FULL-SCALE TESTING AND NUMERICAL MODELING OF A MULTISTORY MASONRY STRUCTURE SUBJECTED TO INTERNAL BLAST LOADING

by

Brian Jarvis Zapata

A dissertation submitted to the faculty of
The University of North Carolina at Charlotte
in partial fulfillment of the requirements
for the degree of Doctor of Philosophy in
Infrastructure and Environmental Systems

Charlotte

2012

Approved by:

_____
Dr. David C. Weggel

_____
Dr. David T. Young

_____
Dr. Janos Gergely

_____
Dr. Howie Fang

_____
Mr. David Thaddeus

ABSTRACT

BRIAN JARVIS ZAPATA. Full-scale testing and numerical modeling of a multistory masonry structure subjected to internal blast loading. (Under the direction of DR. DAVID C. WEGGEL)

As military and diplomatic representatives of the United States are deployed throughout the world, they must frequently make use of local, existing facilities; it is inevitable that some of these will be load bearing unreinforced masonry (URM) structures. Although generally suitable for conventional design loads, load bearing URM presents a unique hazard, with respect to collapse, when exposed to blast loading. There is therefore a need to study the blast resistance of load bearing URM construction in order to better protect US citizens assigned to dangerous locales. To address this, the Department of Civil and Environmental Engineering at the University of North Carolina at Charlotte conducted three blast tests inside a decommissioned, coal-fired, power plant prior to its scheduled demolition. The power plant's walls were constructed of URM and provided an excellent opportunity to study the response of URM walls in-situ.

Post-test analytical studies investigated the ability of existing blast load prediction methodologies to model the case of a cylindrical charge with a low height of burst. It was found that even for the relatively simple blast chamber geometries of these tests, simplified analysis methods predicted blast impulses with an average net error of 22%. The study suggested that existing simplified analysis methods would benefit from additional development to better predict blast loads from cylinders detonated near the ground's surface. A hydrocode, CTH, was also used to perform two and three-

dimensional simulations of the blast events. In order to use the hydrocode, Jones Wilkins Lee (JWL) equation of state (EOS) coefficients were developed for the experiment's Unimax dynamite charges; a novel energy-scaling technique was developed which permits the derivation of new JWL coefficients from an existing coefficient set. The hydrocode simulations were able to simulate blast impulses with an average absolute error of 34.5%. Moreover, the hydrocode simulations provided highly resolved spatio-temporal blast loading data for subsequent structural simulations.

Equivalent single-degree-of-freedom (ESDOF) structural response models were then used to predict the out-of-plane deflections of blast chamber walls. A new resistance function was developed which permits a URM wall to crack at any height; numerical methodologies were also developed to compute transformation factors required for use in the ESDOF method. When combined with the CTH derived blast loading predictions, the ESDOF models were able to predict out-of-plane deflections with reasonable accuracy. Further investigations were performed using finite element models constructed in LS-DYNA; the models used elastic elements combined with contacts possessing a tension/shear cutoff and the ability to simulate fracture energy release. Using the CTH predicted blast loads and carefully selected constitutive parameters, the LS-DYNA models were able to both qualitatively and quantitatively predict blast chamber wall deflections and damage patterns. Moreover, the finite element models suggested several modes of response which cannot be modeled by current ESDOF methods; the effect of these response modes on the accuracy of ESDOF predictions warrants further study.

DEDICATION

To my son, Cole.

ACKNOWLEDGEMENTS

I would like to express my gratitude to my wife, Kristin, to my parents, and to my brother for their patience, encouragement, and support during the long process of completing this work. I would like to thank Dr. David Weggel for his patient guidance and for the many research opportunities he has given me. I would also like to thank Dr. Janos Gergely for the opportunity to work as an undergraduate research assistant, an experience largely responsible for my decision to pursue a graduate degree. Finally, I would like to thank the other members of my committee, Dr. David Young, Dr. Howie Fang, and Mr. David Thaddeus, for their time and assistance.

TABLE OF CONTENTS

LIST OF FIGURES

CHAPTER 1: INTRODUCTION

The last three decades have witnessed a marked increase in the number and severity of terrorist bombings worldwide (US Department of State, 2004). From mosques in Iraq to skyscrapers in New York to resorts in Indonesia, no landmark building can, with certainty, be removed from a list of potential terrorist targets. Given this climate, the current philosophy among security specialists is to recommend that all landmark level facilities and surrounding structures receive, at a minimum, cursory blast and security evaluations. These evaluations may be performed as remedial measures for existing structures or included in the planning of new facilities.

To support these security evaluations, methodologies have been developed to analyze individual structural elements and structural systems subjected to blast loading. Much of this research has focused on masonry, both reinforced and unreinforced, as it is a commonly used construction material throughout the world. In the United States (US), building code wind and seismic lateral force requirements have caused unreinforced masonry (URM) to be typically used as an infill material, rather than as a load bearing structural system. As a result, most research regarding the blast resistance of URM has focused on reducing the hazard presented by collapsing infill panels. Davidson (2008) writes, "most casualties and injuries sustained from terrorist attacks are not caused by the pressure, heat or container fragments resulting from a bomb detonation, but are typically

blunt trauma and penetration injuries caused by the disintegration and fragmentation of walls…" A focus on minimizing damage and injuries caused by debris from collapsing URM infill panels is therefore amply justified.

Outside the US, however, different building codes and the prevalence of old buildings means that URM is frequently used as a load bearing structural system. This practice, combined with the frequency of overseas terrorist bombings creates the need to study the blast resistance of load bearing URM construction. As additional impetus, many older US buildings utilize load bearing masonry as a primary structural system. In order to address this perceived knowledge gap, the Department of Civil and Environmental Engineering at the University of North Carolina at Charlotte conducted three blast tests inside a decommissioned, coal-fired, power plant prior to its scheduled demolition. The power plant's walls were constructed of URM and provided an excellent opportunity to study the response of URM in-situ. Post-test analytical studies were conducted to simulate blast loads and the resulting structural responses of the tested walls. These studies were intended to determine the capability of existing analytical techniques to simulate the performance of load bearing URM. This dissertation will document these experiments and analyses which were funded as part of National Science Foundation Grant CMS-0342103.

The decommissioned power plant was a multistory, steel framed building with unreinforced masonry walls used in both bearing-wall and infill configurations. The choice of an existing structure provided the rare opportunity to study the blast response of a "real" structure, possessing the boundary conditions, geometry, and construction characteristics typical of unreinforced masonry. Although the in-situ test program

created complex conditions for subsequent analyses, this very challenge provided many insights into the simplifications required for engineering-level blast load and structural response predictions. Later chapters will provide a thorough discussion of these approximations and will assess their accuracy.

As is apparent in the preceding paragraphs, the present study encompasses both experimental and analytical work in the fields of explosives, shock physics, and structural engineering. Given the breadth and complexity of this investigation, it was necessary to conduct an extensive literature review of the relevant disciplines. To analyze even a single structural member, a blast analyst must have a basic understanding of explosive compounds, air shocks, structural dynamics, numerical methods, and material and building design codes. As an added complication, the sources from which this information is drawn span over a half-century and are sometimes not released to the public due to security concerns. The following paragraphs will document all sources that could be reasonably obtained, including a handful that are export controlled and/or for official use only. First, literature describing the prior testing of masonry walls will be reported and will include quasi-static, dynamic, and blast tests. Second, literature describing the analysis of masonry walls loaded out-of-plane will be discussed. The discussion will address separate descriptions of simplified and high fidelity computational analyses. And third, a review of blast load prediction methods will conclude the chapter. As with the structural analysis, blast load prediction methods will be divided into simplified and computationally intensive techniques.

1.1. Prior Non-Blast Masonry Testing

Much of what is known about the out-of-plane resistance of masonry is the result of earthquake engineering research. Even by the mid-twentieth century, engineers were still largely unsure how to analyze cracked masonry systems subjected to out-of-plane loads. This was probably a by-product of the allowable stress design (ASD) methodologies dominant at the time. The analysis of "extreme loads" and by association large deformations only became of interest after the development of nuclear weapons. Typical of the ASD method of thinking, studies like that by Yokel and Dikkers (1971) reported the results of 192 tests of masonry walls with an eccentric vertical load. Using simple linear stress/strain distributions, the authors were able to develop interaction curves that conservatively estimated the strength of the load bearing walls. The authors stated "the design of masonry structures is to a large extent empirical and does not rely extensively on the rational application of engineering principals. As a result, even the most advanced masonry design standards fail to fully recognize all the variables and in effect deprive the designer of the insight and flexibility provided by rational analysis."

Many experiments were performed in an effort to provide insight into the complexities of post-elastic behavior. Thomas (1953) showed that the post-elastic (meaning after the formation of flexural tensile cracks) capacity of walls loaded out-of-plane can be significant as a result of arching action. The ultimate load of a masonry infill panel could be two to three times higher than the cracking load and, furthermore, the failure deflection was likely more than a third of the wall thickness, though the study did not positively identify the onset of geometric instability. Hendry (1973) documented a series of 19 tests on masonry infill panels under a variety of boundary conditions to

investigate the effect of axial precompression and number of edges supported. The study showed that for cracked infill panels not restrained against axial motion, increasing axial precompression led to an increased out-of-plane resistance. It should be noted that "strength" and "resistance" are used synonymously.

Dawe and Seah (1989) load tested nine concrete masonry infill panels in order to study the effect of boundary conditions on out-of-plane deflection and resistance. The study found that infill compressive strength, panel dimensions, and frame rigidity have a significant impact on lateral capacity. Hill (1994) documented in-situ tests of three masonry infill walls in a building scheduled for demolition. The panels were built with little to no edge gap (i.e. bounding structural members butted up against panel edges) which resulted in significant out-of-plane strength. Equivalent lateral seismic loads of 1g were attained before the tests were stopped. During the test, Hill noted that members framing the wall panel developed significant deflections as a result of the wall's arching action.

Al-Chaar et al. (1994) performed dynamic tests on masonry infill panels bounded by reinforced concrete frames. After causing cracking using in-plane accelerations (as if it were a shear wall), the infills were rotated 90 degrees and accelerated out-of-plane to study post-crack capacity. In a related test of eight clay and concrete masonry panels, Angel and Uzarski (1996) loaded infill walls out-of-plane quasi-statically after first causing cracking as a result of in-plane shears. They noted that despite having been damaged, the walls were able to resist significant out-of-plane loads as a result of arching effects. Henderson et al. (2003) documented similar findings during an exhaustive research program in which over 700 tests were conducted on infill panels.

Adham (1994) documented a series of 22 tests on both reinforced and unreinforced masonry walls. In the unreinforced test series it was noted that a wall would "crack above its midheight and one course above base. In general, the walls would develop these cracks and respond as two rocking blocks, cycling on the cracks." The tests showed a direct correlation between a cracked URM wall's overburden and its maximum out-of-plane resistance. Unlike Adham (1994) who concluded that peak midheight velocity was of importance in predicting collapse, Griffith et al. (2004) determined that midheight deflection is the determinant of stability. In Griffith's test program, which included quasi-static, harmonic excitation, free vibration, and impulse loads, tests showed that walls did not collapse until their midheight deflection was equal to the wall thickness. Analytically, this failure deflection was described as the point at which midheight wall deflection moved past the line of vertical thrust, leading to geometric instability. This study is probably the best illustration of the full post-elastic range of deflections that unreinforced walls can achieve dynamically. The tests also provided important guidance on the cracked natural frequency of vibration and associated damping ratio which was found to be, at minimum, 5% of critical. The wealth of experimental data from Griffith's tests is unparalleled with regard to the dynamic, out-of-plane behavior of unreinforced masonry.

1.2. Masonry Blast Tests

As a compliment to the in-lab dynamic and quasi-static tests, significant experimentation has been performed on the response of reinforced and unreinforced masonry walls subjected to blast loading. This research, primarily focused on minimizing flying wall debris, has been conducted for over 50 years and traces its

beginnings to nuclear weapons effects studies in the 1950's. In the earliest studies, masonry walls and structures were exposed to the effects of nuclear weapons in order to study their qualitative survivability and the effect on human occupants. (Johnston (1956) and Gabrielsen and Wilton (1972) are well documented examples of the semi-qualitative nature of the early nuclear effects studies). In Gabrielsen and Wilton (1972), the authors report the results of blast tests on axially loaded, unreinforced brick masonry panels under a variety of support conditions. The investigation utilized a shock tube to generate waveforms similar to those expected from a distant nuclear weapon. The study provided details on specimen material parameters, measured blast loads, and measured structural responses. Data collected during studies such as this were eventually incorporated into the original comprehensive Department of Defense (DoD) manual on blast resistance, TM5-1300 (US Army, 1990, originally published in 1969).

Between the end of nuclear survivability studies in the 60's and the mid 90's, little masonry wall testing was performed and even less made public. Moradi (2008) provides a good narrative of the blast testing performed in the 90's which although not always specific to masonry, provides insight into programmatic motivations and the development of analytical techniques. Beginning in 1994, the United States and Israel began cooperatively researching blast retrofit techniques using Israeli test facilities (it can only be inferred based on timing that the programs were spurred by the 1992 bombing of the Israeli Embassy in Buenos Aires, Argentina, and the 1993 bombing of the World Trade Center in New York). Immediately following the April 1995 bombing of the Murrah Federal Building in Oklahoma City, the US began an intensive blast mitigation research program on home soil.

In September 1995 a large reinforced concrete building was blast tested at Eglin Air Force Base (AFB) in order to evaluate composite retrofits. This test was the first to receive pre-test predictions from LS-DYNA finite element models. Taun et al. (1995) found that the results of the finite element models were not accurate, due to lack of an adequate constitutive model for concrete. In 1996, the Israeli test program continued with blast tests on a retrofitted concrete masonry bearing-wall structure (simulated by using post-tensioned steel bars on a single story masonry panel). In comparing pre-test predictions made with SDOF, semi-empirical, and finite element models, Whiting and Coltharp (1996) concluded that the "finite element code is the most accurate means of damage prediction for complex masonry cross sections." Moradi (2008) goes on to state that beginning in 1999, the focus on masonry wall research then shifted to protecting common exterior (infill) walls by means of composite retrofit rather than more traditional techniques such as adding mass with reinforced concrete cladding.

Dennis et al. (2002) documents static and blast tests on unreinforced concrete masonry infill panels; the purpose of the test program was to assess the ability of existing finite element models to correctly predict the failure of unreinforced concrete masonry. The study concluded that while there were often significant differences between analysis and experiment as a result of material variability, the analyses tended to provide conservative results. This work served as the foundation for many subsequent studies of masonry retrofit techniques. Davidson et al. (2004), Davidson et al. (2005), and Baylot et al. (2005b) document experimental and analytical programs in which composite materials were used to retrofit unreinforced masonry against blast. The result of all this research was the development of resistance functions capable of allowing design engineers to

quickly calculate blast induced wall deflections before and after a retrofit. It should be noted that for all of the literature discussed in this section, masonry walls are merely considered a cladding element used to protect building occupants. Studies are primarily concerned with wall collapse and subsequent debris intrusion rather than the structural stability of load bearing masonry.

Wesevich et al. (2002) is the DoD's comprehensive database of all masonry testing performed to date, however could not be obtained for review. Aside from DoD sources, one of the few masonry blast testing studies available in the literature is that of Varma et al. (1997). The experiments blast loaded 27 wall panels in order to investigate the effect of boundary conditions and to develop a correlation between qualitative damage levels and the reflected impulse. The study found that the impulse required to cause wall collapse is almost linearly proportional to the wall thickness.

One alternative to performing experimental investigations of masonry is the study of terrorist bombings or accidental explosions (Hinman and Hammond 1997). In these forensic investigations, the TNT equivalence and pressure loads are difficult to determine with precision, and damage can be too severe to permit a full understanding of the specific events that occurred and their sequence. Nonetheless, studying the behavior of full-scale structures subjected to blast loads provides information that controlled laboratory experiments often cannot. The experimental program of this dissertation therefore provides a unique opportunity to examine, with a higher degree of accuracy, the behavior of a masonry bearing wall building that was formerly in service (i.e. a non-purpose-built structure) and to make comparisons to the results from nonlinear dynamic analyses.

1.3. Single-Degree-of-Freedom Structural Analysis

Engineers tasked with analyzing the response of complex systems subjected to dynamic loading frequently rely on techniques that reduce analytical complexity, yielding more tractable problems. This is often done by idealizing structural members or even entire structures as a single-degree-of-freedom (SDOF) system. This one-dimensional idealization translates the distributed mass and stiffness of a real structure into a representative point mass, having a single stiffness and capable of deflection in only one spatial direction (Tedesco et al., 1999). A mass attached to a spring is an example of an SDOF system (see Figure 1.1). Such one-dimensional systems have the advantage that their solutions are relatively simple and can be computed even for systems with significant nonlinearities. Biggs (1964) makes the point that such solution techniques are more than adequate for the vast majority of problems as uncertainties in the loading or material properties render even rigorous closed formed solutions somewhat approximate as well.

The transient motion of a single-degree of freedom system is governed by the equation of motion (EOM) given by

$$m\ddot{x} + c\dot{x} + kx = F(t) \tag{1.1}$$

where m is the effective mass of the system, c is the effective viscous damping constant, k is the effective spring constant, and $F(t)$ is the effective forcing function (dynamic loading). The term "effective" is applied to the system's parameters because Eq (1.1) abstracts the system as being a single point in space. This is in contrast to reality, where most dynamic systems possess distributed mass and stiffness. Consider, for example, a beam spanning between two supports in which the mass, stiffness, and applied forces are

distributed spatially in at least one dimension. Some sort of transformation is then necessary to convert systems with distributed parameters into equivalent lumped parameter models.

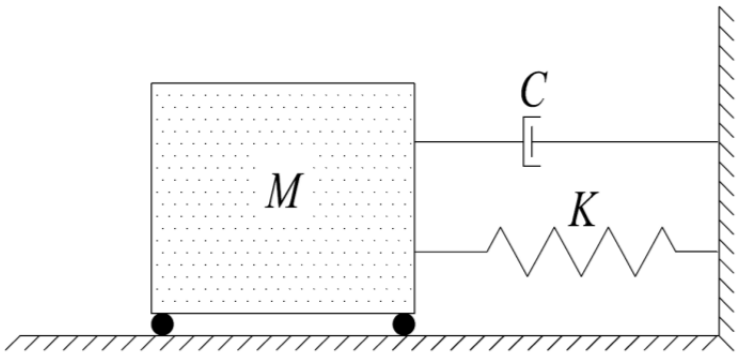

FIGURE 1.1: Typical single degree of freedom system with damping.

One such transformation technique widely used in the physical security community is known as the "equivalent SDOF" (ESDOF) method, which replaced an older technique referred to as the "modal SDOF method" (Morrison, 2006). The ESDOF method was first introduced in 1957 in USACE Engineer Manual EM 1110-345-415. The method is based on using transformation factors to make the kinetic and internal energy of the SDOF system equal to that of the real system. Due to its wide adoption in the physical security community, the ESDOF method is used in this investigation for all SDOF computations. The ESDOF methods from this manual (which is out of print) are conveniently summarized in Biggs (1964). In his text, Biggs rewrites the equation of motion given by Eq. (1.1) as

$$K_M m\ddot{x} + K_L c\dot{x} + K_L kx = K_L F(t) \tag{1.2}$$

The *K* factors in front of each term of the EOM are constants that transform a distributed (real) system into an idealized discrete system. As an additional simplification, Eq. (1.2) can be divided by the term K_L to yield Eq. (1.3), where $K_{LM} = K_M/K_L$.

$$K_{LM}m\ddot{x} + c\dot{x} + kx = F(t) \tag{1.3}$$

The *K* factors in Eq. (1.2) are computed as shown in Eq. (1.4) and Eq. (1.5) for a one-dimensional structure (i.e. a beam or one-way slab).

$$K_M = \frac{\int_0^L m(x)\varphi^2(x)dx}{\int_0^L m(x)dx} \tag{1.4}$$

$$K_L = \frac{\int_0^L p(x)\varphi(x)dx}{\int_0^L p(x)dx} \tag{1.5}$$

In Eq. (1.4) and Eq. (1.5), *m(x)* is the mass at location *x*, *L* is the span length, *p(x)* is the applied load, and $\varphi(x)$ represents the normalized deflected shape of the structure. These transformation factors may be generalized to two-dimensional structures (i.e. a two-way slab) by replacing the single integral with a double integral over the two spatial dimensions.

The ESDOF method is based on an assumed deformed shape of the structure. Therefore, if the structure transitions from elastic to plastic behavior through yield or cracking (thus changing the deflection function, $\varphi(x)$) a different K_{LM} factor must be employed in each phase of the response in order for the analysis to be correct. As an example, consider a vertically spanning masonry wall which cracks at midheight under the action of a uniformly distributed lateral load. Figure 1.2 illustrates the deflected shape during the elastic part of the response (at left) and then after a crack forms at mid-height (at right).

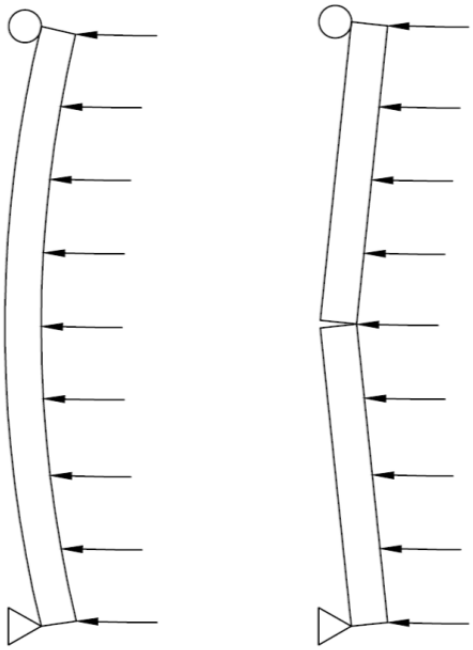

FIGURE 1.2: Simply-supported URM wall deflected shape before (at left) and after (at right) crack forms at midheight.

For this particular scenario, the deflection function $\varphi(x)$ is represented by Eq. (1.6) for the elastic wall and Eqs. (1.7) for the wall after the midheight crack forms.

$$\varphi(x) = \frac{16}{5L^4}(L^3x - 2Lx^3 + x^4) \tag{1.6}$$

$$\varphi(x) = \frac{2x}{L} \qquad for \quad x \leq \frac{L}{2} \tag{1.7a}$$

$$\varphi(x) = \frac{2x}{L} - \frac{4}{L}(x - \frac{L}{2}) \qquad for \quad x > \frac{L}{2} \tag{1.7b}$$

In these equations, L is the height of the wall and x is the vertical coordinate, measured starting from either the top or bottom. Assuming that both the mass per unit length and the lateral load are uniform and have a unit value (the load and mass values do not affect the results for the case of a uniform distribution), combining Eq. (1.6) with Eq. (1.4) and Eq. (1.5) yields Eq. (1.8) which gives the mass transformation factor and Eq. (1.9) which

gives the load transformation factor for the elastic shape. This yields an elastic K_{LM} of 0.50/0.64 = 0.78.

$$K_M = \frac{1}{L}\int_0^L \left[\frac{16}{5L^4}(L^3x - 2Lx^3 + x^4)\right]^2 dx = \frac{1}{2} \tag{1.8}$$

$$K_L = \frac{1}{L}\int_0^L \frac{16}{5L^4}(L^3x - 2Lx^3 + x^4)dx = \frac{16}{25} \tag{1.9}$$

Again, assuming both a uniformly distributed mass and loading with a unit value, combining Eqs. (1.7) with Eq. (1.4) and Eq. (1.5) yields Eq. (1.10) which gives the mass factor and Eq. (1.11) which gives the load factor for the post-elastic wall. This yields a post-elastic K_{LM} of 0.33/0.50 = 0.66.

$$K_M = \frac{1}{L}\left[\int_0^{L/2}\left(\frac{2x}{L}\right)^2 dx + \int_{L/2}^{L}\left[\frac{2x}{L} - \frac{4}{L}\left(x - \frac{L}{2}\right)\right]^2 dx\right] = \frac{1}{3} \tag{1.10}$$

$$K_L = \frac{1}{L}\left[\int_0^{L/2}\frac{2x}{L}dx + \int_{L/2}^{L}\frac{2x}{L} - \frac{4}{L}\left(x - \frac{L}{2}\right)dx\right] = \frac{1}{2} \tag{1.11}$$

Having transformed a real system into an ESDOF system, it is then usually necessary to solve the EOM using numerical methods. Bigg's (1964) solution method has been widely adopted in the physical security community due to its relative simplicity. In his text he details a method called the constant velocity method, so named because the computation of deflection increments between two time steps assumes a constant velocity. Eqs. (1.12) through (1.19) show the steps required for Bigg's numerical solution. As reproduced here, they have been adapted for the case of a system initially at rest and loaded by a time varying function that starts at time *t=0*. In the equations, subscripts denote time increment. For example, U_0 is the deflection at time zero and U_{t+1} is the deflection at time *t +1* (i.e. the next iterative step).

$$A_0 = \frac{F_0}{m} \tag{1.12}$$

$$V_0 = 0 \tag{1.13}$$

$$U_0 = 0 \tag{1.14}$$

$$U_1 = \frac{A_0 \Delta t^2}{2} \tag{1.15}$$

$$V_1 = \frac{U_1}{\Delta t} \tag{1.16}$$

$$A_t = \frac{F_t - k(U_t)U_t - c(k)V_{t-1}}{m} \tag{1.17}$$

$$U_{t+1} = 2U_t - U_{t-1} + A_t(\Delta t)^2 \tag{1.18}$$

$$V_t = \frac{U_{t+1} - U_t}{\Delta t} \tag{1.19}$$

In the equations, A is acceleration, V is velocity, and U is the deflection. F is the force, m is the mass premultiplied by the K_{LM} factor, k is the stiffness at the current deflection (assumed to be a nonlinear function of deflection), c is the current viscous damping (the dependence of c on k is not in Bigg's original formulation), and Δt is the time step size. The numerical solution is started using the assumptions embedded in Eqs. (1.12) through (1.14). Eqs. (1.15) and (1.16) compute the first increment of deflection and velocity using the simplifying assumption that acceleration is constant over the first time step. Using these first estimates of deflection and velocity, a loop is entered in which Eqs. (1.17) through (1.19) are repeated to update the system's configuration at each time step. Biggs states that the solution yielded by this procedure approaches the analytical solution as the time step is decreased. A more thorough discussion of nonlinear damping will follow in Chapter 6 as post-elastic damping requires careful consideration.

1.4. Resistance Functions for SDOF Models

One crucial input necessary for an SDOF model of URM walls loaded out-of-plane, is the nonlinear force versus mid-height deflection relationship, hereafter called the resistance function ($k(U_t)$ in Eq. (1.17)). The research performed to date to generate resistance functions can be separated into three groups, largely based on who performed the work. The first group consists of scattered efforts among a number of laboratories independently working on masonry and/or seismic performance research. The second group consists of a New Zealand research center with an emphasis on the earthquake resistance of masonry walls loaded out-of-plane. The third and most important group is the DoD. The following paragraphs will describe the existing state-of-the-art, categorized according to these groupings and presented in the order in which they are listed above.

The out-of-plane resistance of cracked URM walls is entirely attributable to the action of in-plane forces; these forces can be generated by a wall's contact with bounding members or its self weight. McDowell et al. (1956) presents one of the first attempts to provide a theoretical framework for why cracked URM walls are able to resist large out-of-plane loads. The investigation correctly identified that in-plane forces created by rigid boundary conditions are the principal cause of out-of-plane resistance. This departure from conventional thinking was then extended in a number of studies. Abrams et al. (1996) studied the interaction of arching masonry infill panels with reinforced concrete boundary members. Flanagan and Bennet (1999) performed a review of available arching formulations and compared them to out-of-plane test data. These three studies were primarily focused on the maximum quasi-static load; the post-peak softening

behavior of the walls was of little consequence. During a study on the effect of the flexibility of bounding steel members on out-of-plane resistance Dawe and Seah (1989) observed that after the maximum load was attained, the walls would gradually lose strength until their eventual collapse. In their tests, the walls deflected to more than 50% of the wall thickness. They did not, however, extend their resistance function beyond the peak resistance of the wall panels.

An important advance in resistance function development occurred when Gabrielsen and Wilton (1972) developed resistance functions for vertically preloaded URM panels. This new formulation did not rely on rigid bounding members to generate in-plane forces. Rather, any axial load carried by a masonry panel could provide out-of-plane resistance. Equally as important, the report was concerned with high amplitude dynamic response and therefore the full form of the resistance function (i.e. failure deflection) was required. Using simple statics (their model is shown in Figure 1.3) the researchers identified the point of wall failure as being a lateral deflection equal to the wall's thickness. This corresponds to the point where the midheight of the wall has displaced laterally beyond the line of action of vertical forces.

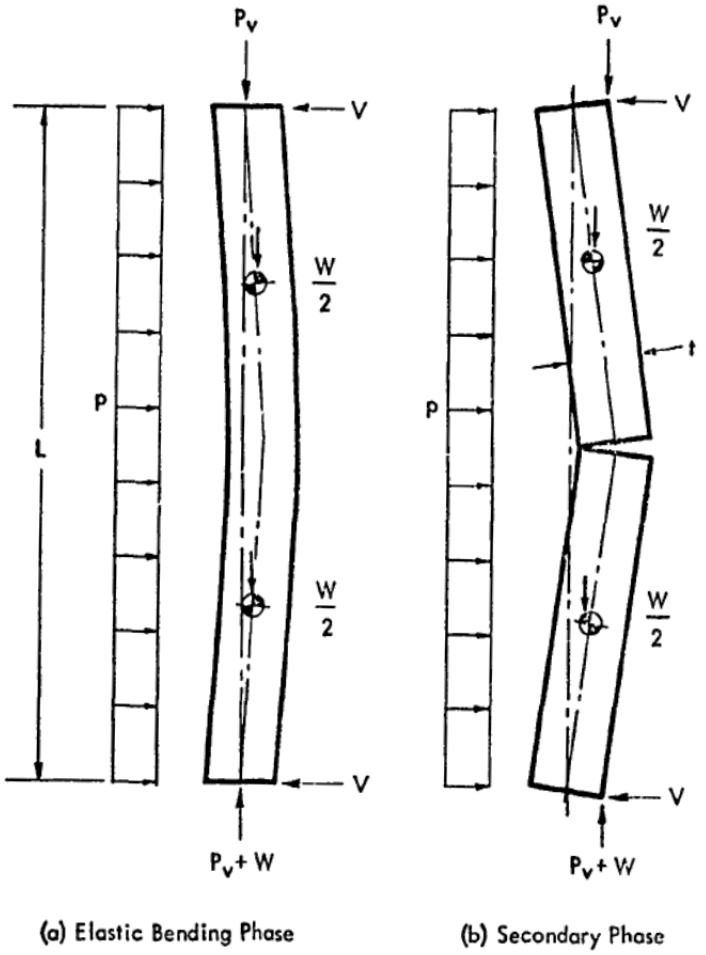

FIGURE 1.3: Simple statics formulation for the lateral resistance of a vertically preloaded masonry wall (Gabrielsen and Wilton, 1972).

Priestley (1985) also investigated resistance functions of this form and came to similar conclusions. A follow-up paper by Priestley and Robinson (1986) discussed Priestley's out-of-plane models and made several corrections to the formulation. Errors aside, the paper essentially validated many of Priestley's ideas. The notable difference between Priestley and Gabrielsen and Wilton is that they assumed different locations of the line of vertical force. For example, Priestly located his line of vertical force using something similar to the principles of reinforced concrete while Gabrielsen and Wilton simply assumed it was located at the extreme tension face. The resistance functions

developed by Gabrielsen, Wilton, and Priestly can be essentially described as bi-linear; resistance increases from zero to the maximum resistance which occurs at a deflection only a few percent of wall thickness. Resistance then decreases linearly to zero which occurs at the failure deflection.

Building on the work of Gabrielsen, Wilton, and Priestley, a group of researchers in New Zealand engaged in an extensive investigation of the post-elastic, out-of-plane response of URM walls. Their research was motivated by the observation that URM walls could deflect significantly beyond the deflection corresponding to peak resistance. Thus a dynamic analysis using deflection as the failure criterion was a more accurate measure of a wall's likelihood of collapse than the ratio of applied load to maximum resistance. The ability to model this in an analysis would enable design engineers to more accurately assess the seismic stability of existing URM structures, potentially reducing the cost of structural retrofits (an important accomplishment in earthquake prone New Zealand). The testing component of the program is thoroughly described in Griffith (2004). Using this wealth of experimental data, the researchers authored at least three papers describing their analytical approach. Doherty et al. (2002), Lam et al. (2003), and Derakhshan et al. (2009) document the development of a resistance function and explain the translation of a real system into an ESDOF system for dynamic analysis. Another important distinction between prior efforts and those of the New Zealanders was that they idealized the resistance function as being tri-linear to account for softening at cracks. Their cyclic test data supports this model which is best applied to seismic loading.

While all of this information can be adapted to blast loaded masonry, only the work produced by the DoD is specifically intended for blast analysis. Two organizations have lead roles in blast mitigation: the United States Army Corps of Engineers (USACE) provides engineering design guidance while the Air Force Research Laboratory (AFRL) performs in-depth research and development on retrofit techniques and high fidelity modeling. USACE has traditionally been the lead engineering agency for civil works; however the Air Force has unique testing facilities at Eglin and Tyndal Air Force Bases in Florida, and the AFRL is therefore intimately involved in blast mitigation research.

Building on the test data reviewed in the prior section and the simple models of Gabrielsen and Wilton (1972), AFRL and USACE have developed extensive analytical tools for the design and analysis of structures subjected to blast. Moradi et al. (2009), Moradi (2008), USACE (2008a), and USACE (2008b) document the results of research directed at developing resistance functions for masonry walls loaded out-of-plane. The resistance functions can simulate unreinforced, reinforced, and retrofitted masonry under the action of out-of-plane blast loads. In order to effectively utilize these models in design, USACE integrated these resistance functions with a nonlinear SDOF analysis tool, implemented in an Excel Spreadsheet that utilizes Biggs's constant velocity method. The program, SDOF Blast Effects Design Spreadsheet, or SBEDS, (USACE, 2008c) is one of USACE's primary tools and is regularly updated as new resistance functions are developed. Sunshine et al. (2004) provides an overview of existing DoD analysis techniques and software.

1.5. Finite Element Structural Analysis

It is usually feasible to formulate analytical models of one-way spanning URM walls loaded out-of-plane. Developing similar models for walls with complex boundary conditions or unique geometries, on the other hand, becomes more difficult. As documented in Dawe and Seah (1989), yield line theory can be applied to such problems; however it is not always accurate, particularly if the crack pattern is not correctly assumed or known a priori. Because blast tests are expensive, many researchers have sought to develop finite element models of masonry to help design better experiments and retrofits and to fill in gaps in the experimental data. There has, therefore, been significant effort invested in the development of finite element models capable of simulating the elastic and post-elastic response of masonry walls loaded out-of-plane.

One modeling approach has been to develop constitutive relations for continuum elements that are capable of simulating the behavior of masonry assemblages. Unfortunately, due to the limitations of finite element codes (deformation limits), these methods usually cannot simulate the full range of possible nonlinear deformations. Cecchi et al. (2005) documented what they term "homogenization techniques" which are used to take what is an inhomogeneous material and render a handful of constitutive parameters for use in elastic finite element models. Others like Lourenco (2000) took this idea one step further and implemented nonlinear constitutive models that could account for crushing and cracking, however are not able to simulate deflections on the order of wall thickness. This is evidenced in studies like that of Ettouney et al. (2003) in which the analytical models were only able to predict deflections of a few tenths of an inch. Ettouney et al. used the concrete element built into the commercial finite element

code ANSYS (Canonsburg, PA). From the author's experience, continuum elements are unable to simulate deformations of the magnitude that are necessary to simulate the deflections of cracked URM.

Lofti and Shing (1994) realized that traditional continuum approaches would not be capable of modeling the full spectrum of nonlinear behaviors in cracked masonry. Their investigation developed constitutive models for masonry and mortar interface elements and integrated them into a custom finite element software to simulate cracked masonry loaded in-plane. Gilbert et al. (1998) took this idea one step further and modified the interface formulation to permit rate effects and a more accurate treatment of the energy release at fractured interfaces. They believed this was necessary to more closely match experimental predictions of interface deflection. Martini (1996a, 1996b) utilized an existing finite element software, ABAQUS (Simulia, Providence, RI) to simulate post-elastic response. In his first 1996 study, Martini modeled brick masonry with each brick comprised of linear and elastic continuum elements connected by contact elements. This permitted large mesh deformations without encountering many of the severe numerical issues normally associated with such simulations. In his study, the simulations were able to reproduce resistance functions of the type developed by Gabrielsen and Wilton (1972). This modeling technique was so successful that it was adopted by nearly every other finite element study of cracking masonry thereafter.

Gilbert et al. (2001) and Burnett et al. (2007) reported on finite element simulations of brick masonry walls and parapets subjected to low velocity vehicle impacts. The researchers used the finite element software LS-DYNA (Livermore, CA) utilizing both contact elements and elastic constitutive models. Material and contact

parameters were derived from an experimental program designed to quantify the dynamic shear and tensile behavior of masonry bonds (Molyneaux, 2002). The studies were able to simulate the large wall deflections observed in empirical data.

AFRL has performed some of the most important research on the use of finite element models to simulate URM. Davidson and Sudame (2006) document experimental and analytical work performed in order to develop an LS-DYNA model of unreinforced concrete masonry walls reinforced with polymer composites. The in-depth investigation examined numerous model parameters including constitutive models, boundary conditions, mesh resolution, damping, material failure, interface elements, and gravity preloading. Moradi (2008) subsequently utilized this model to simulate retrofitted masonry walls exposed to blast loads. The simulations were found to correlate well with experimental data, suggesting the model parameters developed in Davidson and Sudame (2006) might be a good starting point for modeling brick masonry. Davidson (2008) provides a compact overview of the AFRL research program, including directions for further research. In the report, the only recommendation pertaining to modeling masonry is a better understanding of the behavior of masonry at locations where arching causes crushing.

1.6. Empirically Derived Blast Load Predictions

In order to use the preceding structural analysis methods, it is first necessary to estimate the dynamic loads imposed on a structure by high explosive detonations. At the most basic level, an airblast analysis is interested in the computation of airblast pressures and impulses. To accomplish this there are usually two available methods – simplified and computational. Simplified methods are almost always based on extensive empirical

data and can be quite accurate when the analysis is similar to the test scenarios. When an unusual geometry (explosive shape or reflecting surface) or untested explosive compounds are used, it is usually necessary to perform in depth computational analyses which will be discussed in Section 1.7. This section will examine the existing body of experimental data and its translation into simplified (so called engineering-level) guidance.

There are three references (which are inter-related) considered essential to blast designers. The first, TM5-1300 (US Army, 1990) was the original handbook of blast design incorporating simple equations and nomographs which permitted engineers to compute blast loads and the resulting structural responses. This document was then replaced by TM5-855 (US Army, 1998) which provided similar, but updated analytical tools. Both of these documents were superseded by UFC-3-340-01 (USACE, 2002) which is the definitive guidance on blast load prediction for military structures. The document contains a wealth of tabulated blast parameters, both in nomograph and equation forms, which can be used to compute virtually any blast wave parameter of interest ("parameter" in the context of a blast wave refers to pressure, impulse, time of arrival, duration, velocity, etc…).

Figure 1.5 is an example of a typical nomograph for the computation of incident pressure like those found in UFC 3-340-01. In order to use the chart, the user first computes a quantity called the scaled distance (z), which is equal to the radial distance of the target point from the charge's center of mass divided by the charge mass raised to the one third power. Knowing the z value (the chart's x-ordinate), the user then reads the y-ordinate to obtain the overpressure ratio, which is simply the ratio of the blast

overpressure divided by standard atmospheric pressure (101.3 kPa (14.69 psi) for virtually all DoD sources). As an example, using a chemical explosive (TNT in this case) and a *z* value of 1.0, the overpressure ratio is approximately 12. If atmospheric pressure is 101.3 kPa (14.69 psi), then this would correspond to a blast overpressure of 1215 kPa (176.4 psi). There are similar charts that use scaled distance to find most other blast wave parameters of interest such as time of arrival, impulse, positive phase duration, etc.

Also note that scaled distance permits a comparison of two charges. For example, one kilogram at one meter (z=1) produces the same overpressure as 10 kilograms at 2.15 meters (z=1). This cube root scaling, known as Hopkinson Cranz scaling, therefore says that two charges of the same geometry and composition but different weight will produce self-similar blast waves at identical scaled distances. In charts like Figure 1.4, all masses are usually expressed in terms of TNT, the most thoroughly characterized explosive. In order to use the chart with a different explosive compound, equivalency factors are used which convert the mass of an explosive compound into an equivalent mass of TNT; for example, 1 kg of ANFO is equivalent to 0.82 kg of TNT.

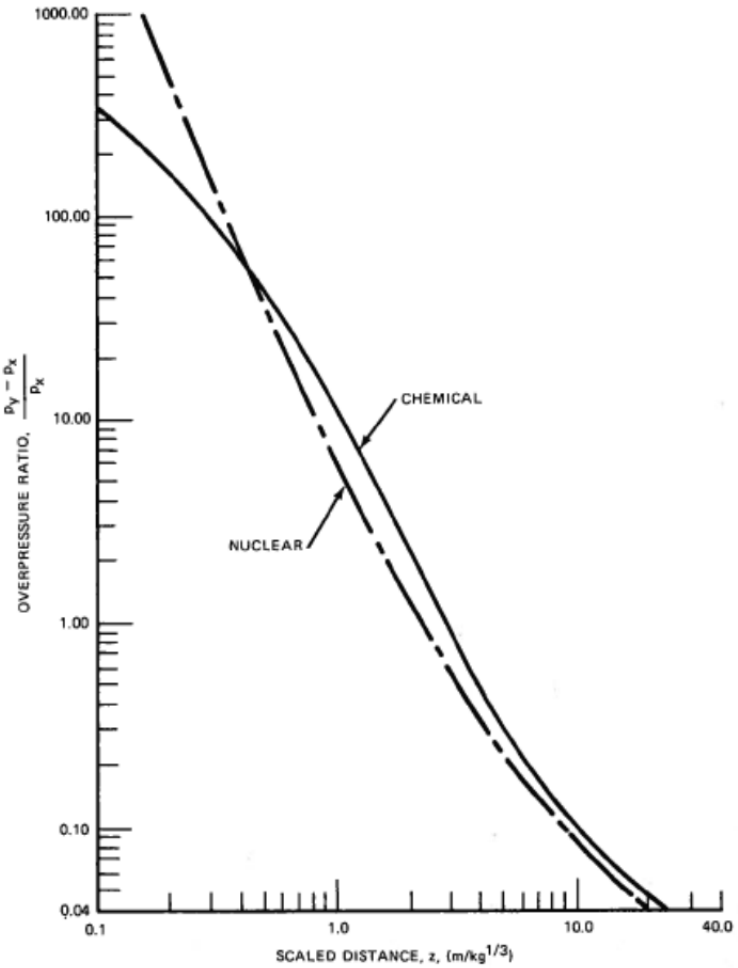

FIGURE 1.4: Example nomograph showing scaled distance versus incident overpressure ratio for nuclear and chemical (TNT) explosions in air from a spherical point source. Note that the nuclear overpressure has been normalized to 1 kg TNT equivalence to qualitatively compare blast parameters (from Kinney and Graham, 1985).

As a companion to the military handbooks and a substitute for nomographs and equations, USACE released two software programs, ConWep (2005) and BlastX (2006), which utilize the data contained in these DoD manuals to enable rapid computation of shockwave (blast) parameters. ConWep was written to predict pressures and impulses created on reflecting surfaces by conventional weapons such as bare high explosive (HE) or common ordnance like a 500 lb bomb. BlastX was written to predict the pressures and

impulses created by confined explosions, using a ray tracing algorithm to compute the multiple reflections encountered in blast environments in enclosed structures.

These DoD blast documents and the associated software are not summaries of single research programs, but instead are aggregations of the best empirical data gathered from several studies to date. Many of the studies from which the data were obtained are not public domain or can no longer be readily acquired. Furthermore, these documents do not always specify from what source data are derived. It is known though, that much of the airblast data for TNT comes from Kingery and Bulmash (1984), a limited distribution document. Other sources like Kinney and Graham (1985) provide similar data, but are not considered the reference standard for airblast design. Bogosian et al. (2002) provide a comprehensive comparison between the Kingery-Bulmash equations and a wide array of other available blast test data. Their study showed that the Kingery-Bulmash data provides an excellent curve fit to other available test data and that ConWep exactly reproduces predictions provided by the Kingery-Bulmash equations.

Although the Kingery and Bulmash report could not be obtained, there were several documents available that illustrate how data was collected for the DoD manuals. Stoner and Bleakney (1948) document the results of 56 airblasts designed to quantify the maximum overpressure versus scaled distance for several charge compositions and geometries. The study demonstrated a novel method of measuring overpressure using shockwave velocity that eliminated the need for piezoelectric pressure gages, considered inaccurate at the time. Kinney and Graham (1985) describe a similar method of overpressure measurement which uses the relation between shockwave Mach number and overpressure ratio. Philipchuk (1955) documented 210 blast tests using seven different

types of explosives in three different configurations (uncased, cased in steel, cased in aluminum). The study found that charges cased in steel jackets yielded the highest pressures and therefore the most damage. The experiments also determined the relative power of each of the seven explosive compounds tested. Tancreto (1975) describes work performed in developing the blast cubicle charts for TM5-1300. Specifically, the 1975 study determined the TNT equivalence of RDX and Comp-B cyclinders to be used in subsequent blast tests. This was done as a result of difficulties experienced in performing the tests with cast TNT (poor detonation performance). Esparza (1986) describes experiments in which spheres of six different explosives were detonated to measure the resulting blast wave parameters. Specifically, the study was interested in the pressures and impulses at small scaled distances due to known deficiencies in the TM5-1300 data at the time. Esparza also provides a helpful narrative regarding how blast data was gathered from multiple sources to form TM5-1300.

Aside from the major DoD manuals (TM5-1300, TM5-855, and UFC 3-340-01), there are quite a few other sources that provide summaries of blast test results, provide simplified analysis techniques, or both. Cooper (1996) and Kinney and Graham (1985) are two excellent general textbooks that provide all of the fundamentals necessary to understand and analyze blast loads. Beshara (1994a and 1994b) are typical examples of generalized review papers. The author covers equivalency, scaling, and provides simple equations for the computation of pressure and impulse. Olatidoye et al. (1998) and Remennikov et al. (2007) are similar in nature, providing only the most general guidance and a qualitative description of blast phenomena.

Advanced computational techniques have permitted the creation of a new type of simplified guidance. Wu and Hoa (2005) used numerical models to create simplified design guidance for analyzing structures subjected to combined air blast and ground shock loads. Rose et al. (1997) used computer simulations to study the interaction of blast waves with a protective barrier wall. The authors provided guidance on the pressure and impulse reductions which could be expected based on wall and site geometries.

The vast majority of simplified blast load prediction techniques assume that the explosive charge is spherical or hemispherical. Guerke and Cheklinski-Glueck (1982) state that for certain cases this assumption can cause errors of a factor of 2 or more. In many instances, however, this is an acceptable approximation because at large standoff distances the shape effect is often small. Esparza (1992) found that for scaled distances greater than 4.0 $m/kg^{1/3}$ (10 $ft/lb^{1/3}$), the shape of the charge had minimal effect on blast overpressure while at a scaled distance of 1.2 $m/kg^{1/3}$ (3 $ft/lb^{1/3}$) this could cause an error of 300% or more. Therefore, when the reflecting surface is relatively close to the explosive charge it is critical to consider shape effects in the computation of blast loads. This is particularly true of cylindrical charges because much more of the explosive energy flows outward radially from the cylinder wall than from the top and bottom. Figure 1.5 shows computer simulations of the pressure produced by a hemisphere (at left) and a cylinder (at right) of TNT detonated on the ground's surface. The simulations show the axisymmetric simulation domain with the center of the charge (and axis of symmetry) at the left-hand vertical edge of each image. High pressure is contoured in white while lower ambient pressures are black. As is visible, the hemisphere produces a

uniform distribution of pressure while the cylinder's pressure distribution is highly non-uniform.

Despite the difficulties in providing simplified guidance for cylindrical charge effects, several researchers have made attempts. Ismail and Murray (1992) performed experiments in order to determine fitting parameters to permit use of the modified Friedlander equation with cylindrical charges (this equation computes blast overpressure as a function of time at a fixed point). Their experiments showed that, due to the non-uniform distribution of blast energy, traditional scaling methodologies do not work well in close proximity to the charge (scaled distances less than 0.8 $kg/m^{1/3}$).

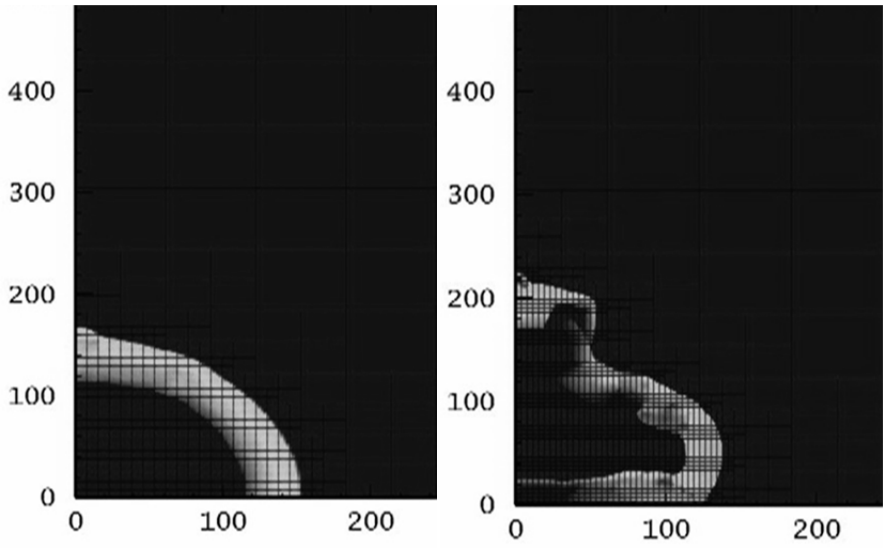

FIGURE 1.5: Pressure distribution in two spatial dimensions through the centerline of an axially symmetric CTH simulation showing qualitative difference in energy distribution between a hemispherical (at left) and cylindrical (at right) surface burst.

Guerke and Checklinski-Glueck (1982) document an experimental program in which cylindrical charges were detonated near the ground's surface at a range of angles relative to the vertical. The research was designed to aid in the construction of

nomographs for cylindrical charges. The researchers found that charge orientation and length to diameter ratio could significantly affect blast pressures and impulses. UFC 3-340-01 (USACE, 2002) provides nomographs similar to Figure 1.4 for cylindrical charges with several different charge length to diameter ratios. Held (1998) and Held (2001) made use of non-electronic measurement devices to study the distribution of blast momentum (and energy) around a cylindrical charge. Qualitatively, the experiments found a distribution of blast energy similar to that presented in UFC 3-340-01. Esparza (2002) provides one of the simplest and most readily applicable methods of predicting the airblast from cylindrical charges. In his study, Esparza provides nomographs that detail a spherical equivalency factor based on charge aspect ratio, scaled distance, and azimuth angle. The spherical equivalency factor is multiplied by the cylindrical charge weight to arrive at an equivalent spherical charge weight for which predictions can be readily made using ConWep.

1.7. Computational Blast Load Predictions

It is preferable to use simple, empirically-derived blast load prediction techniques when possible. However, due to the charge geometry and explosive composition used in this investigation, more advanced analytical methods were required. An advanced computational tool called CTH (McGlaun et al. 1990) was investigated for its ability to model the blast loads generated by the cylindrical dynamite charges of this investigation. CTH is a shock physics hydrocode that was specifically designed to model multi-dimensional, multi-material, large deformation and shock wave physics problems in one, two, and three-dimensional domains with several symmetry options for one and two-dimensional analyses. CTH has a variety of material models which can simulate dynamic

phenomena including fracture, yielding and plasticity, and of particular importance to this work, high explosive detonation.

CTH utilizes the Jones-Wilkins-Lee equation of state (hereafter called the JWL EOS) to describe the expansion of explosive material from the time at which detonation is complete to the final state at which detonation product gases have expanded to ambient pressures. A more thorough discussion of the JWL EOS will follow in Chapter 5, however for now it is sufficient to know that it describes the pressure, energy, and density of detonation products as they expand from a highly compressed state. Lee et al. (1968) describe the development and calibration of the JWL EOS, Souers (2005) describes its common implementation in computer software, and Souers et al. (1996) discuss some methods used to develop JWL parameters.

The need to employ computational methods (instead of engineering-level methods) is not an uncommon situation. There are a number of published studies that necessitated advanced simulations because of reflecting surface geometry, charge composition, or charge geometry. Wilke (2004) documents an experimental and analytical program at Los Alamos National Laboratory which studied the performance of blast relief panels in a decommissioned explosive processing facility. The study used AUTODYN (ANSYS Inc, Canonsburg PA) to perform a fully coupled hydrodynamic/structural simulation to model the confined explosion and resulting failure of structural elements. Lind et al. (1998) documents simulations of an explosives demolition chamber. The study utilized the software FAST3D (publisher unknown) to simulate the blast loading associated with operation of an ordnance destruction facility.

Marconi (1994) describes a numerical study conducted in order to examine the shock loading created by internal explosions. The study found that during shockwave interaction a specific kind of instability develops which further complicates the blast analysis, particularly in the case of a large charge inside a small blast chamber. Chan and Klein (1994) also studied the complex dynamics of internal explosions. The study included subjecting livestock to an enclosed blast environment and was intended to better understand the lethality of armor penetrating explosive rounds. In the experiments, 1 lb of C4 created more than a dozen identifiable reflected blast waves inside the blast chamber. Their numerical simulations were able to approximate the many reflections recorded during the experiment.

Brundage et al. (2007) investigated the ability of CTH to simulate the pressure time history created by a confined explosion. The software was found to be in excellent agreement with experimental results. The researchers then performed a one-way coupling with a finite element program and were able to accurately simulate the response of a thin walled vessel subjected to an internal blast. Zhang et al. (2007) also used CTH to simulate the response of vehicle underbody panels to the blast created by buried mines. Again, CTH was able to accurately simulate the loading created by the explosive device. The pressure time histories were one-way coupled to LS-DYNA (LSTC, Livermore, CA) to simulate vehicle underbody response and the ensuing effect on vehicle occupants.

Some of the more interesting computational work has focused on using numerical methods to study the blast loading on entire structures or even whole city blocks. Armstrong et al. (2002) studied the ability of the software SHAMRC (Applied Research Associates, Albuquerque, NM) to model blast loading on a rectangular building with and

without a protective blast wall. The software was found to be in agreement with experimental data derived from blast tests on scaled models. Ozog et al. (1996) used the software AutoReaGas (Ansys, Inc., Canonsburg, PA) to study the propogation of a vapor cloud explosion inside a refinery structure. No comparisons to experimental data were provided but on a qualitative level the software was able to show the effects of plant layout on the propagation of the blast wave, something that traditional hand calculations are unable to do.

Luccioni et al. (2005) used the software AUTODYN to simulate the blast loads imposed on buildings in a city block. The study compared various simplified prediction methods (nomographs, scaling, reflection charts, etc.) to computational results and the comparison clearly showed that simplified prediction methods are unable to capture the more complex aspects of such a blast scenario and can lead to an underprediction of blast loads. Remennikov and Rose (2005) used the software Air3D (Royal Military Science College, Cranfield University) to study how the proximity of buildings can influence blast loads. Using simulations and comparisons to experimental data, the researchers showed that the presence of buildings in close proximity can greatly increase blast loads as a result of reflections, something that simplified prediction methods cannot model. Baylot et al. (2004 and 2005a) simulated the effects of a more complex urban geometry which included up to nine structures. Again, the studies showed that the complex geometry led to increased blast loading relative to that which would be predicted by simplified methods.

1.8. Problem Statement

The preceding paragraphs have discussed the analytical techniques required to accurately simulate blast loads and the resulting structural responses of load bearing unreinforced masonry walls. These analytical methods are supported by an extensive database of empirical evidence derived from relatively simple experiments. What has not been performed, however, is full-scale testing of these methodologies on a real multi-story bearing wall building that, by definition, posesses representative dead loads, non-ideal boundary conditions, and the inherent characteristics resulting from the design and construction practices in the United States in the 1940s. In order to address this knowledge gap, the Department of Civil and Environmental Engineering at the University of North Carolina at Charlotte conducted three blast tests inside a decommissioned, coal-fired power plant prior to its scheduled demolition. Post-test analytical studies to simulate blast loads and structural responses are documented here to assess the capability of existing analytical techniques to simulate the performance of a load bearing, unreinforced masonry structure.

This document is organized into eight chapters. Chapter 1 reviews the existing state of the art in the various disciplines required to perform a comprehensive blast analysis. Chapter 2 will detail the experimental program executed for this investigation and its results. Chapter 3 compares measured blast loads to those predicted by simplified analysis methods. Chapters 4 and 5 will present relevant shock physics background material and will discuss the results of blast load simulations using CTH. First, a convergence study is performed using CTH to establish the meshing required for airblast simulations. Then, equation of state data available in the literature for commercial

dynamites is reviewed. This data is modified using an energy scaling technique to develop coefficients for the JWL EOS for a previously uncharacterized type of dynamite, Unimax. The adjusted JWL coefficients are then used in CTH to simulate two different blast events. Simulations will show that good agreement between experimental and analytical results can be achieved for impulse using the newly developed JWL coefficients.

Following the analysis of blast loads, Chapters 6 and 7 will apply SDOF and finite element modeling techniques to simulate the structural response of the walls from blast chamber B. The pressures and impulses (both experimental and analytical), along with the basic structural geometry, material properties, and boundary conditions, are used as inputs for both simplified and computationally intensive structural response models. The SDOF models – with the advantage of observing post-test crack patterns before choosing support conditions – are able to predict the experimental permanent deflections well. As a complimentary result, the finite element models predict crack patterns similar to those observed in the field. Finally, Chapter 8 contains a summary of this investigation's primary findings along with recommendations for further research.

CHAPTER 2: EXPERIMENTAL PROGRAM

The Department of Civil and Environmental Engineering at the University of North Carolina at Charlotte conducted three blast tests inside a decommissioned, coal-fired power plant prior to its scheduled demolition. The power plant was composed of three structurally independent buildings – two identically constructed boiler houses and a turbine house. There was also a two-story bearing wall structure attached to the facade of one of the boilerhouses. Figure 2.1 is a photo of the facility showing the front elevation of the power plant and the three charge locations (A1, A2, and B). In the photo, the boiler houses are the taller structures visible in the foreground and the turbine house is the long, low-rise structure in the background.

Figures 2.2 through 2.4 are views of a three-dimensional cut-away model of the structure in the vicinity of locations A1 and B that are intended to illustrate the basic structural configuration of the boilerhouse and bearing wall building (the bearing wall building is at the far right of Figure 2.1). Figure 2.2 is an external isometric view that is representative of the right half of Figure 2.1. Figure 2.3 is a cutaway view of the location B blast chamber as viewed from inside the structure. Figure 2.4 is another cutaway view from higher inside the structure showing the location A1 and location B blast chambers. The illustration shows that location A1 (and A2) is a long corridor located over the coal bunkers. The A1 and A2 blast chambers housed a conveyor and tripper system that was used to transfer coal from the coal yard to the storage bunkers inside the plant.

The primary structural system, structural details, and architectural details (such as infill walls) were determined primarily by inspection because structural and architectural drawings of the facility were incomplete. In shot locations A1 and A2 (the fourth floor of the boiler houses), the structure was a multistory steel framed building with unreinforced brick infill walls. Structurally and architecturally, locations A1 and A2 were very nearly identical. The boilerhouses were built in two phases: the first boilerhouse was completed in the 1940's and the second was completed in the 1970's. While the time between phases of construction was significant, on-site investigation showed the two structures had nearly identical designs and materials. The structure at charge location B consisted of two unreinforced exterior, load-bearing, brick walls and two interior unreinforced infill walls which were part of the location A1 boiler house structure. Section 2.2 will provided detailed narrative descriptions of the construction of each blast chamber.

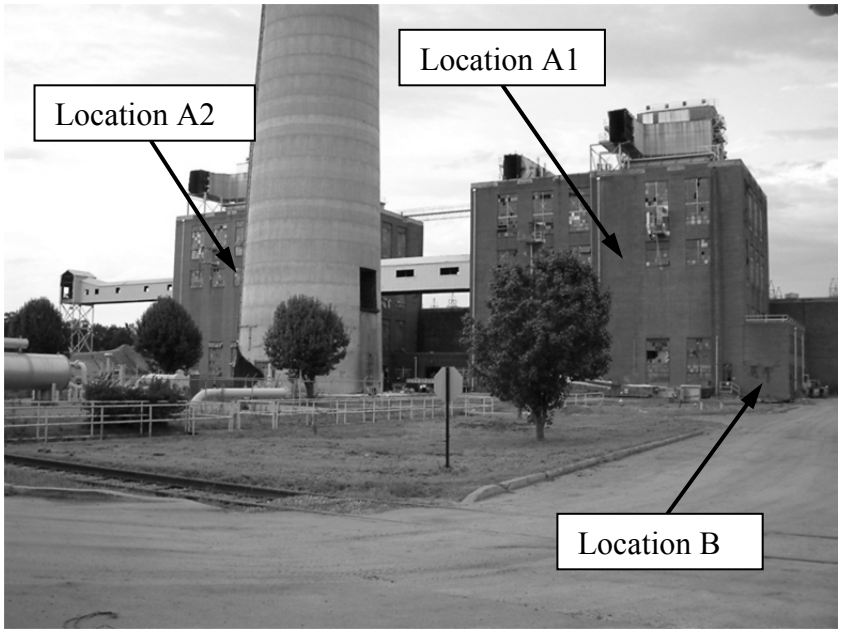

FIGURE 2.1: Photograph of front elevation of power plant showing location of three blast chambers. (Location A2 is behind the left edge of the stack in the foreground).

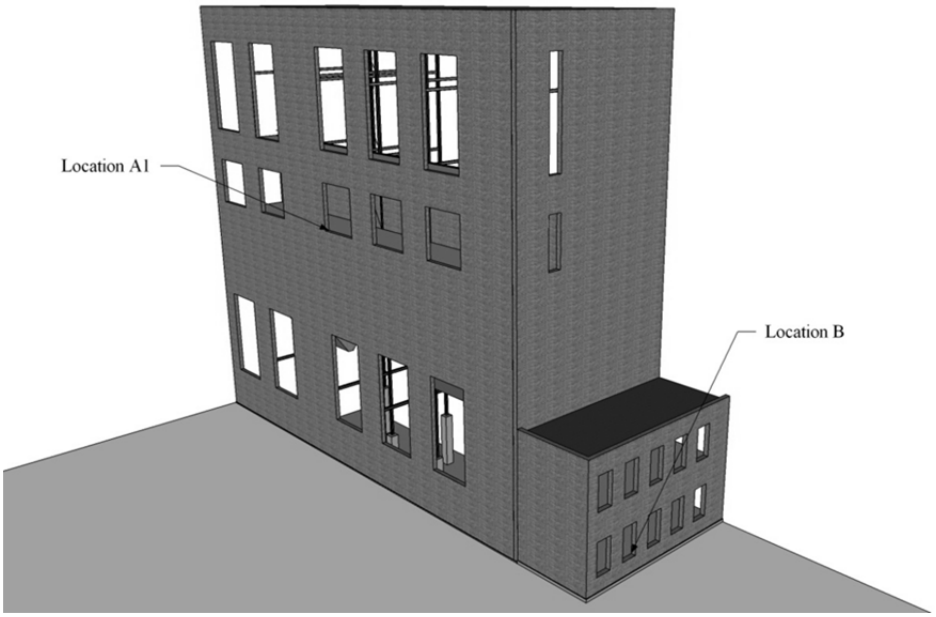

FIGURE 2.2: Isometric view of three-dimensional model of locations A1 and B. The diagram represents the right half of Figure 2.1.

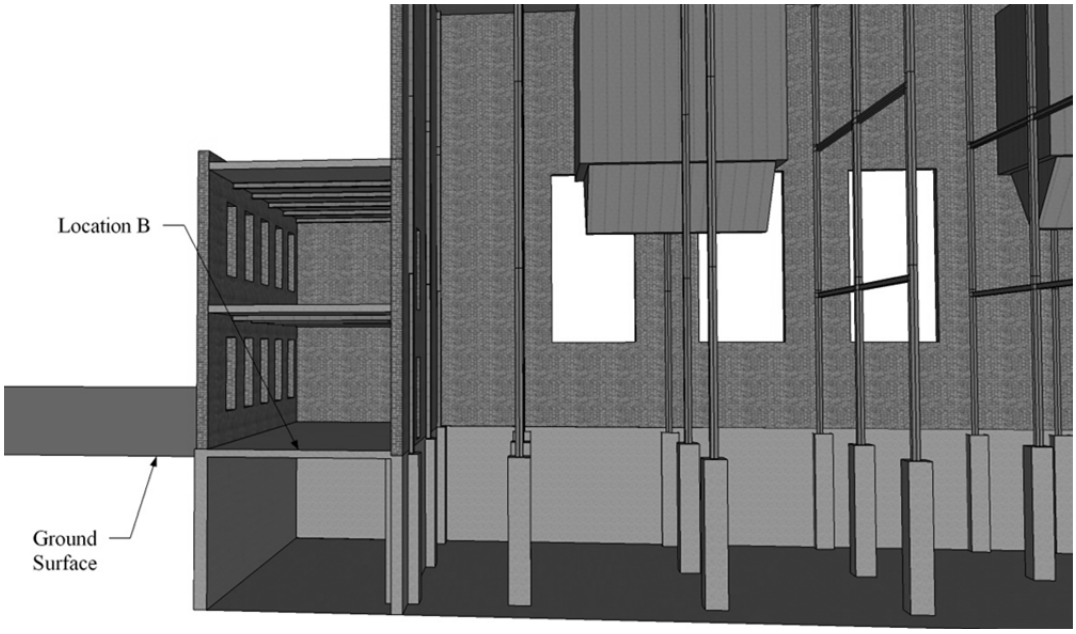

FIGURE 2.3: Isometric view of three-dimensional model from inside showing a section through the structure at location B.

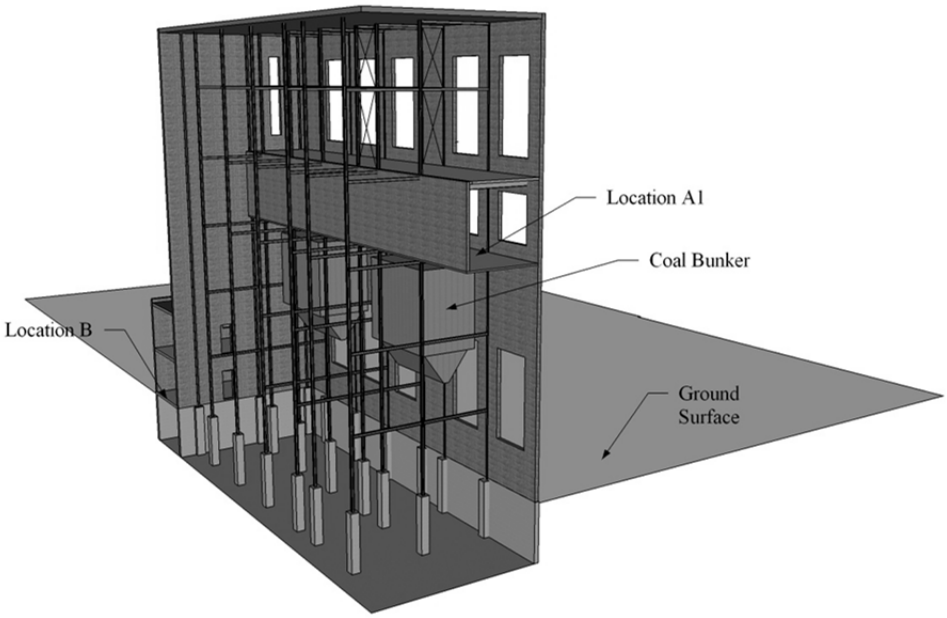

FIGURE 2.4: Isometric view of three-dimensional model showing the configuration of the structure at location A1.

2.1. Instrumentation

Figures 2.5, 2.6, and 2.7 are plan views of each blast chamber showing chamber geometry and the locations of the charges and sensors. Sensor elevations are measured relative to the top of finished floor slabs inside the chambers. In all three blast chambers, the walls and ceilings were instrumented with piezoelectric sensors supplied by PCB Piezotronics (Depew, New York). All sensors (pressure and acceleration) utilized PCB's proprietary integrated circuit piezoelectric (ICP) design which permits signals to be transmitted over two conductor coaxial cables. Flush mount pressure sensors were PCB model 102A03, 69 MPa peak pressure (10 ksi), high-frequency sensors; they were flush mounted on prefabricated metal plates mounted to the interior surfaces of the blast chamber with mechanical anchors and epoxy. This created a reflecting surface flush with the wall or ceiling in order to measure reflected pressures and impulses. Immediately behind these flush mounted plates, a three inch diameter core was drilled through the masonry or concrete substrate to allow the passage of sensor cables through the walls or slabs.

For charges A1 and A2, one PCB model 137A21, 6.9 MPa (1 ksi) peak pressure, high frequency pressure pencil was used to measure incident (side-on) overpressure and impulse. The pressure pencils were mounted to a rigid stand approximately 61 cm (24 in) above the finished floor height; the longitudinal axis of the pressure pencils pointed directly at the charge's center of mass. Shock accelerometers were PCB model 350B21 with a 100,000g measurement range. The shock accelerometers had no integrated electrical or mechanical filtration. The shock accelerometers were mounted on

prefabricated steel plates attached to the exterior surfaces of the blast chamber walls and slabs with mechanical anchors and epoxy. The exterior placement served to protect shock accelerometers and electrical connections from the blast environment. Both the flush mount pressure sensors and shock accelerometers had threaded cases that screwed into tapped holes in the flush mounted plates. Figures 2.8 and 2.9 illustrate the sensor mounting methodology for flush mount pressure sensors and shock accelerometers, respectively. No shock isolators were used to shield sensors from resonant vibrations of their steel mounting plates. Recorded data shows that this was acceptable as very few sensors recorded unexpectedly high amplitude signals indicative of resonance. Plots of time history data for each sensor are included in Appendices A through C and will be discussed in greater detail in Section 2.4.

Data acquisition for the pressure sensors and shock accelerometers was provided by National Instruments (NI) 4472 modules with on-board signal conditioning (bandpass filtration and 4 milliamp (mA) driving current). The NI modules sampled all channels simultaneously at 100 kHz using independent analog to digital converters (ADCs) synchronized to a common system clock. The 4472 modules were configured for AC coupling (meaning a -3dB, or approximately 20% amplitude, attenuation for frequencies at 3.3 Hz, with attenuation increasing for lower frequencies). This high-pass filter is primarily useful for removing a DC bias in sensor signals which is convenient as PCB's piezoelectric sensors typically have an 11 volt bias. The 4472 modules also have integrated analog and digital anti-aliasing filters which eliminate all signal

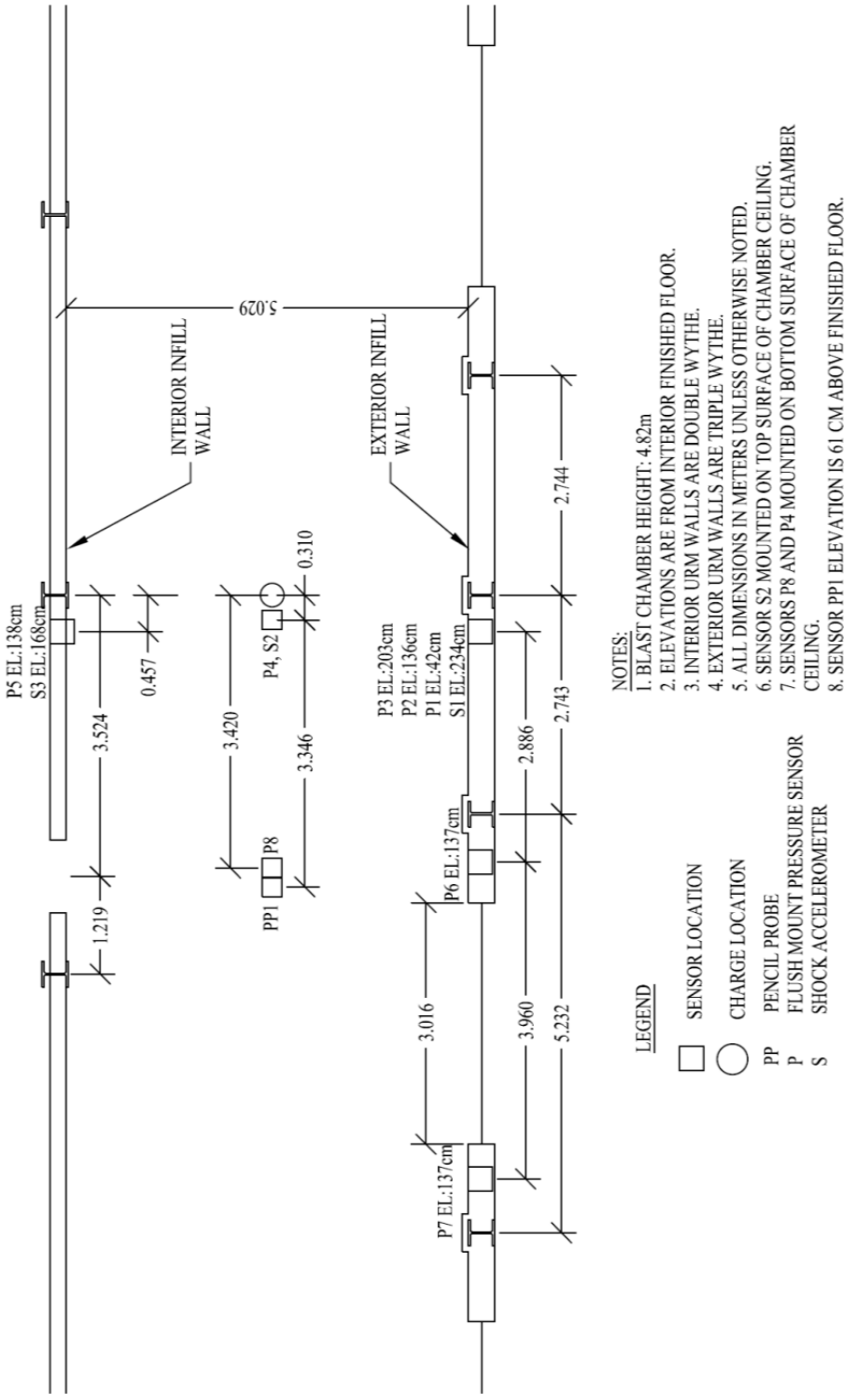

FIGURE 2.5: Plan view of blast chamber A1.

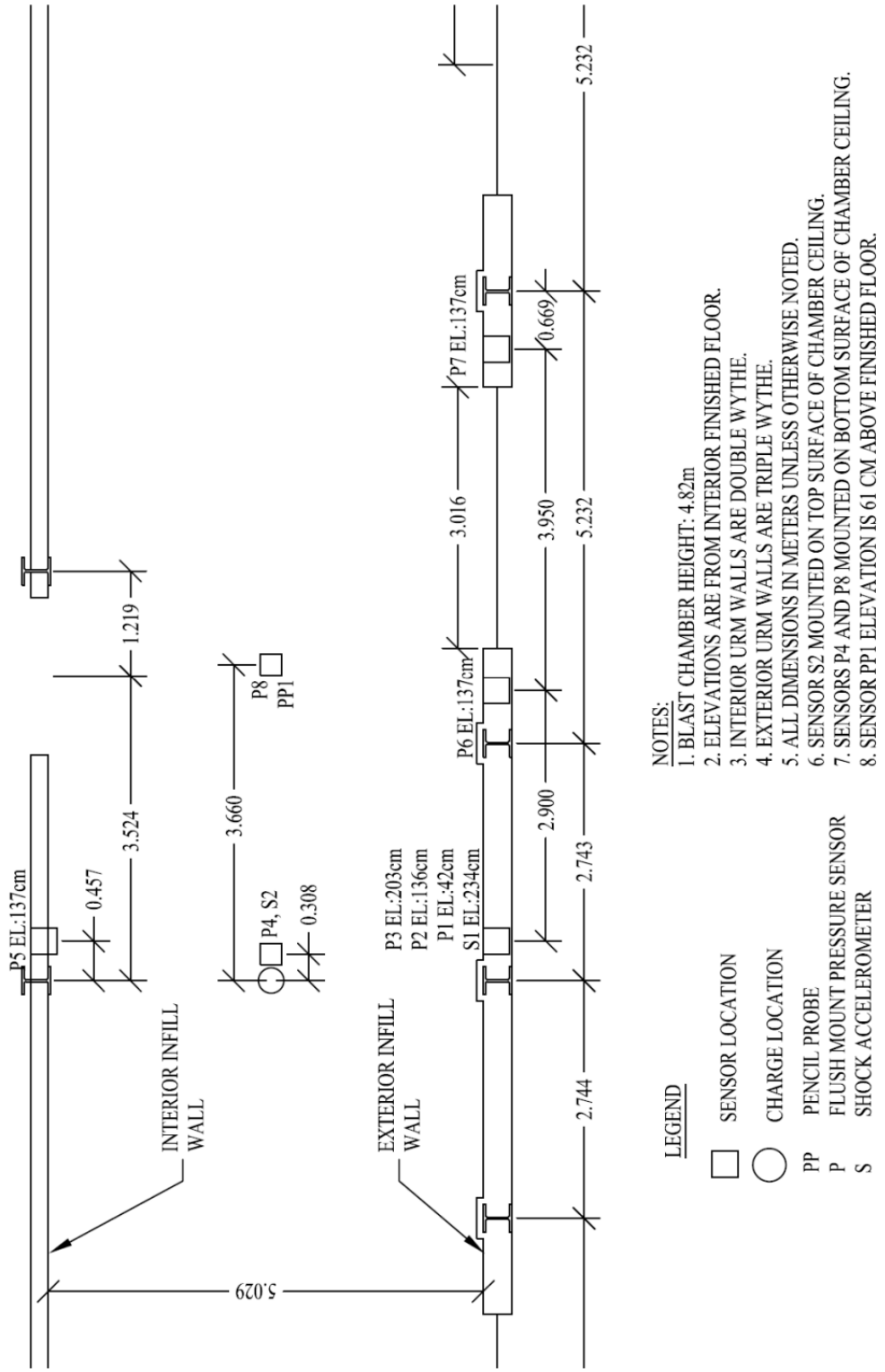

FIGURE 2.6: Plan view of blast chamber A2.

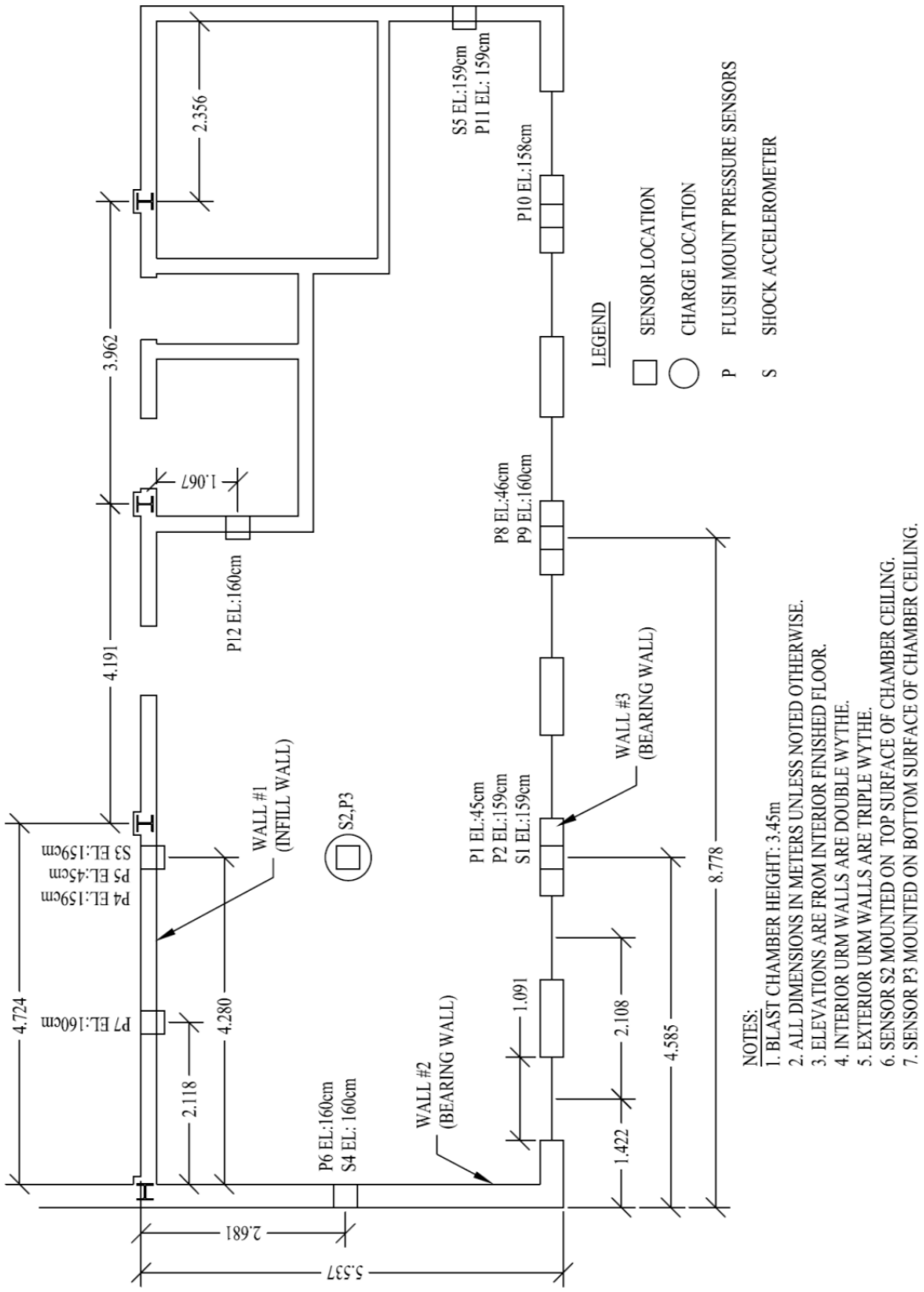

FIGURE 2.7: Plan view of blast chamber B.

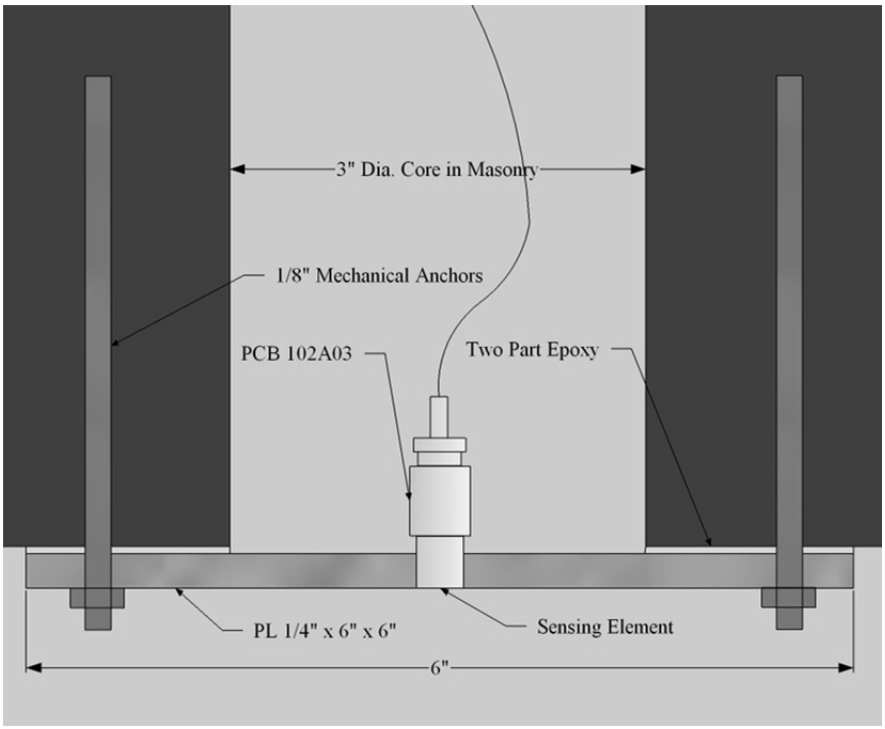

FIGURE 2.8: Cross section through flush mount pressure sensor mounting.

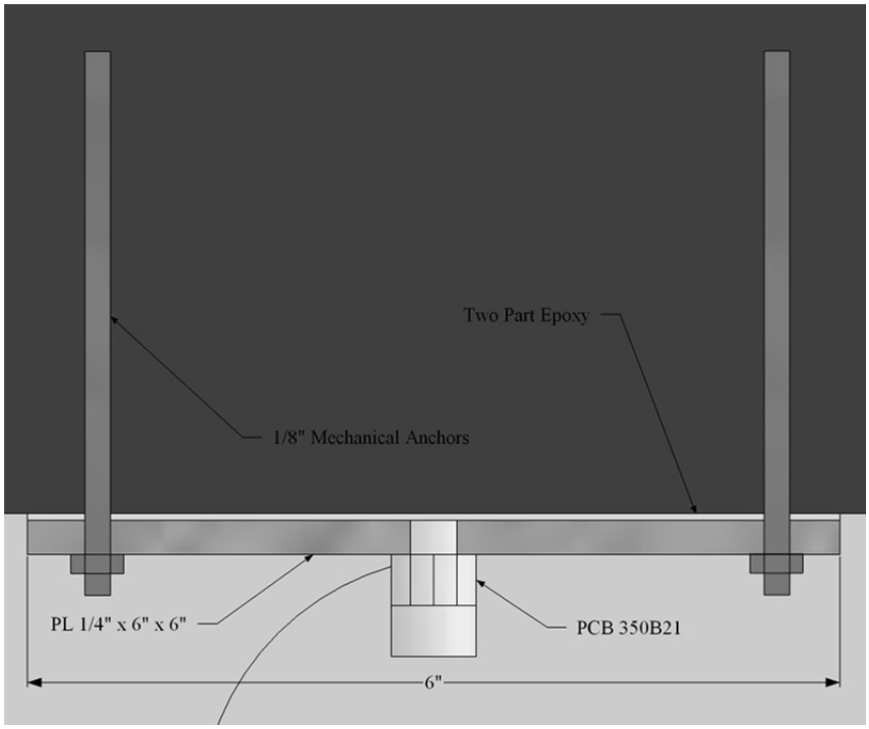

FIGURE 2.9: Cross section through shock accelerometer mounting.

frequency content greater than 45 kHz. This configuration assured that aliasing would not affect measured signals. Sensors were connected to the data acquisition system using 305 meter (1000 foot) long, low capacitance coaxial cables supplied by PCB. All connection hardware and cabling were impedance matched and assembled by PCB.

The combination of long cables and low driving current produced a limitation on the highest frequencies the NI 4472-cable-sensor circuit could transmit. Simplified tests using a sensor simulator and an analog oscillator showed that frequencies above 20 kHz would be significantly attenuated by the capacitive effects of the long cables. Using Eq. (2.1) (from PCB literature), and assuming the 305 meter cable has a capacitance of 98.4 picoFarads per meter (C=98.4 pF/m * 305 m =30012 pF) with a 4 mA excitation (I_c=4) and using a 10.3 MPa (1500 psi) measurement corresponding to 0.75 volt peak output (V=0.75) from a 102A03, the maximum system frequency is approximately 7 kHz.

$$f_{max} = \frac{10^9}{\frac{2\pi CV}{I_c - 1}} \tag{2.1}$$

Unfortunately it is not possible to experimentally verify that the high and low frequency attenuation did not impact the quality of measured pressures and impulses. It is, however, possible to at least simulate the effects of frequency attenuation by a simple numerical experiment. Figure 2.10 shows an artificially constructed blast wave before and after the application of two filters implemented using Matlab (see Appendix D, script D.1). One filter simulated AC coupling and was modeled as a one pole high pass filter with a -3dB point of 3.3 Hz. The second filter simulated the high frequency attenuation of the long cables and was modeled as a first order butterworth low pass filter with a -3dB point of 7 kHz. As Figure 2.10 shows, the filtration does have an effect on the peak

measured pressure (and thus impulse). The frequency attenuation appears to cause an undermeasurement of the peak pressure by 8.7%, which in turn leads to a computation of impulse which is 4.4% below the actual impulse. With respect to shock accelerometer measurements, the dominant frequencies of structural vibration should have been well below 7 kHz and thus the high frequency attenuation is unimportant. Unfortunately, the AC coupling (high pass filter) likely interfered with structural response measurements; this deficiency will be discussed in greater detail in Section 2.4.

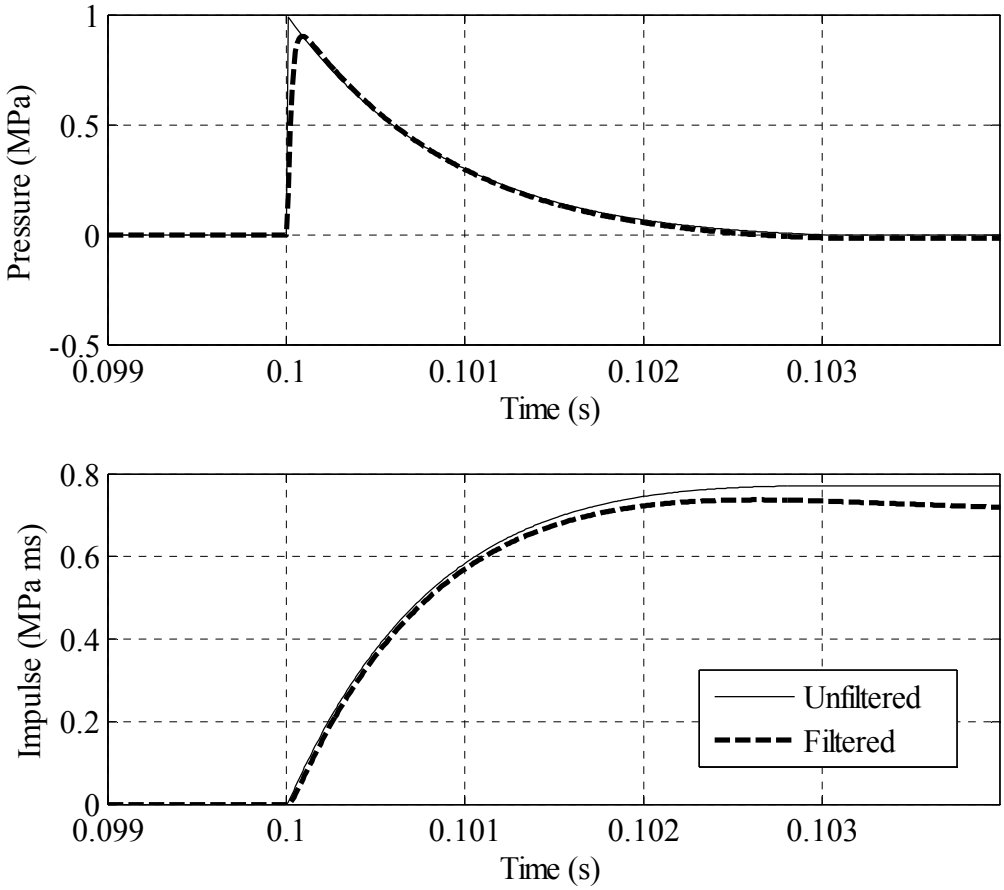

FIGURE 2.10: Example pressure and impulse time history before and after filtration similar to that of NI4472 data acquisition modules.

2.2. Charge Data and Blast Chamber Construction

Complete structural drawings were not available due to the age of the facility. It was therefore necessary to visually identify details of the structural configuration which would be important for subsequent structural modeling. Pre-test samples of masonry and concrete were cut from blast chamber walls and slabs to determine Young's modulus and the compressive and tensile strength of the materials. The following paragraphs provide a narrative description of the explosive charge, field observations of the structural system, and the results of material tests performed in the laboratory.

2.2.1. Charge and Blast Chamber Description — A1

Charge A1 consisted of thirty 0.227 kg nominal (0.204 kg (0.450 lbs) actual) dynamite cartridges formed into an upright cylinder with a total gross weight of 6.53 kg (14.4 lbs). Note that due to cartridge variability, the total gross weight is only approximately the nominal cartridge weight multiplied by the number of cartridges. The net explosive weight was 5.88 kg (13.0 lbs) after subtracting 10% to account for the weight of the cartridge packaging. Dynamite was supplied by Dyno Nobel under the product name Unimax and contained approximately 26% nitroglycerin gel by weight. At detonation the bottom of the cylindrical charge was at a height of 30 cm (12 in) above the blast chamber floor and rested on a lightweight timber stand. The height of the cylindrical charge was approximately 41 cm (16 in); its diameter was approximately 15 cm (6 in). The charge was detonated at its center of mass with two instant electric blasting caps.

Charge location A1 was on the fourth floor of one of the boiler houses (see Figures 2.1 and 2.5). The blast chamber housed a conveyor system that transferred coal

from the coal yard stockpile to the coal bunkers below the blast chamber floor. The floor of the blast chamber was a 10 cm (4 in) thick, reinforced concrete slab, cast-in-place on steel plates and supported by 51 cm (20 in) deep steel I-sections spaced at 4.88 m (16 ft) on center. The ceiling consisted of a reinforced concrete slab and joist system with embedded 46 cm (18 in) deep I-sections spaced at 1.4 m (4.5 ft) on center; the ceiling slab thickness in this region averaged 43 cm (17 in). The exterior brick infill wall was 32 cm (12.5 in) thick and included embedded steel columns with intermittent lateral bracing. The interior brick infill wall was 20 cm (8 in) thick with two door openings, one on either side of the charge; heavy structural beams and columns were embedded in the wall. The average compressive strength of masonry tested from location A1 was 22.3 MPa (3240 psi), the average modulus of elasticity was 6.41 GPa (930 ksi), and the average masonry density was 1900 kg/m^3 (118 lb/ft^3).

Inside the blast chamber, eight flush-mount pressure sensors measured reflected pressures and one pressure pencil measured incident pressure. Three shock accelerometers, mounted to the outer surfaces of the blast chamber walls and ceiling slab, measured structural accelerations. The internal height of the blast chamber was 482 cm (190 in). Figure 2.5 shows the geometry of the blast chamber, the location of the charge, and the locations of the sensors.

2.2.2. Charge and Blast Chamber Description – A2

Charge A2 consisted of fifty 0.091 kg nominal (0.201 lb) cast booster cartridges formed into an upright cylinder with a triangular prism on top. The total gross explosive weight was 4.54 kg (10.0 lbs) and the net explosive weight was 4.09 kg (9.02 lbs) after subtracting 10% for the weight of cartridge packaging. Cast booster was supplied by

Austin Powder Co. under the product name “Cast Booster” and contained predominantly TNT (on a weight basis). The manufacturer’s data sheet specifies that the product contains between 30% and 70% TNT by weight with the remainder made up of RDX, PETN, and/or HMX as a sensitizer. At detonation the bottom of the cylindrical charge was at a height of 30 cm (12 in) above the blast chamber floor and rested on a lightweight timber stand. The height of the cylindrical charge was approximately 30 cm (12 in); its diameter was approximately 14 cm (5.5 in). The charge was detonated at its center of mass with two instant electric blasting caps.

Charge location A2 was on the fourth floor of one of the boiler houses (see Figures 2.1 and 2.6). Like the A1 blast chamber, the A2 blast chamber housed a conveyor system that transferred coal from the coal yard stockpile to the coal bunkers below the blast chamber floor. The floor of the blast chamber was a 10 cm (4 in) thick, reinforced concrete slab, cast-in-place on steel plates supported by 51 cm (20 in) deep steel I-sections spaced at 4.88 m (16 ft) on center. The ceiling consisted of a reinforced concrete slab and joist system with embedded 46 cm (18 in) deep I-sections spaced at 1.4 m (4.5 ft) on center. The ceiling slab thickness in this region averaged 39 cm (15.5 in). The exterior brick infill wall was 32 cm (12.5 in) thick and included embedded steel columns with intermittent lateral bracing. The interior brick infill wall was 20 cm (8 in) thick with two door openings, one on either side of the charge; heavy structural beams and columns were embedded in the wall. Unlike the A1 blast chamber, A2 had an open end wall to accommodate the entrance of a conveyor system. The average compressive strength of masonry tested from location A2 was 18.5 MPa (2690 psi), the average

modulus of elasticity was 6.38 GPa (925 ksi), and the average masonry density was 1840 kg/m^3 (115 lb/ft^3).

Inside the blast chamber, eight flush-mount pressure sensors measured reflected pressures and one pressure pencil measured incident pressure. Two shock accelerometers, mounted to the outer surfaces of the blast chamber walls and ceiling slab, measured structural accelerations. The internal height of the blast chamber was 482 cm (190 in). Figure 2.6 shows the geometry of the blast chamber, the location of the charge, and the locations of the sensors.

2.2.3. Charge and Blast Chamber Description — B

Charge B consisted of forty 0.227 kg nominal (0.204 kg (0.450 lbs) actual) dynamite cartridges formed into an upright cylinder with a total gross weight of 8.71 kg (19.2 lbs). The net explosive weight was 7.84 kg (17.3 lbs) after subtracting 10% for the weight of cartridge packaging. Dynamite was supplied by Dyno Nobel under the product name Unimax and contained approximately 26% nitroglycerin gel by weight. At detonation the bottom of the cylindrical charge was at a height of 30 cm (12 in) above the blast chamber floor, and the charge rested on a lightweight timber stand. The height of the cylindrical charge was approximately 41 cm (16 in); its diameter was approximately 17 cm (6.5 in). The charge was detonated at its center of mass with two instant electric blasting caps. Inside the blast chamber, twelve flush-mount pressure sensors measured reflected pressures. Five shock accelerometers, mounted to the outer surfaces of the blast chamber walls and ceiling slab, measured structural accelerations. Figure 2.7 shows the geometry of the blast chamber, the location of the charge, and the locations of the sensors.

The structure at location B was a two-story, unreinforced, brick, bearing wall building, which was built as an addition adjacent to the larger steel-framed boiler house of location A1. The structure had locker rooms on the ground floor and laboratory space on the second floor. Exterior walls were load-bearing brick while interior walls were non-load-bearing brick infill panels bounded by the steel columns and beams of the adjacent boiler house. The internal height of the blast chamber was 345.4 cm (136 in). Figure 2.7 is a plan of the ground-floor of the building (this figure also establishes the naming convention for the three walls to be studied subsequently). Figures 2.2 and 2.3 show three-dimensional models of the structure at location B.

Interior infill walls were 20 cm (8 in) thick and exterior bearing walls were 30 cm (12 in) thick. The internal face of all walls of the blast chamber had a 5 cm (2 in) thick tile veneer bonded to the brick with mortar. The floor of the blast chamber was a 25 cm (10 in) thick reinforced concrete slab cast integrally with the reinforced concrete foundation walls and caissons. The ceiling of the chamber was a 20 cm (8 in) thick reinforced concrete slab supported by 23 cm (9 in) deep steel wide flange beams spaced at 229 cm (90 in) on center. The beams spanned 495 cm (16.2 ft) and were supported by a steel girder at one end (at the location of Wall #1) and an unreinforced, brick bearing wall (Wall #3) at the other. The one-way spanning floor system meant that collapse of the ground floor bearing wall (Wall #3) would cause a large part of the two-story building to collapse. Compression tests on material samples found that the average compressive strength of the masonry assemblages was 13.5 MPa (1960 psi), the average modulus of elasticity was 4.23 GPa (614 ksi), and the average masonry density was 1850 kg/m^3 (115 lb/ft^3). Bond wrench tests indicated a masonry flexural tensile strength perpendicular to

the bed joints of 0.862 MPa (125 psi) while simple beam bending tests indicated a flexural tensile strength of 0.752 MPa (109 psi). Prior to the blast test, geotextile fabric was hung in front of exterior windows to shield nearby structures from blast generated debris.

2.3. Shot Results – Observed Damage

The results of the three blast tests will be reported in two sections. In this section, narrative descriptions of damage will be provided, accompanied by supporting figures and photographs. Then, Section 2.4 will present a quantitative summary of measured airblast parameters and structural accelerations. Appendices A through C contain a complete set of plotted sensor data for each blast event, showing pressure and impulse time histories, acceleration time histories, and acceleration frequency spectra.

2.3.1. Blast Chamber A1

The explosion caused all windows in the blast chamber to shatter and glass fragments were found as far as 45.7 m (150 ft) from the structure. (This large glass throw distance can be explained by the fact that the blast chamber was on the fourth floor of the boilerhouse). One of the interior doors was blown off its hinges while the other was violently thrown open by the positive overpressure. The reinforced concrete floor slab under the charge showed no significant damage. Nonstructural elements in the blast chamber suffered considerable damage (piping and lighting). The infill walls suffered little to no damage, except for a small fractured region near the closest embedded column and several fine cracks in mortar joints. See Figure 2.11 for a post-test view of the A1 blast chamber.

No structural steel members (beams, columns, or bracing) in the blast chamber were damaged as a result of the blast. The ceiling of the chamber was cracked around the embedded I-sections, particularly in the area immediately above the charge location (Figure 2.12). The crack ran the full width of the blast chamber parallel to the embedded I-section directly above the charge location. Other smaller cracks were observed parallel to the embedded I-shapes.

FIGURE 2.11: Post-test view of A1 blast chamber showing little to no structural damage.

FIGURE 2.12: Crack on top surface of A1 blast chamber ceiling directly above charge location. Crack aligned with embedded I-shaped member supporting the slab.

2.3.2. Blast Chamber A2

The blast caused all windows in the chamber to shatter and glass fragments were found as far as 30 m (100 ft) from the building. (Again, this large glass throw distance can be explained by the fact that the blast chamber was on the fourth floor of the boilerhouse). One of the interior doors was blown off its hinges while the other was violently thrown open by the positive overpressure. The reinforced concrete floor slab under the charge showed no significant damage. Nonstructural elements in the blast chamber suffered considerable damage (Figure 2.13). The infill walls suffered little damage as a result of the explosion; no structural steel members in the blast chamber were damaged. The ceiling of the blast chamber was cracked around the embedded I-sections and very minor flexural cracking of the slab was observed above the charge location (observed from above on the floor slab that was the chamber's ceiling). A small

area of spall was observed on the top surface of the blast chamber ceiling (Figure 2.14). It is worth noting that while charge A1 was larger than A2, it produced less damage to the ceiling slab and the steel plates attached to the floor. This is largely because of the difference in charge shapes. Charge A1 was a perfect cylinder while charge A2 was a cylinder topped with a triangular prism. The effect of the triangular prism was to direct more blast energy both upward and downward than would an ordinary cylinder of the same weight, thus causing greater damage to the floor and ceiling.

FIGURE 2.13: Post-test view of A2 blast chamber showing damage to non-structural components. Note the bent steel plates at lower left.

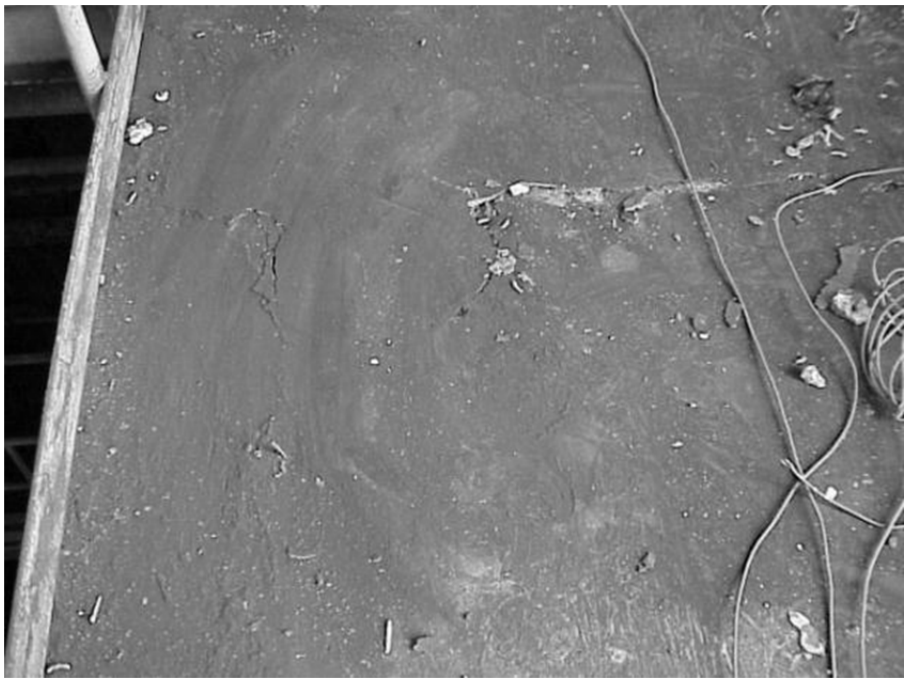

FIGURE 2.14: Floor above blast chamber A2 showing area of spalled concrete.

2.3.3. Blast Chamber B

The blast caused several steel window mullions, all remaining glass, and the protective geotextile fabric covering the windows to be ejected away from the building. The door located in the infill wall was blown open and its frame was severely bent. Sinks and toilets fastened to the walls were either shattered or torn from their supports. Other nonstructural elements such as ductwork, heating fans, and lights hanging from the ceiling were crushed and scattered throughout the room (Figure 2.15).

The three walls closest to the charge (Walls #1, #2, and #3) were severely damaged. Figure 2.7 shows the naming convention used for the blast chamber walls. In particular, the internal infill wall (Wall #1) closest to the charge cracked in an inverted Y-pattern between two interior steel columns; the wall was permanently displaced outward by more than 25 cm (10 in) at its top (Figure 2.16 shows a photo of this damage). This

crack pattern is indicative of a wall that is supported along three edges (left, right, and the bottom). Dawe and Seah (1989) observed an identical crack pattern in one of their experimental tests in which the wall was supported on 3 sides. Regions of the exterior bearing walls (Walls #2 and #3) closest to the charge were also heavily damaged and appeared to be near collapse. The smaller load bearing wall (Wall #2) cracked in an X-pattern. This crack pattern was expected since the wall's aspect ratio (less than 2:1) indicated it should behave as a two-way element if it was adequately supported on all four edges.

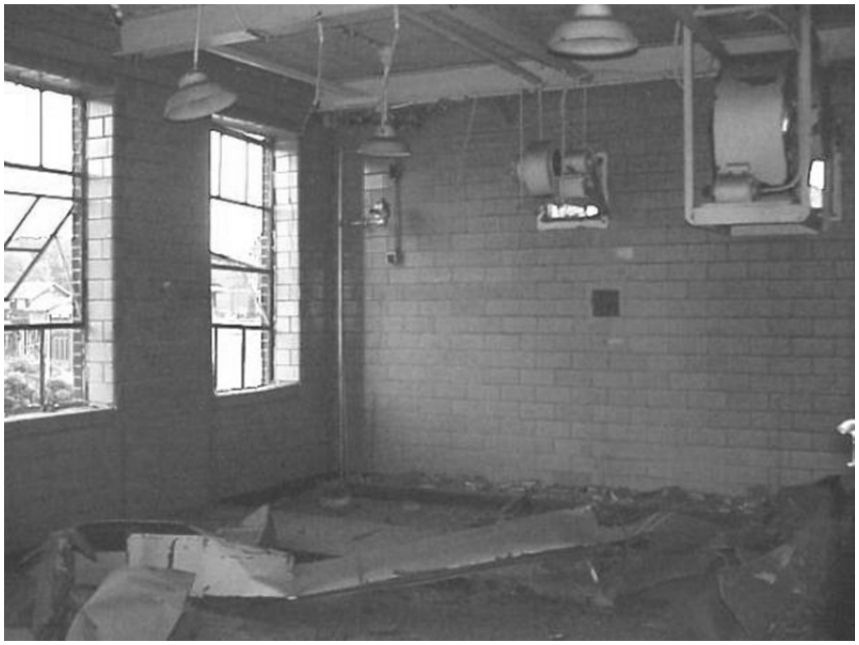

FIGURE 2.15: Post-test view of the location B blast chamber showing extensive damage to nonstructural items.

FIGURE 2.16: Post-test view of Wall #1 from outside the blast chamber showing heavily damaged infill panel.

FIGURE 2.17: Post-test exterior view of Wall #3 where it intersects Wall #2.

FIGURE 2.18: Post-test exterior view of intersection of Wall #3 and Wall #2. Note the area of spall on Wall #3 at upper right. The remaining geotextile fabric used to catch ejecta is visible at right.

The larger bearing wall (Wall #3), which supported one side of the entire second story, exhibited cracking consistent with floor-to-floor, one-way bending. This crack pattern was expected due to the large aspect ratio of the wall (greater than 2:1) and the placement of window openings. Wall #3 was cracked at about one-quarter of its height for approximately 610 cm (20 ft) along the bottom of its windows and approximately 460 cm (15 ft) along the top of its windows; one wythe of brick spalled off the outside of the wall near the charge location (Figure 2.18 is a photo of the damage). Figures 2.17 and 2.18 show the intersection of Wall #3 and Wall #2; this corner of the building suffered extensive damage due to the internal blast loading. Figures 2.19, 2.20, and 2.21 are illustrations of the crack/ damage patterns observed on each wall

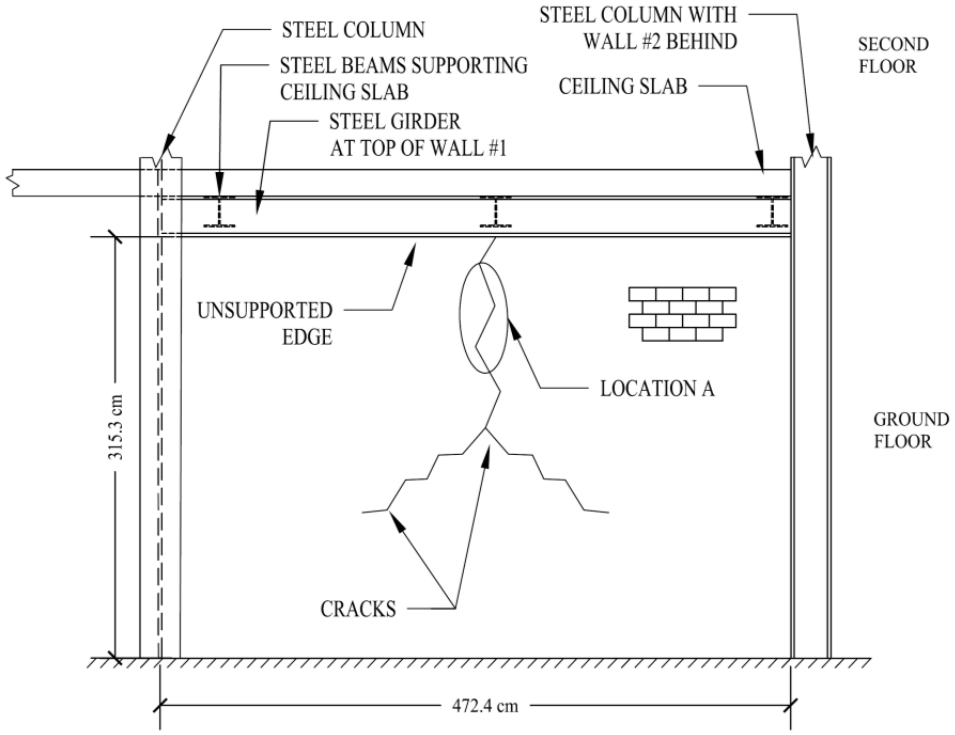

FIGURE 2.19: Post-test crack pattern of ground floor infill wall (Wall #1), outside blast chamber looking in.

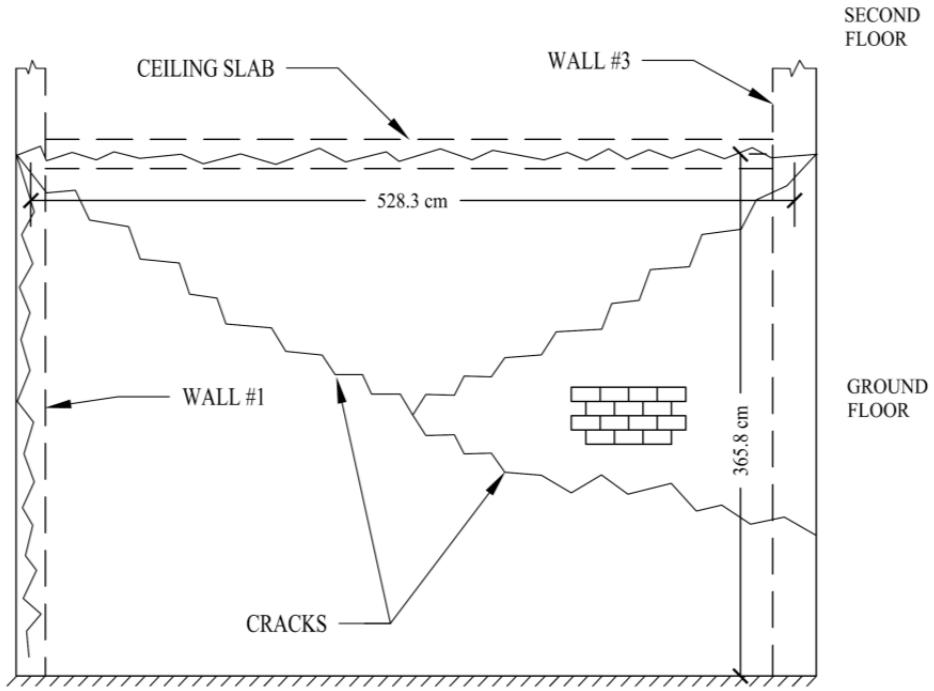

FIGURE 2.20: Post-test crack pattern of smaller bearing wall (Wall #2) at ground floor level, outside blast chamber looking in.

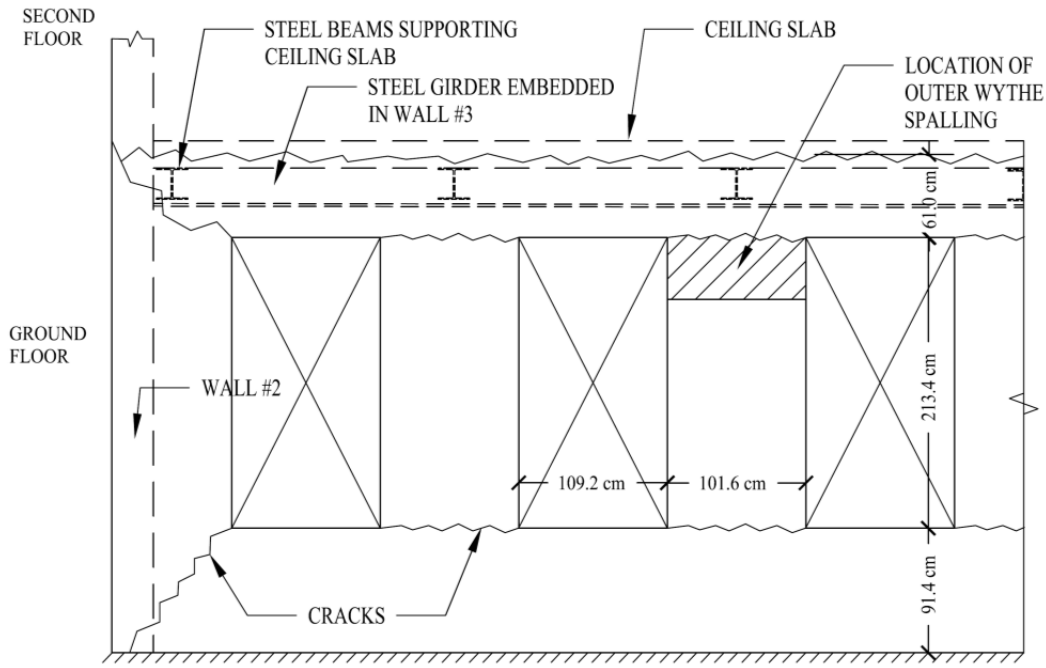

FIGURE 2.21: Post-test crack/damage pattern of larger bearing wall (Wall #3) at ground floor level, outside blast chamber looking in.

2.4. Shot Results – Sensor Measurements

This section provides a summary of measurements made using piezoelectric pressure sensors and shock accelerometers. Before discussing measured quantities, it is necessary to first discuss certain problems discovered after conducting the blast tests. Generally speaking, pressure (and therefore also impulse) measurements are thought to be of acceptable quality with the caveat that any sustained gas pressures were likely not measured due to the data acquisition system's AC coupling. This, however, is acceptable because the blast chambers were only partially confined due to the extensive area of windows. Gas pressures (and corresponding impulses) should have therefore been negligible.

With regard to shock accelerometer measurements, however, problems associated with high range sensors and low frequency attenuation were found to yield semi-unusable data. The first problem, the high measurement range of the shock accelerometers, means that the signal had a high noise floor (greater than +/- 10 g, or greater than 20g total); this is in contrast to the measurements which peak from several hundred to several thousand g's. This background noise can be attributed to a combination of digitization error and noise induced in unshielded instrumentation cables. A high g-limit was chosen because prior to the test there was limited ability to specify the exact location and size of charges. It was therefore believed prudent to over-estimate possible accelerations rather than to select under-ranged sensors which could saturate under blast loading, yielding unusable data.

The second and more serious problem, the AC coupling built into the NI 4472 modules, significantly attenuated (20% or more) signals with frequencies below 3.3 Hz. This feature was enabled by UNC Charlotte's instrumentation vendor without consultation because it solved the difficult problem of removing sensor bias voltages without the use of external signal conditioners. As a result, the majority of masonry wall nonlinear response was not measured by the accelerometers due to its relatively low frequency content (easily below 3.3 Hz as shown by Figure 2.22, a plot of data contained in Griffith et al. (2004)). Therefore, shock accelerometer data could not be integrated accurately enough to obtain structural velocities or deflections.

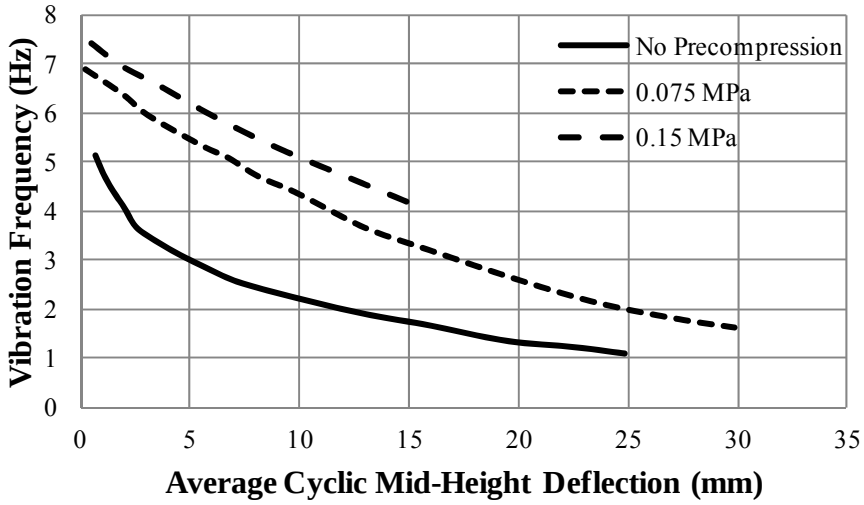

FIGURE 2.22: Natural frequency versus midheight deflection for 50 mm thick brick masonry walls cracked at midheight with various levels of precompression. Simply-supported height of 1500 mm. Data plotted from Griffith et al. 2004.

The remainder of this chapter will, therefore, focus on measured blast pressures, and shock accelerometer measurements will only be used to obtain the natural frequencies of structural elements where possible. The results of interest with regard to structural analyses will primarily be post-blast crack patterns and permanent deflections. In future tests using this data acquisition system, it is strongly recommended that structural accelerations be recorded using external PCB signal conditioners with the NI 4472 modules set to DC coupled mode (which has been permanently enabled for channels 3_0 to 3_7) and using lower range accelerometers with appropriate integrated mechanical and electrical filtration. Recent experimental work has shown that using PCB model 483C signal conditioners with PCB model 350B24 shock accelerometers yields acceptable measurements of blast-induced structural acceleration.

The data summarized in the tables that follow were gathered from the figures compiled in Appendices A through C. In those appendices, each sensor's measured time-

history is plotted on a time scale common to each blast event. Pressure time histories were integrated using the trapezoidal rule to obtain impulse time histories. Fourier amplitude spectra were constructed for acceleration time histories and are shown for two different frequency windows. Where a hardware malfunction (sensor, cable, or connector damage) is suspected, comments are made in the figure captions. In a qualitative sense, the pressure time history plots show what was expected during the tests - textbook-like positive phase pressure waves with no significant gas phase pressures, and a significant number of internal reflections.

Note that the data appear to show negative pressures in some of the time histories. Given the apparent magnitude of computed negative phase impulses the author would have expected to have observed tremendous structural damage from these negative pressures; but no such damage was observed. This indicates that the pressure sensors were likely affected by some thermal or mechanical phenomena which caused their zero state to shift negatively following the blast events. These non-physical signals cannot be separated from any real negative phase pressures that did exist.

Tables 2.1 through 2.3 summarize the data contained in the figures of Appendices A through C by listing the primary blast wave parameters - relative arrival time, positive phase duration, peak positive pressure, and positive impulse. No time of arrival device (TOAD) was used to synchronize the data acquisition system with the detonation of the charges. The data acquisition system was therefore started well in advance of charge detonation and the raw data files were each over a gigabyte in size. In order to decrease the length of time histories (thus facilitating data processing and file handling), start and end times were chosen that windowed the first and last blast generated signals measured

by the sensors. Each blast event's time history was then trimmed to contain data from only this window. As a result, the column "Time of Arrival" is measured relative to the arbitrarily selected start time of each shot's time history, not the actual detonation of a charge. The second column, "Positive Phase Duration", was simply taken as the time required for the initial positive pressure wave to decay to zero, regardless of whether or not this included one or more reflections. The column "Peak Pressure" was taken as the maximum pressure recorded by a given sensor, even if it occurred in a later reflected blast wave rather than the first reflected blast wave. The column "Positive Phase Impulse" was computed as an integral of pressure time histories using the trapezoidal rule. Appendix D contains the Matlab scripts used for post-processing and plotting sensor data.

TABLE 2.1: Shot A1 measured blast parameters.

Sensor	Time of Arrival (ms) [c]	Positive Phase Duration (ms)	Peak Pressure[e] MPa (psi)	Positive Impulse MPa ms (psi ms)
P1	41.9	1.7	5.437 (788.6)	1.257 (182.3)
P2	42.1	1.4	2.329 (337.8)	0.628 (91.1)
P3	42.7	2.8	0.8101 (117.5)	0.363 (52.6)
P4	46.5	6.8	0.483 (70.0) [a]	0.8301 (120.4)
P5	42.2	1.5	2.295 (332.9)	0.7384 (107.1)
P6	44.4	2.7	0.6964 (101.0)	0.341 (49.5)
P7	51.2	3.8	0.119 (17.3)	0.208 (30.1) [b]
P8	48.7	6.0	0.252 (36.6)	0.554 (80.3)
PP1	48.7	2.9	0.087 (12.6) [a]	0.437 (63.4) [b]

Notes for Tables 2.1 through 2.3:

a. Maximum pressure from secondary reflection.

b. Impulse computation includes at least one reflection from the floor, a wall, or the ceiling.

c. Arrival time is taken relative to arbitrary point in raw time series; however, the start time is the same for all sensors in a given shot.

d. Sensor manifested non-physical signals. Data integrity questionable.

e. Flush mount sensors measured reflected pressures while pressure pencils measured incident pressures.

NM. Channel malfunction, no measurements recorded.

TABLE 2.2: Shot A2 measured blast parameters.

Sensor	Time of Arrival (ms) [c]	Positive Phase Duration (ms)	Peak Pressure[e] MPa (psi)	Positive Impulse MPa ms (psi ms)
P1	196.7	1.8	3.605 (522.9)	0.9708 (140.8)
P2	197.2	1.9	3.466 (502.7)	0.7908 (114.7)
P3	197.8	2.1	1.064 (154.3)	0.468 (67.9) [b]
P4	201.5	6.7	0.515 (74.7) [a]	0.754 (109.4) [b]
P5	197.1	1.7	3.093 (448.6)	0.7798 (113.1)
P6	199.0	2.5	0.609 (88.3)	0.350 (50.8)
P7	205.3	3.9	0.160 (23.2)	0.458 (66.4) [b]
P8	203.0	5.1	1.068 (154.9) [a]	0.8763 (127.1) [b]
PP1	198.4	1.3	0.322 (46.7)	0.163 (23.6) [b]

TABLE 2.3: Shot B measured blast parameters.

Sensor	Time of Arrival (ms) [c]	Positive Phase Duration (ms)	Peak Pressure[e] MPa (psi)	Positive Impulse MPa ms (psi ms)
P1	100.5	0.5	10.999 (1595.4)	1.260 (182.7)
P2	100.8	1.6	1.500 (217.6)	0.593 (86.0)
P3	NM	NM	NM	NM
P4	101.0	1.5	1.850 (268.3)	0.627 (90.9)
P5 [d]	100.4	0.8	1.230 (178.4)	0.655 (95.0)
P6	103.1	7.2	1.060 (153.7)	1.061 (153.9) [b]
P7	101.7	1.9	1.050 (152.3)	0.872 (126.5)
P8	103.6	2.5	0.7257 (103.8)	0.590 (85.6) [b]
P9	103.9	3.0	0.468 (67.9)	0.565 (82.0) [b]
P10	112.5	1.6	0.167 (24.2) [a]	0.228 (33.1) [b]
P11	116.6	10.3	0.117 (17.0)	0.683 (99.1) [b]
P12	103.5	3.2	1.080 (156.6)	0.677 (98.2) [b]

Examining the data in Tables 2.1, 2.2, and 2.3 provides some insight into the performance of the explosive charges and the distribution of blast pressures. In shots A1 and A2, sensors P2 and P5 were located at the same elevation but on opposite sides of the charge. Table 2.1 shows that for blast A1, the pressure waves arrived at nearly the same time and were of similar magnitude at both P2 and P5 (1.5% difference in measured peak pressure and 17.6% difference in impulse). In shot A2, the charge was not radially symmetric, but Table 2.2 shows the time of arrival and duration at P2 and P5 were reasonably similar; the difference in measured peak pressure was 10.8% while the

difference in impulse was only 1.4%. For shot B, there were two pairs of sensors that were at the same elevation and standoff on opposite sides of the charge. Sensors P1 and P5 were equidistant from the charge and at an elevation of 44.5 cm above the floor. Unfortunately sensor P5 (or its cabling) malfunctioned and the data was deemed unreliable for comparison. Sensors P2 and P4 were also equidistant but at an elevation of 158.8 cm above the floor. For these sensors, the measured peak pressure difference was 23.3% and the impulse difference was 5.7%. These simple comparisons suggest that the distribution of blast energy was radially symmetric for all three shots, which would also imply that the charges detonated in an approximately symmetric manner.

With regard to the blast pressure distribution on a particular wall, it is only possible to examine the vertical distribution where groups of sensors were spaced vertically at the same horizontal distance from the charge. Figure 2.23 shows the reflected pressure data from sensors in each of the three shots. Sensors P1, P2, and P3 are plotted for shots A1 and A2 and only sensors P1 and P2 for shot B. On the horizontal axis, the peak reflected pressure is normalized to the measurement recorded by P1 (which was always maximum in all three shots, and thus 100%). The vertical axis is the height of the sensor above the blast chamber floor. The plot suggests that a linear reflected pressure distribution up the height of the blast chamber walls might be a reasonably accurate approximation, but there are too few data points to determine this conclusively.

A similar plot was constructed for the vertical distribution of reflected impulse. Figure 2.24 shows impulse data from all three shots using the same sensors as were used to construct Figure 2.23. On the horizontal axis the peak reflected impulse is normalized to the measurement at sensor P1 (which was always maximum in all three shots, and thus

100%). The vertical axis is the height of the sensor above the blast chamber floor. Again the data suggests a linear distribution of reflected impulse vertically might be a reasonable approximation, but as with pressure, there are too few data points to be conclusive.

The relatively similar pressure and impulse distributions observed in the A1 and B data might suggest that the distributions are only a function of the charge's shape and distance to reflecting surfaces (which was nearly identical for charges A1 and B), and not a function of charge mass. Note that the plots for A1 and B are nearly co-linear with regard to pressure and impulse. However the plot of A2 shows a "hump" near midheight. This might be explained by the unusual shape of the A2 charge (cylinder topped by a triangular prism) which produced a different pressure distribution than the other two charges. Chapter 5 will utilize computational simulations to study pressure and impulse distributions in greater detail.

As previously discussed, the acceleration time histories could not be satisfactorily integrated to obtain velocity or deflection time histories. Consequently, the primary use of acceleration data is to provide information regarding dominant structural frequencies. As shown in Tables 2.4, 2.5, and 2.6 none of the sensors registered over 4,000 g, and therefore the 100,000 g limit was a poor sensor choice. In comparing shots A1 and A2 (where accelerometers would have been mounted on nearly identical structures) one can see that shock sensors S1 and S2 recorded accelerations for both shots of similar order of magnitude. For shot B, accelerations are an order of magnitude higher which can be explained by the higher blast loading and the resulting larger structural deformations. Further analyses of the accelerometer data will be presented in Chapter 6, where

measured natural frequencies will be compared to the natural frequencies estimated as part of the ESDOF analyses.

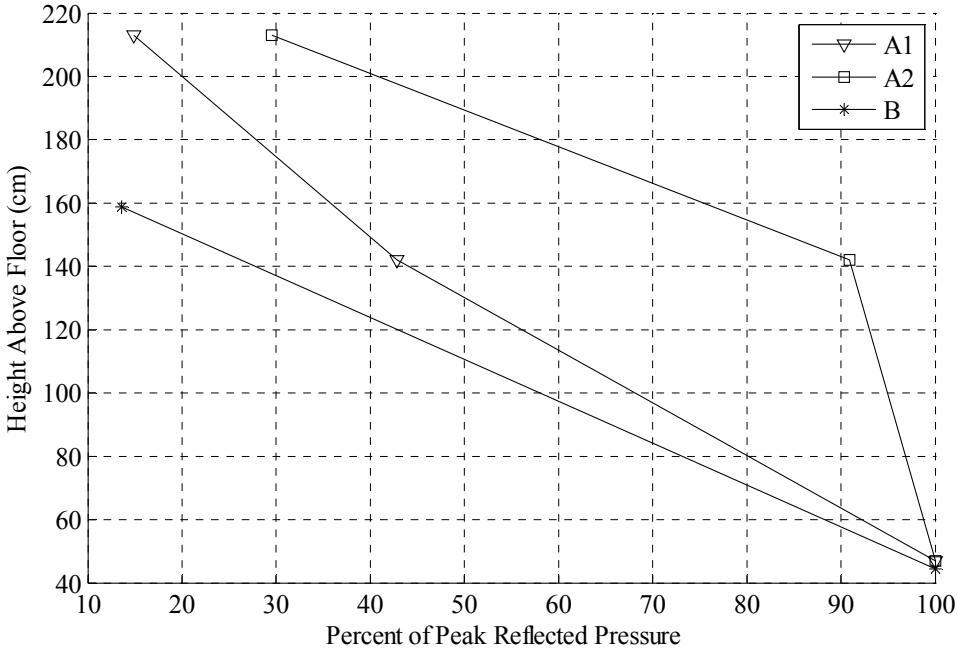

FIGURE 2.23: Vertical peak reflected pressure distributions from all three shots.

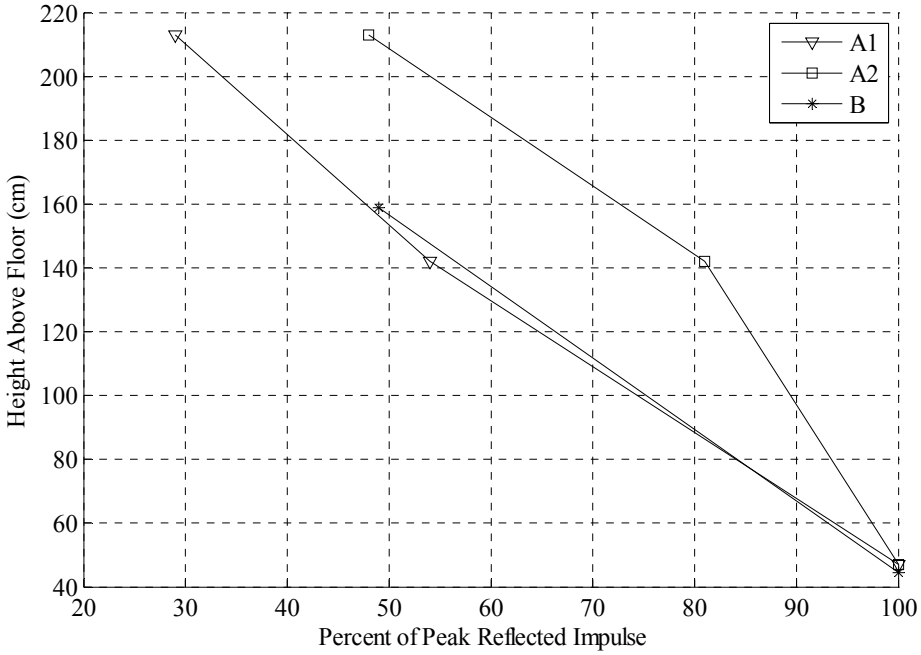

FIGURE 2.24: Vertical peak reflected positive phase impulse distribution from all three shots.

TABLE 2.4: Peak accelerations and natural frequencies processed from Shot A1 data.

Sensor	Peak Acceleration (g)	First Mode (Hz)	Second Mode (Hz)	Third Mode (Hz)	Fourth Mode (Hz)
S1	-39.9/+72.0	6.25	16.3	28.8	40.0
S2	-255.9 / +89.6	6.56	13.8	28.8	38.8
S3	-3380/3976	7.5	42.5	56.3	81.25

TABLE 2.5: Peak accelerations and natural frequencies processed from Shot A2 data.

Sensor	Peak Acceleration (g)	First Mode (Hz)	Second Mode (Hz)	Third Mode (Hz)	Fourth Mode (Hz)
S1	-64.7/+195	0.8	3.2	5.2	13.2
S2	-43.1/+103.5	2.0	2.8	4.4	6.0

TABLE 2.6: Peak accelerations and natural frequencies processed from Shot B data.

Sensor	Peak Acceleration (g)	First Mode (Hz)	Second Mode (Hz)	Third Mode (Hz)	Fourth Mode (Hz)
S1	-2195/+1174	4.3	12.7	29.0	71.7
S2	-79.7/+151.5	5.0	56.0	N/A	N/A
S3	-1669/+2782	4.7	36.4	59.7*	68.7
S4	-99/+230.5	3.7	19.3	60.3*	81.3
S5	NM	NM	NM	NM	NM

*Frequency spike likely from nearby power lines

CHAPTER 3: ENGINEERING LEVEL BLAST LOAD PREDICTION

Chapter 1 illustrated that there are a variety of methods that may be used to predict airblast loading. Before proceeding to computational methods, it is of interest to at least attempt using simple (so called engineering level) analysis methods. These are the tools and techniques that would typically be employed by engineers engaged in the design of blast resistant facilities. Advanced tools like computational fluid dynamics (CFD) codes are expensive with respect to time and money and few structural engineers have access to or the know-how to utilize them. It is therefore of interest to study the accuracy of engineering level analysis tools applied to two different airblast scenarios relevant to this investigation. The comparisons that follow will help show why it was of interest to employ more advanced computational modeling techniques.

The first airblast scenario consists of data collected during an ISERRT Facility (Infrastructure Security and Emergency Responder Research and Training Facility) explosive yield study. The ISERRT data consists of fifteen airblast measurements (incident pressures and impulses) collected during nine different blast events in which bundled cylinders of Unimax dynamite were detonated near the ground's surface in an open arena. These blast tests provide a relatively simple scenario for which to compare predicted and measured blast wave parameters. As an added benefit, the explosive charges were

very similar to those used in shots A1 and B described in Chapter 2. The second scenario is the A1 blast event described in Chapter 2. This scenario is more complex as it includes oblique reflections and the potential for gas phase pressure. Engineering level methods will be used to predict the airblast parameters measured during both of these experiments to assess the accuracy of these simple predictive techniques.

The most rudimentary airblast parameter prediction involves the use of nomographs derived from hundreds of blast tests of Trinitrotoluene (TNT) spheres or hemispheres (Kingery and Bulmash (1984) is the source for many nomographs). From these nomographs, airblast parameters can be quickly computed. The computed incident airblast parameters are then used with reflection coefficient charts that account for shock strength and angle of incidence to translate incident pressures and impulses into reflected pressures and impulses.

Conveniently, these nomographs have been electronically implemented in two software programs written by USACE. ConWep (2005) is the de-facto analysis program used throughout the Army for computing blast wave parameters resulting from hemispherical surface bursts and spherical free air bursts. BlastX (2006), a more advanced software program, is designed to compute shock and gaseous phase blast loads in confined environments produced by spherical, hemispherical, or cylindrical charges. ConWep and BlastX will be applied to both of the previously described airblast scenarios.

Before proceeding with the analyses, it is worth pausing for a moment to discuss the selection of blast prediction methods utilized in this investigation. Chapter 1 showed

there are many airblast prediction methods. With respect to nomographs for hand computation, engineers use those from Kinney and Graham (1985), UFC 3-340-02 (USACE, 2008d), UFC 3-340-01 (USACE, 2002), Kingery and Bulmash (1984), and an array of journal articles with empirically derived equations. Similarly, with respect to software tools engineers can use ConWep, BlastX, SHOCK (NAVFAC, 2005), and FRANG (NAVFAC, 1989). Experience has shown that different branches of government have differing opinions on which tool is the "best" for the job. In the past, the author has seen USACE use ConWep, BlastX, and SHOCK – all for the same analysis. Given this diverse set of tools and conflicting opinions on what constitutes best practice, how is an engineer to select one tool/method over another?

As an answer to this question Bogosian et al. (2002) published a clear and enlightening comparison between many of these tools. In their paper, the authors first compare the Kingery and Bulmash (1984) curve fits to any reliable airblast data that could be obtained. The comparison showed that Kingery and Bulmash's (KB) curve fits are indeed a good representation of TNT airblast data and its use as the standard is well founded. UFC 3-340-01 and UFC 3-340-02 are based on the KB data and should therefore also be given precedent over other references like Kinney and Graham (1985).

With respect to software tools, Bogosian et al. (2002) found that ConWep most accurately represented the KB curve fits while the other tools showed error relative to the KB standard. With regard to positive reflected pressure, the study showed that, compared to the test data, BlastX predicted the highest pressures, SHOCK the lowest, and ConWep represented the average. With regard to reflected positive impulse, SHOCK predicted the

highest impulses while ConWep and BlastX predicted similar, but lower impulses more in agreement with test data. Comparing Bogosian's findings to past experience, the author believes that DoD agencies likely specify the software tool to be used on a project based on which one provides the most conservative answer, regardless of its accuracy relative to test data. Based on this information, ConWep and BlastX were selected as the analysis tools which were likely to be the most accurate.

3.1. Equivalent Explosive Weight

Before using these software programs, it is first necessary to develop a mass equivalency factor which translates a unit weight of Unimax dynamite into an equivalent weight of TNT. This equivalency factor is required because different explosive compounds have different chemical compositions, different detonation velocities, and different energy contents. Thus, one kilogram of dynamite does not produce the same airblast as one kilogram of TNT. There are several methods of determining weight equivalency, but the most straightforward is an equivalency based on the ratio of the energy of Unimax to the energy of TNT at their standard densities (TNT's reference density is 1.63 grams per cubic centimeter, Unimax's is 1.5 grams per cubic centimeter).

At this juncture it is necessary to define terminology used to describe the energy content of explosive materials. Perusing any reference text like Kinney and Graham (1985) or Cooper (1996) the reader will encounter a number of terms including "chemical energy," "available energy," "specific energy," "thermodynamic work function," "hydrodynamic work function," "energy of explosion," "heat of combustion," or "heat of detonation." Clearly, the type of "energy" under consideration must be carefully defined

as it has a very specific meaning that describes how the energy was computed or measured. Experience has shown that practitioners use these terms interchangeably, sometimes without regard for their correctness. Substituting one term for another is not technically correct; however it can be an acceptable estimate for certain explosives for which these quantities are approximately equal. For example, Cooper (1996) reports the heat of detonation of TNT as 1089 cal/g, the thermodynamic work function as 1160 cal/g, and the experimentally measured energy content to be 1120 cal/g. Kinney and Graham (1985) report the theoretically derived energy of explosion to be 1158 cal/g and the experimentally measured energy to be 1118 cal/g. These energies all report the same quantity – the energy released during a detonation.

Four of these energy definitions have relevance to this investigation and are worth expounding upon. The heat of combustion is found by a bomb calorimeter test. In this test, a small amount of the explosive material under study is burned inside a sealed chamber with sufficient oxygen and water to permit the material to react completely, liberating all energy that could be feasibly released. The heat of detonation is similarly measured in an inert (e.g. Nitrogen) atmosphere without any water; this attempts to mimic the conditions that occur during a detonation. The heat of combustion is therefore larger than the heat of detonation due to the additional energy released as combustion products react with oxygen and water to form stable compounds. The difference between the heat of combustion and the heat of detonation is termed the heat of afterburn and is the energy released by the fireball following most explosions. Finally, the hydrodynamic work function is computed as the integral of the expansion isentrope of the detonation

product gases as they expand from the point of detonation to atmospheric pressure. It is usually derived from the equation of state of the detonation product gases which will be discussed at length in a subsequent chapter. Given the variety of available energy definitions it is important that the energy of the explosive material under consideration was found in the same manner as that for TNT. So, for example, comparing the heat of combustion to the heat of detonation would produce a misleading energy equivalence.

Table 3.1 provides two estimates of the energy equivalency factor for Unimax dynamite. The first equivalency was computed using the energy (heat of detonation) of Unimax. The second equivalency was taken from UFC 3-340-01 and is for 20% strength dynamite. The difference in equivalencies is quite large and this investigation will use the 0.94 equivalence computed using heats of detonation because the UFC 3-340-01 equivalence factor likely does not account for the additional energetic materials included in Unimax (e.g. ammonium nitrate). In some instances, references will provide both an impulse equivalence and a pressure equivalence factor. Without extensive airblast testing it is not possible to determine different equivalence factors for pressure and impulse and we must therefore rely exclusively on the energy equivalence.

BlastX can directly utilize equivalent TNT weight along with built in airblast models of cylindrical bombs (which are based on extensive test data and/or CFD simulations). ConWep, on the other hand, requires the user make adjustments to charge properties to account for charge geometry as it only natively models spheres or hemispheres of TNT. Esparza (1992) provides such an adjustment methodology to translate a cylindrical charge into an equivalent spherical charge for use in ConWep. To

develop this equivalency, Esparza compared free air test data (pressures and impulses) from cylindrical bombs to those of spherical bombs. He used this data to compute the weight of a spherical TNT bomb that would produce the same pressure or impulse as a given cylindrical TNT bomb.

TABLE 3.1: Estimated TNT equivalency of UNIMAX dynamite.

Reference Charge Weight	Internal Energy (cal/g) [a]	Energy Equivalence Factor	Equivalent Weight TNT (kg)	UFC 3-340-01 Equivalence Factor[b]	Equivalent Weight TNT (kg)
Unimax 1 kg	1055	0.94	0.94	0.70	0.70
Standard TNT 1 kg	1120	1.0	1.0	1.0	1.0

Notes:
a. Data for Unimax from manufacturer, data for TNT from Cooper (1996). Heats of detonation.
b. Assumes dynamite classified as 20% strength.

Esparza provides this information for several different azimuth angles (azimuth angle is defined as the vertical angle between the horizontal and a radial line extending from the charge center of gravity to the point of interest). He found that for an azimuth angle of zero degrees (the measurement point is at the same elevation as the center of gravity of the charge), the spherical equivalency factor could be as high as three or as low as one, decreasing as you get progressively further away from the charge; the equivalency factor is defined as the weight of the equivalent spherical bomb divided by the weight of the real cylindrical bomb. Section 3.2 will document the application of BlastX, ConWep, and Esparza's equivalency to the free air test data provided by the ISERRT study. Section 3.3 will perform similar comparisons to data from Shot A1.

3.2. Free Air Tests – Experiments versus Predictions

This section will document the experimental airblast data collected during the ISERRT study and compare these measurements to predictions made using ConWep and BlastX. Table 3.2 provides a summary of the charge weight (gross weight as measured by a scale), height of burst (measured from the ground to charge center of gravity), the standoff from the pressure sensor, and the measured incident pressures and impulses. Incident pressures were measured using PCB model 137A21 free air pressure pencils. Signal conditioning for the free air pencils was provided by PCB model 483C signal conditioners which were configured for DC coupling. Data was recorded at a rate of 100 kHz using the National Instruments system described in Section 2.1, with on-board signal conditioning and AC coupling (high pass filtration) disabled. Impulses were computed as the numerical integrals (using the trapezoidal rule) of the pressure time histories measured by the free air pencils.

All dynamite charges were composed of sticks of Unimax bundled together with electrical tape. Each stick measured 20.3 cm (8 in) tall by 3.175 cm (1.25 in) in diameter. Each stick weighed approximately 0.231 kg (0.51 lb). The bombs were detonated from the top center using shocktube driven blasting caps and a small high explosive booster. All charges rested on small timber stands or were affixed to timber poles to achieve the desired height of burst. The EY series of charges represent the closest approximation to free air tests as they had no reflecting surfaces present other than the ground. The BV, BPS, and BPG tests used the cylindrical bombs to generate blast loads on test specimens,

but the test arena geometry and sensor locations were such that there should be little to no impact on the free air measurements presented in the table.

Table 3.2 shows that for blast measurements made at the same distance on similarly sized charges, the measured blast parameters are relatively consistent and repeatable. There is only one significant discrepancy visible in the data. Shots BV-5 and BPS-7 both had a charge size of approximately 1.43 kg. In BPS-7, the free air pencil was further from the charge than in BV-5. One would therefore expect the pressure and impulse to be greater in shot BV-5 than in BPS-7. But the data clearly shows that the opposite is true. Simplified hand calculations showed that neither oblique reflections from the ground nor the formation of a Mach stem can explain the observed discrepancy. One explanation is that the charge in BV-5 was directly affixed to a 2x4 timber while charge BPS-7 rested on a table on the ground. Thus, BV-5 might have lost energy in splintering the 2x4 support timber while BPS-7 did not. Although there is no direct comparison available in the test data, the same is likely true of the BV-4 measurements.

Another point worth briefly discussing is the behavior of bundled dynamite charges as compared to a solid, cast TNT charge. In the very near field (within several charge diameters) the bundled dynamite sticks likely created a highly irregular blast waveform. Examination of the measured blast waveforms show, however, that by the time the blast waves arrived at the pressure sensors they had the appearance of an ideal blast overpressure waveform. Insufficient data has been collected to identify the distance from the charge at which the effect of stick bundling becomes critical. It seems,

however, that for all shots in this investigation measurements were taken at least this far from the charges and the effect of bundling sticks together may be ignored.

TABLE 3.2: Summary of free air data for cylindrical UNIMAX charges.

Shot	Sensor	Charge Weight[a] kg (lbs)	Standoff cm (in)	Height Of Burst[b] cm (in)	Incident Pressure kPa (psi)	Incident Impulse kPa ms (psi ms)
EY-1	PP1	0.953 (2.10)	308.6 (121.5)	30.5 (12.0)	72.5 (10.5)	52 (7.6)
EY-1	PP2	0.953 (2.10)	226.1 (89.0)	30.5 (12.0)	131 (19.0)	71.6 (10.4)
EY-2	PP1	0.953 (2.10)	313.1 (123.25)	30.5 (12.0)	77.2 (11.2)	52 (7.5)
EY-2	PP2	0.953 (2.10)	226.1 (89.0)	30.5 (12.0)	143 (20.7)	74.3 (10.8)
EY-3	PP1	0.953 (2.10)	304.8 (120)	30.5 (12.0)	80.7 (11.7)	54 (7.8)
EY-3	PP2	0.953 (2.10)	224.8 (88.5)	30.5 (12.0)	152 (22.0)	74.5 (10.8)
BV-4	PP1	0.234 (0.515)	203.8 (80.25)	213.4 (84.0)	49 (7.2)	15 (2.1)
BV-4	PP2	0.234 (0.515)	218 (86.0)	213.4 (84.0)	35 (5.1)	18 (2.6)
BV-5	PP2	1.43 (3.15)	220.3 (86.75)	213.4 (84.0)	131 (19.0)	78.4 (11.4)
BPS-7	PP2	1.45 (3.20)	308.6 (121.5)	30.5 (12.0)	185 (26.9)	101 (14.6)
BPS-10	PP1	1.91 (4.20)	293.4 (115.5)	50.8 (20.0)	134 (19.4)	98.4 (14.3)
BPS-10	PP2	1.91 (4.20)	297.8 (117.25)	50.8 (20.0)	142 (20.6)	90.4 (13.1)
BPS-12	PP1	2.37 (5.23)	313.7 (123.5)	50.8 (20.0)	201 (29.1)	N/A[c]
BPS-12	PP2	2.37 (5.23)	309.9 (122.0)	50.8 (20.0)	146 (21.2)	N/A[c]
BPG-14	PP1	1.91 (4.20)	297.2 (117.0)	50.8 (20.0)	145 (21.0)	89.7 (13.0)

Notes:
a. Gross weight as measured in field using a scale.
b. Measured from the ground to charge center of gravity.
c. Sensor malfunction prevented impulse integration.

Table 3.3 provides a comparison between the experimental incident blast wave parameters summarized in Table 3.2 and those predicted by BlastX. In BlastX, there are several options available for cylindrical charges. The best results were obtained using the "cylindrical tabular" model with a bare TNT cylinder with a length to diameter ratio of 1.0. Other models such as the "EMRTC Low Height of Burst" were investigated, but their results were significantly worse. The BlastX help file indicates that the cylindrical tabular model was created through parametric CFD studies, rather than experiment.

TABLE 3.3: Comparison between incident pressures and impulses predicted by BlastX compared to experimental measurements.

Shot	Sensor	Equivalent TNT Charge[a] kg (lbs)	Predicted Pressure[d] kPa (psi)	Percent Error[b]	Predicted Impulse[d] kPa ms (psi ms)	Percent Error[b]
EY-1	PP1	0.806 (1.78)	104 (15.1)	43.5	42.1 (6.1)	-20
EY-1	PP2	0.806 (1.78)	219 (31.7)	66.5	52.6 (7.6)	-27
EY-2	PP1	0.806 (1.78)	101 (14.7)	31.4	41.6 (6.0)	-20
EY-2	PP2	0.806 (1.78)	219 (31.7)	53.0	52.6 (7.6)	-30
EY-3	PP1	0.806 (1.78)	107 (15.5)	32.5	42.4 (6.2)	-21
EY-3	PP2	0.806 (1.78)	225 (32.6)	48.0	52.8 (7.7)	-29
BV-4	PP1	0.198 (0.436)	50 (7.3)	1.9	26.2 (3.8)	81
BV-4	PP2	0.198 (0.436)	44 (6.4)	27	24.8 (3.6)	38
BV-5	PP2	1.21 (2.66)	177 (25.6)	34.9	73.8 (10.7)	-6.5
BPS-7	PP2	1.23 (2.71)	114 (16.6)	-38.2	125 (18.1)	24
BPS-10	PP1	1.62 (3.55)	175 (25.4)	30.7	64.9 (9.4)	-34
BPS-10	PP2	1.62 (3.55)	170 (24.6)	19.3	64.1 (9.3)	-29
BPS-12	PP1	2.01 (4.42)	179 (25.9)	-38.0	70.3 (10.2)	-59
BPS-12	PP2	2.01 (4.42)	184 (26.7)	-24.3	71.0 (10.3)	-50
BPG-14	PP1	1.62 (4.20)	170 (24.7)	17.8	64.2 (9.3)	-28
			Average Absolute Error[c]	37		28

Notes:
a. Equivalent charge weight computed as gross charge weight multiplied by 0.94 for energy equivalence and 0.90 to account for inert packaging weight.
b. Positive error indicates predicted quantity greater than measured quantity.
c. BV-4 and BV-5 not included in average absolute error computation.
d. Predictions made using order of rays equal to 5.

As Table 3.3 shows, BlastX tended to over predict incident pressures while under predicting impulses. This might be of concern if used for structural design, as it is often desirable to over predict impulses rather than pressures due to the impulse sensitivity of many structural elements. Note that this statement is only true in a general sense. For any given component, there are actually an infinite number of pressure-impulse combinations that will produce the same peak response (deflection, rotation, resistance, etc). The relationship between blast pressure and impulse for a consistent level of response can be conveniently visualized on a pressure-impulse (P-I) diagram which shows a line of constant response plotted in pressure-impulse space. It is interesting to note that the BlastX predictions significantly overestimate the impulse for the BV-4 test while underestimating the impulse for all of the other tests. This lends credibility to the theory that the BV series had a reduced explosive output as a result of work done in splintering timber supports.

Given the errors observed in the BlastX comparisons, it was desirable to investigate ConWep as an alternative. As previously discussed, in order to use ConWep it was necessary to calculate spherical equivalency factors using Esparza's (1992) method. Table 3.4 provides a summary of this process, listing the equivalency factors for pressure and impulse (the new weight of an equivalent spherical charge is computed as the original equivalent TNT charge weight multiplied by Esparza's equivalency factor). Note that the column "Equivalent TNT Charge" is the original Unimax charge weight multiplied by 0.94 to account for energy equivalence and by 0.90 to account for packaging weight.

Table 3.5 compares airblast predictions made using ConWep (with the spherical free air burst option and the spherical equivalency data in Table 3.4) to the experimental data from Table 3.2. As with the BlastX predictions, the BV series of tests had the highest errors, grossly overpredicting both pressure and impulse. This lends further credence to the idea that the timber supports used in the BV series of tests absorbed energy that would have otherwise gone into blast wave formation. Comparing the ConWep and BlastX analyses, ConWep is significantly more accurate. ConWep's greater accuracy was partially expected because, as previously discussed, ConWep was found to be an accurate representation of the original test data used to create the software (Bogosian et al., 2002). ConWep also appears to normally over predict both incident pressure and impulse, making it a suitably conservative design tool. In studying the errors in Table 3.5, particularly the EY series of tests, it does not appear that any adjustments to assumed equivalency factors (for either energy or Esparza's shape conversion method) would be of benefit as errors are relatively low and well within the bounds of normal expectation (as defined in Bogosian et al., 2002).

TABLE 3.4: Equivalency factors to convert cylindrical charge to spherical charge of TNT.

Shot	Sensor	Equivalent TNT Charge[a] kg (lbs)	Standoff m (ft)	Scaled Distance $m/kg^{1/3}$ ($ft/lb^{1/3}$)	Pressure Equivalence Factor[b]	Impulse Equivalence Factor[b]
EY-1	PP1	0.806 (1.78)	3.09 (10.1)	3.32 (8.36)	1.16	1.08
EY-1	PP2	0.806 (1.78)	2.26 (7.42)	2.43 (6.12)	1.35	1.07
EY-2	PP1	0.806 (1.78)	3.13 (10.3)	3.36 (8.47)	1.16	1.08
EY-2	PP2	0.806 (1.78)	2.26 (7.42)	2.43 (6.12)	1.35	1.07
EY-3	PP1	0.806 (1.78)	3.05 (10.0)	3.28 (8.25)	1.16	1.09
EY-3	PP2	0.806 (1.78)	2.25 (7.38)	2.42 (6.10)	1.37	1.07
BV-4	PP1	0.198 (0.436)	2.04 (6.69)	3.50 (8.82)	1.16	1.06
BV-4	PP2	0.198 (0.436)	2.18 (7.17)	3.74 (9.46)	1.17	1.03
BV-5	PP2	1.21 (2.66)	2.20 (7.23)	2.07 (5.22)	1.59	1.08
BPS-7	PP2	1.23 (2.71)	3.09 (10.1)	2.88 (7.27)	1.14	1.10
BPS-10	PP1	1.62 (3.55)	2.93 (9.63)	2.50 (6.31)	1.31	1.08
BPS-10	PP2	1.62 (3.55)	2.98 (9.77)	2.54 (6.41)	1.30	1.08
BPS-12	PP1	2.01 (4.42)	3.14 (10.3)	2.49 (6.27)	1.33	1.08
BPS-12	PP2	2.01 (4.42)	3.10 (10.2)	2.46 (6.20)	1.35	1.08
BPG-14	PP1	1.62 (4.20)	2.97 (9.75)	2.53 (6.04)	1.37	1.07

Notes:

a. Equivalent charge weight computed as gross charge weight multiplied by 0.94 for energy equivalence and 0.90 to account for inert packaging weight.

b. Equivalency factors are taken from charts contained in Esparza (1992) and are along radial lines emanating from charge c.g. at 90 degrees to cylindrical charge wall.

TABLE 3.5: Pressures and impulses predicted by ConWep using spherical equivalency method of Esparza (1992).

Shot	Sensor	Predicted Pressure kPa (psi)	Percent Error[b]	Predicted Impulse kPa ms (psi ms)	Percent Error[b]
EY-1	PP1	73.6 (10.7)	1.5	58 (8.3)	9.8
EY-1	PP2	158 (22.9)	20.4	75.3 (10.9)	5.1
EY-2	PP1	71.6 (10.4)	-7.1	56 (8.1)	8.0
EY-2	PP2	158 (22.9)	10.6	75.3 (10.9)	1.4
EY-3	PP1	75.6 (11.0)	-6.3	59 (8.5)	8.6
EY-3	PP2	162 (23.5)	6.5	75.6 (11.0)	1.5
BV-4	PP1	66 (9.6)	34	34 (4.9)	131
BV-4	PP2	58 (8.4)	67	31 (4.5)	76.7
BV-5	PP2	255 (37.0)	94.9	99.8 (14.5)	27.4
BPS-7	PP2	97.0 (14.1)	-47.6	75.8 (11.0)	-24.7
BPS-10	PP1	145 (21.0)	8.1	92.8 (13.5)	-5.7
BPS-10	PP2	139 (20.2)	-2.0	91.6 (13.3)	1.3
BPS-12	PP1	148 (21.5)	-48.5	100 (14.6)	-41.1
BPS-12	PP2	154 (22.3)	-36.8	101 (14.7)	-27.9
BPG-14	PP1	164 (23.9)	13.8	101 (14.7)	13.0
Average Absolute Error[a]			17.4		12.3

Notes:
a. BV series of tests excluded from average absolute error computation.
b. Positive error indicates predicted quantity greater than measured quantity.

Note that the results in Table 3.5 do not include reflections from the ground or Mach stem effects. BlastX treats these reflections as part of its formulation, but ConWep does not. The case of a "near surface burst" is difficult to analyze using simplified tools like ConWep. A near surface burst's apparent blast energy output for an observer near ground level will be higher than a free air burst, but lower than a surface burst. Using the provisions of UFC 3-340-02, the scaled height of burst (height of burst divided by charge weight to the one third power) was used with Figure 2.13 (from the UFC) to compute the expected height of the triple points for all shots. The UFC predicts that the triple point should have been above the height of the sensors for all shots except BV-4 and BV-5. An

examination of the experimental data showed this to be true as only a single incident pressure spike was measured in all shots except BV-4 and BV-5. As an example, Figure 3.1 shows the pressure time history of sensor PP1 from shot BPG-14.

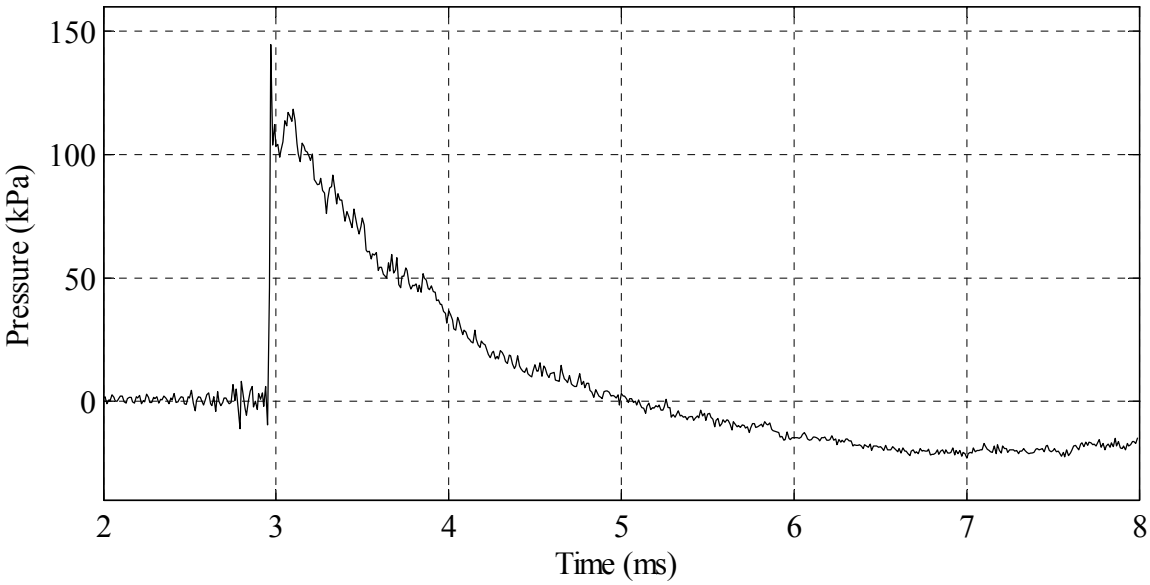

FIGURE 3.1: Incident pressure time history of sensor PP1 from shot BPG-14. No ground reflections are visible in the time history, suggesting sensor was below the triple point.

It was of interest to see the effect of including the Mach stem on predicted pressures and impulses. Unfortunately, ConWep does not offer any method by which to incorporate the effects of a Mach stem. In order to calculate the incident shock parameters in the Mach stem (below the triple point), it is necessary to use Figures 2.9 and 2.10 from UFC 3-340-02. The charts are primarily intended for spherical free air bursts of TNT. Without any other convenient method to account for cylindrical charge geometry, Esparza's equivalency factors were used again and are the same as documented in Table 3.4. Table 3.6 shows the results of this analysis. The table shows

that utilizing standardized guidance for the Mach stem in this case significantly overestimates incident pressures and impulses. This might suggest that if pressures must be accurately estimated for a near surface burst, it would be best to use ConWep and the Esparza coefficients. If a conservative design estimate must be made, then using Esparza's coefficients with standard Mach stem calculations is recommended.

TABLE 3.6: Pressures and impulses predicted by UFC 3-340-02 Figures 2.9 and 2.10 for Mach stem region using spherical equivalency method of Esparza (1992).

Shot	Sensor	Predicted Pressure kPa (psi)	Percent Error	Predicted Impulse kPa ms (psi ms)	Percent Error
EY-1	PP1	108 (15.7)	49.5	109 (15.8)	110
EY-1	PP2	250 (36.3)	91.1	136 (19.7)	89.4
EY-2	PP1	104 (15.1)	34.8	108 (15.7)	110
EY-2	PP2	250 (36.3)	75.4	136 (19.7)	82.4
EY-3	PP1	108 (15.7)	34.2	110 (16.0)	110
EY-3	PP2	251 (36.4)	65.5	137 (19.8)	83.3
BPS-7	PP2	217 (31.5)	17.1	165 (23.9)	63.7
BPS-10	PP1	306 (44.4)	129	199 (28.8)	101
BPS-10	PP2	298 (43.2)	110	197 (28.6)	118
BPS-12	PP1	276 (40.1)	4.1	237 (34.4)	39.3
BPS-12	PP2	285 (41.4)	17.3	224 (32.5)	59.3
BPG-14	PP1	316 (45.8)	118	223 (32.3)	148
		Average Error	+62.2		+92.9

Note: BV series not included because sensors above triple point

As a point of interest, it is instructive to visualize what a Mach stem looks like in terms of traveling pressure waves. Figure 3.2 is a series of images taken from a CTH simulation which will be discussed more in Chapter 5. This simulation is for the BPG-14 blast event. In the images, the pressure sensor is shown as a white dot, the triple point shown as a white triangle, and the path of the triple point as a white dotted line. The series of images graphically demonstrate how the triple point moves with time and how it

would affect the results of an airblast analysis. It is interesting that, in this case, CTH predicted the triple point passes just below the sensors while the experimental data (Figure 3.1) show that the triple point was above the sensors. No cause for this discrepancy could be readily identified.

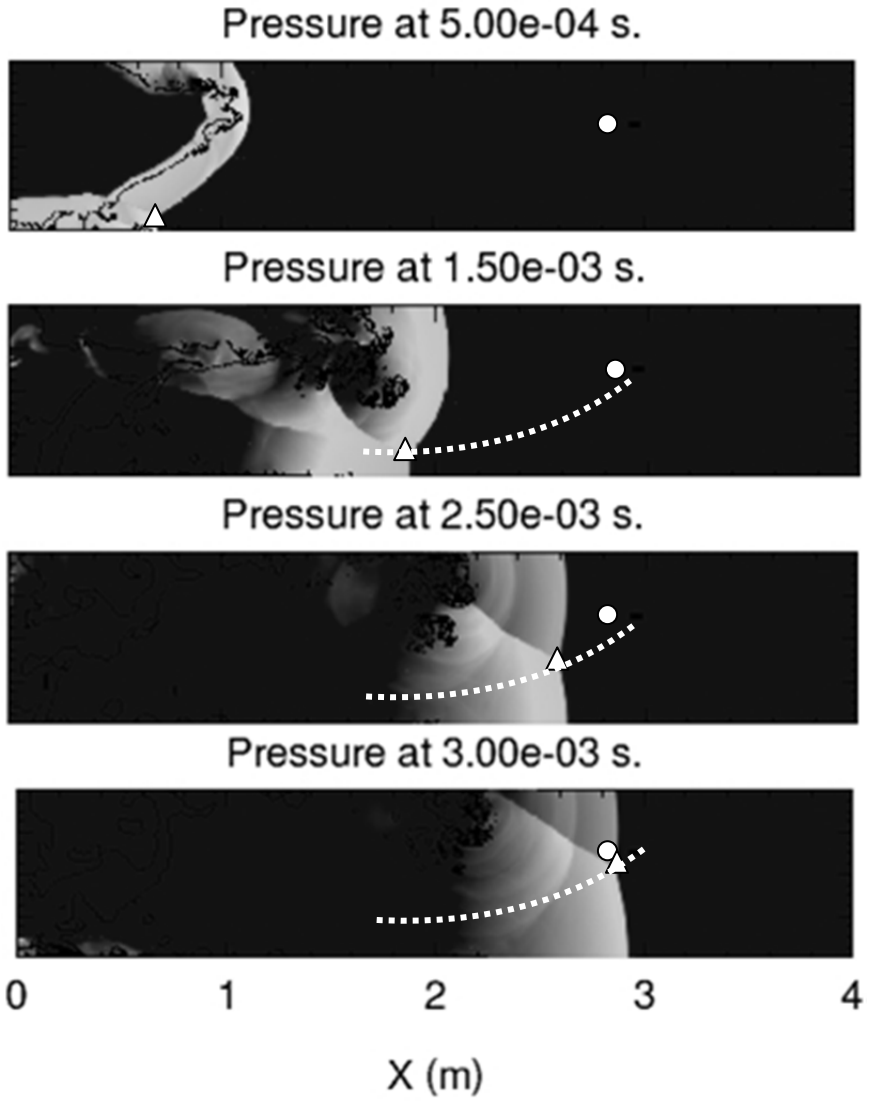

FIGURE 3.2: Plots of pressure from four different times in a two-dimensional cylindrical CTH simulation of shot BPG-14. Pressure is contoured from high (white) to low (black). White circle is pressure sensor. White triangle is location of triple point. Dotted line is path of the triple point.

As a final exercise, it is of interest to see whether or not modeling the near surface burst as a surface burst would provide an improvement in accuracy. This was done using the surface burst module of ConWep. No cylindrical equivalency factors were used and the charge weight was as shown in the second column of Table 3.4. Table 3.7 shows the surface burst analysis predictions for the arena test data. The table shows this leads to higher predicted blast loads relative to the coupled Esparza-Conwep method, but lower blast loads than accounting for the effect of the Mach stem. In comparing the three predictive methods attempted, it appears as though assuming a free air burst and applying Esparza's equivalency factors yields the best results for this particular scenario.

TABLE 3.7: Pressures and impulses predicted by ConWep using a surface burst option along with the equivalent TNT charge weights listed in the second column of Table 3.4.

Shot	Sensor	Predicted Pressure kPa (psi)	Percent Error[b]	Predicted Impulse kPa ms (psi ms)	Percent Error[b]
EY-1	PP1	(13.6)	29.5	(11.5)	51
EY-1	PP2	(26.5)	39.5	(15.1)	45
EY-2	PP1	(13.3)	18.8	(11.3)	51
EY-2	PP2	(26.5)	28.0	(15.1)	39.8
EY-3	PP1	(14.0)	19.7	(11.6)	48.7
EY-3	PP2	(26.8)	21.8	(15.2)	40.7
BV-4	PP1	(12.2)	69	(6.9)	230
BV-4	PP2	(10.7)	110	(6.4)	150
BV-5	PP2	(38.5)	103	(20.1)	76.3
BPS-7	PP2	(18.3)	32.0	(14.9)	2.06
BPS-10	PP1	(24.8)	27.8	(18.5)	29.4
BPS-10	PP2	(24.0)	16.5	(18.3)	39.7
BPS-12	PP1	(25.2)	-39.7	(20.1)	-18.6
BPS-12	PP2	(25.8)	-26.9	(20.3)	-0.49
BPG-14	PP1	(27.3)	30.0	(20.4)	56.9
Average Absolute Error[a]			27.5		32.4

Notes:
a. BV series of tests excluded from average absolute error computation.
b. Positive error indicates predicted quantity greater than measured quantity.

3.3. Shot A1–Experiment versus Predictions

As shown in Section 3.2, ConWep can be very accurate and BlastX less so when predicting the airblast generated by cylindrical charges of Unimax dynamite in an open arena test. As a different (and more complex) comparison, both programs were used to predict the airblast pressures and impulses measured during the A1 blast event described in Chapter 2. It is a relatively cumbersome process to use ConWep for this particular analysis. First, blast chamber geometry and sensor locations were used to develop spherical equivalency factors using the method of Esparza et al. (2002). The results of this preparatory work are shown in Table 3.8 (refer to Figure 2.5 for a plan view of the A1 blast chamber). Based on the Mach reflection analysis shown in Table 3.6, the ConWep analysis will not take into account any secondary reflections from the blast chamber floor. This approach was taken partly because the inclusion of Mach stem and ground reflection effects increased rather than decreased errors. The approach was also of interest because BlastX should capture this phenomena automatically due to its formulation, and it is of interest to see the comparison between the two programs with and without ground reflections.

The equivalency factors, the blast chamber geometry, and the sensor locations were then used with ConWep's slab loading module (set to free air burst, not hemispherical surface burst) to predict the reflected pressure and impulse at each sensor location. These predictions are compared to airblast measurements from the A1 blast event in Table 3.9. The table shows that ConWep coupled with Esparza's method does not yield accurate predictions for this scenario; the software consistently under predicted

both pressure and impulse. This is in contrast to the ConWep comparisons documented in Section 3.2, which had much better agreement with experimental data. This discrepancy suggests that the added complications of azimuth angle and oblique shock reflection reduce the accuracy of the coupled Esparza-ConWep method.

TABLE 3.8: Esparza's spherical equivalency factors for use with ConWep.

Sensor	Slant Distance cm (in)	Azimuth Angle degrees	Scaled Distance[a] $m/kg^{1/3}$ ($ft/lb^{1/3}$)	Pressure Equivalency Factor[b]	Impulse Equivalency Factor[b]
P1	255.6 (100.6)	0.0	1.45 (3.64)	2.5	1.75
P2	272.3 (107.2)	20.2	1.54 (3.88)	1.15	0.95
P3	302.9 (119.3)	32.5	1.71 (4.32)	0.78	0.90
P4	503.8 (198.4)	86.5	2.85 (7.18)	0.8	1.2
P5	273.2 (107.6)	20.7	1.55 (3.90)	1.1	0.95
P6	429.8 (169.2)	12.8	2.43 (6.13)	1.1	1.2
P7	779.4 (306.8)	7.0	4.41 (11.1)	1.1	1.2
P8	608.7 (239.6)	55.7	3.44 (8.68)	0.75	1.2
PP1	365.8 (144.0)	0.0	2.07 (5.22)	1.75	1.2

Notes:
a. Charge weight computed as gross charge weight multiplied by 0.94 for energy equivalence and 0.90 to account for inert packaging weight.
b. Equivalency factors taken from charts contained in Esparza (1992).

It was somewhat less cumbersome to apply BlastX to the A1 blast scenario. The BlastX model was constructed to dimensionally represent the A1 blast chamber and included a full representation of venting areas in the chamber's exterior walls. Virtual sensors were placed in the BlastX model to represent the pressure sensors shown in Figure 2.5. As with the free air modeling of Section 3.2, the "cylindrical tabular" option was used to predict pressures and impulses. A free air burst charge model was selected and the code was allowed to model blast waves reflected from the blast chamber floor. BlastX offers the option of computing shock loads, gas phase loads, or a combination of

both. Brief experimentation showed that including gas phase pressures grossly over predicted all quantities of interest. Therefore, only the shock load output option was selected.

TABLE 3.9: ConWep predictions of peak reflected pressures and impulses compared to measured peak reflected pressures and impulses.

Sensor	Predicted Pressure MPa (psi)	Measured Pressure MPa (psi)[a]	Percent Error[b]	Predicted Impulse kPa ms (psi ms)	Measured Impulse Mpa ms (psi ms)[a]	Percent Error[b]
P1	4.134 (599.6)	5.437 (788.6)	-24.0	0.9142 (132.6)	1.257 (182.3)	-27.3
P2	1.518 (220.1)	2.329 (337.8)	-34.8	0.506 (73.4)	0.628 (91.1)	-19.5
P3	0.736 (106.7)	0.8101 (117.5)	-9.2	0.396 (57.4)	0.363 (52.6)	9.0
P4	0.200 (29.0)	0.483 (70.0)	-58.6	0.310 (44.9)	0.8301 (120.4)	-62.7
P5	1.435 (208.1)	2.295 (332.9)	-37.5	0.503 (72.9)	0.7384 (107.1)	-32.0
P6	0.290 (42.0)	0.6964 (101.0)	-58.4	0.264 (38.3)	0.341 (49.5)	-22.7
P7	0.0731 (10.6)	0.119 (17.3)	-38.7	0.119 (17.3)	0.208 (30.1)	-42.6
P8	0.121 (17.6)	0.252 (36.6)	-51.9	0.222 (32.2)	0.554 (80.3)	-59.9
PP1	0.274 (39.8)	0.087 (12.6)	215.9	0.175 (25.4)	0.437 (63.4)	-60.0
Average Absolute Error			58.8			37.3

Notes:
a. Measured quantities repeated from Table 2.1 for convenience.
b. Positive error indicates predicted quantity greater than measured quantity.

Another parameter that must be selected in a BlastX analysis is called "order of rays." This quantity represents the number of reflections a shockwave is allowed to have before being removed from the model. BlastX suggests a default value of five. In order to study the effect of this value, simulations were performed using values of five and two.

Table 3.10 compares pressures and impulses measured during the A1 blast event and BlastX predictions made using an order of rays equal to five. This comparison is performed again in Table 3.11, except using an order of rays equal to two. As the tables show, the average error for impulse is significantly better using an order of rays equal to two; the converse is true for reflected pressures. In the BlastX user manual, it is recommended that a higher order of rays be used for design while a lower order of rays be used for analysis, and Tables 3.10 and 3.11 show that this would be a conservative approach, at least for impulse-critical structures.

TABLE 3.10: Comparison between predicted and measured blast pressures and impulses for shot A1 using BlastX with an order of rays equal to five.

Sensor	Measured Peak Pressure MPa (psi)	Predicted Peak Pressure MPa (psi)	Percent Error[a,b]	Measured Positive Impulse MPa ms (psi ms)	Predicted Positive Impulse MPa ms (psi ms)	Percent Error[a,b]
P1	5.437 (788.6)	3.294 (477.7)	-39.4	1.257 (182.3)	1.073 (155.6)	-14.6
P2	2.329 (337.8)	1.709 (247.9)	-26.6	0.628 (91.1)	1.183 (171.6)	88.4
P3	0.8101 (117.5)	0.8232 (119.4)	1.6	0.362 (52.6)	1.189 (172.5)	228
P4	0.483 (70.0)	0.479 (69.5)	-0.8	0.8300 (120.4)	2.213 (321.0)	167
P5	2.295 (332.9)	1.688 (244.8)	-26.4	0.7381 (107.1)	1.184 (171.7)	60.4
P6	0.6961 (101.0)	0.492 (71.3)	-29.3	0.341 (49.5)	0.8363 (121.3)	145
P7	0.119 (17.3)	0.130 (18.8)	9.24	0.208 (30.1)	0.7564 (109.7)	264
P8	0.253 (36.6)	0.410 (59.5)	62.1	0.554 (80.3)	1.056 (153.2)	90.6
PP1	0.0872 (12.6)	0.325 (47.2)	272	0.437 (63.4)	0.9025 (130.9)	107
Average Absolute Error %			24.4			132

TABLE 3.11: Comparison between predicted and measured blast pressures and impulses for shot A1 using BlastX with an order of rays equal to two.

Sensor	Measured Peak Pressure MPa (psi)	Predicted Peak Pressure MPa (psi)	Percent Error[a,b]	Measured Positive Impulse MPa ms (psi ms)	Predicted Positive Impulse MPa ms (psi ms)	Percent Error[a,b]
P1	5.437 (788.6)	2.686 (389.5)	-50.6	1.257 (182.3)	0.538 (78.0)	-57.2
P2	2.329 (337.8)	1.302 (188.9)	-44.1	0.628 (91.1)	0.541 (78.4)	-13.9
P3	0.8101 (117.5)	0.6709 (97.3)	-17.2	0.362 (52.6)	0.503 (73.0)	39.0
P4	0.483 (70.0)	0.4792 (69.5)	-0.8	0.8300 (120.4)	1.108 (160.7)	33.5
P5	2.295 (332.9)	1.2817 (185.9)	-44.2	0.7381 (107.1)	0.539 (78.1)	-27.0
P6	0.6961 (101.0)	0.365 (52.9)	-47.6	0.341 (49.5)	0.165 (23.9)	-51.7
P7	0.119 (17.3)	0.0903 (13.1)	-24.1	0.208 (30.1)	0.126 (18.3)	-39.3
P8	0.253 (36.6)	0.1793 (26.0)	-29.1	0.554 (80.3)	0.443 (64.3)	-20.0
PP1	0.0872 (12.6)	0.325 (47.2)	273	0.437 (63.4)	0.174 (25.3)	-60.1
Average Absolute Error %			32.2			35.2

Notes for Tables 3.10 and 3.11:
a. Positive error indicates predicted quantity greater than measured quantity.
b. Average error computation excludes PP1 because it is an extreme outlier with respect to pressure.

As the preceding analyses show, predictions of blast pressures and impulses for cylindrical charges inside a confining structure can have large errors when estimated with the most common engineering level analytical methods. If only used for design, then it would be acceptable to use something like BlastX with the order of rays set to five or higher. This would result in a conservative design for impulse dominated structures. But given that the objective of this investigation is to accurately simulate experimental observations (i.e. analysis), this is an unsatisfactory result.

Given the desire for greater accuracy, there are only two options that would provide significantly better results. The first (and most expensive) is to perform more airblast experiments in order to develop a comprehensive understanding of the blast loading experienced at different locations within the blast chamber. This data would be

specific to the geometry of the charge and reflecting surfaces. A more affordable and expedient alternative is the use of high fidelity computational fluid dynamics (CFD) models to simulate the explosive events. One such software program, called CTH, is a three-dimensional shock physics hydrocode written and maintained by Sandia National Laboratories. The following chapters will describe the software's capabilities, document convergence studies, perform simple comparisons to existing TNT airblast data (KB standard), and finally apply the software to the A1 and B blast events described in Chapter 2. (The A2 blast event will not be simulated due to a lack of adequate data regarding charge composition. The manufacturer, Austin Powder Company, was contacted for more information; however, their representatives were unable to state with certainty the content of their product.)

CHAPTER 4: HYDRODYNAMIC MODELING WITH CTH

Chapter 3 demonstrated that simplified methods of airblast prediction can have large errors (between 30% and 50%) when charge and reflecting surface geometry differ from the simplest configuration (i.e. non hemispherical or non-spherical charges, oblique reflections, etc.) In order to simulate conditions like those in the experimental program, it is usually necessary to utilize a class of software programs known collectively as hydrocodes (short for hydrodynamic codes). These software tools simulate the transient motion of fluids by numerically solving the Euler or Navier Stokes equations. This investigation will utilize CTH, a three-dimensional shock physics hydrocode written and maintained by Sandia National Laboratories (McGlaun et al. 1990 and Hertel et al. 1993). CTH can model many different phenomena including shockwaves in fluids and solids, detonation, penetration, brittle failure, strain rate dependent constitutive behavior, plasticity, and viscoplasticity, among others (Hertel et al. 1993).

For the remainder of this investigation, the primary interest will be CTH's ability to simulate detonations and the resulting shockwaves in air. Section 4.1 will provide an introduction to some of the underlying theory of CTH, documenting the original theoretical work upon which the code is based. Although the implementation of this theory in CTH is significantly more involved than what will be presented here, it is still representative of how the code operates. Enough information will be presented regarding

one-dimensional hydrodynamic formulations that a numerical simulation tool could be coded from the information contained in this chapter. Following the theoretical development, Section 4.2 will document convergence studies performed in one dimension to identify the mesh size required for accurate simulations. Section 4.3 will then test this convergence criteria in a two-dimensional simulation to demonstrate that it extends to higher dimensionality. As an additional measure, the results of CTH airblast simulations in Sections 4.2 and 4.3 will be compared to empirical data for spherical free-air blasts to show the code's accuracy at predicting pressures and impulses. Empirical data will be represented by predictions made using the software tool ConWep (2005) and Kinney and Graham's textbook (1985).

4.1. Background Theory

With the publication of his 1757 "Principes généraux du mouvement des fluids," Leonhard Euler provided the first mathematical framework for the treatment of inviscid (non-viscous) fluid flow (Dartmouth, 2011). Euler is credited with developing two of the three equations that are today termed "Euler's equations." These two equations were found to require a third which was supplied by Pierre Laplace in 1789; it is called the energy equation. Collectively, all three equations are usually referred to as Euler's equations. The equations as reproduced in this chapter are taken from Richtmyer (1964). The first of Euler's equations is termed the continuity equation, given by Eq. (4.1a), and states that total mass is conserved. The second equation is the equation of motion, given by Eq. (4.1b), and states that momentum is conserved. The third equation (Eq. (4.1c)) is a statement of the conservation of energy (Eq. (4.1a) and (4.1b) do not independently

guarantee energy conservation under all conditions). Eqs. (4.1) have the variables $\boldsymbol{u}$ (vectorial material velocity), ρ (mass density), P (pressure of the fluid), and ε (energy in the fluid volume).

$$\left(\frac{\partial}{\partial t} + \boldsymbol{u} \cdot \nabla\right)\rho = -\rho \nabla \cdot \boldsymbol{u} \tag{4.1a}$$

$$\rho\left(\frac{\partial}{\partial t} + \boldsymbol{u} \cdot \nabla\right)\boldsymbol{u} = -\nabla P \tag{4.1b}$$

$$\rho\left(\frac{\partial}{\partial t} + \boldsymbol{u} \cdot \nabla\right)\varepsilon = -P \nabla \cdot \boldsymbol{u} \tag{4.1c}$$

Eqs. (4.1) are written in vectorial form that applies to one, two, or three dimensions. Their apparent simplicity is, however, deceiving as increasing the number of dimensions significantly increases the complexity of the analysis. For the rest of this section, the one-dimensional form of the equations will be discussed to shed light on their solution. Wilkins (1999) provides more information on two-dimensional methods for hydrodynamics. Eqs. (4.2) are the one-dimensional form of Eqs. (4.1) and allow a slightly more intuitive understanding of the conservation equations.

$$\frac{\partial \rho}{\partial t} + u\frac{\partial \rho}{\partial X} = -\rho\frac{\partial u}{\partial X} \tag{4.2a}$$

$$\rho\frac{\partial u}{\partial t} + \rho u\frac{\partial u}{\partial X} = -\frac{\partial P}{\partial X} \tag{4.2b}$$

$$\rho\frac{\partial \varepsilon}{\partial t} + \rho u\frac{\partial \varepsilon}{\partial X} = -P\frac{\partial u}{\partial X} \tag{4.2c}$$

These three equations for inviscid fluid flow, however, are not sufficient to determine the state of a system. A fourth equation is required to make the system solveable. This fourth equation is called the equation of state (EOS). EOS's will be discussed in greater detail in Chapter 5, but for now it is sufficient to know that an EOS

determines the pressure of a material given two other state variables (e.g. energy, temperature, and/or density). As written in Eq. (4.3), the EOS determines the energy as a function of the pressure and density.

$$\varepsilon = f(P, \rho) \tag{4.3}$$

Eqs. (4.1) and (4.2) are written in a formulation referred to as the Eulerian form (which is not the same as saying Euler's equations). In this form, the equations describe fluid motion as though observed from a spatially fixed reference. Thus the *X* variable is a location in Cartesian coordinate space. While convenient under certain circumstances, this form of Euler's equations presents problems when implemented in hydrocodes. In particular, tracking thin bands of high velocity material (e.g. explosively driven plates, moving shocks in air) is cumbersome as the mesh must be finely resolved. In addition, the inclusion of strength models is inconvenient when using the Eulerian form (Noh, 1976). Thus the Lagrangian forms of Eqs. (4.1) and (4.2) are widely used instead. Lagrangian in this context means that the equations are formulated from the perspective of an observer that moves with material in the domain. A popular comparison is to say that if one were observing a river's flow, the Eulerian observer would stand on the bank watching the water flow past. The Lagrangian observer, on the other hand, would observe the water from a boat travelling with the flow. Thus to the Lagrangian observer, the water appears not to move, rather the bank of the river passes by.

The Lagrangian form of Euler's equations are shown in Eqs. (4.4) for the case of one spatial dimension in a rectangular coordinate frame. The extension of these equations to a cylindrical or spherical geometry is somewhat trivial, only requiring a

change of variables. Eqs. (4.4) are strikingly simple in comparison to their Eulerian counterparts (Eqs. (4.2)). Note that in Eqs. (4.4), *X* is the Cartesian spatial coordinate while *x* is the Lagrangian coordinate.

$$u = \frac{\partial X}{\partial t} \tag{4.4a}$$

$$\frac{\partial u}{\partial t} = -\frac{1}{\rho_o}\frac{\partial P}{\partial x} \tag{4.4b}$$

$$\frac{\partial \varepsilon}{\partial t} = -P\frac{\partial V}{\partial t} \tag{4.4c}$$

$$V = \frac{1}{\rho_o}\frac{\partial X}{\partial x} \tag{4.4d}$$

$$P = f(\varepsilon, \rho) \tag{4.5}$$

Noh (1976) provides an excellent discussion on the merits of the Eulerian and Lagrangian approaches. His conclusions could be paraphrased as Eulerian formulations eliminate problems related to mesh distortion while Lagrangian requires less mesh resolution and is much better at tracking moving material. CTH hybridizes these approaches by utilizing a Lagrangian formulation of Euler's equations wherein the mesh is remapped after each computational step to the configuration it had prior to the step. Thus, it has the power and capabilities of a Lagrangian formulation while the remapping results in what is essentially a static Eulerian mesh (Hertel et al. 1993), avoiding the pitfalls of mesh distortion (e.g. negative volumes).

These equations which describe the motion of inviscid fluids do not, however, describe fluid flow which experiences shock compression. This is because a shock (which is a supersonic, finite amplitude wave) introduces a discontinuity in every variable – pressure, density, energy, velocity, etc. - and does so nearly instantaneously.

The Euler equations applied to this discontinuity do not correctly predict the state of material after passage of a shock. In 1885 Pierre Henri Hugoniot (Johnson and Cheret, 1998) found that a set of conservation equations could describe the initial and final states of material undergoing shock compression (it should also be mentioned that Lord Rankine discovered these same relations nearly simultaneously, however credit is usually ascribed to Hugoniot). These equations, referred to as the Hugoniot equations, are given by:

$$\rho(u - U_S) = \rho_o(u_o - U_S) \tag{4.6a}$$

$$P - P_o = \rho_o(u - u_o)(U_S - u_o) \tag{4.6b}$$

$$E - E_o = \frac{Pu - P_o u_o}{\rho_o(U_S - u_o)} - \frac{1}{2}(u^2 - u_o^2) \tag{4.6c}$$

Eqs. (4.6) describe the conservation of mass, momentum, and energy across a shock discontinuity, respectively, where ρ is the density, u the particle velocity, U_s the shock velocity, P the pressure, and E the energy. The zero subscript indicates the pre-shock value and absence of the zero subscript indicates the post-shock value.

Building on Euler's equations and the Hugoniot equations, American scientists began hydrocode development in earnest in the mid-20th century following the invention of the first computers. By the mid 50's, researchers had developed what can be described as Eulerian hydrocodes (their choice of coordinate frame was largely driven by the desire to avoid the problems of mesh distortion). These hydrocodes utilized Euler's equations with one special modification. The algorithms would track the location of a moving shock and would then apply the Hugoniot equations at the location of the shock at each time step in what could be described as a moving boundary condition. Although this

worked for simple one-dimensional problems, the method did not scale well to accommodate multi-dimensional, multi-shock simulations.

Von Neumann and Richtmyer (1950) solved this problem with a clever modification to Euler's equations – they introduced a fictitious viscosity pressure. Eqs. (4.7) are nearly identical to Eqs. (4.4) except there now appears a viscosity pressure that is additive to the pressure. Eq. (4.8) is the associated EOS and Eq. (4.9) is the definition of the viscosity pressure. In these equations, X is the Cartesian coordinate, P the pressure, q the artificial viscosity pressure, x the Lagrangian coordinate, ε the energy, ρ the density, c a constant coefficient, U the velocity, and V the specific volume (which is equal to $1/\rho$). Von Neumann and Richtmyer reasoned that in real shockwaves, dissipative mechanisms (viscosity and heat conduction) tend to smear the shock spatially. This smearing effect is convenient in a numerical simulation because it causes the shock dimension to be equal to or greater than the discretization length (mesh size).

$$u = \frac{\partial X}{\partial t} \tag{4.7a}$$

$$\frac{\partial u}{\partial t} = -\frac{1}{\rho_o}\frac{\partial (P+q)}{\partial x} \tag{4.7b}$$

$$\frac{\partial \varepsilon}{\partial t} = -(P+q)\frac{\partial V}{\partial t} \tag{4.7c}$$

$$V = \frac{1}{\rho_o}\frac{\partial X}{\partial x} \tag{4.7d}$$

$$P = f(\varepsilon, \rho) \tag{4.8}$$

$$q = -\frac{(c\Delta X)^2}{V}\frac{\partial U}{\partial x}\left|\frac{\partial U}{\partial x}\right| \tag{4.9}$$

Von Neumann and Richtmyer placed four requirements on the effects of q:

1. Eqs. (4.7) must possess solutions without discontinuities

2. The thickness of shock layers must at all locations be of the same order as the interval length ΔX used in the numerical computation
3. The effect of the q term must be negligible outside of the shock layers and
4. The Hugoniot equations must hold when all other dimensions characterizing the flow are large compared to the shock thickness.

In their 1950 paper through a series of mathematical tests, Von Neumann and Richtmyer indeed showed these requirements to be satisfied by the system of Eqs. (4.7) through (4.9). Richtmyer (1964) states that the artificial viscosity term only needs to be evaluated for compression. It is not required for stability or correctness when materials undergo tensile loading as tensile shocks violate the second law of thermodynamics (they require a decrease in entropy), and thus do not exist.

All that remains to solve the set of Eqs. (4.7) through (4.9) is to provide a numerical solution scheme. Von Neumann and Richtmyer (1950) and Richtmyer (1964) both provide very similar finite difference formulations. In the following paragraphs, the version of Noh (1976) will be presented and represents only a slight modification of Von Neumann and Richtmyer's approach. In Eqs. (4.10), subscripts denote the grid point number (spatial Lagrangian coordinate) while superscripts denote the time step (temporal coordinate). Note that many of the spatial coordinates call for point $k \pm 1/2$. This half step refers to the center of a mesh cell. So for example, cell number 1 has grid point 1 as its left-hand boundary, grid point 2 as its right-hand boundary, and grid point 1+ ½ as its center. This cell centering is physically motivated as a quantity like pressure only makes sense if it is uniform throughout the cell (i.e. the left-hand and right-hand boundary

cannot be different). With respect to temporal discretization, the ½ step doesn't have any physical meaning, but rather flows from the mathematics of the finite difference method itself.

In Eq. (4.10a), U is the node centered Lagrangian material velocity, Δt the time step, ΔX the mesh size, P the cell pressure, q the cell artificial viscosity pressure, and ρ the cell mass density. The equation essentially says that velocity is related to the acceleration (in the form of pressure divided by density and cell size) multiplied by the time increment. Eq. (4.10b) updates the current location of the mesh nodes in Cartesian space by the quantity velocity multiplied by time. Eq. (4.10c) computes the current specific volume as a function of the original density and the current relative distance between node points. Eq. (4.10d) computes the cell centered artificial viscosity pressure as a function of a constant C_o, the density, and the velocity.

$$U_k^{n+\frac{1}{2}} = U_k^{n-\frac{1}{2}} - \frac{\Delta t}{\rho_k^0 \Delta X}\left(P_{k+\frac{1}{2}}^n + q_{k+\frac{1}{2}}^{n-\frac{1}{2}} - P_{k-\frac{1}{2}}^n - q_{k-\frac{1}{2}}^{n-\frac{1}{2}}\right) \tag{4.10a}$$

$$X_k^{n+1} = X_k^n + \Delta t U_k^{n+\frac{1}{2}} \tag{4.10b}$$

$$V_{k+\frac{1}{2}}^{n+1} = \frac{1}{\rho_{k+\frac{1}{2}}^0 \Delta X}(X_{k+1}^{n+1} - X_k^n) \tag{4.10c}$$

$$q_{k+\frac{1}{2}}^{n+\frac{1}{2}} = -C_0^2(\Delta X)^2\left(\rho_{k+\frac{1}{2}}^{n+\frac{1}{2}} + \rho_{k+\frac{1}{2}}^n\right)\frac{\left[\left|U_{k+1}^{n+\frac{1}{2}} - U_k^{n+\frac{1}{2}}\right|\left(U_{k+1}^{n+\frac{1}{2}} - U_k^{n+\frac{1}{2}}\right)\right]}{(\Delta X)^2} \tag{4.10d}$$

Eq. (4.10e) is where Noh breaks from Von Neumann and Richtmyer as he claims the form shown is more accurate than the original method. The equation essentially says that the energy of the next time step is equivalent to the original energy plus or minus

PΔV, which is a statement of the first law of thermodynamics for a reversible process (Van Ness, 1969). Finally, Eq. (4.10f) is a statement of the EOS that computes pressure as a function of energy and density.

$$\varepsilon_{k+\frac{1}{2}}^{n+1} = \varepsilon_{k+\frac{1}{2}}^{n} - \frac{1}{2}\left[\left(P_{k+\frac{1}{2}}^{n+1} + q_{k+\frac{1}{2}}^{n+\frac{1}{2}}\right) + \left(P_{k+\frac{1}{2}}^{n} + q_{k+\frac{1}{2}}^{n-\frac{1}{2}}\right)\right]\left(V_{k+\frac{1}{2}}^{n+1} - V_{k+\frac{1}{2}}^{n}\right) \tag{4.10e}$$

$$P_{k+\frac{1}{2}}^{n+1} = f\left(\varepsilon_{k+\frac{1}{2}}^{n+1}, \rho_{k+\frac{1}{2}}^{n}\right) \tag{4.10f}$$

Eqs. (4.10) can be implemented directly and computed in order from Eq. (4.10a) to (4.10f) (after establishing initial conditions). Eq. (4.10f) shows the only missing piece of information required to arrive at a complete solution is the EOS, representing the pressure as a function of energy and density (CTH computes pressure as a function of temperature and density). If one wished to directly implement these difference equations for the case of a low-level airblast, it would be a reasonable approximation to use an EOS for air of the form:

$$P = \frac{\varepsilon}{V}(1 - \gamma) \tag{4.11}$$

In this simple EOS, which is based on the ideal gas law, γ is the ratio of the specific heat of air at constant volume to that at constant pressure. For air this can be reasonably taken as equal to 1.4. In reality gamma changes as a function of pressure, however for low pressure shocks the value 1.4 is sufficiently accurate. If greater accuracy is required for strong shocks, there are variable gamma approximations available that compute the specific heat ratio as a function of energy and density. Doan and Nickel (1963) provide one such formulation for gamma which is shown in Eq. (4.12). Their expression is easily used in conjunction with Eq. (4.11). Note that the function

$f(\rho, \epsilon)$ requires a number of supporting calculations and due to length is not reproduced here.

$$(\gamma - 1) = f(\rho, \epsilon) \tag{4.12}$$

According to Noh (1976), Eqs. (4.10) are fully second order accurate and are stable provided Eq. (4.13) is satisfied for all cells in the domain. In this equation, *S* is the local sound speed which can be computed as shown in Eq. (4.14) for an ideal gas. The more mathematically formal definition of sound speed is shown in Eq. (4.15) and can be applied to any EOS provided the adiabat is defined. Eq. (4.13) must be evaluated for each mesh cell at each time step, and the most restrictive value of Δt must be chosen for the entire domain's next time step.

$$S\frac{\Delta t}{\Delta X} + 4C_o^2\frac{\Delta t}{\Delta X}|\Delta U| < 1 \tag{4.13}$$

$$S = \sqrt{\frac{\gamma P}{\rho}} \tag{4.14}$$

$$S = \sqrt{\frac{\partial P}{\partial \rho}} \tag{4.15}$$

4.2. One-Dimensional Convergence

Like any numerical method, the results of a hydrodynamic simulation are affected to a great extent by the mesh size. Eq. (4.13) shows that the stability criteria are explicitly governed by the ratio of time step to mesh size. In a finite difference hydrodynamic system, energy is usually well conserved regardless of mesh size (energy conservation is, after all, one of the Euler equations). Sharp pressure and velocity gradients, on the other hand, only become sufficiently resolved with increasing discretization. This investigation will show that mesh refinement in CTH is primarily

needed to resolve peak pressure, while impulse is, by comparison, much less sensitive to cell size. The purpose of this convergence study is not to determine how quickly or accurately CTH approaches some theoretical solution, but instead to identify a meshing scheme which produces a reasonable accuracy when compared to empirical data.

An airblast simulation in CTH can be idealized as a having three events of interest. In the first event, the solid explosive material is replaced with an equivalent mass of detonation product gases at high density, pressure, and energy. A simulation of this event should seek to accurately insert the required amount of energy and define a moving shock sharply enough to simulate the ensuing air shock. Experience has shown that "sharp" definition can be attained using a mesh discretization one to two orders of magnitude smaller than the dimensions of the explosive charge being modeled. The second event is the propagation of an air shock from the explosive source through the simulated air toward a target. In this interval, the simulation should resolve the moving shock sufficiently to predict incident pressures and impulses. The third event of interest is the period during which the travelling air shock is reflected by a surface. During this event the simulation should accurately predict the rise in pressures and impulses associated with shock front reflection. This convergence study will seek to determine the most efficient mesh size to use for simulating each of these three critical events.

One complication with studying mesh resolution is that refinement requirements depend on the intensity of the shock being modeled. The larger the explosion, the steeper the pressure gradient, and the higher the resulting shock velocity. To avoid this problem, mesh resolution was studied as a function of scaled distance (i.e standoff divided by the

cube root of the charge weight). This provides a convenient simplification because the air shock Mach number is a single valued function of the scaled distance. Kinney and Graham (1985) demonstrate this in a table in the back of their text (Table 10 in Kinney and Graham). It shows that the overpressure ratio can be reduced to a function of only one variable – the Mach number of the shock. If a standard airblast nomograph (like Figure 1.4 in Chapter 1) is considered, two shocks with the same scaled distance will have the same overpressure, and Kinney and Graham show that this is equivalent to having identical shock velocities (Mach number). Mesh refinement requirements will therefore be comparable between two simulations modeling blast waves at equal scaled distances. As will be demonstrated, this method of studying convergence allows the formulation of simple guidelines that can be used in establishing first-guesses for mesh size.

For the convergence studies that follow, mesh dimensions are reported in native CTH units of centimeters. Rather than picking an even English dimension, it was easier to pick a sensible metric dimension, even though the conversion to English units appears nonsensical. Also, results for pressure and impulse will only be reported to the first decimal (with respect to English units). Discussions with Sandia personnel and sensor specifications suggest that the accuracy of empirical data would be even less than one decimal place in pressure (with respect to English units).

All CTH convergence simulations and comparisons to empirical data were performed using air at a state referred to as "US Standard Atmosphere, 1976" for altitudes below 11 km as described by UFC-3-340-01 (2002). This corresponds to an

atmospheric pressure of 101.3 kPa (14.69 psi), a temperature of 15 degrees Celsius (59 degrees Fahrenheit), and an air density of 0.001225 grams per cubic centimeter (g/cm^3). CTH's built in EOS for air has a slightly different standard state of 24.8 degrees Celsius (76.7 degrees F), a density of 0.001218 g/cm^3, and a pressure of 101.3 kPa (14.69 psi). In order to provide an accurate comparison, CTH's air was set to an initial density of 0.001225 g/cm^3 and a temperature of 23.0 degrees Celsius (73.5 degrees Farenheit), which together yielded an air pressure of 101.3 kPa. Although the temperature is different than the US Standard Atmosphere, this adjustment yields the correct pressure and density, which are of greater importance.

The explosive charges used in the convergence study were composed of TNT with a density of 1.63 g/cm^3, a detonation velocity of 6.93 km/s, a detonation pressure of 21 GPa, and an energy of 7.0×10^{10} ergs/cc (7.0 kJ/cc). All convergence simulations were performed using a one-dimensional, spherically symmetric mesh. Figure 4.1 is a qualitative illustration of a typical one-dimensional mesh. At the left-hand boundary is a "symmetry boundary condition." Immediately beside the symmetry boundary is the explosive material and then, further to the right, the air. Either a transmissive boundary condition (to simulate infinite air and thus incident pressure and impulse) or a reflecting boundary condition (to simulate reflected pressure and impulse) is located at the right-most boundary.

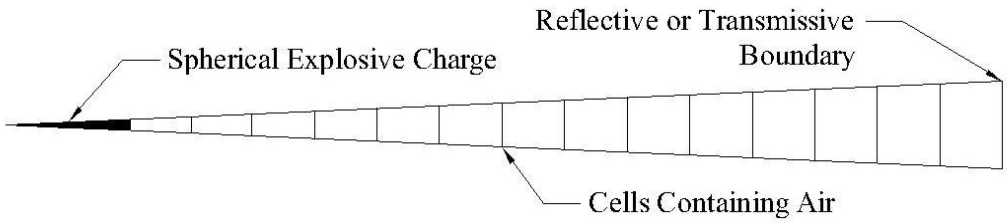

FIGURE 4.1: Diagram of spherically symmetric mesh.

Section 4.2.1 will study the mesh discretization necessary to accurately capture the insertion and initiation of explosive material in the CTH mesh. Section 4.2.2 will study the mesh discretization required for cells containing air to simulate incidence pressures and impulses. Finally, Section 4.2.3 will study the mesh discretization required to accurately simulate the pressures and impulses of a shock reflection. In Section 4.3, the cell sizing guidance developed in Sections 4.2.1 and 4.2.2 will be tested in a two-dimensional analysis to show that the one-dimensional guidance indeed extends to simulations of higher dimension.

4.2.1. Cells Containing Explosive Material

Unlike cells containing air, mesh cells within the explosive have a standoff (distance) of zero, and scaled distance could therefore not be utilized there. Mesh refinement of the explosive material itself was thus based on the explosive charge size. The larger the charge, the more energy present, the higher the pressure, and thus a requirement for higher refinement. Pressure was measured at two locations in the model domain – one location was near the center of the spherical explosive charge while the other was fixed at 75 centimeters. Impulse was only quantified at the 75 cm standoff as impulse inside the charge does not have any physical meaning with respect to an airblast.

Tables 4.1 and 4.2 present the results of this convergence study for a 10 kg and 50 kg charge. The left-hand columns show the uniform cell size used throughout the simulation domain. The purpose of these two tables is to identify the point at which the entire domain could be termed converged. This provides a useful basis – it is now known what a converged result should be (as the tables show, the 0.001 cm cell size is for all intents and purposes, converged). In order to speed computations in later convergence studies, some error relative to the "converged solution" will be tolerated. The mesh corresponding to a 5% error (relative to the 0.001 cm converged result) was arbitrarily selected as tolerable. In looking at the simulated pressure and impulse at 75 cm, both Tables 4.1 and 4.2 show that a cell size of 0.125 cm provides this level of accuracy.

The tables show that within the explosive (x=5 cm), the peak simulated pressure very slowly approaches the theoretically expected pressure of 21 GPa. This corresponds to a pressure known as the CJ state which will be discussed at length in Chapter 5. Outside the charge, the simulated pressure and impulse more rapidly converge. But these ultrafine levels of mesh resolution require significant computational time, even in one dimension. A 0.001 cm mesh resolution in two or three dimensions would be infeasible due to the required computational resources (at least those currently available at UNC Charlotte). It was therefore desirable to see if a courser mesh could be used for cells containing explosive material, while still maintaining an acceptable accuracy. Tables 4.3 and 4.4 show the pressure and impulse results at x=75 cm when the cell size within the explosive charge is progressively coarsened. A constant cell size for air of 0.125 cm was

used when the explosive cell size was at least this large (based on the previously discussed 5% error criteria).

TABLE 4.1: CTH simulation results for a 10 kg charge as a function of discretization.

Mesh Size (cm)	Pressure at x=5 cm GPa (kpsi)	Pressure at x=75 cm MPa (kpsi)	Impulse at x=75 cm MPa ms (psi ms)
0.5	9.959 (1444)	6.039 (0.8759)	0.1843 (26.73)
0.25	11.61 (1684)	6.337 (0.9191)	0.1890 (27.41)
0.125	13.14 (1906)	6.588 (0.9555)	0.1914 (27.76)
0.05	15.60 (2263)	6.739 (0.9774)	0.1929 (27.98)
0.025	16.67 (2418)	6.799 (0.9861)	0.1935 (28.06)
0.01	18.02 (2614)	6.833 (0.9910)	0.1939 (28.12)
0.005	18.64 (2704)	6.848 (0.9932)	0.1941 (28.15)
0.001	19.63 (2847)	6.859 (0.9948)	0.1942 (28.17)

Note: For Tables 4.1 through 4.4, x is measured from the center of the explosive charge.

TABLE 4.2: CTH simulation results for a 50 kg charge as a function of discretization.

Mesh Size (cm)	Pressure at x=5 cm GPa (kpsi)	Pressure at x=75 cm MPa (kpsi)	Impulse at x=75 cm MPa ms (psi ms)
0.5	9.959 (1444)	12.81 (1.858)	0.4908 (71.18)
0.25	11.61 (1684)	14.03 (2.034)	0.4825 (69.98)
0.125	13.40 (1944)	14.26 (2.068)	0.4804 (69.68)
0.05	15.33 (2223)	14.51 (2.104)	0.4797 (69.57)
0.025	16.67 (2418)	14.62 (2.120)	0.4794 (69.53)
0.01	17.99 (2609)	14.70 (2.132)	0.4792 (69.50)
0.005	18.64 (2704)	14.73 (2.136)	0.4792 (69.50)
0.001	19.69 (2856)	14.75 (2.139)	0.4792 (69.50)

TABLE 4.3: CTH simulation results for 10 kg charge as explosive mesh is coarsened.

Air Mesh Size (cm)	Explosive Mesh Size (cm)	Pressure at x=75 cm Mpa (kpsi)	Impulse at x=75 cm MPa ms (psi ms)	Pressure* Error %
0.001	0.001	6.859 (0.9948)	0.1942	0%
0.125	0.125	6.588 (0.9555)	0.1914	-4.0
0.125	0.25	6.612 (0.9590)	0.1897	-3.6
0.125	0.5	6.621 (0.9603)	0.1865	-3.5
0.125	0.75	6.808 (0.9874)	0.1834	-0.7
0.125	1.0	6.506 (0.9436)	0.1812	-5.1

Note: *Errors computed as relative to pressure predicted for 0.001cm mesh.

TABLE 4.4: CTH simulation results for a 50 kg charge as explosive mesh is coarsened.

Air Mesh Size (cm)	Explosive Mesh Size (cm)	Pressure at x=75 cm MPa (kpsi)	Impulse at x=75 cm MPa ms (psi ms)	Pressure* Error %
0.001	0.001	14.75 (2.139)	0.4792	0%
0.125	0.125	14.26 (2.068)	0.4804	-3.3
0.125	0.25	13.98 (2.028)	0.4835	-5.2
0.125	0.5	14.23 (2.064)	0.4890	-3.5
0.125	0.75	13.34 (1.934)	0.4944	-9.6
0.125	1.0	12.95 (1.878)	0.4990	-12.2

Note: *Errors computed as relative to pressure predicted for 0.001cm mesh.

Table 4.3 (and Table 4.4 to a lesser degree) shows an unusual trend – as mesh refinement of the explosive decreases, predicted pressure increases. It is difficult to ascribe this to a particular cause, but the magnitude is not sufficient to raise concern. Examining the errors in Tables 4.3 and 4.4, it is seen that using a mesh resolution of 0.5 cm for the explosive material is adequate, provided the air is sufficiently resolved at the point of interest. For additional conservatism, the convergence studies that follow will use an explosive cell size of 0.25 cm.

4.2.2. Convergence of Shocks in Air – Incident Parameters

The convergence of simulations of shocks propagating through air was studied to determine the discretization required to accurately simulate incident pressures and impulses. The study was conducted using a fixed mesh size of 0.25 cm for the explosive material. The air was meshed using several different sizes for each of the scaled distances investigated. A virtual sensor was placed at the standoff of interest to "measure" the simulated incident pressure and impulse. The convergence study for incident parameters was performed twice – once for a charge of 5 kg and once for a charge of 200 kg. The results of both the 5 and 200 kg simulations should yield nearly

identical pressures (at equal scaled distances), but the 200 kg charge will generate larger impulses. As will be shown, the ratio of impulse to pressure has an interesting relationship with convergence.

The data generated during the incident parameter convergence study will be presented in Tables 4.5 through 4.16 followed by a discussion of the results. Incident pressure and impulse results for the 5 kg charge will be followed by those for the 200 kg charge. Each parameter (pressure or impulse) is reported in a three table group for each charge size. In each group of three, the first table, for example Table 4.5, presents the raw simulated parameter as a function of mesh size. The second, like Table 4.6, reports the error in the simulated quantity relative to the smallest cell size studied (which was always 0.125 cm). The cell corresponding to an error less than 5% has been highlighted for each standoff, and this result is considered to be sufficiently converged. Finally, the third table, such as Table 4.7, compares the simulated CTH result to empirical data, using the result from the mesh cell size determined to be converged. Empirical predictions were made using ConWep (2005) and Kinney and Graham's (K&G) text (1985).

TABLE 4.5: 5 kg charge – simulated incident pressure.

Scaled Distance m/kg $^{1/3}$	Pressure as a Function of Cell Size (cm) kPa (psi)					
	0.125 cm	0.25 cm	0.5 cm	1.0 cm	2.0 cm	4.0 cm
0.5	3573.6 (505.8)	3535.6 (495.2)	3471.6 (478.2)	3383.0 (442.8)	3283.4 (380.0)	2932.5 (386.7)
1	879.8 (125.9)	880.6 (123.6)	869.6 (118.4)	849.8 (113.1)	814.4 (106.8)	752.9 (86.5)
2	158.6 (22.9)	158.0 (22.5)	157.4 (22.2)	156.4 (21.7)	154.4 (20.9)	146.9 (20.2)
4	41.4 (5.9)	40.7 (5.9)	40.7 (5.8)	40.7 (5.8)	40.7 (5.6)	40.0 (5.5)
5	28.3 (4.1)	28.3 (4.1)	28.3 (4.1)	28.3 (4.0)	28.3 (4.0)	27.6 (3.8)
10	10.3 (1.5)	10.3 (1.5)	10.3 (1.5)	10.3 (1.4)	10.3 (1.4)	9.7 (1.4)

TABLE 4.6: 5 kg charge – incident pressure error relative to 0.125 cm cell result.

Scaled Distance m/kg $^{1/3}$	Percent Error Relative to 0.125 cm Cell Size					
	0.125 cm	0.25 cm	0.5 cm	1.0 cm	2.0 cm	4.0 cm
0.5	-	2.1	5.5	12.5	24.9	23.5
1	-	1.8	6.0	10.2	15.2	31.3
2	-	1.7	3.1	5.2	8.7	11.8
4	-	0.0	1.7	1.7	5.1	6.8
5	-	0.0	0.0	2.4	2.4	7.3
10	-	0.0	0.0	6.7	6.7*	6.7

Note: *choice of number of significant figures in simulation result caused error to be greater than 5% due to decimal rounding

TABLE 4.7: 5 kg charge - comparison between converged pressure and empirical data.

Scaled Distance m/kg $^{1/3}$	Converged Cell Size (cm)	CTH kPa (psi)	ConWep kPa (psi)	Percent Error	K&G kPa (psi)	Percent Error
0.5	0.25	3536 (495.2)	3885 (563.5)	-12.1	3950 (572.9)	-13.6
1	0.25	880.6 (123.6)	934.9 (135.6)	-8.8	995.6 (144.4)	-14.4
2	0.5	157 (22.2)	195 (28.3)	-21.6	205 (29.7)	-25.3
4	1	41 (5.8)	47 (6.8)	-14.7	44 (6.4)	-12.5
5	2	28 (4.0)	31 (4.5)	-11.1	29 (4.2)	-2.4
10	2	10 (1.4)	11 (1.6)	-12.5	9.7 (1.4)	6.2
			Average Error %	-13.5		-12.4

TABLE 4.8: 5 kg charge – simulated incident impulse.

Scaled Distance m/kg $^{1/3}$	Impulse as a Function of Cell Size (cm) kPa ms (psi ms)					
	0.125 cm	0.25 cm	0.5 cm	1.0 cm	2.0 cm	4.0 cm
0.5	200 (29.0)	210 (30.4)	192 (27.8)	185 (26.9)	174 (25.3)	161 (23.3)
1	192 (27.9)	192 (27.8)	190 (27.5)	190 (27.5)	188 (27.2)	189 (27.4)
2	116 (16.8)	114 (16.6)	114 (16.6)	115 (16.7)	115 (16.7)	115 (16.7)
4	65 (9.4)	64 (9.3)	64 (9.3)	64 (9.3)	65 (9.4)	65 (9.4)
5	52 (7.6)	52 (7.5)	52 (7.5)	52 (7.6)	52 (7.6)	53 (7.7)
10	26 (3.8)	26 (3.8)	26 (3.8)	26 (3.8)	27 (3.9)	27 (3.9)

TABLE 4.9: 5 kg charge – incident impulse error relative to 0.125 cm cell result.

Scaled Distance m/kg $^{1/3}$	Percent Error Relative to 0.125 cm Cell Size					
	0.125 cm	0.25 cm	0.5 cm	1.0 cm	2.0 cm	4.0 cm
0.5	-	-4.8	4.1	7.2	12.8	19.7
1	-	1.4	1.4	1.4	2.5	1.8
2	-	1.2	1.2	0.6	0.6	0.6
4	-	1.1	1.1	1.1	0.0	0.0
5	-	1.3	1.3	0.0	0.0	-1.3
10	-	0.0	0.0	0.0	-2.6	-2.6

TABLE 4.10: 5 kg charge - comparison between converged impulse and empirical data.

Scaled Distance m/kg $^{1/3}$	Converged Cell Size (cm)	CTH kPa ms (psi ms)	ConWep kPa ms (psi ms)	Percent Error	K&G kPa ms (psi ms)	Percent Error
0.5	0.5	210 (30.4)	242 (35.1)	-13.4	183 (26.5)	14.7
1	4	189 (27.4)	299* (43.3)	-36.7	174 (25.2)	8.7
2	4	115 (16.7)	158 (22.9)	-27.1	136 (19.7)	-15.2
4	4	65 (9.4)	85.5 (12.4)	-24.2	66 (9.5)	-1.1
5	4	53 (7.7)	69.6 (10.1)	-23.8	51 (7.4)	4.1
10	4	27 (3.9)	36 (5.2)	-25.0	26 (3.7)	5.4
			Average Error %	-25.0		2.8

Note: *result unexpected as smaller scaled distance had lower impulse

TABLE 4.11: 200 kg charge – simulated incident pressure.

Scaled Distance m/kg $^{1/3}$	Pressure as a Function of Cell Size (cm) kPa (psi)					
	0.125 cm	0.25 cm	0.5 cm	1.0 cm	2.0 cm	4.0 cm
0.5	3574 (518.3)	3536 (512.8)	3472 (503.5)	3383 (490.7)	3283 (476.2)	2932 (425.3)
1	879.8 (127.6)	880.5 (127.7)	869.4 (126.1)	850.1 (123.3)	816.3 (118.4)	752.9 (109.2)
2	159 (23.0)	158 (22.9)	157 (22.8)	157 (22.7)	154 (22.4)	167 (21.3)
4	41 (6.0)	41 (5.9)	41 (5.9)	41 (5.9)	41 (5.9)	40 (5.8)
5	28 (4.1)	28 (4.1)	28 (4.1)	28 (4.1)	28 (4.1)	28 (4.0)
10	10 (1.5)	10 (1.5)	10 (1.5)	10 (1.5)	10 (1.5)	10 (1.4)

TABLE 4.12: 200 kg charge – incident pressure error relative to 0.125 cm cell result.

Scaled Distance m/kg$^{1/3}$	Percent Error Relative to 0.125 cm Cell Size					
	0.125 cm	0.25 cm	0.5 cm	1.0 cm	2.0 cm	4.0 cm
0.5	-	-1.1	-2.9	-5.3	-8.1	-17.9
1	-	0.1	-1.2	-3.4	-7.2	-14.4
2	-	-0.3	-0.7	-1.3	-2.6	-7.3
4	-	-1.7	-1.7	-1.7	-1.7	-3.3
5	-	0.0	0.0	0.0	0.0	-2.4
10	-	0.0	0.0	0.0	0.0	-6.7*

Note: *choice of number of significant figures in simulation result caused error to be greater than 5% due to decimal rounding

TABLE 4.13: 200 kg charge - comparison between converged pressure and empirical data.

Scaled Distance $m/kg^{1/3}$	Converged Cell Size (cm)	CTH kPa (psi)	ConWep kPa (psi)	Percent Error	K&G kPa (psi)	Percent Error
0.5	0.5	3472 (503.5)	3885 (563.5)	-10.6	3950.0 (572.9)	-12.1
1	1	850.1 (123.3)	934.9 (135.6)	-9.1	995.6 (144.4)	-14.6
2	2	154 (22.4)	194 (28.2)	-20.6	204.8 (29.7)	-24.6
4	4	40 (5.8)	47 (6.8)	-14.7	44.1 (6.4)	-9.4
5	4	28 (4.0)	31 (4.5)	-11.1	29.0 (4.2)	-4.8
10	4	10 (1.4)	11 (1.6)	-12.5	9.7 (1.4)	0.0
			Average Error %	-13.1		-10.9

TABLE 4.14: 200 kg charge – simulated incident impulse.

Scaled Distance $m/kg^{1/3}$	Impulse as a Function of Cell Size (cm) kPa ms (psi ms)					
	0.125 cm	0.25 cm	0.5 cm	1.0 cm	2.0 cm	4.0 cm
0.5	695.0 (100.8)	687 (99.6)	683 (99.0)	675 (97.9)	660 (95.7)	630 (91.4)
1	658.4 (95.5)	672 (97.5)	672 (97.5)	670 (97.2)	662 (96.0)	649 (94.2)
2	396 (57.4)	391 (56.7)	392 (56.8)	392 (56.8)	392 (56.8)	380 (55.1)
4	221 (32.0)	219 (31.8)	220 (31.9)	220 (31.9)	221 (32.0)	221 (32.0)
5	179 (25.9)	178 (25.8)	179 (25.9)	179 (25.9)	179 (26.0)	179 (26.0)
10	90.3 (13.1)	90.3 (13.1)	90.3 (13.1)	91.0 (13.2)	91.0 (13.2)	91.0 (13.2)

TABLE 4.15: 200 kg charge – incident impulse error relative to 0.125 cm cell result.

Scaled Distance m/kg $^{1/3}$	Percent Error Relative to 0.125 cm Cell Size					
	0.125 cm	0.25 cm	0.5 cm	1.0 cm	2.0 cm	4.0 cm
0.5	-	-1.2	-1.8	-2.9	-5.1	-9.3
1	-	2.1	2.1	1.8	0.5	-1.4
2	-	-1.2	-1.0	-1.0	-1.0	-4.0
4	-	-0.6	-0.3	-0.3	0.0	0.0
5	-	-0.4	0.0	0.0	0.4	0.4
10	-	0.0	0.0	0.8	0.8	0.8

TABLE 4.16: 200 kg charge - comparison between converged impulse and empirical data.

Scaled Distance m/kg$^{1/3}$	Converged Cell Size (cm)	CTH kPa ms (psi ms)	ConWep kPa ms (psi ms)	Percent Error	K&G kPa ms (psi ms)	Percent Error
0.5	1	675 (97.9)	826.7 (119.9)	-18.3	626 (90.8)	7.8
1	4	649 (94.2)	1021 (148.1)	-36.4	594 (86.1)	9.4
2	4	380 (55.1)	538 (78.1)	-29.4	464 (67.3)	-18.1
4	4	221 (32.0)	291 (42.2)	-24.2	223 (32.4)	-1.2
5	4	179 (26.0)	238 (34.5)	-24.6	175 (25.4)	2.4
10	4	91.0 (13.2)	123 (17.9)	-26.3	88.3 (12.8)	3.1
Average Error %				-26.5		0.6

The 5 kg incident pressure results (Tables 4.5 through 4.7) show that, at the worst case, a 0.25 cm cell size is required to accurately simulate incident pressure. Using the converged cell sizes presented in Table 4.6, Table 4.7 shows that the average error between CTH and empirical data for incident pressure is approximately 14%. Looking at the 5 kg incident impulse results, Table 4.9 shows that impulse may be accurately modeled using a cell size that is two or more times greater than the cell size required for incident pressure. In comparing the simulated impulse to empirical data in Table 4.10,

CTH underpredicted the ConWep result by 25% while overpredicting the K&G result by only 2.8%. The difference between CTH and ConWep is not surprising because Bogosian et al. (2002) noted that ConWep tended to overpredict the incident impulse of the experimental data they examined by about 15%.

The 200 kg incident pressure study (Tables 4.11 through 4.13) shows results that are similar to the 5 kg incident pressure study. The notable difference, however, is that the larger charge size required less mesh resolution at each standoff. This observation leads to an interesting result which will be discussed shortly. As with the 5 kg study, the 200 kg study had an error of approximately 11% in incident pressure when comparing CTH and empirical data. Finally, the 200 kg incident impulse study showed that, similar to the pressure, the 200 kg charge required less mesh resolution than the 5 kg charge. In comparing simulated impulse, CTH underpredicted the ConWep result by 26.5% and overpredicted the K&G result by only 0.6%.

As mentioned earlier, it is of interest to study why the 200 kg charge, with its larger impulse, would require less refinement than a small charge. After some examination, it was found that plotting the converged cell size as a function of peak impulse divided by peak pressure provides a revealing result. This is shown in the log-log plot of Figure 4.2. This can be thought of as a measure of the time required for the blast wave to deliver its impulse. The lower this ratio, the more impulse is being delivered per unit time. As an illustration, using a scaled distance of 0.5 $m/kg^{1/3}$, the 5 kg charge has an *I/P* ratio of 0.06 while the 200 kg charge has an ratio *I/P* of 0.20. A power law curve fit was added to Figure 4.2 and it is given by

$$Cell\ Size \approx\ 1.0436\left(\frac{Impulse}{Pressure}\right)^{0.6358} \tag{4.16}$$

This equation has an R^2 value of 0.92 and is thus a good fit. Note that the equation could be simplified to

$$Cell\ Size \approx\ \left(\frac{Impulse}{Pressure}\right)^{0.64} \tag{4.17}$$

and the R^2 value would still be 0.91 which is, for all intents and purposes, just as good. Also note that the scatter of the data points is largely due to the 5% error criterion and, if several of the converged cell sizes were changed by one increment, the points would likely lay on the straight line in Figure 4.2.

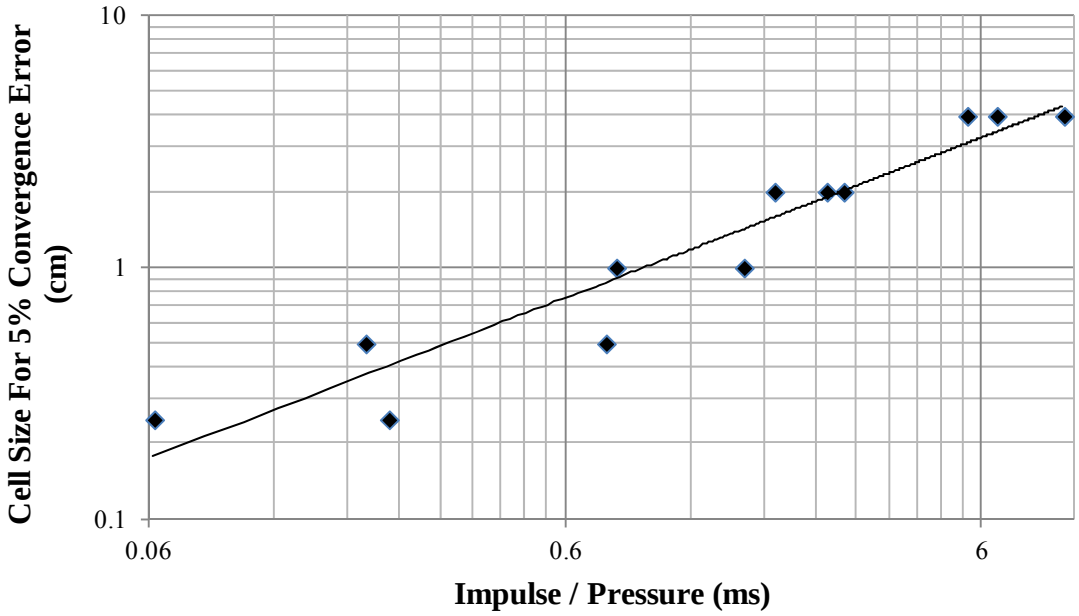

FIGURE 4.2: Log-log plot of converged cell size as a function of impulse divided by pressure.

4.2.3. Convergence of Shocks in Air – Reflected Parameters

Having determined the mesh size necessary to refine shocks travelling through air, the final (and key) convergence that needed to be studied was the mesh size required to accurately model reflected pressures and impulses. These quantities are of particular importance as they will ultimately be used in structural response simulations. As with the incident parameter study, a fixed cell size of 0.25 cm was used for the explosive material. The size of the cells used to mesh air was varied to determine the mesh size required for convergence of reflected pressure and impulse. As with the incident parameter study, an attempt will be made to identify a rule of thumb that can be used to construct a sufficiently refined model from the outset.

The reflected parameter results that follow in Tables 4.17 through 4.28 will be presented in exactly the same manner as the results of the incident parameter study. Thus each parameter (reflected pressure or impulse) will be reported in a three table group. There are two important differences between the reflected parameter study and the incident parameter study. First, cell convergence was not identified based on error relative to some hyper-fine resolution. Rather, convergence was determined based on the rate at which the simulated reflected pressure increased with respect to decreasing cell size. When the change between one cell size and the next smaller size was less than 5%, the simulation was deemed to be converged at the smaller cell size. The second difference with the incident parameter study is that only ConWep was used as a source of empirical data; Kinney and Graham (1985) do not provide sufficient information regarding reflected impulse. An analysis of the results follows the tables.

TABLE 4.17: 5 kg charge – simulated reflected pressure.

Scaled Distance m/kg $^{1/3}$	Peak Reflected Pressure as a Function of Mesh Cell Size kPa (psi)					
	0.01 cm	0.05 cm	0.125 cm	0.25 cm	0.5 cm	1.0 cm
0.5	26631 (3862.6)	25567 (3708.3)	24374 (3535.2)	22445 (3255.3)	19883 (2883.8)	17238 (2500.2)
1	4902 (711.0)	4817 (698.6)	4702 (682.0)	4540 (658.5)	4244 (615.6)	3780 (548.3)
2	496 (71.9)	494 (71.6)	490 (71.1)	485 (70.3)	476 (69.0)	460 (66.7)
4	95.1 (13.8)	95.1 (13.8)	95.1 (13.8)	95.1 (13.8)	94.5 (13.7)	94.5 (13.5)
5	NS	63 (9.2)	63 (9.2)	63 (9.1)	63 (9.1)	62 (9.0)
10	NS	NS	21 (3.1)	21 (3.1)	21 (3.0)	21 (3.0)

Notes for Tables 4.17 through 4.19:

NS means not simulated because convergence was already achieved.

NR means no result obtained because secondary shock interfered with impulse quantification.

TABLE 4.18: Reflected pressure errors relative to one cell size larger.

Scaled Distance m/kg $^{1/3}$	Percent Error Relative to One Cell Size Larger					
	0.01 cm	0.05 cm	0.125 cm	0.25 cm	0.5 cm	1.0 cm
0.5	4.2	4.9	8.6	12.9	15.3	-
1	1.8	2.4	3.6	7.0	12.3	-
2	0.4	0.7	1.1	1.9	3.5	-
4	0	0	0	0.7	1.5	-
5	NS	0	1.1	0	1.1	-
10	NS	NS	0	3.3	0	-

TABLE 4.19: 5 kg charge - comparison between converged reflected pressure and empirical data.

Scaled Distance $m/kg^{1/3}$	Converged Cell Size (cm)	CTH kPa (psi)	ConWep kPa (psi)	Percent Error
0.5	0.05	25567 (3708.3)	30357 (4403.0)	-15.8
1	0.125	4702 (682.0)	5006 (726.0)	-6.1
2	0.5	476 (69.0)	646 (93.7)	-26.4
4	1.0	94.5 (13.5)	110 (16.0)	-15.6
5	1.0	62 (9.0)	70.3 (10.2)	-11.8
10	1.0	21 (3.0)	23 (3.4)	-11.8
			Average Error %	-14.6

TABLE 4.20: 5 kg charge – simulated reflected impulse.

Scaled Distance $m/kg^{1/3}$	Peak Reflected Impulse as a Function of Mesh Cell Size kPa ms (psi ms)					
	0.01 cm	0.05 cm	0.125 cm	0.25 cm	0.5 cm	1.0 cm
0.5	NR	NR	NR	NR	NR	NR
1	NR	NR	NR	NR	NR	NR
2	461 (66.8)	461 (66.8)	460 (66.7)	459 (66.6)	459 (66.6)	460 (66.7)
4	180 (26.1)	180 (26.1)	180 (26.1)	181 (26.2)	181 (26.2)	181 (26.3)
5	NS	136 (19.7)	136 (19.7)	136 (19.7)	137 (19.8)	136 (19.7)
10	NS	NS	61 (8.8)	61 (8.8)	61 (8.8)	61 (8.9)

Notes for Tables 4.20 through 4.22:

NS means not simulated because convergence was already achieved.

NR means no result obtained because secondary shock interfered with impulse quantification.

TABLE 4.21: Reflected impulse errors relative to one cell size larger.

Scaled Distance m/kg $^{1/3}$	Percent Error Relative to One Cell Size Larger					
	0.01 cm	0.05 cm	0.125 cm	0.25 cm	0.5 cm	1.0 cm
0.5	NR	NR	NR	NR	NR	NR
1	NR	NR	NR	NR	NR	NR
2	0.0	0.1	0.2	0	-0.1	-
4	0.0	0	0	-0.4	-0.4	-
5	NS	0	0	-0.5	0.5	-
10	NS	NS	0	0.0	-1.1	-

TABLE 4.22: 5 kg charge - comparison between converged reflected impulse and empirical data.

Scaled Distance m/kg$^{1/3}$	Converged Cell Size (cm)	CTH kPa ms (psi ms)	ConWep kPa ms (psi ms)	Percent Error
0.5	NR	-	-	-
1	NR	-	-	-
2	1	460 (66.7)	403 (58.5)	14.0
4	1	181 (26.3)	182 (26.4)	-0.4
5	1	136 (19.7)	143 (20.7)	-4.8
10	1	61 (8.9)	68 (9.9)	-10.1
			Average Error %	-0.3

TABLE 4.23: 200 kg charge – simulated reflected pressure.

Scaled Distance m/kg $^{1/3}$	Peak Reflected Pressure as a Function of Mesh Cell Size kPa (psi)					
	0.01 cm	0.05 cm	0.125 cm	0.25 cm	0.5 cm	1.0 cm
0.5	26901 (3901.7)	26564 (3852.8)	26337 (3819.8)	25578 (3709.8)	24285 (3522.3)	22054 (3198.6)
1	NS	NS	4845 (702.7)	4786 (694.1)	4677 (678.3)	4493 (651.7)
2	NS	NS	494 (71.7)	492 (71.4)	490 (71.0)	484 (70.2)
4	NS	NS	95.8 (13.9)	95.8 (13.8)	95.8 (13.8)	95.8 (13.8)
5	NS	NS	880 (9.2)	880 (9.2)	880 (9.2)	880 (9.2)
10	NS	NS	NS	21 (3.1)	21 (3.1)	21 (3.1)

Notes for Tables 4.23 through 4.25:

NS means not simulated because convergence was already achieved.

NR means no result obtained because secondary shock interfered with impulse quantification.

TABLE 4.24: Reflected pressure errors relative to one cell size larger.

Scaled Distance m/kg $^{1/3}$	Percent Error Relative to One Size Larger					
	0.01 cm	0.05 cm	0.125 cm	0.25 cm	0.5 cm	1.0 cm
0.5	1.3	0.9	3.0	5.3	10.1	-
1	NS	NS	1.2	2.3	4.1	-
2	NS	NS	0.4	0.6	1.1	-
4	NS	NS	0.7	0.0	0.0	-
5	NS	NS	0.0	0.0	0.0	-
10	NS	NS	NS	0.0	0.0	-

TABLE 4.25: 200 kg charge - comparison between converged reflected pressure and empirical data.

Scaled Distance $m/kg^{1/3}$	Converged Cell Size (cm)	CTH kPa (psi)	ConWep kPa (psi)	Percent Error
0.5	0.125	26337 (3819.8)	30219 (4383.0)	-12.8
1	0.5	4677 (678.3)	5001 (725.3)	-6.5
2	1	484 (70.2)	645 (93.6)	-25.0
4	1	95.8 (13.8)	110 (16.0)	-13.8
5	1	880 (9.2)	70.3 (10.2)	-9.8
10	1	21 (3.1)	23 (3.4)	-8.8
			Average Error %	-12.8

TABLE 4.26: 200 kg charge – simulated reflected impulse.

Scaled Distance $m/kg^{1/3}$	Peak Reflected Impulse as a Function of Mesh Cell Size kPa ms (psi ms)					
	0.01 cm	0.05 cm	0.125 cm	0.25 cm	0.5 cm	1.0 cm
0.5	NR	NR	NR	NR	NR	NR
1	NR	NR	NR	NR	NR	NR
2	NS	NS	1575 (228.4)	1573 (228.1)	1571 (227.9)	1573 (228.2)
4	NS	NS	616 (89.3)	615 (89.2)	616 (89.3)	617 (89.5)
5	NS	NS	465 (67.4)	465 (67.4)	465 (67.4)	466 (67.6)
10	NS	NS	NS	206 (29.9)	207 (30.0)	207 (30.0)

Notes for Tables 4.26 through 4.28:

NS means not simulated because convergence was already achieved.

NR means no result obtained because secondary shock interfered with impulse quantification.

TABLE 4.27: Reflected impulse errors relative to one cell size larger.

Scaled Distance m/kg $^{1/3}$	Percent Error Relative to One Cell Size Larger					
	0.01 cm	0.05 cm	0.125 cm	0.25 cm	0.5 cm	1.0 cm
0.5	NR	NR	NR	NR	NR	-
1	NR	NR	NR	NR	NR	-
2	NS	NS	0.1	0.1	-0.1	-
4	NS	NS	0.1	-0.1	-0.2	-
5	NS	NS	0.0	0.0	-0.3	-
10	NS	NS	NS	-0.3	0.0	-

TABLE 4.28: 200 kg charge - comparison between converged reflected impulse and empirical data.

Scaled Distance m/kg$^{1/3}$	Converged Cell Size (cm)	CTH kPa ms (psi ms)	ConWep kPa ms (psi ms)	Percent Error
0.5	-	-	-	-
1	-	-	-	-
2	1	1573 (228.2)	1378 (199.9)	14.2
4	1	617 (89.5)	623 (90.3)	-0.9
5	1	466 (67.6)	487 (70.7)	-4.4
10	1	207 (30.0)	232 (33.7)	-11.0
			Average Error %	-0.5

The 5 kg reflected pressure results (Tables 4.17 through 4.19) show that at the worst case, a simulation using a 0.05 cm cell size is required to accurately simulate reflected pressure. This is over five times smaller than the resolution required for incident pressure. Using the converged cell sizes presented in Table 4.18, Table 4.19 shows that, on average, CTH underpredicts ConWep reflected pressure predictions by 14.6%. Note that even using the smallest mesh size tested does not improve this result considerably. Looking at the 5 kg reflected impulse results, Table 4.21 shows that impulse may be accurately simulated using a cell size that is twice the cell size required

for reflected pressure. In comparing the simulated reflected impulse to empirical data, CTH underpredicted the ConWep result by an average of only 0.3%. It is not clear why CTH's simulated reflected impulses would agree with ConWep better than its simulated incident impulses.

The 200 kg reflected pressure results (Tables 4.23 through 4.25) show that the larger charge requires less mesh resolution than the 5 kg charge. This result was also obtained when comparing incident pressures for the 5 kg and 200 kg charges. The 200 kg study found that CTH underpredicts reflected pressure by an average of 12.8% when comparing CTH and ConWep predictions. Finally, both the 5 kg and the 200 kg studies showed that reflected impulse is readily simulated using 1 cm cells for the scaled distances tested. In comparing simulated impulse, CTH underpredicted the ConWep result by an average of 0.5%. These error percentages (this statement applies to both incident and reflected parameters) are in excellent agreement with the empirical data, as Bogosian et al. (2002) show that even the most highly calibrated airblast prediction tools have errors between 6% and 15% when compared to experimental data.

There is one final complication that must be investigated. Because it is desirable to minimize the number of cells in the domain, and thus computational effort, it is preferable to use large cells where possible. In order to do this, the explosive material will be highly refined, the air much less so, and the reflecting surface again more refined. It was therefore of interest to check whether or not there was some minimum thickness that a zone of highly refined reflecting cells (the cells modeling the "film" of air at the reflecting surface) needed to be in order to provide an accurate result. Table 4.29 shows

the results of this investigation. As the data show, the thickness of the zone of highly refined cells for reflected pressure makes virtually no difference and so 10 centimeters will be used.

TABLE 4.29: Results of reflection zone thickness tests, 5kg charge, z=2 m/kg$^{1/3}$.

Explosive Cell Size (cm)	Air Cell Size (cm)	Refl. Zone Cell Size (cm)	Refl. Zone Thickness (cm)	Refl. Press. kPa (psi)	Refl. Imp. kPa ms (psi ms)
0.25	0.50	0.25	10	487 (70.7)	460 (66.7)
0.25	0.50	0.25	25	488 (70.8)	461 (66.9)
0.25	0.50	0.25	50	488 (70.8)	461 (66.8)

4.3. Two-Dimensional Test

The run times required to repeat the convergence study in two dimensions would have been prohibitive. Each simulated standoff could equate to days of simulation time, even using the University computing cluster. It was therefore decided to perform the convergence study in one dimension and then test whether or not the rules of thumb developed in one dimension worked well in two dimensions. Because all of this work will ultimately be applied to the A1 and B blast events, it was desirable to test the convergence criteria in a two-dimensional simulation at a similar scaled distance as the experiments. Thus, the following simulations were performed for a 9 kg spherical charge of TNT at a standoff distance of 2.5 meters. This corresponds to a scaled distance of 1.2 m/kg $^{1/3}$ which is slightly smaller than the scaled distance from the experiments and should thus be representative. Using ConWep, the impulse to pressure ratio was estimated to be 0.31 ms. Using this value in Eq. (4.16) yields a cell size estimate of 0.5

cm for incident pressures. Looking at Table 4.18 for a scaled distance between 1.0 and 2.0, a cell size of approximately 0.25 cm should be sufficient to simulate reflected parameters. Note that these exact cell sizes could not be used in the trial two-dimensional simulation because CTH determines cell sizes based on factors including the domain size and user specified level of refinement. Thus, the cell sizes tested had to be slightly smaller than the 0.5 cm and 0.25 cm sizes selected. Also, CTH requires that cells containing explosive materials always have the highest level of refinement of any material in the mesh. Therefore, the explosive charge and the reflection zone were refined using the same mesh size, even though the explosive could have been modeled with a courser mesh.

One additional complication is the desire to use adaptive mesh refinement (AMR) in multi-dimensional simulations. This software feature allows the problem to continuously adapt the mesh based on user instructions. In doing so, a significant computational savings is achieved, permitting very highly refined simulations to be performed in reasonable periods of time. Figures 4.3 and 4.4 are simulation results from two instants during the two-dimensional CTH simulations reported here. The left hand figures correspond to time t=0, and the right-hand figures correspond to approximately 1ms after detonation is complete. Figure 4.3 shows the configuration of the CTH mesh. The black lines represent the borders of mesh blocks, and each block contains approximately 100 cells. The figure shows that AMR indeed provides a finer mesh where it is needed, i.e. in regions of the model where high pressure and density gradients exist. Figure 4.4 are grayscale colormap plots of pressure at the same time periods shown

in Figure 4.3. White corresponds to high pressure and black corresponds to ambient pressure. The dark lines within the shock front represent the boundaries between gaseous detonation products and air.

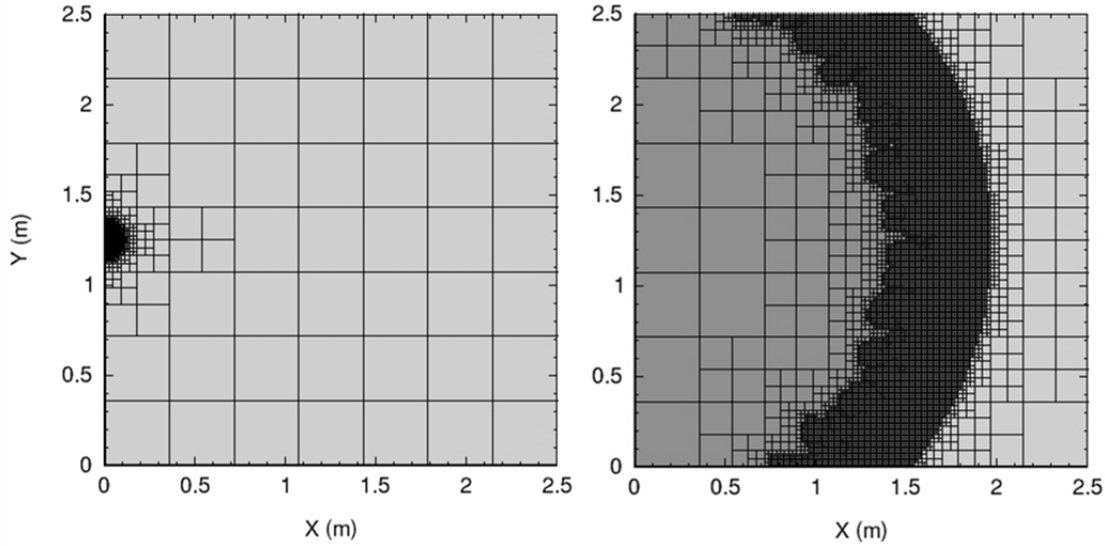

FIGURE 4.3: CTH Plot of materials at two different times during blast simulation.

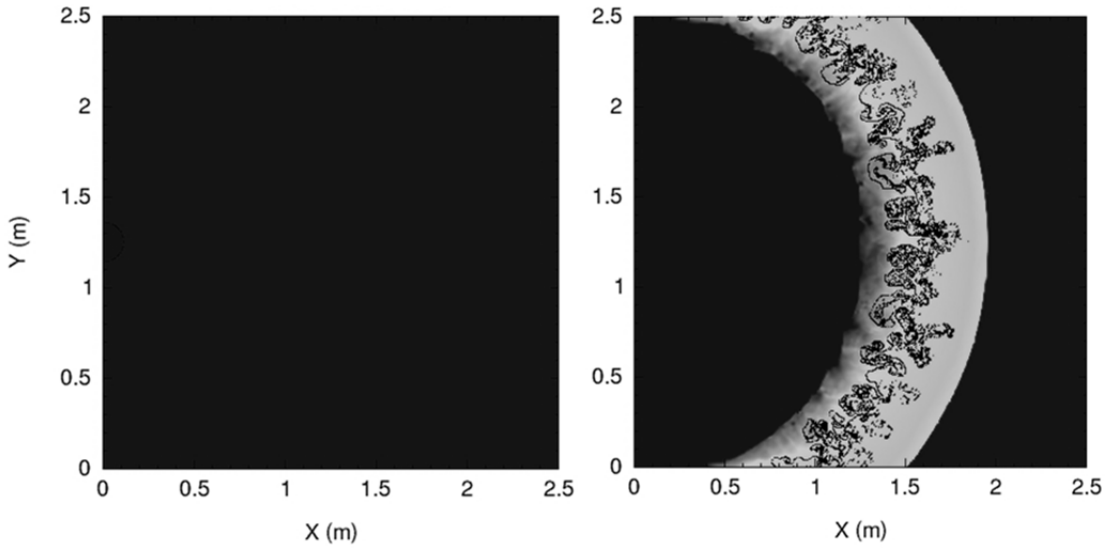

FIGURE 4.4: CTH Plot of pressure at two different times during blast simulation.

Table 4.30 shows the meshing scheme used in the two-dimensional simulations. Three different levels of resolution were tested to be certain that convergence had been achieved. Table 4.31 presents the results of the two-dimensional tests for each refinement level. The table shows that despite a nearly fourfold increase in resolution, the results did not change appreciably, and indeed the lowest mesh resolution was sufficient; this confirms that the convergence criteria previously identified can be applied to two-dimensional simulations.

TABLE 4.30: Cell sizes used in two-dimensional comparison.

Refinement Level	Explosive Mesh Size (cm)	Air Mesh Size (cm)	Reflection Mesh Size (cm)
1	0.22	0.44	0.22
2	0.11	0.22	0.11
3	0.055	0.11	0.055

TABLE 4.31: CTH results for three levels of refinement. 9 kg charge at 2.5 m standoff.

Level	CTH Pressure kPa (psi)	Percent Error* (pressure)	CTH Impulse kPa ms (psi ms)	Percent Error* (impulse)
1	2508 (363.7)	-14.0	895.6 (129.9)	-2.4
2	2475 (358.9)	-15.2	870.8 (126.3)	-5.1
3	2467 (357.8)	-15.4	881.1 (127.8)	-4.0

Notes:
*Error relative to ConWep which predicted 2916 kPa (423.0 psi) and 917.7 kPa ms (133.1 psi ms).

To summarize, the guidance developed in this chapter for creating a converged simulation can be restated as follows:

1. Knowing the charge size and standoff, use some simplified method (ConWep, nomograph, etc.) to predict the incident pressure and impulse.

2. Using the ratio of impulse divided by pressure, use Eq. (4.16) to estimate the cell size required for incident pressure.
3. As a starting point, the cell size required for reflected pressure will be approximately half the size predicted using Eq. (4.16), but could be up to five times smaller.
4. Run several simulations, each time decreasing the cell size by 50% until the results do not change significantly between one simulation and the next.

CHAPTER 5: THE JWL EQUATION OF STATE AND CTH SIMULATION RESULTS

Section 4.1 showed that an equation of state (EOS) is required to solve Euler's equations. An EOS must therefore be supplied for every material in the hydrodynamic model. Normally EOS are found experimentally due to the complexity of material behavior over the wide range of densities typically encountered in shock physics simulations. These complex behaviors can include phase changes, dissociation, ionization, etc. A study of Doan and Nickel's (1963) plots of the EOS of air quickly illustrates the challenge. Only recently has it been possible to develop an EOS using advanced thermochemical computer simulations, but even these are subject to interpretation by the user and are usually verified experimentally.

From a calculational standpoint, there are two primary types of EOS available – tabular and analytic. Tabular EOS consist of table-like data structures which describe the pressure, density, and energy states of a material across a wide range of the state variables. A tabular form can be useful when the EOS is based on experimental data for which a closed form expression cannot be readily developed. Analytic EOS are somewhat more convenient, providing closed-form mathematical expressions for the pressure, density, and energy. This chapter will develop the coefficients necessary to use an analytic EOS known as the Jones-Wilkins-Lee (JWL) equation of state.

An exhaustive discussion of the EOS for air is beyond the scope of this investigation. Moreover, there are few, if any, adjustments to the EOS that a user may

make in CTH, rendering it of lesser interest. It is sufficient to say that CTH uses a tabular EOS for air based on extensive empirical data; the airblast comparisons performed in Chapter 4 demonstrate it is well calibrated for the purpose of this investigation. The only adjustments that may be made to the EOS for air are defining its initial density and temperature as described in Section 4.2.

In CTH the JWL EOS is one option for simulating high explosive detonation. There are other EOS available that include models of reactive detonations (i.e. it simulates what happens during the transition from solid explosive to gaseous detonation products); however such a complex EOS is unnecessary for airblast simulations. The JWL EOS describes the adiabatic expansion of gaseous detonation products from the point immediately after detonation (i.e. after the completion of the thermochemical reactions of detonation are complete) to the final state at which the gasses have expanded to ambient pressure. This EOS does not model the behavior of the solid explosive. Instead, CTH replaces the solid explosive in the model with an equivalent mass of highly compressed detonation products which are described by the JWL EOS. The sequence and rate at which this replacement occurs is governed by the HEBURN algorithm of the software.

It is worth briefly discussing whether or not dynamite can be considered an ideal explosive. This is important as the theory presented in this chapter (and used in CTH to simulate detonation) is formulated for ideal explosives. Penn et al. (1975) defines an ideal explosive as one in which there is a constant rate of energy release over a wide range of diameters. Souers et al. (1996) defines an ideal explosive as one which follows

Zel'dovich-von Neumann-Doring (ZND) theory and possesses a true CJ state (to be defined shortly) under heavy confinement. Powerful military explosives like PETN are ideal explosives. Composite explosives like dynamite and ANFO (ammonium nitrate and fuel oil), typically do not display these characteristics. Penn et al. (1975) noted that, while ANFO's behavior was highly irregular and requires a more complex equation of state, dynamite can be approximated as an ideal explosive and thus the JWL EOS may be used.

5.1. Elementary Shock Physics Theory

Before proceeding with the development of JWL coefficients for Unimax, it is helpful to provide some background on the theory of shockwaves and detonations. Of primary importance to any shock physics analysis are the Hugoniot equations (Eqs. (4.6)). They are the fundamental equations that describe the state of matter undergoing shock compression. The Hugoniot equations hold true, irrespective of how a shock was generated or its strength. The precise pre/post shock states described by the Hugoniot equations must usually be determined experimentally for a given material. This is done by conducting a series of shock loading experiments in which the same material under test is subjected to shocks of varying strength. Using this experimental data, a curve is constructed which plots post-shock pressure as a function of specific volume. Such a plot is referred to as the Hugoniot curve and it is the graphical description of Hugoniot's mathematical relationships for a particular material. Figure 5.1 (the curved line) is an example of a Hugoniot curve for air, where P is pressure and V is specific volume, computed as $1/\rho$. It is important to understand that the Hugoniot does not represent a

path of compression or expansion, but rather is only the locus of all possible shock end states.

Instead, the path followed by shock loading is a straight line in *P*-*V* space, referred to as the Rayleigh Line (the straight line in Figure 5.1). This line is drawn using two points. The first point is the specific volume and pressure of the material before shock loading. The second point is located by the intersection of the Rayleigh line leaving the first point with a slope of $-\rho_o^2 U_s^2$ and intersecting the Hugoniot curve at a higher density and pressure (ρ_o is the unshocked density and U_s is the shock velocity). This second point on the Hugoniot curve is the post-shock state of the material.

As an example, consider a shockwave moving through air. Figure 5.1 shows the Hugoniot for air initially at US Standard Atmosphere (solid curve) and the Rayleigh line for a shock with a U_s of Mach 2.2 (dashed line). The diamond points on the solid curve represent data from Table 10 in Kinney and Graham's text (1985). As the graph shows, the passage of a shock travelling at Mach 2.2 will create an overpressure of 0.455 MPa (66.0 psi). The process of "jumping" from one state to another along the Rayleigh line is irreversible as a result of the entropy increase across the shock. After passage of the shockwave, the compressed material is typically assumed to expand along an adiabat or an isentrope. Note that isentropes are always adiabatic, but adiabats are not necessarily isentropic. The choice of an adiabat or isentrope is usually driven by the mathematical assumptions necessary to solve a particular problem, not the physics of the problem itself. In assuming isentropy, the problem becomes thermodynamically reversible, greatly simplifying certain types of calculations.

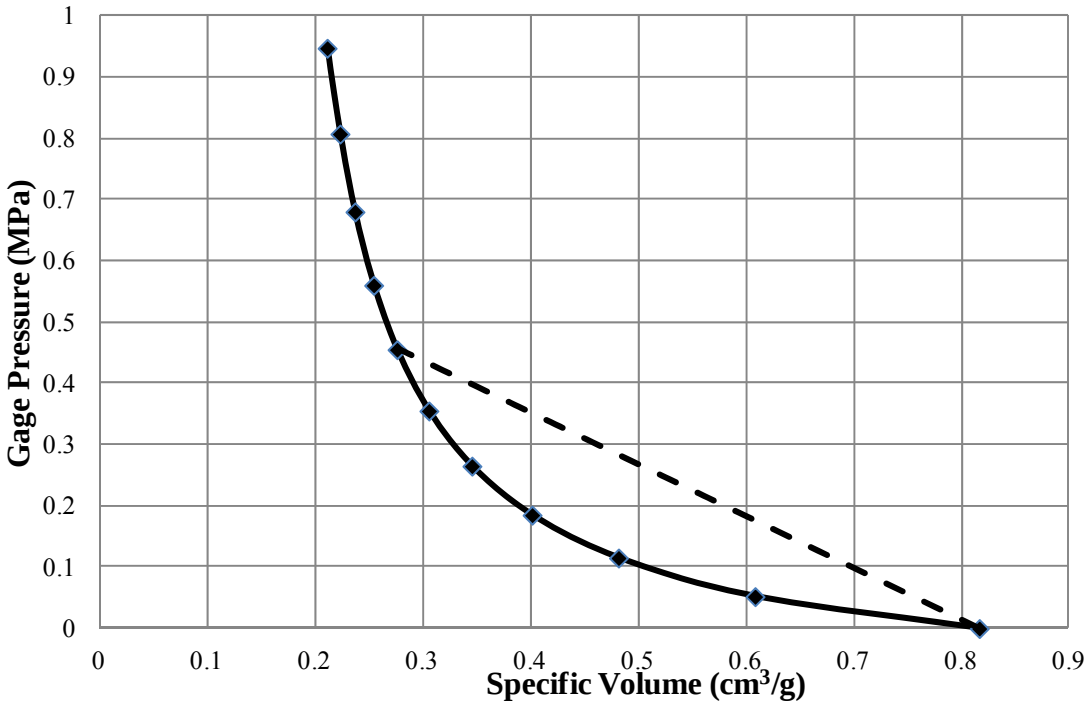

FIGURE 5.1: Hugoniot (solid curve) and Rayleigh line (dashed curve) for air initially at US Standard Atmosphere subject to a shock travelling at Mach 2.2.

As an interesting aside, many engineers do not recognize that airblast nomographs or tabulated airblast data are in fact a Hugoniot for air. Consider for example a typical nomograph of scaled distance versus peak pressure (like that shown in Figure 1.4). In such charts, each scaled distance corresponds to exactly one Mach number. In turn, this unique Mach number corresponds to exactly one overpressure ratio, which in turn corresponds to only one specific volume. Thus, the nomograph is actually a Hugoniot (or at least contains the same information as the Hugoniot) represented in a manner convenient for engineering calculations.

Rearranging the Hugoniot equations provides two useful expressions. Hugoniot's statement of the conservation of mass is given by:

$$\frac{\rho_o}{\rho} = 1 - \frac{u}{U_s} \tag{5.1}$$

This equation allows computation of relative volume based on the shock and particle velocities (u is the particle velocity). Hugoniot's conservation of momentum equation allows computation of pressure based on shock and particle velocities and is given by:

$$P = \rho_o U_s u \tag{5.2}$$

In these equations ρ_o is the pre-shock density, ρ is the post-shock density, u is the post-shock particle velocity, U_s is the shock front velocity, and P the pressure rise created by the shock. As written, these equations assume the material is at rest before being shocked (i.e. pre-shock velocity and pressure are zero).

These two simple equations permit transformation of experimental measurements into a Hugoniot. A good example of this is Deal (1957) which documents an experiment performed to develop a high pressure Hugoniot for air. In the experiment, a plate was explosively driven to high velocity. As the plate accelerated, the air in front of the plate was rapidly compressed causing an air shock to form. After formation, the shock front in the air traveled faster than the plate. Using a high speed camera, the velocity of the plate was measured (this is the particle velocity) and the velocity of the air shock was measured (this is the shock velocity). The experiment was repeated several times using different explosive quantities to achieve different plate velocities. This created different U_s-u pairs which were used to create a Hugoniot using Eqs. (5.1) and (5.2). This type of experiment is representative of how Hugoniot data can be generated for many materials.

The analysis of an explosive detonation requires one additional complication. The JWL EOS is based on an idea known as the Chapman Jouguet (CJ) theory of detonation. CJ theory assumes detonation is an instantaneous thermochemical reaction and places certain mathematical requirements on the state of gaseous detonation products. This special post-detonation state is termed the CJ state and can be found mathematically; however, a graphical illustration is helpful to comprehension. Figure 5.2 will be used to locate the CJ state of solid TNT. Finding the CJ state requires three overlaid curves in pressure-specific volume space. The first required curve is TNT's unreacted Hugoniot (solid curve at the bottom). It was produced from Gibbs and Popolato (1980) who provide the following expression for U_s. Cooper (1996) cites this equation as well.

$$U_S = 2.57 + 1.88u \tag{5.3}$$

Using Eq. (5.3), a set of U_s-u coordinates was calculated. Then using Eq. (5.2) the velocity pairs were used to compute pressure. Finally, using Eq. (5.1) the density and specific volume were calculated, thus producing the unreacted Hugoniot curve.

The second curve required to find the CJ state is the Rayleigh line for the detonation products. This corresponds to the straight line leaving the point P=0 MPa, V=0.61 cm^3/g on the unreacted Hugoniot with a slope of $-\rho_o^2 U_s^2$ (ρ_o = 1.63 g/cm^3 and U_s = 6.93 km/s) and intersecting the unreacted Hugoniot again at high density and pressure. The high pressure intersection of the Rayleigh line with the unreacted explosive Hugoniot is referred to as the Von Neumann spike and describes an intense mechanical compression. This shock compression leads to the thermochemical process of detonation.

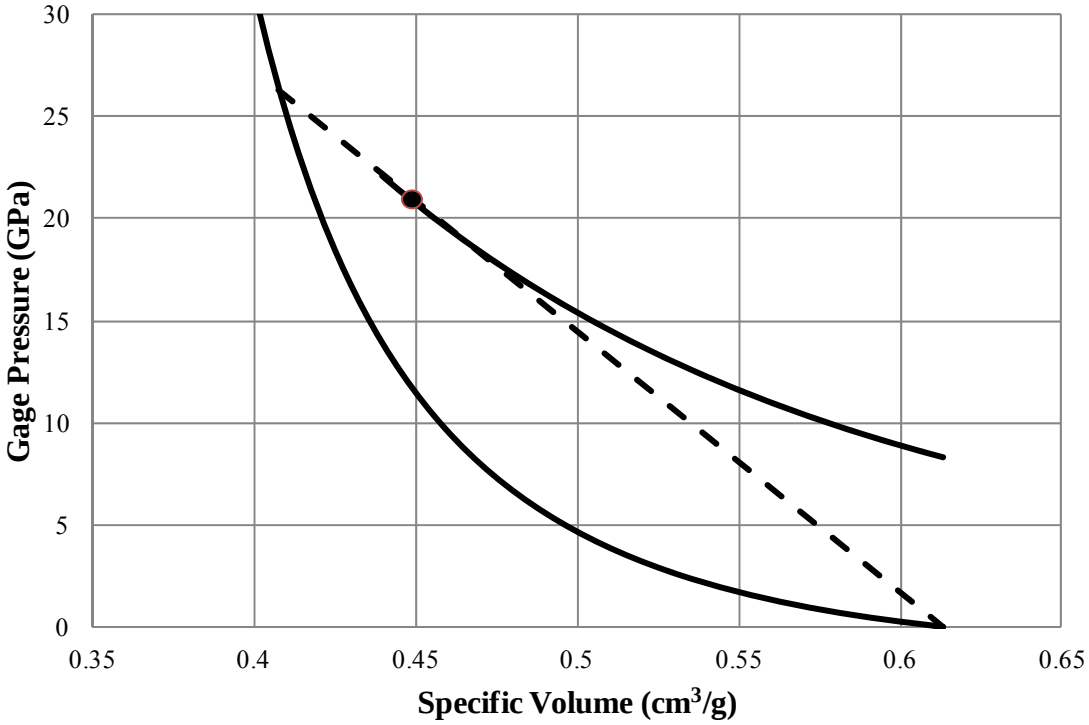

FIGURE 5.2: Unreacted Hugoniot (lower solid line), detonation products Hugoniot (upper solid line), Rayleigh line (dashed line) and CJ state (solid dot) for TNT.

As the thermochemical reaction proceeds to completion, the material unloads along some path (that is not important for our purposes) until it reaches the point where the Rayleigh line is tangent to the Hugoniot curve of the detonation products. This detonation product Hugoniot (the upper solid curve) is the third curve necessary to specify the CJ state. Several simple methods presented by Cooper (1996) were tested to generate a detonation products Hugoniot but they did not produce satisfactory results. Instead, the BCAT utility within CTH was used to output the Hugoniot of the detonation products in the region of interest. This Hugoniot is plotted as the upper solid Hugoniot curve in Figure 5.2.

The CJ state, identified by a solid dot in Figure 5.2, corresponds to the only intersection between the Rayleigh line and the detonation products Hugoniot which yields a stable detonation. At this point, CJ theory requires the slope of the Rayleigh line, the detonation products Hugoniot, and the expansion isentrope to all be equal. Recalling Eq. (4.17), which says that the square root of the slope of lines in *P*-*V* space equals the sound speed, this CJ theory requirement simply means that the velocity of all parts of the detonation wave must be equal. If the slopes were different it could mean, for example, that the detonation front is overtaken by its rarefaction wave, or that the reaction zone between the detonation front and the rarefaction wave expands to be very large (Cooper 1996). Such results are not observed in real detonations and thus CJ theory is believed to be a reasonable approximation of reality.

Once the detonation products are formed at the CJ state, they expand along the detonation products isentrope, which is defined by the JWL EOS. For clarity the isentrope is not shown in Figure 5.2 because it lies directly over the Hugoniot in the region of interest. Many authors will state that for engineering purposes, the Hugoniot and isentrope for detonation products may be assumed to be equivalent, but this is only a good approximation near the CJ state. For the remainder of this document, a variable with the subscript "CJ" implies that the variable is computed at the CJ state. This convention will be used often, as the properties of detonation products at the CJ state are very important in defining JWL coefficients.

5.2. The JWL Equation of State

From the CJ state, the detonation products expand along an adiabatic path until they have equilibrated with the surrounding atmosphere. Adiabatic means that the expanding detonation products are assumed to have a constant energy throughout expansion. For convenience, this adiabatic path is normally also assumed to be isentropic (entropy does not change), allowing an integral of the expansion isentrope to compute the energy released. Although the real process of expansion isn't reversible or isentropic, Van Ness (1969) amusingly explains "our choice in thermodynamics often is to do calculations for reversible processes or to do no calculations at all." Given that the JWL EOS is only an approximation (a curve fit) of the expansion process observed in real high explosive detonations, these thermodynamic assumptions are acceptable.

The JWL EOS is essentially a curve fit describing this expansion path from the CJ state to ambient conditions. In all of the equations that follow, V_r is the relative volume computed as ρ_o/ρ. V_{CJ} is V_r evaluated at the CJ state. The standard form of the JWL EOS given by Lee et al. (1968) is

$$P(V_r, E) = A\left[1 - \frac{\omega}{R_1 V_r}\right] e^{-R_1 V_r} + B\left[1 - \frac{\omega}{R_2 V_r}\right] e^{-R_2 V_r} + \frac{\omega E_S}{V_r} \tag{5.4}$$

In the equation, the pressure, P, is computed as a function of the relative volume, V_r, and the energy, E. The variables A, B, ω, R_1, and R_2 are material-specific constants derived for use with the JWL. Eq. (5.5) shows how the variable E_s is computed as a function of V_r.

$$E_S(V_r) = \frac{A}{R_1} e^{-R_1 V_r} + \frac{B}{R_2} e^{-R_2 V_r} + \frac{C}{\omega V_r^{\omega}} \tag{5.5}$$

In the equation, C is yet another material-specific JWL constant. The form of the JWL equations used by CTH are given by

$$P(V_r, T) = Ae^{-R_1 V_r} + Be^{-R_2 V_r} + \omega \rho C_V T \tag{5.6}$$

$$E(V_r, T) = \frac{1}{\rho_o}\left[\frac{A}{R_1} e^{-R_1 V_r} + \frac{B}{R_2} e^{-R_2 V_r} - E_o\right] + C_V T \tag{5.7}$$

$$C_V = \frac{C}{\omega T_{CJ} \rho_o}\left(1 - \frac{P_{CJ}}{\rho_o D_{CJ}^2}\right)^{-\omega} \tag{5.8}$$

In these equations, T is the temperature, C_v the specific heat at constant volume, E_o is the explosive's per unit volume chemical energy, T_{CJ} is the detonation temperature, P_{CJ} the detonation pressure, and D_{CJ} the detonation velocity. The equations show that CTH uses temperature, rather than energy, as a state variable. When certain assumptions are made regarding the detonation temperature, the energy and temperature forms are equivalent. The transformation between the two forms may be made using Eq. (5.8) with T_{CJ} assumed to be 0.35 eV (electron volts, 1 eV is equal to 11604.5 Kelvin).

There are a few rules for values the JWL coefficients must take, and rigorous analysis (Souers and Haselman, 1994) has found no useful relationship between the physical properties or performance of an explosive and its JWL coefficients. Despite this, there are several rules of thumb that appear to hold true. R_1 is normally approximately equal to four while R_2 is approximately equal to one. The ω term is usually between 0.2 and 0.4. The A term is roughly 100 times the B term and 1000 times the C term (Lee et al. 1968). Souers (2005) cautions users that the JWL coefficients should be reported to at least five decimal places. The author of this dissertation has

found this to be true, as using fewer significant figures leads CTH to calculate the wrong CJ state. Section 5.3 will discuss in greater detail how JWL coefficients are developed.

There are three critical conditions that any set of JWL coefficients must satisfy. First, when evaluated, the chosen coefficients must predict an energy release consistent with the available chemical energy, E_o, computed by

$$E_o = \frac{A}{R_1} e^{-R_1 V_{CJ}} + \frac{B}{R_2} e^{-R_2 V_{CJ}} + C_V T_{CJ} \rho_o - \frac{P_{CJ}(1-V_{CJ})}{2} \tag{5.9}$$

Also, when evaluated at the CJ state, Eq. (5.10) must predict the correct CJ pressure.

$$P_{CJ} = \frac{A\left[1-\frac{\omega}{R_1 V_{CJ}}\right] e^{-R_1 V_{CJ}} + B\left[1-\frac{\omega}{R_2 V_{CJ}}\right] e^{-R_2 V_{CJ}} + \frac{\omega E_o}{V_{CJ}}}{1+\frac{\omega\left(1-\frac{1}{V_{CJ}}\right)}{2}} \tag{5.10}$$

Eq. (5.11) is the third condition that must be satisfied; it relates the detonation velocity, detonation pressure, and initial density.

$$D_{CJ} = \sqrt{\frac{P_{CJ}}{\rho_o(1-V_{CJ})}} \tag{5.11}$$

Hydrocodes (including CTH) perform these checks to determine if the JWL coefficients specified are consistent with the specified CJ state. If the JWL coefficient set is found to be inconsistent, the hydrocodes usually redefine the CJ state to produce consistency, often leading to an incorrect representation of the explosive material.

5.3. Developing JWL Coefficients

Coefficients for the JWL EOS are normally derived from a calibration process that involves experiments and simulation (Lee et al. 1968). The experimental component of calibration can be summarized as follows: a machined hollow copper cylinder with an inner diameter of at least three centimeters, a wall thickness of 5 to 10 millimeters, and a

length to diameter ratio of four or more is filled with the explosive for which the JWL coefficients are sought. The cylinder is then detonated from one end which causes a rapid expansion and disintegration of the copper cylinder. As the detonation progresses, cameras or laser velocimeters are used to record the deflection or velocity time history of the copper cylinder's wall. LS-DYNA, a commercially available finite element code (LSTC, Livermore, CA), or some other hydrocode like CTH is then used to simulate the experiment. LS-DYNA has a built-in JWL EOS as well as material models that are well calibrated for the type of copper used in the experiment; LS-DYNA is thus a popular code for this problem. The JWL coefficients are adjusted in LS-DYNA until the simulated wall deflection/velocity time history closely matches the experimental data. Souers and Haselman (1994) provide an excellent discussion of this and other processes for determining JWL coefficients.

This experimentally based calibration method is thought to provide the most accurate set of JWL coefficients over a broad range of pressures (as compared to coefficients merely estimated from experience or computed using thermochemical equilibrium software programs). This calibration, however, is quite expensive and requires specialized equipment (e.g. cameras with frame rates of 100,000 fps and greater) to measure the expansion of the copper cylinder. JWL coefficients that are determined using this method are only available for traditional military explosives.

The dynamite used in this study has not been characterized by this process. When JWL coefficients are not available for a particular explosive, there are methods of estimating the required coefficients using those of another already characterized

explosive. Section 5.4 will document the JWL coefficients of previously characterized dynamites found in peer reviewed literature or government technical reports. Section 5.5 will use these existing coefficients as the basis for developing new JWL coefficients for Unimax dynamite. Finally, Sections 5.6 and 5.7 report simulation results for the A1 and B blast events using the newly-developed JWL coefficients.

5.4. Existing Dynamite JWL Coefficients

There is limited data available regarding the performance and modeling of commercial explosives like the dynamite used in this work. Typically, defense laboratories or the Department of Energy in the United States are tasked with characterizing explosives to support ongoing weapons related programs. Within the government explosives community, the characterization of an explosive is typically project specific, and dynamite is no longer used for military applications because more powerful and easily molded compounds are available. Over the last 50 years, TNT and PETN have emerged as the "standard" explosive compounds (with a large body of research) to which all others are compared. While the use of precisely manufactured TNT charges would have greatly simplified the airblast modeling in this investigation, logistical considerations required the use of readily available dynamite in the experimental program.

Much of the information in this dissertation regarding dynamite is from personal communications with Bob LeVan, an engineer with Dyno Nobel (Salt Lake City, UT). In the 1980's there were still several nitroglycerin dynamite manufacturers as evidenced by Cooper (1996). Of the commercially manufactured dynamites, Unigel (made by

Hercules) was considered the standard gelatin dynamite. Dyno Nobel acquired Hercules in 1985 and began manufacturing Unigel as its own product. With the rising use of bulk explosives like ANFO, the demand for dynamites decreased and Dyno Nobel became the sole manufacturer of nitroglycerin dynamites in North America. Dyno Nobel currently manufactures two nitroglycerin dynamite products, Unigel and Unimax. Their energetic and chemical properties are shown in Table 5.1. As shown in the table, Unimax is more powerful than Unigel. No test data was available regarding detonation pressure, so the following expression from Cooper (1996) was used to estimate it:

$$P_{CJ} = \rho_o D_{CJ}^2 (1 - 0.7125\rho_o^{0.04}) \tag{5.12}$$

Cooper claims that, when compared to experimental measurements, the predicted pressure is usually within 5%.

TABLE 5.1: Properties of Dyno Nobel dynamites from LeVan (2007).

	Unimax	Unigel
Detonation Velocity (D_{CJ})	5856 m/s	4300 m/s[a]
Detonation Pressure (P_{CJ})	14.2 GPa[b]	6.73 GPa[b]
Unreacted Density (ρ_o)	1.50 g/cc	1.30 g/cc
Relative Weight Strength	1.20	1.09
Nitroglycerin Ether Extract	26.2 %	19.5 %
Ammonium Nitrate	39.2 %	67.0 %
Sodium Nitrate	25.6 %	7.40 %
Heat of Explosion (≈energy)	6.322 kJ/cc	5.191 kJ/cc

Notes:
a. Unigel's detonation velocity is minimum guaranteed
b. Values computed using Eq. (5.12)

Table 5.2 provides a listing of dynamites and the associated detonation velocities that could be located in published literature. The Unigel currently manufactured by Dyno Nobel is similar in density to that manufactured at the time of previous studies. It also

appears as though Unimax is similar to the ammonia gelatin dynamite from Sadwin et al. (1965); it is reassuring to see that their detonation velocities are so similar. Unimax is called an "extra gelatin dynamite" by the manufacturer. The designation "extra" means that the composite explosive contains additional oxidizers. The "gelatin" designation refers to the nitroglycerin component which is combined with another agent to form a gel (Cooper, 1996).

TABLE 5.2: Summary of CJ parameters for dynamites from other researchers.

Product Description	ρ_o (g/cc)	P_{CJ} (GPa)	D_{CJ} (m/s)	Charge Diameter (mm)	Reference
Unigel	1.26	12.8	5760	Not Listed	Edwards et al. (1994)
Unigel	1.294	12.0	5477	Not Listed	Hornberg (1986)
Unigel	1.262	12.0	5760	Not Listed	Penn et al. (1975)
Gelatin Dynamite	1.50	15.4*	6090	100	Souers et al. (2004)
Permissible Dynamite	1.10	2.25*	2680	45	Souers et al. (2004)
Ammonia Gelatin Dynamite	1.50	14.8*	5980	100	Sadwin et al. (1965)
Extra Dynamite	1.36	6.37*	4100	100	Sadwin et al. (1965)

Note: *Value computed using Eq. (5.12)

The most important properties to know when simulating the performance of an explosive are its unreacted density and the two Chapman Jouguet (CJ) state parameters: detonation velocity and detonation pressure. Table 5.2 shows that while Unigel's density has not varied considerably, there is a discrepancy between the manufacturer's detonation velocity D_{CJ} (shown in Table 5.1) and that obtained by other researchers. This might be

explained by the fact that Unigel's detonation velocity in Table 5.1 was provided by the manufacturer as a minimum, but Unimax's detonation velocity, on the other hand, was determined experimentally. The gelatin dynamite and ammonia gelatin dynamite shown in Table 5.2 have a similar density and detonation velocity as Unimax, suggesting the Dyno Nobel supplied detonation velocity is reasonably accurate.

Table 5.3 lists three Unigel JWL coefficient sets from the literature. The energy (or heat of explosion) provided by Dyno Nobel for Unigel in Table 5.1 is similar to the E_o value for two of the coefficient sets listed in Table 5.3. Penn et al. (1975) explicitly state that their E_o value was based on the heat of formation of the detonation products at the CJ state, but Hornberg et al. (1986) and Edwards et al. (1994) do not provide a clear indication of how they arrived at their energy values. E_o is an important parameter because it is used to make the energy of the JWL isentrope consistent with the explosive's available chemical energy (Lee et al., 1968). As will be shown, this is by far the single most important property of an explosive compound with respect to airblast results.

A previously undefined parameter appears in Table 5.3, γ_{CJ}. This term, called the adiabatic gamma, is the ratio of the detonation products' specific heat at constant pressure to the specific heat at constant volume. This coefficient varies with density and, as written in the table, is specifically for the CJ state. As the detonation products expand, the value of gamma varies nonlinearly until eventually decreasing to a value of 1.4 at atmospheric pressure (which is the same as the adiabatic gamma of air at sea level). Note that in this chapter, JWL coefficients are presented in units of GPa, meters per second,

and kJ. CTH uses dynes/cm^2 for pressure, centimeters per second for velocity, and ergs for energy. To convert pressure, multiply GPa by 1x10^{10} to get dynes/cm^2. To convert velocity, multiply m/s by 100 to get cm/s. To convert energy, multiply kJ by 1x10^{10} to get ergs.

TABLE 5.3: Summary of available JWL coefficients for dynamite in literature.

	Unigel by Penn et al. (1975)	Unigel by Hornberg (1986)	Unigel by Edwards et al. (1994)
ρ_o (g/cc)	1.262	1.294	1.26
P_{CJ} (GPa)	12.0	12.0	12.8
D_{CJ} (m/s)	5760	5477	5760
E_o (kJ/cc)	5.1	5.1	4.04
γ_{CJ}	2.49	Not Reported	2.49
A (GPa)	190.7	121.831	109.70
B (GPa)	7.58	1.857	7.58
R_1	4.4	3.60150	4.4
R_2	1.4	0.86185	1.4
ω	0.23	0.20	0.23
C (GPa)	0.627	0.549	Not Reported

5.5. Obtaining JWL Coefficients

An exhaustive search was undertaken to identify procedures for computing JWL coefficients. The search revealed two primary methods of obtaining "new" coefficients. One method would be to use advanced thermochemical equilibrium codes to directly compute JWL coefficients. Such tools, however, require significant experience and training beyond what was reasonable for this investigation. Even when used by experienced scientists, these tools may still yield results which are questionable and require tests for validation.

The method eventually adopted for this study was to scale new JWL coefficients from those of another similar explosive. There are, however, very few methods available for engineers to perform such scaling procedures. Souers et al. (1996) presents one scaling technique, but only for very small variations in density. Small density adjustments of this type are typically required when analyzing multiple blasts from a test series in which charge properties vary slightly between shots. In Lee et al. (1968), where the JWL EOS is first presented, another method of scaling JWL coefficients is described for density changes on the order of 10%. While the density scaling used in this investigation is approximately 15%, the method of Lee et al. (1968) was still employed due to both its relative simplicity and a lack of better options.

The scaling procedure from Lee et al. (1968) is shown in Eqs. (5.13) through (5.19).

$$P'_{CJ} = \frac{\rho'_o D^{2\prime}}{\gamma_{CJ}+1} \tag{5.13}$$

$$E'_o = \frac{\rho'_o}{\rho_o} E_o \tag{5.14}$$

$$V_{CJ} = V'_{CJ} = \frac{\gamma_{CJ}}{\gamma_{CJ}+1} \tag{5.15}$$

$$P'_{CJ} = A'e^{-R_1 V_{CJ}} + B'e^{-R_2 V_{CJ}} + \frac{C'}{V_{CJ}^{(\omega+1)}} \tag{5.16}$$

$$-E_o{}' = -E'_{CJ} + \frac{1}{2} P'_{CJ}(1 - V_{CJ}) \tag{5.17}$$

$$E'_{CJ} = \frac{A'}{R_1} e^{-R_1 V_{CJ}} + \frac{B\prime}{R_2} e^{-R_2 V_{CJ}} + \frac{\frac{C\prime}{\omega}}{V_{CJ}^{\omega}} \tag{5.18}$$

$$\gamma_{CJ} = \frac{V_{CJ}}{P'_{CJ}} \left[-R_1 A' e^{-R_1 V_{CJ}} - R_2 B' e^{-R_2 V_{CJ}} - (\omega + 1) \frac{C'}{V_{CJ}^{(\omega+2)}} \right] \tag{5.19}$$

In these equations, the scaled JWL coefficients are primed. The original γ_{CJ} value, the new unreacted density, and the new detonation velocity are used to compute the new CJ state pressure according to Eq. (5.13). The new E_o is linearly scaled from the original E_o by the ratio of new to original density using Eq. (5.14). The new relative volume at the CJ state is assumed to be identical to the old relative volume as shown in Eq. (5.15). The original values of R_1, R_2, γ_{CJ}, and ω are used in conjunction with the new values of E_o' and P_{CJ}' to solve three simultaneous equations for the three unknowns *A'*, *B'*, and *C'*. The three equations are the system given by Eqs. (5.16), (5.17), and (5.19), with Eq. (5.18) showing the calculation of energy at the CJ point. The full procedure is well documented in Lee et al. (1968) and it was found that implementing the process using Excel's (Microsoft, Redmond, WA) solver feature was both simple and accurate.

The three sets of JWL coefficients listed in Table 5.3 were compared to the Unigel currently manufactured by Dyno Nobel (Table 5.1). The first two have similar energies (E_o) while the third is significantly lower. The third set was therefore discarded. The second set of coefficients from Hornberg (1986) had unusual values for R_1 and R_2, and this caused the adjustment method to produce a negative value for *B*, which is unacceptable. The second set was therefore also discarded. The density-based adjustment scheme was therefore applied to the JWL coefficients from Penn et al. (1975). Without knowledge of how Dyno Nobel derived Unimax's heat of explosion, it was thought unwise to rely on this value to determine the explosive's energy. Thus, the Penn et al. (1975) E_o for Unigel was scaled up based on the density ratio, rather than directly

specifying the manufacturer-supplied energy from Table 5.1. The results of the JWL coefficient scaling procedure are provided in Table 5.4.

TABLE 5.4: Adjusted EOS coefficients using method of Lee et al. (1969).

	Unigel Penn et al. (1975)	Adjusted Unimax per Lee et al. (1968)
ρ_o (g/cc)	1.262	1.50
P_{CJ} (GPa)	12.0	14.7390
D_{CJ} (m/s)	5760	5856
E_o (kJ/cc)	5.1	6.062
γ_{CJ}	2.49	2.49
A (GPa)	190.7	234.350
B (GPa)	7.58	9.5127
C (GPa)	0.627	0.50064
R_1	4.4	4.4
R_2	1.4	1.4
ω	0.23	0.23

Although the new coefficients set was self-consistent and could be justified based on the literature, it did not produce satisfactory results with respect to airblast. Table 5.5 shows a preliminary CTH simulation of the A1 blast event using the adjusted JWL coefficients. The table shows that the adjusted coefficient set produced an average absolute error of 23.2% in reflected pressure and 21.2% in reflected impulse for Shot A1. As will be shown in Chapter 6, the structural response of the blast chamber walls is predominately impulse driven. It was therefore desirable to try to decrease the impulse error, even at the expense of reflected pressure accuracy.

Having attempted one of the few adjustment methods available, an alternative, more unconventional approach was sought. Using the consistency conditions of Eqs. (5.9) through (5.11), the effect of changing JWL coefficients on airblast simulation

results was studied to determine what, if any, effect changes in the JWL coefficients had on the results of an airblast simulation. The investigation included varying detonation velocity, detonation pressure, and all of the JWL coefficients. The study found that, as long as E_o remained constant, changing any or all of the JWL coefficients in concert yielded very little change in the results of an airblast simulation.

TABLE 5.5: Simulation of Shot A1 using E_o=6.06 kJ/cc.

	P1	P2	P3	P5
CTH Reflected Pressure kPa (psi)	7033.3 (1020.1)	1801 (261.2)	681 (98.7)	1729 (250.8)
Measured Reflected Pressure kPa (psi)	5437 (788.6)	2329 (337.8)	810.1 (117.5)	2295 (332.9)
% Error	29.4	-22.7	-16.0	-24.7
CTH Reflected Impulse kPa ms (psi ms)	1600 (232.0)	746.0 (108.2)	498 (72.3)	729.5 (105.8)
Measured Reflected Impulse kPa ms (psi ms)	1257 (182.3)	628 (91.1)	363 (52.6)	738.4 (107.1)
% Error	27.3	18.8	37.5	-1.2

Note:
Air was meshed with 0.38 cm cells, reflection zone meshed with 0.19 cm cells.

Initially this appeared to be counterintuitive. After some consideration, however, this seems feasible given that the JWL coefficients are primarily tuned to reproduce cylinder wall velocities. In all of the references describing the JWL EOS and its coefficients, there is no information or procedure presented for calibration for far field results. Based on this simple study it would appear that outside the gaseous detonation products, it is only the initial energy of the charge that matters for sufficiently accurate airblast simulations using the JWL EOS. The JWL coefficients are thus only important in that they define the CJ state properly (the problem's initial conditions). The only

significant change in airblast results occurs by changing E_o – the greater the energy, the greater the resulting pressure and impulse.

With this simple but important finding, an alternate JWL coefficient adjustment scheme was sought. In Chapter 3, an adjustment factor of 0.9 was applied to the explosive's net weight to account for packaging, and then another factor of 0.94 was applied to account for the lower energy content relative to TNT. Thus, the relative strength of charges comprised of dynamite sticks to TNT was taken to be about 84.6% by gross weight. Table 3.5 showed that this produced reasonably good results when compared to open arena tests using Unimax. Based on this observation, a new E_o was directly selected (rather than scaled based on density). Because the 84.6% equivalence utilized in Chapter 3 was only an estimate, a decision was made to simply select a new "round" number for E_o rather than strictly adhering to this equivalency. E_o was therefore adjusted from 6.06 kJ/cc to 5.0 kJ/cc. This corresponds to a 71.4% TNT equivalence based on energy. It is interesting to note that, had Edwards (1994) Unigel data in the original density scaling process been used, an E_o of 4.8 kJ/cc would have been computed.

The adjustment procedure for changing only E_o is somewhat different than the one from Lee et al. (1968). This new procedure starts with the density adjusted JWL coefficients shown in Table 5.4. The consistency conditions at the CJ state (Eqs. (5.9) through (5.11)) were implemented in an Excel spreadsheet. The problem was constrained to require that the predicted E_o be 5.0 kJ/cc and that D_{CJ} be 5856 m/s. Maintaining the measured D_{CJ} was justifiable as measurements of detonation velocity are usually accurate. The Excel solver was then used to adjust the coefficients A, B, C, R_1, R_2, and ω

until the consistency conditions were satisfied. No restriction was imposed on the value of P_{CJ} or the adiabatic gamma (and by extension the CJ state relative volume). Rather, CTH's own nonlinear solver algorithm was utilized to find V_{CJ} which in turn dictated P_{CJ}. The nonlinear solver works by iteratively solving the consistency conditions (Eqs. (5.9) through (5.11)) for a V_{CJ} that satisfies the three equations. The algorithm was borrowed from the CTH Fortran source code file eosjwi.F and is not reproduced in this document due to export control and copyright considerations. The algorithm was implemented such that the Excel solver could iteratively use the calculation of V_{CJ} as it solved for new JWL coefficients. The resulting set of energy-modified JWL coefficients are shown in the right-hand column of Table 5.6 along with the density-scaled coefficients of Table 5.4 for comparison. The Excel solver preferentially changed R_1, R_2, and ω and not A, B, or C, presumably because R_1 and R_2 have a larger influence on energy and velocity. Although it would be possible to make an adjustment in which only A, B, and C are modified, there is no reason to believe that such an adjustment is any better than the one presented in Table 5.6.

Using the energy-adjusted JWL coefficients, shot A1 was again simulated. Table 5.7 shows the results of this simulation, and indeed the reflected impulse agreement has improved, albeit at the cost of reflected pressure accuracy. Using an E_o of 5.0 kJ/cc, the CTH simulations had an average pressure error of 32.0% and an average impulse error of 15.2%. As an added check of these new coefficients, a simulation was conducted for shots BPS-10 and BPG-14 (documented in Table 3.2). These shots were chosen because of the relative consistency of the measurements and because of the larger charge size,

which helps reduce variability due to small inconsistencies in dynamite stick weight. As Table 5.8 shows, the adjusted JWL coefficients do a good job of predicting incident impulse, but are less accurate for incident pressure. It is not clear why CTH overpredicts the free air incident pressures but underpredicts the A1 reflected pressures. Note that although the simulations in Tables 5.7 and 5.8 used different mesh sizes, both simulations were found to be converged. The primary reason for the difference in cell sizes was because the simulation domains were of different dimensions and thus the CTH cell size selection algorithm required a slightly different mesh dimension.

TABLE 5.6: Adjusted EOS coefficients based on Lee et al. and energy scaling.

	Unigel Penn et al. (1975)	Adjusted Unimax per Lee et al. (1968)	Adjusted Unimax Based on E_o=5kJ/cc
ρ_o (g/cc)	1.262	1.50	1.50
P_{CJ} (GPa)	12.0	14.7390	14.6502
D_{CJ} (m/s)	5760	5856	5856
E_o (kJ/cc)	5.1	6.062	5.000
γ_{CJ}	2.49	2.49	N/A*
A (GPa)	190.7	234.350	234.350
B (GPa)	7.58	9.5127	9.5127
C (GPa)	0.627	0.50064	0.50064
R_1	4.4	4.4	4.35917
R_2	1.4	1.4	1.39147
ω	0.23	0.23	0.24975

Note: *The adiabatic gamma is not required for this calculation.

There is no clear reason why the E_o in CTH and Dyno Nobel's supplied heat of explosion should be so different. It is likely that the Dyno Nobel value is the inaccurate energy quantity because the usual user of dynamite only cares about the maximum energy the product will yield. This value can be used for calculations regarding safe

standoff and storage. Thus, an inaccurate estimate of energy on the part of the manufacturer has minimal impact provided the estimate is conservatively high; the findings of this investigation would suggest this is indeed the case.

TABLE 5.7: Simulation of Shot A1 using E_o=5.0 kJ/cc.

	P1	P2	P3	P5
CTH Reflected Pressure kPa (psi)	4933 (715.5)	1213 (175.9)	635 (92.1)	1171 (169.9)
Measured Reflected Pressure kPa (psi)	5437 (788.6)	2329 (337.8)	810.1 (117.5)	2295 (332.9)
% Error	-9.3	-47.9	-21.6	-49.0
CTH Reflected Impulse kPa ms (psi ms)	1553 (225.3)	704.0 (102.1)	431 (62.5)	692.2 (100.4)
Measured Reflected Impulse kPa ms (psi ms)	1257 (182.3)	628 (91.1)	363 (52.6)	738.4 (107.1)
% Error	23.6	12.1	18.8	-6.3

Note: Air was meshed with 0.38 cm cells, reflection zone meshed with 0.19 cm cells.

TABLE 5.8: Simulation of Shots BPS-10 and BPS-14.

	Sensor PP1	Sensor PP2
CTH Incident Pressure kPa (psi)	169 (24.5)	171 (24.8)
Average Measured Incident Pressure kPa (psi)	134 (19.4)	143 (20.8)
% Error	26.2	19.2
CTH Predicted Incident Impulse kPa ms (psi ms)	109 (15.8)	108 (15.7)
Average Measured Incident Impulse kPa ms (psi ms)	94.5 (13.7)	90.3 (13.1)
% Error	15.3	19.8

Note: Charge bottom detonated. Air cells meshed using a 0.25 cm cells.

5.6. Two-Dimensional CTH Simulations – Shots A1 and B

Using the adjusted JWL coefficients (based on an E_o of 5.0 kJ/cc), two-dimensional (cylindrically symmetric) CTH models were constructed for Shots A1 and B. Several different levels of refinement were studied to ensure that the data reported in the

following tables and figures represents a converged result. The explosive in these models was meshed with 0.048 cm cells, the air with 0.096 cm cells, and the air near reflecting surfaces with 0.048 cm cells. With such high levels of refinement, two-dimensional simulations required nearly 1000 CPU hours of compute time each. The input files for this and all other CTH models that follow can be found in Appendix E.

Table 5.9 presents results for the two-dimensional simulation of Shot A1. The average absolute reflected pressure error was 30.9% and the average absolute reflected impulse error was 16.8%. Although reflected pressure agreement was relatively poor, the reflected impulse agreement was very good and is typical of the errors seen in other analytical methods under good conditions (Bogosian et al., 2002). Tables 5.10 and 5.11 show the tabulated CTH predictions of reflected pressure and impulse at intervals of 50 cm up the height of the A1 blast chamber walls. Note that for all results that follow in this section, reflected blast pressures are typically reported up the full height of the wall but impulse results do not always cover the full height. This is because near the top of the walls in the simulation, nonphysical reflections from the symmetry boundary condition sometimes could not be separated from real reflections from the ceiling or floor. Thus no impulse is reported in this region as it would be an inaccurate estimate.

TABLE 5.9: Comparison between CTH predictions for Shot A1 and experimental data.

	P1	P2	P3	P5
CTH Reflected Pressure kPa (psi)	4551 (660.1)	1331 (193.1)	618 (89.7)	1363 (197.7)
Measured Reflected Pressure kPa (psi)	5437 (788.6)	2329 (337.8)	810.1 (117.5)	2295 (332.9)
% Error	-16.3	-42.8	-23.7	-40.6
CTH Reflected Impulse kPa ms (psi ms)	1607 (233.1)	683 (99.1)	443 (64.2)	677 (98.2)
Measured Reflected Impulse kPa ms (psi ms)	1257 (182.3)	628 (91.1)	363 (52.6)	738.4 (107.1)
% Error	27.9	8.8	22.1	-8.3

TABLE 5.10: Vertical pressure profile of Shot A1 simulation.

Height Above Chamber Floor (cm)	Peak Reflected Pressure kPa (psi)	Peak Reflected Pressure as a Percentage of Simulated Reflected Pressure at 50 cm
0	8011.0 (1161.9)	181.9
50	4403 (638.6)	100.0
100	2304 (334.2)	52.3
150	1127 (163.5)	25.6
200	632 (91.6)	14.3
250	431 (62.5)	9.8
300	343 (49.7)	7.8
350	302 (43.8)	6.9
400	253 (36.7)	5.7
450	213 (30.9)	4.8
503[b]	592 (85.9)	13.5

Notes for Tables 5.10 and 5.11:

a. N/A means reflected blast waves interfered with impulse quantification.
b. Simulated chamber height was slightly greater than actual chamber height in order to obtain square mesh cells.

TABLE 5.11: Vertical impulse profile of Shot A1 simulation.

Height Above Chamber Floor (cm)	Peak Reflected Impulse kPa ms (psi ms)	Peak Reflected Impulse as a Percentage of Simulated Reflected Impulse at 50 cm
0	1874 (271.8)	135.6
50	1382 (200.5)	100.0
100	783 (113.6)	56.7
150	621 (90.1)	44.9
200	447 (64.9)	32.4
250	413 (59.9)	29.9
300	387 (56.2)	28.0
350	366 (53.1)	26.5
400	346 (50.2)	25.0
450	N/A[a]	N/A[a]
503[b]	N/A[a]	N/A[a]

The data in the preceding tables is represented graphically in Figures 5.3 and 5.4. The figures show that both qualitatively and quantitatively, the CTH predicted pressure and impulse profiles are representative of the experimentally measured quantities.

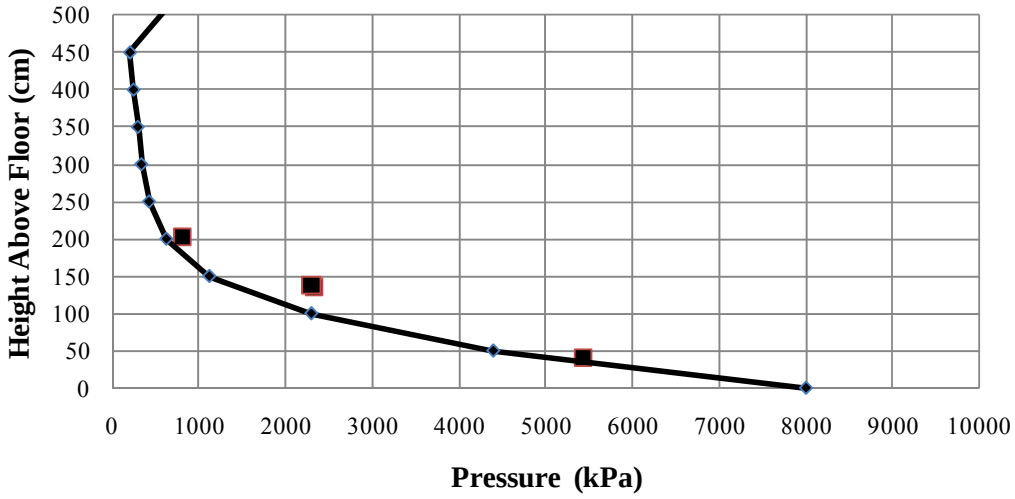

FIGURE 5.3: Plot of peak reflected pressure versus height above blast chamber floor (Shot A1). Solid line is CTH simulation. Square data points are experimental measurements.

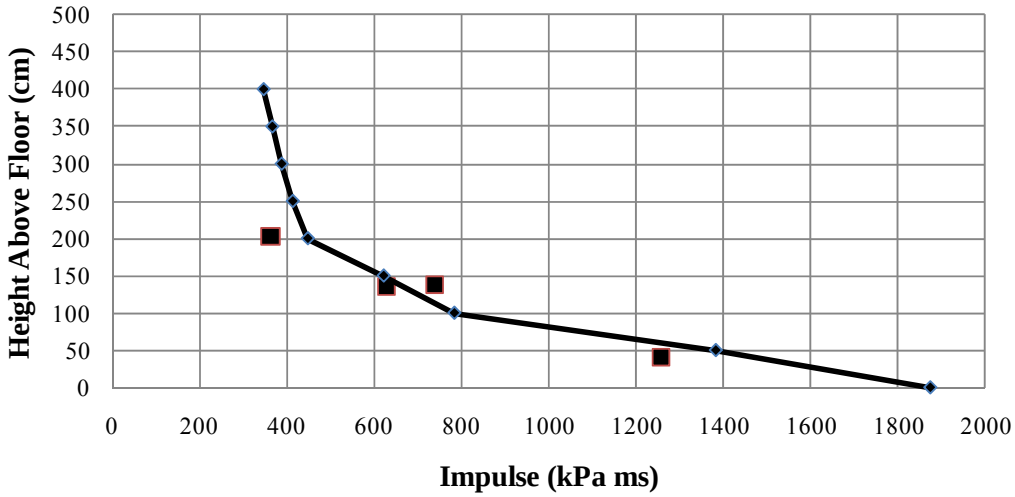

FIGURE 5.4: Plot of peak reflected impulse versus height above blast chamber floor (Shot A1). Solid line is CTH simulation. Square data points are experimental measurements.

Two similar models were developed for Shot B. One model was used to predict reflected pressures and impulses for Wall #2 while the other predicted reflected pressures and impulses for Wall #3. The models used nearly identical mesh dimensions as the model for A1. Table 5.12 shows that the Shot B simulations underpredicted peak reflected pressures by an average of 30.1% and overpredicted peak reflected positive impulse by 19.3%. Note that the error in the P6 reflected impulse simulation is not included in the average error computation. This is because subsequent reflected blast waves in the experimental data could not be removed from the first reflected wave. The two-dimensional CTH model could not reproduce these reflections. Comparison of the P6 pressure time history overlay included in Appendix F (Figure F.7) suggests that, if only the first reflected blast wave was considered, CTH and the experimental data might agree reasonably well. Tables 5.13 and 5.14 show the tabulated peak reflected pressure and reflected impulse as a function of height above the blast chamber floor for Wall #2.

TABLE 5.12: Comparison between CTH predictions for Shot B to experimental data.

	P1	P2	P4	P6
CTH Pressure	7474.6 (1084.1)	1227 (177.9)	1227 (177.9)	674 (97.8)
Measured	11000 (1595.4)	1500 (217.6)	1850 (268.3)	1060 (153.7)
% Error	-32.0	-18.2	-33.7	-36.4
CTH Impulse	1699 (246.4)	679 (98.5)	679 (98.5)	574 (83.3)
Measured	1260 (182.7)	593 (86.0)	627 (90.9)	1061 (153.9)
% Error	34.9	14.5	8.4	-45.8

Note: Experimental data included numerous reflections; inspection of time history overlays in Appendix F suggests errors reported in this table would be less if reflections were removed from experimental data.

TABLE 5.13: Vertical reflected pressure profile of Shot B simulation (Wall #2).

Height Above Chamber Floor (cm)	Peak Reflected Pressure kPa (psi)	Peak Reflected Pressure as a Percentage of Simulated Reflected Pressure at 50 cm
0	1411 (204.6)	112.9
50	1250 (181.3)	100.0
100	861.8 (125.0)	68.9
150	688 (99.8)	55.0
200	583 (84.6)	46.7
250	465 (67.5)	37.2
300	680 (98.6)	54.4
321	1158 (168.0)	92.7

TABLE 5.14: Vertical reflected impulse profile of Shot B simulation (Wall #2).

Height Above Chamber Floor (cm)	Peak Reflected Impulse kPa ms (psi ms)	Peak Reflected Impulse as a Percentage of Simulated Reflected Impulse at 50 cm
0	868.0 (125.9)	109.1
50	795.7 (115.4)	100.0
100	661 (95.9)	83.1
150	588 (85.3)	73.9
200	501 (72.7)	63.0
250	406 (58.9)	51.0
300	N/A	N/A
321	N/A	N/A

Note: N/A means reflected blast waves interfered with impulse quantification.

Figures 5.5 and 5.6 provide a graphical representation of the tables, showing the distribution of pressure and impulse up the wall's height. Due to the multiple reflections observed in the experimental data, the figures show a large error in CTH predicted blast quantities. As previously mentioned, however, if comparing only the first reflected shocks, CTH would exhibit a higher accuracy. Unfortunately, this is only a qualitative judgment because removing the first shock from subsequent reflections in the experimental data would be subject to error and thus an exact quantitative comparison would not be reliable. This perceived agreement, combined with the accuracy observed in the other two-dimensional simulations, provides some confidence that the results for Wall #2 are fairly representative of the first shock load experienced by the wall.

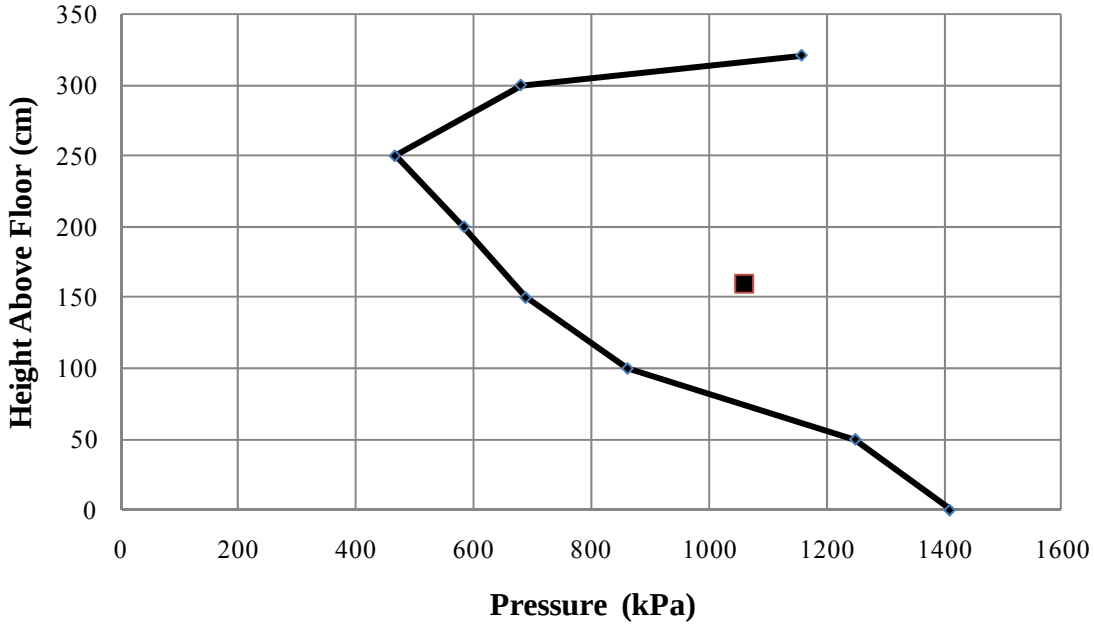

FIGURE 5.5: Plot of peak reflected pressure versus height above blast chamber floor (Shot B, Wall #2). Solid line is CTH simulation. Square data points are experimental measurements.

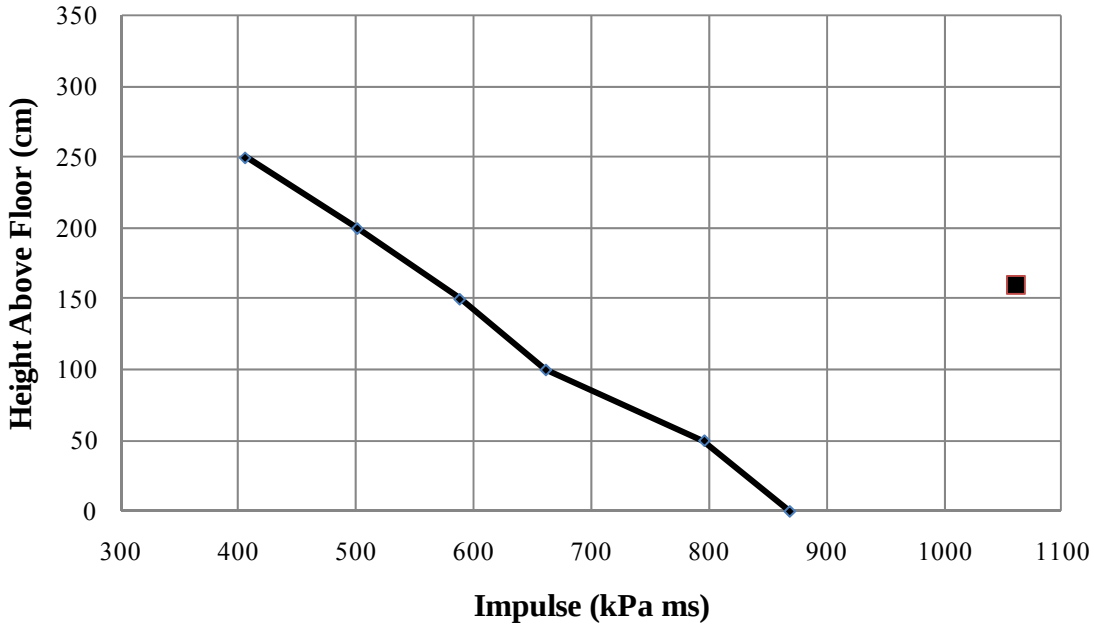

FIGURE 5.6: Plot of peak reflected impulse versus height above blast chamber floor (Shot B, Wall #2). Solid line is CTH simulation. Square data points are experimental measurements.

Tables 5.15 and 5.16 tabulate the peak reflected pressures and reflected impulses as a function of height above the blast chamber floor for Wall #3. Figures 5.7 and 5.8 are the graphical representation of this data. The figures show that both qualitatively and quantitatively, the CTH predicted pressure and impulse profiles are in agreement with the experimental data.

TABLE 5.15: Vertical reflected pressure profile of Shot B simulation (Wall #3).

Height Above Chamber Floor (cm)	Peak Reflected Pressure kPa (psi)	Peak Reflected Pressure as a Percentage of Simulated Reflected Pressure at 50 cm
0	10632 (1542.0)	142.2
50	7474.6 (1084.1)	100.0
100	2845 (412.6)	38.1
150	1404 (203.6)	18.8
200	937.0 (135.9)	12.5
250	609 (88.4)	8.2
300	408 (59.2)	5.5
350	1287 (186.7)	17.2
372	1395 (202.4)	18.7

TABLE 5.16: Vertical reflected impulse profile of Shot B Simulation (Wall #3).

Height Above Chamber Floor (cm)	Peak Reflected Impulse kPa ms (psi ms)	Peak Reflected Impulse as a Percentage of Simulated Reflected Impulse at 50 cm
0	2410 (349.6)	141.8
50	1700 (246.5)	100.0
100	1085 (157.4)	63.9
150	789.4 (114.5)	46.5
200	500 (72.5)	29.4
250	494 (71.7)	29.1
300	468 (67.9)	27.5
321	N/A	N/A

Note: N/A means reflected blast waves interfered with impulse quantification.

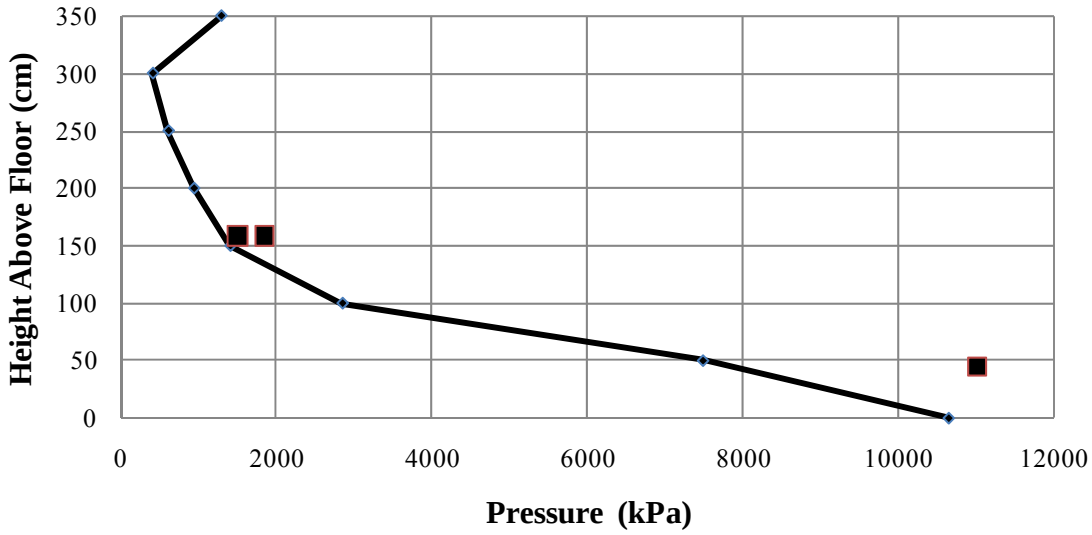

FIGURE 5.7: Plot of peak reflected pressure versus height above blast chamber floor (Shot B, Wall #3). Solid line is CTH simulation. Square data points are experimental measurements.

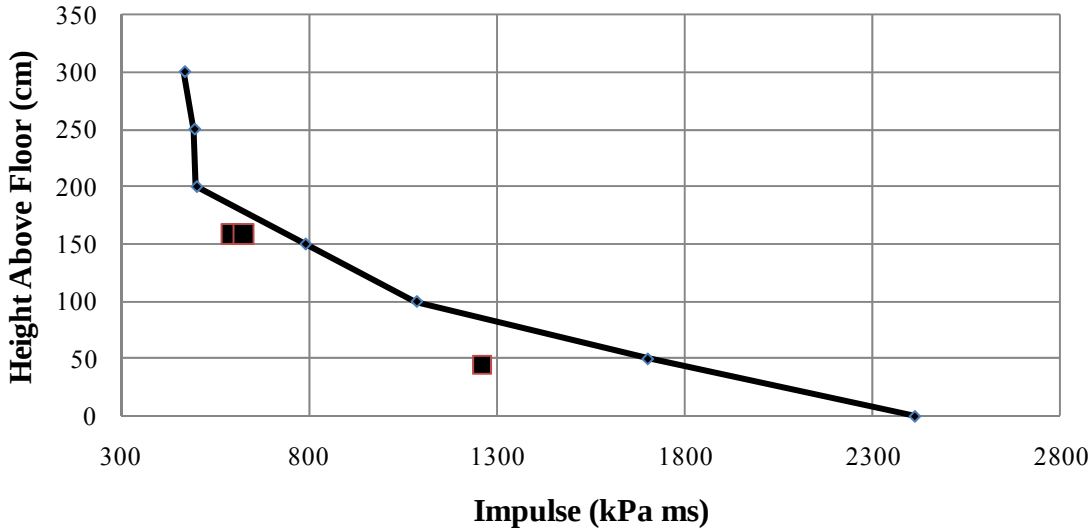

FIGURE 5.8: Plot of peak reflected impulse versus height above blast chamber floor (Shot B, Wall #3). Solid line is CTH simulation. Square data points are experimental measurements.

The preceding tables and figures are useful independently, but providing a comparison of the results might shed light on what "rules of thumb" might be developed from the hydrocode simulations. Figure 5.9 is a plot of the normalized peak reflected pressure as a function of height for all three simulations. The figure shows that, despite a difference in the charge size, the Shot A1 simulation and the Shot B Wall #3 simulations yielded nearly identical peak pressure distributions, which could be reasonably approximated by a bi-linear function. The Shot B Wall #2 simulation predicted a blast pressure distribution which was linear up until the dramatic rise in pressure which occurs near the wall-ceiling intersection. Figure 5.10 provides the same type of comparison of the three simulations, but with respect to reflected impulse. This time it appears that the Shot A1and Shot B Wall #3 impulse distributions could be approximated as trilinear while the Shot B Wall #2 impulse distribution could be approximated as essentially linear.

Studying Figure 5.9, it appears that as a rule of thumb, the bottom 50 to 100 cm nearest a wall's intersection with the floor receives significantly larger loads than any other portion of the wall. The Shot A1 and Shot B Wall #3 simulations both had scaled distances of approximately 1.3 $m/kg^{1/3}$; the Shot B Wall #2 simulation had a scaled distance of 2.1 $m/kg^{1/3}$. It appears that somewhere between those two scaled distances, a cutoff could be established where the shape of the pressure and impulse distributions change.

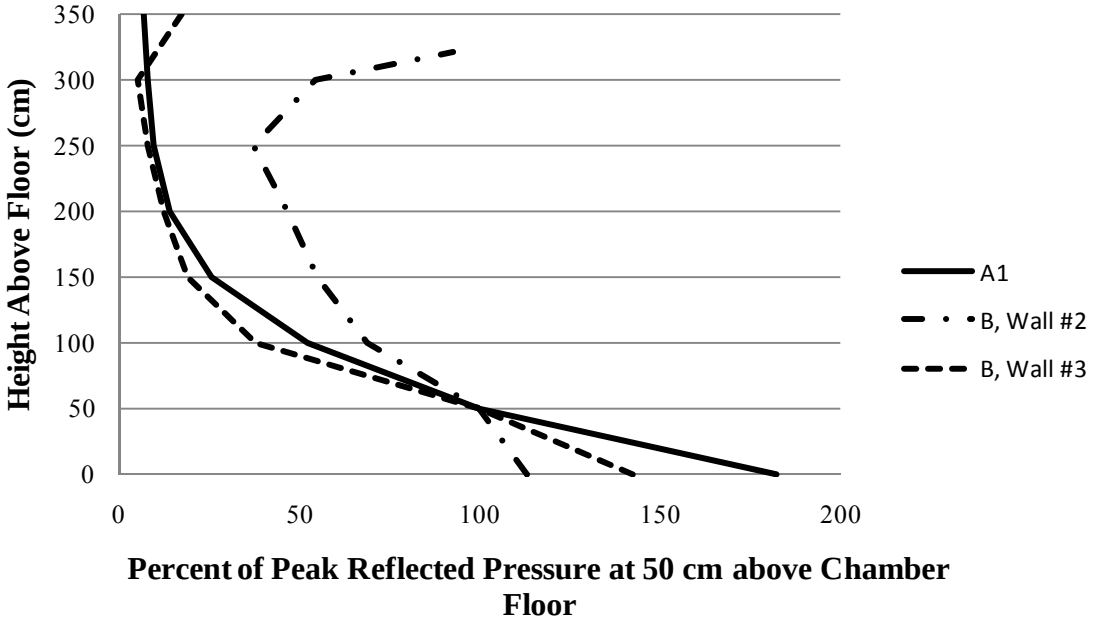

FIGURE 5.9: Comparison of normalized peak reflected pressure profiles from the three CTH simulations.

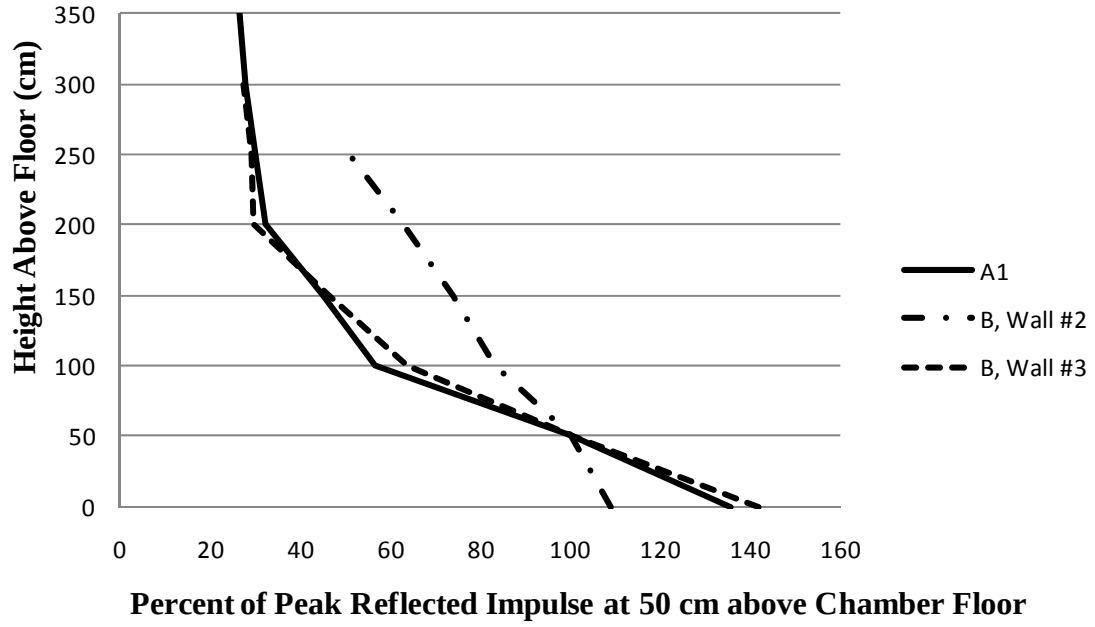

FIGURE 5.10: Comparison of normalized peak reflected impulse profiles from the three CTH simulations.

It bears repeating that for all impulse data, the impulse near the intersection of the wall with the ceiling was not computed because reflections from the floor could not be reliably separated from reflections created by the symmetry boundary which arrived at nearly the same time. These artifacts of the symmetry boundary do not have any basis in reality. If it were possible to remove these nonphysical reflections, there would still likely be a jump in impulse at the top of the wall, but for the purposes of the structural analyses performed in this dissertation, this will not have much of an effect. As will be described in Chapter 6, the pressure/impulse at the ends of a flexural member matter much less those near midspan for a flexural analysis.

Further comparisons between the CTH simulations and the experimental results are included in Appendix F. There the CTH pressure time histories are overlaid with the time histories measured by sensors during Shots A1 and B. The plots show that qualitatively, the CTH waveforms are similar to those measured by pressure sensors in the blast chambers. Although the simulated peak reflected pressures often differed significantly from the experimental measurements, the area under the curves was similar and thus the total impulse of the blast waves compared well between simulation and experiment. In the plots, the CTH waveforms were synchronized to the arrival of the first blast wave at sensor P1 in the Shot A1 or Shot B recorded data. Thus the P1 waveforms for simulation and experiment artificially appear to have coincident times of arrival. In examining the waveforms of other CTH simulated sensors in Appendix F, however, it is clear that CTH underpredicts shock velocity, as the simulated waveforms (of sensors other than P1) arrive later than their experimental counterparts. This is logical, given that

the pressures predicted by CTH were also lower (recall that higher shock velocities yield higher pressures). The accuracy of impulse and the relative inaccuracy of pressure suggest that dynamite (or at least charges comprised of dynamite sticks) may not be able to be modeled as an ideal explosive compound. If more accurate predictions of pressure are required, a complicated reactive burn model might need to be used, rather than the simple JWL EOS.

During the JWL EOS adjustment trials, an effort was made to artificially increase the reflected pressures (and thus shock velocities) predicted by CTH. This was done by increasing D_{CJ} and P_{CJ} while holding E_o constant. Such adjustments, however, did not yield the desired result. These efforts seemed to suggest that the constraints imposed by CJ theory (namely, the required isentrope slope at the CJ state) and the JWL EOS might very well prevent such adjustments (i.e. increasing pressure while decreasing impulse). This realization suggests that for airblast modelers, a simpler and less constrained EOS might be of use; because it is accurate airblast predictions that are of much more importance than the precise thermodynamic behavior of the explosive compound.

5.7. Shot B – Three-Dimensional Simulation

A three-dimensional simulation was also conducted for Shot B. The simulation was performed in order to develop two-dimensional loading profiles for the blast chamber walls; these will be used in the structural analyses that follow in Chapters 6 and 7. The boundaries of the simulation domain included most of the length of Wall#1 and #3, and all of Wall #2. Figure 5.11 is a plan view of Blast Chamber B showing the hatched volume included in the CTH simulation. The domain was 500 cm wide, 350 cm

tall, and 500 cm long. Note that these dimensions are slightly different than those of the actual blast chamber (as shown in Figure 2.7). This was necessary in order to provide a domain that could be meshed with perfectly cubic cells; this produces better simulation results for a given number of cells.

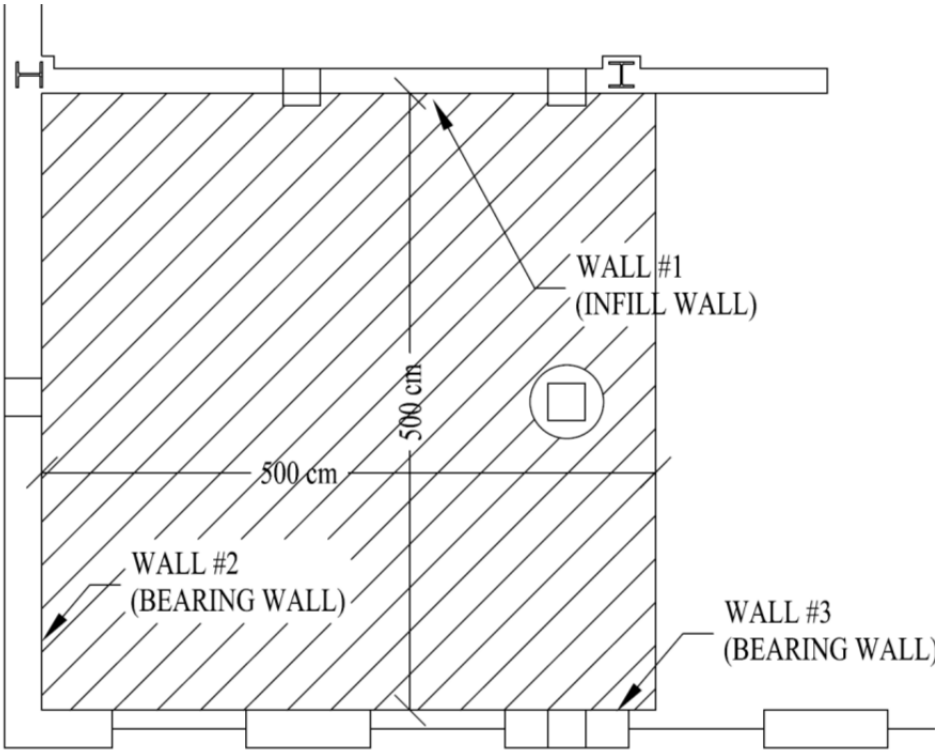

FIGURE 5.11: Plan view of Blast Chamber B. Hatched area represents chamber volume included in three-dimensional CTH simulation domain.

Convergence in the domain was investigated using cubic mesh sizes ranging from 1.563 cm to 0.0488 cm. An effort was made to use sizes smaller than 0.0488 cm; however, numerical difficulties that could not be resolved were encountered at these finer discretizations (negative energies developed in the expanding explosive material). Fortunately, the convergence study showed that the 0.0488 cm cell size was essentially

converged with respect to impulse. Note that this cell size is nearly identical to that used in the final two-dimensional simulations. Figure 5.12 is a three-dimensional image from the CTH simulation that shows a grayscale isosurface of pressure at the location of the shockfront immediately following detonation. Note that, despite the highly refined mesh size, artificial structures are still visible in the isosurface. *Z*=5 meters corresponds to the right-hand boundary shown in Figure 5.11.

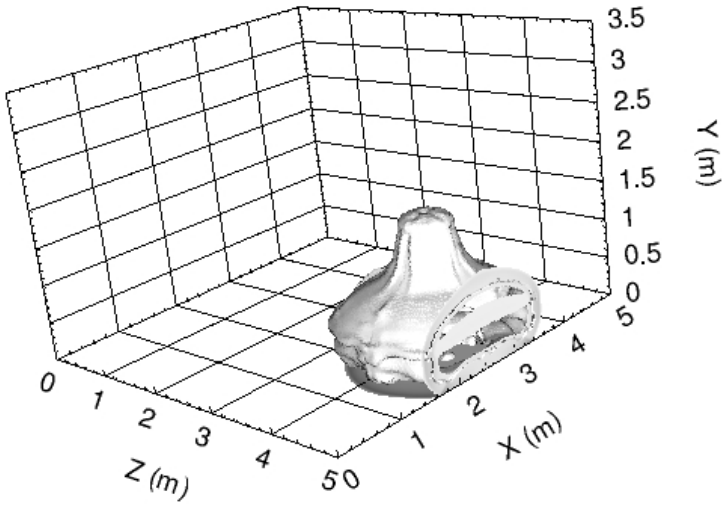

FIGURE 5.12: Image from CTH simulation showing pressure isosurface just after detonation.

An effort was made to include rigid material in the CTH domain to allow a direct simulation of the window openings in Wall #3. This would have been beneficial because it would have allowed an accurate representation of blast pressure venting through window openings; venting clearly occurred because pressure sensors in the blast chamber did not measure any quasi-static gas pressures. Unfortunately, CTH's rigid material feature (which is relatively new) does not appear to be fully functional, as inclusion of the

rigid material caused a variety of simulation errors including spurious fluctuations in virtual sensor measurements and artificially low reflected pressures. The rigid material option was therefore not included. Instead, the symmetry boundary condition (perfectly reflecting) was used to simulate walls and ceilings. This also led to difficulties as inclusion of Walls #1, #2, #3 and the blast chamber ceiling led to higher impulses than were measured in the experiment. Clearly then, shock venting through the window openings was important to dissipating blast chamber reflections.

Without the ability to use the rigid material model, it was necessary to simulate shock dissipation due to the windows by other means. It was determined that the best available option was to remove a blast chamber wall or the ceiling from the simulation domain. In doing so, reflected shocks were allowed to leave the simulation domain, thus decreasing the impulses from subsequent reflections and in principle relieving internal loads in a similar manner as the window openings would. An infinite transmitting medium was used to simulate the removal of a reflecting surface. Note that, for a given boundary, CTH requires that the entire boundary be of a single type; i.e. an infinite transmitting boundary condition cannot share the same plane as a perfectly reflecting boundary condition. Tables 5.17 through 5.19 tabulate the reflected pressures and impulses predicted by CTH using three different assumptions of reflecting surface.

TABLE 5.17: Load Case 1 - Walls #1, #2, #3, and ceiling included as reflecting surfaces.

Sensor	CTH Reflected Pressure kPa (psi)	Percent Error	CTH Reflected Impulse kPa ms (psi ms)	Percent Error
P1	5128 (743.8)	-53.4	2324 (337.1)	84.5
P2	854.9 (124.0)	-43.0	777.7 (112.8)	31.2
P4	854.9 (124.0)	-53.8	777.7 (112.8)	24.1
P5[a]	5128 (743.8)	-53.4	2324 (337.1)	84.5
P6	525 (76.1)	-50.5	1135 (164.6)	7.0
P7	541 (78.5)	-48.5	986.6 (143.1)	13.1
Average Absolute Error		50.4		40.7

TABLE 5.18: Load Case 2 - Walls #1, #2, and ceiling included as reflecting surfaces.

Sensor	CTH Reflected Pressure kPa (psi)	Percent Error	CTH Reflected Impulse kPa ms (psi ms)	Percent Error
P1	5128 (743.8)	-53.4	1757 (254.8)	39.5
P2	854.9 (124.0)	-43.0	482 (69.9)	-18.7
P4	854.9 (124.0)	-53.8	482 (69.9)	-23.1
P5[a]	5128 (743.8)	-53.4	1757 (254.8)	39.5
P6	525 (76.1)	-50.5	611 (88.6)	-42.4
P7	541 (78.6)	-48.5	491 (71.2)	-43.7
Average Absolute Error		50.4		34.5

TABLE 5.19: Load Case 3 - Walls #1, #2, and #3 included as reflecting surfaces.

Sensor	CTH Reflected Pressure kPa (psi)	Percent Error	CTH Reflected Impulse kPa ms (psi ms)	Percent Error
P1	5128 (743.7)	-53.4	1755 (254.6)	39.4
P2	854.3 (123.9)	-43.1	527 (76.4)	-11.2
P4	854.3 (123.9)	-53.8	527 (76.4)	-16.0
P5[a]	5128 (743.7)	-53.4	1755 (254.6)	39.4
P6	556 (80.7)	-47.5	797.7 (115.7)	-24.8
P7	541 (78.5)	-48.5	369 (53.5)	-57.7
Average Absolute Error		50.0		31.4

Notes for Table 5.17-5.19:

a. The P5 measurement was deemed unreliable due to non-physical signals in time history, thus the P1 measurements were used as a substitute to compute error.

Table 5.17 presents simulated sensor measurements for a simulation in which Walls #1, #2, #3, and the ceiling were included as reflecting surfaces (Load Case 1). Table 5.18 (Load Case 2) is the same simulation, having removed Wall #3 from the model (note that because of chamber symmetry, it was still possible to simulate all sensors). Table 5.19 (Load Case 3) is a simulation including Walls #1, #2, and #3 as reflecting surfaces but omitting the ceiling. All three tables show that, in general, peak reflected pressure is not well modeled; the average absolute error was slightly greater than 50%. It is not clear why the two-dimensional simulations had better pressure agreement using similar mesh sizes because, in principle, the three-dimensional model should have better represented the physics of the problem. This finding suggests it might be of use to compare several generic two and three-dimensional airblast simulations with identical mesh sizes; the comparisons might show there is some difference in convergence or simulation error between two and three-dimensional models. The pressure error observed here, however, is acceptable given that the out-of-plane response of blast chamber walls is impulse dominated, rather than pressure dominated; this assertion is based on the ratio of wall natural period to blast wave duration and will be further discussed in Section 6.1.2.

In comparing the impulse error across all sensors at once, including all walls but excluding the ceiling yields the best average absolute error (Load Case 3). But unfortunately this produces an impulse distribution which is artificially skewed toward the base of the walls. Studying the tables, it appears as though Load Case 2 (Table 5.18) represents a reasonable compromise – it includes the ceiling but provides a mechanism by which blast energy is vented. Load Case 2 produces an impulse error of -42.4% for

Wall #2 and of -43.7% for Wall #1; note that these errors are based on single points of measurement on each wall. For Wall #3, Load Case 2 yields an average absolute impulse error of 30.2% (based on sensors P1, P2, P4, and P5). Summing the errors (including sign) for all simulated sensors on all walls from Load Case 2, the net average error was -8.2%. Figures 5.13 through 5.18 show the CTH-predicted peak reflected pressures and impulses as contour plots over the surface of blast chamber walls in units of MPa and MPa ms, respectively. The contours were generated from the CTH data using the "griddata" feature and the "v4" interpolator of Matlab (see script D.6 in Appendix D for more information). Several different interpolation schemes were tried, including linear and cubic, but all showed generally the same result. The "v4" interpolation scheme yielded smoother looking contours and was therefore selected for final contouring.

In each plot, the "sensor locations" from the CTH simulations are shown as small circles. Although the pattern of observation points may appear somewhat haphazard, they actually correspond to wall quarter and midpoints, the location of the charge, and the location of instruments in the actual blast chamber of the test program. Given the number of observation points and the fact that all investigated interpolation methods produced similar results, the contour plots shown are probably accurate representations of the simulated peak pressures and impulses computed by CTH. Note that for Wall #2, symmetry was artificially created by using the CTH-predicted pressures from the half of Wall #2 adjacent to Wall #1. This was done because removing Wall #3 from the simulation created very low pressures near the transmitting boundary and it was thought more realistic to use the data closer to Wall #1.

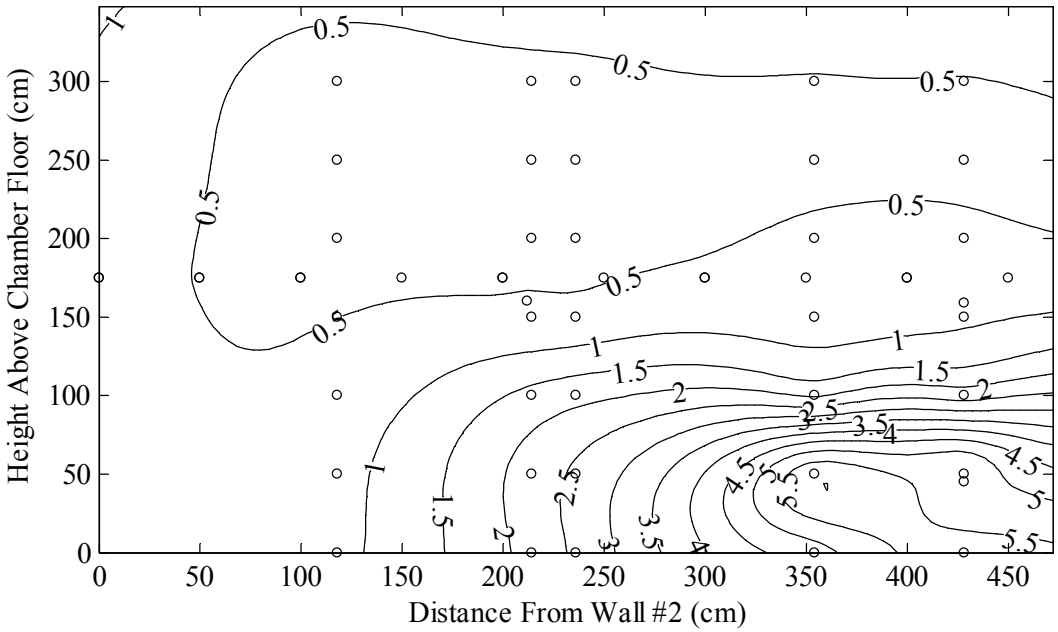

FIGURE 5.13: Contours of peak reflected pressure (MPa) computed by CTH for the surface of Wall #1, between Wall #2 and the end of Wall #1. Viewed from inside the blast chamber looking out.

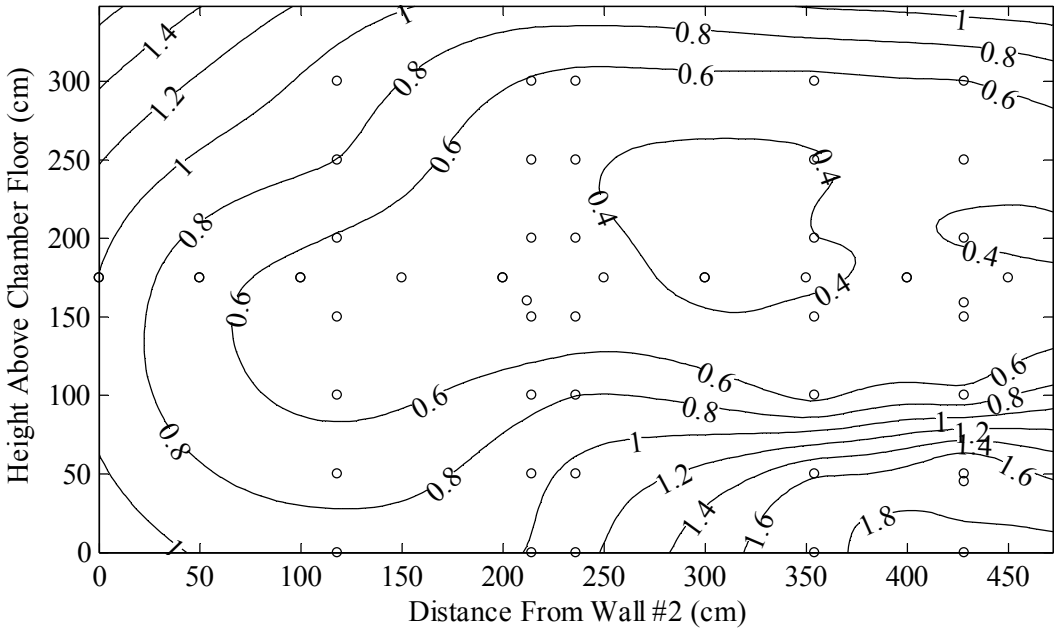

FIGURE 5.14: Contours of peak reflected impulse (MPa ms) computed by CTH for the surface of Wall #1, between Wall #2 and the end of Wall #1. Viewed from inside the blast chamber looking out.

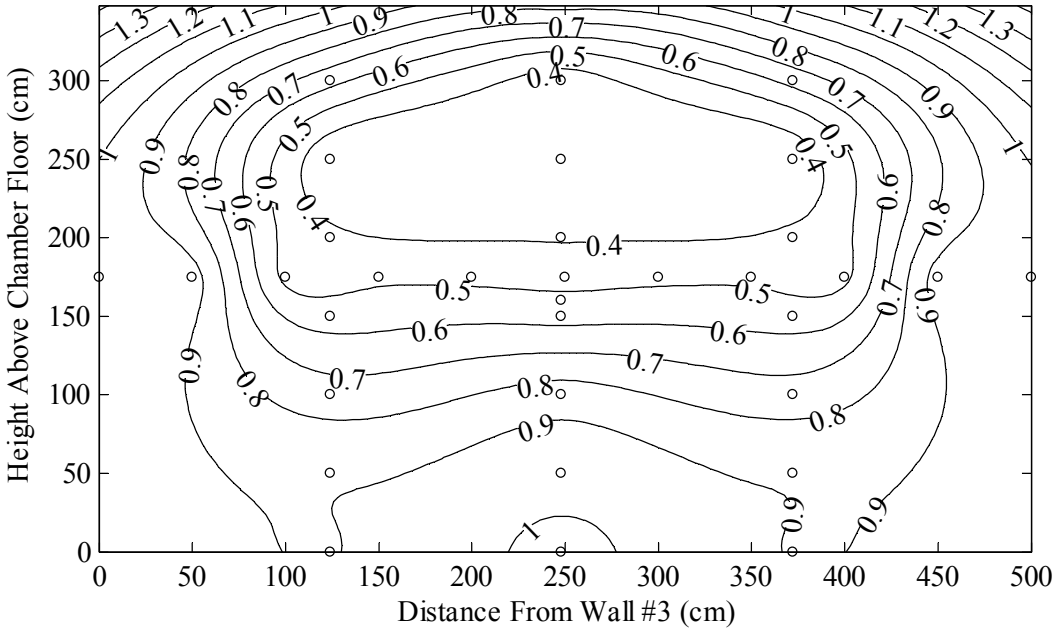

FIGURE 5.15: Contours of peak reflected pressure (MPa) computed by CTH for the surface of Wall #2. Viewed from inside the blast chamber looking out.

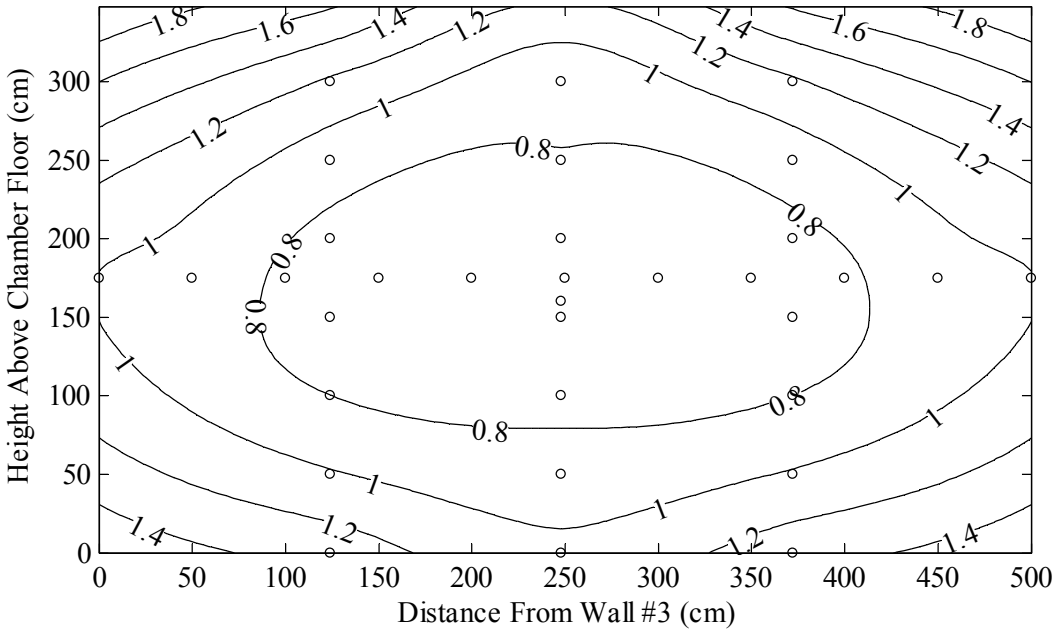

FIGURE 5.16: Contours of peak reflected impulse (MPa ms) computed by CTH for the surface of Wall #2. Viewed from inside the blast chamber looking out.

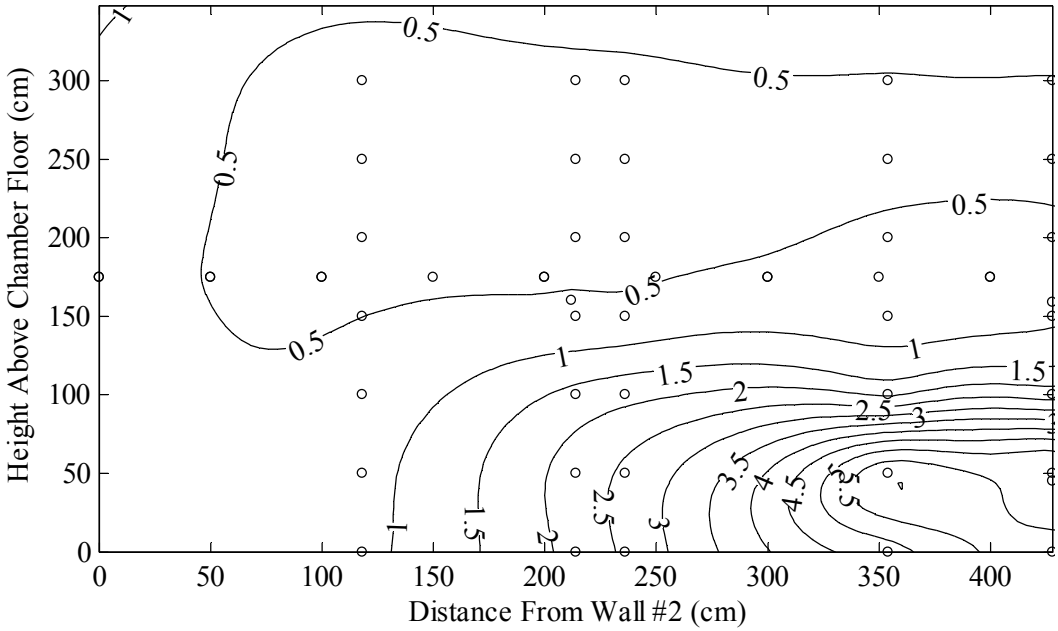

FIGURE 5.17: Contours of peak reflected pressure (MPa) computed by CTH for the surface of Wall #3 between Wall #2 and the charge centerline. Viewed from outside the blast chamber looking in.

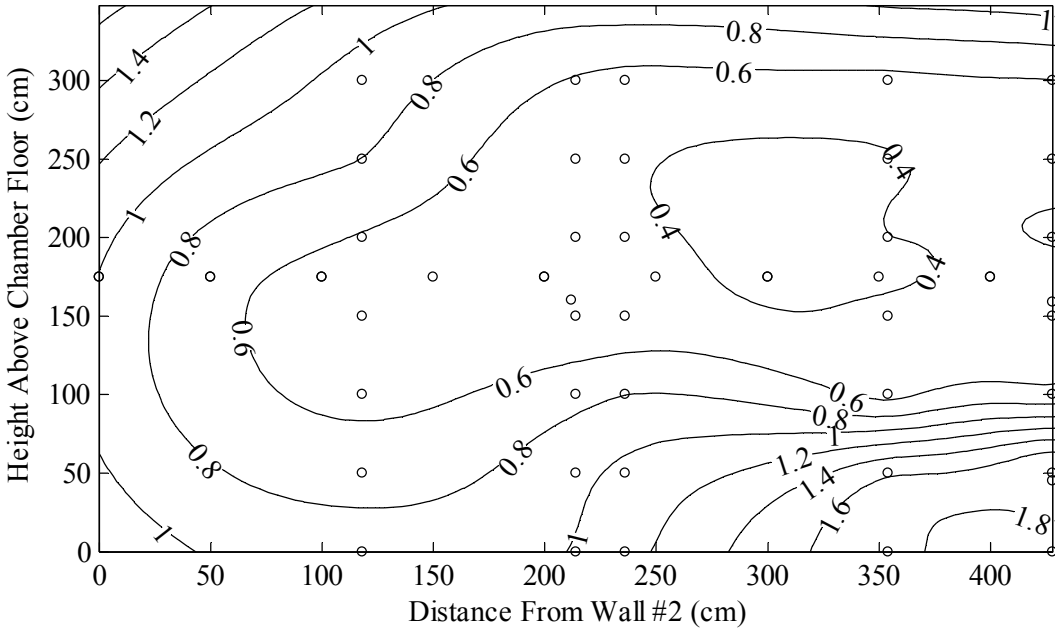

FIGURE 5.18: Contours of peak reflected impulse (MPa ms) computed by CTH for the surface of Wall #3 between Wall #2 and the charge centerline. Viewed from outside the blast chamber looking in.

CHAPTER 6: SINGLE DEGREE OF FREEDOM STRUCTURAL ANALYSIS

This investigation has gone to great lengths to develop representative blast load profiles for the Shot B blast chamber. The accurate prediction of blast loads, although interesting in its own right, is important because it provides the loading information necessary to conduct accurate structural response simulations. Chapters 6 and 7 will utilize this blast loading data to develop models of the Shot B blast chamber walls (Walls #1, #2, and #3 as labeled in Figure 2.7). The structural analyses that follow in this chapter and in Chapter 7 will only simulate the responses of the chamber walls of Shot B because the walls of the chambers of Shots A1 and A2 did not experience significant structural deformations. This chapter will use the equivalent single degree of freedom (ESDOF) method to simulate the response of blast chamber walls while Chapter 7 will utilize finite element models for the same purpose.

Chapter 1 documented the basics of the ESDOF method for creating and solving SDOF representations of real structures. This chapter will document the application of the ESDOF method to both one and two-way spanning structures with non-uniform loading, mass, and stiffness. Herein, the ESDOF method is combined with Biggs' (1964) transient numerical solution scheme as implemented in Single degree of freedom Blast Effects Design Spreadsheet (SBEDS), distributed by USACE (2008c). The software is built around the methodologies contained in UFC 3-340-02 (USACE, 2008d). SBEDS is approved by USACE for blast design calculations and is widely used throughout the

physical security community as a standard tool. It is therefore of interest to study its ability to predict the out-of-plane wall deflections observed in Shot B. More information on USACE software code development can be found in Sunshine et al. (2004).

It is worth emphasizing that the methods presented in this chapter represent the standard analysis methodology accepted by USACE for blast design calculations. Despite their simplicity, the methods have been proven adequate for the design of components including masonry, reinforced concrete, steel plates, and light gage wall systems, among others. Although more accurate methods are available, FEA for example, understanding the inputs and results of such analyses can be cumbersome, and FEA is often too expensive for design purposes unless no other proven analysis method exists. Further, in some structural analyses, the variations in material properties, geometry, construction workmanship, and uncertainties in the applied loading can limit a high fidelity structural simulation from providing results that are any more reliable than an ESDOF analysis.

This chapter will describe the development and application of an ESDOF model for each of the three Shot B blast chamber walls. First, a general discussion of brick URM resistance functions will be presented. This will be followed by a discussion of how resistance function ordered pairs were computed for each wall. Following that are details of how each of the three walls was converted from a real to an ESDOF system. Then using the ESDOF models and applied loading, simulations were performed to predict the out-of-plane deflections of the blast chamber walls. Finally, two criteria are employed to estimate the post-blast residual capacity of blast chamber bearing walls. The criteria are used to estimate how close the structure was to collapse.

6.1. Resistance Functions

Thus far this dissertation has provided information regarding every parameter required for an ESDOF simulation save one critical piece of information – the resistance function. In order to simulate the out-of-plane response of brick URM, a resistance function is required to describe the nonlinear force deflection relationship of the wall. Although there are many formulations, the models of out-of-plane resistance of URM walls can be grouped into two categories.

The first category is called rigid arching response. As first described by McDowell et al. (1956), "…the resistance of the wall to lateral loads is due entirely to forces set up in the plane of the panel as a result of the tendency of the masonry material to be crushed at the midspan and at the end supports." These in-plane forces can be attributed to beams or columns surrounding an infill panel which, as the wall rocks out-of-plane, restrict the wall's edge rotations. A variety of formulations have been developed for rigid arching, ranging from the early expression contained in McDowell et al. (1956) to the formulation contained in TM5-1300 (US Army, 1990). Flanagan and Bennett (1999) review a number of rigid arching models which accounted for the flexibility of bounding beams and columns. Through careful comparisons to experimental data, the authors were able to identify the most accurate formulation for including the flexibility of bounding members. In all cases, however, as pointed out by Henderson et al. (2003), the rigid arching resistance of infill panels tends to be significant and the walls are able to sustain large out-of-plane deflections.

While the rigid arching resistance function has been well developed for ESDOF analyses, it is not the best resistance function for the walls in this test program. This is

primarily because rigid arching relies on a stiff frame bounding a wall panel on at least two opposite edges. In the Shot B blast chamber, the load-bearing walls (Walls #2 and #3) had no such bounding members and the infill wall (Wall #1) had sufficient gaps along its edges to make rigid arching less applicable. Furthermore, the rigid arching resistance function was not used because it produces permanent deflections only after very large dynamic deflections and, as indicated by some authors (USACE, 2008c), the permanent deflections are unreliable. It was thus necessary to consider an alternative resistance function in this study.

The second out-of-plane resistance function can best be classified as a combination of elastic flexure (up to first cracking) and the arching action of axial loads (both self-weight and applied vertical loads). This resistance function, called brittle flexural response with axial load, is incorporated in SBEDS as a composite of two behaviors. Initially, the wall behaves as an uncracked flexural element until the formation of the first tensile crack; then the wall behaves as two rocking rigid bodies. This resistance function relies on the arching action of axial loads similar to those found by Griffith et al. (2004) experimentally and Doherty et al. (2002) analytically (though the SBEDS arching formulation predicts a greater resistance than Doherty's). An explanation of how arching resistance develops from axial load can be found in Doherty et al. (2002) and Gabrielsen and Wilton (1972). Figure 6.1 shows the general resistance-deflection relationship for this resistance function.

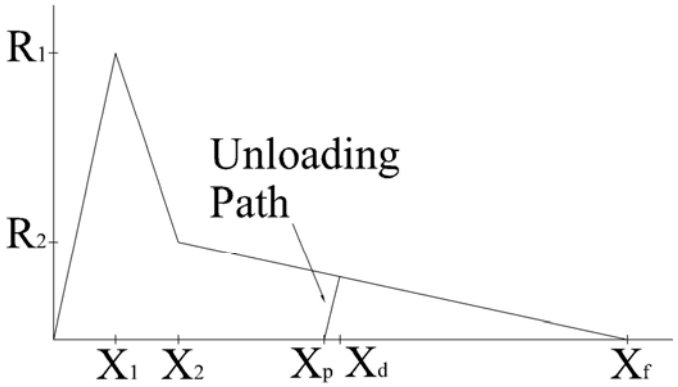

FIGURE 6.1: Resistance (pressure) versus mid-height deflection for the brittle flexural response with axial load resistance function.

In Figure 6.1, X_1 is the out-of-plane deflection at the formation of the first flexural tension crack; R_1 is the corresponding out-of-plane load causing this crack. X_2 is the deflection at which the maximum arching resistance is developed; R_2 is the out-of-plane wall capacity at this deflection. X_f is the wall deflection at failure and is equal to the wall's thickness. During a dynamic analysis, the deflection will reach some dynamic maximum, X_d; if the wall has cracked, then there will be a permanent deflection, X_p. Note that unloading between X_d and X_p occurs along the same slope as the elastic wall stiffness; since, as shown in Figure 6.1, X_d and X_p are approximately the same value, considering X_d as the permanent deflection often results in a negligible error.

First, the calculations necessary to compute the ordered pairs of the resistance function will be presented for a one-way spanning, simply-supported wall (like Wall #3) using the default SBEDS methodology. The SBEDS formulation (for all wall types/spans) assumes that the first flexural tension crack forms at midspan of a wall panel. While this is a reasonable representation of Walls #1 and #2, Wall #3 cracked above and below the wall's window openings (the bottom crack corresponds to

approximately the quarter point) and thus the mid-height crack representation limits the accuracy of the analysis. To address this, a new resistance function will be presented for one-way spanning walls which permits a crack at any height. The methodology, used to compute the ordered pairs of the new resistance function, will account for a non-uniform distribution of mass, stiffness, and loading (applicable to a wall with window openings for example; window openings will be assumed to be frangible and thus will not add out-of-plane load to the wall). This will be followed by the SBED's methodology of computing resistance function ordered pairs for a two-way spanning wall with four sides simply-supported (like Wall #2). Finally, the SBEDS methodology for computing resistance function ordered pairs for a two-way spanning wall with three sides simply-supported (like Wall #1) will be presented.

6.1.1. Wall #3 - One-Way Spanning Wall, Mid-Height Crack

Wall #3 will first be modeled as a one-way spanning, simply-supported member which cracks at mid-height. The wall's large aspect ratio (width to height) along with post-test observations of the crack pattern suggests that assuming one-way action is a good approximation. In this case, the default SBEDS methodology will be employed which assumes that the wall has a uniform loading, mass, and stiffness; resistances are thus given as a force per unit area and taken as constant. The ordered pairs of the resistance function (X_1,R_1), (X_2,R_2), and (X_f,0) are given by Eqs. (6.1) through (6.6).

$$R_1 = \frac{8 f_t^* S}{L^2} \tag{6.1}$$

$$f_t^* = f_t - \frac{P}{A} \tag{6.2}$$

$$X_1 = \frac{5R_1L^4}{384EI} \tag{6.3}$$

$$R_2 = \frac{8}{L^2}(t - X_1)\left(P + \frac{WL}{2}\right) \tag{6.4}$$

$$X_2 = X_1 + \frac{\left|(R_1 - R_2)\right|}{\frac{R_1}{X_1}} \tag{6.5}$$

$$X_f = t \tag{6.6}$$

In the equations, f_t *is* the tensile strength of mortar perpendicular to the bed joints, S is the per unit length section modulus, L is the span (wall height), P the axial load above the top of the wall, A the cross sectional area per unit length, E the modulus of elasticity, I the moment of inertia per unit length, W the self weight per unit height, and t the wall's thickness. Eq. (6.1) represents the wall's out-of-plane resistance at formation of the midheight flexural crack (resistances are assumed to be spatially uniform and are given in force per unit area). Eq. (6.2) represents the flexural tensile strength of the mortar joints, adjusted to account for the precompression of the axial load (compressive loads are negative, thus increasing the effective tensile strength of the masonry). Eq. (6.3) is the elastic lateral deflection of the wall at midheight, corresponding to the cracking load (R_1). Eqs. (6.1), (6.2), and (6.3) can be easily derived from elastic mechanics principles.

Eq. (6.4) is the cracked wall's out-of-plane (maximum) resistance as a result of the arching action of axial loads. Eq. (6.5) is the corresponding cracked wall's mid-height lateral deflection at the maximum arching resistance (R_2). Note that the change in resistance between R_1 and R_2 is assumed to occur along a line with a slope equal to the

wall's elastic stiffness. Finally, Eq. (6.6) is the maximum deflection the wall can experience before losing stability. Beyond this limiting deflection (equal to its thickness) the wall will collapse.

A constant axial load (P) is the only option available in SBEDS simulations, but simplified analytical investigations showed that Walls #2 and #3 may have experienced multiple axial load oscillations as a result of blast-induced uplift on the concrete floor slab system of the second story (the ceiling of the blast chamber) and its resulting vertical oscillations. These axial load oscillations can significantly influence the response of the wall; however there is no automated procedure to simulate this complex dynamic interaction in SBEDS. Modeling approximations are left to the discretion of the analyst. Although it is difficult to determine the precise phasing of the wall's out-of-plane response relative to the ceiling slab's reaction force time history, simplified analyses suggested that the axial load in the walls due to loads from the ceiling slab were minimal. It was thus assumed that Walls #2 and #3 carried no axial load (beyond their self-weight and the weight of the walls above) during their out-of-plane responses; this assumption will be shown to yield good agreement with the experimental permanent deflections.

Another resistance function parameter required in SBEDS is a strength adjustment factor B_w to account for window or door openings in a wall. In SBEDS the B_w factor directly scales the resistance and stiffness. Although easy to implement, this assumes that the blast load is entirely uniform and planar; this was not the case in this investigation. The SBEDS user manual recommends that for a one-way member, B_w be taken as the ratio of wall width resisting lateral loading (total width minus window width) to the total width. An alternate ratio, first proposed by Mays et al. (1998) for reinforced

concrete walls and later examined by Flanagan and Bennett (1999) in the context of masonry, is an area ratio, rather than a width ratio. This alternate reduction factor is computed as the ratio of the area of solid wall to the total area of the wall. Both methods of calculating B_w will be used to analyze Wall #3.

As stated previously, these equations assume the wall cracks at mid-height. In the next section, a new resistance function will be presented which allows a one-way wall to crack at any height; the location of the crack must be estimated beforehand as an input to the resistance function. Of equal importance, the accompanying methodology used to compute the ordered pairs of the resistance function will allow a better formulation for inclusion of nonuniform loading, mass, and stiffness quantities.

6.1.2. Wall #3 - One-Way Spanning Wall, Variable Height Crack

Section 6.1.1 provides the SBEDS formulation for a URM wall that is assumed to crack at midheight. In the experimental program, Wall #3 was observed to crack above and below the window openings in the wall. The bottom crack corresponds to approximately the quarter point while the top crack corresponds to approximately the three quarter point of the span. Examination of the post-test shape of the wall showed that the majority of out-of-plane deflection occurred at the crack that formed at the bottom of the window openings; the crack above the window openings will therefore be ignored. The large out-of-plane deflection at the lower quarter point makes sense, given the bottom-skewed impulse distribution shown in Figure 5.18.

To better model Wall #3's out-of-plane response, this section will present a resistance function (presented here for the first time) for a one-way spanning, simply-supported URM wall that can crack at any height. Equally as important, the method in

which the resistance function ordered pairs are computed will account for the wall's non-uniform stiffness and mass and the nonuniform blast loading. Initially an attempt was made to develop closed form methods of computing the resistance function ordered pairs. It quickly became apparent, however, that the only realistic approach was to solve the problem numerically.

The first step in creating the resistance function is to obtain the ordered pair R_1,X_1. These points are calculated by performing four successive numerical integrations of the nonlinear loading function; the constants of integration are determined between each successive integral to satisfy the boundary conditions. The integrals provide the shear curve, the moment curve (which is used to compute cracking resistance R_1), the rotation curve, and the deflection curve (to calculate deflection X_1 corresponding to R_1). In order to evaluate these integrals, the loading on Wall #3 (from Load Case 2, Table 5.18) had to be reduced from the two-dimensional contours shown in Figure 5.18 to a one-dimensional function. A 421.8 cm width of wall was taken as the width over which to average the blast loading. This corresponds to the center to center distance between masonry piers on either side of the window openings on either side of the charge centerline (as looking laterally along the wall's length). Figure 6.2 shows the one-dimensional vertical impulse profile used for computing transformation factors required in the ESDOF model.

Note that for all calculations that follow, the reflected impulse contours are used as the load, rather than the pressure contours. This is because the out-of-plane response of the blast chamber walls is impulse dominated. This assertion is justified by considering the ratio of the wall's elastic natural period to the duration of the blast load.

A common structural dynamics rule of thumb states that if the ratio is greater than 10, then dynamic response is impulse dominated; in this case the ratio is closer to 25.

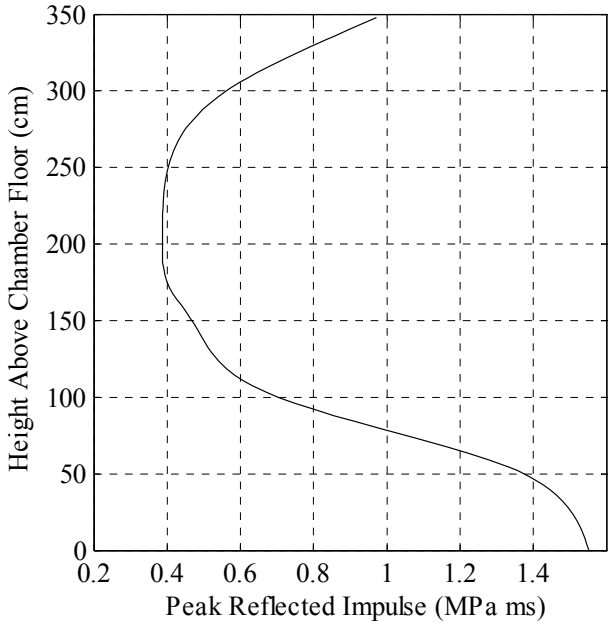

FIGURE 6.2: Plot of reflected impulse (averaged across effective wall width) versus height above blast chamber floor for Wall #3.

Figure 6.3 shows the free body diagram used to develop the post-elastic (cracked) resistance. Note that only the top half self-weight is included in the formulation. This was the basis upon which the SBEDS arching formulation was developed, and it was also adopted here. As will be shown in Chapter 7, using a reduced self weight is not an unreasonable assumption because the dynamic rocking action of the wall segments tends to cause vertical acceleration (and thus reduced apparent self weight). Moreover, if the weight of the upper wall segment were not included, the wall would have no resistance to lateral loads in the absence of a concentrated load at the top (P). Summing moments about the points of rotation yields:

$$\sum M_A = -\frac{R_2 {L_2}^2}{2} + (WL_2 + P)(t - X_1) = 0 \quad (6.7)$$

$$\sum M_B = \frac{R_1 {L_1}^2}{2} - (WL_2 + P)(t - X_1) = 0 \quad (6.8)$$

Eq. (6.7) is the summation of moments about the top segment's assumed point of rotation, while Eq. (6.8) is a similar summation for the bottom segment. In Eqs. (6.7) and (6.8), W is the weight per unit length, P is the axial load per unit length applied at the top of the wall, t is the wall thickness, X_1 is the lateral deflection at the crack height at the cracking load, L_1 is the span of wall segment between the bottom of the wall and the crack, and L_2 is the span of the wall segment between the crack and the top of the wall. Simplifying these expressions yields Eq. (6.9) which is the maximum resistance of the top half of the wall, while Eq. (6.10) is the resistance of the bottom half of the wall.

$$R_2 = \left[\frac{2W}{L_2} + \frac{2P}{L_2^2}\right](t - X_1) \quad (6.9)$$

$$R_1 = \frac{2(WL_2+P)(t-X_1)}{L_1^2} \quad (6.10)$$

Both equations must be evaluated, and the minimum value is taken as the overall uniform arching capacity.

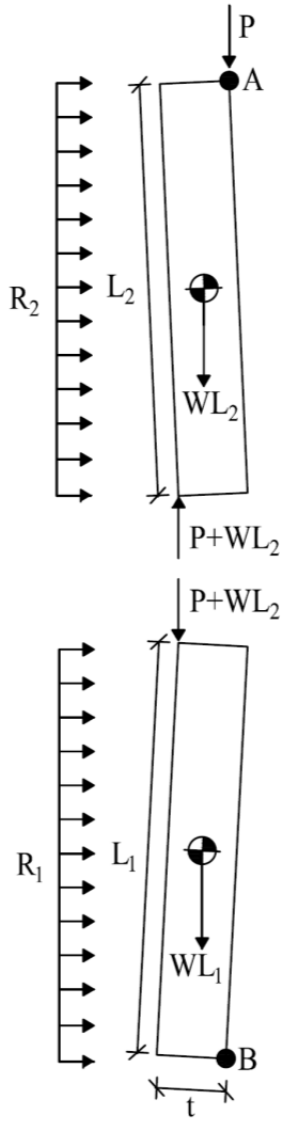

FIGURE 6.3: Free body diagram of upper (at left) and lower (at right) wall segments for derivation of arching resistance for wall with variable height crack, uniform load, and uniform mass.

Note that, as presented here, the equations for arching resistance are formulated for a uniform loading and mass. It is relatively straightforward to reformulate the moment summations shown in Eqs. (6.7) and (6.8) for any specific nonuniform distribution of loading and mass. In the Matlab scripts used to compute post-elastic resistance, the nonuniform distributions were treated by numerically finding the centroids

of the loading distribution and the mass distribution, and using these in refined moment summations to better estimate the arching resistance. Refer to Matlab script D.7 in Appendix D for details of the computations.

6.1.3. Wall #2 - One or Two-Way Spanning Wall, Midheight Crack

Wall #2 will be modeled as both a one-way and a two-way spanning element. The wall's aspect ratio and the post-test crack pattern suggested that a two-way spanning element would be a good physical approximation. Both one-and two-way spanning analyses were investigated because there was such extensive damage to the intersection of Walls #2 and #3 that it appeared as though the two-way action could have been compromised.

First, Wall #2 will be modeled as a one-way spanning element. The ordered pairs of this resistance function can be computed using Eqs. (6.1) through (6.6) as presented in Section 6.1.1 or using the methodology developed in Section 6.1.2 which accounts for general loading, mass, and stiffness distributions. To permit a one-way spanning analysis, it was necessary to perform lateral averaging in order to develop a one-dimensional load profile (from the two-dimensional impulse profile from Load Case 2). This averaging was performed across the wall's entire width and yielded the reflected impulse versus height distribution shown in Figure 6.4

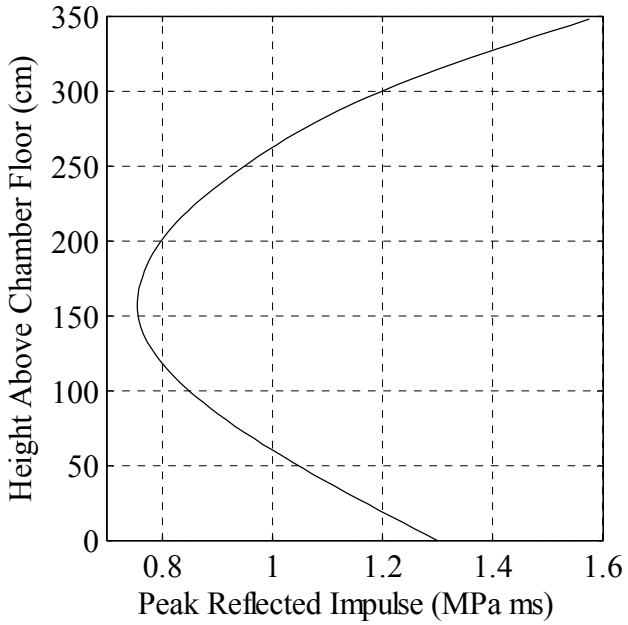

FIGURE 6.4: Plot of reflected impulse (averaged across wall width) versus height above blast chamber floor for Wall #2.

Wall #2 will also be modeled as a two-way spanning element with four edges simply-supported. Although there are a variety of methods to compute the elastic resistance of a plate (wall) simply-supported along four edges, the method preferred by USACE is to look up the stiffness and deflection from charts in Chapter 3 of UFC 3-340-02. The charts provide nomographs of several useful variables, but this analysis only requires one, γ. The user selects the chart which corresponds to the appropriate boundary conditions and then, using the wall's aspect ratio (ratio of height to width), selects the value of γ. For this particular case, the appropriate nomograph is Figure 3-36 in UFC 3-340-02. This coefficient is then used in

$$K_e = \frac{D}{\gamma H^4} \tag{6.11}$$

to compute the elastic stiffness K_e , the out-of-plane stiffness at the point of greatest deflection – mid-span in both the horizontal and vertical directions. In Eq. (6.11) H is the

clear vertical span of the wall and *D* is the wall's flexural rigidity computed by Eq. (6.12), where *E* is the modulus of elasticity, *I* is the moment of inertia per unit width, and *v* is Poisson's ratio (taken as 0.22).

$$D = \frac{EI}{1-v^2} \tag{6.12}$$

In addition to the elastic stiffness, it is also necessary to calculate the resistance at which the first flexural crack forms. Table 3-2 in UFC 3-340-02 provides guidance on computing the ultimate resistance of two-way plates with a variety of boundary conditions. Note that "ultimate resistance" usually means the literal maximum resistance (load) that a structure achieves. Normally this term is applied to a steel or reinforced concrete structure; this would correspond to a fully plastic cross section deformed along yield lines. In the context of this analysis, "ultimate resistance" corresponds to the wall's cracking load. The UFC 3-340-02 guidance has been simplified and more compactly presented in Table 4-4 of the SBEDS Methodology Manual (USACE, 2008c). The cracking resistance (under uniform load) of the wall is found by setting Eqs. (6.13) and (6.14) equal to each other and solving for *x,* where *x* is the horizontal distance from the panel's vertical edges where yield lines intersect one another.

$$r_1 = \frac{5.4M}{x^2} \tag{6.13}$$

$$r_2 = \frac{8.64M(3W-x)}{H^2(3W-4x)} \tag{6.14}$$

Back-substituting the value of *x* into either equation yields the wall's cracking resistance. In the equations *M* is the moment capacity per unit width ($M=f_t S$), *W* is the width of the wall, and *H* is the height of the wall.

Eqs. (6.13) and (6.14) assume that the wall cracks along yield lines emanating from the corners. The capacity determined by these equations is a yield line equilibrium solution. While computing the ultimate resistance for steel plates or reinforced concrete panels along yield lines makes sense, it is questionable as to why this would be a good choice for unreinforced masonry. To study the accuracy of this method, a linear and elastic, static finite element model was built using ANSYS (Canonsburg, PA). The model used the linear shell element Shell 43, which has three translational and three rotational degrees of freedom at each node and is well suited to model moderately-thick shell structures. The wall was meshed with elements having square aspect ratios with an edge length of 10.16 cm (4.0 in). The edge nodes of the model were supported using a roller-type constraint. Loading was applied to the model by writing a one-way coupling algorithm that took the impulse profile shown in Figure 5.16 and applied it as nodal loads in the ANSYS model. This permitted an accurate assessment of both the effective stiffness and the cracking load of the wall panel under the action of the nonuniform blast loading.

The finite element model shows that, as expected, the yield line solution overestimates the wall's capacity. It is likely that, because yield line analysis is simple and relatively close to the correct answer, it was applied to unreinforced masonry for the sake of convenience. For comparison, Eqs (6.13) and (6.14) predict the uniform load causing cracking of Wall #2 to be 33.9 kPa (4.91) psi while the ANSYS finite element model predicts the cracking load to be 29.1 kPa (4.22 psi) (based on tensile stress normal to the mortar joints). Both the ANSYS-derived and SBEDS-derived stiffnesses and cracking resistances will be used in ESDOF simulations for comparison.

The treatment of two-way spanning URM walls is only different than that of a one-way spanning wall during the elastic phase of response. After the first flexural crack has formed, a two-way spanning wall is assumed to respond as a vertically spanning one-way wall. Its post-elastic resistance is as defined by Eqs. (6.4), (6.5), and (6.6) or using the methodology developed in Section 6.1.2 which permits nonuniform loading and mass distributions. The transition from a two-way element to a one-way element is logical because vertical loads are the only mechanism of out-of-plane resistance after cracking occurs. There should be no in-plane horizontal loads for this particular case because bounding members do not inhibit panel edge rotations. Note that, although the post-elastic resistance is computed based on one-way action, the post-elastic ESDOF transformation factors are still computed with the deflected shape of a two-way spanning plate.

6.1.4. Wall #1, Two-Way, Three Edges Supported

Wall #1 was modeled as a two-way spanning element with three edges simply-supported (bottom and vertical edges). These boundary conditions were chosen based on engineering judgement and supported by post-test observations of the wall's deflected shape, which showed that the top edge of the wall panel was, for all intents and purposes, free to displace out-of-plane. The analysis of this wall panel's elastic deflection and resistance is only slightly different than the analysis presented in Section 6.1.3 for the case of a two-way wall with four edges simply-supported. Like Wall #2, the elastic stiffness of Wall #1 was determined using the appropriate nomograph for γ (Figure 3-30 in UFC 3-340-02). This coefficient is then used in Eqs. (6.11) and (6.12) to compute the

elastic stiffness K_e , which is the out-of-plane stiffness of the wall panel at the point of greatest deflection – at the top of the wall and midspan horizontally.

In addition to the elastic stiffness, it is also necessary to calculate the peak resistance at which the first flexural crack forms. Like Wall #2, this wall's ultimate resistance can be calculated from the figures in Table 4-4 of the SBEDS Methodology Manual. The cracking resistance of Wall #1 is found by setting the following equations equal to each other and solving for *y*,

$$r_1 = \frac{5.4M}{y^2} \tag{6.15}$$

$$r_2 = \frac{4.32M(6H-y)}{W^2(3H-2y)} \tag{6.16}$$

where *y* is the vertical distance from the bottom of the panel to the height where yield lines intersect. Back-substituting the value of *y* into either equation yields the wall's cracking resistance.

Like Eqs. (6.13) and (6.14), Eqs. (6.15) and (6.16) assume that the wall fails along yield lines emanating from the corners. The capacity determined by these equations is a yield line equilibrium solution. Again, the accuracy of this methodology was investigated using a linear and elastic, static finite element model like the one described in Section 6.1.3. A one-way coupling algorithm was again used to transfer the impulse contours from Figure 5.14 into nodal loads in the FEA model. Like before, the finite element model showed that the yield line solution overestimates the wall's capacity. For comparison, Eqs (6.15) and (6.16) predict the cracking resistance of the wall to be 9.10 kPa (1.32 psi) while the ANSYS finite element model predicts the cracking resistance to be 8.00 kPa (1.16 psi) based on tensile stress normal to the mortar joints. Both the

ANSYS-derived and SBEDS-derived stiffness and cracking resistances will be used in the SDOF analyses for comparison.

Wall #1's post-elastic resistance is defined by Eqs. (6.4), (6.5), and (6.6) or using the methodology presented in Section 6.1.2 for a wall with a nonuniform loading and mass distribution. The transition from a two-way element to a one-way element is logical because vertical loads are the only mechanism of out-of-plane resistance after cracking occurs. Since there should be no in-plane horizontal loads for Wall #1, only the vertical forces resist out-of-plane motion.

6.2. Equivalent SDOF Systems

In addition to resistance function ordered pairs, the ESDOF transformation factors must also be developed. Chapter 1 provided an overview of how the ESDOF transformation factors (K_L, K_M, and K_{LM}) are computed for one-way spanning structures with uniform loading, mass, and stiffness distributions. Unfortunately, Chapter 5 showed that the Shot B blast chamber walls were subjected to complex loading distributions. Furthermore, Wall #3 also had nonuniform mass and stiffness due to the presence of the window openings. Initially, an effort was made to derive a closed form solution which would permit development of the ESDOF transformation factors for any of the blast chamber walls. It quickly became apparent, however, that such a solution was intractable, particularly for the elastic phase of wall response. It was therefore desirable to numerically derive the transformation factors for all three walls. The following sections will describe the methodology used in deriving transformation factors and Appendix D contains the corresponding Matlab scripts.

First, ESDOF transformation factors will be derived for Walls #2 and #3 assuming one-way spans. Following that, the transformation factors will be derived for Walls #1 and #2 assuming two-way spans; note that Wall #1's response is termed "two-way" despite being supported on only three sides. For each type of support condition, an elastic and post-elastic deformed shape will be computed. These will be combined with the CTH-derived impulse loading contours to derive the ESDOF transformation factors.

6.2.1. One-Way Spanning Elements

Walls #2 and #3 were modeled as one-way spanning elements (Wall #2 will also be modeled as a two-way element in the next section). The loading profiles shown in Figures 6.2 and 6.4 will be used as the applied loading. It is also necessary to compute deflected shapes for the elastic and post-elastic phases of wall response. Figure 6.5 shows the normalized deflected shapes used for the elastic and post-elastic phases of Wall #2's response, assuming a one-way span that cracks at mid-height. The elastic deflected shape was computed using the quadruple integration scheme described in Section 6.1.2. The post-elastic deflected shape was computed as two straight lines intersecting at the assumed height of the tensile crack.

Computing the deflected shape of Wall #3 was even more complicated than Wall #2 due to its nonuniform mass and stiffness. The loading profile from Figure 6.2 was used for this analysis. Figure 6.6 shows the stiffness (moment of inertia) and mass of Wall #3 as a function of height above the base of the wall. Note that the plots have been normalized so that a value of one represents the stiffness or mass (per unit length) in the absence of a window opening.

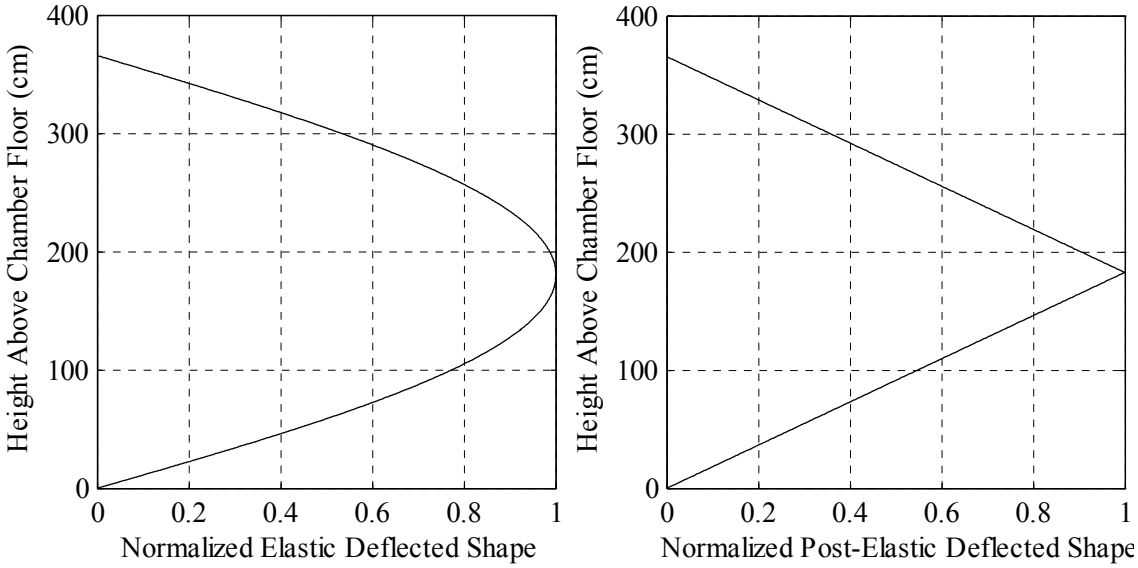

FIGURE 6.5: Wall #2 normalized deflected shapes for the elastic phase of response (at left) and the post-elastic phase of response (at right).

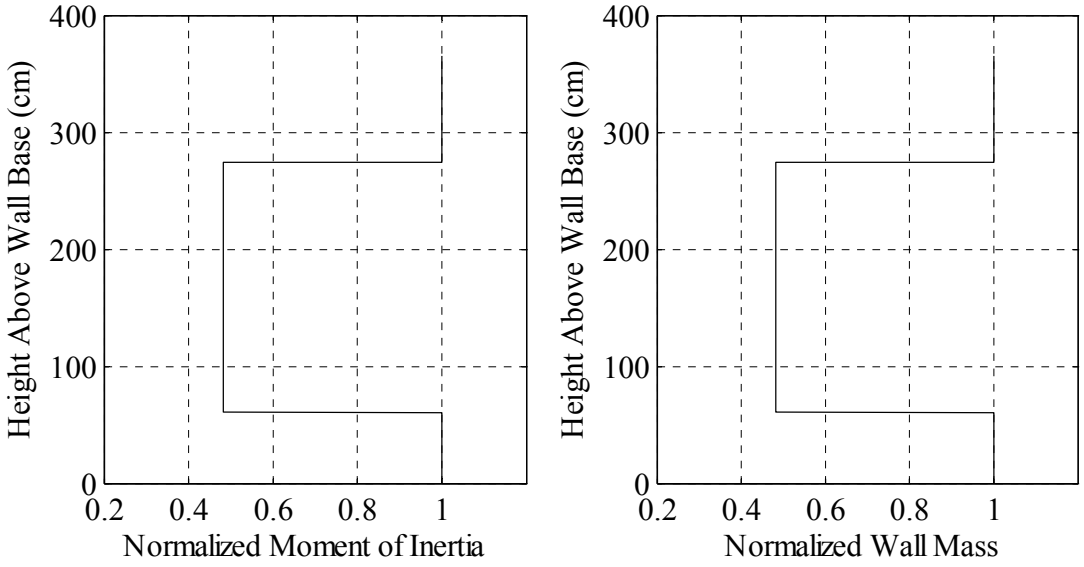

FIGURE 6.6: Plots of normalized moment of inertia (at left) and normalized wall mass (at right) as a function of height for Wall #3, which had numerous window openings.

Using this data along with the quadruple integration scheme described earlier, deformed shapes were developed for Wall #3. Figure 6.7 shows the normalized deflected shapes computed for the elastic and post-elastic phases of wall response assuming a one-

way span that cracks just below the bottom of the window openings. Note that for the elastic deformed shape, the normalization was performed relative to a point on the wall's span which was not the maximum deflection (i.e. at the assumed crack location). Thus, the normalized elastic deflected shape has a maximum value greater than 1.0.

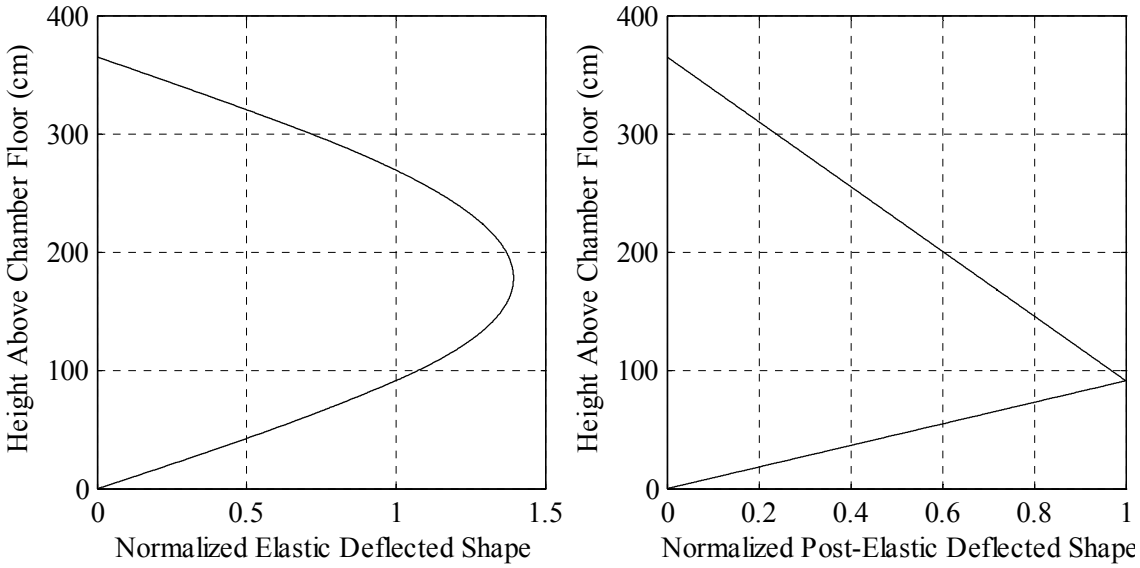

FIGURE 6.7: Wall #3 Normalized deflected shapes for the elastic phase of response (at left) and the post-elastic phase of response (at right) with the flexural crack forming just below the window openings.

Having developed all of the necessary inputs, the K_M and K_L factors are computed respectively by

$$K_M = \frac{\sum_x m(x)\varphi(x)^2}{\sum_x m(x)} \tag{6.17}$$

$$K_L = \frac{\sum_x p(x)\varphi(x)}{\sum_x p(x)} \tag{6.18}$$

Note that these equations are the discrete analogs of Eqs. (1.4) and (1.5). These summations are performed over the height of the one-way elements, where the variable *x* is the position up the height. In the equations, *m(x)* represents the spatially variable mass, *p(x)* the spatially variable load, and *φ(x)* is the normalized deflected shape. Using this

methodology, Wall #2 was computed to have an elastic K_M of 0.51, an elastic K_L of 0.58, an elastic K_{LM} of 0.88 ($K_{LM} = K_M/K_L$), a post-elastic K_M of 0.33, a post-elastic K_L of 0.44, and a post-elastic K_{LM} of 0.75. Wall #3 was computed to have an elastic K_M of 0.75, an elastic K_L of 0.60, an elastic K_{LM} of 1.25, a post-elastic K_M of 0.29, a post-elastic K_L of 0.42, and a post-elastic K_{LM} of 0.69. The Matlab program used to perform these computations is included in Appendix D as script D.7.

6.2.2. Two-Way Spanning Members

The development of ESDOF transformation factors for two-way elements is more difficult than for one-way spanning elements. Most of the added difficulty comes from computing the shape functions required to perform two-dimensional integrals. The two-dimensional analogs of Eqs. (6.17) and (6.18) are

$$K_M = \frac{\sum_{xy} m(x,y)\varphi(x,y)^2}{\sum_{xy} m(x,y)} \tag{6.19}$$

$$K_L = \frac{\sum_{xy} p(x,y)\varphi(x,y)}{\sum_{xy} p(x,y)} \tag{6.20}$$

The variables in the equations are as defined previously. Section 5.7 developed the necessary loading profiles *p(x,y),* which are shown in Figures 5.14 and 5.16. Walls #1 and #2 have uniform mass, making *m(x,y)* a constant. The only additional information required for the two-dimensional integrals is the deflected shape *φ(x,y)*.

Initially an attempt was made to use Navier's solution to compute the deflection of a simply-supported rectangular plate. Navier's solution is

$$p_{mn} = \frac{4}{ab}\int_0^b \int_0^a p(x,y) sin\frac{m\pi x}{a} sin\frac{n\pi y}{b} dxdy \tag{6.21}$$

$$w = \frac{1}{\pi^4 D}\sum_{m=1}^{\infty}\sum_{n=1}^{\infty} \frac{p_{mn}}{\left[\frac{m^2}{a}+\frac{n^2}{b}\right]^2} sin\frac{m\pi x}{a} sin\frac{n\pi y}{b} \tag{6.22}$$

where $p(x,y)$ is the applied loading, a and b are the dimensions of the plate, D is the flexural rigidity, x and y are spatial variables, and m and n are summation terms. This approach has the advantage in that Navier's solution permits arbitrary loading, which would have made using the impulse profiles from Chapter 5 relatively straightforward. Using between three and five terms in the summations of Navier's solution along with Eqs. (6.19) and (6.20) yielded transformation factors that were very similar to the transformation factors reported by Biggs (1964). This result, however, is merely coincidence.

After researching other published studies of the ESDOF transformation factors, it turns out that the vast majority available in the literature (Biggs' included) are inaccurate for two-way elements. Morrison (2006) states that the original transformation factors (from Biggs (1964) and other places) were derived using very rough approximations of the elastic deflected shapes of plates and are thus inaccurate. This results in errors of up to nearly 50% for certain transformation factors. Morrison attempted to use closed form solutions to obtain the elastic deflected shape of a rectangular plate. The author reported it necessary to use over a thousand terms in the summations in Navier's solution to obtain an accurate result for transformation factors. This would be overly time intensive, even on a very fast computer. This led Morrison to, instead, use FEA to compute two-dimensional deflected shapes. These deflected shapes were then used in Eqs. (6.19) and (6.20) to obtain transformation factors which are substantially different than those in Biggs (1964).

Based on the work of Morrison (2006) the decision was made to use FEA to compute the deformed shapes for two-way spans in this investigation. Using both Matlab

and the ANSYS coding tool, a program was written that allowed the complex two-dimensional impulse contours from Chapter 5 to be converted to nodal loads in an ANSYS model of Wall #1. Figure 6.8 shows the resulting normalized elastic deflected shape computed by ANSYS using a static analysis. Figure 6.9 is the corresponding normalized post-elastic deflected shape based on the yield line geometry used by SBEDS.

Again, using the previously described Matlab and ANSYS coding, an ANSYS model was constructed to simulate the elastic deflection of Wall #2. Figure 6.10 is the normalized elastic deflected shape computed by ANSYS (using a static analysis) under the action of the impulse loading profile from Figure 5.16. Figure 6.11 is the corresponding normalized post-elastic deflected shape based on the yield line geometry used by SBEDS.

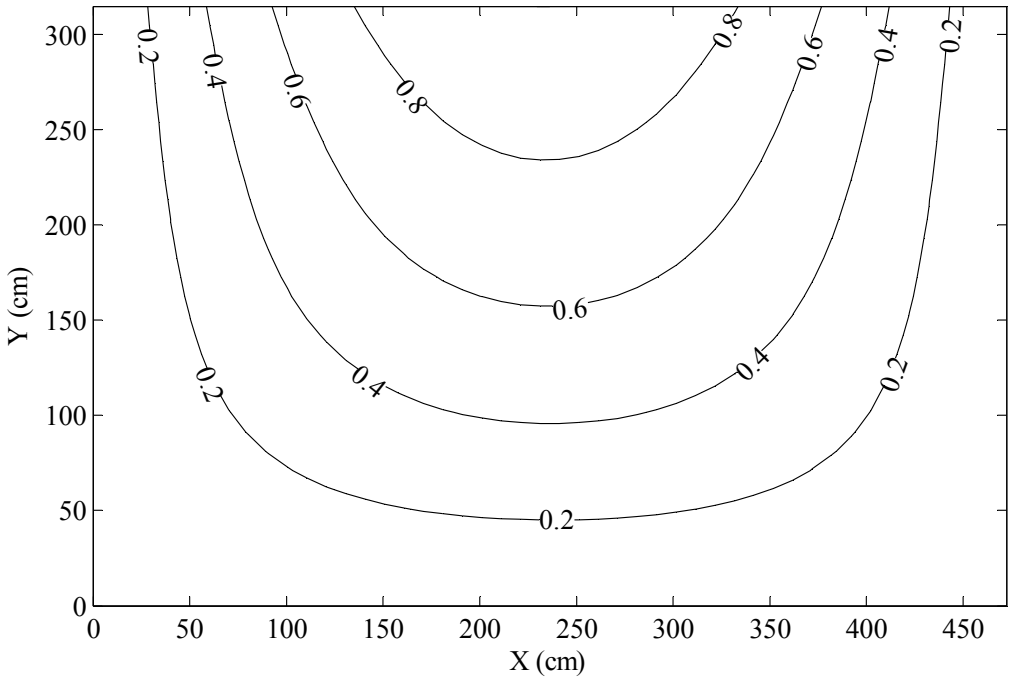

FIGURE 6.8: Wall #1 normalized elastic deflected shape as viewed from inside the blast chamber looking out.

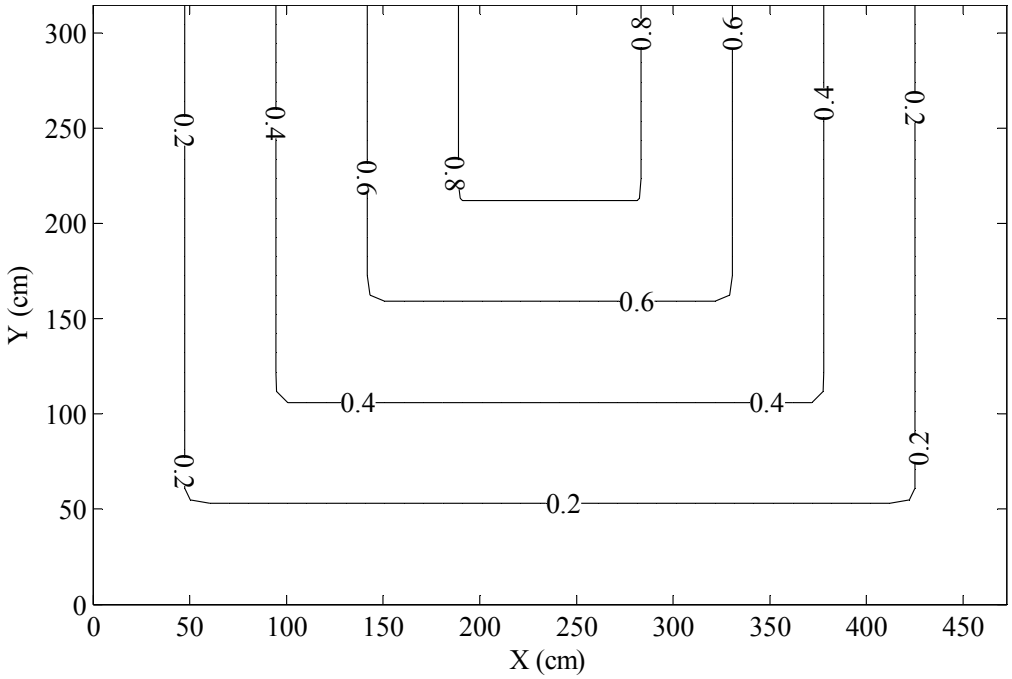

FIGURE 6.9: Wall #1 normalized post-elastic deflected shape as viewed from inside the blast chamber looking out.

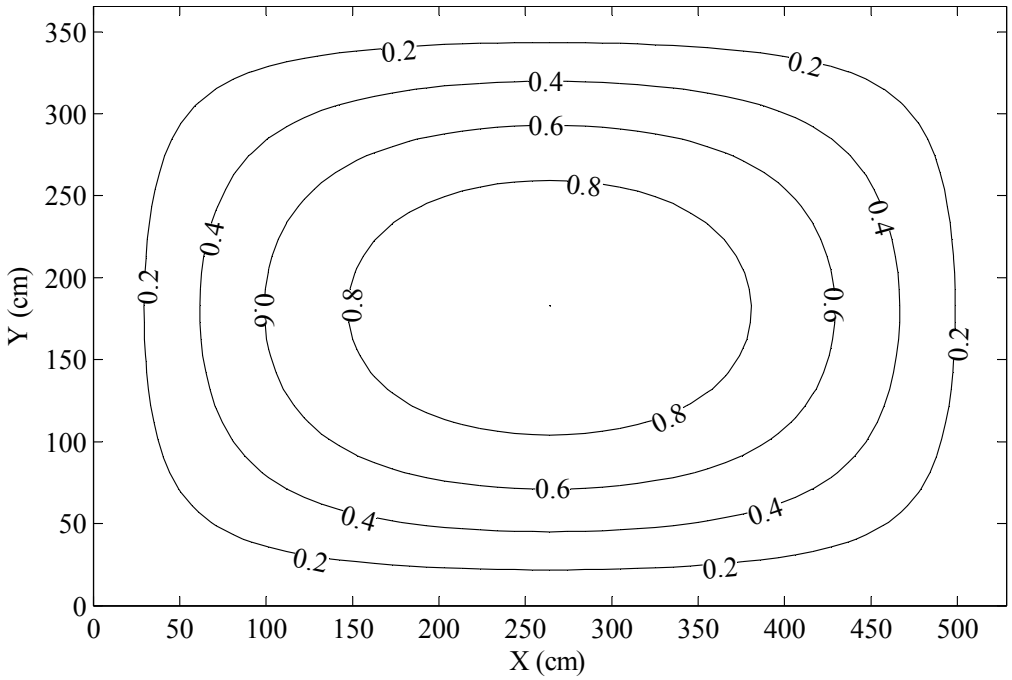

FIGURE 6.10: Wall #2 normalized elastic deflected shape as viewed from inside the blast chamber looking out.

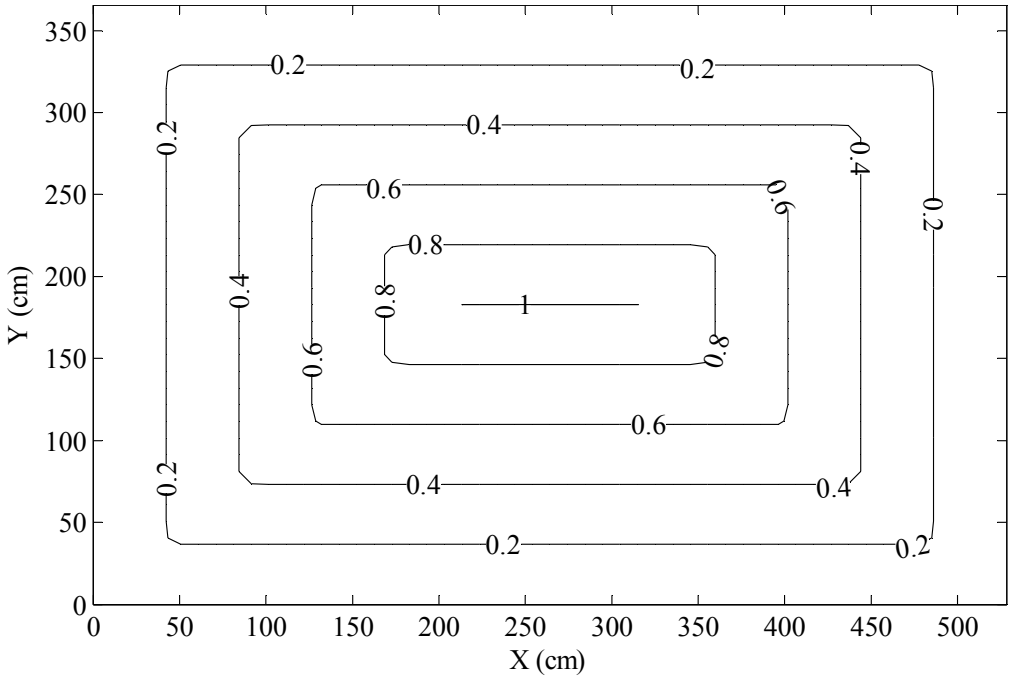

FIGURE 6.11: Wall #2 normalized post-elastic deflected shape as viewed from inside the blast chamber looking out.

The normalized deflected shapes and the reflected impulse profiles from Chapter 5 were used with Eqs. (6.19) and (6.20) to compute the ESDOF transformation factors. In order to facilitate computations, Matlab programs were written to perform the integrations using the deflected shape and the loading distributions. The programs are included in Appendix D as scripts D.8 and D.9. For Wall #1 the program computed the elastic K_M factor to be 0.19, the K_L factor to be 0.30, and the K_{LM} factor to be 0.63. The post-elastic K_M factor was 0.19, the K_L factor 0.30, and the K_{LM} factor 0.63. For Wall #2 the program computed the elastic K_M factor to be 0.28, the K_L factor to be 0.37, and the K_{LM} factor to be 0.76. The post-elastic K_M factor was 0.20, the K_L factor 0.31, and the K_{LM} factor 0.65. Note that, as a validation, the Matlab program and the ANSYS FEA model were used to model the plates studied in Morrison (2006); they were able to closely replicate his ESDOF transformation factors.

6.3. Summary of SDOF Input Parameters

Using the methods outlined previously, ESDOF and resistance function ordered pairs were calculated for the walls of Blast Chamber B. Both directly computed and default (those assuming uniform distributions of loading and mass) ESDOF transformation factors were calculated. Similarly, resistance function ordered pairs were calculated using both the newly developed resistance function as well as the default SBEDS resistance function. These data were used as inputs for the simulations listed in Table 6.1. As an additional measure, the effect of using a directly measured, versus an SBEDS default modulus of elasticity for masonry, was considered.

Table 6.2 provides a summary of the ESDOF transformation factors corresponding to the analysis cases in Table 6.1. The non-computed (default) factors in the table were taken from UFC 3-340-02 and are the same ones which would be SBEDS defaults. In comparing the computed values to the default values, the errors for the K_{LM} factor range from as low as 8% to as high as 38%. Most of the computed factors appear close to the default factors, with the exception of those for Wall #3, which has an elastic K_{LM} value of 1.25; values greater than 1.0 are not normally encountered in practice. A K_{LM} factor greater than 1.0 is best explained through an example.

Consider a simply-supported beam with a uniform loading. If the deflection of the beam was monitored at midspan, the K_{LM} factor would be 0.78. But suppose the deflection of the same beam was instead monitored at a quarter point of the span. Applying a uniform load to the beam would yield a higher deflection at the midspan than at the quarter point. Thus, the apparent stiffness of the system (loading divided by deflection) would be higher at the quarter point. But regardless of where deflection is

monitored, the natural frequency of the beam must remain the same. Recall that the ESDOF elastic natural frequency is computed by

$$\omega = \sqrt{\frac{K_e}{K_{LM}M}} \tag{6.23}$$

where ω is the undamped elastic natural frequency, K_e the elastic stiffness, and M the total system mass. Thus, to make the calculated natural frequency of the quarter point the same as at midspan, one would expect the K_{LM} value to be larger at the quarter point than at midspan. Using simple beam theory, the ratio of midspan to quarter point deflection will be 1.4 for a uniformly loaded, simply-supported beam. Thus, the K_{LM} for the quarter point will be 1.4 x 0.78 = 1.1. Wall #3's elastic K_{LM} value of 1.25 is computed similarly, but is larger than 1.1 because of a difference in the location of deflection tracking and the wall's nonuniform loading.

Table 6.3 shows the ordered pairs of the resistance functions computed using the methods outlined in the preceding sections. Note that for both the default SBEDS procedures and the newly developed procedures - the self-weight of the interior tile veneer (122 kg/m^2 or 25 lb/ft^2) is included in the arching resistance calculation as well as in the wall's mass. Although a post-test inspection of the blast chamber showed significant delamination of the tile veneer from the brick masonry backup, it was assumed to be bonded long enough to have contributed to the post-elastic arching resistance.

TABLE 6.1: Summary of ESDOF analysis cases.

Analysis Case	Wall	R_I Source	K_L, K_M, K_{LM} Source	Span & Support	Masonry Modulus GPa (ksi)
1A	1	ANSYS FEA (Section 6.1.4)	2D Integral w/ Matlab Script	Two-Way Simple	4.23 (614)
1B	1	SBEDS Default	SBEDS Default	Two-Way Simple	4.23 (614)
1C	1	SBEDS Default	SBEDS Default	Two-Way Simple	13.44 (1950)
2A	2	ANSYS FEA (Section 6.1.3)	2D Integral w/ Matlab Script	Two-Way Simple	4.23 (614)
2B	2	Matlab Script (Section 6.1.2)	1D Integral w/ Matlab Script	One-Way Simple	4.23 (614)
2C	2	SBEDS Default	SBEDS Default	Two-Way Simple	4.23 (614)
2D	2	SBEDS Default	SBEDS Default	Two-Way Simple	13.44 (1950)
3A	3	Matlab Script (Section 6.1.2)	1D Integral w/ Matlab Script	One-Way Simple	4.23 (614)
3B*	3	Matlab Script (Section 6.1.2)	1D Integral w/ Matlab Script	One-Way Simple	4.23 (614)
3C	3	SBEDS Default B_w=1	SBEDS Default	One-Way Simple	4.23 (614)
3D	3	SBEDS Default B_w=0.482	SBEDS Default	One-Way Simple	4.23 (614)
3E	3	SBEDS Default B_w=0.698	SBEDS Default	One-Way Simple	4.23 (614)
3F	3	SBEDS Default B_w=0.698	SBEDS Default	One-Way Simple	13.44 (1950)

Notes: SBEDS default modulus of elasticity is 13.44 GPa; 4.23 GPa determined by compression test. *All Wall #2 and #3 analysis cases used 245 N/cm (140 lbs/in) axial load except Case 3B which used no axial load.

TABLE 6.2: Summary of directly computed and default ESDOF transformation factors.

Analysis Case	ELASTIC			POST-ELASTIC		
	K_L	K_M	K_{LM}	K_L	K_M	K_{LM}
1A	0.30	0.19	0.63	0.30	0.19	0.63
1B	*	*	0.70	*	*	0.53
1C	*	*	0.70	*	*	0.53
2A	0.37	0.28	0.76	0.31	0.20	0.65
2B	0.58	0.51	0.88	0.44	0.33	0.75
2C	*	*	0.70	*	*	0.54
2D	*	*	0.70	*	*	0.54
3A	0.60	0.75	1.25	0.42	0.29	0.69
3B	0.60	0.75	1.25	0.42	0.29	0.69
3C	0.64	0.5	0.78	0.5	0.33	0.66
3D	0.64	0.5	0.78	0.5	0.33	0.66
3E	0.64	0.5	0.78	0.5	0.33	0.66
3F	0.64	0.5	0.78	0.5	0.33	0.66

Notes: *Neither SBEDS nor UFC 3-340-02 provide the default values of K_L or K_M, only K_{LM}. Directly computed ESDOF factors are shaded in gray to permit easier comparison with default values.

Equivalent uniform impulses were computed for each wall of the blast chamber by integrating each two-dimensional impulse contour (for example Figure 5.16 in Chapter 5) over its area and then dividing the total impulse by the wall area. This is suitable for use with the computed K_{LM} factors because they inherently account for the actual nonuniform loading distribution. The default K_{LM} factors, on the other hand, do not account for the nonuniform loading; they were instead developed assuming a uniform load and it is of interest to study the errors created by this assumption. Studying Table 2.3, the sensors embedded in Walls #1, #2, and #3 had average positive phase durations of approximately 2.25 ms. This information was substituted into

$$P_{eq} = \frac{2I_{eq}}{t_d} \tag{6.23}$$

to compute the equivalent uniform pressure from the equivalent uniform impulse. Eq. (6.23) represents a decaying triangular pressure pulse where P_{eq} is the equivalent uniform

pressure acting over the blast wave duration t_d and I_{eq} is the equivalent uniform impulse. Note that this method of back-computing pressure from impulse and blast wave duration is standard practice as described in UFC 3-340-02. The equivalent uniform loads computed using this methodology are shown in Table 6.4.

TABLE 6.3: Summary of resistance function ordered pairs for analysis cases investigated.

Analysis Case	ELASTIC			POST-ELASTIC		
	R_1 kPa (psi)	X_1 mm (in)	K_e kPa/cm (psi/in)	R_2 kPa (psi)	X_2 mm (in)	X_f cm (in)
1A	8.00 (1.16)	9.86 (0.388)	8.12 (2.99)	1.17 (0.170)	18.3 (0.719)	20.3 (8.00)
1B	9.10 (1.32)	13.9 (0.548)	6.54 (2.41)	1.17 (0.170)	26.2 (1.03)	20.3 (8.00)
1C	9.10 (1.32)	4.39 (0.173)	20.8 (7.66)	1.23 (0.178)	8.18 (0.322)	20.3 (8.00)
2A	29.1 (4.22)	3.48 (0.137)	83.6 (30.8)	8.00 (1.16)	5.99 (0.236)	30.5 (12.0)
2B	19.0 (2.75)	3.96 (0.156)	47.8 (17.6)	8.00 (1.16)	6.25 (0.246)	30.5 (12.0)
2C	33.9 (4.91)	4.27 (0.168)	79.0 (29.1)	6.61 (0.959)	7.75 (0.305)	30.5 (12.0)
2D	33.9 (4.91)	1.35 (0.053)	251 (92.6)	6.67 (0.968)	2.41 (0.095)	30.5 (12.0)
3A	12.2 (1.77)	2.64 (0.104)	46.1 (17.0)	9.72 (1.41)	3.18 (0.125)	30.5 (12.0)
3B	11.7 (1.69)	2.54 (0.100)	45.9 (16.9)	2.24 (0.325)	4.57 (0.180)	30.5 (12.0)
3C	16.7 (2.42)	3.89 (0.153)	42.9 (15.8)	6.62 (0.960)	6.22 (0.245)	30.5 (12.0)
3D	8.41 (1.22)	4.06 (0.160)	20.7 (7.63)	3.19 (0.462)	6.60 (0.260)	30.5 (12.0)
3E	11.9 (1.72)	3.96 (0.156)	30.1 (11.1)	4.62 (0.670)	6.38 (0.251)	30.5 (12.0)
3F	11.9 (1.72)	1.24 (0.049)	95.3 (35.1)	4.66 (0.676)	2.01 (0.079)	30.5 (12.0)

TABLE 6.4: Summary of equivalent reflected uniform impulses and pressures.

Analysis Case	Uniform Impulse MPa ms (psi ms)	Uniform Pressure MPa (psi)	Duration (ms)
1A, 1B, 1C	0.770 (111.7)	0.6845 (99.29)	2.25
2A, 2B, 2C, 2D, 2E	0.9996 (144.98)	0.8885 (128.87)	2.25
3A, 3B	0.5739 (83.23)*	0.5101 (73.98)	2.25
3C, 3D, 3E, 3F	0.7357 (106.7)	0.6539 (94.84)	2.25

Note: *This equivalent uniform impulse is reduced to account for the area of window openings.

All wall response simulations were performed twice, once using viscous damping of 2% of critical and once using 5% of critical. The SBEDS Methodology Manual (USACE, 2008c) indicates that SBEDS compares favorably to experimental data when 2% viscous damping is used. Griffith et al. (2004) performed out-of-plane free vibration tests on cracked brick masonry walls and determined that 5% of critical damping is a reasonable estimate of damping in rocking URM wall segments. Applying this directly, however, is problematic. SBEDS computes the damping coefficient only once based on the elastic natural frequency. This damping coefficient would therefore be too high for the post-elastic phase of wall response in which the rocking wall segments have a much lower natural frequency than the uncracked elastic structure.

SBEDS addresses this by including a binary switch for damping in the calculation. Prior to reaching the cracking resistance, a constant damping coefficient is applied, the input value. After exceeding the ultimate resistance, damping is reduced by a factor of 100. Thus after cracking, 5% damping would become 0.05% damping (as computed using the natural frequency of the elastic, uncracked structure). This is important because use of the elastic damping coefficient during post-elastic response would significantly underestimate peak out-of-plane deflections. The SBEDS manual

states that damping is turned "off" after the ultimate resistance is achieved, but this is not actually the case. The scale factor of 0.01 was verified by comparing SBEDS outputs to hand calculations. It is questionable as to whether or not this is an appropriate treatment of post-crack damping, as its inclusion tends to reduce deflections.

6.4. Experimental Versus Analytical Deflections

Simulations were performed for the analysis cases in Table 6.1 using the inputs contained in Tables 6.2 through 6.4. Tables 6.5 and 6.6 compare the observed permanent deflections of the Shot B blast chamber walls to the peak dynamic deflections predicted by SBEDS. Calculations, where experimental acceleration data were double integrated, did not produce reliable deflection results. Therefore, the measured permanent deflections (at several key locations) were used in the comparisons. Note that, because unloading of the resistance function occurs along a path with a stiffness equal to its elastic stiffness, rebound is small and thus using peak dynamic deflection instead of permanent deflection yields only a small error. The tables show that SBEDS analyses–with the advantage of observing post-test crack patterns before choosing support conditions–were able to predict the experimental permanent deflections reasonably well.

TABLE 6.5: Comparison between SBEDS predicted peak dynamic deflection and experimental permanent deflection. Simulations use 2% damping.

Analysis Case	SBEDS X_d cm (in)	Experimental Result cm (in)
1A	FAILURE	25 (10)
1B	FAILURE	25 (10)
1C	FAILURE	25 (10)
2A	7.57 (2.98)	8.9 (3.5)
2B	7.44 (2.93)	8.9 (3.5)
2C	8.18 (3.22)	8.9 (3.5)
2D	7.24 (2.85)	8.9 (3.5)
3A	1.14 (0.45)	6.4 (2.5)
3B	3.00 (1.18)	6.4 (2.5)
3C	5.31 (2.09)	6.4 (2.5)
3D	27.7 (10.9)	6.4 (2.5)
3E	11.1 (4.36)	6.4 (2.5)
3F	9.25 (3.64)	6.4 (2.5)

Note: An analytical result of "FAILURE" means that the analytical deflection exceeded wall thickness. (t= 20.34 cm for Wall #1 and t=30.48 cm for Wall #2)

TABLE 6.6: Comparison between SBEDS predicted peak dynamic deflection and experimental permanent deflection. Simulations use 5% damping.

Analysis Case	SBEDS X_d cm (in)	Experimental Results cm (in)
1A	FAILURE	25 (10)
1B	FAILURE	25 (10)
1C	16.1 (6.33)	25 (10)
2A	5.18 (2.04)	8.9 (3.5)
2B	5.49 (2.16)	8.9 (3.5)
2C	5.44 (2.14)	8.9 (3.5)
2D	4.19 (1.65)	8.9 (3.5)
3A	1.02 (0.40)	6.4 (2.5)
3B	2.08 (0.82)	6.4 (2.5)
3C	4.06 (1.60)	6.4 (2.5)
3D	14.0 (5.52)	6.4 (2.5)
3E	7.54 (2.97)	6.4 (2.5)
3F	5.66 (2.23)	6.4 (2.5)

Note: An analytical result of "FAILURE" means that the analytical deflection exceeded wall thickness. (t=20.34 cm for Wall #1 and t=30.48 cm for Wall #2)

Comparing Table 6.5 to 6.6, it can be seen that going from 2% to 5% viscous damping reduces the predicted deflections by 30% to 50%. The best results were obtained using the 2% damping coefficient, validating the SBEDS recommendations. Table 6.5 shows that all of the analyses correctly predicted that Wall #1 should have failed. For Wall #2, the best prediction of permanent deflection was made using default SBEDS parameters (case 2C) although the newly developed parameters (Cases 2A and 2B) performed only slightly worse. The permanent deflection of Wall #3 was somewhat underpredicted by the newly developed resistance function and transformation factors (Cases 3A and 3B) while the best prediction was made by Case 3C. This could be caused by one of two factors - the blast loads were under predicted by CTH and/or the dynamic tensile strength of the masonry was overestimated.

As an additional comparison, the ESDOF elastic natural frequencies of the walls were compared to frequencies derived from experimental data. Table 6.7 shows the comparison between the analytical fundamental natural frequency and the two closest frequencies derived from shock accelerometer measurements. For Wall #1, analysis cases 1A and 1B predict elastic natural frequencies relatively close to those from the experimental data. For Wall #2, Case 2C which accurately predicted the deflection also predicted the natural frequency reasonably well; Case 2A which was based on an FEA model also predicted the natural frequency reasonably well. For Wall #3, all cases except 3F agreed reasonably well with the experimental data.

TABLE 6.7: Natural frequencies from SBEDS as compared to experimental data.

Analysis Case	SDOF Hz	Experimental Frequency 1 Hz	Experimental Frequency 2 Hz
1A	8.1	4.7	36.4
1B	6.9	4.7	36.4
1C	12.4	4.7	36.4
2A	20.2	3.7	19.3
2B	14.2	3.7	19.3
2C	20.4	3.7	19.3
2D	36.4	3.7	19.3
3A	11.7	4.3	12.7
3B	11.7	4.3	12.7
3C	14.3	4.3	12.7
3D	14.3	4.3	12.7
3E	14.3	4.3	12.7
3F	25.5	4.3	12.7

6.5. Collapse Prediction

When analyzing the blast resistance of a load-bearing masonry structure, after computing the response of the walls, it is also necessary to assess the impact of wall deflections on structural stability. Two criteria were used to quantify the state of a bearing wall structure relative to its collapse limit-state. The first criterion is based on wall midheight deflection as suggested by Doherty et al. (2002) for seismic analyses and implied in the definition of the resistance functions in SBEDS (USACE, 2008c). The second criterion makes use of the brittle flexural response with axial load resistance function to quantify the remaining out-of-plane resistance of a damaged wall. These will be referred to as the deflection criterion and the resistance criterion, respectively.

Although these criteria are very simple, they represent two of three obvious options available for assessing the capacity of unreinforced masonry walls. The third possible criterion is based on the wall's axial load capacity. For unreinforced masonry, methods to analyze the stability of cracked (damaged) assemblages have been developed

(La Mendola et al. 1995, Lu et al. 2004, and Tesfaye and Broome 1977). The walls of the test structure reported in this article, however, had low slenderness values and load eccentricities which acted to restore the wall to equilibrium (rather than exacerbating deflections), implying that this method of stability analysis would predict only a negligible reduction in axial resistance.

Using the deflection criterion, the state of a bearing wall structure (relative to its collapse limit-state) is defined as the ratio of the actual permanent out-of-plane deflection of key bearing walls Δ_{mid} relative to their failure deflections $\Delta_{failure}$. This is represented mathematically as a percentage by

$$Percent\ of\ collapse\ limit\ state = \frac{\Delta_{mid}}{\Delta_{failure}}\ x\ 100 \tag{6.24}$$

Alternatively, and slightly more accurately, Δ_{mid} could represent the peak dynamic deflection of the wall. However, since unloading occurs along the same slope as the initial wall stiffness of the brittle flexural response resistance function, the values of permanent deflections are only slightly smaller than peak dynamic deflections if the wall has been pushed beyond the (X_2, R_2) point on its resistance function. For the brittle flexural response resistance function, USACE recommends that the wall thickness be used as the failure deflection (USACE, 2008c). This is in agreement with the findings of Doherty et al. (2002) which showed that walls would not fail dynamically until the mid-height deflection was equal to the wall's thickness.

The resistance criterion is defined as the ratio of the residual (post-blast) out-of-plane resistance to the maximum (cracking in this case) resistance as given by the

equations/methodology in the preceding sections. This is represented mathematically as a percentage by

$$Pecent\ of\ collapse\ limit\ state = \left(1 - \frac{R_{residual}}{R_{max}}\right)\ x\ 100 \tag{6.25}$$

R_{max} is taken as the larger of the cracking resistance or the post-elastic arching resistance. $R_{residual}$ is determined by locating the intersection of the brittle flexure resistance function with a line (having a slope equal to the elastic stiffness, which represents the unloading/reloading path) drawn through the permanent deflection. This intersection represents the maximum resistance that would be achieved by the damaged wall if it were to be subjected to another out-of-plane load. Note that, for these comparisons, Wall #2 will use the resistance function from Case 2A and Wall #3 will use the resistance function from Case 3A.

6.6. Post-Blast State of the Test Structure

The internal infill wall (Wall #1) was extensively damaged and had a permanent deflection of approximately 25 cm (10 inches). Field observations indicated the wall was being held together by the frictional interlock between broken wall regions. The wall appeared unstable and probably would have collapsed under the action of a small lateral load. The extreme deflection (greater than its thickness) of the infill wall meant it attained its collapse limit-state for all practical purposes. The two load bearing walls, Walls #2 and #3, had permanent deflections equal to 8.9 cm (3.5 in) and 6.4 cm (2.5 in), respectively. Therefore, these walls attained a relatively low percentage of their collapse limit-states according to the deflection criterion. According to the resistance criterion, however, the walls had only a small fraction of their maximum resistance remaining, and

were thus vulnerable to further out-of-plane loading. Table 6.8 uses Eqs. (6.24) and (6.25) to quantify the states of Walls #2 and #3 based on experimental deflections. Walls #2 and #3 were 29%-79% and 21%-83% of their collapse limit-states, respectively, depending on the choice of collapse criterion.

TABLE 6.8. State of Walls #2 and #3 as a percentage of the collapse limit-state based on analytical deflections.

Criterion	Wall #2	Wall #3
Deflection	29%	21%
Resistance	79%	83%

Note: Wall #2 used case 2A resistance function, Wall #3 used case 3A resistance function.

The deflection criterion applied to Wall #3, the critical load-bearing wall of this building, indicates that the building attained approximately one fifth of its collapse limit-state. While the load-bearing walls continued to support the structure above and their deflections were not as extreme as the infill wall's, field observations indicated that the damage to these walls was extensive enough to require significant repairs before going back into service or total demolition of the building. Further, the application of the resistance criterion supports this conclusion, since the building attained 83% of its collapse limit-state as far as subsequent out-of-plane loading is concerned.

CHAPTER 7: FE MODELS OF THE SHOT B BLAST CHAMBER WALLS

Chapter 6 investigated the ability of the ESDOF method to predict the permanent deflections of the Shot B blast chamber walls (Walls #1, #2, and #3). The ESDOF method is frequently utilized for blast resistant structural design and it is reassuring to see that it was able to predict deflections with reasonable accuracy. It is of interest to study whether or not more complex simulations using FEA would predict deflections and damage patterns with greater accuracy. It is difficult to foresee an FE model being used in practice for the blast-resistant design of a URM structure due to the cost of the man-hours the analysis would require; however development of such a model might prove to be tremendously useful for other applications. An FE model which predicts the deformations and damage patterns observed in this experimental program could be used for detailed analyses, used to assist in retrofit designs of URM, and applied to other types of loading (for example seismic).

This chapter will investigate the ability of a commercial finite element software, LS-DYNA (LSTC, Livermore, CA), to simulate the response of the blast loaded URM walls of the Shot B blast chamber. LS-DYNA is a general purpose, transient, explicit and implicit, nonlinear, parallelized finite element software with a wide array of capabilities. The software has been successfully used to simulate phenomena including airblast, shockwaves, nonlinear stress/strain, large deformation, and contact problems among others. This chapter will describe the FEA modeling performed for this investigation

including details of the meshing, element types, boundary conditions, loading, contact considerations, constitutive properties, and simulation results.

7.1. Simple Models

Simpler FEA models were constructed prior to development of the full-scale wall models in order to study the various available contact algorithms and basic model parameters. Single integration point, constant stress elements were used in all of the simplified analyses reported in this section. Davidson and Sudame (2006) found that this element was a better choice than the fully integrated solid element because it yielded similar results at greatly reduced computational cost (i.e. faster run times). Brick material was modeled with a linear and elastic constitutive law; very little crushing was expected (and observed) in the blast chamber walls and the use of a non-linear material model would have added significant complexity to the model for little to no gain. The solid elements had an elastic modulus of 4233 MPa (614 ksi) and a density of 1842 kg/m^3 (115 pcf); these values were derived from laboratory tests of samples taken from blast chamber walls. Note that an additional 400 kg/m^2 (25 psf) aerial mass was applied to the walls to represent the interior tile veneer.

Contact entities were used to simulate the tensile and shear failure of masonry assemblages. This approach is very similar to that adopted by Burnett et al. (2007) in their FEA models. Only contacts which possess a "tiebreak" feature were considered. Tiebreaks permit a failure stress or force to be specified for the contact to represent the tensile and/or shear capacity of the URM assemblage. The contact option TIEBREAK_NODE_TO_NODE was not considered because once a tiebreak has failed, the contact is deactivated entirely. This is unacceptable because the contact must permit

compressive loads and sliding friction after failure in order to simulate cracked URM. The best remaining contact options available were TIEBREAK_NODES_TO_SURFACE, TIEBREAK_SURFACE_TO_SURFACE, and AUTOMATIC_SURFACE_TO_SURFACE_TIEBREAK. All three contacts are similar, with the exception that the nodes to surface contact specifies failure in terms of nodal forces while surface to surface contacts define failure in terms of stress on the contact surfaces. Using a stress based definition yields desirable simplifications because not all nodes in a model have the same tributary area. Thus different contacts would have different effective failure forces (on a per node basis); this would make it very difficult to manually write the contact cards accurately. Also, the nodes to surface contact would only check for penetration of the slave nodes through the master surface. This is less robust than a surface to surface contact in which overall segment to segment penetration is checked. For this investigation, segmental penetration is important because once two bricks slide relative to one another, slave nodes might be located outside the boundaries of the master surface; a nodes to surface contact might therefore allow surfaces to penetrate one another.

The two surface to surface contacts were tested using a simplified model like that shown in Figure 7.1. Trial simulations found that the non-automatic contact produced unexpected segment penetrations that could not be explained. Regardless of which supplemental options were utilized (e.g. SOFT=2), the penetrations could not be eliminated. The automatic contact option did not produce these unusual penetrations and thus AUTOMATIC_SURFACE_TO_SURFACE_TIEBREAK was used to simulate the tensile and shear capacities of the blast chamber walls. The only feature of the contact

which was “automatic” was the orientation of surface normals. Otherwise, the contact definition was essentially identical to the non-automatic definition. This contact algorithm has several options for defining failure. Trial and error showed that Option 2 worked well and determines failure in accordance with:

$$\left[\frac{\sigma_n}{NFLS}\right]^2 + \left[\frac{\sigma_s}{SFLS}\right]^2 \geq 1 \tag{7.1}$$

where σ_n is the computed normal tensile stress, *NFLS* the user specified normal tensile failure stress, σ_s the computed shear stress, and *SFLS* the user specified shear failure stress. When the left-hand side of the equation is greater than or equal to 1.0, the shear and tensile strengths are deactivated, but the contact continues to support compressive loads and sliding friction.

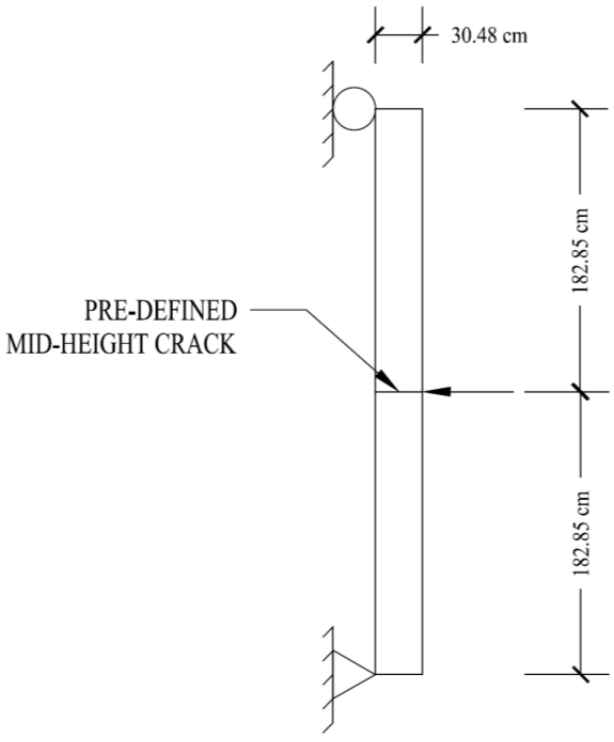

FIGURE 7.1: Simply-supported, point loaded wall strip.

A simple four element model was constructed to verify that the selected contact type functioned as expected. Figure 7.2 shows the model used for these tests.

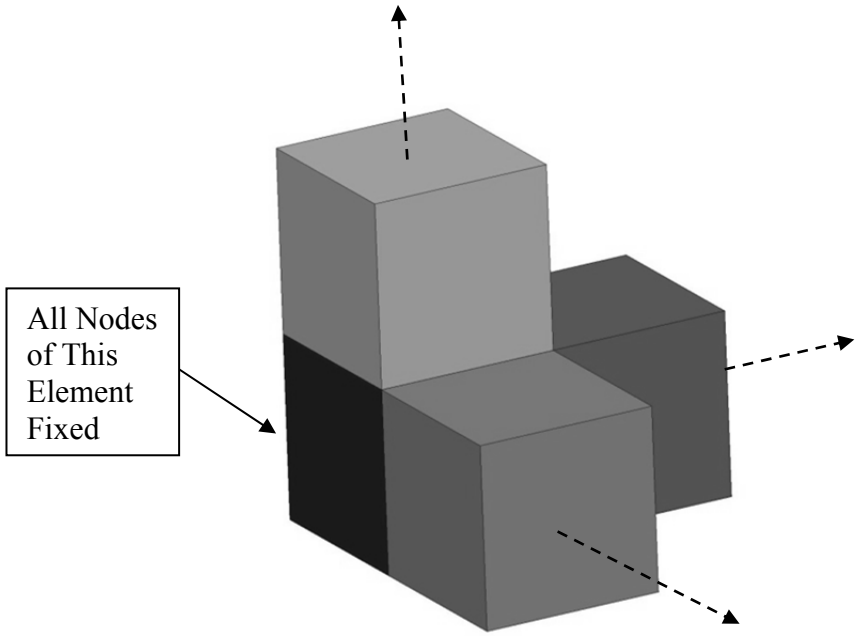

FIGURE 7.2: Four element model used to test normal and shear tiebreak features.

In Figure 7.2, the base (darkest shaded) element was fixed against all translation. The remaining three elements were attached to the base element using only the AUTOMATIC_SURFACE_TO_SURFACE_TIEBREAK contact. A gradually ramped normal tensile force was applied to each of the three elements in turn. The simulation found that the contacts indeed failed at the specified normal tensile failure stress (NFLS). A similar simulation was conducted in shear and that test confirmed the tiebreak failed at the user specified shear stress (SFLS).

This simple model also permitted tests which identified the method best suited to defining contacts. At first, the automatic part-based contact search feature was tested (each of the four elements was given a different part number). Using this code feature,

LS-DYNA automatically identifies contacts by detecting parts which have segments which are initially in contact. This feature simplifies the input deck to a single contact definition card for the entire model. Unfortunately, a part-based search created extraneous contacts for this model's cubic parts. It appears as though the automatic search algorithm generated contacts for segments which are at 90 degrees to one another. This occurs because segments at 90 degrees are close enough to touch and appear to be in contact as a result of master surface enlargement during the automated LS-DYNA search. It was therefore necessary to use a more cumbersome manual specification of every contact. This means that for all the models that follow, each contact is defined by two segment (individual element face) definition cards and one contact definition card, which references the segment cards.

The four element model shown in Figure 7.2 was only useful for testing contact behavior when forces were perfectly normal or perfectly parallel to the plane of contact. This will not usually be the case in the full-scale models. The specification of failure stress is only straightforward when the applied stress is entirely normal or parallel and uniform across the contact surface. LS-DYNA documentation indicates that when a user specifies a failure stress, that stress is apportioned as a force to the contact's nodes based on their tributary areas. Thus the failure stress must be specified in a manner that accounts for how stress will be calculated and apportioned during a simulation. The limited available documentation did not clearly explain how the entire computation would be performed and thus it was necessary to determine the required value of *NFLS* by trial and error. This was done using the pin-roller supported, three point bending model shown schematically in Figure 7.1.

The model was 30.5 cm (12.0 in) thick, 365.8 cm (144.0 in) tall, and 30.5 (12.0 in) wide. The model was meshed with solid elements with a 10.16 cm (4 in) edge length. The location of a crack was predetermined by inclusion of a tiebreak contact definition at midspan. Gravity was not included in the model. The midspan point load was slowly increased until the contacts failed in tension. The specified value of NFLS was adjusted until the FE model failed at a load of 4448 N (1000 lbs). This failure load was calculated from beam theory using a failure stress of 0.862 MPa (125 psi) in flexural tension. The shear failure stress was specified as 0.689 MPa (100 psi) based on guidance contained in Drysdale et al. (1999) derived from laboratory tests of clay masonry; this shear failure stress is less than would be permitted for strength design by the MSJC code (MSJC, 2008). From this model, the required value of NFLS was found to be 0.643 MPa (93.2 psi), or a 25.4% reduction.

After calibrating the NFLS, another FEA model was constructed which was similar to the three point bending model. The model was intended to simulate a unit width of Wall #3 from the Shot B blast chamber. It was of interest to see how dynamic deflections predicted by LS-DYNA compared to those predicted by SBEDS for this simple case. The FEA model was 30.5 cm (12 in) wide, 30.5 cm (12 in) thick, and 365.8 cm (144 in) tall. Figure 7.3 schematically shows the dimensions, loading, boundary conditions, and assumed crack location for the LS-DYNA model; these conditions are essentially identical to those assumed in SBEDS for the brittle flexural response resistance function described in Section 6.1. The model was meshed with cubic solid elements with a 10.16 cm (4 in) edge length. At its base, the model was supported in the vertical direction using a rigid wall boundary condition to provide vertical support; a

rigid wall boundary effectively establishes a contact plane through which no nodes may pass. A pin boundary condition was applied at the bottom and a roller boundary condition at the top of the model to provide the out-of-plane restraint. Gravity was applied using dynamic relaxation. The crack location was predefined at midspan using contacts with an NFLS equal to 0.643 MPa (93.2 psi) and SFLS equal to 0.689 MPa (100 psi). Figure 7.4 shows the finite element model at rest and during out-of-plane response after the mid-height contacts have failed in flexural tension.

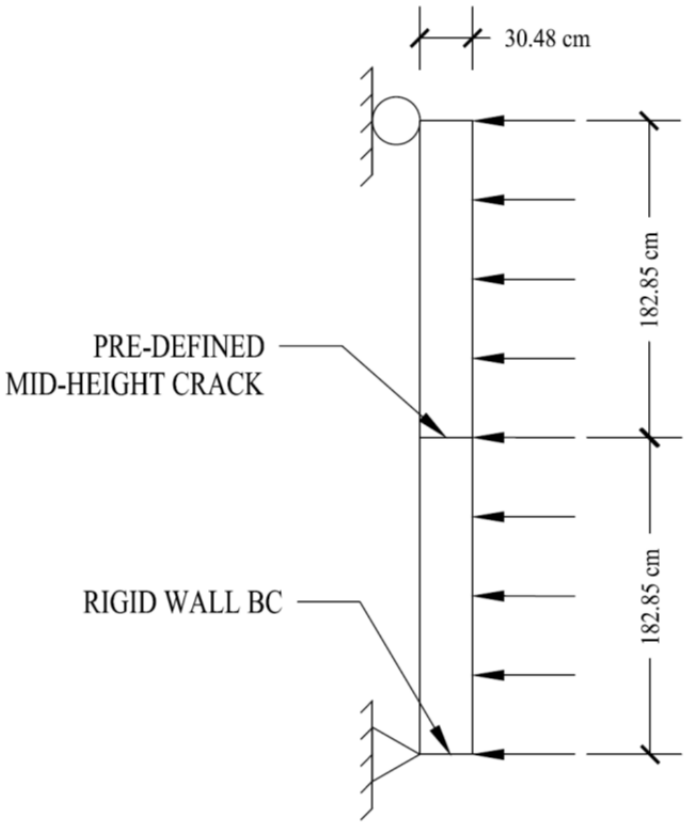

FIGURE 7.3: Illustration showing LS-DYNA model for simplified comparisons to SBEDS.

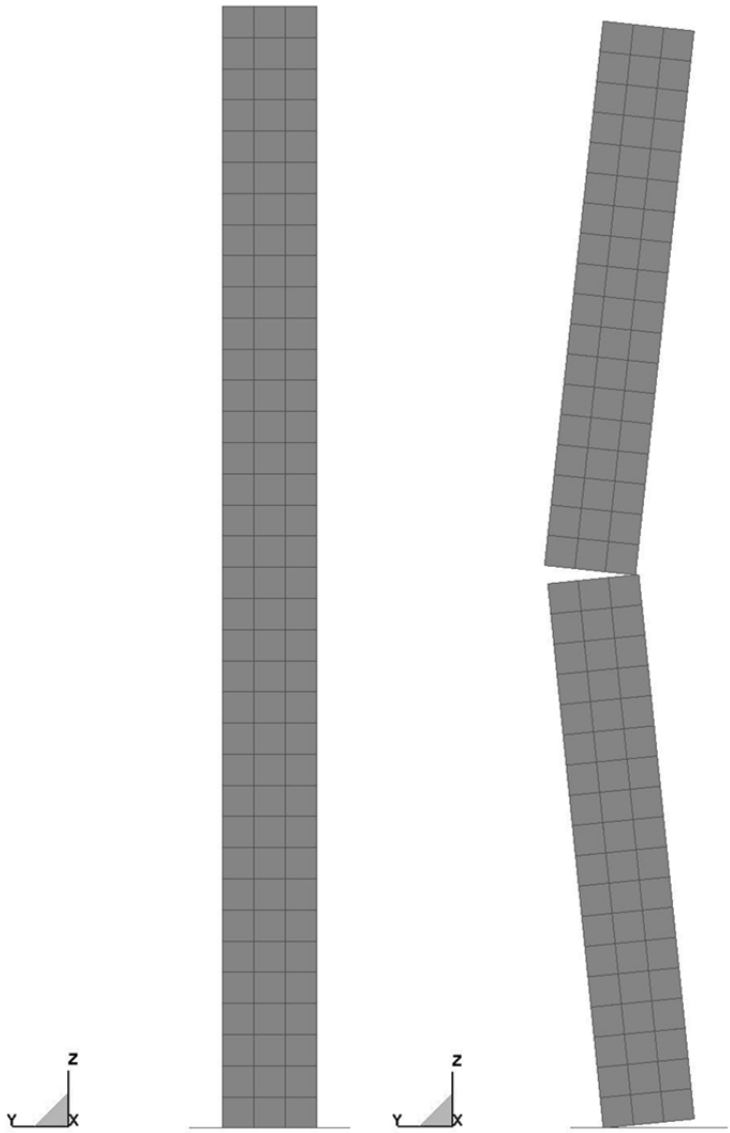

FIGURE 7.4: View of LS-DYNA model showing model at rest and after formation of mid-height crack. Loading was applied to the –Y face in the +Y direction. Gravity was applied in the –Z direction. The horizontal line at the bottom of the wall represents the rigid wall boundary condition.

For all comparisons, an idealized triangular blast wave was applied as a uniform surface pressure. The load was assumed to have a near instantaneous rise time and a 2 ms duration. Table 7.1 shows this as normalized ordered pairs, where 1.0 represents the normalized peak reflected pressure. Note that both LS-DYNA and SBEDS interpolate

between these ordered pairs so it is unnecessary to define more points. The loading was applied starting at t=100 ms in order to verify that the model had stabilized after gravity initialization.

TABLE 7.1: Normalized time history profile for simplified comparisons.

Time (ms)	Peak Reflected Pressure (normalized)
100.0	0
100.1	1.0
102.1	0.0
∞	0.0

Chapter 6 showed that the results of an ESDOF simulation could be very sensitive to the magnitude of applied damping. It was therefore of interest to study the effect of damping on LS-DYNA simulations. For the simplified comparisons that follow, 2% of critical damping was used in all SBEDS analyses. For the LS-DYNA analyses, both 2% and zero damping were used. In order to compute the damping coefficient in LS-DYNA, it was first necessary to determine the model's elastic natural frequency. This was accomplished by observing the model's natural period of vibration during a simulated free vibration test. SBEDS predicted the model's elastic natural frequency to be 14.3 Hz while LS-DYNA predicted a natural frequency of 17.2 Hz. There are a number of factors which could contribute to this apparent difference of stiffness, including LS-DYNA's rigid wall boundary condition and the hourglass control algorithms; also, FE formulations are commonly known to be stiffer than the structures they model. Using the natural frequency, the nodal damping coefficient in LS-DYNA was determined by

$$C = \zeta(2\omega)\, m \tag{7.2}$$

where C is the damping coefficient which is computed as the damping ratio ζ multiplied by twice the elastic natural frequency ω (in radians per second) and the nodal mass m. Note that the user only supplies the value $\zeta(2\omega)$ in LS-DYNA using the DAMPING_GLOBAL card; the software automatically multiplies this value by appropriate nodal masses. During the elastic phase of response, both SBEDS and LS-DYNA utilized 2% of critical damping; after cracking, however, SBEDS reduces damping by a factor of 100 while LS-DYNA continues to use the 2% value.

Tables 7.2 through 7.4 compare the out-of-plane wall deflections predicted by LS-DYNA to those predicted by SBEDS using 2% viscous damping. Then, Tables 7.5 through 7.7 repeat the same simulations, except damping in the LS-DYNA model has been reduced to zero. In all tables, percent differences are computed relative to the values predicted by SBEDS, where a positive difference indicates LS-DYNA predicted a greater deflection/time/reaction than SBEDS.

TABLE 7.2: Comparison of peak deflections as predicted by LS-DYNA and SBEDS; 2% of critical damping.

Load Case	Peak Reflected Pressure kPa (psi)	Reflected Impulse kPa ms (psi ms)	LS-DYNA Deflection cm (in)	SBEDS Deflection cm (in)	Percent Difference
1*	41 (6.0)	43 (6.3)	0.08 (0.03)	0.08 (0.03)	0.0
2*	82.7 (12.0)	86.9 (12.6)	0.18 (0.07)	0.18 (0.07)	0.0
3	165 (24.0)	174 (25.2)	1.0 (0.40)	0.71 (0.28)	43
4	331 (48.0)	347 (50.4)	4.17 (1.64)	3.10 (1.22)	34
5	496 (72.0)	521 (75.6)	9.35 (3.68)	6.68 (2.63)	40
6	827.4 (120.0)	868.7 (126.0)	23.1 (9.10)	16.6 (6.55)	39

Note: *Wall remains elastic.

TABLE 7.3: Comparison of time to peak deflection predicted by LS-DYNA and SBEDS; 2% of critical damping.

Load Case	LS-DYNA Time to Peak Deflection (ms)	SBEDS Time to Peak Deflection (ms)	Percent Difference
1*	17	18	5.6
2*	18	18	0.0
3	65	51	27
4	133	108	23.1
5	198	162	22.2
6	443	289	53.3

Note: *Wall remains elastic.

TABLE 7.4: Peak dynamic reactions predicted by LS-DYNA and SBEDS; 2% of critical damping.

Load Case	LS-DYNA** Peak Dynamic Reaction kN (lb)	SBEDS Peak Dynamic Reaction kN (lb)	Percent Difference
1*	5.427 (1220)	5.075 (1141)	6.5
2*	8.007 (1800)	10.15 (2281)	-21.1
3	17.81 (4004)	20.29 (4562)	-12.2
4	38.47 (8648)	40.20 (9037)	-4.3
5	58.676 (13191)	60.878 (13686)	-3.6
6	95.103 (21380)	98.924 (22239)	-3.9

Notes: *Wall remains elastic. **Peak LS-DYNA reaction is from summation of nodal reaction forces at bottom of wall.

TABLE 7.5: Comparison of peak deflections predicted by LS-DYNA and SBEDS; SBEDS using 2% and LS-DYNA 0% of critical damping.

Load Case	Peak Reflected Pressure kPa (psi)	Reflected Impulse kPa ms (psi ms)	LS-DYNA Deflection cm (in)	SBEDS Deflection cm (in)	Percent Difference
1*	41 (6.0)	43 (6.3)	0.08 (0.03)	0.08 (0.03)	0.0
2*	82.7 (12.0)	86.9 (12.6)	0.18 (0.07)	0.18 (0.07)	0.0
3	165 (24.0)	174 (25.2)	1.3 (0.50)	0.71 (0.28)	79
4	331 (48.0)	347 (50.4)	6.32 (2.49)	3.10 (1.22)	104
5	496 (72.0)	521 (75.6)	19.9 (7.82)	6.68 (2.63)	197
6	827.4 (120.0)	868.7 (126.0)	FAILURE**	16.6 (6.55)	N/A

Notes: *Wall remains elastic. **Failure means max wall deflection greater than wall thickness.

TABLE 7.6: Comparison of time to peak deflection predicted by LS-DYNA and SBEDS; SBEDS using 2% and LS-DYNA 0% of critical damping.

Load Case	LS-DYNA Time to Peak Deflection (ms)	SBEDS Time to Peak Deflection (ms)	Percent Difference
1*	17	18	5.6
2*	18	18	0.0
3	79	51	55
4	190	108	75.9
5	442	162	173
6	N/A	289	N/A

Note: *Wall remains elastic.

TABLE 7.7: Peak dynamic reactions predicted by LS-DYNA and SBEDS; SBEDS using 2% and LS-DYNA 0% of critical damping.

Load Case	LS-DYNA** Peak Dynamic Reaction kN (lb)	SBEDS Peak Dynamic Reaction kN (lb)	Percent Difference
1*	5.716 (1285)	5.075 (1141)	12.6
2*	8.514 (1914)	10.15 (2281)	-16.1
3	17.84 (4011)	20.29 (4562)	-12.1
4	38.53 (8662)	40.20 (9037)	-4.1
5	58.774 (13213)	60.878 (13686)	-3.5
6	95.263 (21416)	98.924 (22239)	-3.7

Notes: *Wall remains elastic. **Peak LS-DYNA reaction is from summation of nodal reaction forces at bottom of wall.

In the case of both 2% and 0% critical damping the tables show that, once the models have cracked at midheight, LS-DYNA predicted deflections that are 50 to 100% larger than those predicted by SBEDS. This difference can be explained by considering Figure 7.5 which shows the contact force at the midheight crack for Load Case 5 from Table 7.2. Until time t=0.1 seconds, the midheight force is constant and equal to the weight of the upper wall half. When the blast load is applied, the upper wall segment is pushed upward as the two segments rock, causing the wall halves to lose contact; this corresponds to the first region on the plot where there is a contact force of zero. The subsequent spikes and zero force regions of the plot show that the upper wall half in fact "bounces" off the bottom several times during the wall's response. Recalling from Chapter 6 that URM's post-elastic out-of-plane resistance is predicated on axial force alone, the discrepancy between LS-DYNA and SBEDS begins to make sense. If there is no axial force on the lower wall segment, then there is effectively no out-of-plane resistance. SBEDS is simply incapable of simulating this vertical deflection of one wall half relative to another.

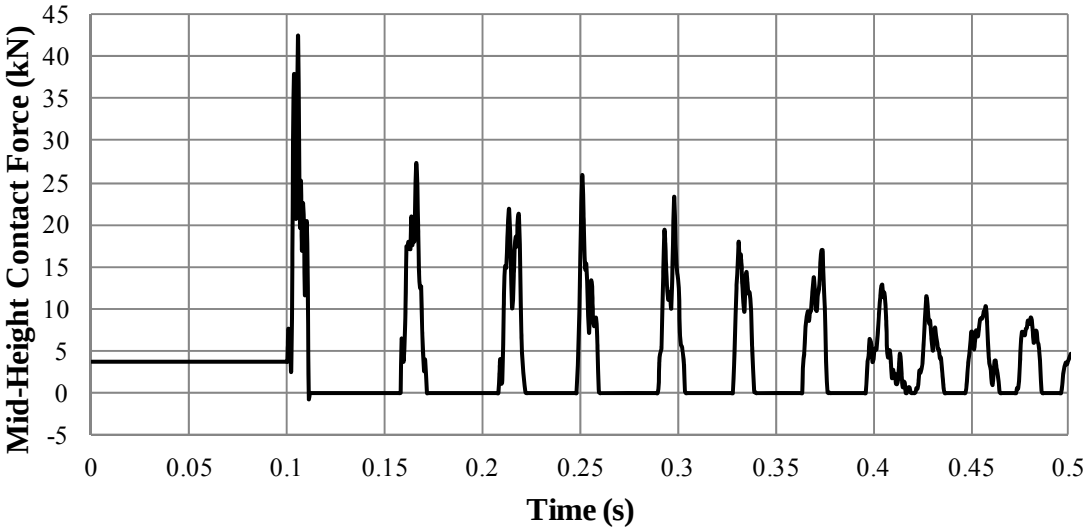

FIGURE 7.5: Contact force at mid-height crack as a function of time. From LS-DYNA simulation for Load Case 5 from Table 7.2.

Although this phenomenon makes sense with regard to the LS-DYNA model, it is likely less pronounced in an actual structure. In the LS-DYNA model the materials are perfectly elastic, but a real structure would likely see highly localized crushing of mortar at a crack. In addition, a real structure has more complex boundary conditions which would likely inhibit vertical movement; both of these factors would act to mitigate the bouncing shown in Figure 7.5. It would be interesting to experimentally measure this phenomenon and find out what, if any, effect the dynamic vertical interaction of wall segments might have on the out-of-plane response of URM walls. Based on this comparison, it is tempting to label SBEDS as somewhat unconservative relative to LS-DYNA. Examining validation data, however, USACE (2008) shows that SBEDS predictions are normally conservative when compared to experimental data for URM walls. This means that, in fact, LS-DYNA's predictions might be overly-conservative.

Tables 7.3 and 7.6 compare the LS-DYNA and SBEDS predictions of the time required to achieve maximum deflection. Given the difference in predicted peak deflections, it is not surprising that the predicted time to peak deflection also differed between SBEDS and LS-DYNA by a similar degree. Tables 7.4 and 7.7 compare the maximum reactions predicted by LS-DYNA to those predicted by SBEDS. In SBEDS, the maximum reaction forces are computed as a summation of the applied loading and the computed element resistance, both multiplied by ESDOF transformation factors. In LS-DYNA, the peak reactions were computed by summing the nodal reaction forces at the pin at the bottom of the model. It is interesting to note that the ESDOF computed dynamic reactions are normally conservative for cases in which the wall cracks, but slightly unconservative for fully elastic simulations. Studying the force-time history produced by LS-DYNA it appears that, for elastic simulations, there are several modes (with frequencies higher than the fundamental mode) involved in wall response and their combined effect tended to cause FEA reactions to be higher than the ESDOF reactions. Regardless, it appears that the FEA and ESDOF predicted reaction forces are generally in close agreement.

Comparing Tables 7.2 and 7.5 shows that damping can considerably change the results of the LS-DYNA simulations. This same effect was observed in the SBEDS results from Chapter 6. As previously mentioned, SBEDS reduces the damping coefficient by a factor of 100 once the model is no longer elastic. LS-DYNA does have the ability to specify damping as a function of time, but this is difficult to use because the moment of cracking depends on the damping specified. It is easier to simply specify a constant damping coefficient. This is problematic because the model's natural frequency

decreases significantly after cracking, thus also changing what would be the critical damping coefficient. Compare, for example, Load Cases 1 and 4 from Table 7.3. The elastic model had a natural period of 58 milliseconds (frequency of 15 Hz) while the cracked structure had a natural period of approximately 532 milliseconds (frequency of 1.88 Hz). Specifying 2% of critical damping in LS-DYNA, Load Case 1 would require a damping value of 3.8 rad/s while Load Case 4 would require a damping value of 0.47 rad/s, a change of nearly a factor of 8. Further evidence of the effect of damping on post-elastic response is shown in Figure 7.6, which compares simulation total energy to damping energy as a function of time (for Load Case 5 from Table 7.2). The figure shows that after cracking (which occurs shortly after t=0.1 seconds) damping energy quickly approaches total energy. This result implies that most of the model's kinetic energy is quickly dissipated by damping; this should not be the case for a structure with 2% viscous damping.

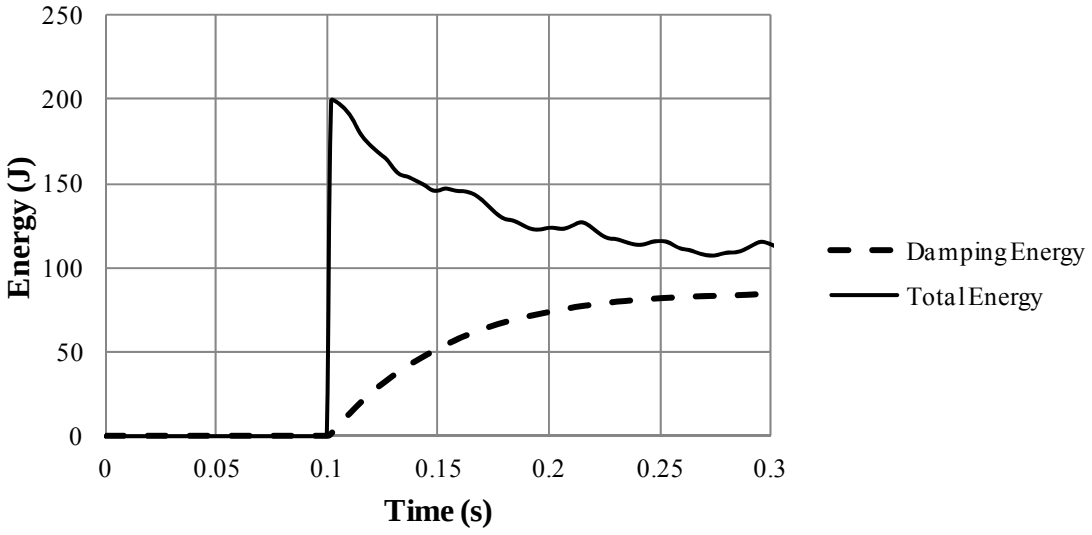

FIGURE 7.6: Comparison of total energy to damping energy for 2% of critical damping. LS-DYNA results from Load Case 5, Table 7.2.

This apparent sensitivity to damping is contrary to what Davidson and Sudame (2004) found in their study of fiber reinforced polymer (FRP) strengthened CMU walls. They found that specifying 2% or 5% of critical damping yielded essentially the same out-of-plane deflections. It is important to note, however, that because their walls had FRP laminates, they were stiffer after cracking than a plain URM wall would have been. Thus the change in natural frequency between the uncracked and cracked states was small enough that the damping coefficient and therefore the results were only minimally affected. For this investigation, however, the damping must be carefully chosen to prevent erroneous energy dissipation after formation of a crack.

The single integration point element used in the preceding simulations requires a special algorithm to prevent excessive hourglass energy. When hourglass energy escalates significantly, the model can become unstable or parts attached by contacts can spuriously break apart. Davidson and Sudame (2004) reported that the hourglass energy should be less than 10% of the internal energy in the model. Figures 7.7 though 7.9 show plots of internal energy and hourglass energy for Load Case 1 (with 2% damping) using none and two different hourglass control schemes. Clearly, the Type 4 hourglass control provided the best results, yielding an hourglass energy well below 10% of the model's internal energy.

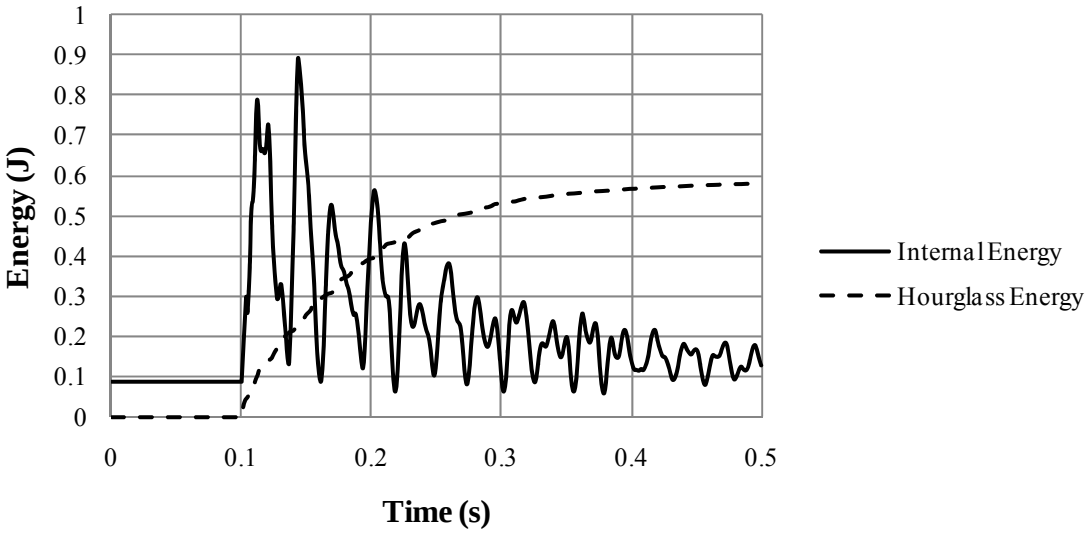

FIGURE 7.7: Internal energy compared to hourglass energy with no hourglass control.

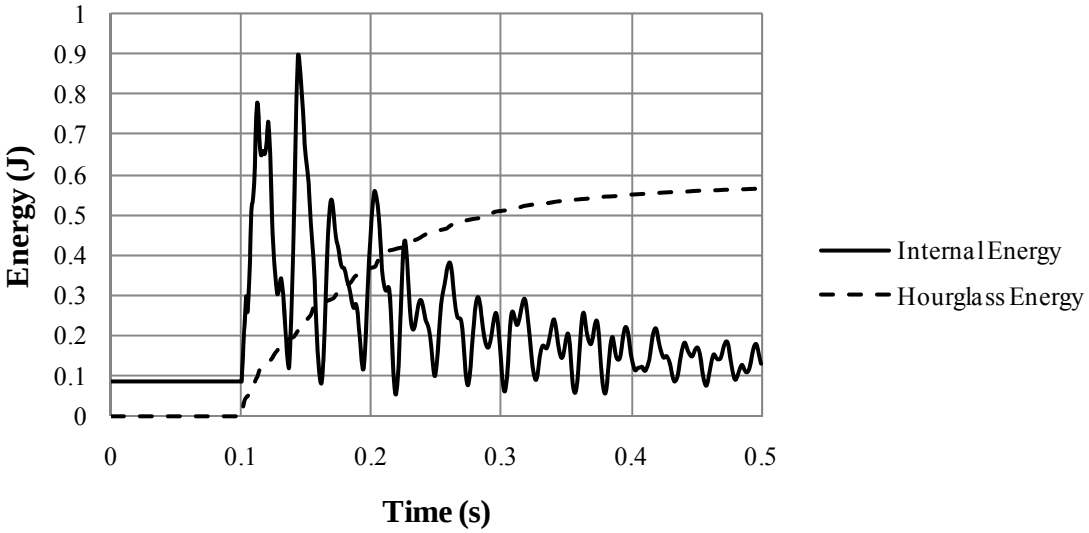

FIGURE 7.8: Internal energy compared to hourglass energy with Type 1 hourglass control.

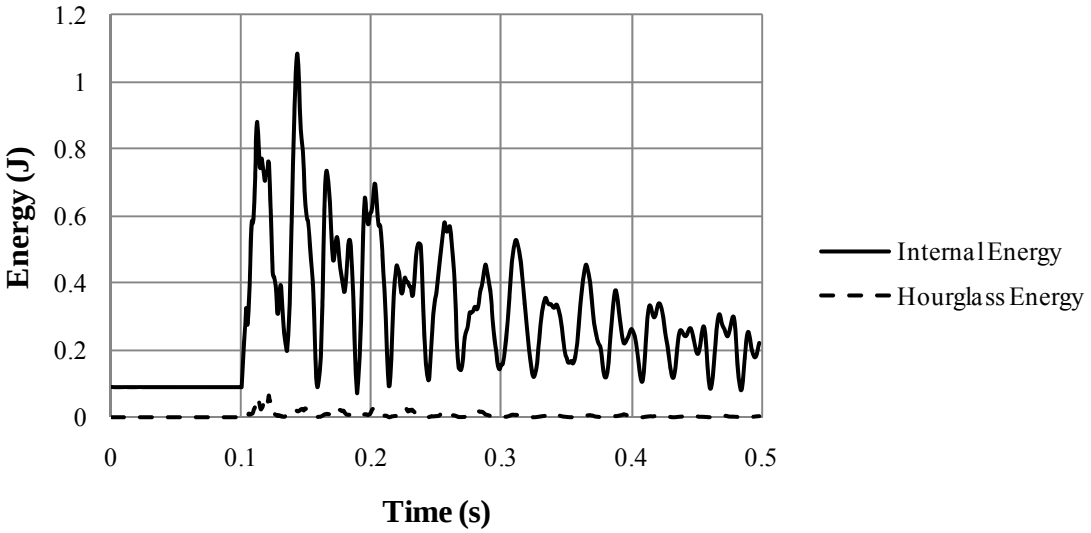

FIGURE 7.9: Internal energy compared to hourglass energy with Type 4 hourglass control.

7.2. Full-Scale Models

Using the information learned from the simplified investigations, two FE models were developed for the Shot B blast chamber walls. One model contained both Wall #2 and Wall #3 because they connected at a common corner; the other model contained only Wall #1 because it was structurally independent from the other walls. This was advantageous because the model of Wall #1 ran quickly (approximately 20 minutes using fifteen nodes of the University cluster) and thus permitted several simulations to be performed to facilitate choosing the final parameter sets for use in both models.

7.2.1. Element Size and Type

Initially, an attempt was made to use 5.08 cm (2 in) cubic solid elements to model the walls. Unfortunately, this led to the creation of more contacts in the model of Walls #2 and #3 than LS-DYNA would allow; the model would have required approximately 120,000 contacts, which is more than the internal limit of UNC Charlotte's current

version of LS-DYNA. The limitation in software version 971 was confirmed in personal communication with LS-DYNA technical support. Therefore, the models were meshed with 10.16 cm (4 in) cubic elements to allow all the necessary contact definitions to be included; this reduced the number of contacts to 23,864. Unfortunately, this larger element size created problems controlling hourglass energy for the Type 1 solid element. All of the previously discussed hourglass control schemes were investigated, but the hourglass energy could never be adequately limited to 10% of the internal energy. In order to resolve this issue, a different element formulation was utilized. For the full-scale models that follow, all solid elements are Type 2, the selectively reduced fully integrated solid.

Since bricks were modeled as 10.16 cm (4in) thick, 10.16 cm (4 in) wide and 20.32 cm (8 in) long, two of these Type 2 elements were joined together to form each brick; this is double the thickness of standard bricks which are nominally 5.08 cm (2 in) thick. The bricks were modeled as 10.16 cm (4 in) thick primarily to reduce the number of contact entities, but this also created a favorable 1:1 element aspect ratio. Each brick was given a separate part number.

7.2.2. Calibration of Failure Stress

The simplified models tested in Section 7.1 showed that trial-and-error calibration was required to determine the correct tensile failure stress (NFLS). These models examined bending perpendicular to the bed joints; this is representative of how Wall #3 was expected to behave. Walls #1 and #2, however, experienced two-way bending, meaning that bending would also occur parallel to the bed joints. It was therefore of interest to also calibrate the tensile (normal) failure stress using a model with bending

parallel to the bed joints. Figure 7.10 shows the model used for Wall #1 before (at bottom) and after (at top) formation of mid-span tensile cracks. The model was pin-roller supported and had a uniform load applied along its span. An identical model was constructed for Wall #2, but with three bricks through the wall's thickness.

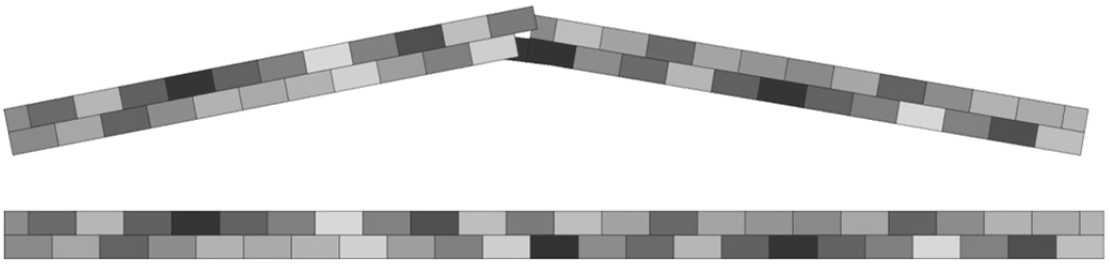

FIGURE 7.10: LS-DYNA model of a strip of Wall #1 with bending parallel to the bed joints. Initial unloaded state at bottom and immediately after tensile failure at top.

Tests with the model yielded two surprises. First, the shear failure stress must be set appreciably lower than the tensile failure stress. Otherwise, even after tensile failure, the shear capacity between bricks will continue to sustain load. Based on parametric studies, it appears as though specifying the shear failure stress (SFLS) to be less than 75% of the tensile failure stress (NFLS) will yield the correct failure load. The failure stresses employed in the full-scale simulations require one additional piece of information, – the dynamic increase factor - which will be described in Section 7.2.4; thus the calibrated failure stresses will be presented there.

The second and more surprising discovery was that the user-specified contact penalty force scale factor controls the bending stiffness of the model. This scale factor is specified in the CONTROL_CONTACT card. The LS-DYNA user manual suggests a value of 0.10 and tests showed that this value leads to a bending stiffness approximately

half of what traditional beam theory predicts. Attempts to use a higher value (0.3 for example) did increase the bending stiffness, but also created problems with shooting nodes (large, non-physical deflections of individual nodes) and unexpected node penetrations. The default recommended value of 0.10 was therefore used in the simulations that follow. Methods to accurately represent bending stiffness while avoiding numerical problems warrant further investigation; this is likely something which must be investigated by LS-DYNA's creators as it might involve modifications to the contact algorithms.

7.2.3. Failure Stresses Including the Dynamic Increase Factor

For many materials, the failure stress (strength) is directly proportional to the rate at which the material is strained. Higher strain rates produce higher apparent failure stresses. Masonry under compressive or tensile loading experiences this phenomenon. One-way engineers account for this is by using a multiplier called the dynamic increase factor (DIF). Using the results of several SBEDS simulations from Section 7.1, it appears as though a strain rate of 1 s^{-1} is a reasonable estimate of the rate experienced by the blast chamber walls. Wei and Hao (2009) report that for a strain rate of 1 s^{-1}, the DIF for masonry under tension can be estimated as 1.4. Burnett et al. (2007) utilized a split Hopkinson bar apparatus and experimentally found that a mortar joint in brick masonry could have a DIF of up to 3.1. Given this wide range and a sparsity of experimental data for URM (and no such tests performed on the masonry in this investigation), the numerical analyses reported here will utilize a mid-range value of the DIF, where DIF = 2.0. Note that this DIF makes the specified tensile failure stress consistent with the maximum dynamic tensile stress recommended for analysis by UFC 3-340-02, which is

1.72 MPa (250 psi); USACE found that this value created the best agreement between analyses using SBEDS and experiments. Based on the NFLS and SFLS calibration trials from Sections 7.1 and 7.2.2 and a DIF of 2.0, the tensile and shear failure stresses for each wall are summarized in Table 7.8.

TABLE 7.8: Failure stresses utilized in LS-DYNA models.

Wall	Failure Stress Type	MPa (psi)
Wall #1	Tensile for Bending	0.9367 (135.9)
	Tensile for through-thickness spall	1.724 (250.0)
	Shear	0.6895 (100.0)
Wall #2	Tensile for Bending	1.147 (166.4)
	Tensile for through-thickness spall	1.724 (250.0)
	Shear	0.6895 (100.0)
Wall #3	Tensile for Bending	1.286 (186.5)
	Tensile for through-thickness spall	1.724 (250.0)
	Shear	0.6895 (100.0)

Table 7.8 clearly shows that the LS-DYNA contact cards cannot be written using a single definition. In order to correctly write the contact cards, a Matlab program was written (included as Script D.10 in Appendix D) for convenience. The program takes the node and element definition cards from the FE model input files and uses them to compute the location of every contact in the model. The program then writes the correct segment and contact definition cards with the failure stress based on the location and orientation of the contact. Given that the smallest model (Wall #1) had 5581 contacts, manual specification would have been impractical.

7.2.4. Inclusion of Fracture Energy

Although the simplified comparisons successfully utilized the failure option described by Eq. (7.1), use of this option in the full-scale simulations led to excessive deformations. A similar observation was reported by Gilbert et al. (1998) who modeled

vehicle impacts on masonry parapet walls. The researchers noticed that although the damage pattern was qualitatively similar, use of a simple tiebreak failure model (like Type 2) yielded deflections larger than those observed in experiments. The authors went on to explain that it was necessary to include fracture energy in their FE model in order to obtain quantitatively accurate deformations. Note that inclusion of fracture energy in the SBEDS comparisons from Section 7.1 would not have been appropriate as SBEDS does not account for fracture energy either.

For this investigation, a failure model including fracture energy was available by switching from failure Option 2 to Option 7. Option 7, referred to as the DYCOSS model (Dynamic Behavior of Composite Ship Structures), computes the onset of cracking according to

$$1 = \left(\frac{\max(\sigma_n,0)}{NFLS}\right)^2 + \left(\frac{\sigma_s}{SFLS(1-\sin(\varphi)\min(0,\sigma_n))}\right)^2 \tag{7.3}$$

where σ_n is the applied normal stress, *NFLS* is the specified normal failure stress, σ_s is the applied shear stress, *SFLS* the specified shear failure stress, and φ is the friction angle. Option 7 failure is thus similar to Option 2, however includes shear strengthening with increasing compressive stress. This compression enhanced shear capacity can be compared to a Mohr-Coulomb failure envelope in which the shear capacity of a material is computed as

$$SFLS = \max(\sigma_n, 0)\sin(\varphi) + c \tag{7.4}$$

where *SFLS* is the shear failure stress, σ_n is the normal stress (compressive), φ is the friction angle, and c is the cohesion (i.e. the shear capacity in the absence of normal stress). Interestingly, the shear failure stress component of both the DYCOSS and Mohr-

Coulomb models may be made equal through selection of an appropriate friction angle φ. For example, using φ of 0.4 degrees in Eq. (7.3) yields a similar shear capacity as using $\varphi = 36°$ in Eq. (7.4). Note that although the DYCOSS model was not intended for masonry, it was found to be the best option available in LS-DYNA for this investigation. Failure Option 5 was investigated as an alternate means of including fracture energy, but produced numerical problems when tested; use of this option was therefore abandoned.

In addition to the normal and shear failure stresses, the DYCOSS failure model requires the user to specify a Mode I and Mode II fracture energy. Very limited information regarding masonry fracture parameters was found in the literature. Table 7.9 summarizes the three sets of available data and shows the source reporting this data. It should be noted that fracture parameters for masonry are likely dependent on a number of factors including: mortar type, brick type, surface preparation, tensile and shear strengths of the masonry assembly, etc. Also, the fracture energies should be somewhat correlated to the failure stresses of the masonry specimens. As shear or tensile failure stress increases, so too does the fracture energy (in most cases); it is unclear how this statement applies to stress increases resulting from high strain rate loading. Given all of this variability and uncertainty, the parameters in Table 7.9 can serve only as a rough estimate for the masonry in this investigation.

TABLE 7.9: Summary of brick masonry fracture parameters.

Source	Dilatancy Angle (deg)	Friction Angle (deg)	Mode I ERR N/mm (lb/in)	Mode II ERR N/mm (lb/in)
Burnett et al. (2007)	7.2	Not Listed	0.01 (0.06)	0.059 (0.337)
Gilbert et al. (1998)	17.7	32.6	0.01 (0.06)	0.05 (0.29)
Proft et al. (2011)	Not Listed	36.9	0.018 (0.103)	0.125 (0.714)

Table 7.10 shows the fracture energy release rates (ERR) used in the LS-DYNA simulations; the values are based on the data from Gilbert et al. (1998). This source was selected because the authors derived their energies from several different data sets which supported their final energy value. Furthermore, the study went on to use the data in FE simulations of brick masonry which correlated well with experiments. Therefore, the fracture energies as reported by Gilbert et al. (1998) were adopted, unmodified, to represent those of masonry in flexural tension. For through-thickness tensile failure, the energies were magnified by a factor of 1.5; this corresponds to the ratio of the through thickness tensile failure stress to the average flexural tensile failure stress utilized in the input files. This magnification is based on the hypothesis that the fracture energy should be approximately proportional to the failure stress (tensile or shear); thus if the tensile stress is reduced or increased relative to some baseline, so too should the fracture energy. Given the limited information regarding fracture energies of masonry, more study is warranted, both to experimentally determine the energies as well as how best to specify them in FE models. Moreover, further study is warranted regarding whether or not fracture energy release rates should be scaled by the DIFs for dynamic analyses.

TABLE 7.10: Fracture energies used in LS-DYNA simulations.

Wall And Stress Type	Tensile Strength kPa (psi)	Shear Strength kPa (psi)	Mode I ERR N/mm (lb/in)	Mode II ERR N/mm (lb/in)
Wall #1 Flexural Tension	0.9367 (135.9)	0.6895 (100.0)	0.01 (0.0571)	0.05 (0.2855)
Wall #1 Through Thickness	1.724 (250.0)	0.6895 (100.0)	0.015 (0.0857)	0.075 (0.4283)
Wall #2 Flexural Tension	1.147 (166.4)	0.6895 (100.0)	0.01 (0.0571)	0.05 (0.2855)
Wall #2 Through Thickness	1.724 (250.0)	0.6895 (100.0)	0.015 (0.0857)	0.075 (0.4283)
Wall #3 Flexural Tension	1.286 (186.5)	0.6895 (100.0)	0.01 (0.0571)	0.05 (0.2855)
Wall #3 Through Thickness	1.724 (250.0)	0.6895 (100.0)	0.015 (0.0857)	0.075 (0.4283)

7.2.5. Boundary Conditions

Figure 7.11 shows the elevation view of the LS-DYNA model of Wall #1. In the figure, individual bricks are represented by different shades of gray. Rigid wall boundary conditions are visible above and below the wall (represented by the thin, dark lines). At the bottom of the model, the rigid wall boundary condition is initially in contact with the wall and provides vertical support to resist the force of gravity; the bottom of the wall was also roller supported to prevent out-of-plane deflections along this edge. At the top of Wall #1, a 1.52 cm (0.60 in) gap was included between the top of the wall and the rigid wall boundary condition above; this modeled the gap that existed between the top of the real wall and the beam above. The vertical edges were restrained out-of-plane by roller supports on the non-blast side of the wall. Figure 7.12 schematically shows the boundary conditions applied to the model.

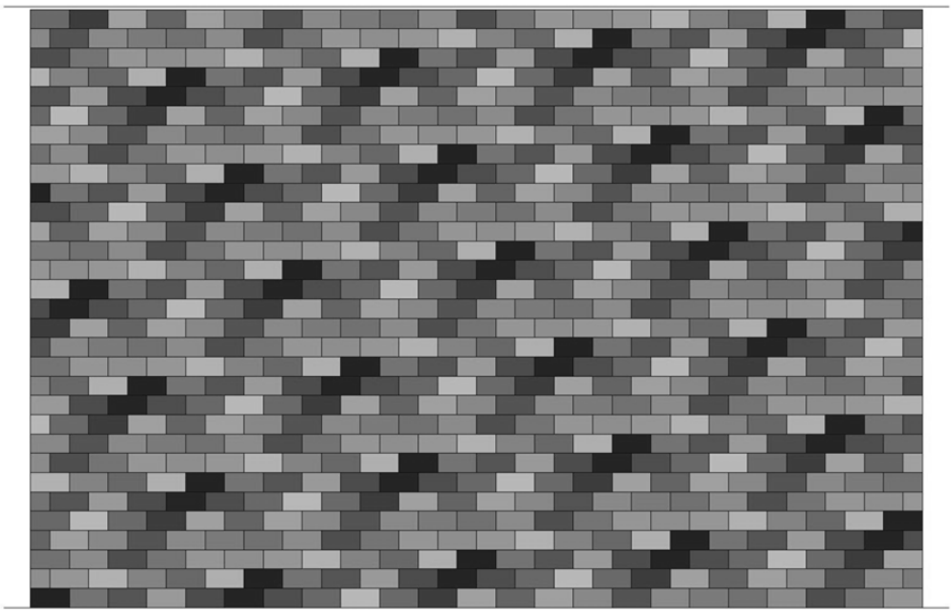

FIGURE 7.11: LS-DYNA model of Wall #1.

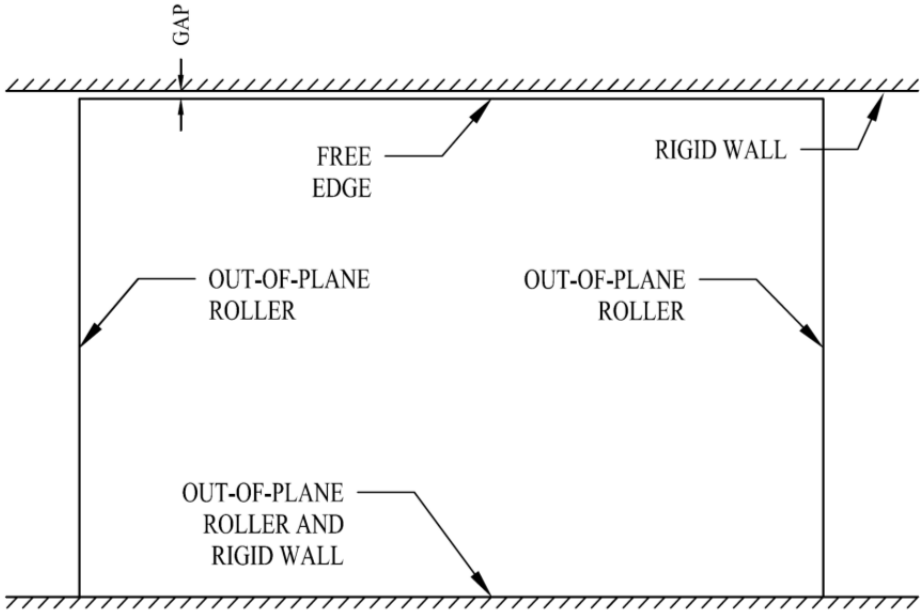

FIGURE 7.12: Schematic illustration of boundary conditions applied to Wall #1.

Figure 7.13 shows the LS-DYNA model of Walls #2 and #3, looking outward from inside the blast chamber. In the figure there are long assemblies of darkly shaded

elements at the top of each wall; they have increased densities to represent the weight of the walls above (i.e. from the second story and its roof). Where these dense elements contact the tops of the walls, a contact with tensile and shear failure was defined to simulate the presumed initial fixity. These dense elements were constrained to prevent rotation but permitted vertical deflections. Figure 7.14 shows vertical sections of both walls to emphasize the out-of-plane restraints applied to the model. Wall #3 had a roller at its top to prevent out-of-plane deflection; this was judged appropriate because the embedded steel framing likely provided some restraint. Wall #2 did not have any such embed and was thus free to displace out-of-plane after failure of the contacts between the top of the wall and the dense elements representing the upper story mass.

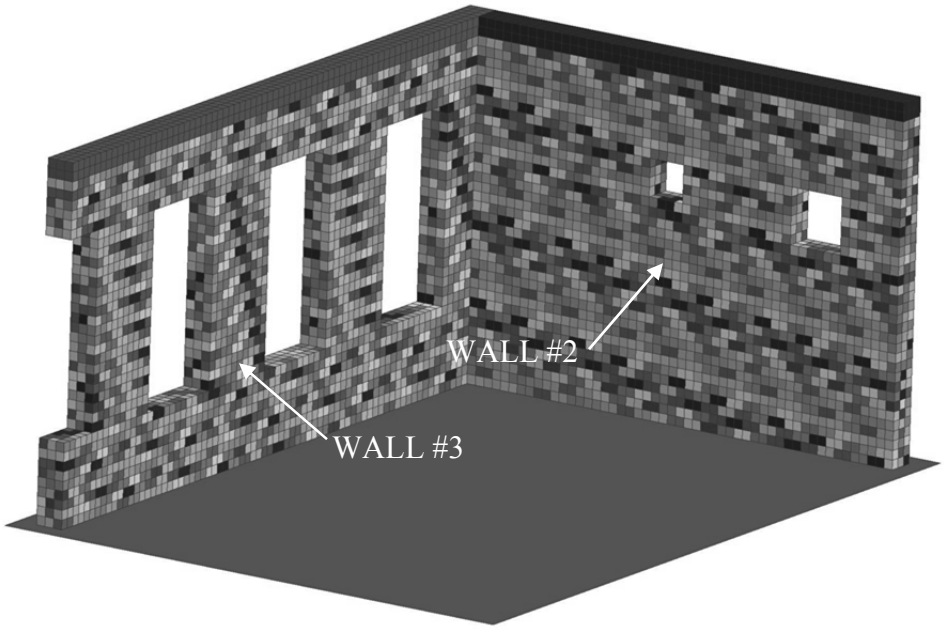

FIGURE 7.13: View of the LS-DYNA model of Walls #2 and #3 viewed from inside the blast chamber.

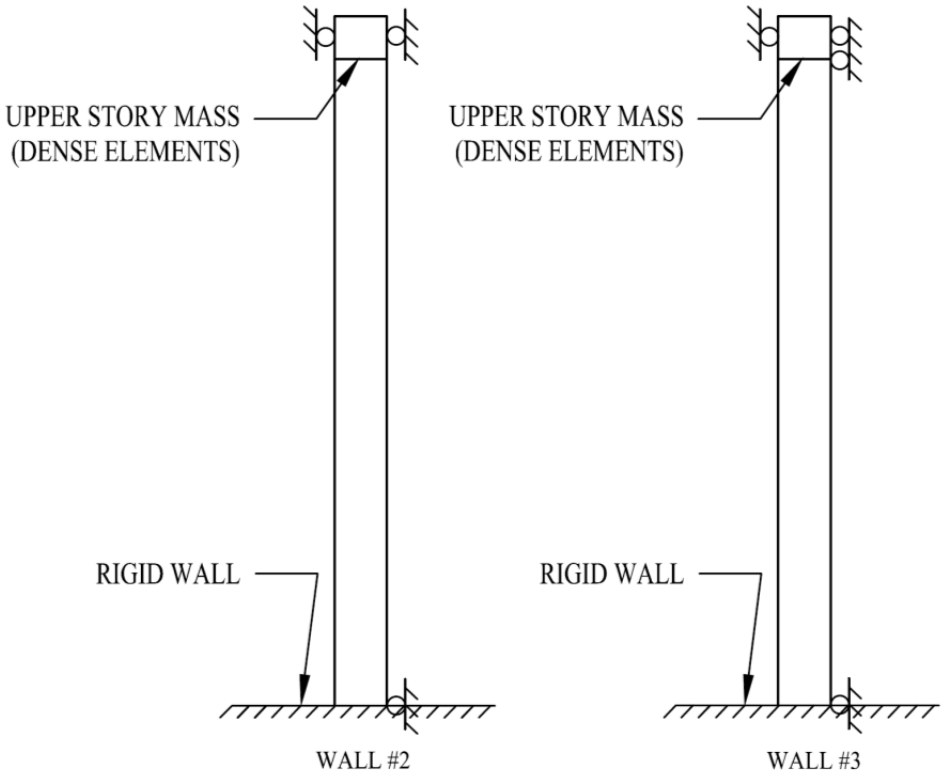

FIGURE 7.14: Sections through Walls #2 and #3 showing applied boundary conditions.

The weight of the second floor slab was not included in the model because rudimentary calculations suggested that its weight was largely counteracted by the uplift resulting from blast pressures inside the blast chamber. (The FE model was found to produce reasonably accurate results without including the weight of the ceiling/floor slab, suggesting that indeed this was a reasonable approximation.) The large gray rectangle at the bottom of Figure 7.13 represents the rigid wall boundary condition which modeled the top of the foundation supporting Walls #2 and #3. At the left-hand side of the figure, the nodes along the vertical edge of Wall #3 were constrained in-plane to simulate continuity with the adjacent in-plane wall segment (not modeled to reduce run times). At

the right-hand side of the figure, the nodes of Wall #2 along the vertical edge (on the exterior face) were constrained against both out-of-plane and in-plane deflections. The wall terminated in a joint in the masonry at this location which would have permitted contraction but resisted expansion; during the outbound blast response, the wall would have experienced expansion and therefore this restraint is a reasonable approximation of the real structure.

7.2.6. Blast Loading

Although the ConWep airblast algorithms are coded in LS-DYNA, the impulse profiles developed in Chapter 5 will be applied to the wall models to provide the most accurate representation of the loading experienced by the blast chamber walls. As discussed in Chapter 5, Load Case 2 results (Table 5.18 and Figures 5.13-5.18) will be used for the loading in the finite element models. It is recalled that this load case had the most realistic vertical distribution of impulse due to inclusion of the ceiling.

In order to simplify application of the loading in the FE models, the face of each wall was divided into regions (rectangular boxes) of approximately equal size. Each box was assigned a uniform blast pressure and associated time history, which was derived from the impulse distributions reported in Chapter 5 for Load Case 2. Figures 7.15 through 7.17 schematically show the loading boxes for Walls #1, #2, and #3, respectively. Tables 7.11 through 7.13 contain the related peak reflected pressures and impulses applied to each box. The tables also show the time of arrival for the pressure in each box as derived from the CTH simulation results. Based on the data contained in Table 2.3, all waveforms were idealized as triangular pulses having 2.25 ms durations. Although it would have been more precise to use the pressure-time histories directly

computed by CTH in the Load Case 2 simulation, this would not have necessarily been more accurate. This is because the CTH simulation did not include the presence of Wall #3 (to simulate venting) and thus the computed time history might not represent the real pressure-time histories any more accurately than the idealized waveforms do.

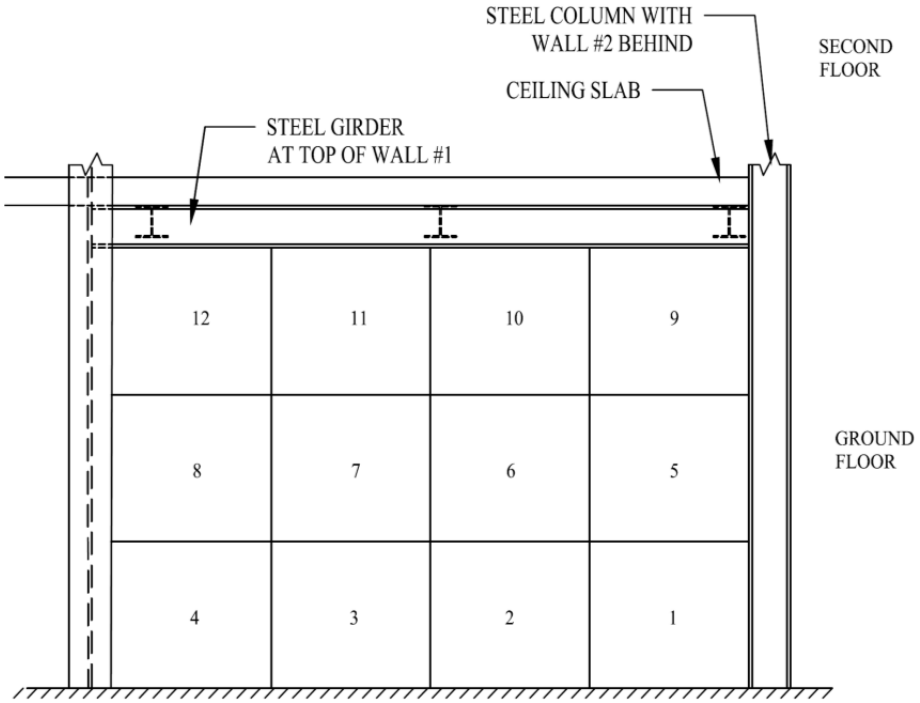

FIGURE 7.15: Loading boxes for Wall #1, outside of blast chamber looking in.

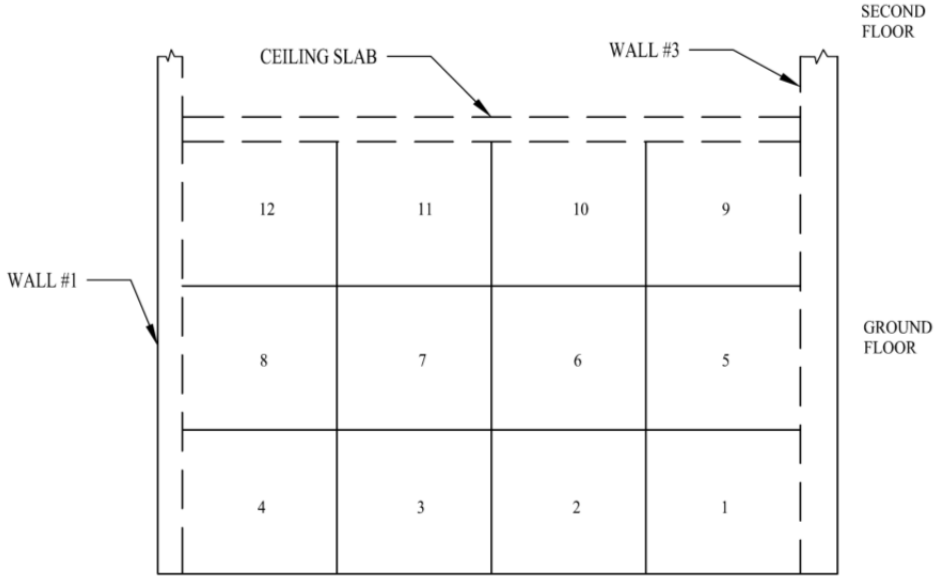

FIGURE 7.16: Loading boxes for Wall #2, outside of blast chamber looking in.

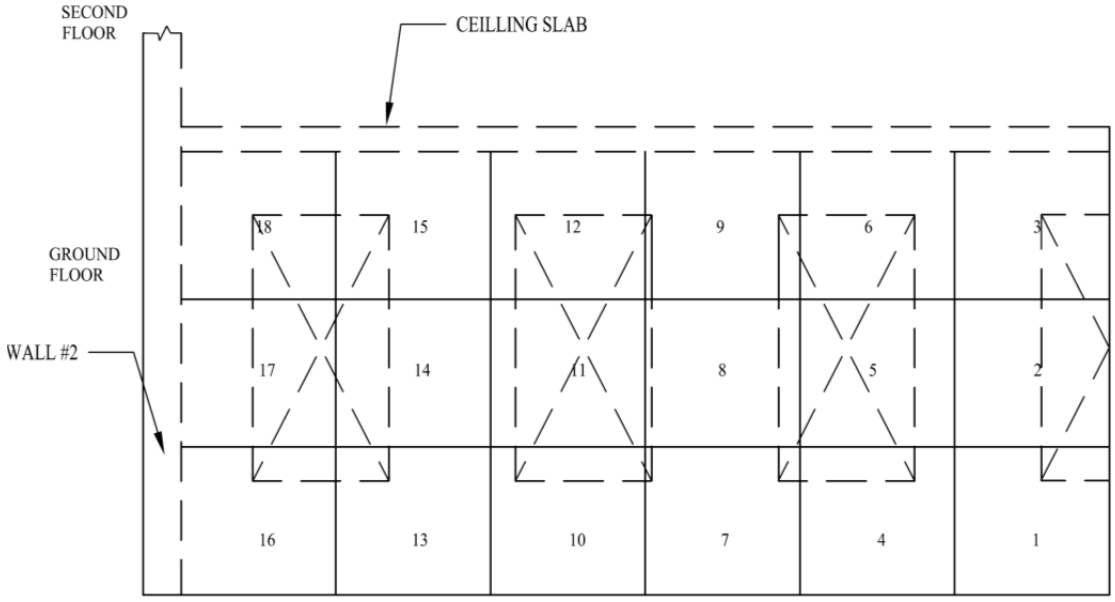

FIGURE 7.17: Loading boxes for Wall #3, outside of blast chamber looking in.

TABLE 7.11: Pressure time history data for loading boxes on Wall #1.

Load Box	Peak Reflected Pressure kPa (psi)	Peak Reflected Impulse kPa ms (psi ms)	Time of Arrival ms
1	728.7 (105.7)	819.8 (118.9)	2.41
2	696.8 (101.1)	783.9 (113.7)	1.72
3	992.2 (143.9)	1116 (161.9)	1.03
4	1230 (178.4)	1384 (200.7)	0.34
5	648 (94.0)	728.8 (105.7)	3.46
6	456 (66.1)	513 (74.4)	2.77
7	382 (55.5)	430 (62.4)	2.08
8	399 (57.9)	449 (65.1)	1.39
9	1005 (145.8)	1131 (164.0)	4.51
10	641 (93.0)	721.2 (104.6)	3.82
11	496 (72.0)	559 (81.0)	3.13
12	550 (79.8)	619 (89.8)	2.44

TABLE 7.12: Pressure time history data for loading boxes on Wall #2.

Load Box	Peak Reflected Pressure kPa (psi)	Peak Reflected Impulse kPa ms (psi ms)	Time of Arrival ms
1	1014 (147.0)	1140 (165.4)	3.808
2	817.0 (118.5)	919.1 (133.3)	3.478
3	829.2 (120.3)	932.9 (135.3)	3.478
4	1017 (147.5)	1144 (165.9)	3.808
5	815.7 (118.3)	917.7 (133.1)	4.948
6	599 (86.9)	674 (97.8)	4.618
7	606 (87.9)	682 (98.9)	4.618
8	807.8 (117.2)	908.7 (131.8)	4.948
9	1212 (175.8)	1364 (197.8)	6.088
10	881.3 (127.8)	991.5 (143.8)	5.758
11	905.2 (131.3)	1018 (147.7)	5.758
12	1218 (176.6)	1370 (198.7)	6.088

TABLE 7.13: Pressure time history data for loading boxes on Wall #3.

Load Box	Peak Reflected Pressure kPa (psi)	Peak Reflected Impulse kPa ms (psi ms)	Time of Arrival ms
1	676 (98.0)	759.8 (110.2)	2.840
2	466 (67.6)	525 (76.1)	3.890
3	679 (98.5)	763.9 (110.8)	4.940
4	977.0 (141.7)	1099 (159.4)	1.920
5	385.4 (55.9)	434 (62.9)	2.970
6	504 (73.1)	567 (82.2)	4.020
7	1222 (177.3)	1376 (199.5)	1.000
8	394 (57.1)	443 (64.2)	2.050
9	543 (78.7)	610 (88.5)	3.100
10	1060 (153.7)	1192 (172.9)	1.000
11	372 (54.0)	419 (60.7)	2.050
12	508 (73.7)	572 (82.9)	3.100
13	739.8 (107.3)	832.2 (120.7)	1.920
14	448 (65.0)	504 (73.1)	2.970
15	604 (87.6)	680 (98.6)	4.020
16	719.1 (104.3)	808.8 (117.3)	2.840
17	639 (92.6)	718.4 (104.2)	3.890
18	992.8 (144.0)	1117 (162.0)	4.940

7.2.7. Additional LS-DYNA Control Parameters

In addition to the material failure parameters, there are a number of other control parameters which must be defined in LS-DYNA. First, a small amount of damping was specified using a load curve and the *DAMPING_GLOBAL card which defined the damping decreasing from 4 to 0.4 rads/sec over the course of blast loading (the LS-DYNA damping coefficient is specified prior to being multiplied by mass). These values correspond to 2% of critical viscous damping for the uncracked and cracked structure, respectively. It was also necessary to use the CONTROL_TIMESTEP card in order to decrease the automatically computed time step. It was found that using a scale factor of 0.25 yielded consistently stable results. Dynamic relaxation was employed to initialize gravity in the simulations; non-automatic control was used. This yielded slightly better results than the automatic control scheme.

The manually-specified AUTOMATIC_SURFACE_TO_SURFACE_TIEBREAK contacts functioned well, except when bricks displaced more than 10.16 cm (4 in) relative to one another causing element faces to lose contact; the elements would then free-fall through the other elements in the mesh. To address this, an AUTOMATIC_GENERAL contact was also specified for the model of Walls #2 and #3 which supported compression only; this was not required for the Wall #1 model as brick-to-brick relative deflections were not greater than 10.16 cm (4 in). The coefficients of friction for this secondary contact were set very low (to 0.01) to avoid double-representation of brick-to-brick frictional forces. Finally, for the AUTOMATIC_GENERAL contact, the default penalty scale factor was changed to 0.01 in order to prevent interference with the primary contacts responsible for defining tensile and shear failures.

7.3. Simulation Results

Multiple simulations were performed using the two FE models of the Shot B blast chamber walls. In Section 7.3.1, simulation results corresponding to "best-estimate" parameters will be presented. Then, in Section 7.3.2, sensitivity studies will be presented in order to determine which model inputs have the greatest impact on simulation results.

7.3.1. Best-Estimate Results

Table 7.14 compares the permanent deflections observed in the experiments to those predicted by LS-DYNA using the best-estimate parameter set. The table shows that, in general, the simulations were able to predict permanent wall deflections of similar magnitude to those in the experiment. Figures 7.18 through 7.20 show the time histories of the key points on each wall; these time histories were used to populate Table 7.14. Two points of measurement (3-1 and 3-2) are presented for Wall #3. Both locations are

at the bottom of a window opening but are on adjacent piers. Figure 7.21 shows locations 3-1 and 3-2 as well as the predicted crack pattern along the length of Wall #3. At the right-hand side of the figure (location 3-2) a sliding failure occurs after the formation of a large flexural crack; the same failure does not occur at location 3-1. One hypothesis for why this occurred is that some combination of factors including the axial stress and degree of through-thickness cracking combined to permit sliding at location 3-2 but not location 3-1. Post-crack sliding occurs when a wall segment slides relative to its adjacent segment at the location of a tensile flexural crack. Field observations suggest that post-crack sliding was responsible for much of the permanent set of Wall #3.

TABLE 7.14: Comparison between experimental measurements and FE simulations.

Wall	Experimental Result	FE Permanent Deflection cm (in)	Percent Error
#1	25 (10)	38 (15)	150
#2	8.9 (3.5)	8.1 (3.2)	-9.7
#3-1	6.4 (2.5)	0.61 (0.24)	-90
#3-2	6.4 (2.5)	8.9 (3.5)	41

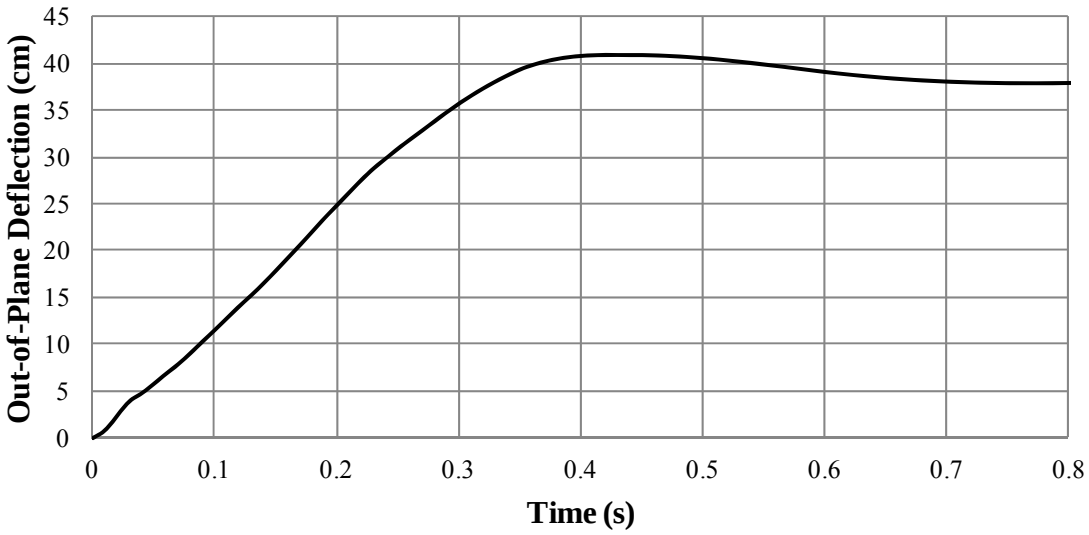

FIGURE 7.18: Deflection time history of Wall #1 at the topmost node located in the horizontal center of the span.

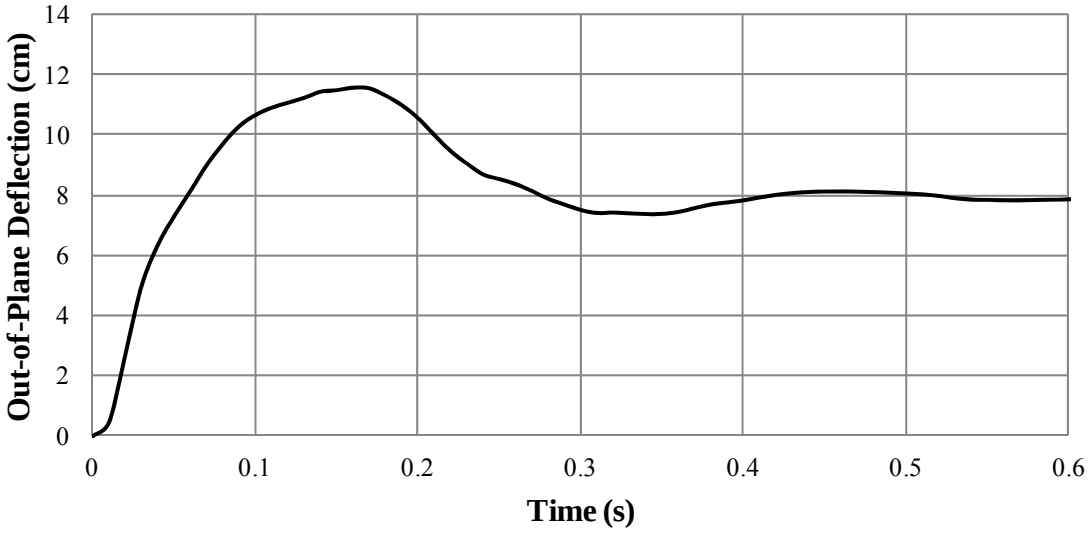

FIGURE 7.19: Deflection time history of Wall #2 at a node located at the center of the span, both vertically and horizontally.

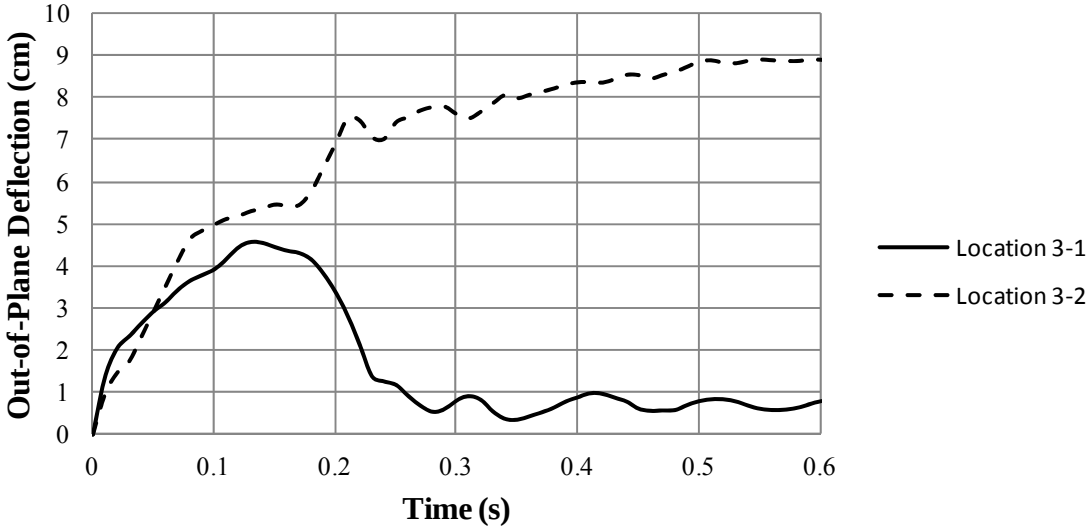

FIGURE 7.20: Deflection time history of Wall #3 at bottom of window opening; location 3-1 was directly in line with charge while location 3-2 was on an adjacent pier.

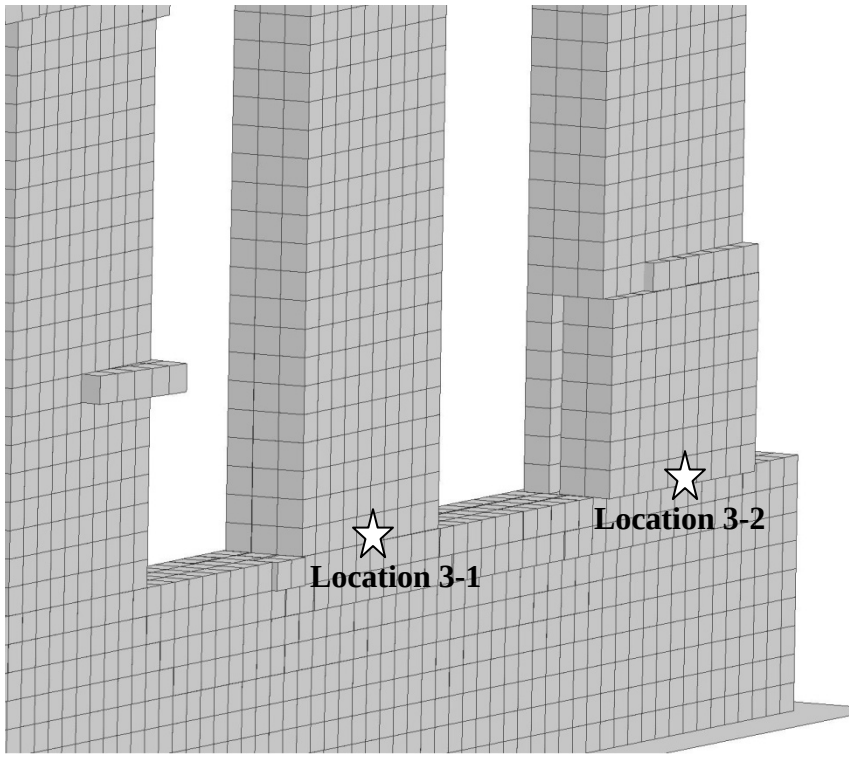

FIGURE 7.21: FE results from Wall #3 showing of points of deflection measurement.

Perhaps even more important than the magnitude of permanent deflections are the qualitative results of the LS-DYNA models. If predicted damage patterns are similar to those observed in the tests, this suggests that the wall models are, indeed, representative of the tested structure and, further, that the complex blast loads were adequately modeled. Visualizing cracks (tiebreak contacts which have experienced tensile or shear failure) presents a problem in LS-DYNA. Extensive investigation did not locate a code feature for identifying contacts which have experienced a tiebreak (i.e. a crack has formed). Therefore crack patterns had to be identified through careful examination of the displaced structure as output by LS-DYNA. By stepping through the deflection time history of a simulation, it was possible to see when gaps opened between adjacent bricks. This careful visual inspection yielded the images that follow; they were generated using the

LS-PREPOST post-processor (LSTC, Livermore, CA). In the figures, bricks which have been ejected or have fallen out of the walls will appear more darkly shaded than others.

Figures 7.22 and 7.23 show, respectively, the experimental and modeled crack patterns for Wall #1. Damage is generally represented by the FE model which also produces an inverted Y-shaped crack pattern. The model also predicts cracking near the upper corners of the wall, a phenomenon not observed in the test. Closer inspection of the simulation outputs revealed that this cracking was the result of the wall's interaction with its upper boundary condition. Figures 7.24 and 7.25 show a similar comparison for Wall #2. The figures show that the predicted crack pattern is similar to that observed in the test. The most obvious difference occurs in the crack which, in the test, was observed to intersect the right-hand opening at the upper left-hand corner (Figure 7.24); the FE model predicted the crack would intersect this opening at the lower left-hand corner (Figure 7.25).

FIGURE 7.22: Photo of damage observed in Wall #1.

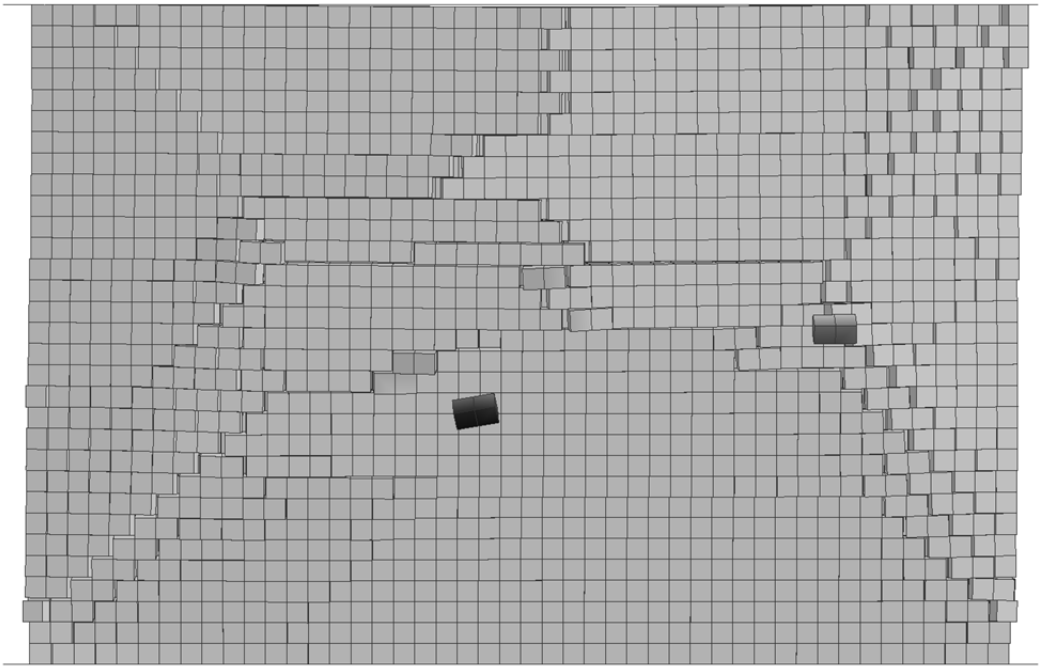

FIGURE 7.23: Modelled crack pattern of Wall #1.

FIGURE 7.24: Photo of damage observed in Wall #2 near mid-panel.

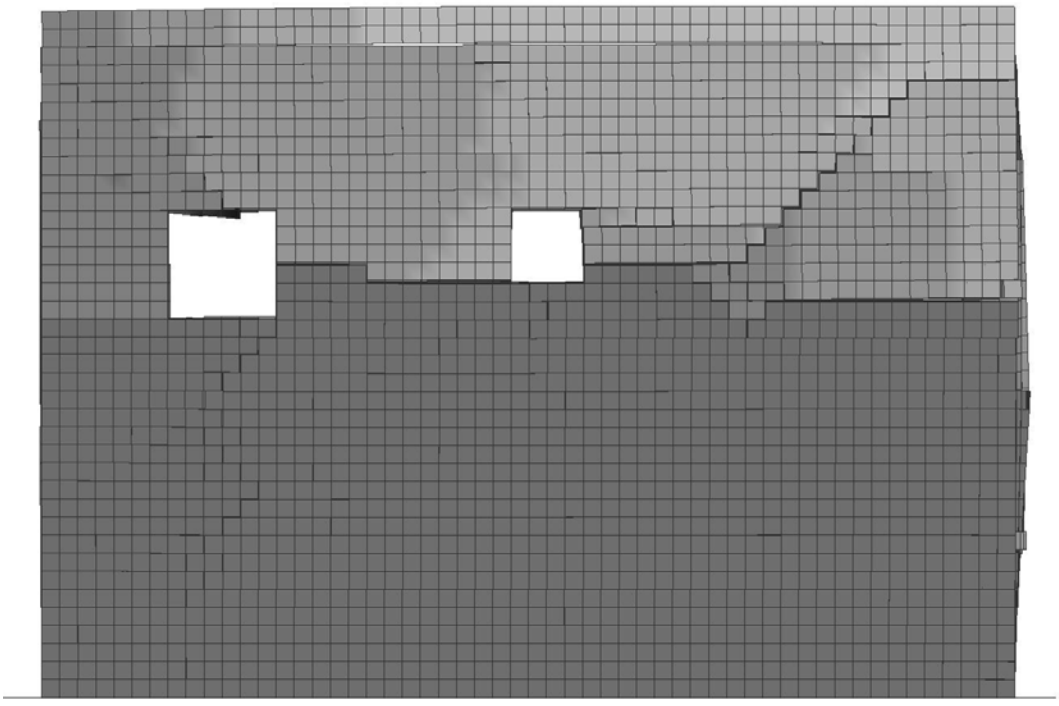

FIGURE 7.25: Modelled crack pattern of Wall #2.

Figures 7.26 and 7.27 compare the crack patterns at the intersection of Walls #2 and #3. The predicted and experimental crack patterns are observed to match closely. Note that the steel lintels, which spanned over the window openings, were not represented in the FE model. This allowed the bricks above the window openings to fall out during the simulations.

Although qualitative damage comparisons were good, the magnitude of the predicted permanent deflections were not as good; however, these FE results must be viewed relative to the required modeling simplifications. First, flexural tensile and shear failure stresses had to be artificially reduced to predict the correct out-of-plane wall capacities; these reductions were spurred by the limited number of contacts that could be utilized. Both of these reduced failure stresses created contact failures where none were anticipated. Moreover, FE results were obtained using estimates (from published studies) for critical modeling parameters including: DIFs, fracture energies, coefficients of friction, and masonry friction angle among others. Section 7.3.2 will illustrate how adjustments to these modeling parameters can affect FE simulation results. However, given the large number of modeling parameters (and their ranges), the uncertainty of actual blast loads/blast load distributions, the approximate nature of wall boundary conditions, and uncertainty regarding material properties, it will be demonstrated that the results presented in this section are of adequate practical accuracy.

FIGURE 7.26: Photo of damage observed at the intersection of Walls #2 and #3.

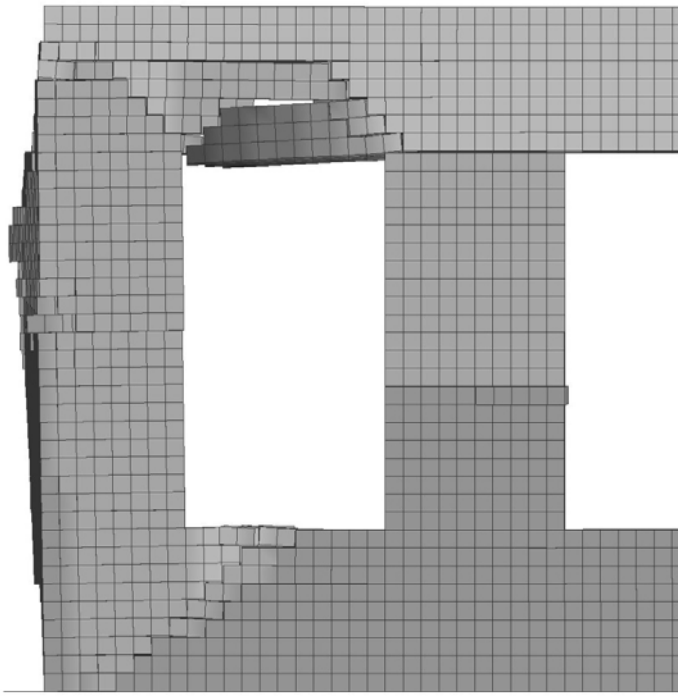

FIGURE 7.27: Modelled crack pattern at the intersection of Walls #2 and #3.

The global statistics output file of each simulation was also reviewed to identify possible simulation errors and to potentially glean insightful information. No problems were identified; however, an interesting observation was made when comparing various system energies. Figure 7.28 compares the external work (which is approximately equal to total energy) to the sliding energy for the Wall #1 simulation; sliding energy is comprised of the frictional energy at all contacts including those at the rigid boundaries. The comparison shows that the majority of the energy absorbed by the system is due to frictional effects. This suggests that the characterization of the frictional properties of the brick masonry assemblage is critical to the accuracy of the simulations.

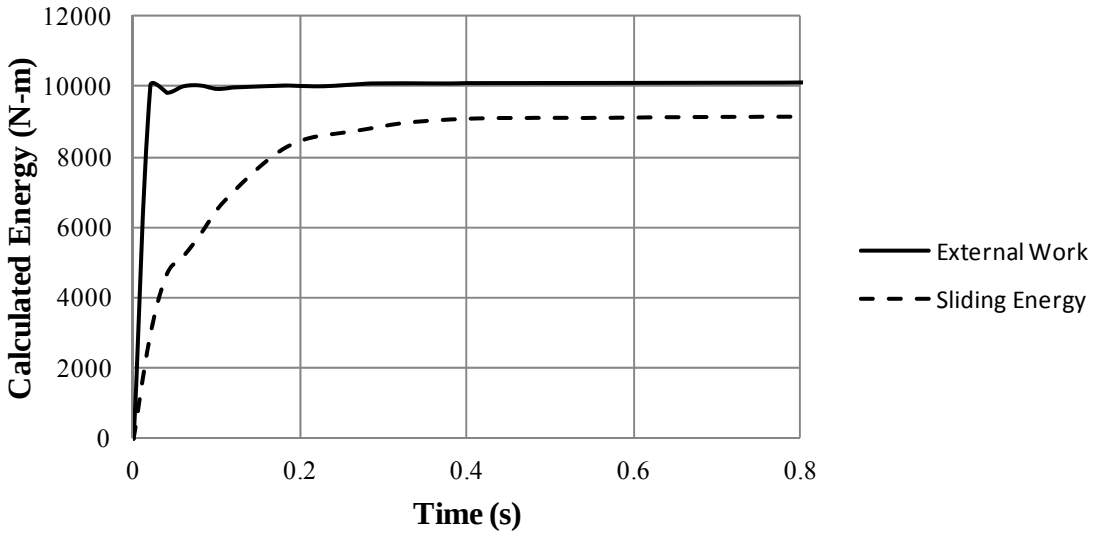

FIGURE 7.28: Energy calculated by LS-DYNA comparing external work to sliding interface energy (for Wall #1).

7.3.2. Parameter Sensitivity Study

The simulation results in Section 7.3.1 were computed using the best estimates of model parameters. It is of practical interest to study the effects of varying the input parameters on the permanent deflections predicted by the FE models. Normally,

bracketing simulation results is done by increasing or decreasing parameters by their standard deviations. Unfortunately, there is insufficient data available to use this approach. For example, even though a standard deviation could be computed for the masonry's tensile strength, it is multiplied by a DIF with an unknown standard deviation. As with the DIF, most parameters needed for this work, taken from peer reviewed literature, do not include standard deviations. Even estimating standard deviations from the available published studies may not be particularly meaningful because each study utilized different masonry materials and different methodologies and thus would lead only to very rough estimates. Therefore it would seem better advised to perform the sensitivity study by varying model parameters using engineering judgment. In reviewing the parameters found in literature, it would appear that varying failure stresses, fracture energies, friction angles, and the elastic modulus by +/- 50% would provide representative results; similarly, the literature suggests that a +/- 25% variability in the coefficients of friction would also be reasonable. The penalty scale factor, damping, density, and wall gap were also adjusted by +/- 25% based on judgment and several trial simulations.

Tables 7.15 through 7.20 report the results of the sensitivity study; each cell of the tables represents one simulation in which a single parameter was varied. The results for each wall are reported in a two table set. The first table reports permanent deflections for simulations in which parameters were varied by +/-50%. The second table reports simulation results when the parameters were varied by +/- 25%. Note that Wall #1 was modeled independently, while the parameters for Walls #2 and #3 were changed simultaneously because they were in the same model. In the tables, the word "collapse"

denotes a simulation in which the wall deflected far enough out-of-plane to become unstable; this usually happened when the peak deflection was greater than the wall's thickness. "Shooting node instability" refers to a numerical issue in which the contact algorithm causes single nodes to rapidly accelerate away from their elements; this usually results in a termination of the simulation.

TABLE 7.15: Wall #1 – Permanent deflections when parameters were varied by +/-50%.

Parameter	Best Estimate Parameter Value	Permanent Deflection cm (in)	
		+50% Variation	-50% Variation
Tensile Failure Stress* MPa (psi)	0.9363 / 1.724 (135.8 / 250.0)	37.3 (14.7)	Collapse
Shear Failure Stress MPa (psi)	0.6895 (100.0)	33.0 (13.0)	Collapse
Mode I Fracture Energy* J/mm (lb/in)	0.0100 / 0.0150 (0.0571 / 0.0857)	5.94 (2.34)	43.4 (17.1)
Mode II Fracture Energy* J/mm (lb/in)	0.0500 / 0.0750 (0.2855 / 0.4283)	42.4 (16.7)	Collapse
Friction Angle Degrees	0.401	1.26 (0.497)	30.5 (12.0)
Elastic Modulus MPa (ksi)	4233 (614.0)	33.0 (13.0)	49.5 (19.5)
Penalty Scale Factor	0.10	53.1 (20.9)	19.3 (7.58)
Damping rads/sec	4.4 / 0.44	40.4 (15.9)	12.8 (5.03)

Notes: *Table cells with two values – first value is always on a plane normal to direction of bending, second value is on a plane normal to through-thickness spall.

TABLE 7.16: Wall #1 – Permanent deflections when parameters were varied by +/-25%.

Parameter	Best Estimate Parameter Value	Permanent Deflection cm (in)	
		+25% Variation	-25% Variation
Coeff. of Static Friction	0.75	38.1 (15.0)	56.4 (22.2)
Coeff. of Kinetic Friction	0.60	38.1 (15.0)	38.1 (15.0)
Material Density kg/m^3 (lb/ft^3)	2443 (152.5)	40.1 (15.8)	Collapse
Gap at Top cm (in)	1.5 (0.60)	54.1 (21.3)	15.4 (6.06)

TABLE 7.17: Wall #2 – Permanent deflections when parameters were varied by +/-50%.

Parameter	Best Estimate Parameter Value	Permanent Deflection cm (in)	
		+50% Variation	-50% Variation
Tensile Failure Stress* MPa (psi)	1.147 / 1.724 (166.4 / 250.0)	3.43 (1.35)	15.2 (5.98)
Shear Failure Stress MPa (psi)	0.6895 (100.0)	10.5 (4.18)	Collapse
Mode I Fracture Energy* J/mm (lb/in)	0.0100 / 0.0150 (.0571 / .0857)	7.72 (3.04)	10.2 (4.01)
Mode II Fracture Energy* J/mm (lb/in)	0.0500 / 0.0750 (0.2855 / 0.4283)	13.4 (5.26)	Collapse
Friction Angle Degrees	0.401	19.6 (7.73)	26.7 (10.5)
Elastic Modulus MPa (ksi)	4233 (614.0)	Shooting Node Instability	3.81 (1.50)
Penalty Scale Factor	0.10	21.6 (8.51)	3.38 (1.33)
Damping rads/sec	4.4 / 0.44	8.36 (3.29)	5.11 (2.01)

Notes: *Table cells with two values – first value is always on a plane normal to direction of bending, second value is on a plane normal to through-thickness spall.

TABLE 7.18: Wall #2 – Permanent deflections when parameters were varied by +/-25%.

Parameter	Best Estimate Parameter Value	Permanent Deflection cm (in)	
		+25% Variation	-25% Variation
Coeff. of Static Friction	0.75	-0.121 (-0.0478)	Shooting Node Instability
Coeff. of Kinetic Friction	0.60	7.90 (3.11)	7.92 (3.12)
Material Density* kg/m^3 (lb/ft^3)	2253 / 33159 (140.7 / 2070.1)	7.98 (3.14)	Collapse

Notes: *First value corresponds to wall density; second value corresponds to density of mesh representing upper story walls.

Table 7.15 shows that changing material failure and contact model parameters can significantly impact simulation results for Wall #1. Sometimes parameter changes yielded intuitive results – i.e. decreasing strength lead to increased deflections. Other changes, however, yielded counterintuitive results – i.e. a decrease in the value of damping actually decreased permanent deformation. What is not shown in the table is that each of these parameter changes altered the manner in which the wall interacted with

the upper rigid wall boundary condition. If a parameter change tended to cause the wall to strike the boundary sooner, this normally led to decreased permanent deflections. Table 7.16 shows the results for Wall #1 parameters that were varied by +/- 25%. The static coefficient of friction, the material density, and the size of the gap at the top of the wall all had a significant impact on the results. Interestingly, the coefficient of kinetic friction had virtually no effect on simulation results for a 25% variation.

TABLE 7.19: Wall #3 – Permanent deflections when parameters were varied by +/-50%.

Parameter	Best Estimate Parameter Value	Permanent Deflection cm (in)	
		+50% Variation	-50% Variation
Tensile Failure Stress* MPa (psi)	1.286 / 1.724 (186.5 / 250.0)	5.49 (2.16)	7.42 (2.92)
Shear Failure Stress MPa (psi)	0.6895 (100.0)	0.0668 (0.0263)	6.20 (2.44)
Mode I Fracture Energy* J/mm (lb/in)	0.0100 / 0.0150 (.0571 / .0857)	2.57 (1.01)	6.22 (2.45)
Mode II Fracture Energy* J/mm (lb/in)	0.0500 / 0.0750 (0.2855 / 0.4283)	-0.0363 (-0.0143)	Collapse
Friction Angle Degrees	0.401	0.189 (0.0746)	0.366 (0.144)
Elastic Modulus MPa (ksi)	4233 (614.0)	Shooting Node Instability	0.716 (0.282)
Penalty Scale Factor	0.10	2.05 (0.808)	3.43 (1.35)
Damping rads/sec	4.4 / 0.44	0.226 (0.0890)	0.218 (0.0859)

Notes: *Table cells with two values – first value is always on a plane normal to direction of bending, second value is on a plane normal to through-thickness spall.

TABLE 7.20: Wall #3 – Permanent deflections when parameters were varied by +/-25%.

Parameter	Best Estimate Parameter Value	Permanent Deflection cm (in)	
		+25% Variation	-25% Variation
Coeff. of Static Friction	0.75	0.328 (0.129)	Shooting Node Instability
Coeff. of Kinetic Friction	0.60	0.947 (0.373)	0.947 (0.373)
Material Density* kg/m^3 (lb/ft^3)	2253 / 33159 (140.7 / 2070.1)	-1.14 (-0.448)	Collapse

Notes: *First value corresponds to wall density; second value corresponds to density of mesh representing upper story walls.

Tables 7.17 through 7.20 for Walls #2 and #3 show similar trends. Many of the strength parameter changes yielded predictable results; lower strength meant higher permanent deflections. Other parameters like the damping coefficient or penalty scale factor showed no predictable trend. In some cases, like decreasing the elastic modulus, numerical instabilities occurred which produced "shooting nodes," causing the simulation to prematurely terminate. For Walls #2 and #3, changing a single parameter could drastically alter the crack pattern predicted by the FE model. This caused particularly unpredictable results in Wall #3. If a shear failure with sliding developed at the point of measurement (bottom of the window openings), then deformations tended to match the experiments. If such a failure did not develop, however, negative permanent deflections could result.

Reviewing Tables 7.15 through 7.20, it becomes apparent that the parameter set selected as the best estimate values do indeed produce some of the better results possible. The only exceptions are the simulations in which flexural and through thickness tensile strengths were increased to 150% of the best estimate values. These simulations produced equal, if not slightly more accurate, permanent deformations. Otherwise, it appears as though modifying the parameters would not yield substantial improvements to the results.

Careful examination of the FEA generated animations and associated crack patterns make one fact clear – the necessity to specify reduced failure stresses is likely a significant reason that experimental and analytical deflections do not compare more closely. This also appears to be the reason that the simulations predict more cracks than were observed in the test. This finding would suggest that those aspects of LS-DYNA

require further development. This includes providing the capacity to run models that have many hundreds of thousands of contacts. Additionally, an automated contact search feature should be developed which does not generate contacts for segments at 90 degrees to one another (or at least an option to turn this feature off should be considered). And lastly, more research on masonry's fracture parameters and post-failure frictional interface properties is required.

CHAPTER 8: SUMMARY AND CONCLUSIONS

Although hydrodynamics and structural dynamics are well established fields, the information required for this investigation had to be cobbled together from a variety of far-flung sources including journals, limited distribution military manuals, research reports, and out-of-print texts. The sources were found to be particularly disparate for ESDOF methods. Although UFC 3-340-02 (a limited distribution document) provides extensive guidance on how to use the ESDOF method, it does not provide any justification for the provided transformation factors. The reader is left to locate other documents, some of which are out of publication. In addition, Morrison (2008) showed that many references for the ESDOF method contain errors in the transformation factors (derivations and/or the factors reported). Given the ESDOF method's widespread use, the development of a comprehensive ESDOF text might prove useful for practicing professionals engaged in any sort of dynamic analysis, ranging from blast or earthquake resistant design, to machine vibration and impact problems. Accompanying the comprehensive text should be basic, open-source software capable of performing the calculations required for an ESDOF analysis (SBEDS is not open-source and much of the program is inaccessible without a password). The Matlab scripts in Appendix D serve as a starting point for this effort.

Chapter 2 described the experimental program in detail. The shock accelerometers used in the experiments were not optimal. Their range (+/- 100,000 g)

created a high noise floor which likely obscured actual structural accelerations. Subsequent testing by the University has shown that DC coupled sensors with a range of +/- 5,000 g that include mechanical and electrical low pass filters perform much better for instrumenting blast loaded structural components. Reassuringly, the investigation also showed that despite both high and low frequency filtration of sensor signals, the pressure measurements were only affected to a small degree. Note that this finding is only true if, in fact, there were no gas phase pressures lasting for several tenths of a second; any such pressure signals would have been attenuated by the AC coupling.

The experimental data showed that, where pressure sensors were placed symmetrically, they registered similar pressures and impulses; this indicates both a symmetric detonation and consistent performance of the sensors. In a few cases the pressure sensors malfunctioned. These malfunctions were mostly attributable to cable damage during prior shots. In a few instances, it appeared as though sensor ringing occurred. This was caused by the sensor mounting which did not isolate the sensor from the metal plate or surrounding structure. Subsequent work at the University has developed methods of mounting pressure sensors in a non-metallic grommet which reduces the chance that ringing will occur.

Chapter 3 documented efforts to use simplified analysis methods to predict the pressures and impulses observed in Shot A1 and from open arena tests; no predictions were made for Shot A2 because information regarding charge composition was lacking. The best open arena predictions were obtained by combining Esparza's method (1992) and ConWep; errors from BlastX predictions were nearly double the Esparza/ConWep method. It is surprising that BlastX would perform so poorly because the BlastX

cylindrical tabular model was generated from hydrocode simulations of cylindrical charges; this would presumably give the code a distinct advantage with respect to the spatial distribution of blast energy. Furthermore, BlastX should also accurately model the effects of reflections from the ground's surface, a blast loading scenario that the ConWep/Esparza method cannot model.

When applied to the A1 blast scenario, however, the results were reversed. The ConWep/Esparza method yielded larger errors than BlastX, although not significantly. It also became clear that the BlastX order of rays option has a tremendous effect on the results and must be chosen carefully depending on whether the objective is design or analysis. Overall, the comparisons between measurements and predictions showed that simplified analysis methods could predict blast impulses with an average absolute accuracy 36% in the case of Shot A1 and 20% for the open arena tests.

Another interesting observation is that the Esparza equivalency method was not accurate when combined with UFC 3-340-02 calculations for incident parameters below the triple point. Blast wave measurements for the open arena tests documented in Chapter 3, however, were made below the triple point. It therefore might have been serendipitous that the coupled Esparza/ConWep calculations agreed so well with the data. It would likely prove useful to extend the Esparza spherical equivalency data to include cylindrical charges with a low height of burst; this would likely have many applications in protective design.

The difficulties encountered using simplified methods led to the use of CTH in Chapter 4. An extensive convergence study was conducted which led to the discovery of a relationship between the converged mesh size and the properties of the blast wave.

This suggests the possibility of some fundamental (and possibly closed form) relationship between the hydrodynamic difference equations and blast wave properties. One example might be a relationship between the mesh size, time step, and resulting errors in predictions of velocity, density, energy, and/or pressure. Comparisons between the converged CTH simulations and empirical data for TNT airblasts showed that CTH could predict pressure and impulse accurately. CTH underpredicted peak incident overpressure by an average of 12% and overpredicted positive incident impulse by 2% when compared to Kinney and Graham's airblast data. With respect to reflected parameters, CTH underpredicted peak reflected pressure by 14% and peak reflected positive impulse by 0.4% when compared to ConWep predictions. These errors are, in comparison to most predictive methods, excellent.

Chapter 5 detailed efforts to develop JWL EOS parameters for Unimax dynamite. Initial attempts to use density scaling to develop new coefficients from those published in technical literature did not yield satisfactory results. Instead, the density scaling procedure was combined with some of CTH's internal coding to develop a new procedure for energy scaling JWL coefficients. The method, which is consistent with respect to the CJ state, tended to preferentially adjust only R_1, R_2, and ω when implemented in an Excel solver. Although these variables are not normally adjusted, this is not necessarily problematic because other trials using a density scaling technique found that A, B, and C could only be adjusted within relatively limited tolerances before the JWL encountered numerical difficulties.

The development of the energy scaling procedure required careful study of the JWL and its implementation in CTH. The restriction on JWL coefficients imposed by

consistency conditions for the CJ state and thermodynamic considerations limit how JWL parameters can be adjusted. For example, it was found that increasing blast overpressure while decreasing blast impulse was essentially infeasible. These limitations, although in adherence to the theoretical framework of the EOS, are somewhat unimportant to airblast modelers primarily concerned with far field results. To such users, the JWL and its implementation represent what is essentially a complicated initial condition used to set up a travelling shockwave. Thus it would be worthwhile to consider development of some simpler explosive EOS for airblast modelers. The new EOS should be calibrated by allowing modelers to adjust pressure and impulse somewhat independently (within certain necessary limitations) to match simple airblast measurements; this would represent a tremendous cost savings over current JWL development methods.

Using the energy-adjusted JWL coefficient set with CTH, simulations were conducted for shots A1 and B. The two-dimensional simulations had an average absolute pressure error of 31% and an absolute impulse error of 21%. The three-dimensional simulations of Shot B had an average absolute pressure error of 50.4% and an average absolute impulse error of 35%. Note that although the two and three-dimensional simulations both used the same mesh resolution, the errors in three dimensions were still higher. Attempts to accurately model the Shot B blast chamber in three dimensions including the window openings in Wall #3 showed that CTH's rigid material algorithm is not fully functional; instead, an entire wall had to be omitted from the simulation in order to model venting through the windows. Although only marginally more accurate than the simplified analytical methods, the CTH analyses provided the necessary spatio-temporal

distribution of blast energy on reflecting surfaces which was vital for subsequent structural simulations.

Chapter 6 investigated the ability of the ESDOF method to simulate the response of the Shot B blast chamber walls. A new resistance function was developed which permits a one-way spanning member to crack at any height. An accompanying software program was written which could take arbitrary loading and compute the required ESDOF input parameters including resistance function ordered pairs and transformation factors. Numerous errors in the traditionally quoted transformation factors were found while developing transformation factors for two-way elements; these errors were corroborated by Morrison (2008). Given that most design engineers would be hard pressed to perform the calculations necessary to develop transformation factors for two-way members, providing an open source software program and comprehensive text geared toward practitioners would be a useful contribution to the state-of-the-art.

Overall, the ESDOF analyses predicted permanent deflections similar to those measured in the field. It is interesting that the predictions made using carefully computed resistance function ordered pairs and transformation factors were not any more accurate than those made using the default values. It should be noted that some of the error in the predictions can be explained by the observation that, in addition to flexural deflections, the blast chamber walls also had relative shearing/sliding motions that occurred between wall segments; these shearing/sliding motions are not modeled by the ESDOF method using current URM resistance functions.

Another source of error is the large number of system properties which had to be estimated, including: the effective span lengths, the degree of fixity, and the dynamic

tensile strength, to name but a few. The number of estimated parameters suggests that an uncertainty analysis of ESDOF-predicted deflections would be quite useful. The investigation might show that, due to the uncertainty in material properties alone, computing more accurate transformation factors is unwarranted because the gain in accuracy from the transformation factors is entirely offset by the spread in resistance function ordered pairs created by material uncertainties. Such a conclusion would provide additional validation to the current state-of-practice for the ESDOF method in protective design.

Analytical investigations into the effects of damping on ESDOF predictions showed that permanent deflections could change dramatically (by 50% or more) based on the choice of damping ratio. This observation is consistent with the SBEDS user manual, which states that the brittle flexural response with axial load resistance function is particularly sensitive to the choice of damping. A review of the SBEDS user manual and Oswald (2005) suggest that the default damping ratio be specified as 2% of critical because it produced the best agreement between analytical and experimental deflections for tests of masonry walls. By contrast, the experimental work performed by Griffith et al. (2004) on cracked masonry walls indicates a minimum damping ratio of 5% over a broad range of frequencies. This investigation seems to reaffirm the use of 2% damping, as that produced the best agreement between analytical predictions and the measured permanent deformations.

Deflection and resistance-based criteria were adopted for quantifying the state of the Shot B URM walls relative to their collapse limit-states. Both criteria, based on simple ratios, provide a straightforward means for estimating how close a building is to

collapsing. If future out-of-plane loads are not of concern, then the deflection criterion can provide a very simple estimate of a structure's state relative to its collapse limit-state. If, however, a structure is to be reloaded by a blast or some other type of out-of-plane force (such as wind pressure), then the resistance criterion should be used to provide a conservative estimate of the building's state relative to its collapse limit-state.

Chapter 7 documented LS-DYNA simulations that were able to reproduce the results of the experimental program in a general sense. The investigation reinforced that the analyst is required to carefully consider wall boundary conditions, compute representative (effective) blast pressures, and determine effective axial loads (accounting for the possible load reduction due to slab uplift) in order to even reproduce qualitatively accurate damage patterns; admittedly, the choice of boundary conditions is easier when experimental results are available a priori. Although the qualitative damage comparisons were good, the magnitudes of the predicted permanent deflections were not as good.

These FEA results, however, must be viewed relative to the required modeling simplifications. First, only a limited number of contacts could be defined; this in turn limited the number of elements and thus mesh resolution. The limited mesh resolution required the tensile failure stress to be artificially reduced so that the flexural capacity of the walls was accurately represented. This in turn required the shear failure stress to be drastically reduced. Examination of simulation results suggest that these stress capacity reductions were the cause of the increased damage observed in simulation results. This finding suggests that LS-DYNA would benefit from further development which increases the number of contacts the code can utilize in a single model. Users of the code would also greatly benefit from some automated contact search algorithm which does not

initially tie segments at 90 degrees to one another; the Matlab code included in Appendix D serves as a starting point for this feature.

In addition to these general modeling difficulties, there were other findings that merit further study. First, an investigation of the contact penalty force scale factor is warranted; this factor appears to have a significant influence on the resulting out-of-plane bending stiffness of the FE wall models. It would also be interesting if a Mohr Coulomb failure option could be added to the LS-DYNA surface to surface contacts; if shear dilatancy could be included, then the contact would be highly representative of masonry failure. To support this failure model, more laboratory tests would be required to develop a better data set of fracture energy release rates, friction angles, and shear dilatancy angles. Also, it might be of use to perform further studies, both experimental and analytical, on the contact forces between rocking wall segments. The simplified unit-width FEA models showed that rocking wall segments can lose contact entirely and this has important implications for the cracked wall's resistance function.

REFERENCES

Abrams, D.P., R. Angel, and J. Uzarski. "Out-of-Plane Strength of Unreinforced Masonry Infill Panels." Earthquake Spectra 12.4 (1996): 825-844.

Adham, S.A., comp. Proceedings from the NCEER Workshop on the Seismic Response of Masonry Infills: Out-of-plane response of masonry walls. Report No. 1994-02-04. National Center for Earthquake Engineering Research. 1994.

Al-Chaar, Ghassan, R. Angle, and D.P. Abrams. (1994). "Dynamic testing of unreinforced brick masonry infills." Proceedings of the 12th Structures Congress, Atlanta, GA, 24-28 April 1994.

Angel, Richard, and Joseph Uzarski. "Estimating Transverse Strength of Masonry Infills." Proceedings of the 14th CCMS Symposium held in conjunction with the 14th Structures Congress, Chicago, IL, 15-18 April 1996.

Armstrong, B.J., D.D. Rickman, J.T. Baylot, T.L. Bevins. "Code Validation Studies for Blast in Urban Terrain." Proceedings of the 2002 HPC Users Group Conference, Austin, TX, 10-14 June 2002.

Baylot, J.T., B.J. Armstrong, D.D. Rickman, and T.L. Bevins. "Three-Building and Typical City Multiple-Building Simulations." Proceedings of the HPCMP Users Group Conference, Los Alamitos, CA, 7-11 June 2004. 211-217.

Baylot, J.T., B.J. Armstrong, D.D. Rickman, and T.L. Bevins. (2005a). "Numerical Simulations of Nine-Building Portions of a Typical City." Proceedings of the HPCMP Users Group Conference, Nasheville, TN, 27-30 June. 207-214.

Baylot, J. T., B. Bullock, T.R. Slawson, and S.C. Woodsen. "Blast Response of Lightly Attached Concrete Masonry Unit Walls." Journal of Structural Engineering 131.8 (2005b): 1186-1193.

Beshara, F.B.A. "Modelling of Blast Loading on Aboveground Structures – I. General Phenomenology and External Blast." Journal of Computers and Structures 51.5 (1994a): 585-596.

Beshara, F.B.A. "Modelling of Blast Loading on Aboveground Structures – II. Internal Blast and Ground Shock." Journal of Computers and Structures 51.5 (1994b): 597-606.

Biggs, J.M. Introduction to Structural Dynamics. New York: McGraw Hill, 1964.

BlastX: Internal and External Blast Effects Prediction. Download. Version 6.4.2.0. USACE Protective Design Center, 2006.

Bogosian, David, John Ferritto, and Yongjiang Shi. "Measuring Uncertainty and Conservatism in Simplified Blast Models." Proceedings of the 30th Explosive Safety Seminar, Atlanta, GA, August 2002.

Brundage, A.L., K. Metzinger, D. Vangoethem, and S. Attaway. "Model Validation of a Structure Subjected to Internal Blast Loading." Proceedings of the 2007 International Modal Analysis Conference, Orlando, FL, 19-22 February 2007.

Burnett, S., M. Gilbert, T. Molyneaux, G. Beattie, and B. Hobbs. "The Performance of Unreinforced Masonry Walls Subjected to Low-Velocity Impacts: Finite Element Analysis." International Journal of Impact Engineering 34.8 (2007): 1433-1450.

Cecchi, Antonella, Gabriele Milani, and Antonio Tralli. "Validation of analytical multiparameter models for out-of-plane loaded masonry walls by means of the finite element method." Journal of Engineering Mechanics 131.2 (2005): 185-198.

Chan, P.C. and H.H. Klein. "Study of Blast Effects Inside an Enclosure." Journal of Fluids Engineering, Transactions of the ASME 116.3 (1994): 450-455.

ConWep: Conventional Weapons Effects. Download. Version 2.1.0.8. USACE Protective Design Center, 2005.

Cooper, P.W. Explosives Engineering. New York: Wiley-VCH, 1996.

Dartmouth College, Department of Mathematics. "Paper E226 – Principes Generaux du Mouvement des Fluides." *The Euler Archive*. Web 9 June 2011. http://www.math.dartmouth.edu/~euler/.

Davidson, J., comp. Advanced Compuational Dynamics Simulation of Protective Structures Research. Air Force Research Laboratory. Report No. AFRL-RX-TY-TR-2008-4610. 2008.

Davidson, J. and S. Sudame, comp. Development of Computational Models and Input Sensitivity Study of Polymer Reinforced Concrete Masonry Walls Subjected to Blast. Air Force Research Laboratory. Report No. AFRL-ML-TY-TR-2006-4522. 2006

Davidson, J. S., Porter, J. R., Dinan, R. J., Hammons, M. I., and Connell, J. D. "Explosive Testing of Polymer Retrofit Masonry Walls." Journal of the Performance of Constructed Facilities 18.2 (2004): 100-106.

Davidson, J. S., J. Fisher, M. Hammons, J. Porter, and R. Dinan. "Failure Mechanisms of Polymer-Reinforced Concrete Masonry Walls Subjected to Blast." Journal of Structural Engineering 131.8 (2005): 1194-1205.

Dawe, J.L. and C.K. Seah. "Out-of-Plane Resistance of Concrete Masonry Infilled Panels." Canadian Journal of Civil Engineering 16.6 (1989): 854-864.

Deal, W.E. "Shock Hugoniot of Air." Journal of Applied Physics 28.7 (1957): 782-784.

Dennis, S. T., J.T. Baylot, and S.C. Woodson. "Response of ¼-Scale Concrete Masonry Unit (CMU) Walls to Blast." Journal of Engineering Mechanics 128.2 (2002): 134-142.

Derakhshan, H., J.M. Ingham, and M.C. Griffith. "Tri-Linear Force-Displacement Models Representative of Out-of-Plane Unreinforced Masonry Wall Behavior." Proceedings of the 11th Canadian Masonry Symposium, Toronto, Canada, 2009.

Doan, L.R. and G.H. Nickel, comp. A Subroutine for the Equation of State for Air. Air Force Weapons Laboratory. Technical Memorandum RTD (WLR) TM-63-2. 1963.

Doherty, K., M.C. Griffith, N. Lam, and J. Wilson. "Displacement-Based Seismic Analysis for Out-of-Plane Bending of Unreinforced Masonry Walls." Journal of Engineering Earthquake Structural Dynamics 31.4 (2002): 833-850.

Drysdale, R.G., A.A. Hamid, and L.R. Baker. Masonry Structures: Behavior and Design. Boulder: The Masonry Society, 1999.

Edwards, C.L., D. Pearson, and D. Baker, comp. Draft Ground Motion Data from the Small-Scale Explosive Experiments Conducted at the Grefco Perlite Mine near Socorro, New Mexico. Los Alamos National Laboratory. Report No. LA-UR-94-1003. 1994.

Esparza, E.D. "Airblast Measurements and Equivalency for Spherical Charges at Small Scaled Distances." Proceedings of the 22nd Department of Defense Explosives Safety Seminar, Anaheim, CA, 26-28 August 1986. 2029-2057.

Ettouney, M., P. DiMaggio, and A. Hapij. "Analysis of Bearing Walls to Blast Threats." Proceedings of the 2003 Structures Congress and Exposition, Seattle, WA, 29-31 May 2003.

Flanagan, R.D., and R.M. Bennett. "Arching of Masonry Infilled Frames: Comparison of Analytical Methods." Practice Periodical on Structural Design and Construction 4.3 (1999): 105-110.

Gabrielsen, B. and C. Wilton. Shock Tunnel Tests of Wall Panels. URS Research Corporation for Defense Civil Preparedness Agency. Report No. URS 7030-7. 1972.

Gilbert, M., B. Hobbs, T.C.K. Molyneaux, S. Burnett, G. Beattie, and P. Newton. "Improving the Impact Resistance of Masonry Parapet Walls." Proceedings of the 3rd International Arch Bridges Conference, Paris, France, 2001. 635-640.

Gilbert, M., T.C.K. Molyneaux, and B. Hobbs. "A Dynamic Finite Element Modeling Approach for Masonry Structures." Proceedings of the British Masonry Society 8 (1998): 182-187.

Griffith, M. C., N.T.K. Lam, J.L. Wilson, and K. Doherty. "Experimental Investigation of Unreinforced Brick Masonry Walls in Flexure." Journal of Structural Engineering 130.3 (2004): 423-432.

Guerke, G. and G. Scheklinski-Gluek. Blast parameters from cylindrical charges detonated on the surface of the ground. Ernst Mach Institute. Fort Belvoir, VA: Defense Technical Information Center, 1982. DTIC Accession No. ADP000430.

Held, Manfred. "Improved Momentum Method." Propellants, Explosives, and Pyrotechnics 26.6 (2001): 290-295.

Held, Manfred. "Impulse Method for the Blast Contour of Cylindrical Explosive Charges." Propellants, Explosives, and Pyrotechnics 24.1 (1998): 17-26.

Henderson, R.C., K.E. Fricke, W.D. Jones, J.E. Beavers, and R.M. Bennett. "Summary of Large and Small-Scale Unreinforced Masonry Infill Test Program." Journal of Structural Engineering 129.12 (2003): 1667-1675.

Hendry, A.W. "The Lateral Strength of Unreinforced Brickwork." The Structural Engineer 51.2 (1973): 43-50.

Hertel, E.S., et al. "CTH: A Software Family for Multi-Dimensional Shock Physics Analysis." Proceedings of the 19th International Symposium on Shock Waves, Marseille, France, 26-30 July 1993.

Hinman, E. and D.J. Hammond. Lessons from the Oklahoma City Bombing: Defensive Design Techniques. New York: ASCE, 1997.

Hill, James A. "Lateral Response of Unreinforced Masonry Infill Frame Panels." Proceedings of the 11th Conference on Analysis and Computation, Atlanta, GA, 24-28 April 1994.

Hornberg, H. "Determination of Fume State Parameters From Expansion Measurements of Metal Tubes." Propellants, Explosives, and Pyrotechnics 11.1 (1986): 23-31.

Ismail, M.M., and S.G. Murray. "Study of the Blast Waves From the Explosion of Nonspherical Charges." Propellants, Explosives, and Pyrotechnics 18.3 (1992): 132-138.

Johnston, B.G., comp. Damage to Commercial and Industrial Buildings Exposed to Nuclear Effects. Federal Civil Defense Administration. Report WT-1189. 1956.

Johnson, J.N. and R. Cheret. Eds. Classic Papers in Shock Compression Science. New York: Springer, 1998.

Kingery, C.N., and G. Bulmash, comp. Airblast parameters from TNT spherical air burst and hemispherical surface burst. U.S. Army Ballistics Research Lab, Aberdeen Proving Ground, MD. Report ARBL-TR-02555. 1984.

Kinney, G.F. and K.J. Graham. Explosive Shocks in Air. New York: Springer-Verlag, 1985.

La Mendola, L., M. Papia, and G. Zingone. "Stability of Masonry Walls Subjected to Seismic Transverse Forces." Journal of Structural Engineering 121.11 (1995): 1581-1587.

Lam, N.T.K., M. Griffith, J. Wilson, and K. Doherty. "Time-History Analysis of URM Walls in Out-of-Plane Flexure." Engineering Structures 25.6 (2003): 743-754.

Lee, E.L., H.C. Hornig, and J.W. Kury, comp. Adiabatic Expansion of High Explosive Detonation Products. Lawrence Radiation Laboratory. Report No. UCRL-50422. 1968.

LeVan, B., Personal communication, January 2007, Dyno Nobel, Salt Lake City, Utah.

Lind, C.A., J.P. Boris, E.S. Oran, W.J. Mitchell, and J.L. Wilcox. "Response of Partially Confined Detonation Facility to Blast Loading." Journal of Pressure Vessel Technology, Transactions of the ASME 120.3 (1998): 306-312.

Lofti, Hamid R., and P. Benson Shing. "Interface Model Applied to Fracture of Masonry Structures." Journal of Structural Engineering 120.1 (1994): 63-80.

Lourenco, Paulo B. "Anisotropic Softening Model for Masonry Plates and Shells." Journal of Structural Engineering 126.9 (2000): 1008-1016.

Lu, M., A.E. Shultz, and H.K. Stolarski. "Analysis of the Influence of Tensile Strength on the Stability of Eccentrically Compressed Slender Unreinforced Masonry Walls Under Lateral Loads." Journal of Structural Engineering 130.6 (2004): 921-933.

Luccioni, B.M., R.D. Ambrosini, and R.F. Danesi. "Assessment of blast loads on structures." WIT Transactions on Engineering Science 49 (2005): 347-358.

Marconi, Frank. "Investigation of the Interaction of a Blast Wave with an Internal Structure." AIAA Journal 32.8 (1994): 1561-1567.

Martini, K. "Finite element studies in the out-of-plane behavior of unreinforced masonry." Ancient Reconstruction of the Pompeii Forum, School of Architecture, University of Virginia, 1996a.

Martini, K. "Finite element studies in the two-way out-of-plane behavior of unreinforced masonry." Ancient Reconstruction of the Pompeii Forum. School of Architecture, University of Virginia, 1996b.

Mays, G.C., Hetherington, J.G., and Rose, T.A. "Resistance-Deflection Functions for Concrete Wall Panels with Openings." Journal of Structural Engineering 124.5 (1998): 579-587.

McDowell, E.L., K.E. McKee, and E. Sevin. "Arching Action Theory of Masonry Walls." Journal of the Structural Division, Proceedings of the American Society of Civil Engineering 82 (1956).

McGlaun, J.M., S.L. Thompson, and M.G. Elrick. "CTH: a Three-Dimensional Shock Wave Physics Code." International Journal of Impact Engineering 10 (1990): 351-360.

Molyneaux T.C.K., G. Beattie, M. Gilbert, S. Burnett, B. Hobbs, and P. Newton. "Assessment Of Static And Dynamic Failure Characteristics Of Mortar Joints In Unreinforced And Reinforced Masonry." Proceedings of the 6th International Masonry Conference, London, 4-6 November 2002. 341-350.

Moradi, L, comp. Resistance of membrane retrofit concrete masonry walls to lateral pressure. Air Force Research Laboratory. Report No. AFRL-RX-TY-TR-2008-4540. 2008.

Moradi, L.G., J.S. Davidson, and R.J. Dinan. "Response of Bonded Membrane Retrofit Concrete Masonry Walls to Dynamic Pressure." Journal of the Performance of Constructed Facilities 23.2 (2009): 72-80.

Morrison, C.M. (2006). "Dynamic Response of Walls and Slabs by Single-Degree-of-Freedom Analysis – A Critical Review and Revision." International Journal of Impact Engineering 32 (2006): 1214-1247.

Masonry Standards Joint Committee (MSJC). Building Code Requirements and Specifications for Masonry Structures. Boulder: The Masonry Society, 2008.

NAVFAC. SHOCK User's Manual Version 1.0. Naval Facilities Engineering Service Center. Report No. UG-2065-SHR. 2005.

NAVFAC. FRANG User's Manual, Draft 3. Naval Civil Engineering Laboratory. Report No. 6046UG. 1989.

Noh, William F., comp. Numerical Methods in Hydrodynamic Calculations. Lawrence Livermore National Laboratory. Report No. UCRL-52112. 1976.

Olatidoye, O., S. Sarathy, G. Jones, C. McIntyre, and L. Milligan, comp. A Representative Survey of Blast Loading Models and Damage Assessment Methods for Buildings Subject to Explosive Blasts. DoD High Performance Computing and Modernization Program, Major Shared Resource Center. Report No. CEWES MSRC/PET TR/98-36. 1998.

Ozog, Henry, Georges A. Melhem, Bert van den Berg, and Paul Mercx. "Facility Siting – Case Study Demonstrating Benefit of Analyzing Blast Dynamics." Proceedings of the International Conference and Workshop on Process Safety Management and Inherently Safer Processes, Orlando, FL, 8-11 October 1996. 293-315.

Penn, L, et al., comp. Determination of Equation-of-State Parameters for Four Types of Explosive. Lawrence Livermore Laboratory. Report No. UCRL-51892. 1975.

Philipchuk, V., comp. Determination of free-air blast of one-pound high explosive cylinders. National Northern. NN-F-6. Fort Belvoir, VA: Defense Technical Information Center, 1955. DTIC Accession No. AD066637.

Priestley, M.J.N. "Seismic behavior of unreinforced masonry walls." Bulletin of the New Zealand National Society for Earthquake Engineering 18.2 (1985): 191-205.

Priestley, M.J.N. and L.M. Robinson. "Discussion: Seismic Behavior of Unreinforced Masonry Walls." Bulletin of the New Zealand National Society for Earthquake Engineering 19.1 (1986): 65-75.

Proft, K.D., H. Koen, and B. Sluys. "Mesoscopic Modeling of Masonry Failure." Engineering and Computational Mechanics 164.1 (2011): 41-46.

Remennikov, A.M. "The State of the Art of Explosive Loads Characterization." Proceedings of the 2007 Australian Earthquake Engineering Society Conference, Wollongong, NSW, 23-25 November 2007. 1-25.

Remennikov, A.M. and T.A. Rose. "Modeling Blast Loads on Buildings in Complex City Geometries." Computers and Structures 83.27 (2005): 2197-2205.

Richtmyer, R.D. Difference Methods for Initial Value Problems. New York: Interscience Publishers, Inc., 1964.

Rose, T.A., P.D. Smith, and G.C. Mays. "Design Charts Relating to Protection of Structures against Airblast from High Explosives." Proceedings of the Institution of Civil Engineers, Structures and Buildings 122.2 (1997): 186-192.

Sadwin, L.D., and N.M. Junk. "Lateral Shock Pressure Measurements at an Explosive Column." Fourth Symposium on Detonation. US Naval Ordnance Laboratory: White Oak, MD. (1965): 92-95.

Souers, P.C., comp. JWL Calculating. Lawrence Livermore National Laboratory. Report No. UCRL-TR-211984. 2005.

Souers, P.C., and L.C. Haselman, Jr., comp. Detonation Equation of State at LLNL, 1993. Lawrence Livermore National Laboratory. Report No. UCRL-ID-116113. 1994.

Souers, P.C., B. Wu, and L.C. Haselman, Jr., comp. Detonation Equation of State at LLNL, 1995. Lawrence Livermore National Laboratory. Report No. UCRL-TD-119262 Rev 3. 1996.

Stoner, R.G. and W. Bleakney. "The Attenuation of Spherical Shock Waves in Air." Journal of Applied Physics 19 (1948): 670-678.

Sunshine, D., Amini, A. and Swanson, M. (2004). "Overview of Simplified Methods and Research for Blast Analysis." Proceedings of the 2004 Structures Congress, Nashville, TN, 22-26 May 2004. 1-11.

Tancreto, J.E. Effects of charge shape and composition on blast environment. Picatinny Arsenal. Report No. AD-A011 807. 1975.

Taun, C.Y., L.C. Muszynski, and W.C. Dass. Explosive Test of an Externally Reinforced Multi-Story Concrete Structure at Eglin AFB, FL. Tyndall AFB, Florida: Applied Research Associates, Inc. - Gulf Coast Division, 1995.

Tedesco, J.W., W.G. McDougal, and C.A. Ross. Structural Dynamics: Theory and Applications. Menlo Park: Addison Wesley Longman, 1999.

Tesfaye, E., and T.H. Broome. "Effect of Weight on Stability of Masonry Walls." Journal of Structural Engineering 103.5 (1977): 961-970.

Thomas, F.G. "The Strength of Brickwork." The Structural Engineer 31.2 (1953): 35-41.

U.S. Army Corps of Engineers. Design and Analysis of Hardened Structures for Conventional Weapons Effects. Report No. UFC 3-340-01. 2002.

U.S. Army Corps of Engineers. Comparison of Calculated Single-Degree-of-Freedom Response to Blast Test Data. USACE Protective Design Center. Report No. PDC TR-08-02. 2008a.

U.S. Army Corps of Engineers. Parameter Study for Single-Degree-of-Freedom Response of Structural Components to Blast Loads. USACE Protective Design Center. Report No. PDC TR-08-01. 2008b.

U.S. Army Corps of Engineers. Methodology Manual for the Single-Degree-of-Freedom Blast Effects Design Spreadsheet (SBEDS). USACE Protective Design Center. Report No. PDC TR 06-01 Rev 1. 2008c.

U.S. Army, U.S. Navy, U.S. Air Force. Structures to Resist the Effects of Accidental Explosions. Department of the Army. Army TM5-1300, Navy NAVFAC P397. 1990.

U.S. Army, U.S. Navy, U.S. Air Force. Design and Analysis of Hardened Structures for Conventional Weapon Effects. Department of the Army. TM 5-855-1, AFPAM 32-1147(1), NAVFAC P-1080. 1998.

U.S. Army Corps of Engineers. Structures to Resist the Effects of Accidental Explosions. USACE Protective Design Center. Report No. UFC 3-340-02. 2008d.

U.S. Department of State. Office of the Historian. Significant Terrorist Incidents, 1961-2003: A Brief Chronology. 1 March 2010. <http://www.state.gov/r/pa/ho/pubs/fs/5902.htm>.

Varma, R. K., C.P.S. Tomar, S. Parkash, and V.S. Sethi. (1997). "Damage to Brick Masonry Wall Panels Under High Explosive Detonations." Structures under Extreme Loading Conditions: Proceedings, ASME/JSME Joint Pressure Vessels and Piping Conference, Orlando, FL, 27-31 July, 1997. 207-216.

Van Ness, H.C. Understanding Thermodynamics. New York: Dover Publications, 1969.

Verghese, Abraham. Home, Life, and Work. New York: Vintage Books, 2010.

VonNeumann, J. and R.D. Richtmyer. "A Method for the Numerical Calculation of Hydrodynamic Shocks." Journal of Applied Physics 21 (1950): 232-237.

Wei, Xueying and Hong Hao. "Numerical Derivation of Homogenized Dynamic Masonry Material Properties with Strain Rate Effects." International Journal of Impact Engineering 36 (2009): 522-536.

Wesevich, J.W., C.J. Oswald, M.T. Edel, M.J. Lowak, and S. S. Alaoui, comp. Compile an Enhance Blast Related CMU Wall Test Database (CMUDS). Wilfred Baker Engineering. Contract No. 41756-00-C-0900. Office of Special Technology, 2002.

Whiting, W.D. and D.R. Colthorp, comp. Retrofit Measures for Conventional Concrete Masonry Unit Building Subject to Terrorist Threat. U.S. Army Engineer Waterways Experiment Station, Vicksburg, Mississippi: Waterways Experiment Station, 1996.

Wilke, J.P. Effects of Various Blowout Panel Configurations on the Structural Response of Los Alamos National Laboratory Building 16-340 to Internal Explosions. Masters Thesis. New Mexico Institute of Mining and Technology. 2004.

Wilkins, M.L. Computer Simulation of Dynamic Phenomena. New York: Springer Verlag Berlin Heidelberg, 1999.

Wu, C. and H. Hao. "Modeling of Simultaneous Ground Shock and Airblast Pressure on Nearby Structures from Surface Explosions." International Journal of Impact Engineering 31.6 (2005): 699-717.

Yokel, Y.F., and R.D. Dikkers. "Strength of Load Bearing Masonry Walls." Journal of the Structural Division, Proceedings of the American Society of Civil Engineering, 97.5 (1971): 1593-1609.

Zhang, G., N. Vlahopoulos, R. Goetz, and R. Van De Velde. "Blast Event Simulation for a Vehicle Subjected to an Explosion." Proceedings of the 2007 International Modal Analysis Conference, Orlando, FL, 19-22 February 2007.

APPENDIX A: SHOT A1 SENSOR MEASUREMENTS

This appendix contains plots for all sensor measurements from Shot A1. Measurements have been plotted on a common time window, where the beginning of the time window is an arbitrarily selected point preceding the detonation of the charge. All time history data are plotted starting at time = 0.04 seconds (regardless of whether tick mark is shown or not).

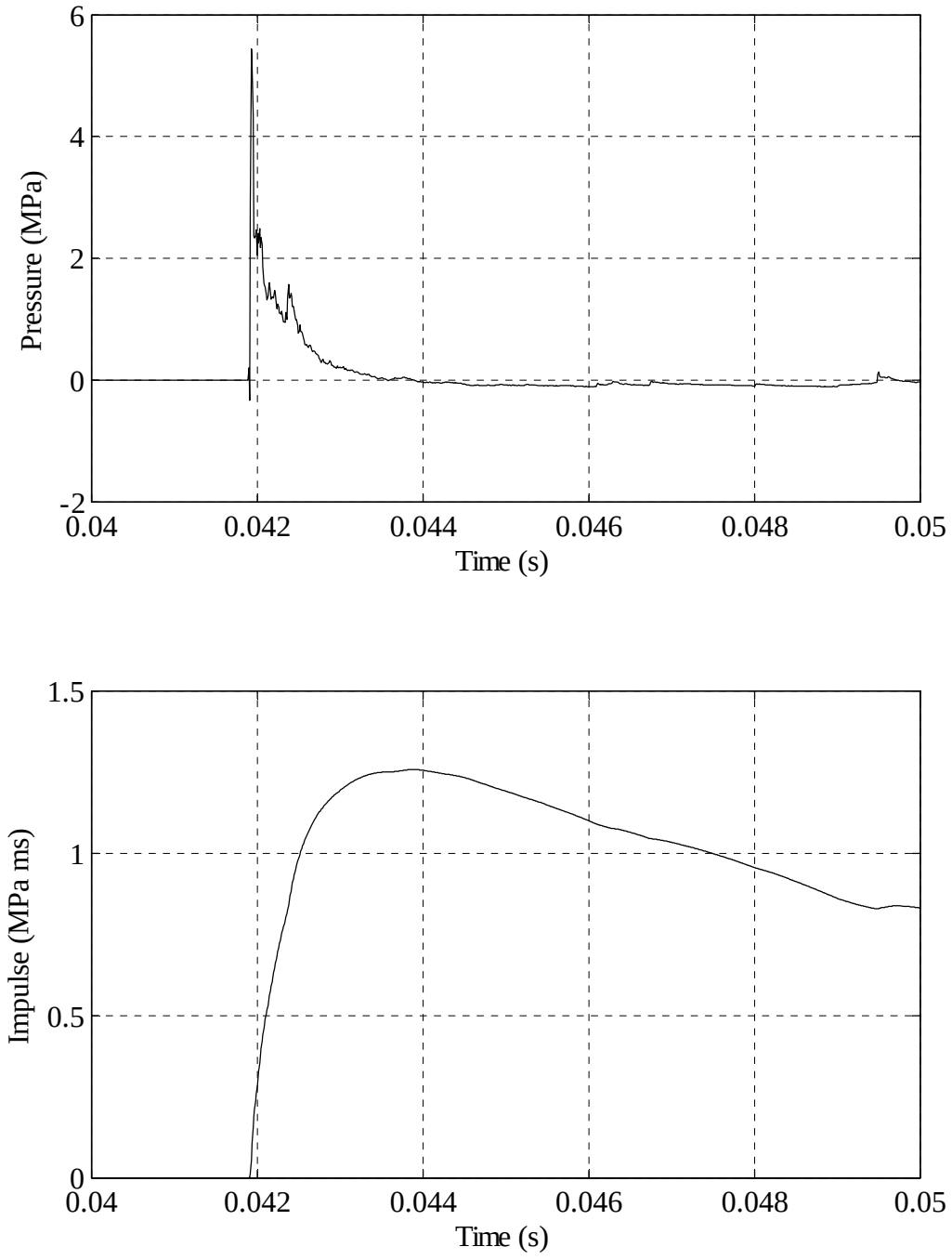

FIGURE A.1. Shot A1 - Flush mount sensor P1 pressure and impulse as a function of time.

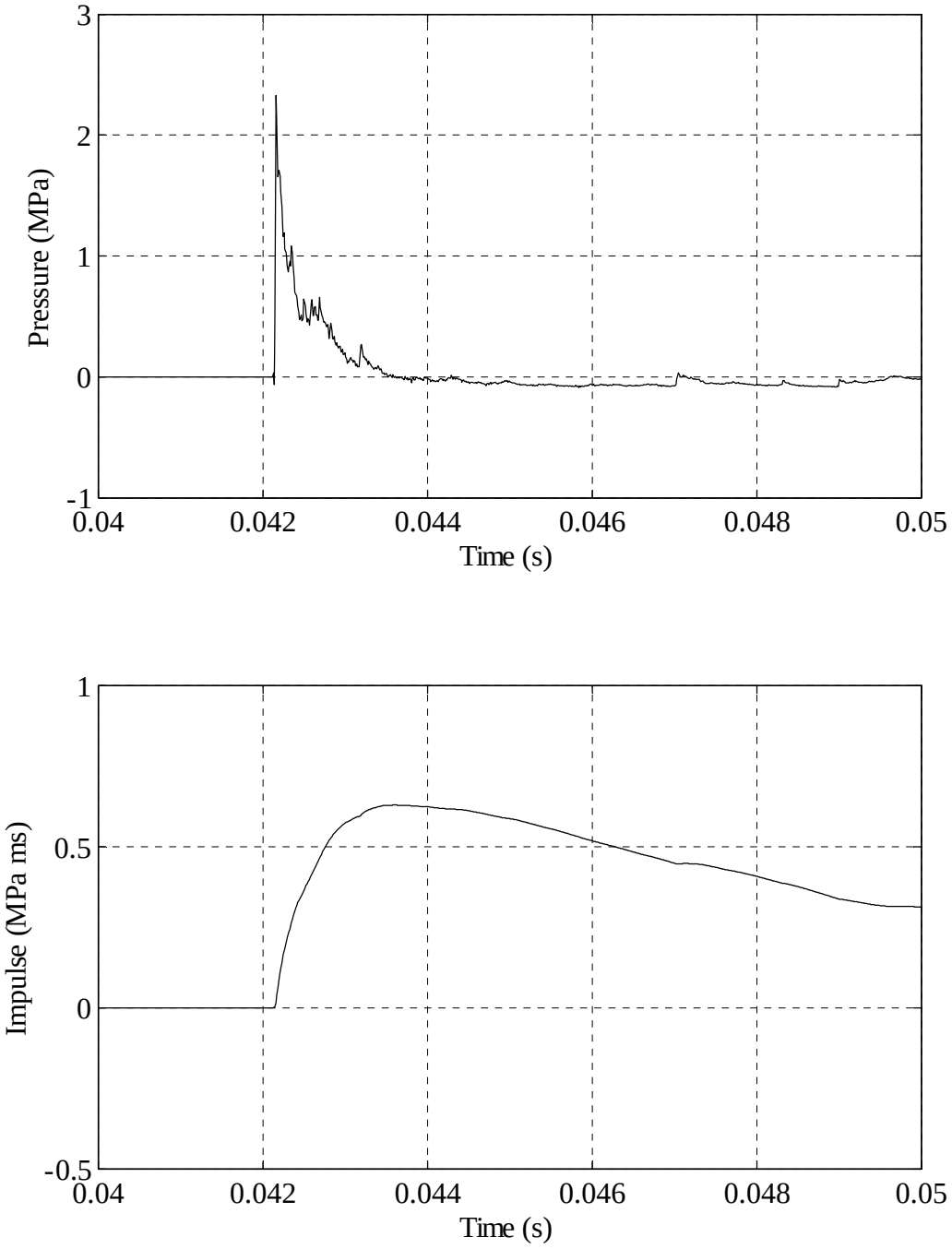

FIGURE A.2. Shot A1 - Flush mount sensor P2 pressure and impulse as a function of time.

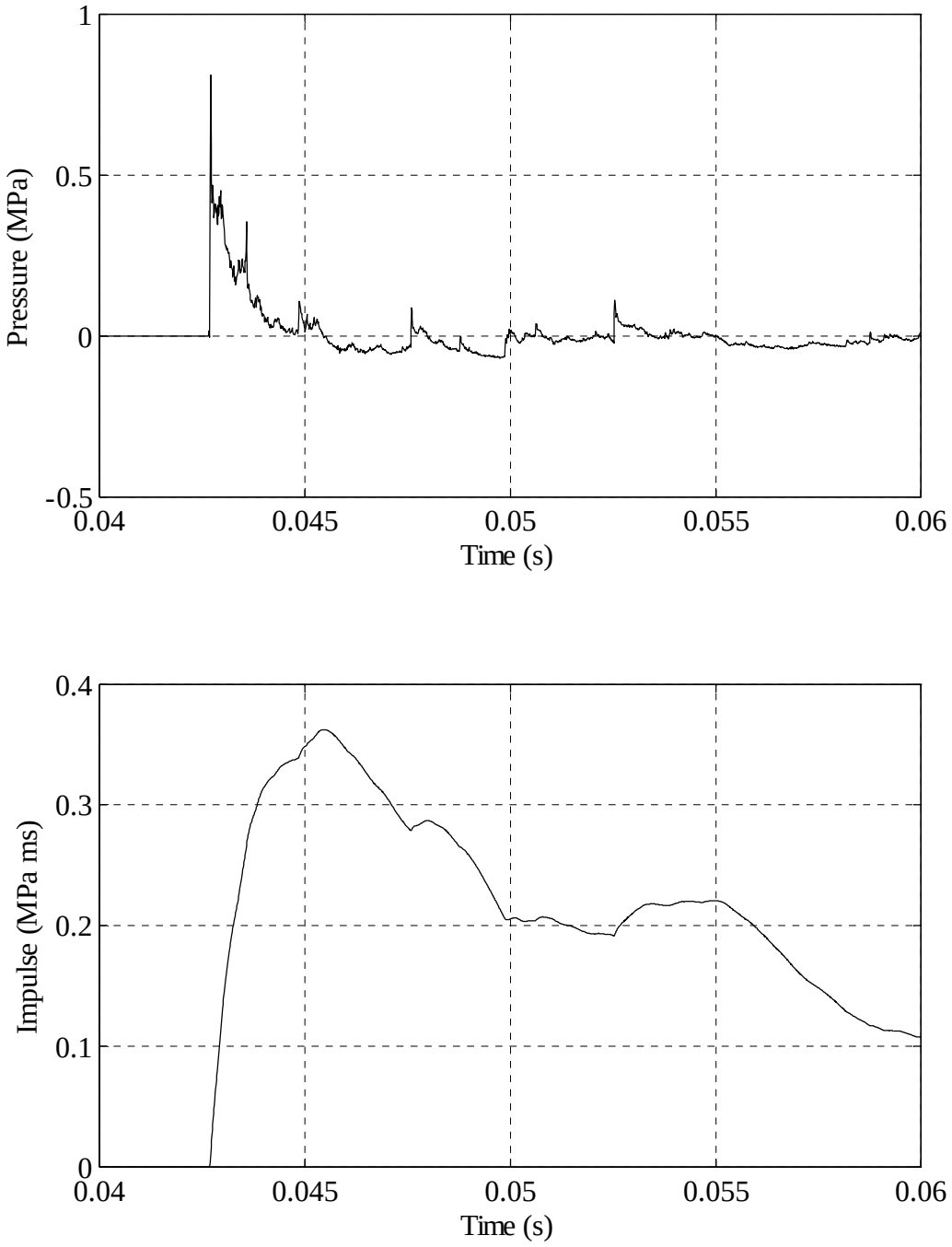

FIGURE A.3: Shot A1 - Flush mount sensor P3 pressure and impulse as a function of time.

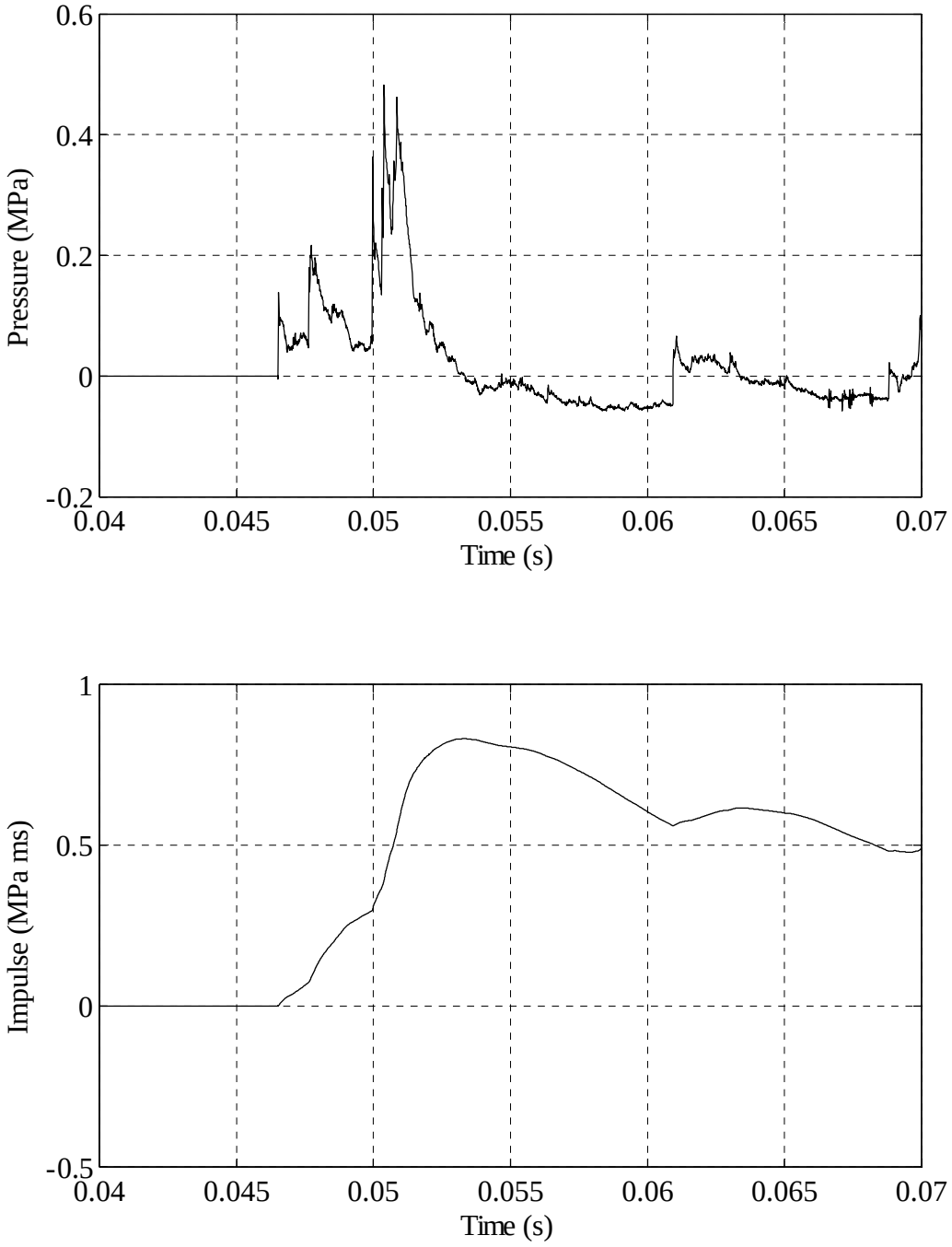

FIGURE A.4: Shot A1 - Flush mount sensor P4 pressure and impulse as a function of time.

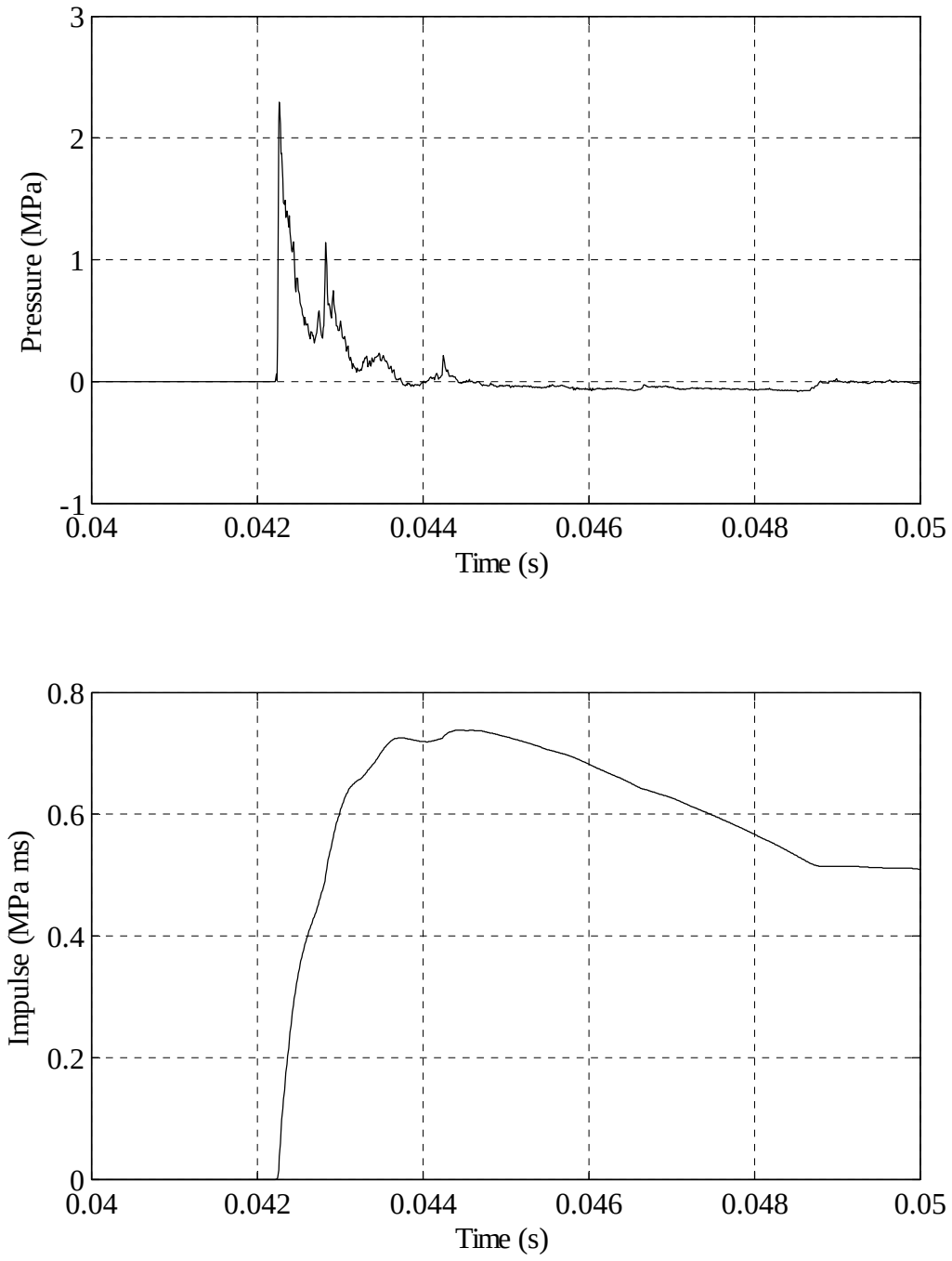

FIGURE A.5: Shot A1 - Flush mount sensor P5 pressure and impulse as a function of time.

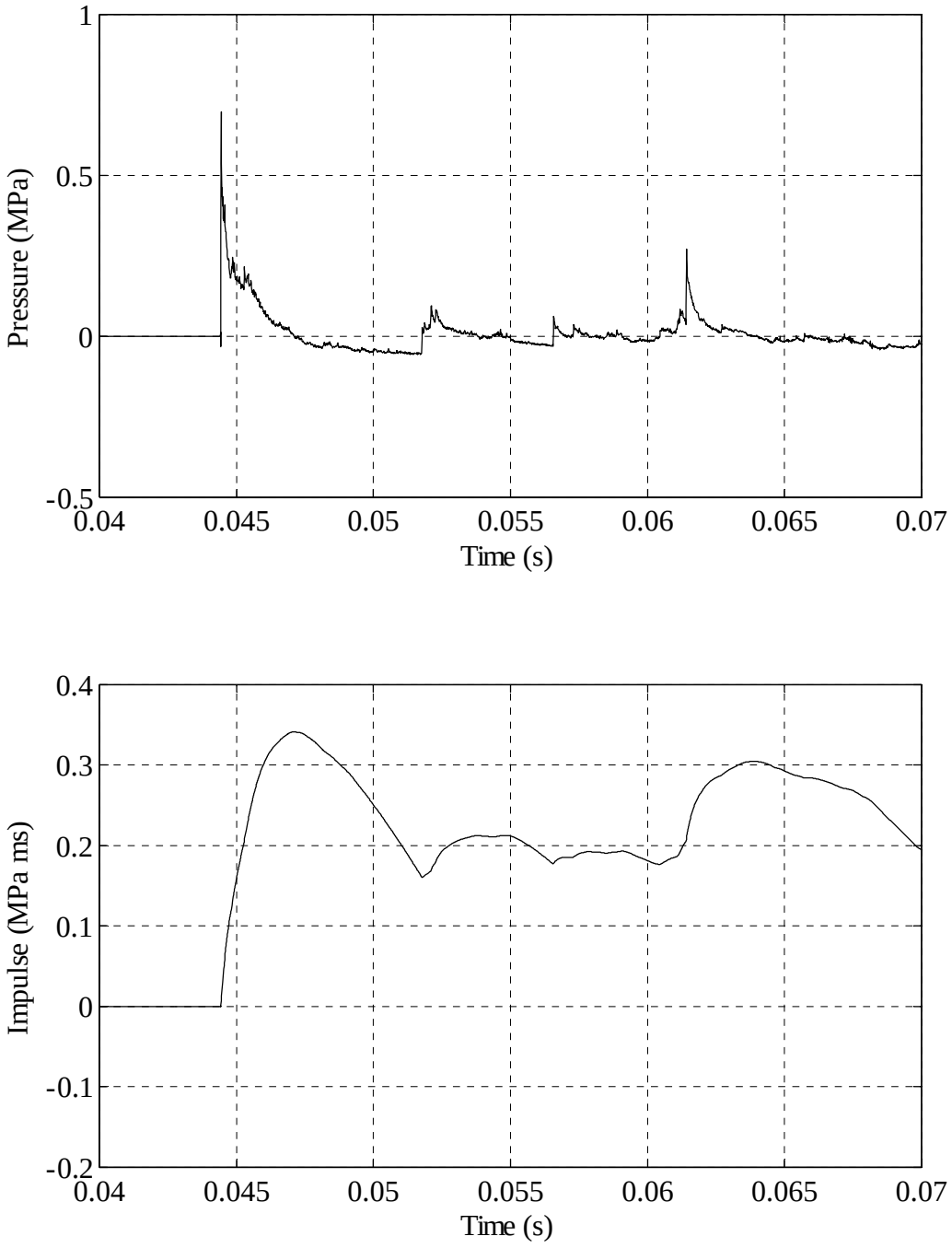

FIGURE A.6: Shot A1 - Flush mount sensor P6 pressure and impulse as a function of time.

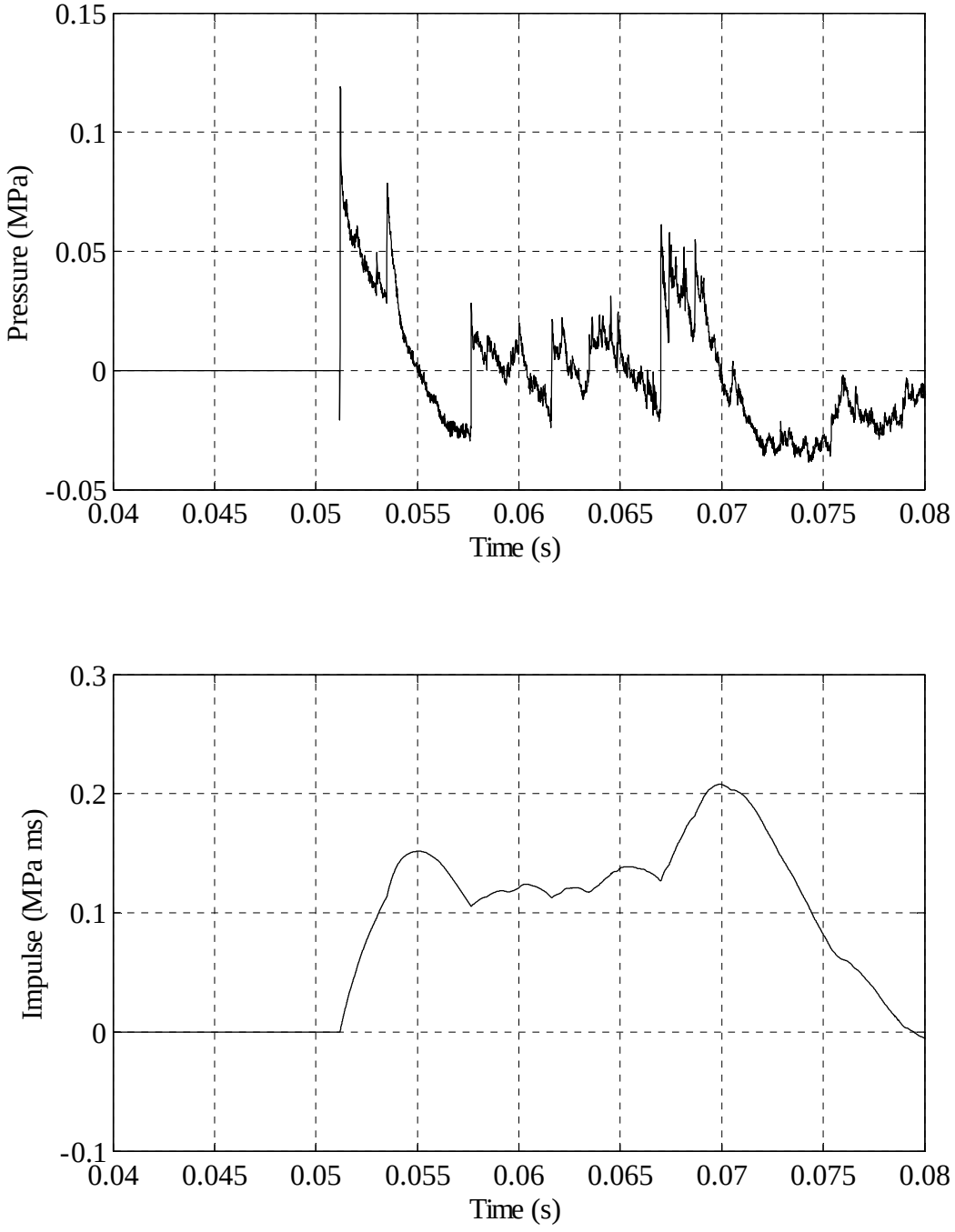

FIGURE A7: Shot A1 - Flush mount sensor P7 pressure and impulse as a function of time.

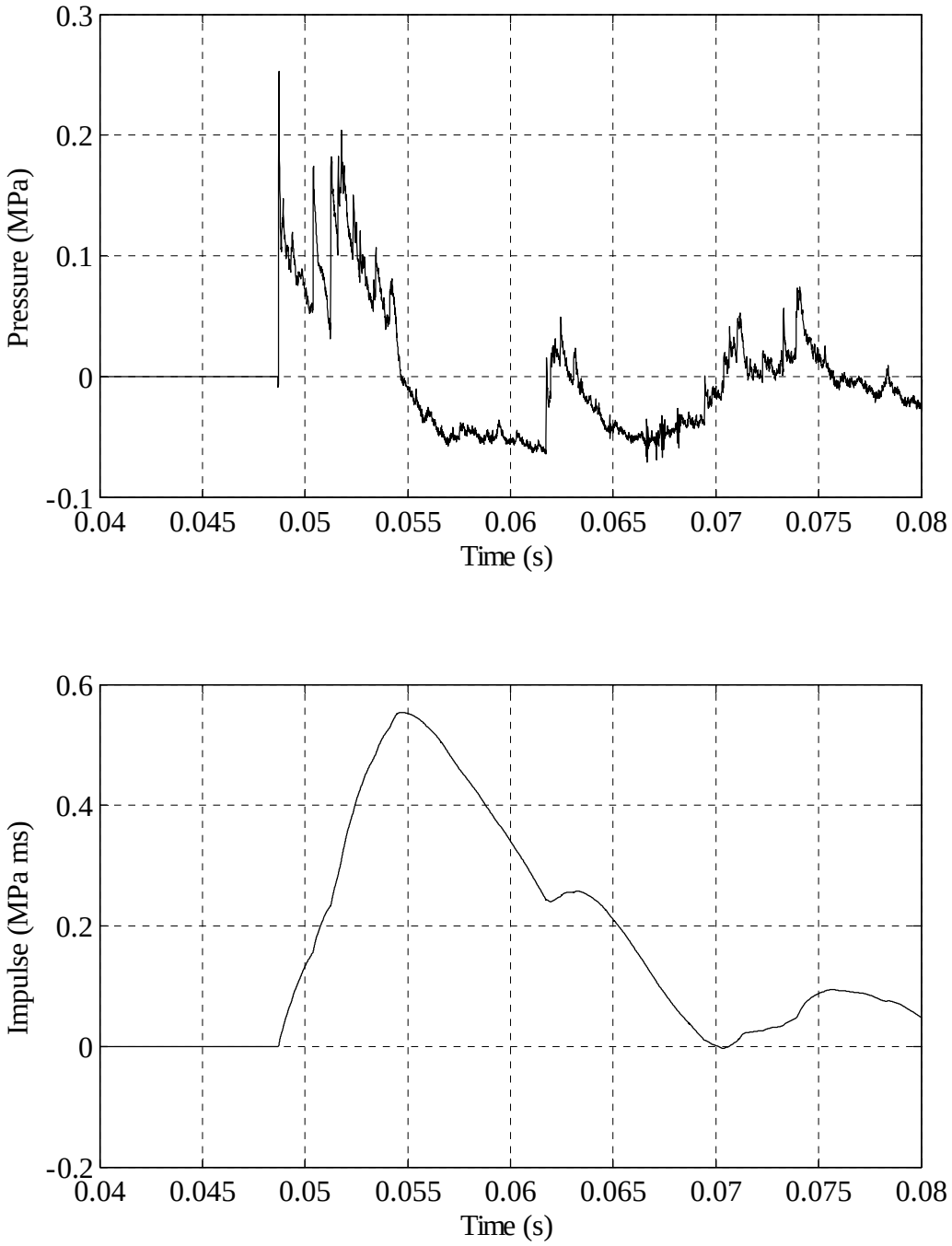

FIGURE A.8: Shot A1 - Flush mount sensor P8 pressure and impulse as a function of time.

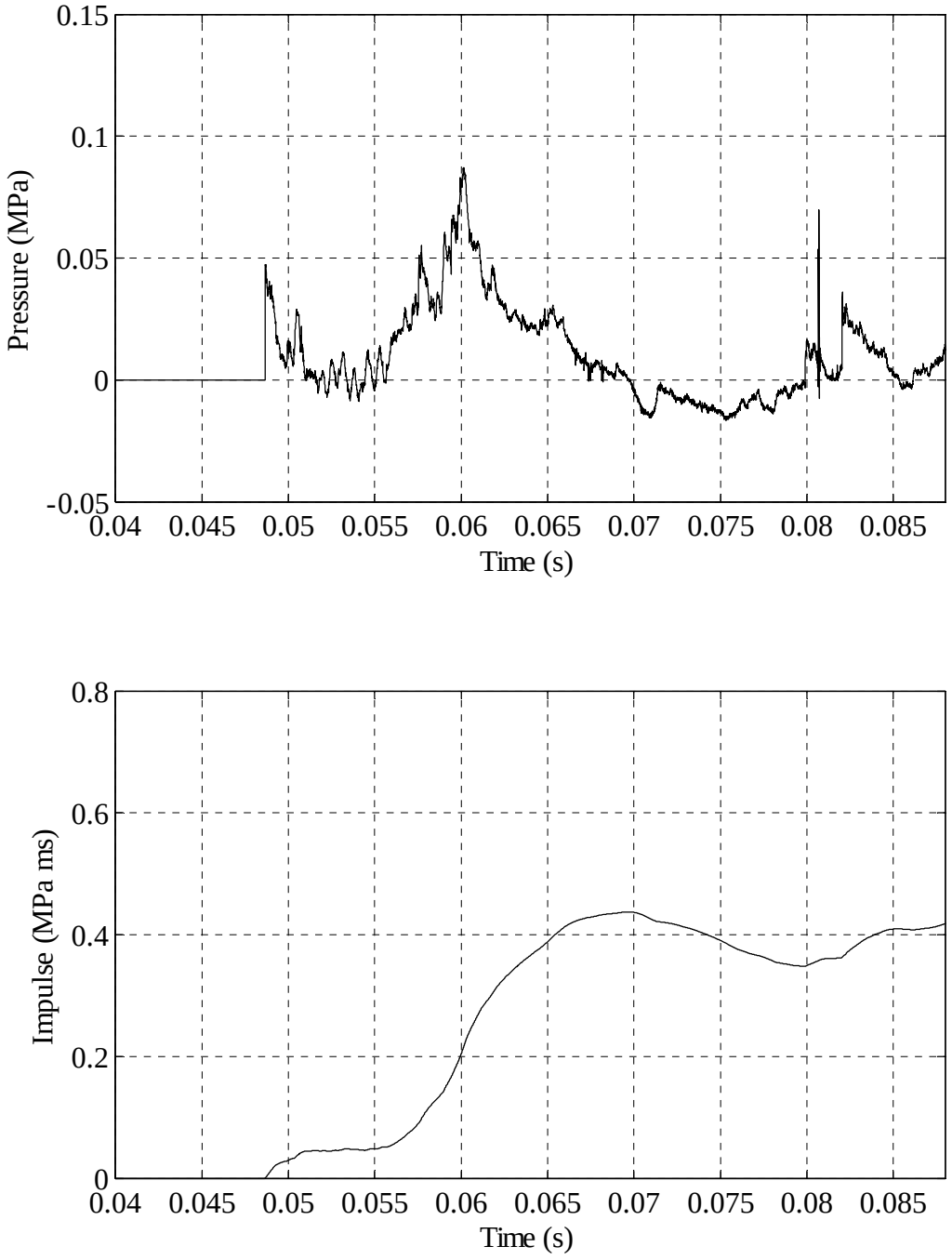

FIGURE A.9: Shot A1 - Pressure pencil PP1 pressure and impulse as a function of time.

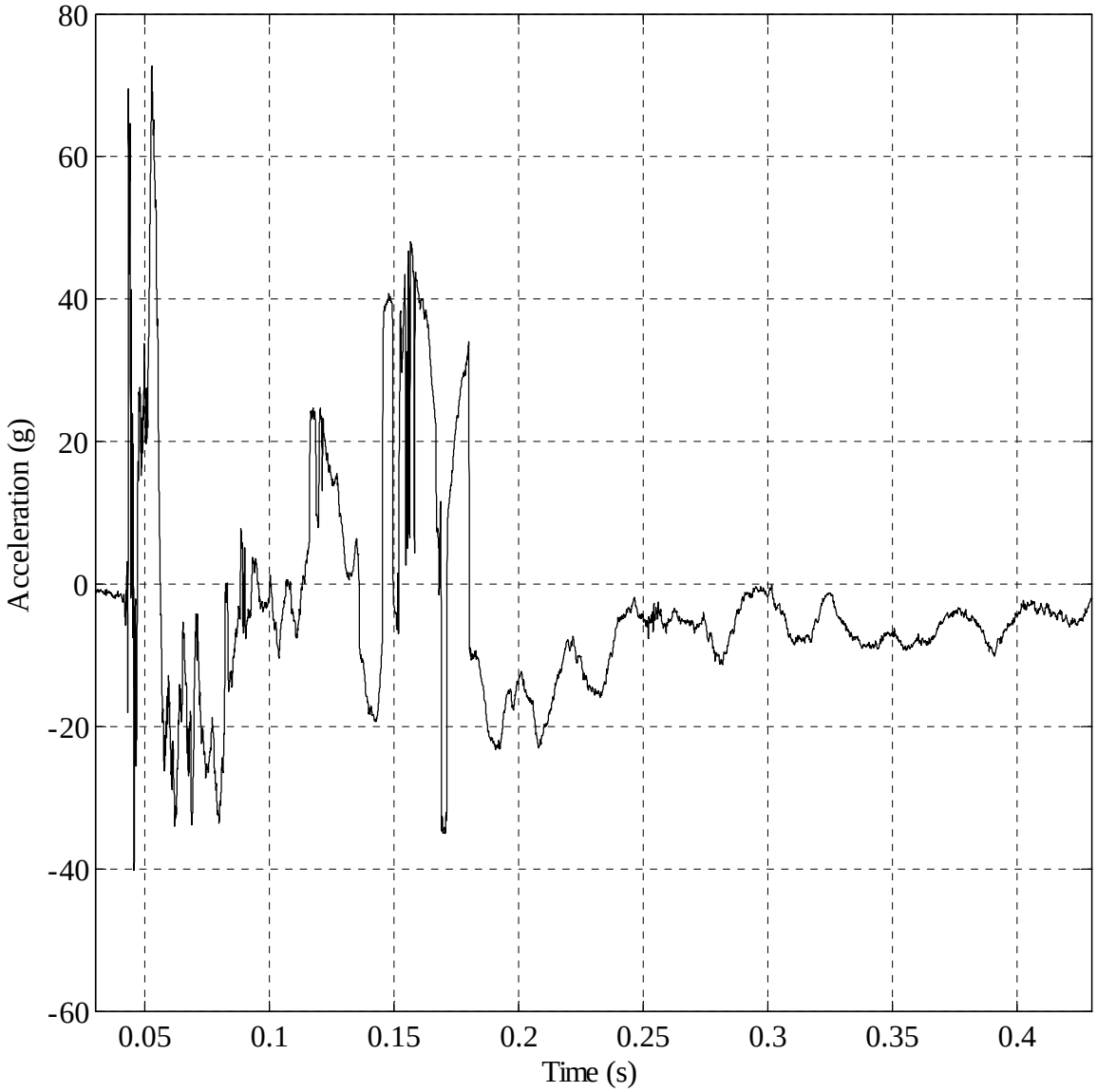

FIGURE A.10: Shot A1 - Acceleration time history measured by sensor S1.

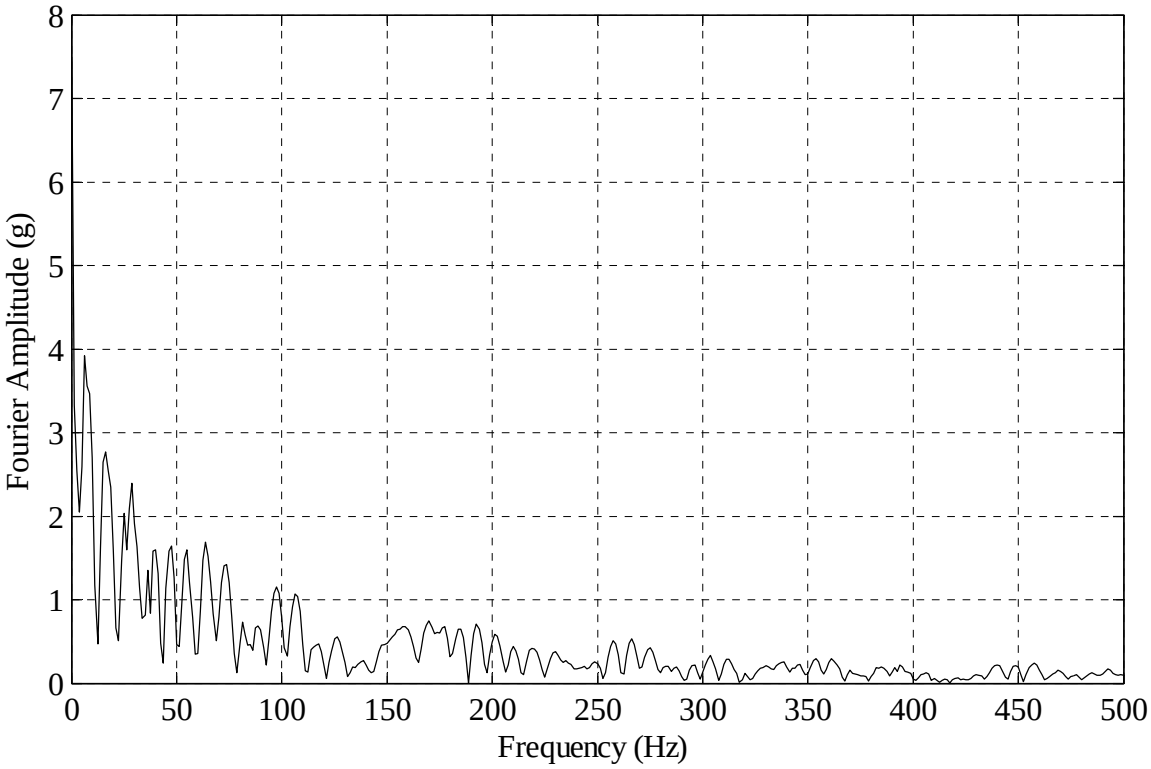

FIGURE A.11: Shot A1 - Fourier amplitude spectrum of acceleration time history measured by sensor S1.

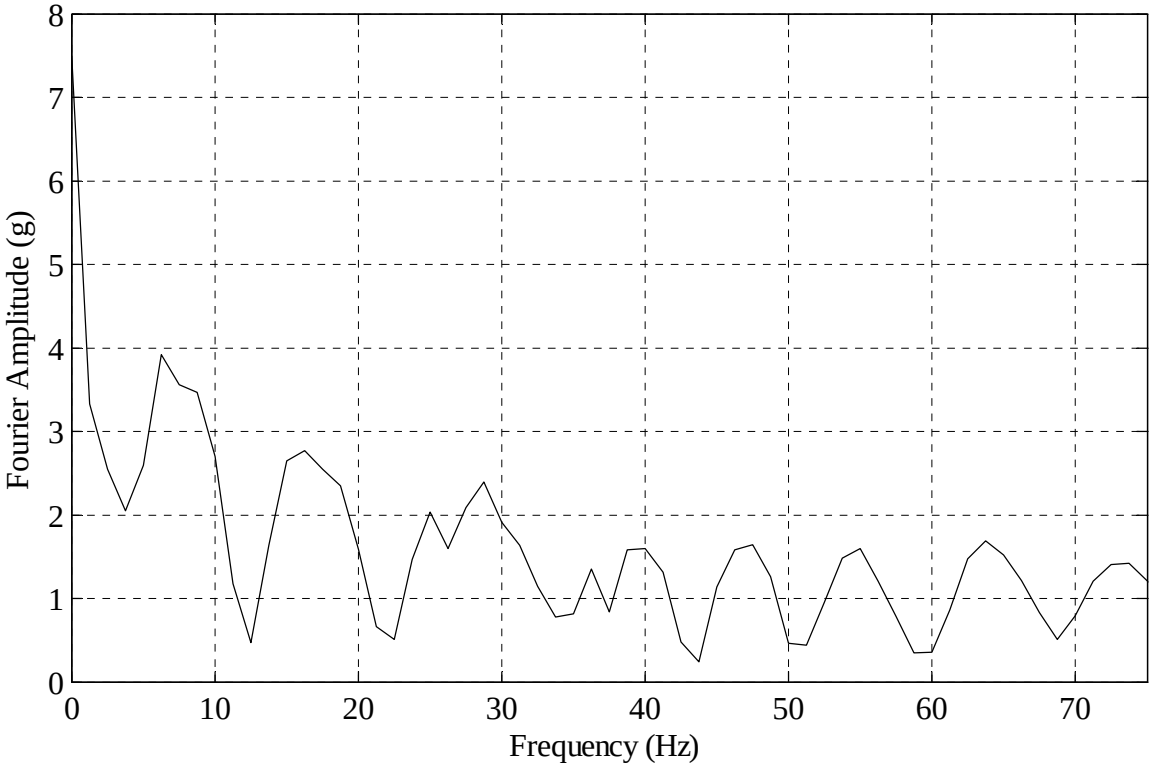

FIGURE A.12: Zoomed in window showing lower frequencies from Figure A.11.

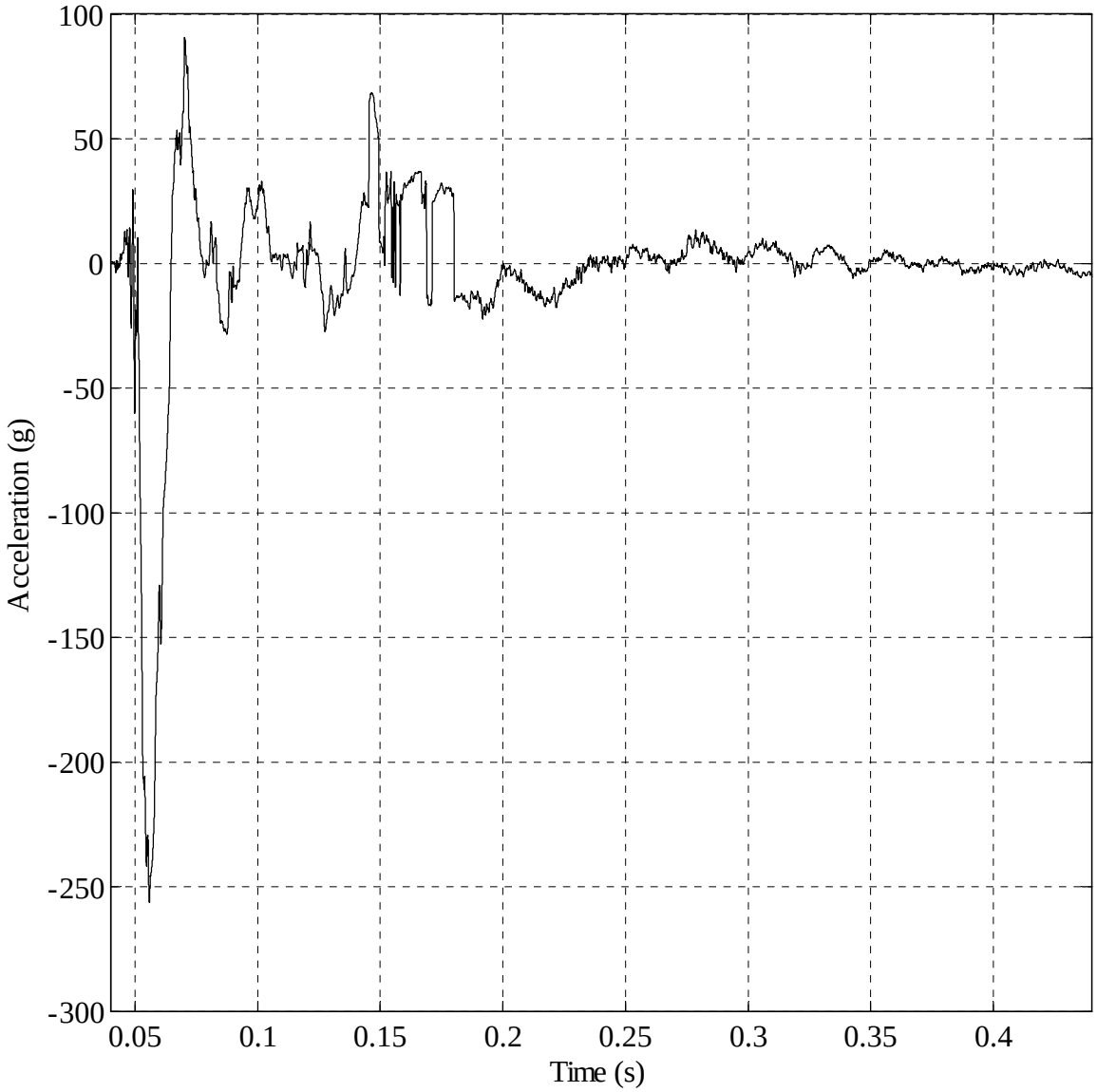

FIGURE A.13: Shot A1 - Acceleration time history measured by sensor S2.

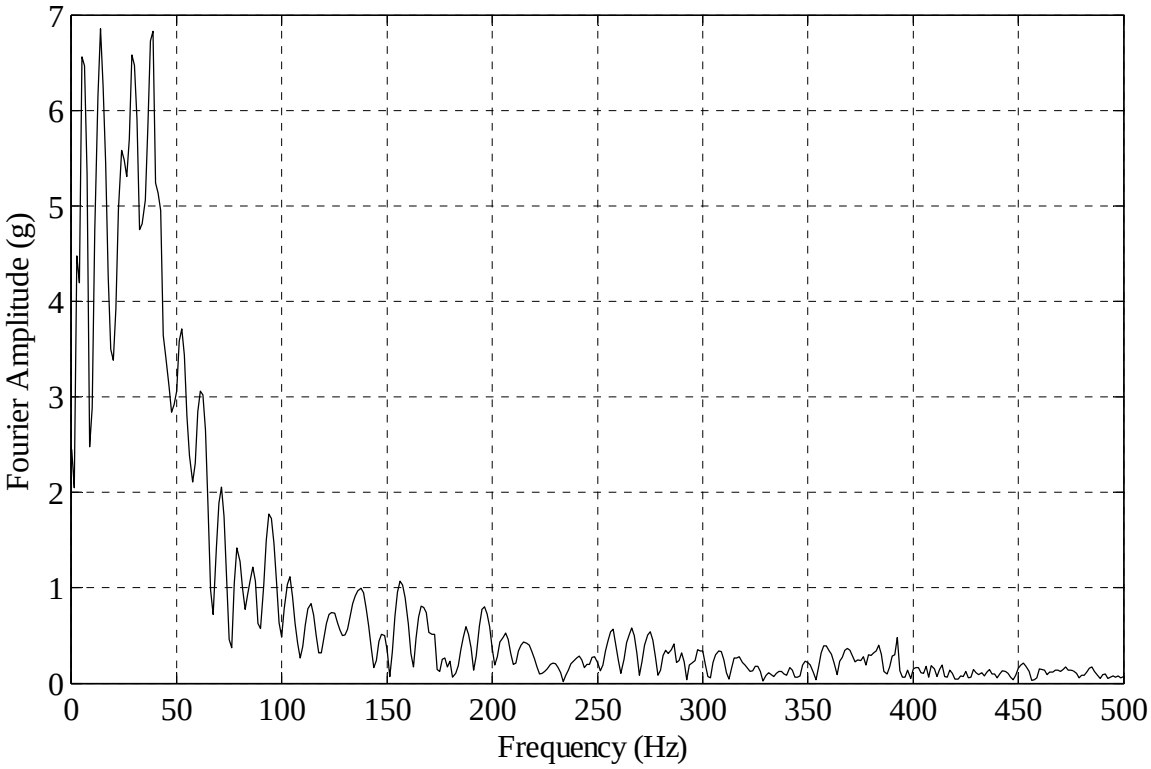

FIGURE A.14: Shot A1 - Fourier amplitude spectrum of acceleration time history measured by sensor S2.

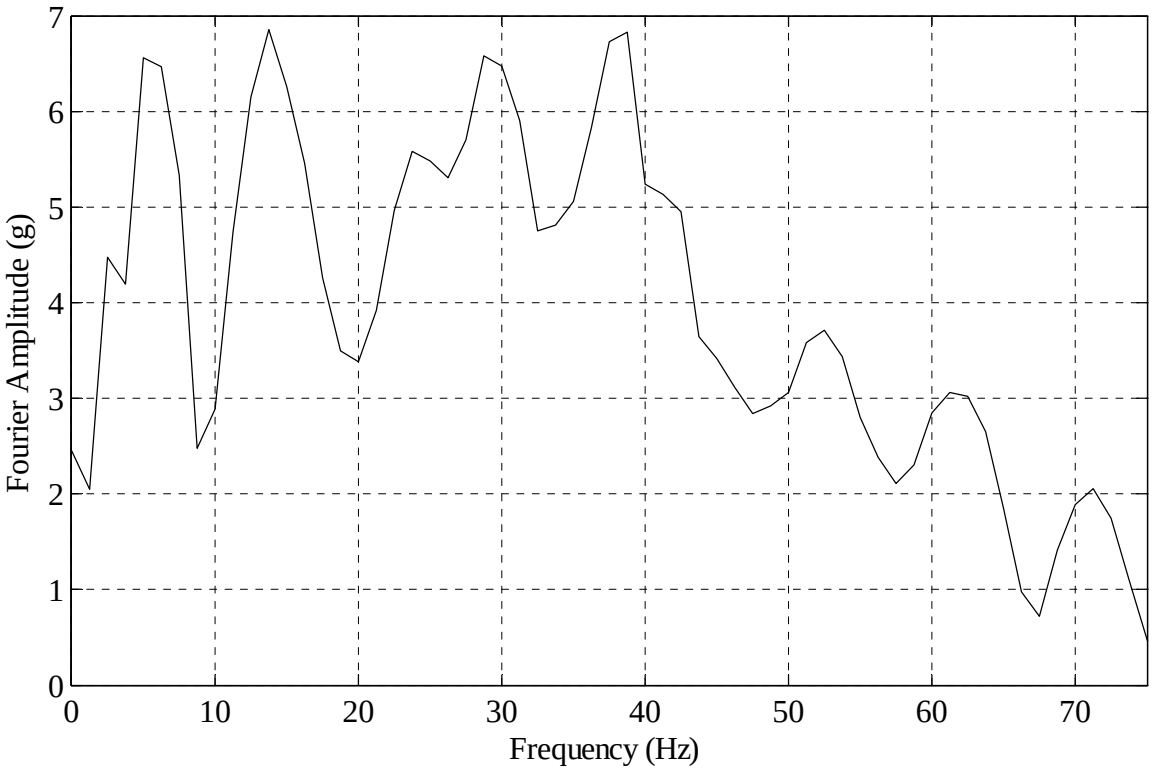

FIGURE A.15: Zoomed in window showing lower frequencies from Figure A.14.

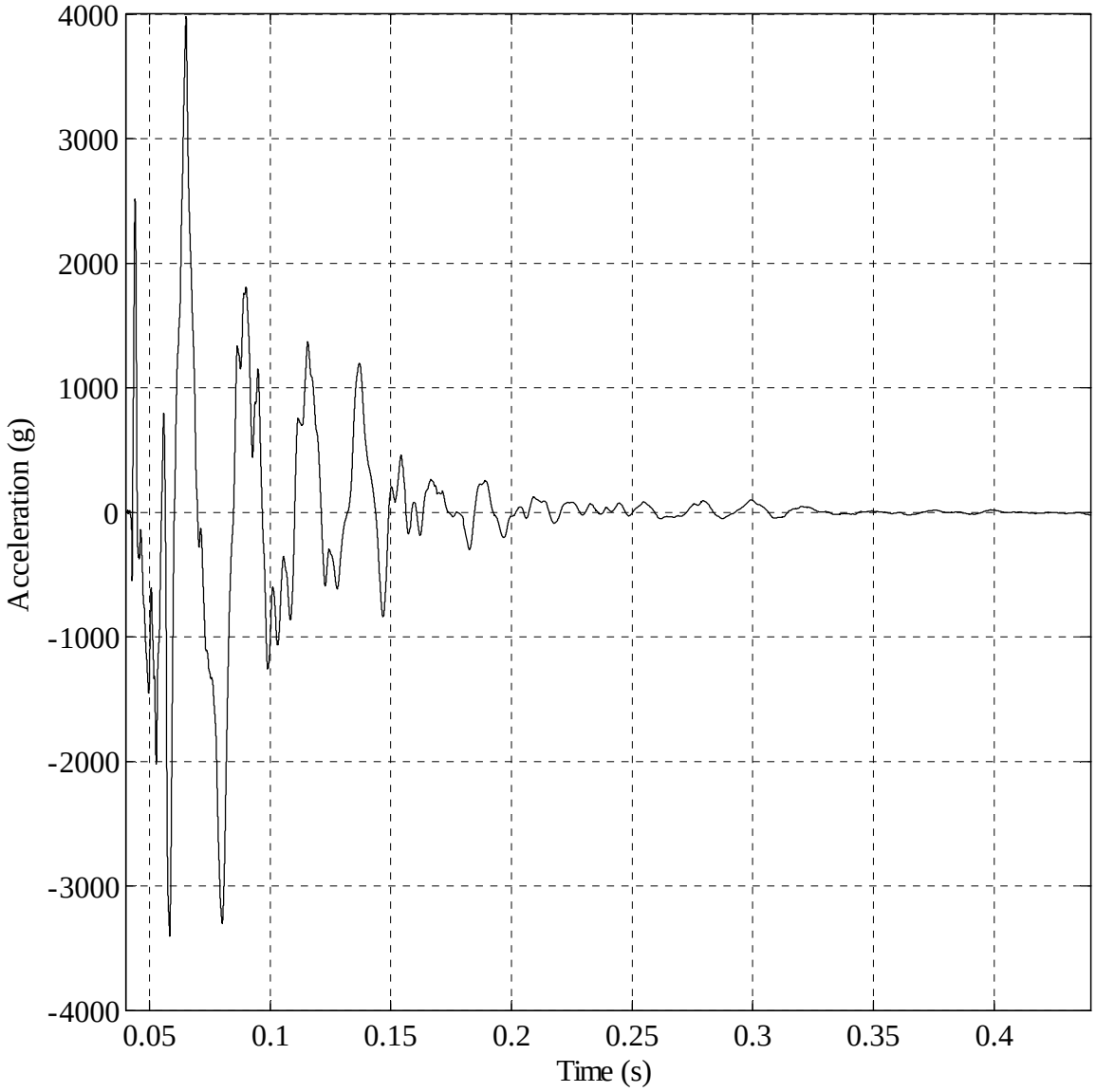

FIGURE A.16: Shot A1 - Acceleration time history measured by sensor S3.

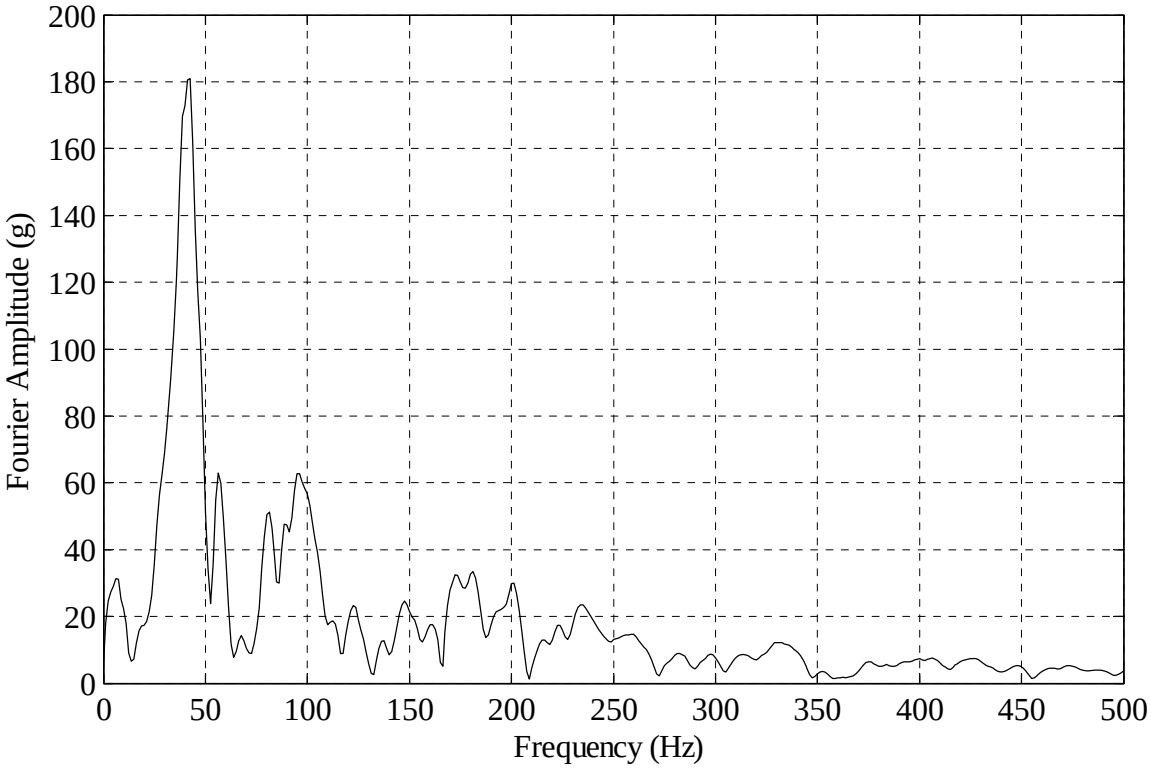

FIGURE A.17: Shot A1 - Fourier amplitude spectrum of acceleration time history measured by sensor S3.

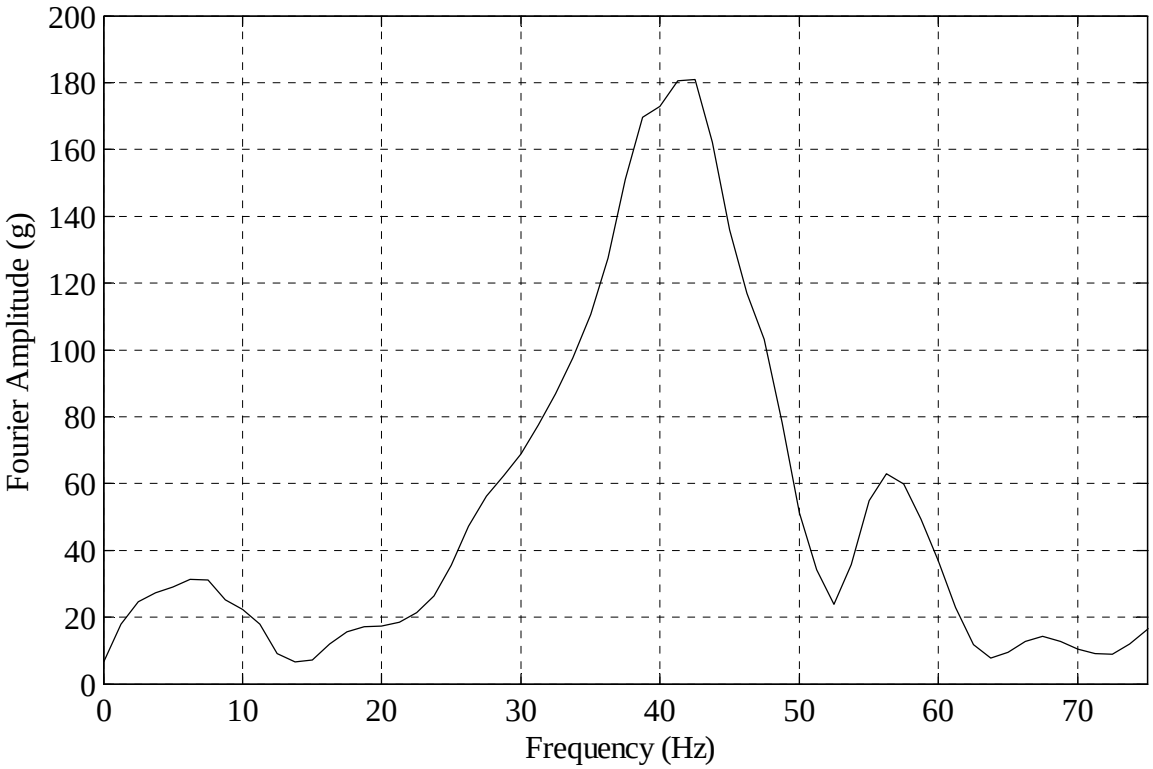

FIGURE A.18: Zoomed in window showing lower frequencies from Figure A.17.

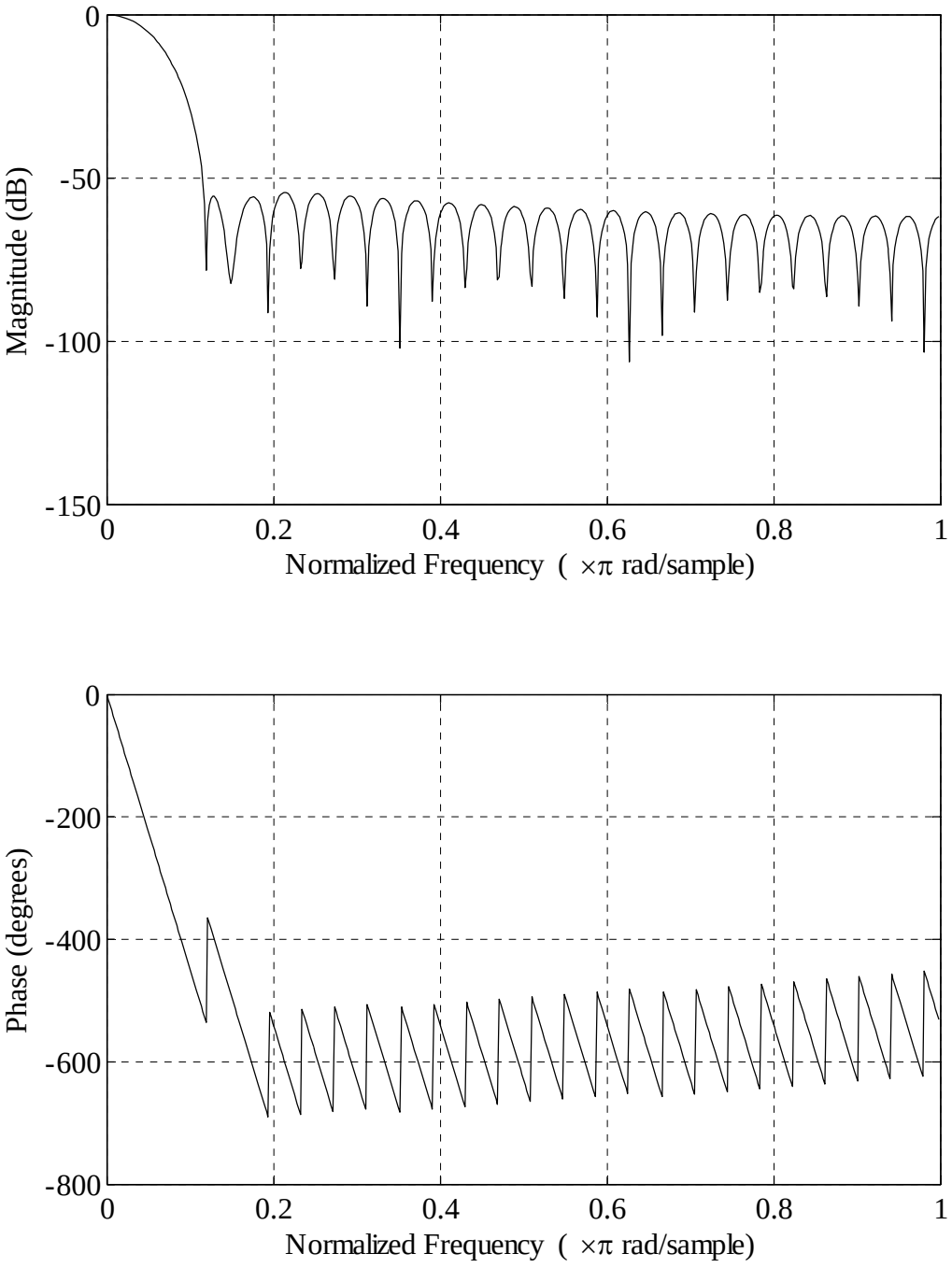

FIGURE A.19: Response of Matlab filter used to post-process shock accelerometer data. Note that in normalized frequency, 1.0 corresponds to the Nyquist frequency (50 kHz in this case).

APPENDIX B: SHOT A2 SENSOR MEASUREMENTS

This appendix contains plots for all sensor measurements from Shot A2. Measurements have been plotted on a common time window, where the beginning of the time window is an arbitrarily selected point preceding the detonation of the charge. All time history data are plotted starting at time = 0.19 seconds (regardless of whether tick mark is shown or not).

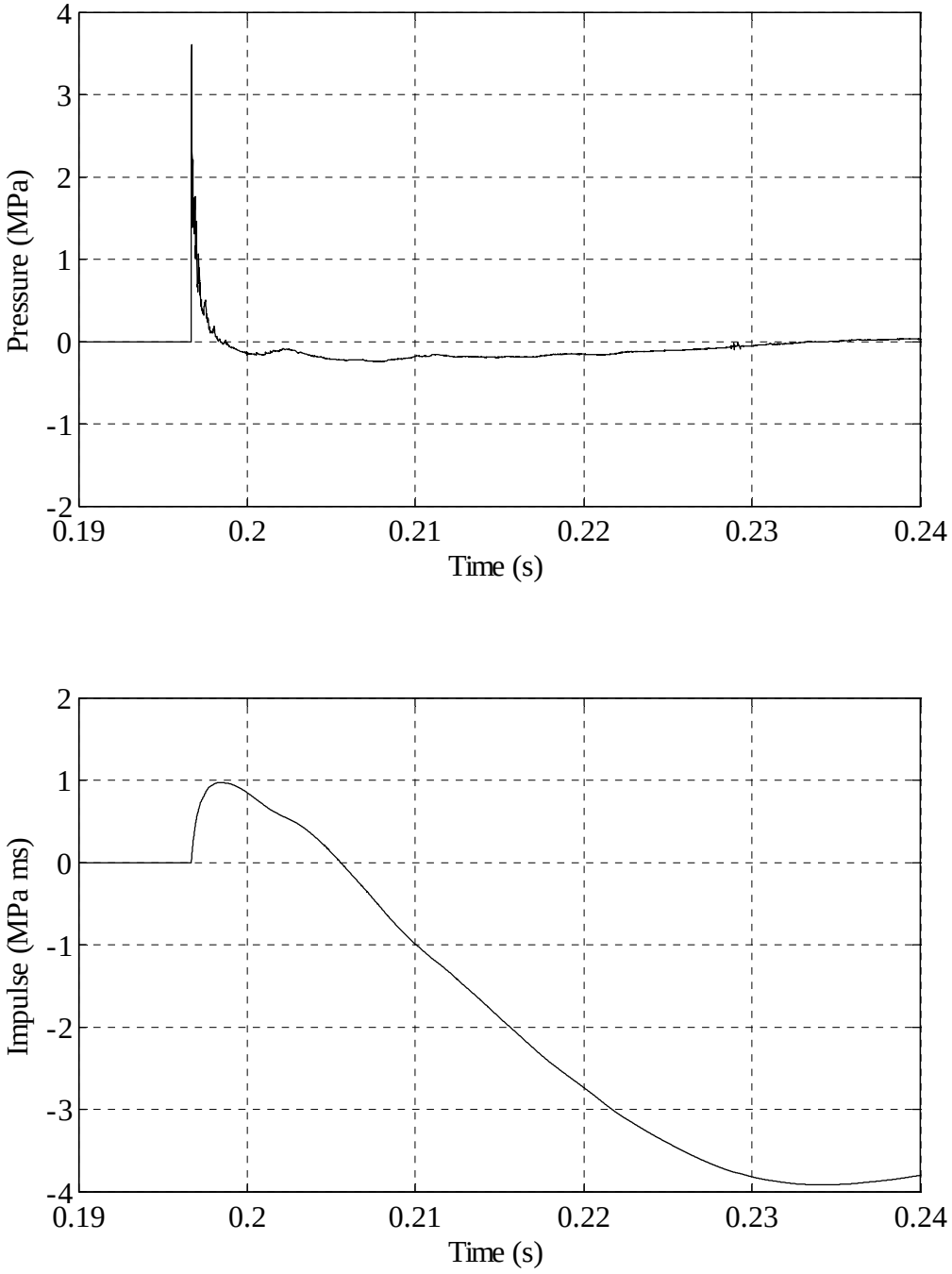

FIGURE B.1: Shot A2 - Flush mount sensor P1 pressure and impulse as a function of time.

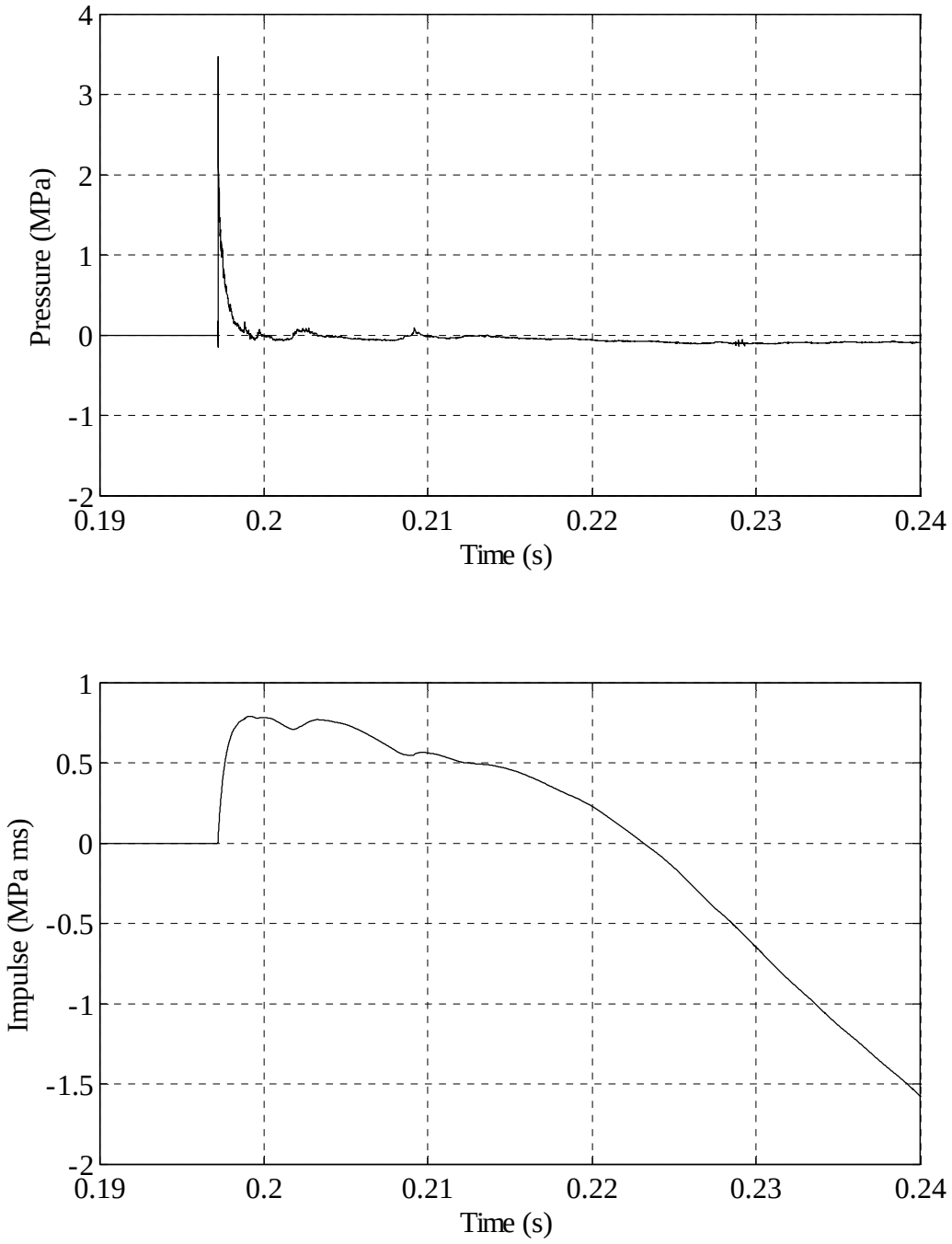

FIGURE B.2: Shot A2 - Flush mount sensor P2 pressure and impulse as a function of time.

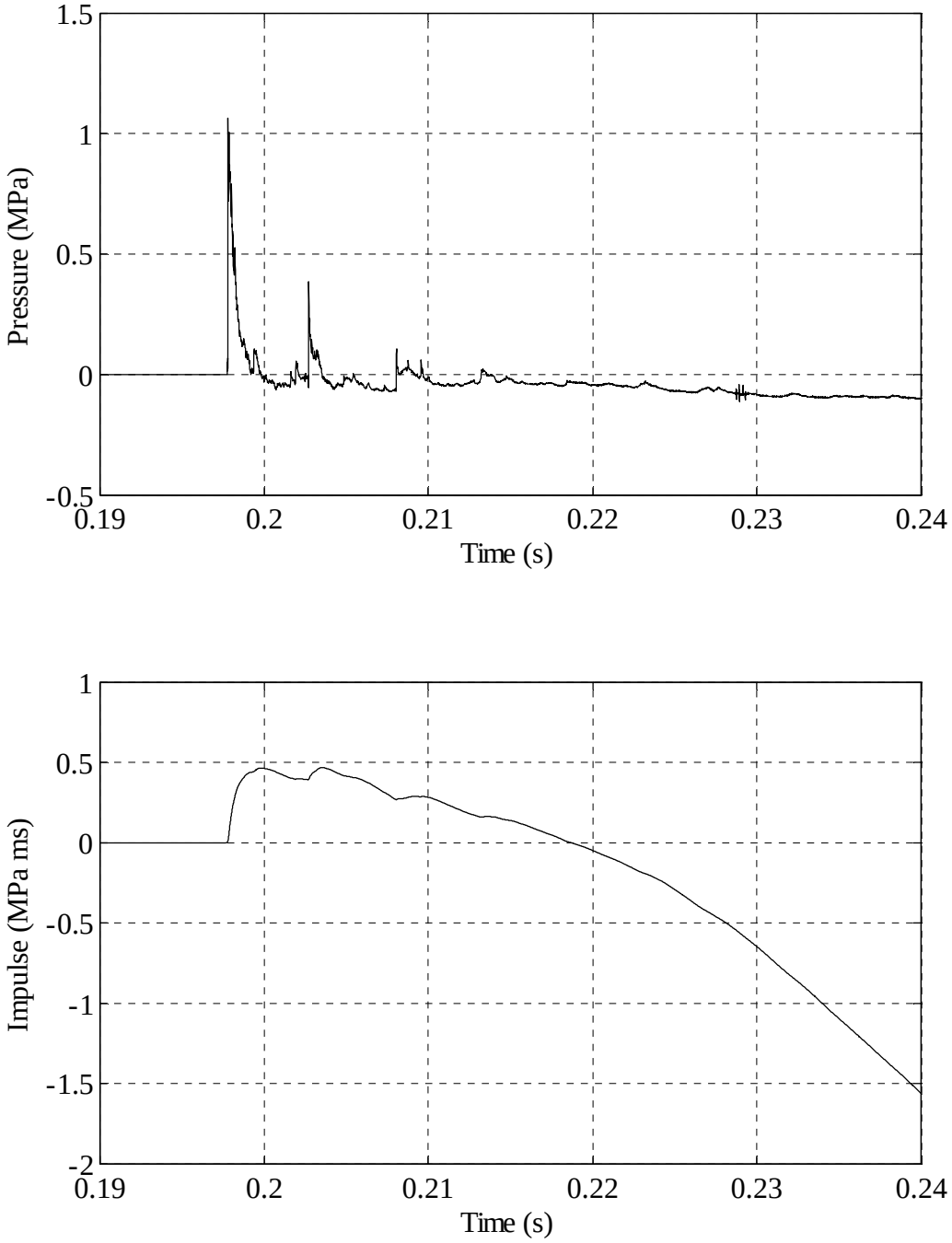

FIGURE B.3: Shot A2 - Flush mount sensor P3 pressure and impulse as a function of time.

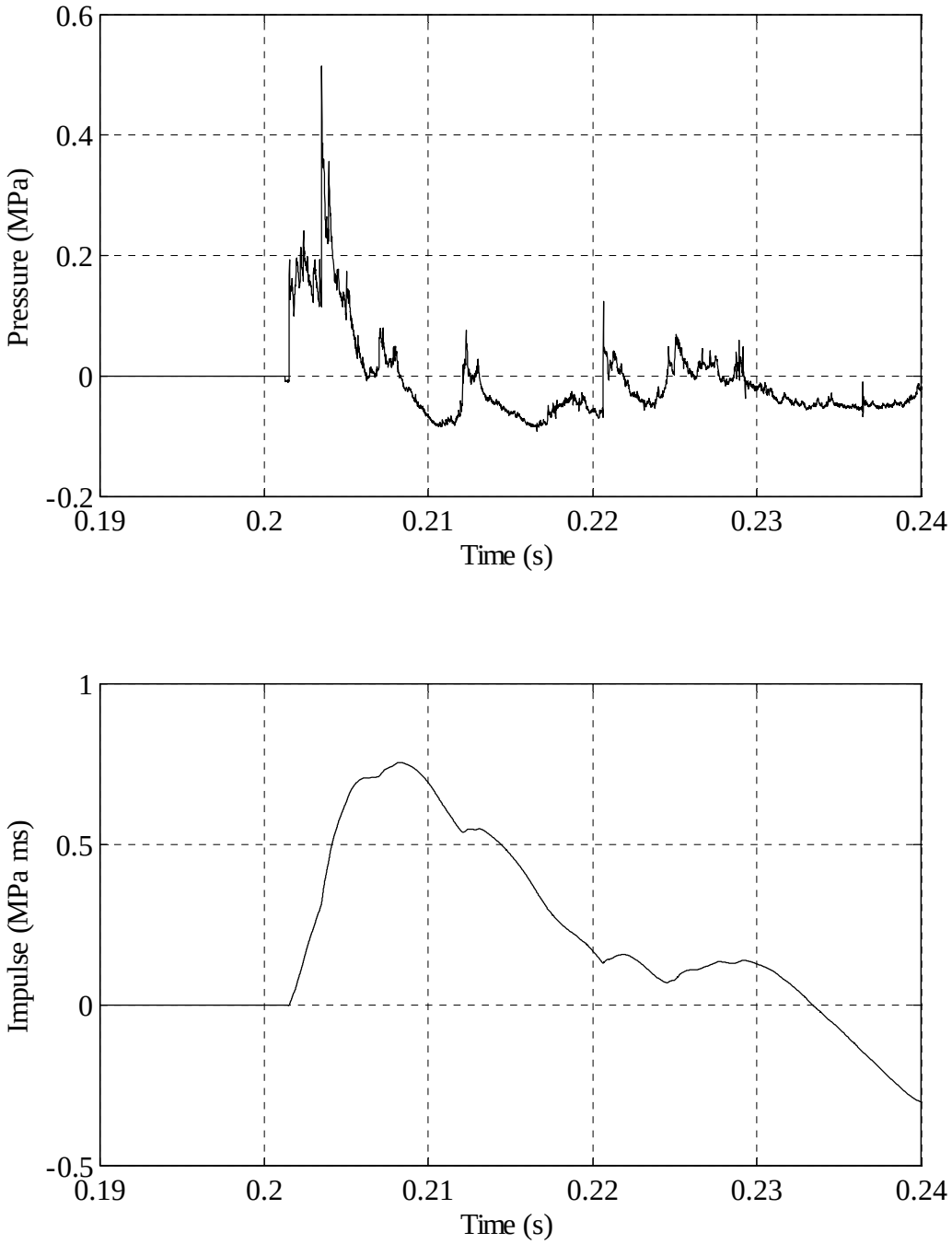

FIGURE B.4: Shot A2 - Flush mount sensor P4 pressure and impulse as a function of time.

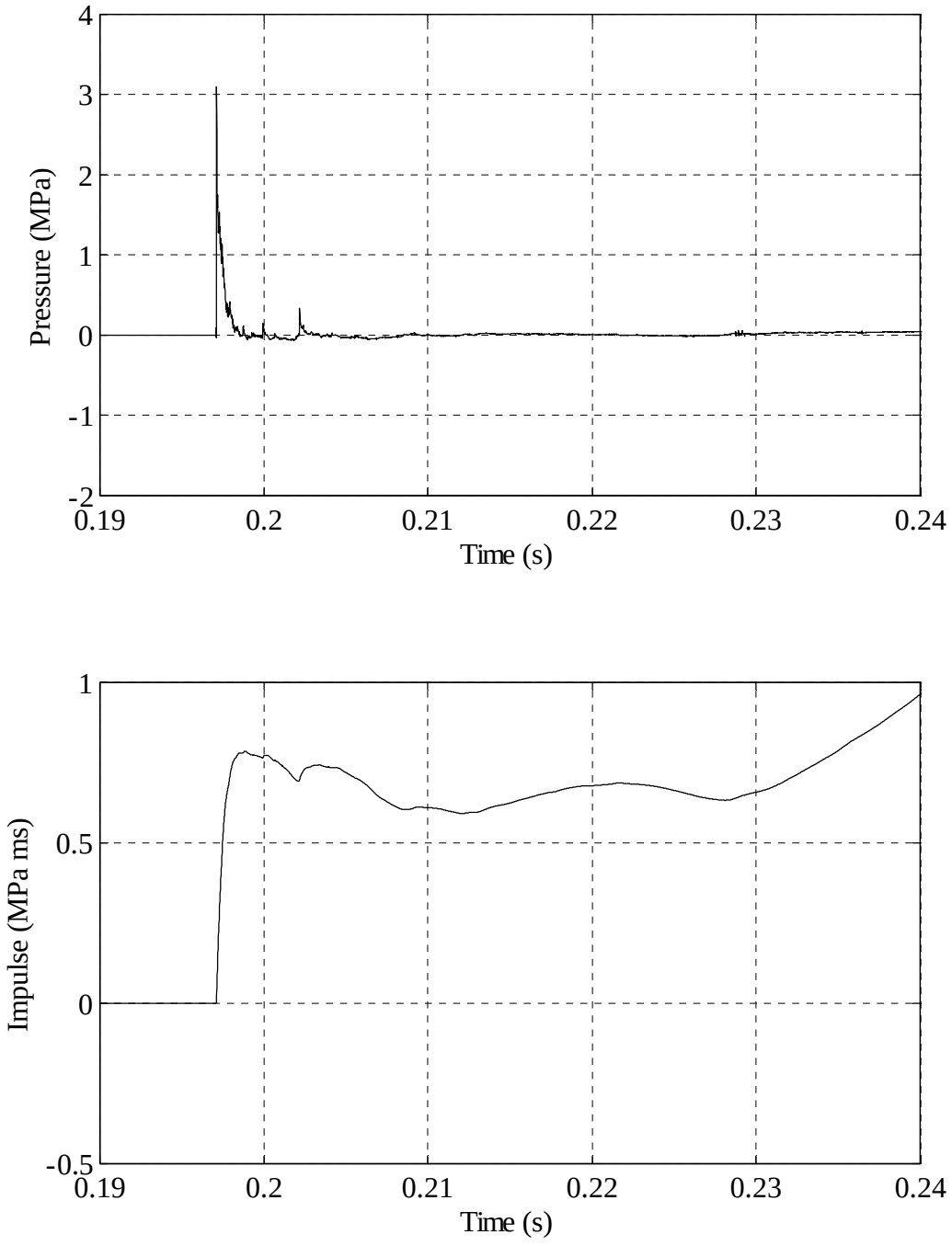

FIGURE B.5: Shot A2 - Flush mount sensor P5 pressure and impulse as a function of time.

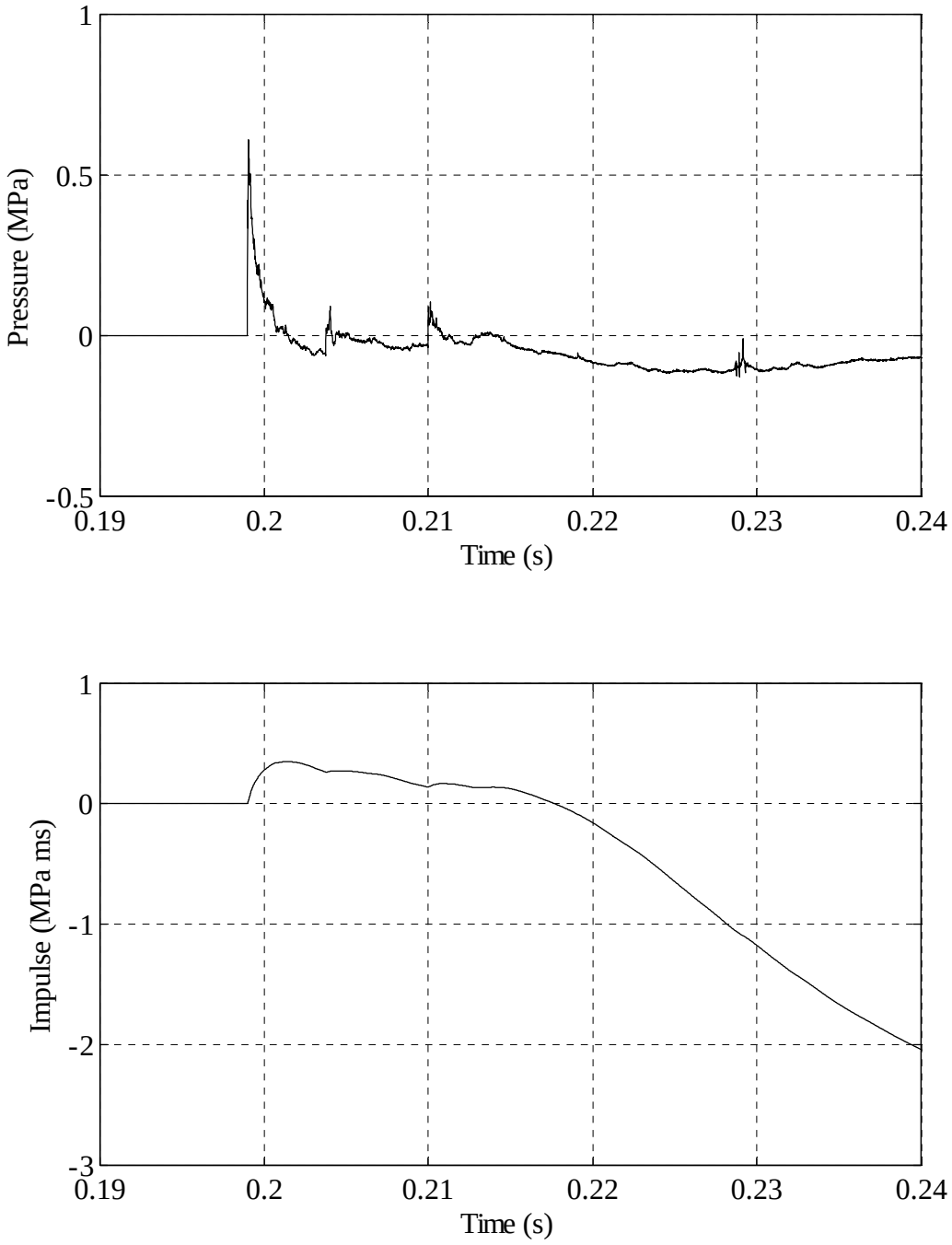

FIGURE B.6: Shot A2 - Flush mount sensor P6 pressure and impulse as a function of time.

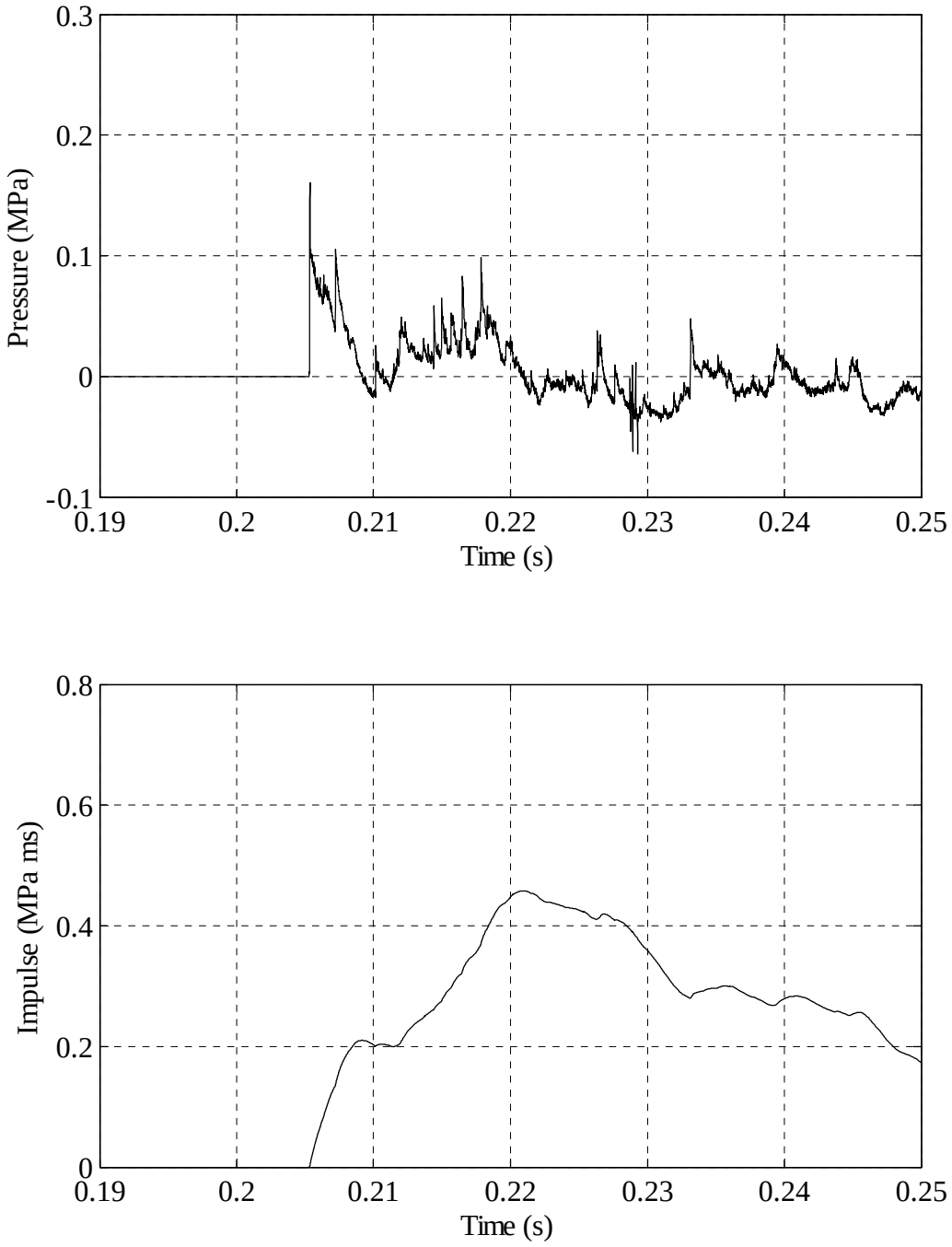

FIGURE B.7: Shot A2 - Flush mount sensor P7 pressure and impulse as a function of time.

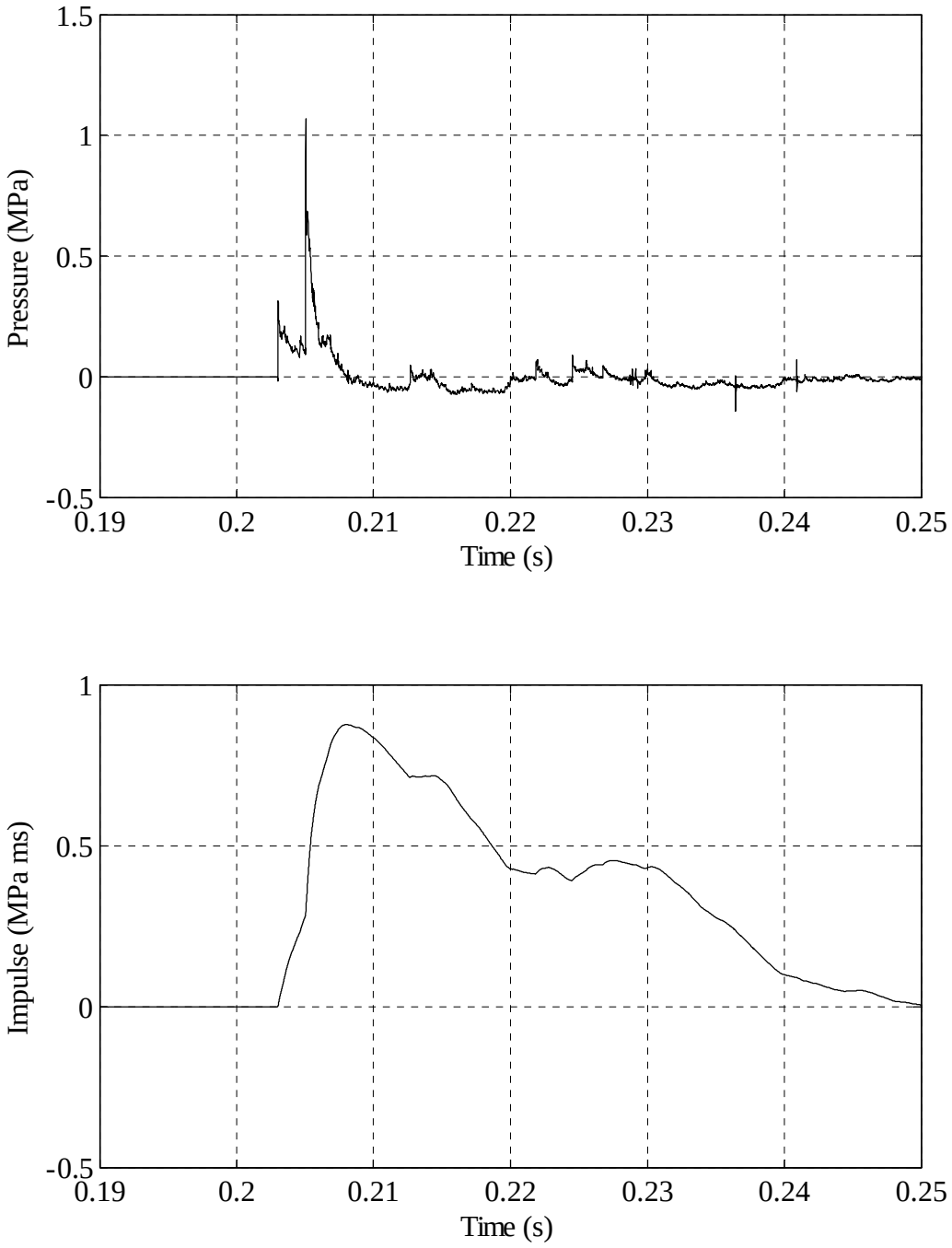

FIGURE B.8: Shot A2 - Flush mount sensor P8 pressure and impulse as a function of time.

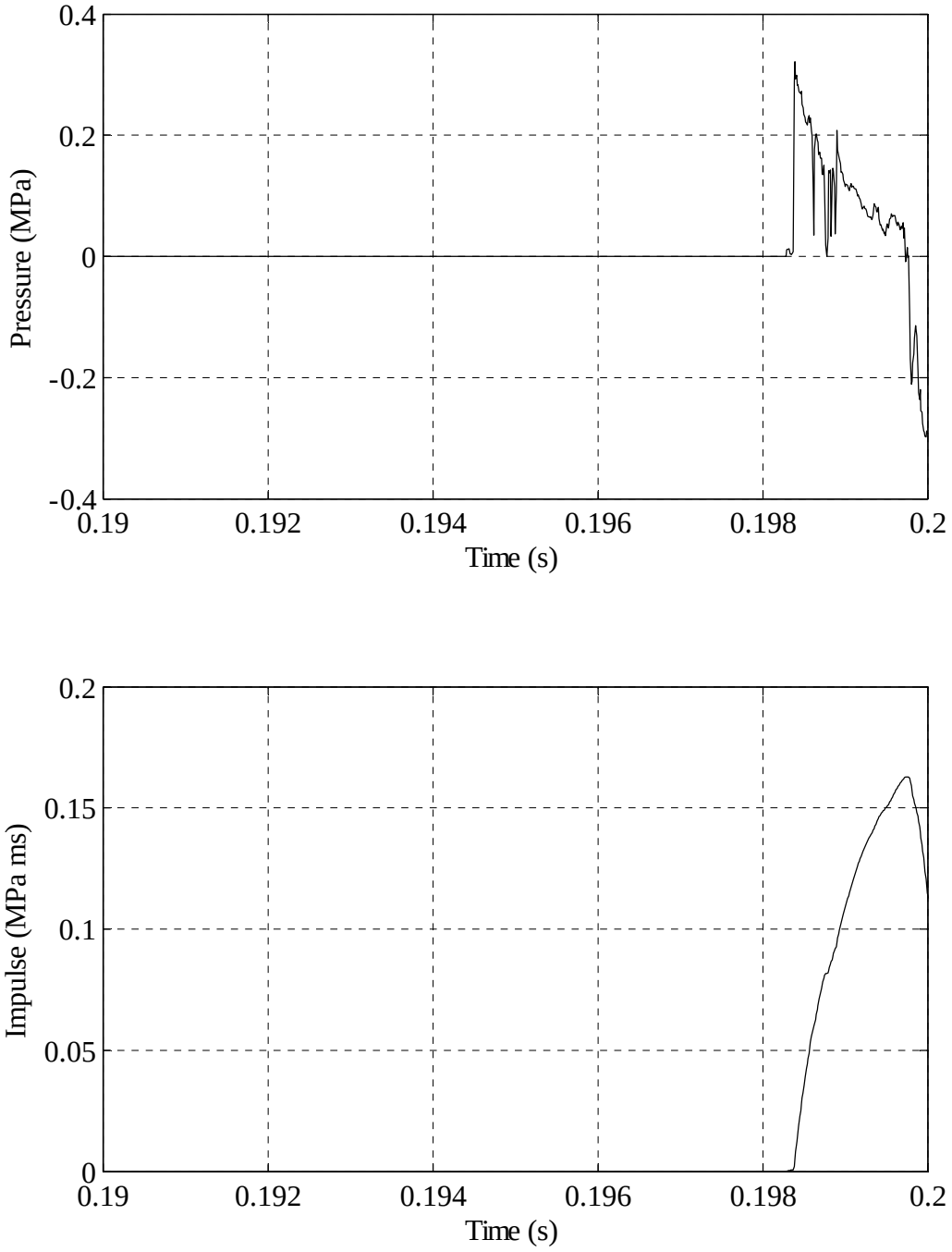

FIGURE B.9: Shot A2 - Pressure pencil PP1 pressure and impulse as a function of time.

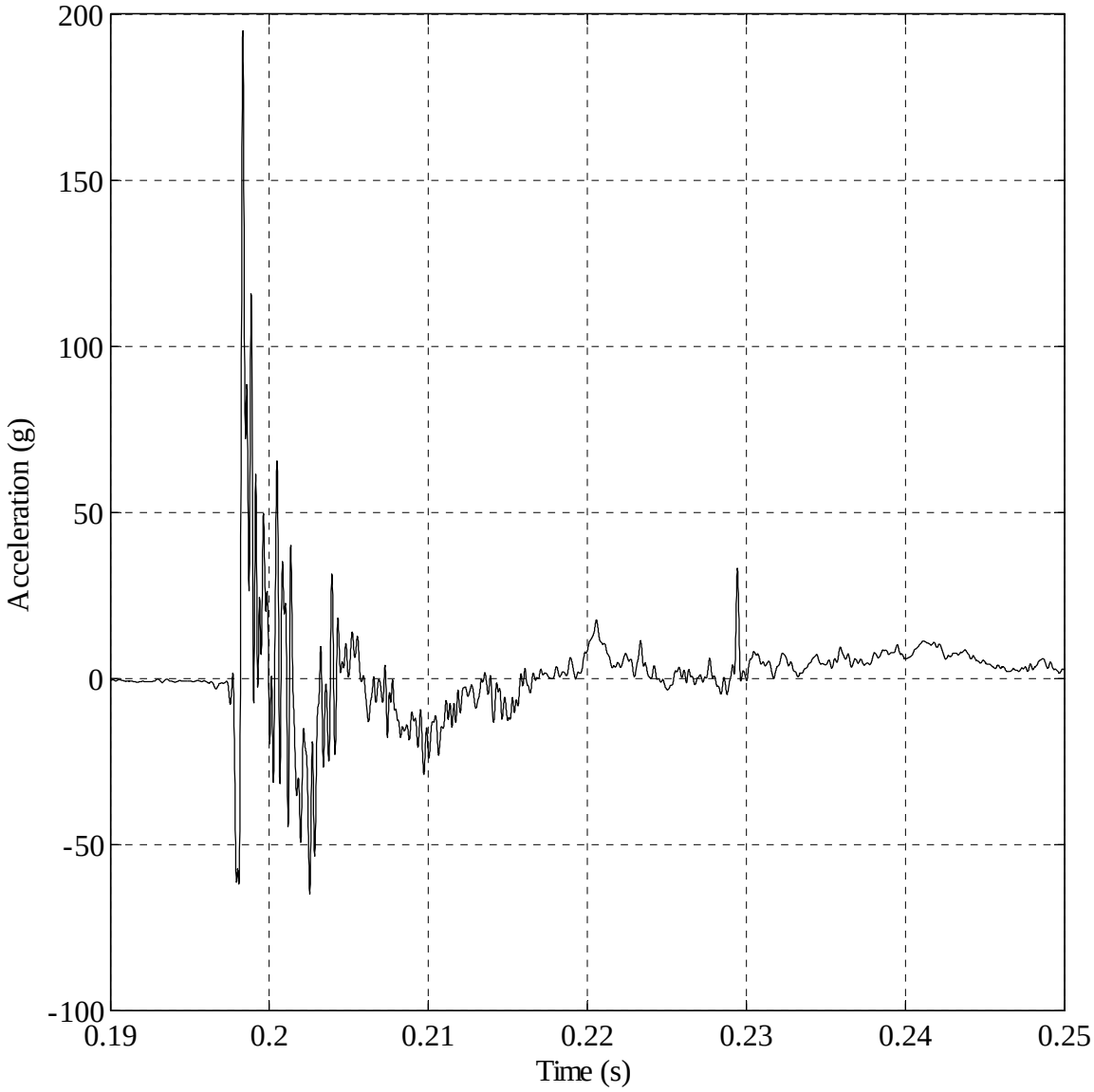

FIGURE B.10: Shot A2 - Acceleration time history measured by sensor S1.

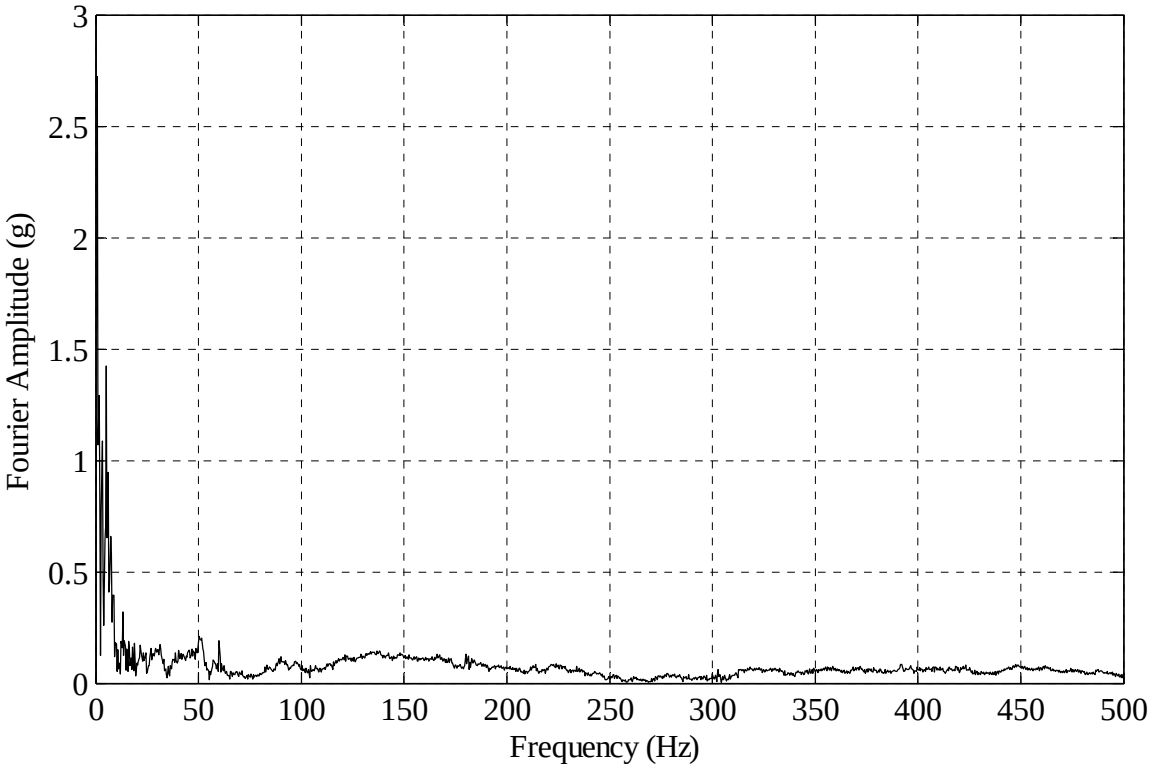

FIGURE B.11: Shot A2 - Fourier amplitude spectrum of acceleration time history measured by sensor S1.

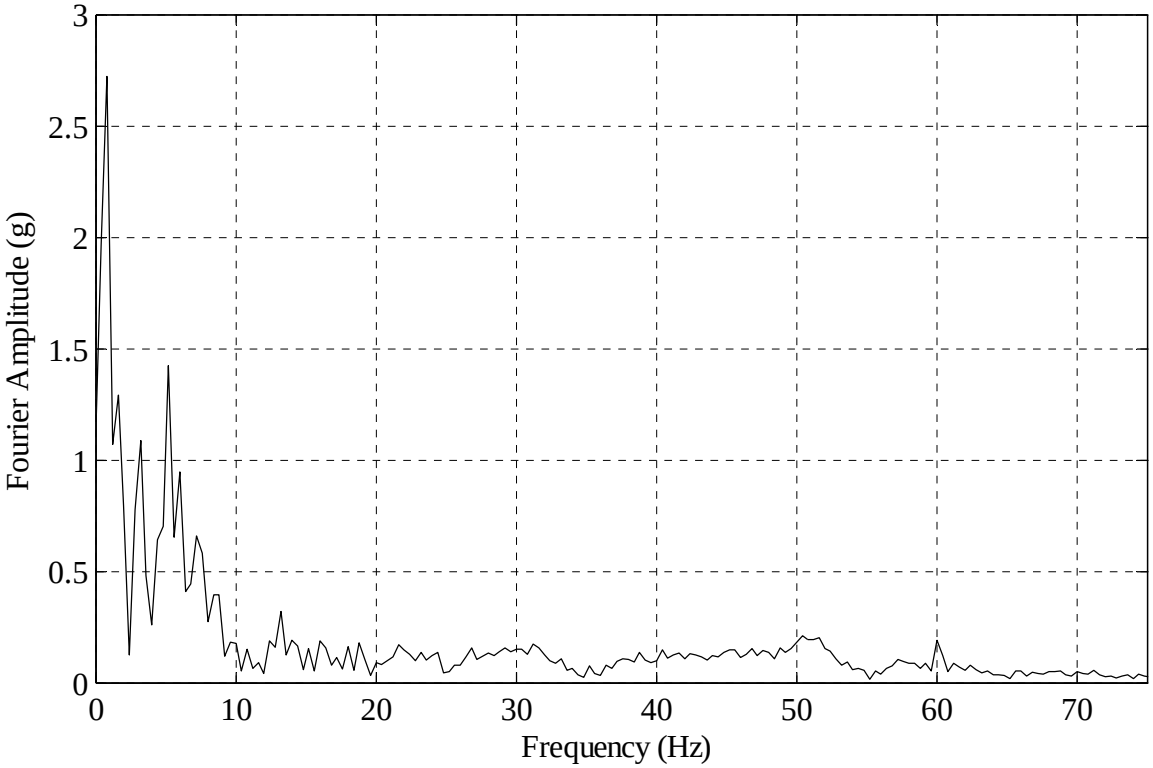

FIGURE B.12: Zoomed in window showing lower frequencies from Figure B.11.

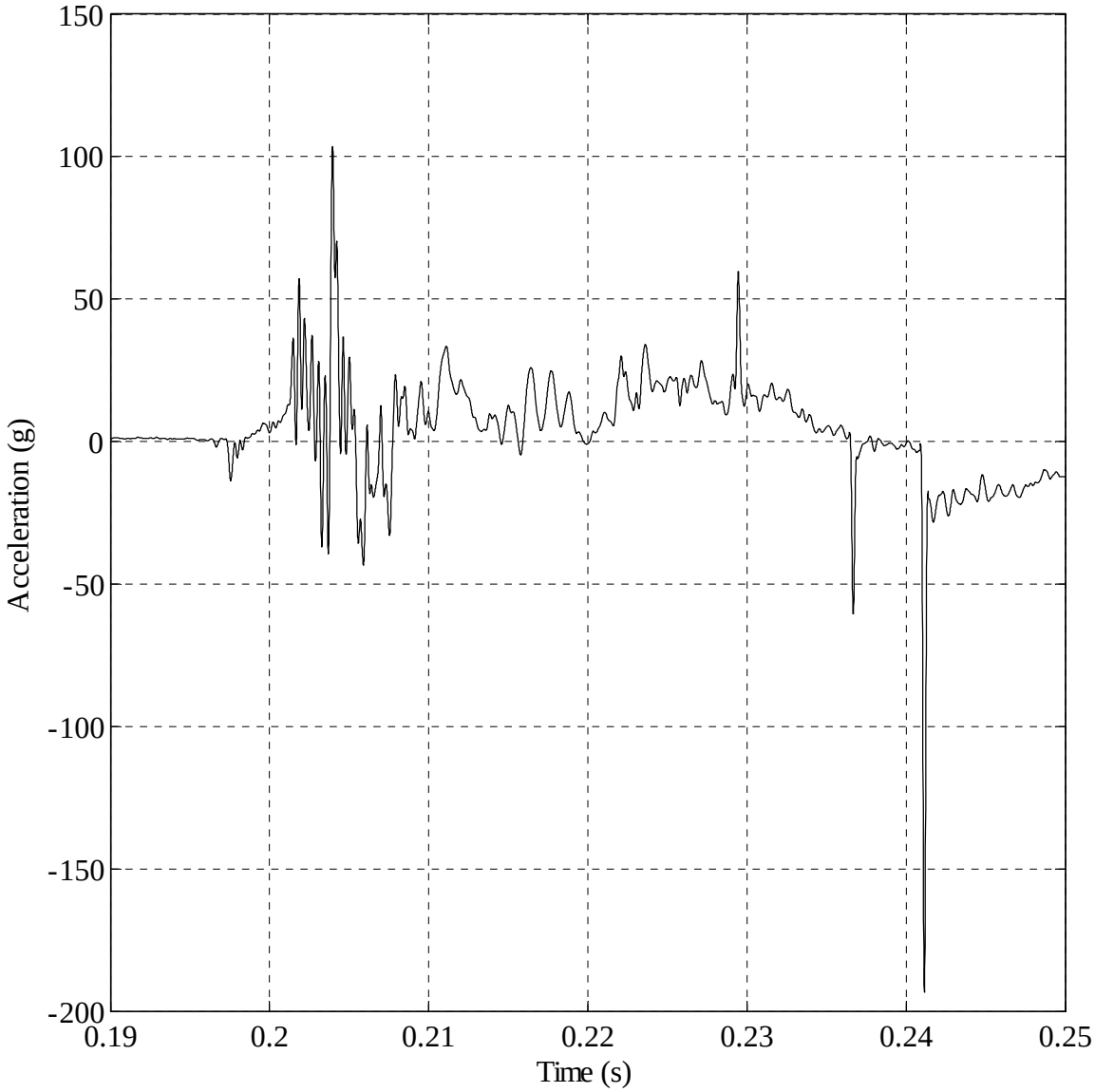

FIGURE B.13: Shot A2 - Acceleration time history measured by sensor S2.

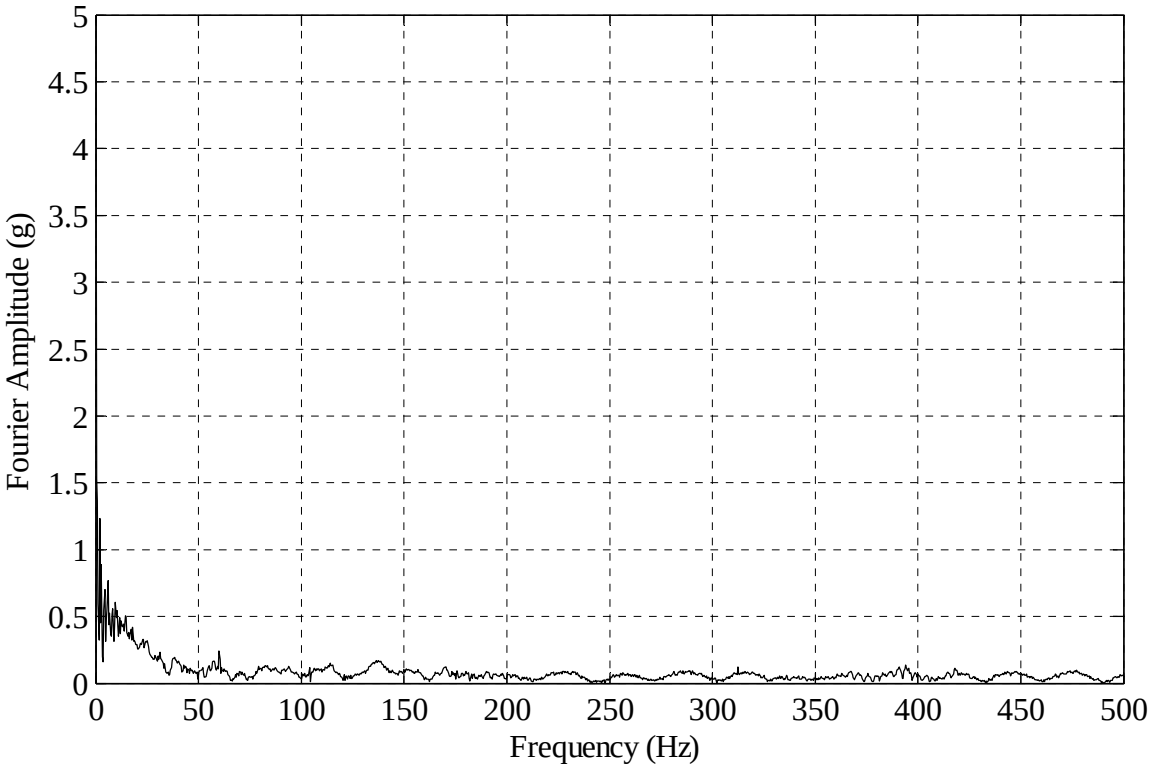

FIGURE B.14: Shot A2 - Fourier amplitude spectrum of acceleration time history measured by sensor S2.

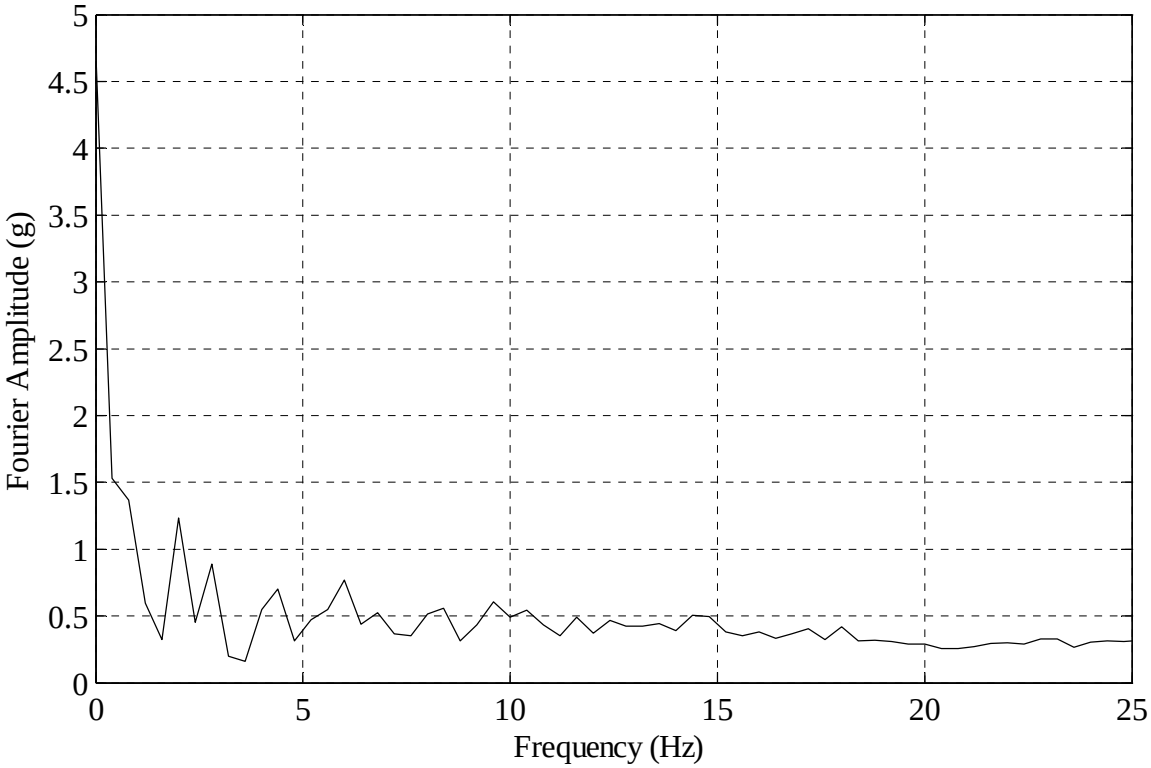

FIGURE B.15: Zoomed in window showing lower frequencies from Figure B.14.

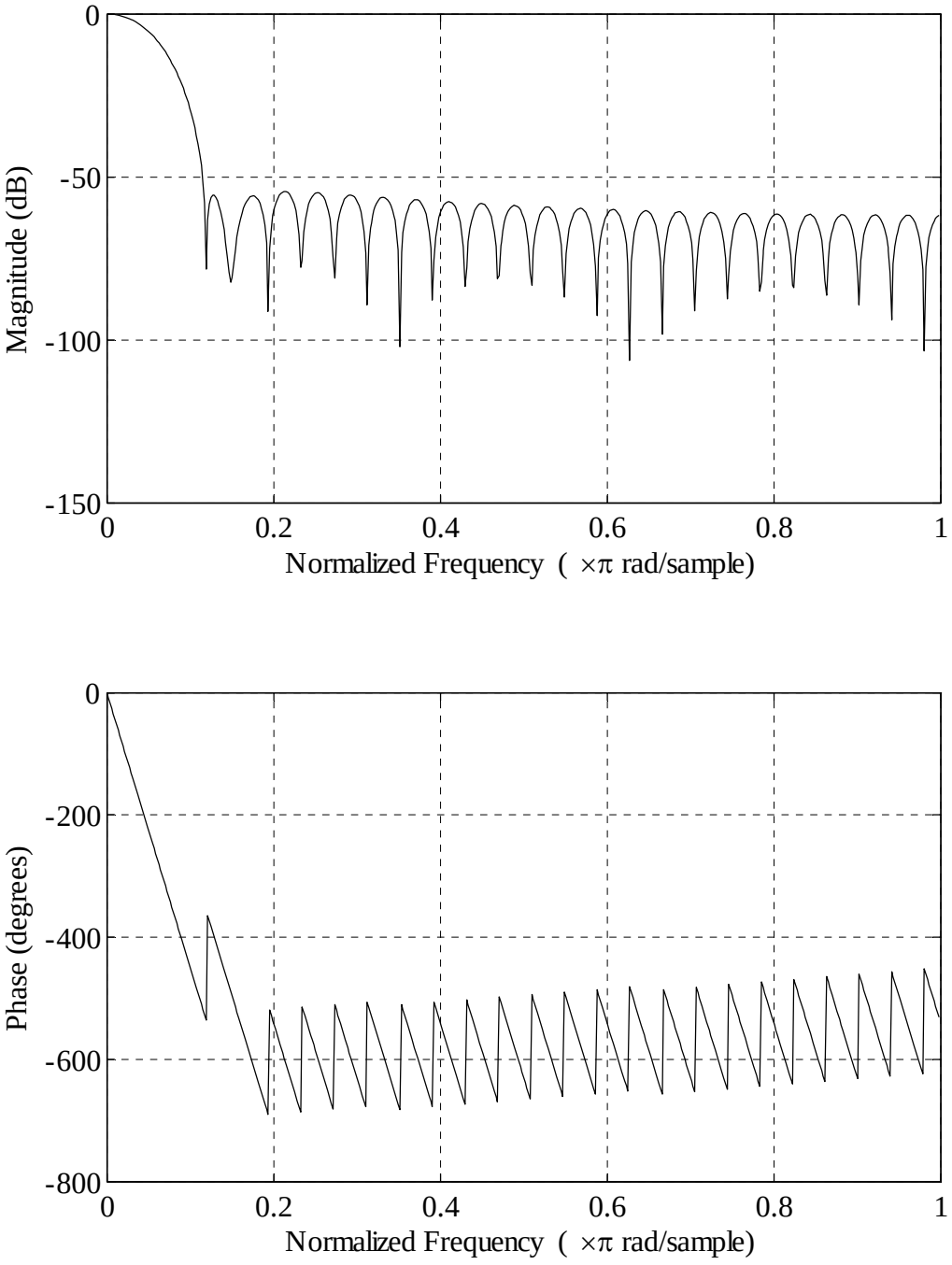

FIGURE B.16: Response of Matlab filter used to post-process shock accelerometer data. Note that in normalized frequency, 1.0 corresponds to the Nyquist frequency (50 kHz in this case).

APPENDIX C: SHOT B SENSOR MEASUREMENTS

This appendix contains plots for all sensor measurements from Shot B. Measurements have been plotted on a common time window, where the beginning of the time window is an arbitrarily selected point preceding the detonation of the charge. All time history data are plotted starting at time = 0.095 seconds (regardless of whether tick mark is shown or not).

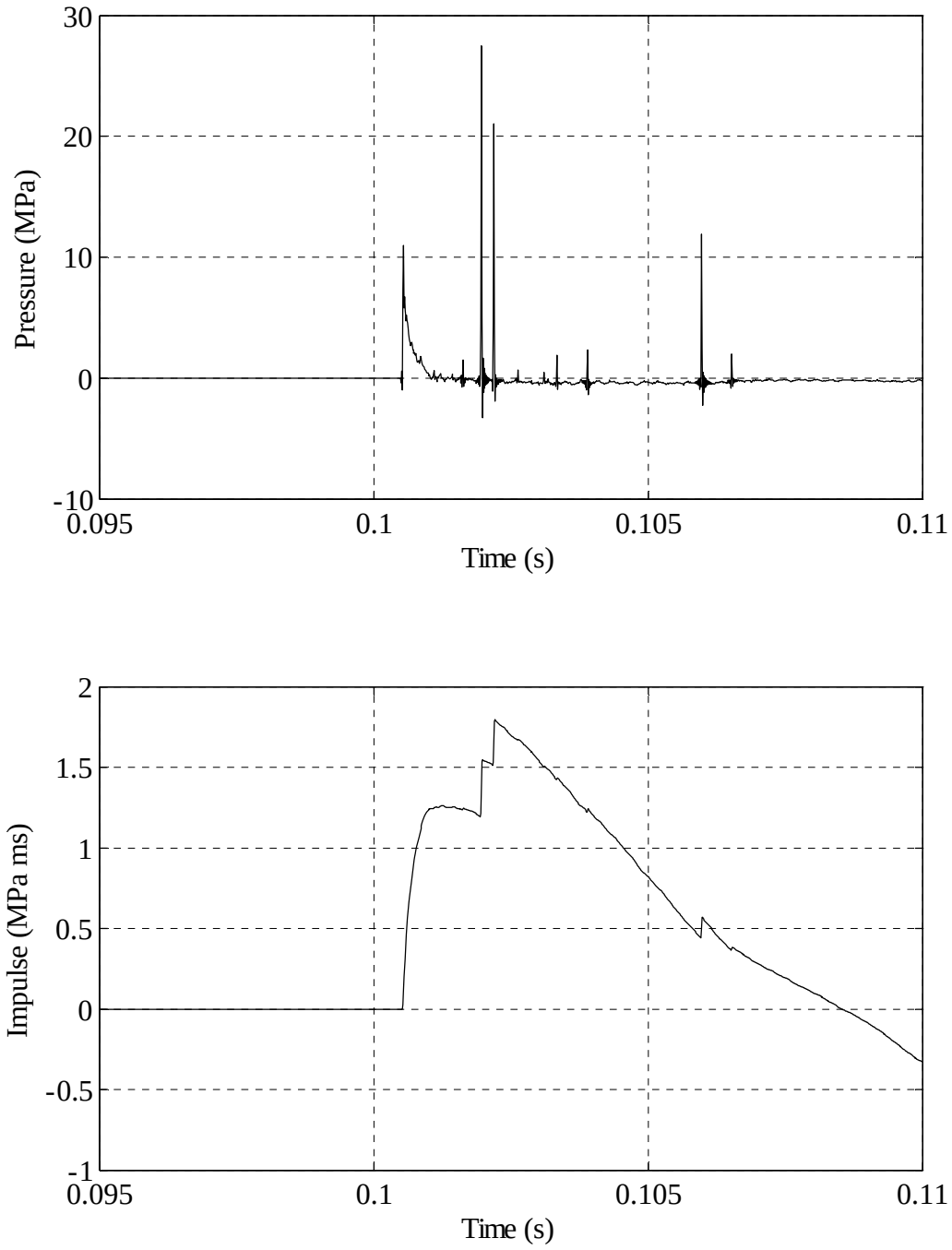

FIGURE C.1: Shot B - Flush mount sensor P1 pressure and impulse as a function of time. Subsequent spikes after first pressure wave appear to be nonphysical, likely cable or connection damage.

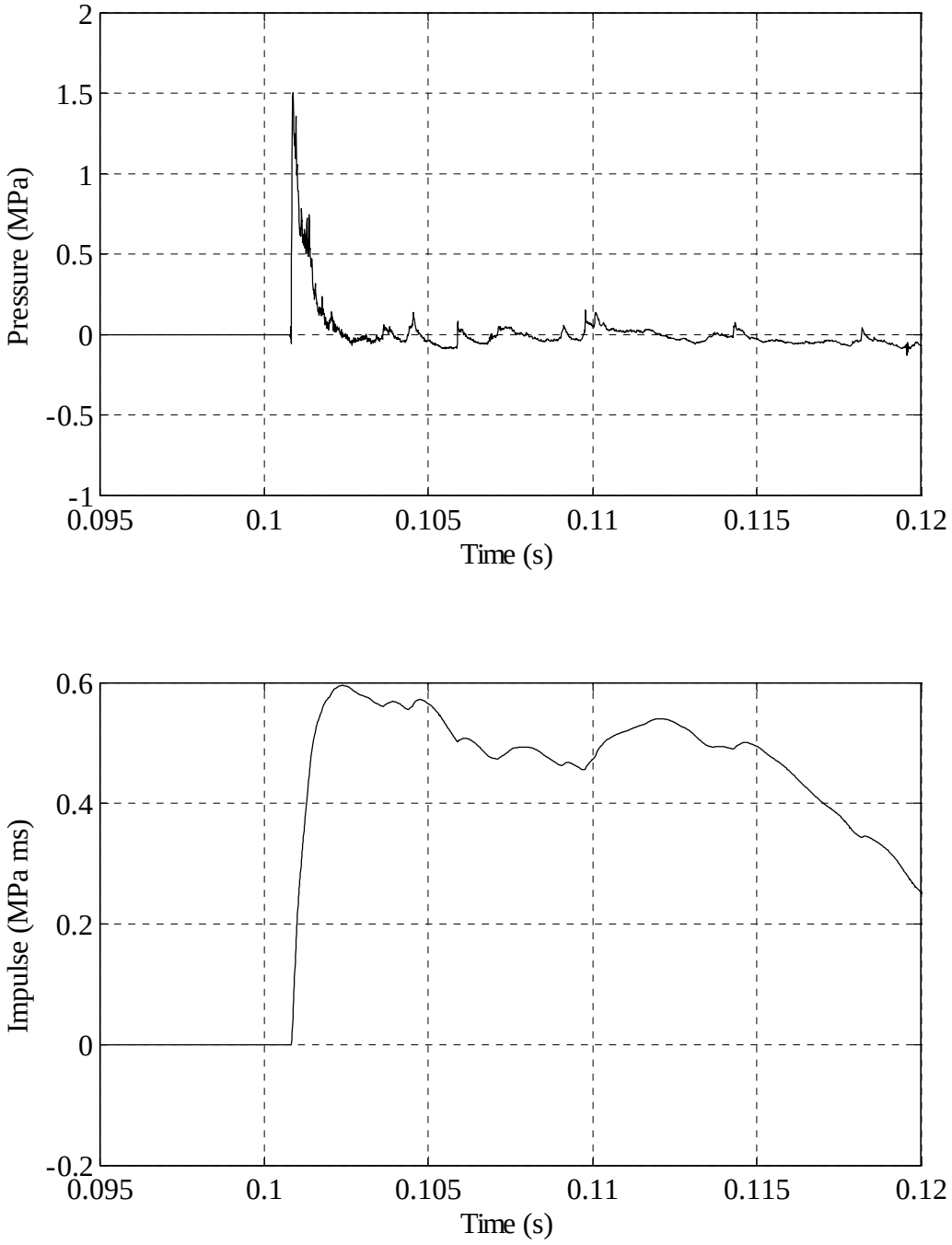

FIGURE C.2: Shot B - Flush mount sensor P2 pressure and impulse as a function of time.

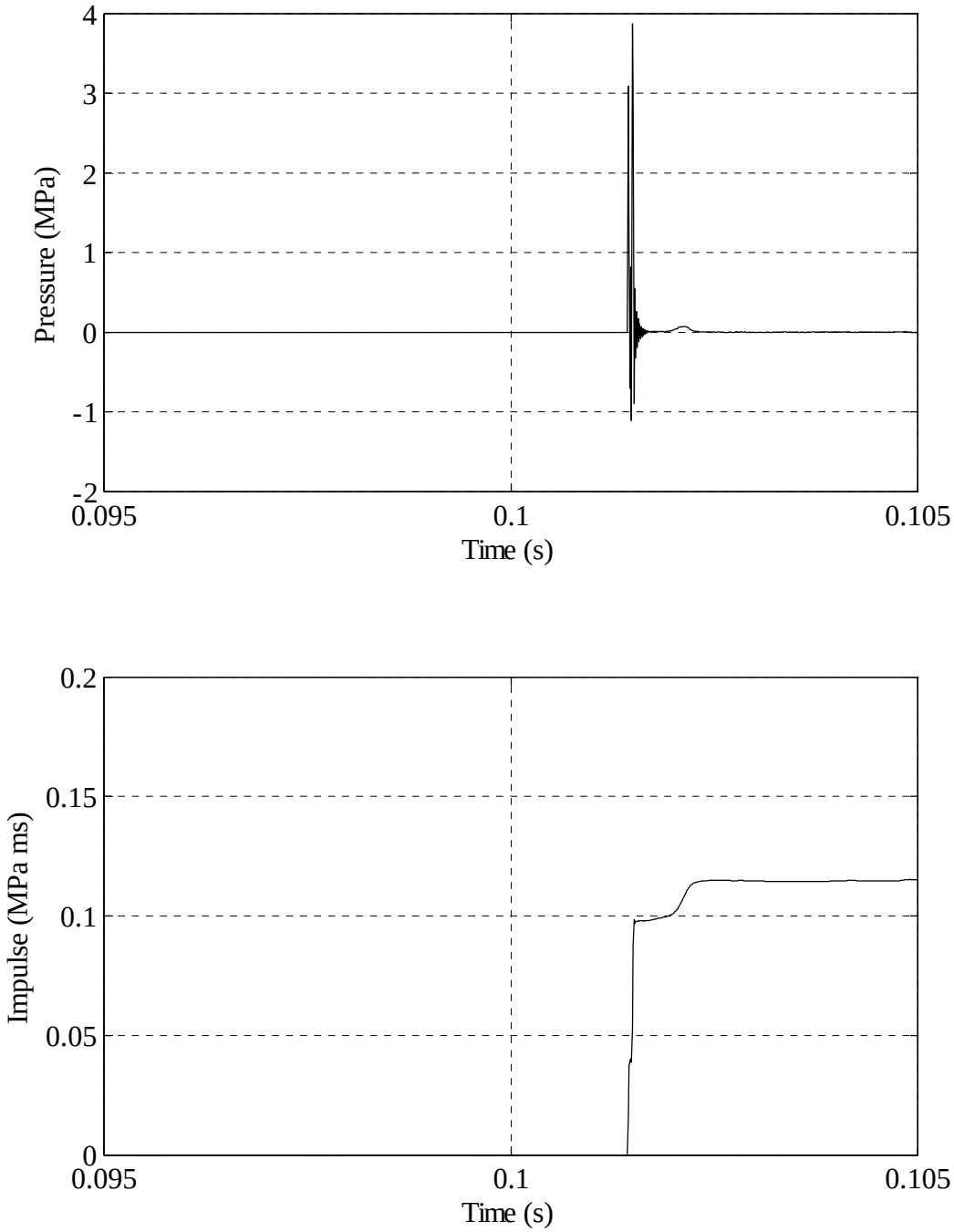

FIGURE C.3: Shot B - Flush mount sensor P3 pressure and impulse as a function of time. Close inspection of time series shows that measurement is non-physical. Either cable/connector damage or sensor damage from prior shot.

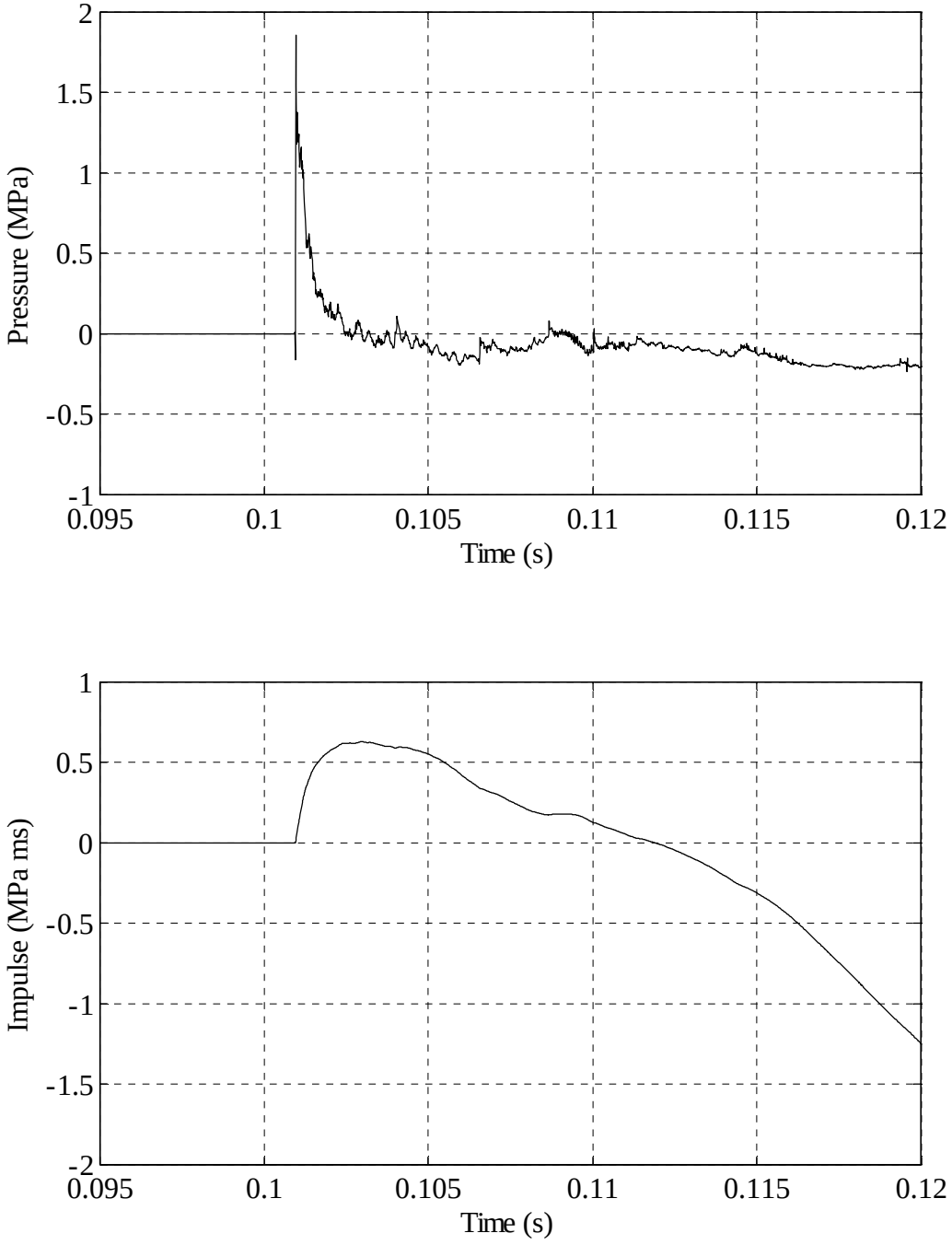

FIGURE C.4: Shot B - Flush mount sensor P4 pressure and impulse as a function of time.

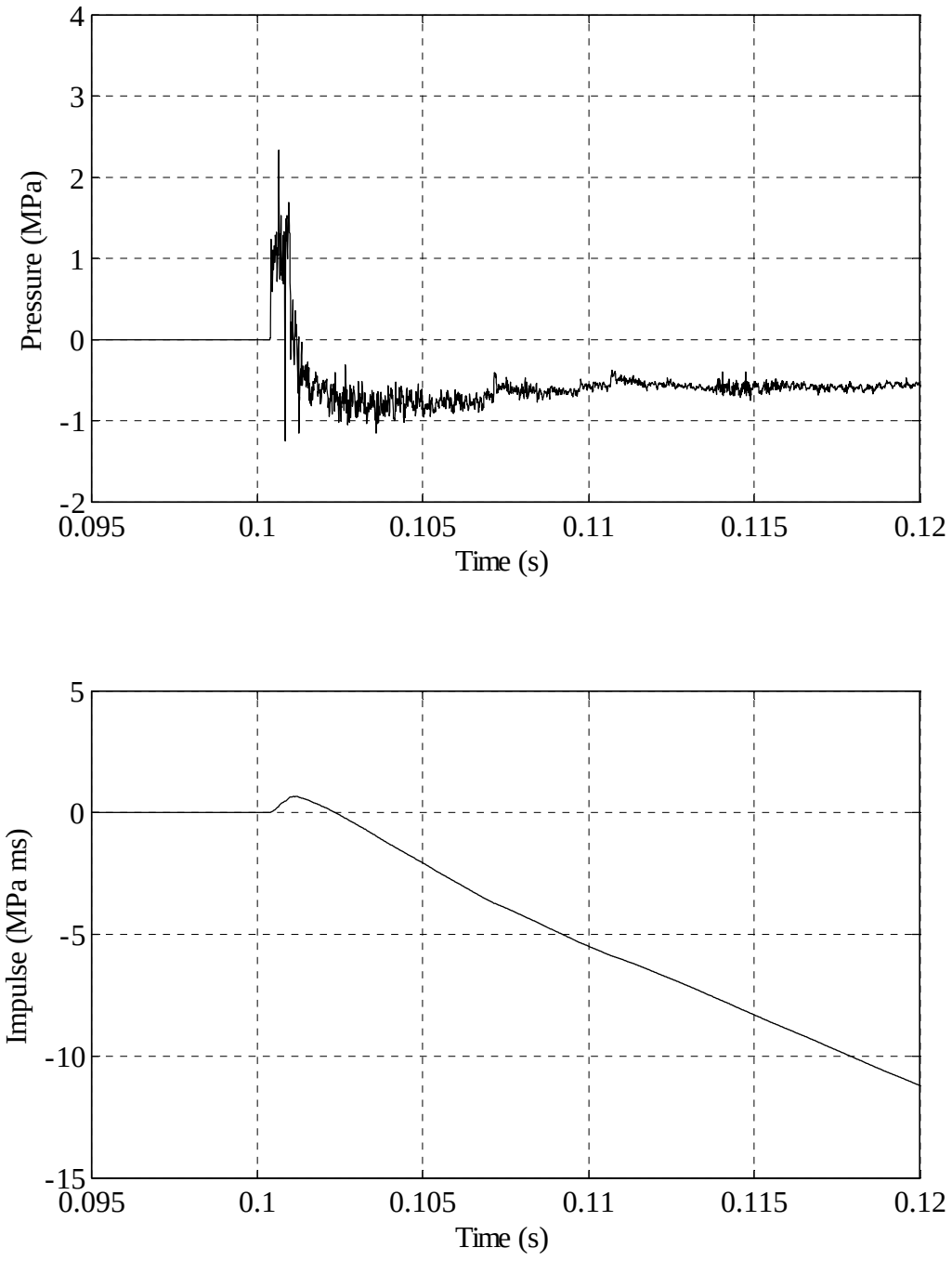

FIGURE C.5: Shot B - Flush mount sensor P5 pressure and impulse as a function of time.

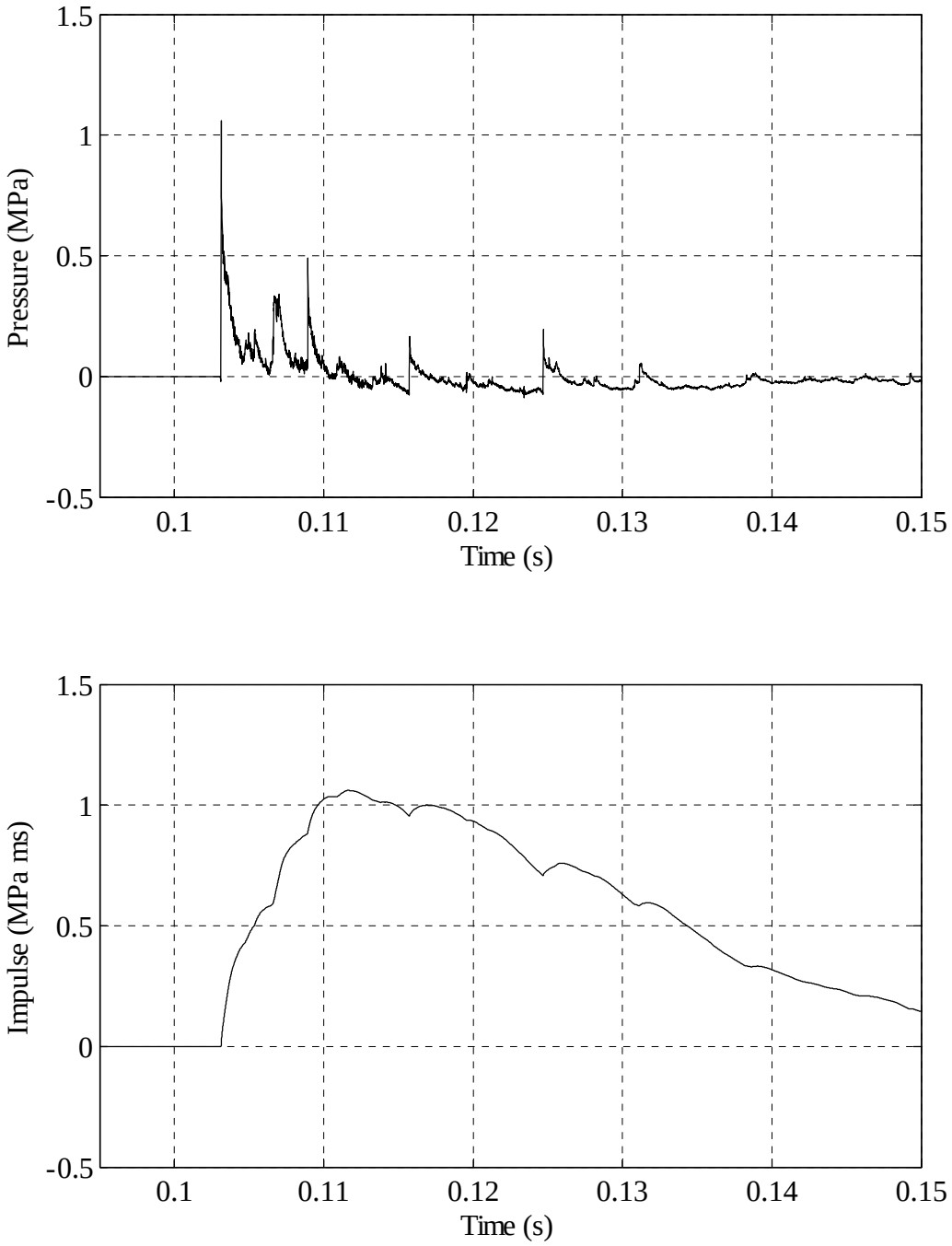

FIGURE C.6: Shot B - Flush mount sensor P6 pressure and impulse as a function of time.

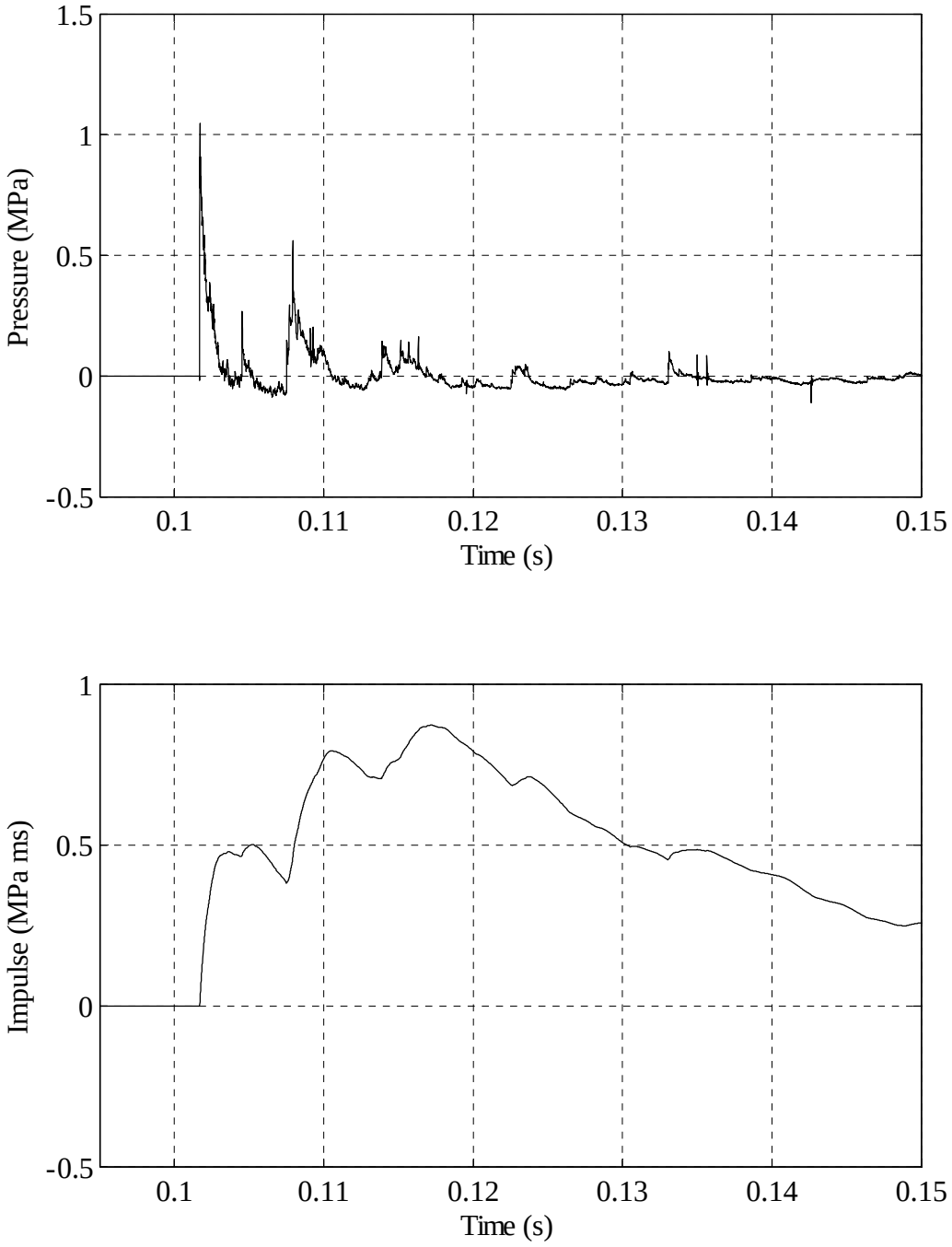

FIGURE C.7: Shot B - Flush mount sensor P7 pressure and impulse as a function of time.

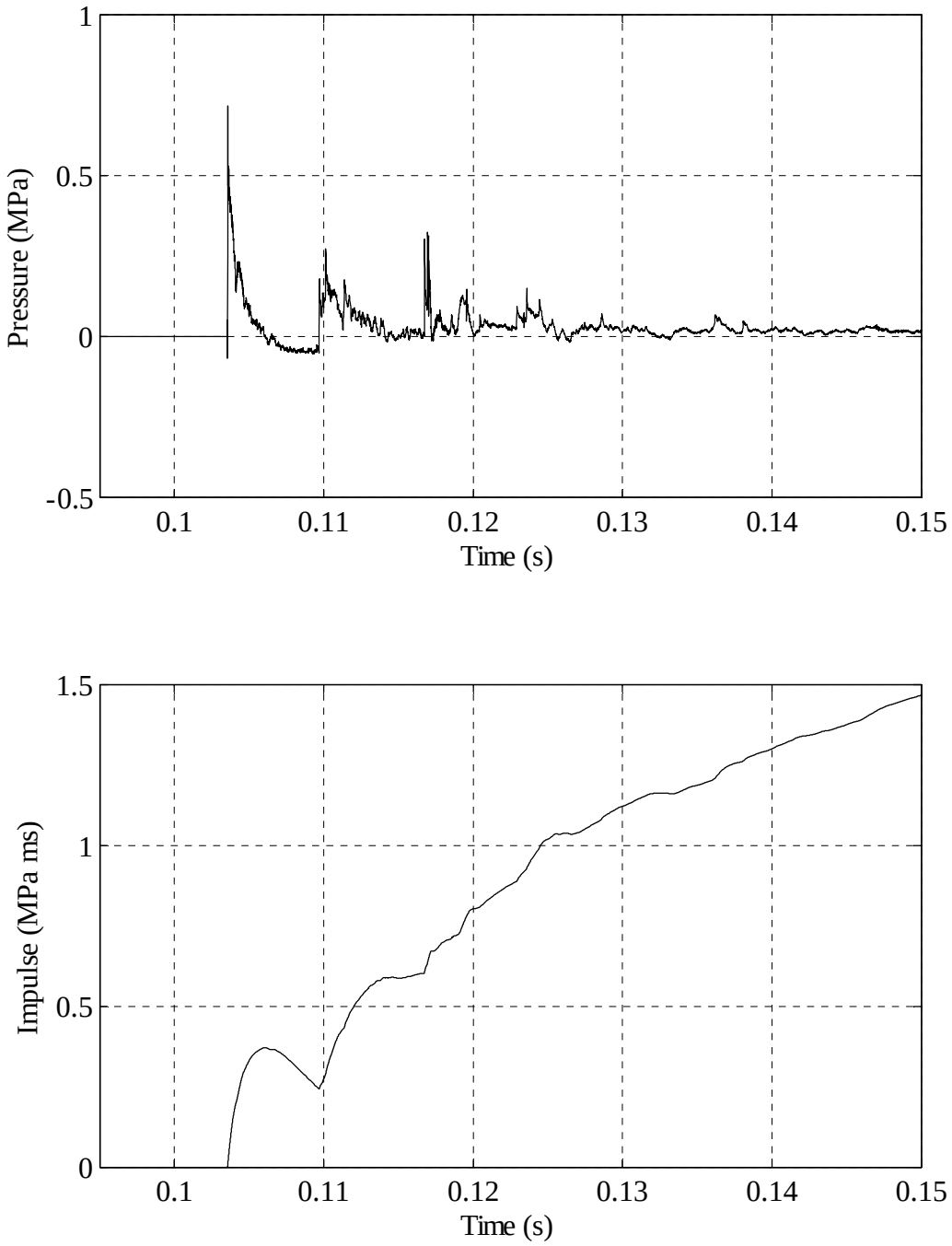

FIGURE C.8: Shot B - Flush mount sensor P8 pressure and impulse as a function of time. Only first two reflected waves included in impulse computation included in Chapter 2.

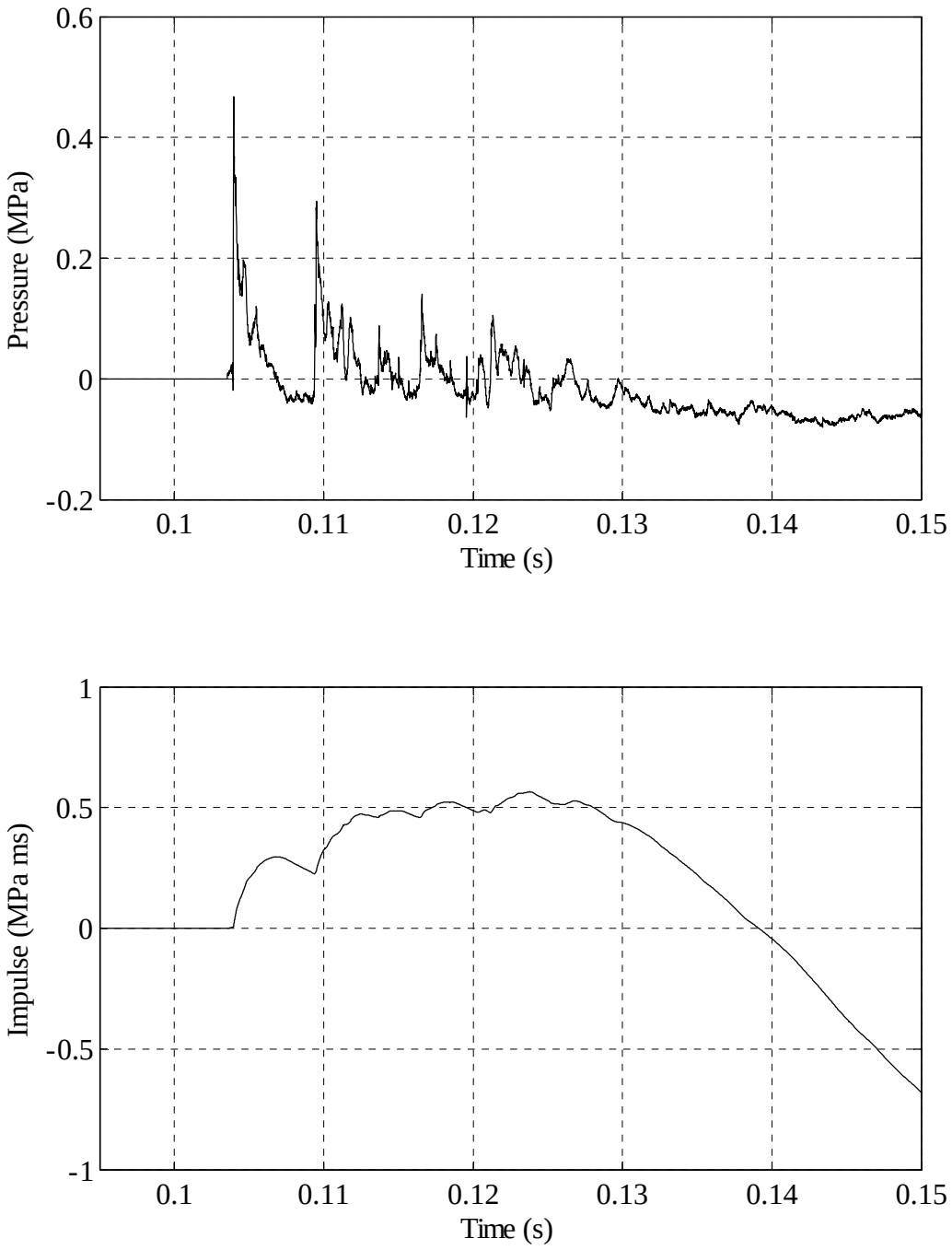

FIGURE C.9: Shot B - Flush mount sensor P9 pressure and impulse as a function of time.

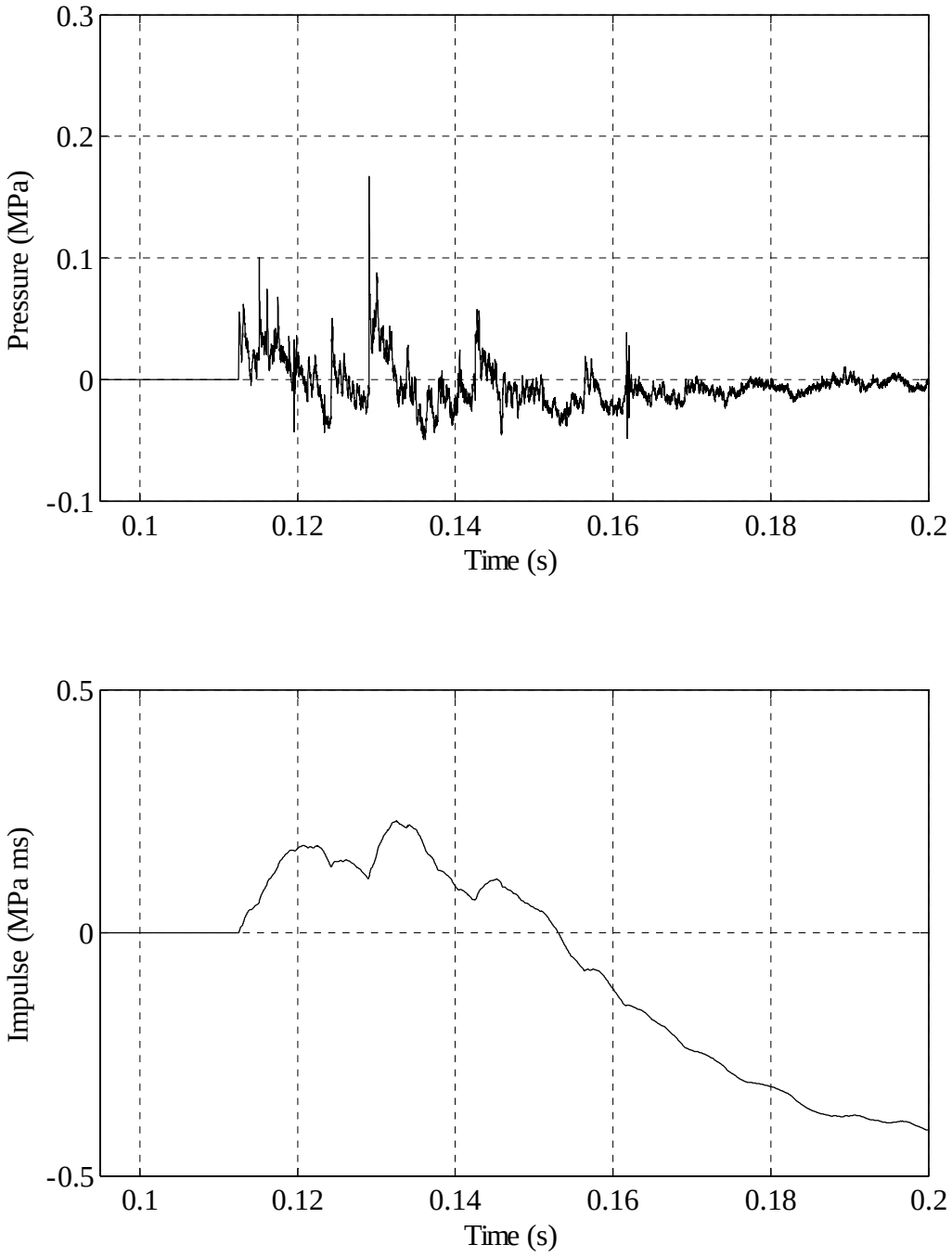

FIGURE C.10: Shot B - Flush mount sensor P10 pressure and impulse as a function of time.

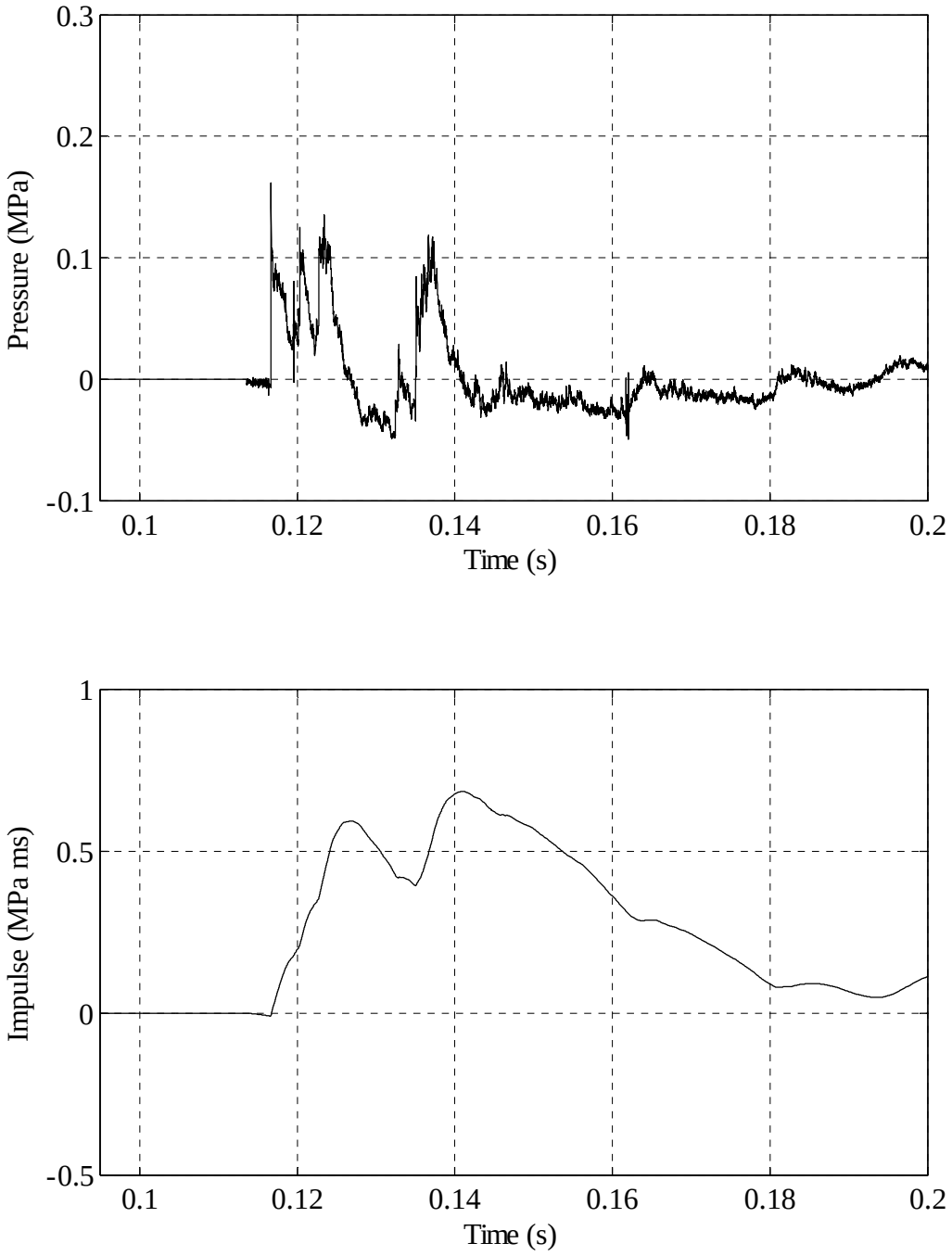

FIGURE C.11: Shot B - Flush mount sensor P11 pressure and impulse as a function of time.

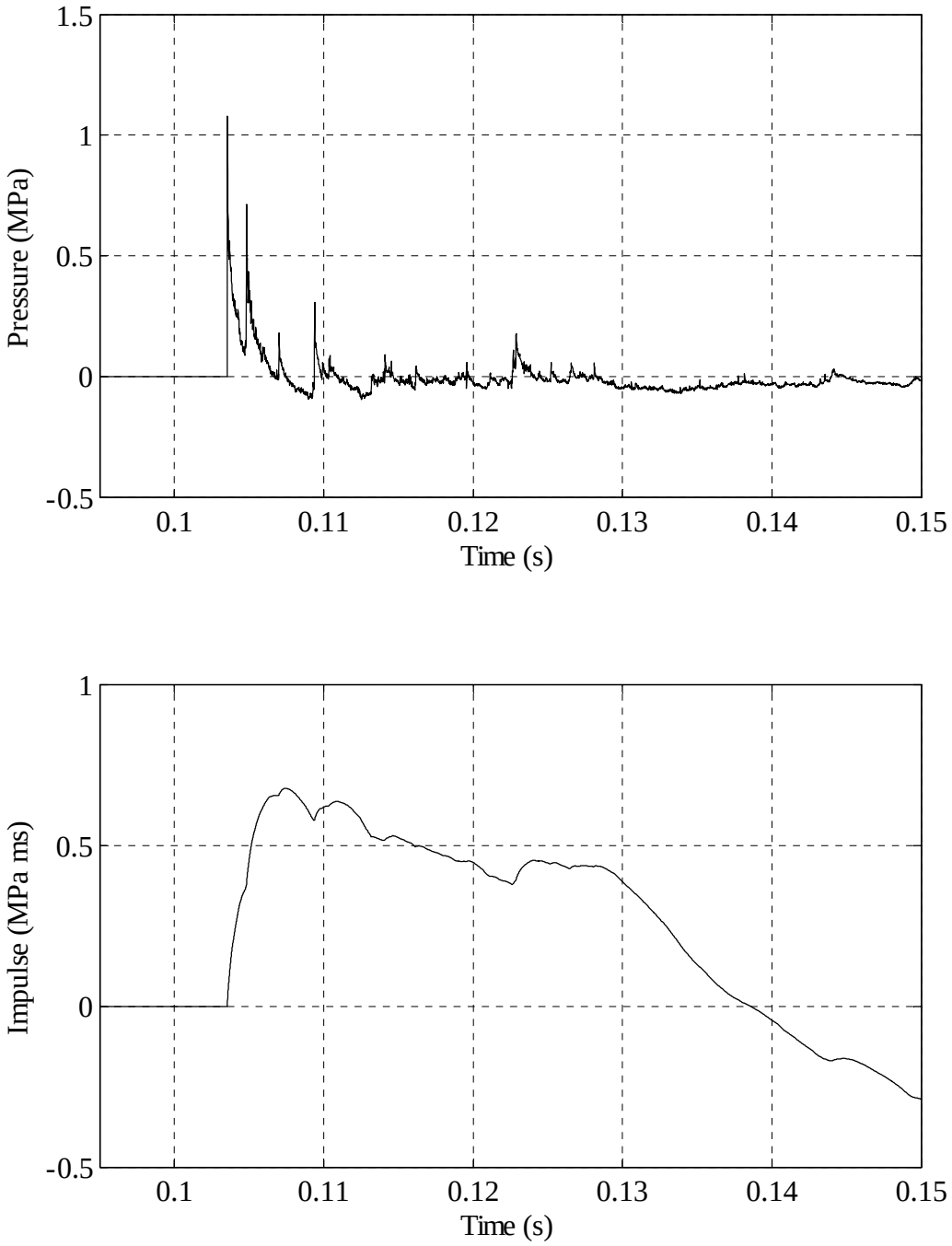

FIGURE C.12: Shot B - Flush mount sensor P12 pressure and impulse as a function of time.

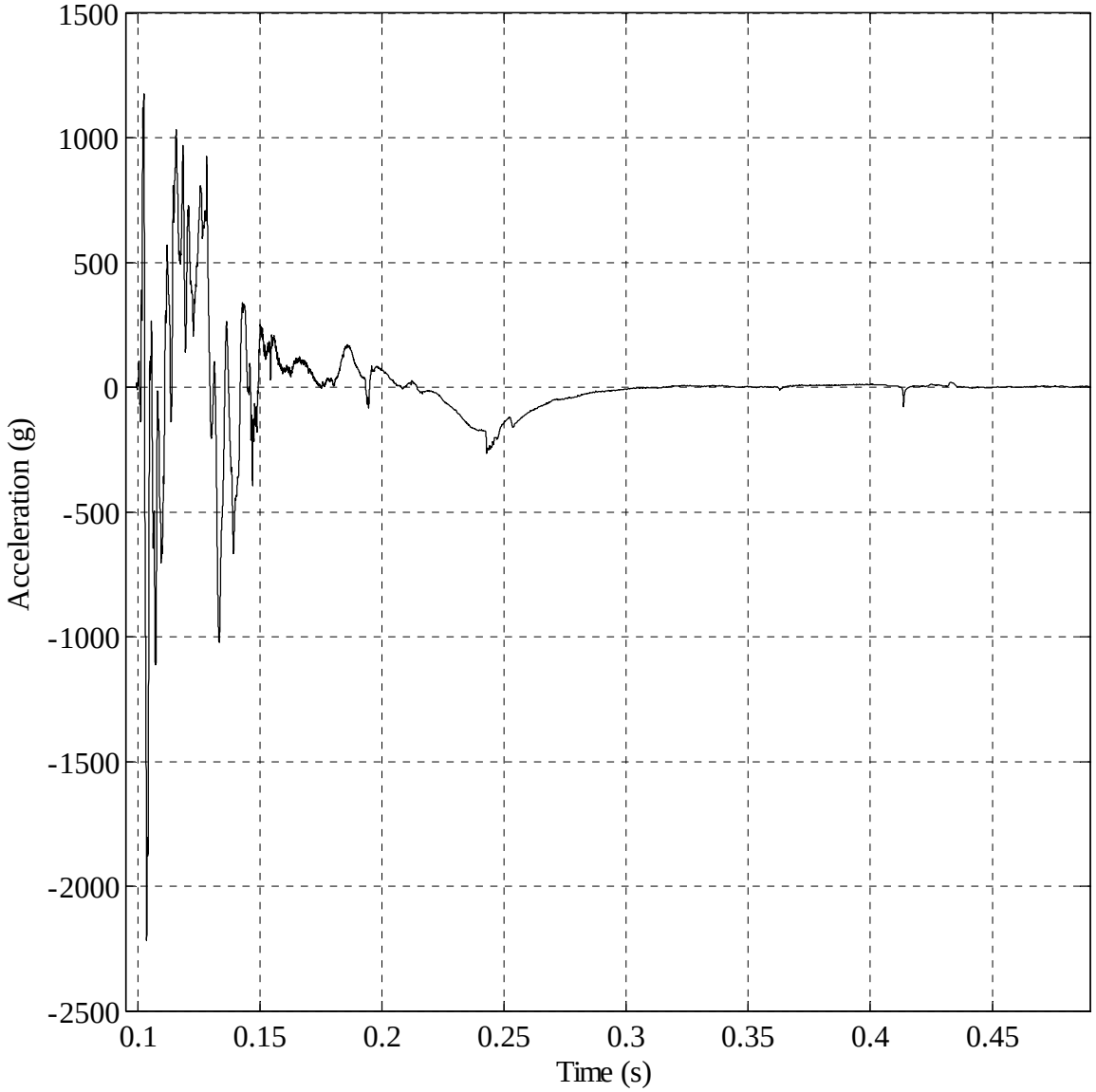

FIGURE C.13: Shot B - Acceleration time history measured by sensor S1.

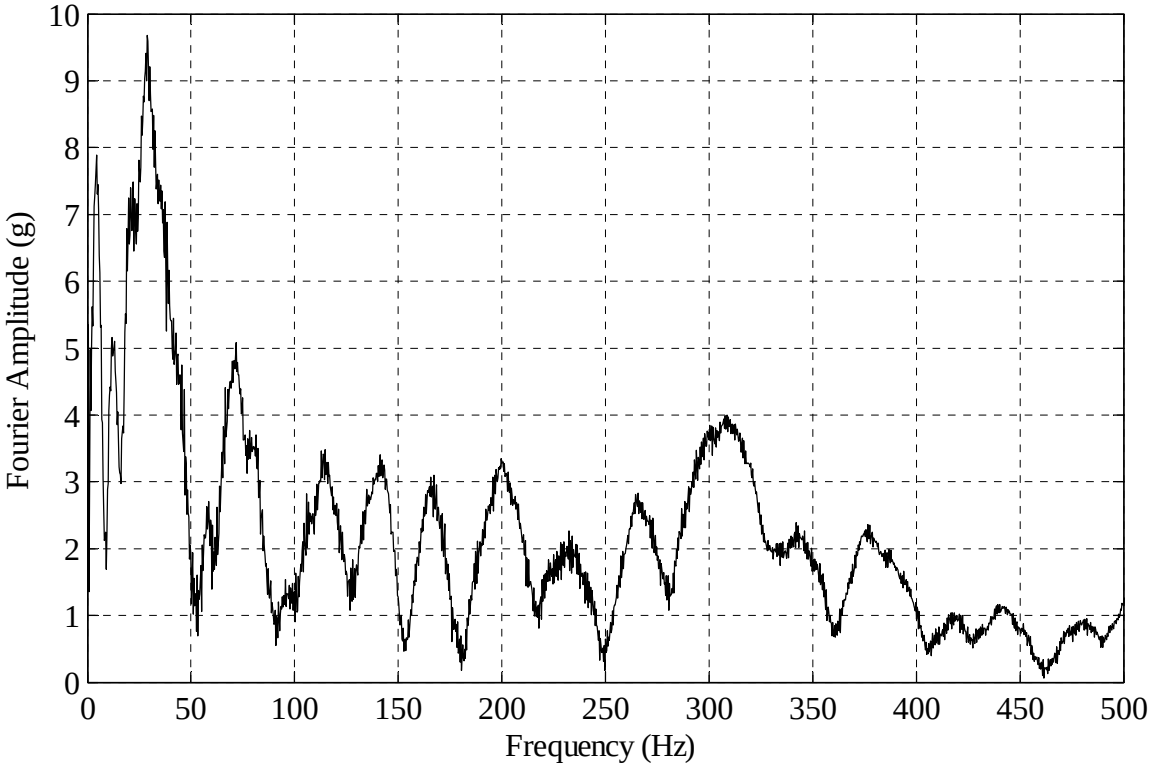

FIGURE C.14: Shot B - Fourier amplitude spectrum of acceleration time history measured by sensor S1.

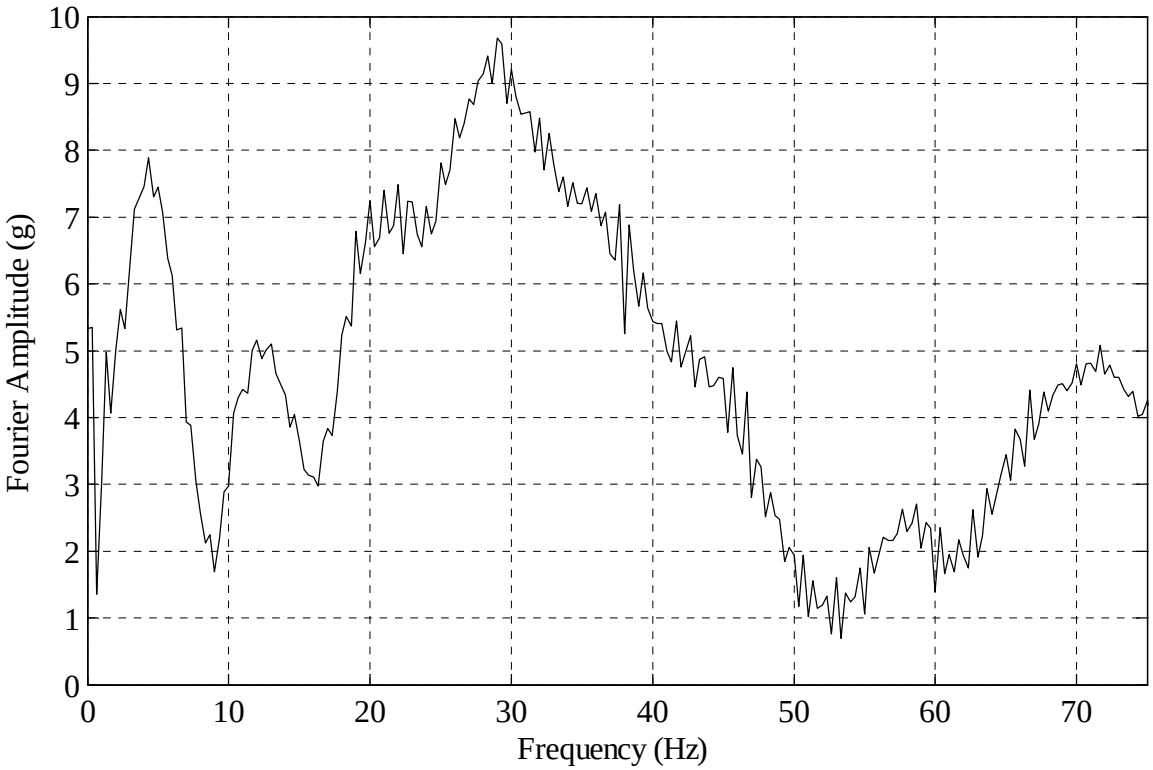

FIGURE C.15: Zoomed in window showing lower frequencies from Figure C.14.

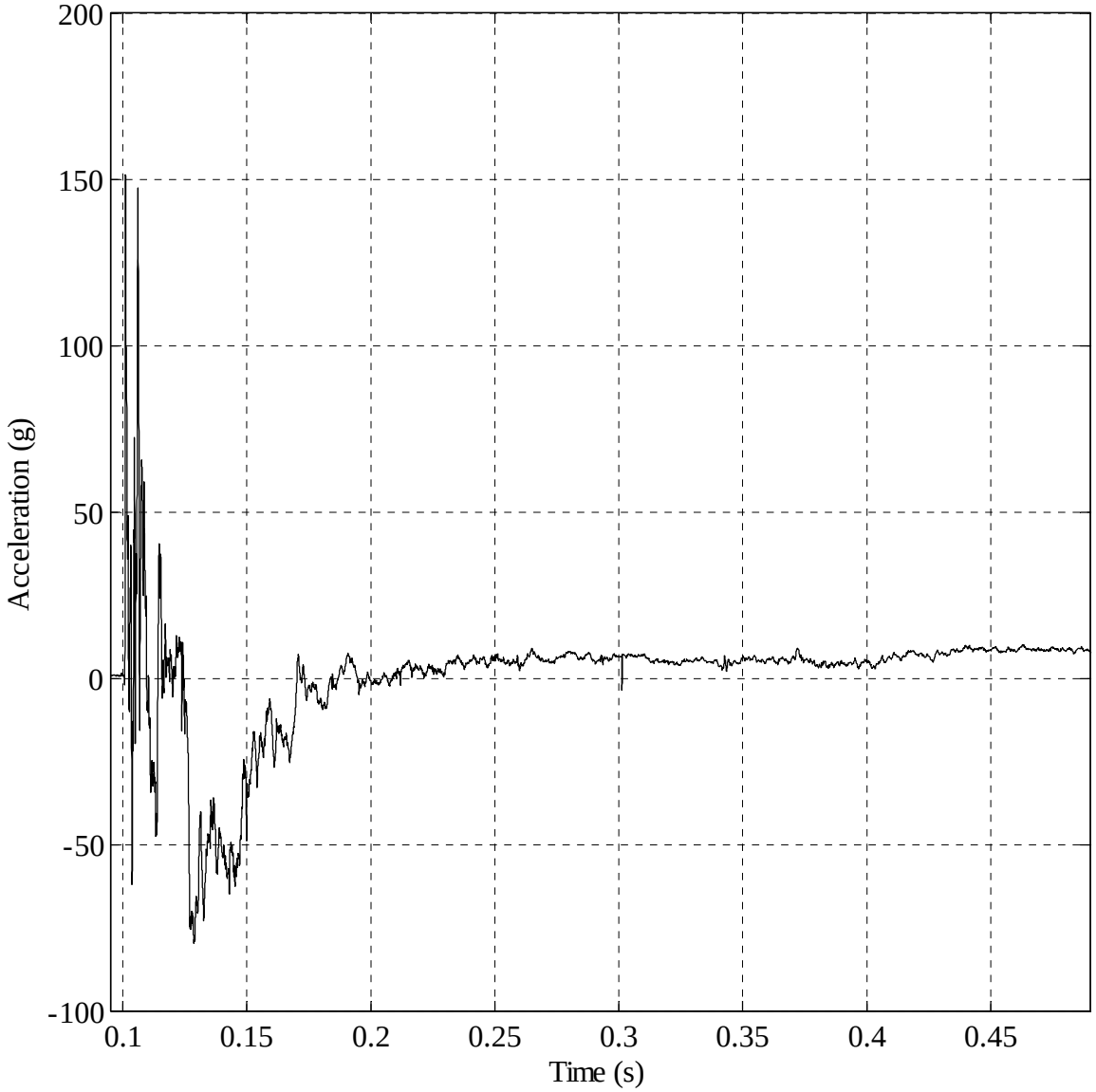

FIGURE C.16: Shot B - Acceleration time history measured by sensor S2.

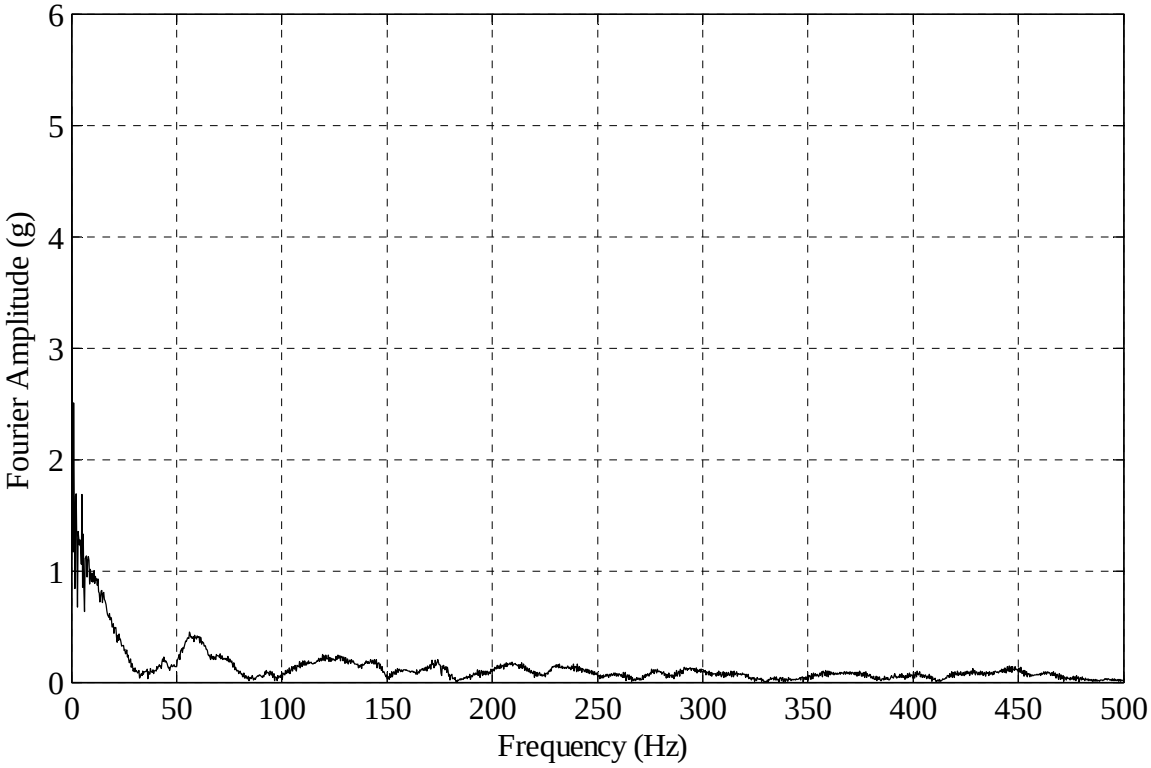

FIGURE C.17: Shot B - Fourier amplitude spectrum of acceleration time history measured by sensor S2.

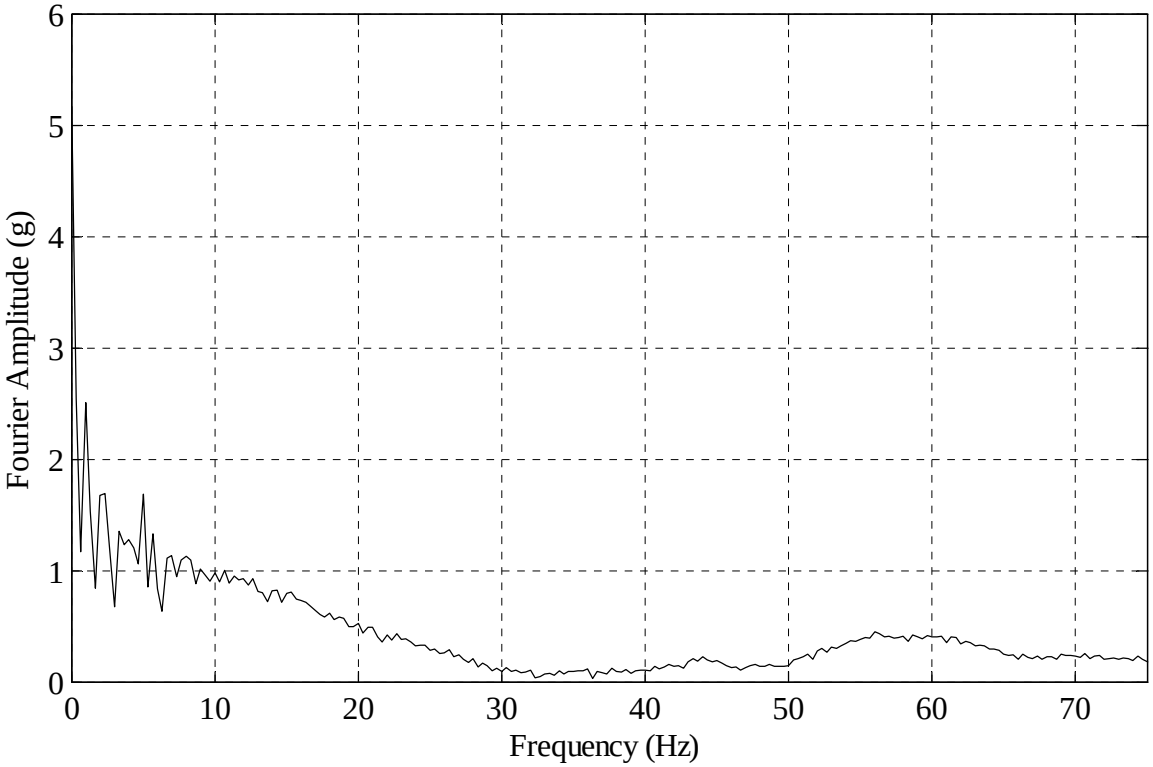

FIGURE C.18: Zoomed in window showing lower frequencies from Figure C.17.

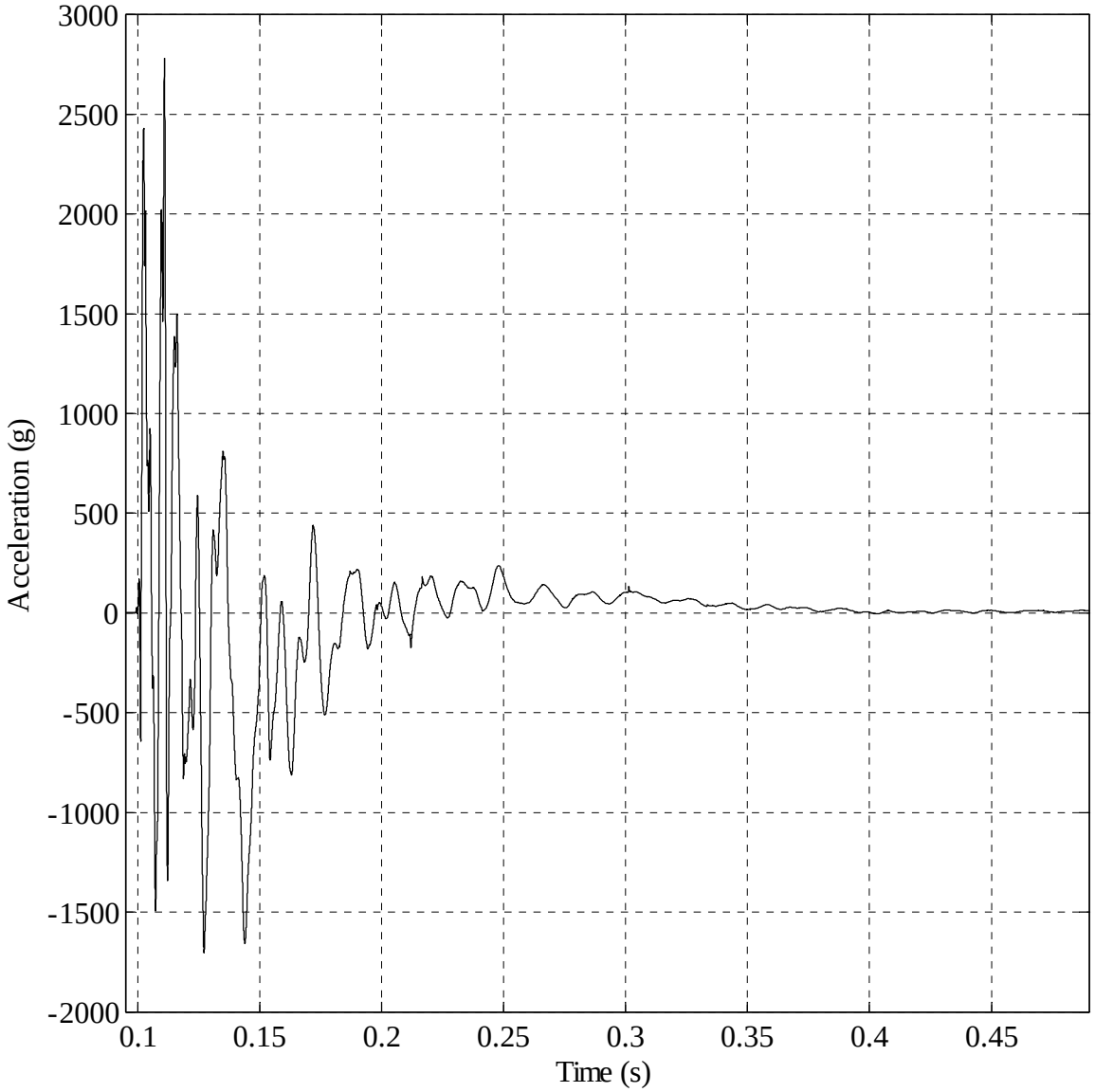

FIGURE C.19: Shot B - Acceleration time history measured by sensor S3.

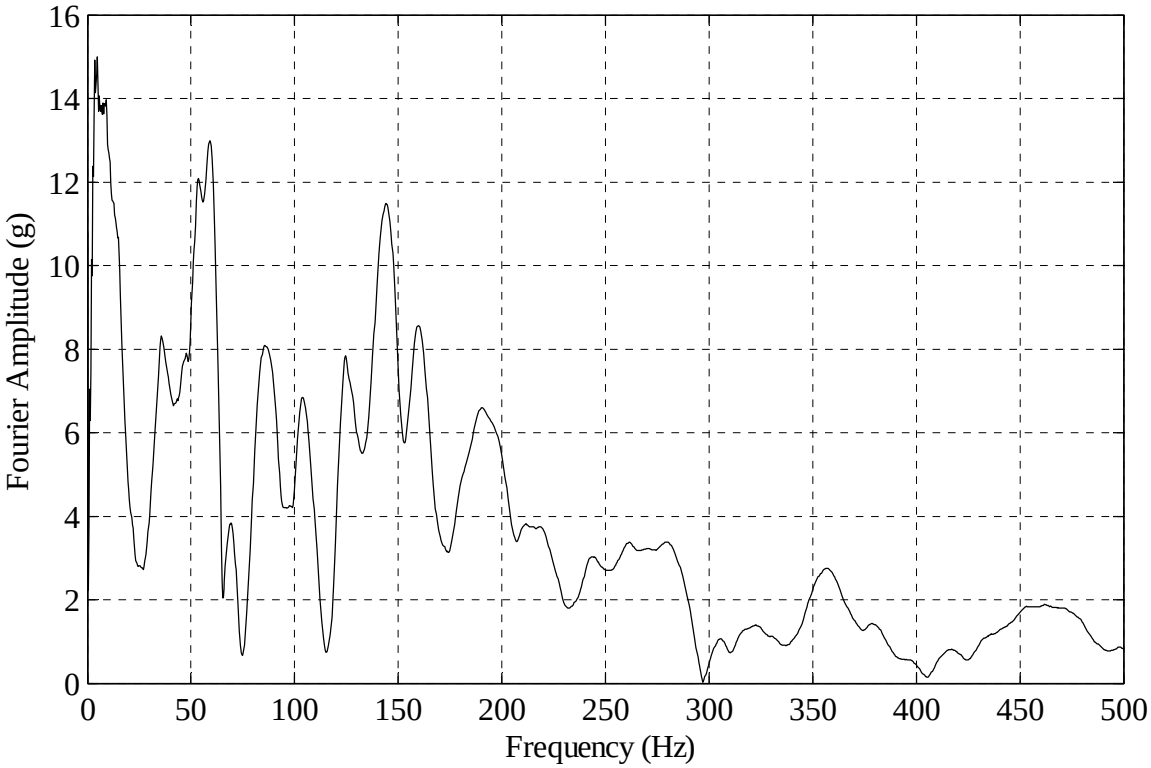

FIGURE C.20: Shot B - Fourier amplitude spectrum of acceleration time history measured by sensor S3.

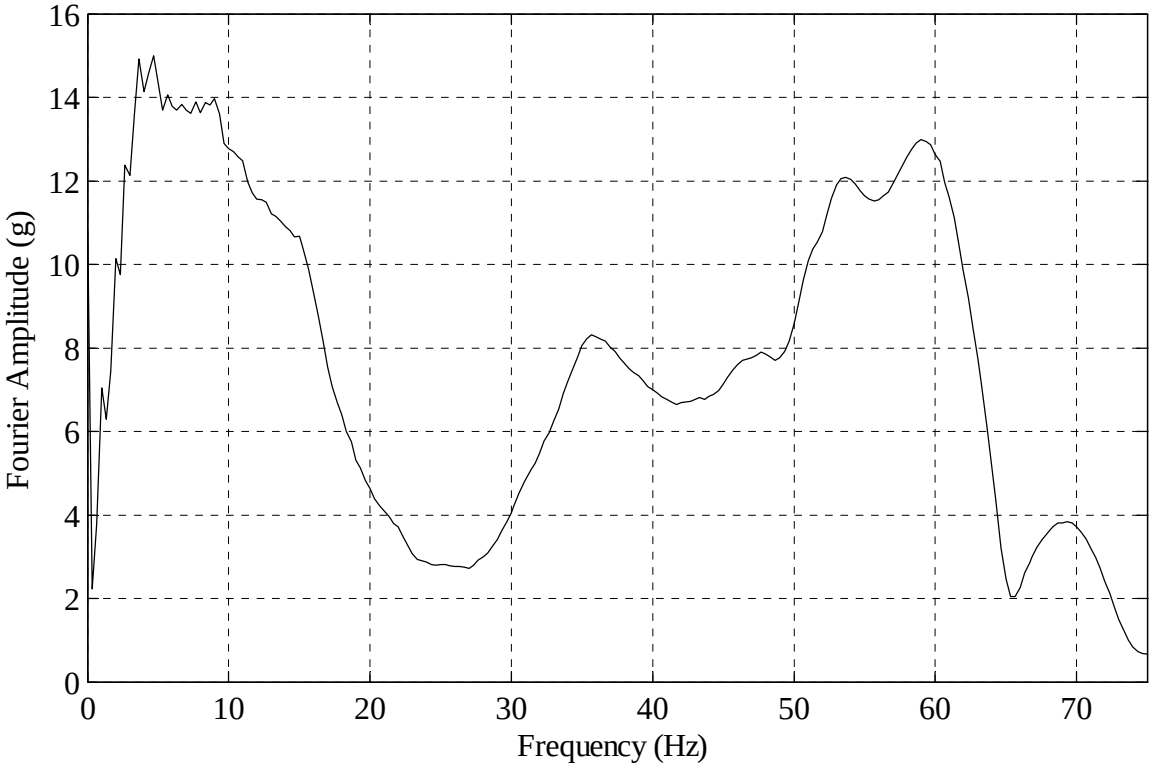

FIGURE C.21: Zoomed in window showing lower frequencies from Figure C20.

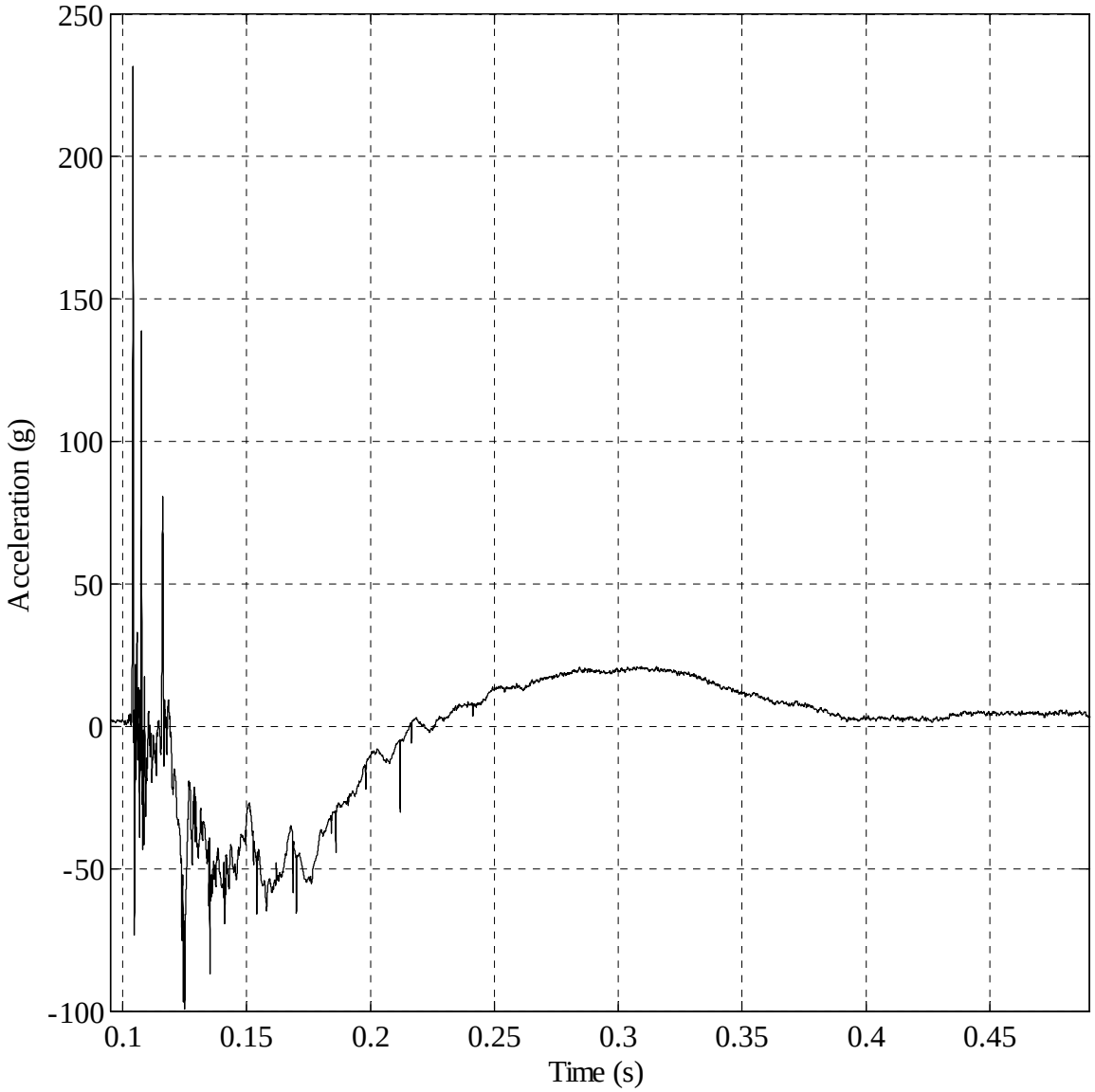

FIGURE C.22: Shot B - Acceleration time history measured by sensor S4.

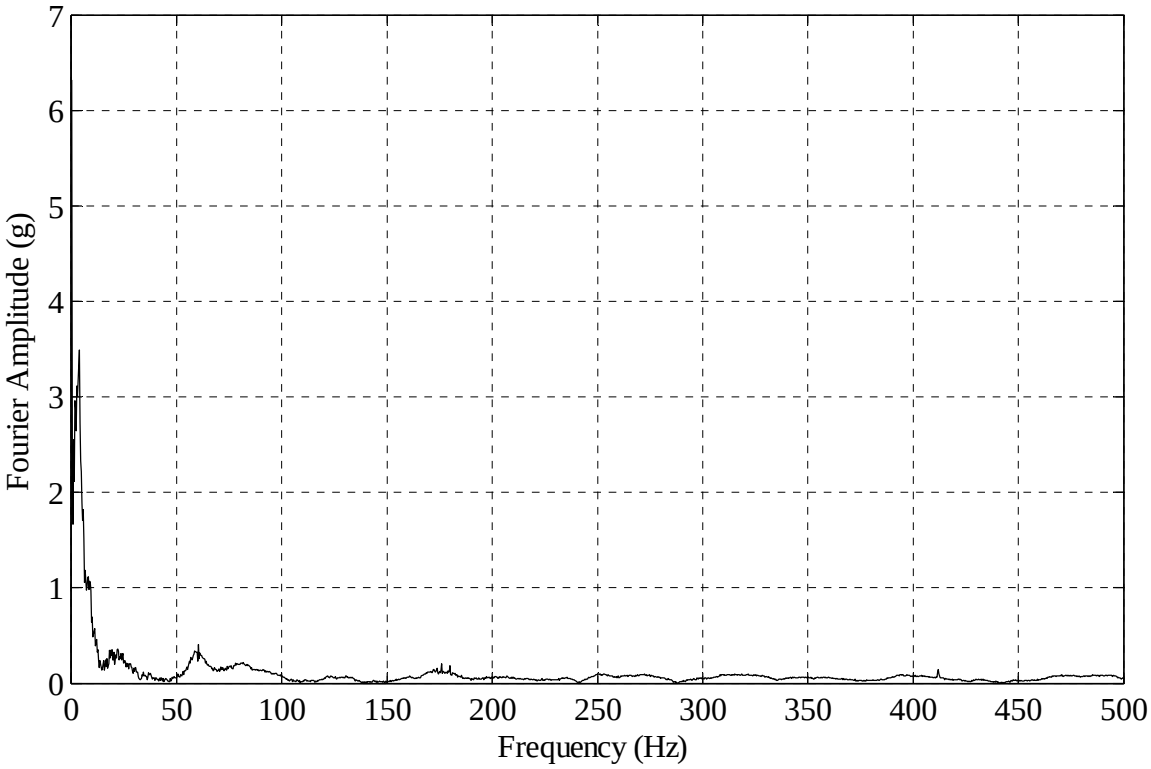

FIGURE C.23: Shot B - Fourier amplitude spectrum of acceleration time history measured by sensor S4.

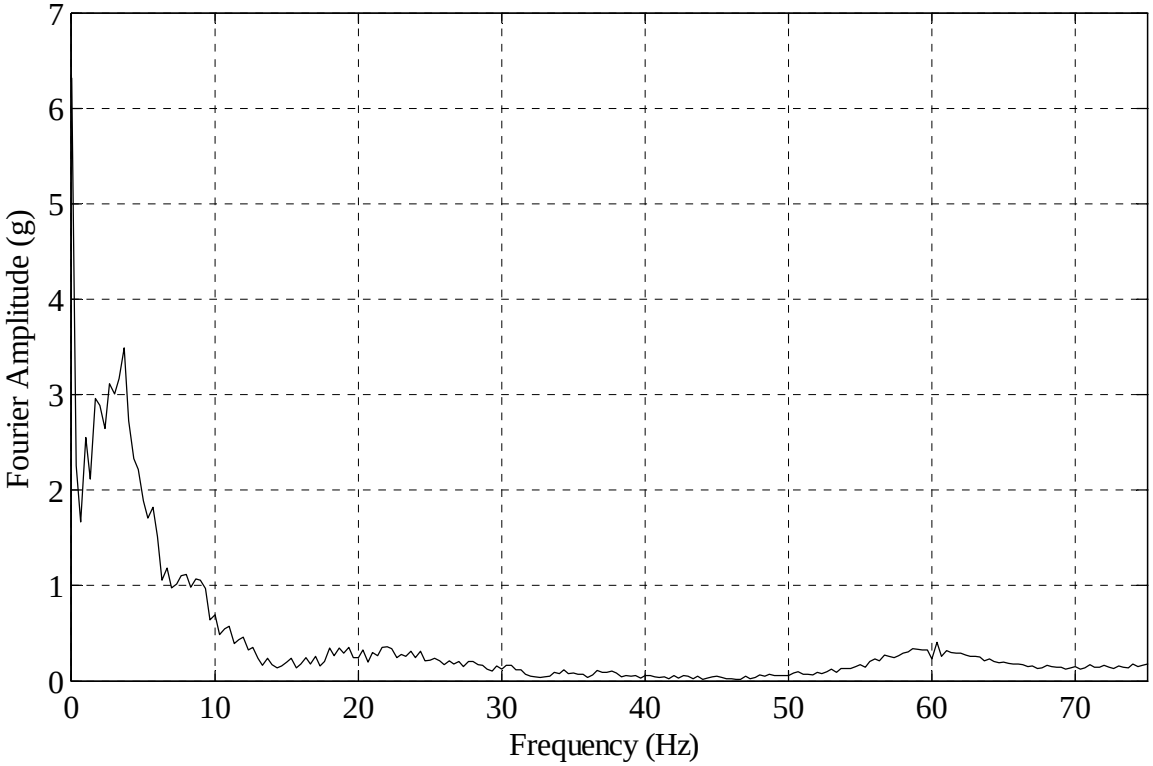

FIGURE C.24: Zoomed in window showing lower frequencies from Figure C23.

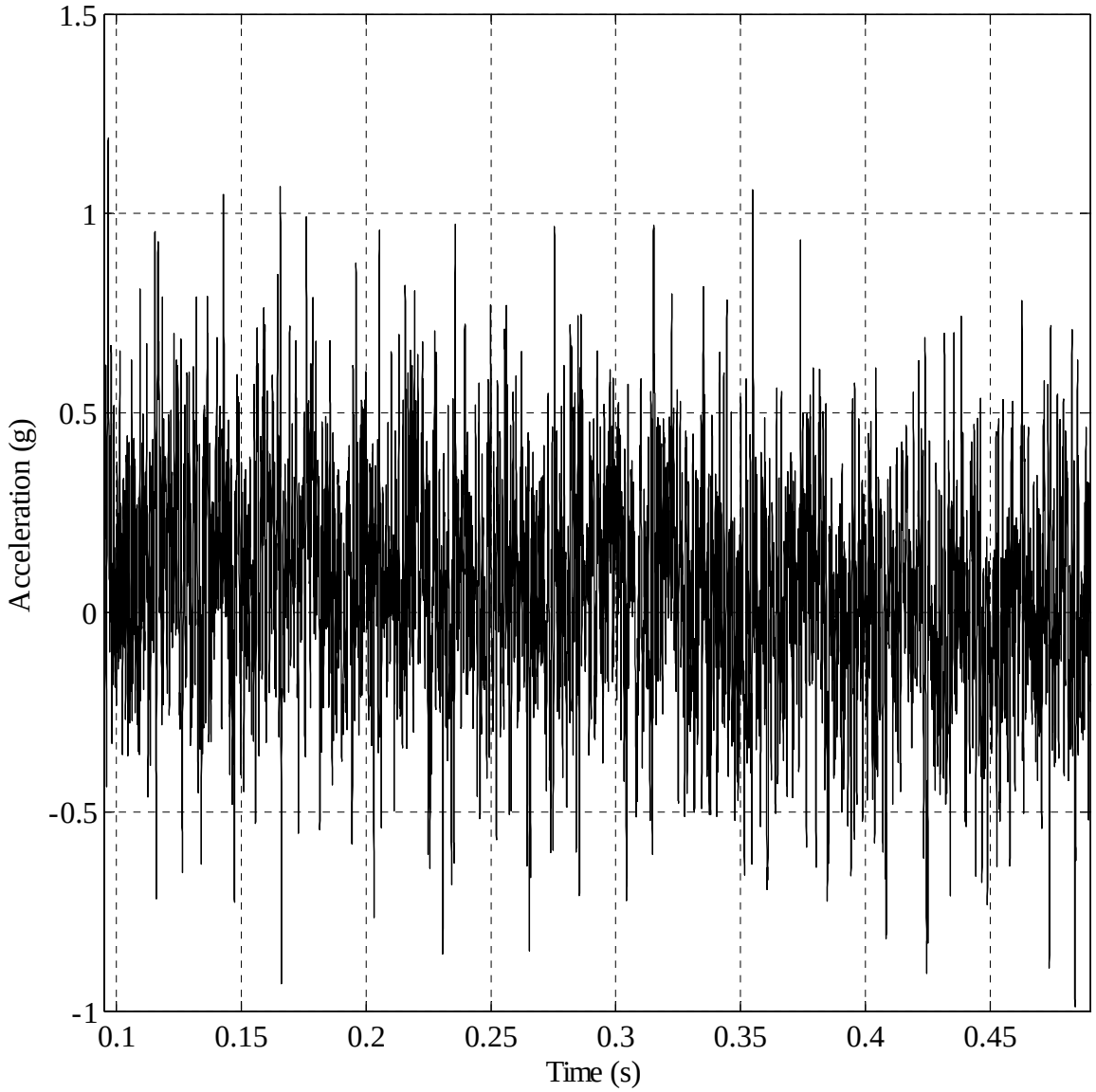

FIGURE C.25: Shot B - Acceleration time history measured by sensor S5. Sensor likely damaged or had faulty cabling, no signal measured.

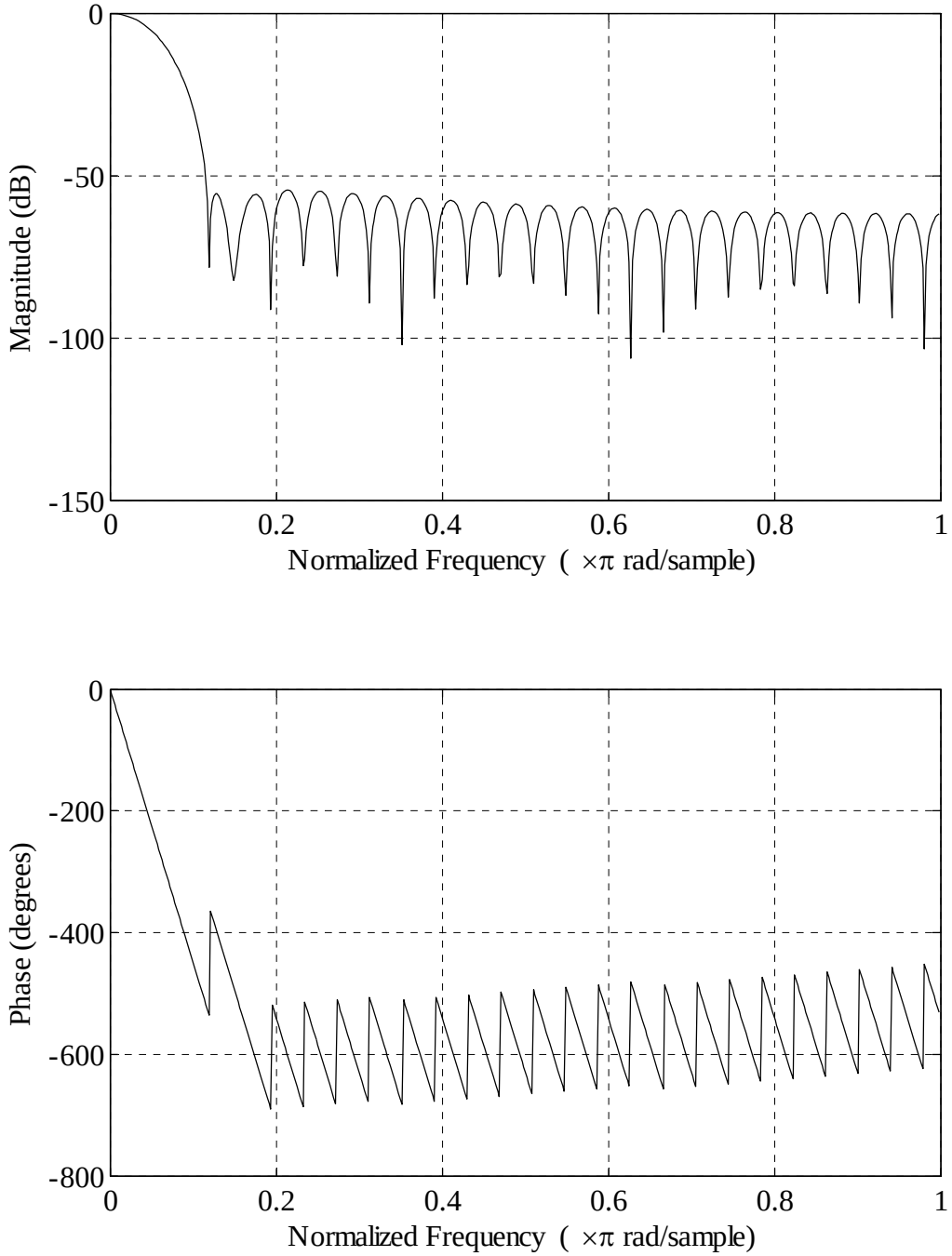

FIGURE C.26: Response of Matlab filter used to post-process shock accelerometer data. Note that in normalized frequency, 1.0 corresponds to the Nyquist frequency (50 kHz in this case).

APPENDIX D: MATLAB SCRIPTS

This appendix contains Matlab scripts used in this investigation. Preceding each script is a brief description of the code's use. This text may be directly copied and pasted into a Matlab window and executed.

D.1. Script for Figure 2.10

This script will create the pressure and impulse time histories shown in Figure 2.10 in Chapter 2. It creates the pressure time history using an equation from page 100 of Kinney and Graham's text. The script then applies two filters to the data to mimic the effects of the data acquisition system's filtration. Following the code see Figure D.1 for an NI supplied high pass frequency curve for NI 4472 modules.

```
%Create the time vector
time=[0.00001:0.00001:0.5];

%Create the positive phase of a blastwave
for j=1:1:300
   p(j)=(1-time(j)/0.003)*exp(-2.4*time(j)/0.003);          %Pressure spike of 1 MPa
end

%Stitch this into a longer time series that is zero-padded
pressure(1:10000)=[0];
pressure(10001:10300)=[p];
pressure(10301:50000)=[0];

%Design a 1 pole high pass filter with the -3dB point at 3.3 Hz
T=1/100000;   %Time between samples
t=0.047   %filter time constant, from NI data sheet on NI4472 DAQ
a=T/t;   %filter coefficient
%freqz([1-a a-1],[1 a-1],50000)            %Plot the frequency response of the high pass filter

%Design a 1st order low pass filter with 7kHz cutoff and 100 kHz Sampling
[B,A]=butter(1,7/50);
%freqz(B,A,50000)   %plot the frequency response of the lowpass filter

pfiltlow=filter(B,A,pressure);  %Apply the lowpass filter
pfilt=filter([1-a a-1],[1 a-1],pfiltlow);   %Apply the highpass filter

impnorm=cumtrapz(pressure)/100;                  %Unfiltered impulse, MPa ms
impfilt=cumtrapz(pfilt)/100;                     %Filtered impulse, MPA ms
```

```
%Plot the results
figure(1)
subplot(2,1,1)
plot(time,pressure)
xlabel('Time (s)')
ylabel('Pressure (MPa)')
hold on
plot(time,pfilt,'--')
xlim([0.099,0.104])
grid on
subplot(2,1,2)
plot(time,impnorm)
xlabel('Time (s)')
ylabel('Impulse (MPa ms)')
xlim([0.099,0.104])
hold on
plot(time,impfilt,'--')
grid on
```

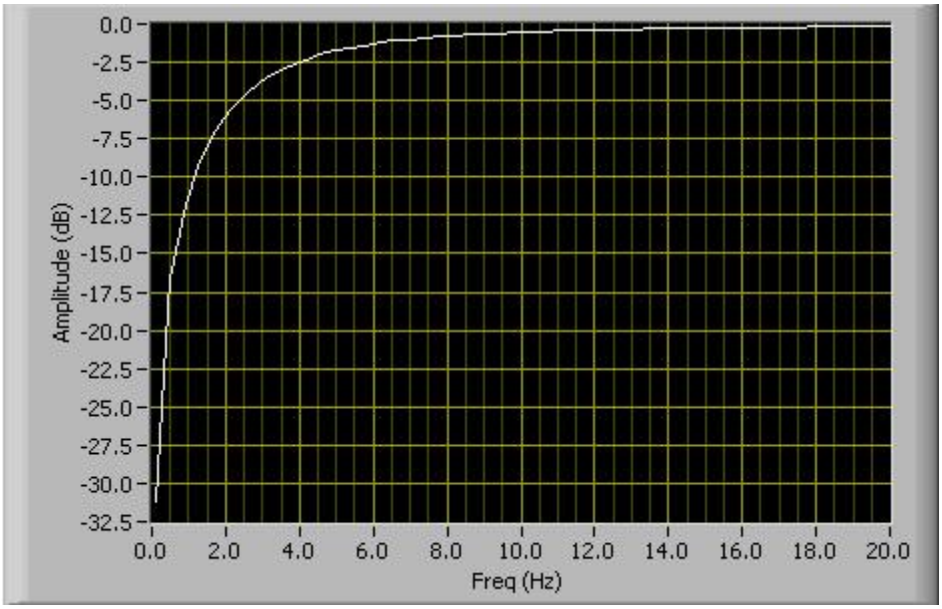

FIGURE D.1: National Instruments supplied frequency versus attenuation amplitude curve for NI 4472 modules. High pass RC filter time constant = 47 milliseconds

Graph Source:
http://digital.ni.com/public.nsf/allkb/E1DC95907C3D7D28862571ED0033D0D1

D.2. Script for Shot A1 in Appendix A

This script post-processes and plots the sensor data for Shot A1 in Appendix A. It requires that the A1 data file be located in the Matlab working directory.

```
%This file will read in the time series data from shot A1.  The file then
%creates a redundant time series for each curve, trims the curve and compute
%impulse.  Finally, a double windowed plot will be made so that pressure
%and impulse can be compared on more or less the same plot.

%Load the basic variables into the workspace
load('shotA1clip.mat');

%Create a time series from each pressure time history for integrating
%impulse.  Use cumulative trapezoidal integration.
P1cc(4191:20000)=P1c(4191:20000)*0.00689475;
P1cc(1:4190)=0;
P1imp=cumtrapz(P1cc)/100;

P2cc(4214:20000)=P2c(4214:20000)*0.00689475;
P2cc(1:4213)=0;
P2imp=cumtrapz(P2cc)/100;

P3cc(4267:20000)=P3c(4267:20000)*0.00689475;
P3cc(1:4266)=0;
P3imp=cumtrapz(P3cc)/100;

P4cc(4651:20000)=P4c(4651:20000)*0.00689475;
P4cc(1:4650)=0;
P4imp=cumtrapz(P4cc)/100;

P5cc(4224:20000)=P5c(4224:20000)*0.00689475;
P5cc(1:4223)=0;
P5imp=cumtrapz(P5cc)/100;

P6cc(4442:20000)=P6c(4442:20000)*0.00689475;
P6cc(1:4441)=0;
P6imp=cumtrapz(P6cc)/100;

P7cc(5118:20000)=P7c(5118:20000)*0.00689475;
P7cc(1:5117)=0;
P7imp=cumtrapz(P7cc)/100;

P8cc(4868:20000)=P8c(4868:20000)*0.00689475;
P8cc(1:4867)=0;
P8imp=cumtrapz(P8cc)/100;

PP1cc(4868:20000)=PP1c(4868:20000)*0.00689475;
PP1cc(1:4867)=0;
PP1imp=cumtrapz(PP1cc)/100;

%Now filter all of the shock sensor data using a low-pass filter at 2500 HZ
b=fir1(50,0.05);    %50th order filter, very sharp.
%freqz(b,1,512); %this command will plot the frequency response function

S1f=filter(b,1,S1c);
```

```
S2f=filter(b,1,S2c);
S3f=filter(b,1,S3c);

%Remove the DC offset in the sensors
S1avg=sum(S1f(1:2000))/2000;
S1f=S1f-S1avg;
S1f=S1f';
S2avg=sum(S2f(1:2000))/2000;
S2f=S2f-S2avg;
S2f=S2f';
S3avg=sum(S3f(1:2000))/2000;
S3f=S3f-S3avg;
S3f=S3f';

%Delete the source vectors
clear P1c
clear P2c
clear P3c
clear P4c
clear P5c
clear P6c
clear P7c
clear P8c
clear PP1c
clear S1c
clear S2c
clear S3c

%Make time series an even number
S1f(80001)=[];
S2f(80001)=[];
S3f(80001)=[];

%Create time array for X-axis of plots
time1=[0:0.00001:0.19999];
time2=[0:0.00001:0.79999];

%Get Fourier Amplitude Spectra of all acceleration data
Ys1=fft(S1f);
FAMPs1=abs(Ys1(1:40000))/40000;
Ys2=fft(S2f);
FAMPs2=abs(Ys2(1:40000))/40000;
Ys3=fft(S3f);
FAMPs3=abs(Ys3(1:40000))/40000;
FREQ=[0:39999]/40000*50000;

%Start plotting sensor data
%Flushmount #1
figure(1)
subplot(2,1,1)
plot(time1,P1cc,'Color',[0 0 0])
```

```
xlabel('Time (s)')
ylabel('Pressure (MPa)')
xlim([0.04,0.05])
grid on
subplot(2,1,2)
plot(time1,P1imp,'Color',[0 0 0])
xlabel('Time (s)')
ylabel('Impulse (MPa ms)')
xlim([0.04,0.05])
grid on
%set(gcf,'PaperPositionMode','manual')
%set(gcf,'PaperType','usletter')
%set(gcf,'PaperPosition',[2 3 6 7])
%print -f1 -r200 -dmeta A1_FM1

%Flushmount #2
figure(2)
subplot(2,1,1)
plot(time1,P2cc)
xlabel('Time (s)')
ylabel('Pressure (MPa)')
xlim([0.04,0.05])
grid on
subplot(2,1,2)
plot(time1,P2imp)
xlabel('Time (s)')
ylabel('Impulse (MPa ms)')
xlim([0.04,0.05])
grid on

%Flushmount #3
figure(3)
subplot(2,1,1)
plot(time1,P3cc)
xlabel('Time (s)')
ylabel('Pressure (MPa)')
xlim([0.04,0.06])
grid on
subplot(2,1,2)
plot(time1,P3imp)
xlabel('Time (s)')
ylabel('Impulse (MPa ms)')
xlim([0.04,0.06])
grid on

%Flushmount #4
figure(4)
subplot(2,1,1)
plot(time1,P4cc)
xlabel('Time (s)')
ylabel('Pressure (MPa)')
```

```
xlim([0.04,0.07])
grid on
subplot(2,1,2)
plot(time1,P4imp)
xlabel('Time (s)')
ylabel('Impulse (MPa ms)')
xlim([0.04,0.07])
grid on

%Flushmount #5
figure(5)
subplot(2,1,1)
plot(time1,P5cc)
xlabel('Time (s)')
ylabel('Pressure (MPa)')
xlim([0.04,0.05])
grid on
subplot(2,1,2)
plot(time1,P5imp)
xlabel('Time (s)')
ylabel('Impulse (MPa ms)')
xlim([0.04,0.05])
grid on

%Flushmount #6
figure(6)
subplot(2,1,1)
plot(time1,P6cc)
xlabel('Time (s)')
ylabel('Pressure (MPa)')
xlim([0.04,0.07])
grid on
subplot(2,1,2)
plot(time1,P6imp)
xlabel('Time (s)')
ylabel('Impulse (MPa ms)')
xlim([0.04,0.07])
grid on

%Flushmount #7
figure(7)
subplot(2,1,1)
plot(time1,P7cc)
xlabel('Time (s)')
ylabel('Pressure (MPa)')
xlim([0.04,0.08])
grid on
subplot(2,1,2)
plot(time1,P7imp)
xlabel('Time (s)')
ylabel('Impulse (MPa ms)')
```

```
xlim([0.04,0.08])
grid on

%Flushmount #8
figure(8)
subplot(2,1,1)
plot(time1,P8cc)
xlabel('Time (s)')
ylabel('Pressure (MPa)')
xlim([0.04,0.08])
grid on
subplot(2,1,2)
plot(time1,P8imp)
xlabel('Time (s)')
ylabel('Impulse (MPa ms)')
xlim([0.04,0.08])
grid on

%Pressure Pencil
figure(9)
subplot(2,1,1)
plot(time1,PP1cc)
xlabel('Time (s)')
ylabel('Pressure (MPa)')
xlim([0.04,.088])
grid on
subplot(2,1,2)
plot(time1,PP1imp)
xlabel('Time (s)')
ylabel('Impulse (MPa ms)')
xlim([0.04,0.088])
grid on

%Shock 1 Time Series
figure(10)
plot(time2,S1f)
xlabel('Time (s)')
ylabel('Acceleration (g)')
xlim([0.04,0.43])
grid on

%Shock 1 Fourier Spectra
figure(11)
plot(FREQ,FAMPs1)
xlabel('Frequency (Hz)')
ylabel('Fourier Amplitude (g)')
xlim([0,500])
grid on

%Shock 1 Zoom Fourier Spectra
figure(12)
```

```
plot(FREQ,FAMPs1)
xlabel('Frequency (Hz)')
ylabel('Fourier Amplitude (g)')
xlim([0,75])
grid on

%Shock 2 Time Series
figure(13)
plot(time2,S2f)
xlabel('Time (s)')
ylabel('Acceleration (g)')
xlim([0.04,0.44])
grid on

%Shock 2 Fourier Spectra
figure(14)
plot(FREQ,FAMPs2)
xlabel('Frequency (Hz)')
ylabel('Fourier Amplitude (g)')
xlim([0,500])
grid on

%Shock 2 Zoom Fourier Spectra
figure(15)
plot(FREQ,FAMPs2)
xlabel('Frequency (Hz)')
ylabel('Fourier Amplitude (g)')
xlim([0,75])
grid on

%Shock 3 Time Series
figure(16)
plot(time2,S3f)
xlabel('Time (s)')
ylabel('Acceleration (g)')
xlim([0.04,0.44])
grid on

%Shock 3 Fourier Spectra
figure(17)
plot(FREQ,FAMPs3)
xlabel('Frequency (Hz)')
ylabel('Fourier Amplitude (g)')
xlim([0,500])
grid on

%Shock 3 Zoom Fourier Spectra
figure(18)
plot(FREQ,FAMPs3)
xlabel('Frequency (Hz)')
ylabel('Fourier Amplitude (g)')
```

```
xlim([0,75])
grid on

%Plot Frequency and Phase Response of Filter
figure(19)
freqz(b)
grid on
```

D.3. Script for Shot A2 in Appendix B

This script post-processes and plots the sensor data for Shot A2 in Appendix B. It requires that the A2 data file be located in the Matlab working directory.

```
%This file will read in the time series data from shot A2.  The file then
%creates a redundant time series for each curve, trim the curve and compute
%impulse.  Finally, a double windowed plot will be made so that pressure
%and impulse can be compared on more or less the same plot.

%Load the basic variables into the workspace
load('shotA2clip.mat');

%Create a time series from each pressure time history for integrating
%impulse.  Use cumulative trapezoidal integration.
P1cc(69671:80000)=P1c(69671:80000)*0.00689475;
P1cc(1:69670)=0;
P1imp=cumtrapz(P1cc)/100;

P2cc(69721:80000)=P2c(69721:80000)*0.00689475;
P2cc(1:69720)=0;
P2imp=cumtrapz(P2cc)/100;

P3cc(69777:80000)=P3c(69777:80000)*0.00689475;
P3cc(1:69776)=0;
P3imp=cumtrapz(P3cc)/100;

P4cc(70130:80000)=P4c(70130:80000)*0.00689475;
P4cc(1:70129)=0;
P4imp=cumtrapz(P4cc)/100;

P5cc(69710:80000)=P5c(69710:80000)*0.00689475;
P5cc(1:69709)=0;
P5imp=cumtrapz(P5cc)/100;

P6cc(69900:80000)=P6c(69900:80000)*0.00689475;
P6cc(1:69899)=0;
P6imp=cumtrapz(P6cc)/100;

P7cc(70530:80000)=P7c(70530:80000)*0.00689475;
P7cc(1:70529)=0;
```

```
P7imp=cumtrapz(P7cc)/100;

P8cc(70300:80000)=P8c(70300:80000)*0.00689475;
P8cc(1:70299)=0;
P8imp=cumtrapz(P8cc)/100;

PP1cc(69830:80000)=PP1c(69830:80000)*0.00689475;
PP1cc(1:69829)=0;
PP1imp=cumtrapz(PP1cc)/100;

%Now filter all of the shock sensor data using a low-pass filter at 2000 HZ
b=fir1(50,0.05);    %50th order filter, very sharp.
%freqz(b,1,512); %this command will plot the frequency response function

S1f=filter(b,1,S1c);
S2f=filter(b,1,S2c);

%Remove the DC offset in the sensors
S1avg=sum(S1f(1:2000))/2000;
S1f=S1f-S1avg;
S1f=S1f';
S2avg=sum(S2f(1:2000))/2000;
S2f=S2f-S2avg;
S2f=S2f';

%Delete the source vectors
clear P1c
clear P2c
clear P3c
clear P4c
clear P5c
clear P6c
clear P7c
clear P8c
clear PP1c
clear S1c
clear S2c

%Trim the junk at the front of all time series
P1cc(1:50000)=[];
P2cc(1:50000)=[];
P3cc(1:50000)=[];
P4cc(1:50000)=[];
P5cc(1:50000)=[];
P6cc(1:50000)=[];
P7cc(1:50000)=[];
P8cc(1:50000)=[];
PP1cc(1:50000)=[];
S1f(1:50000)=[];
S2f(1:50000)=[];
P1imp(1:50000)=[];
```

```
P2imp(1:50000)=[];
P3imp(1:50000)=[];
P4imp(1:50000)=[];
P5imp(1:50000)=[];
P6imp(1:50000)=[];
P7imp(1:50000)=[];
P8imp(1:50000)=[];
PP1imp(1:50000)=[];

%Make time series an even number
S1f(250001)=[];
S2f(250001)=[];

%Create time array for X-axis of plots
time1=[0:0.00001:0.29999];
time2=[0:0.00001:2.49999];

%Get Fourier Amplitude Spectra of all acceleration data
Ys1=fft(S1f);
FAMPs1=abs(Ys1(1:125000))/125000;
Ys2=fft(S2f);
FAMPs2=abs(Ys2(1:125000))/125000;
FREQ=[0:124999]/125000*50000;

%Start plotting sensor data
%Flushmount #1
figure(1)
subplot(2,1,1)
plot(time1,P1cc)
xlabel('Time (s)')
ylabel('Pressure (MPa)')
xlim([0.19,0.24])
subplot(2,1,2)
plot(time1,P1imp)
xlabel('Time (s)')
ylabel('Impulse (MPa ms)')
xlim([0.19,0.24])
set(gcf,'PaperPositionMode','manual')
set(gcf,'PaperType','usletter')
set(gcf,'PaperPosition',[2 1 6 6])
print -f1 -r600 -deps A1_FM1

%Flushmount #2
figure(2)
subplot(2,1,1)
plot(time1,P2cc)
xlabel('Time (s)')
ylabel('Pressure (MPa)')
xlim([0.19,0.24])
subplot(2,1,2)
plot(time1,P2imp)
```

```
xlabel('Time (s)')
ylabel('Impulse (MPa ms)')
xlim([0.19,0.24])

%Flushmount #3
figure(3)
subplot(2,1,1)
plot(time1,P3cc)
xlabel('Time (s)')
ylabel('Pressure (MPa)')
xlim([0.19,0.24])
subplot(2,1,2)
plot(time1,P3imp)
xlabel('Time (s)')
ylabel('Impulse (MPa ms)')
xlim([0.19,0.24])

%Flushmount #4
figure(4)
subplot(2,1,1)
plot(time1,P4cc)
xlabel('Time (s)')
ylabel('Pressure (MPa)')
xlim([0.19,0.24])
subplot(2,1,2)
plot(time1,P4imp)
xlabel('Time (s)')
ylabel('Impulse (MPa ms)')
xlim([0.19,0.24])

%Flushmount #5
figure(5)
subplot(2,1,1)
plot(time1,P5cc)
xlabel('Time (s)')
ylabel('Pressure (MPa)')
xlim([0.19,0.24])
subplot(2,1,2)
plot(time1,P5imp)
xlabel('Time (s)')
ylabel('Impulse (MPa ms)')
xlim([0.19,0.24])

%Flushmount #6
figure(6)
subplot(2,1,1)
plot(time1,P6cc)
xlabel('Time (s)')
ylabel('Pressure (MPa)')
xlim([0.19,0.24])
subplot(2,1,2)
```

```
plot(time1,P6imp)
xlabel('Time (s)')
ylabel('Impulse (MPa ms)')
xlim([0.19,0.24])

%Flushmount #7
figure(7)
subplot(2,1,1)
plot(time1,P7cc)
xlabel('Time (s)')
ylabel('Pressure (MPa)')
xlim([0.2,0.25])
subplot(2,1,2)
plot(time1,P7imp)
xlabel('Time (s)')
ylabel('Impulse (MPa ms)')
xlim([0.19,0.25])

%Flushmount #8
figure(8)
subplot(2,1,1)
plot(time1,P8cc)
xlabel('Time (s)')
ylabel('Pressure (MPa)')
xlim([0.2,.25])
subplot(2,1,2)
plot(time1,P8imp)
xlabel('Time (s)')
ylabel('Impulse (MPa ms)')
xlim([0.19,0.25])

%Pressure Pencil
figure(9)
subplot(2,1,1)
plot(time1,PP1cc)
xlabel('Time (s)')
ylabel('Pressure (MPa)')
xlim([0.198,.2])
subplot(2,1,2)
plot(time1,PP1imp)
xlabel('Time (s)')
ylabel('Impulse (MPa ms)')
xlim([0.19,0.2])

%Shock 1 Time Series
figure(10)
plot(time2,S1f)
xlabel('Time (s)')
ylabel('Acceleration (g)')
xlim([0.19,0.25])
```

```
%Shock 1 Fourier Spectra
figure(11)
plot(FREQ,FAMPs1)
xlabel('Frequency (Hz)')
ylabel('Fourier Amplitude (g)')
xlim([0,500])

%Shock 1 Zoom Fourier Spectra
figure(12)
plot(FREQ,FAMPs1)
xlabel('Frequency (Hz)')
ylabel('Fourier Amplitude (g)')
xlim([0,75])

%Shock 2 Time Series
figure(13)
plot(time2,S2f)
xlabel('Time (s)')
ylabel('Acceleration (g)')
xlim([0.19,0.25])

%Shock 2 Fourier Spectra
figure(14)
plot(FREQ,FAMPs2)
xlabel('Frequency (Hz)')
ylabel('Fourier Amplitude (g)')
xlim([0,500])

%Shock 2 Zoom Fourier Spectra
figure(15)
plot(FREQ,FAMPs2)
xlabel('Frequency (Hz)')
ylabel('Fourier Amplitude (g)')
xlim([0,25])

%Plot Frequency and Phase Response of Filter
figure(16)
freqz(b)
```

D.4. Script for Shot B in Appendix C

This script post-processes and plots the sensor data for Shot B in Appendix C. It requires that the B data file be located in the Matlab working directory.

```
%This file will read in the time series data from shot B.  The file then
%creates a redundant time series for each curve, trim the curve and compute
%impulse.  Finally, a double windowed plot will be made so that pressure
%and impulse can be compared on more or less the same plot.
```

```
%Load the basic variables into the workspace
load('shotBclip.mat');

%Create a time series from each pressure time history for integrating
%impulse.  Use cumulative trapezoidal integration.
P1cc(30050:50000)=P1c(30050:50000)*0.00689475;
P1cc(1:30049)=0;
P1imp=cumtrapz(P1cc)/100;

P2cc(30080:50000)=P2c(30080:50000)*0.00689475;
P2cc(1:30079)=0;
P2imp=cumtrapz(P2cc)/100;

P3cc(30145:50000)=P3c(30145:50000)*0.00689475;
P3cc(1:30144)=0;
P3imp=cumtrapz(P3cc)/100;

P4cc(30095:50000)=P4c(30095:50000)*0.00689475;
P4cc(1:30094)=0;
P4imp=cumtrapz(P4cc)/100;

P5cc(30040:50000)=P5c(30040:50000)*0.00689475;
P5cc(1:30039)=0;
P5imp=cumtrapz(P5cc)/100;

P6cc(30310:50000)=P6c(30310:50000)*0.00689475;
P6cc(1:30309)=0;
P6imp=cumtrapz(P6cc)/100;

P7cc(30170:50000)=P7c(30170:50000)*0.00689475;
P7cc(1:30169)=0;
P7imp=cumtrapz(P7cc)/100;

P8cc(30355:50000)=P8c(30355:50000)*0.00689475;
P8cc(1:30354)=0;
P8imp=cumtrapz(P8cc)/100;

P9cc(30355:50000)=P9c(30355:50000)*0.00689475;
P9cc(1:30354)=0;
P9imp=cumtrapz(P9cc)/100;

P10cc(30355:50000)=P10c(30355:50000)*0.00689475;
P10cc(1:31254)=0;
P10imp=cumtrapz(P10cc)/100;

P11cc(30355:50000)=P11c(30355:50000)*0.00689475;
P11cc(1:31354)=0;
P11imp=cumtrapz(P11cc)/100;

P12cc(30355:50000)=P12c(30355:50000)*0.00689475;
P12cc(1:30354)=0;
```

```
P12imp=cumtrapz(P12cc)/100;

%Now filter all of the shock sensor data using a low-pass filter at 2000 HZ
b=fir1(50,0.05);    %50th order filter, very sharp.
%freqz(b,1,512); %this command will plot the frequency response function

S1f=filter(b,1,S1c);
S2f=filter(b,1,S2c);
S3f=filter(b,1,S3c);
S4f=filter(b,1,S4c);
S5f=filter(b,1,S5c);

%Remove the DC offset in the sensors
S1avg=sum(S1f(1:2000))/2000;
S1f=S1f-S1avg;
S1f=S1f';
S2avg=sum(S2f(1:2000))/2000;
S2f=S2f-S2avg;
S2f=S2f';
S3avg=sum(S3f(1:2000))/2000;
S3f=S3f-S3avg;
S3f=S3f';
S4avg=sum(S4f(1:2000))/2000;
S4f=S4f-S4avg;
S4f=S4f';
S5avg=sum(S5f(1:2000))/2000;
S5f=S5f-S5avg;
S5f=S5f';

%Delete the source vectors
clear P1c
clear P2c
clear P3c
clear P4c
clear P5c
clear P6c
clear P7c
clear P8c
clear P9c
clear P10c
clear P11c
clear P12c
clear S1c
clear S2c
clear S3c
clear S4c
clear S5c

%Make time series an even number
S1f(30001)=[];
S2f(30001)=[];
```

```
S3f(30001)=[];
S4f(30001)=[];
S5f(30001)=[];

%Get Fourier Amplitude Spectra of all acceleration data
Ys1=fft(S1f);
FAMPs1=abs(Ys1(1:150000))/150000;
Ys2=fft(S2f);
FAMPs2=abs(Ys2(1:150000))/150000;
Ys3=fft(S3f);
FAMPs3=abs(Ys3(1:150000))/150000;
Ys4=fft(S4f);
FAMPs4=abs(Ys4(1:150000))/150000;
Ys5=fft(S5f);
FAMPs5=abs(Ys5(1:150000))/150000;

FREQ=[0:149999]/150000*50000;

%Trim the excess time in front of time series
P1cc(1:20000)=[];
P2cc(1:20000)=[];
P3cc(1:20000)=[];
P4cc(1:20000)=[];
P5cc(1:20000)=[];
P6cc(1:20000)=[];
P7cc(1:20000)=[];
P8cc(1:20000)=[];
P9cc(1:20000)=[];
P10cc(1:20000)=[];
P11cc(1:20000)=[];
P12cc(1:20000)=[];
P1imp(1:20000)=[];
P2imp(1:20000)=[];
P3imp(1:20000)=[];
P4imp(1:20000)=[];
P5imp(1:20000)=[];
P6imp(1:20000)=[];
P7imp(1:20000)=[];
P8imp(1:20000)=[];
P9imp(1:20000)=[];
P10imp(1:20000)=[];
P11imp(1:20000)=[];
P12imp(1:20000)=[];

S1f(1:20000)=[];
S2f(1:20000)=[];
S3f(1:20000)=[];
S4f(1:20000)=[];
S5f(1:20000)=[];

%Create time array for X-axis of plots
```

```
time1=[0:0.00001:0.29999];
time2=[0:0.00001:2.79999];

%Start plotting sensor data
%Flushmount #1
figure(1)
subplot(2,1,1)
plot(time1,P1cc)
xlabel('Time (s)')
ylabel('Pressure (MPa)')
xlim([0.095,0.11])
subplot(2,1,2)
plot(time1,P1imp)
xlabel('Time (s)')
ylabel('Impulse (MPa ms)')
xlim([0.095,0.11])
set(gcf,'PaperPositionMode','manual')
set(gcf,'PaperType','usletter')
set(gcf,'PaperPosition',[2 1 6 6])
print -f1 -r600 -deps A1_FM1

%Flushmount #2
figure(2)
subplot(2,1,1)
plot(time1,P2cc)
xlabel('Time (s)')
ylabel('Pressure (MPa)')
xlim([0.095,0.12])
subplot(2,1,2)
plot(time1,P2imp)
xlabel('Time (s)')
ylabel('Impulse (MPa ms)')
xlim([0.095,0.12])

%Flushmount #3
figure(3)
subplot(2,1,1)
plot(time1,P3cc)
xlabel('Time (s)')
ylabel('Pressure (MPa)')
xlim([0.095,0.105])
subplot(2,1,2)
plot(time1,P3imp)
xlabel('Time (s)')
ylabel('Impulse (MPa ms)')
xlim([0.095,0.105])

%Flushmount #4
figure(4)
subplot(2,1,1)
plot(time1,P4cc)
```

```
xlabel('Time (s)')
ylabel('Pressure (MPa)')
xlim([0.095,0.12])
subplot(2,1,2)
plot(time1,P4imp)
xlabel('Time (s)')
ylabel('Impulse (MPa ms)')
xlim([0.095,0.12])

%Flushmount #5
figure(5)
subplot(2,1,1)
plot(time1,P5cc)
xlabel('Time (s)')
ylabel('Pressure (MPa)')
xlim([0.095,0.12])
subplot(2,1,2)
plot(time1,P5imp)
xlabel('Time (s)')
ylabel('Impulse (MPa ms)')
xlim([0.095,0.12])

%Flushmount #6
figure(6)
subplot(2,1,1)
plot(time1,P6cc)
xlabel('Time (s)')
ylabel('Pressure (MPa)')
xlim([0.095,0.15])
subplot(2,1,2)
plot(time1,P6imp)
xlabel('Time (s)')
ylabel('Impulse (MPa ms)')
xlim([0.095,0.15])

%Flushmount #7
figure(7)
subplot(2,1,1)
plot(time1,P7cc)
xlabel('Time (s)')
ylabel('Pressure (MPa)')
xlim([0.095,0.15])
subplot(2,1,2)
plot(time1,P7imp)
xlabel('Time (s)')
ylabel('Impulse (MPa ms)')
xlim([0.095,0.15])

%Flushmount #8
figure(8)
subplot(2,1,1)
```

```
plot(time1,P8cc)
xlabel('Time (s)')
ylabel('Pressure (MPa)')
xlim([0.095,0.15])
subplot(2,1,2)
plot(time1,P8imp)
xlabel('Time (s)')
ylabel('Impulse (MPa ms)')
xlim([0.095,0.15])

%Flushmount #9
figure(9)
subplot(2,1,1)
plot(time1,P9cc)
xlabel('Time (s)')
ylabel('Pressure (MPa)')
xlim([0.095,0.15])
subplot(2,1,2)
plot(time1,P9imp)
xlabel('Time (s)')
ylabel('Impulse (MPa ms)')
xlim([0.095,0.15])

%Flushmount #10
figure(10)
subplot(2,1,1)
plot(time1,P10cc)
xlabel('Time (s)')
ylabel('Pressure (MPa)')
xlim([0.095,0.2])
subplot(2,1,2)
plot(time1,P10imp)
xlabel('Time (s)')
ylabel('Impulse (MPa ms)')
xlim([0.095,0.2])

%Flushmount #11
figure(11)
subplot(2,1,1)
plot(time1,P11cc)
xlabel('Time (s)')
ylabel('Pressure (MPa)')
xlim([0.095,0.2])
subplot(2,1,2)
plot(time1,P11imp)
xlabel('Time (s)')
ylabel('Impulse (MPa ms)')
xlim([0.095,0.2])

%Flushmount #12
figure(12)
```

```
subplot(2,1,1)
plot(time1,P12cc)
xlabel('Time (s)')
ylabel('Pressure (MPa)')
xlim([0.095,0.15])
subplot(2,1,2)
plot(time1,P12imp)
xlabel('Time (s)')
ylabel('Impulse (MPa ms)')
xlim([0.095,0.15])

%Shock 1 Time Series
figure(13)
plot(time2,S1f)
xlabel('Time (s)')
ylabel('Acceleration (g)')
xlim([0.095,0.49])

%Shock 1 Fourier Spectra
figure(14)
plot(FREQ,FAMPs1)
xlabel('Frequency (Hz)')
ylabel('Fourier Amplitude (g)')
xlim([0,500])

%Shock 1 Zoom Fourier Spectra
figure(15)
plot(FREQ,FAMPs1)
xlabel('Frequency (Hz)')
ylabel('Fourier Amplitude (g)')
xlim([0,75])

%Shock 2 Time Series
figure(16)
plot(time2,S2f)
xlabel('Time (s)')
ylabel('Acceleration (g)')
xlim([0.095,0.49])

%Shock 2 Fourier Spectra
figure(17)
plot(FREQ,FAMPs2)
xlabel('Frequency (Hz)')
ylabel('Fourier Amplitude (g)')
xlim([0,500])

%Shock 2 Zoom Fourier Spectra
figure(18)
plot(FREQ,FAMPs2)
xlabel('Frequency (Hz)')
ylabel('Fourier Amplitude (g)')
```

```
xlim([0,75])

%Shock 3 Time Series
figure(19)
plot(time2,S3f)
xlabel('Time (s)')
ylabel('Acceleration (g)')
xlim([0.095,0.49])

%Shock 3 Fourier Spectra
figure(20)
plot(FREQ,FAMPs3)
xlabel('Frequency (Hz)')
ylabel('Fourier Amplitude (g)')
xlim([0,500])

%Shock 3 Zoom Fourier Spectra
figure(21)
plot(FREQ,FAMPs3)
xlabel('Frequency (Hz)')
ylabel('Fourier Amplitude (g)')
xlim([0,75])

%Shock 4 Time Series
figure(22)
plot(time2,S4f)
xlabel('Time (s)')
ylabel('Acceleration (g)')
xlim([0.095,0.49])

%Shock 4 Fourier Spectra
figure(23)
plot(FREQ,FAMPs4)
xlabel('Frequency (Hz)')
ylabel('Fourier Amplitude (g)')
xlim([0,500])

%Shock 4 Zoom Fourier Spectra
figure(24)
plot(FREQ,FAMPs4)
xlabel('Frequency (Hz)')
ylabel('Fourier Amplitude (g)')
xlim([0,75])

%SHOCK 5 RECORDED NO SIGNAL, PLOTTED ONLY FOR COMPLETENESS

%Shock 5 Time Series
figure(25)
plot(time2,S5f)
xlabel('Time (s)')
ylabel('Acceleration (g)')
```

```
xlim([0.095,0.49])

%Shock 5 Fourier Spectra
figure(26)
plot(FREQ,FAMPs5)
xlabel('Frequency (Hz)')
ylabel('Fourier Amplitude (g)')
xlim([0,500])

%Shock 5 Zoom Fourier Spectra
figure(27)
plot(FREQ,FAMPs5)
xlabel('Frequency (Hz)')
ylabel('Fourier Amplitude (g)')
xlim([0,75])

%Plot Frequency and Phase Response of Filter
figure(28)
freqz(b)
```

D.5. Script for Figures 2.23 and 2.24

This script generates the plots of vertical pressure/impulse ratio versus height above blast chamber floor shown in Figures 2.23 and 2.24.

```
y1=[47,142,213];
imp11=[1,.54,.29];
p1=[100,42.8,14.9];
y2=[47,142,213];
imp2=[1,0.81,0.48];
p2=[100,90.9,29.5];
y3=[44.5,158.8];
imp3=[1,0.49];
p3=[100,13.6];

imp1=imp1*100
imp2=imp2*100
imp3=imp3*100

hold on
plot(imp1,y1)
plot(imp2,y2)
plot(imp3,y3,'*')

hold on
plot(p1,y1)
plot(p2,y2)
plot(p3,y3)
```

D.6. Script for Figures 5.13 through 5.18

This script post processes the CTH 3D simulations to generate pressure and impulse contours over Chamber B walls. This script produces Figures 5.13 through 5.18.

```
%Process the pressure time histories from the 3D CTH simulation.
%Extract the pressure vectors after importing them from the HSCTH file:
TIME=data(:,1);
%first subtract the initial reading from all sensors, then convert to psi,
%then integrate
k=0
for j=14:4:378
   k=k+1;
   P(:,k)=(data(:,j)-data(1,j))/68947.5;
end

%convert P to MPa
P=P*0.00689475729;

for j=1:1:92
   imp(:,j)=cumtrapz(TIME,P(:,j));
end

%make it MPa - ms
imp=imp*1000;

%GENERATE LOCATIONS OF SENSORS
%Blast chamber sensors
LOC(1,1:3)=[500,45,428];    %*P1
LOC(2,1:3)=[500,159,428];   %*P2
LOC(3,1:3)=[500,350,428];  %*P3
LOC(4,1:3)=[500,159,428];  %*P4
LOC(5,1:3)=[500,45,428];  %*P5
LOC(6,1:3)=[248,160,0];   %*P6
LOC(7,1:3)=[500,160,212];   %*P7
%Wall 1 midheight horizontal profile
LOC(8,1:3)=[500,175,0];
LOC(9,1:3)=[500,175,50];
LOC(10,1:3)=[500,175,100];
LOC(11,1:3)=[500,175,150];
LOC(12,1:3)=[500,175,200];
LOC(13,1:3)=[500,175,250];
LOC(14,1:3)=[500,175,300];
LOC(15,1:3)=[500,175,350];
LOC(16,1:3)=[500,175,400];
LOC(17,1:3)=[500,175,450];
LOC(18,1:3)=[500,175,500];
%Wall 1 central vertical profile
LOC(19,1:3)=[500,0,236];
```

```
LOC(20,1:3)=[500,50,236];
LOC(21,1:3)=[500,100,236];
LOC(22,1:3)=[500,150,236];
LOC(23,1:3)=[500,200,236];
LOC(24,1:3)=[500,250,236];
LOC(25,1:3)=[500,300,236];
LOC(26,1:3)=[500,350,236];
%Wall 1 quarter point vertical profile
LOC(27,1:3)=[500,0,118];
LOC(28,1:3)=[500,50,118];
LOC(29,1:3)=[500,100,118];
LOC(30,1:3)=[500,150,118];
LOC(31,1:3)=[500,200,118];
LOC(32,1:3)=[500,250,118];
LOC(33,1:3)=[500,300,118];
LOC(34,1:3)=[500,350,118];
%Wall 1 quarter point vetical profile
LOC(35,1:3)=[500,0,354];
LOC(36,1:3)=[500,50,354];
LOC(37,1:3)=[500,100,354];
LOC(38,1:3)=[500,150,354];
LOC(39,1:3)=[500,200,354];
LOC(40,1:3)=[500,250,354];
LOC(41,1:3)=[500,300,354];
LOC(42,1:3)=[500,350,354];
%Wall 2 horizontal profile
LOC(43,1:3)=[0,175,0];
LOC(44,1:3)=[50,175,0];
LOC(45,1:3)=[100,175,0];
LOC(46,1:3)=[150,175,0];
LOC(47,1:3)=[200,175,0];
LOC(48,1:3)=[250,175,0];
LOC(49,1:3)=[300,175,0];
LOC(50,1:3)=[350,175,0];
LOC(51,1:3)=[400,175,0];
LOC(52,1:3)=[450,175,0];
LOC(53,1:3)=[500,175,0];
%Wall 2 vertical profile
LOC(54,1:3)=[248,0,0];
LOC(55,1:3)=[248,50,0];
LOC(56,1:3)=[248,100,0];
LOC(57,1:3)=[248,150,0];
LOC(58,1:3)=[248,200,0];
LOC(59,1:3)=[248,250,0];
LOC(60,1:3)=[248,300,0];
LOC(61,1:3)=[248,350,0];
%Wall 2 vertical quarter point profile
LOC(62,1:3)=[372,0,0];
LOC(63,1:3)=[372,50,0];
LOC(64,1:3)=[372,100,0];
LOC(65,1:3)=[372,150,0];
```

```
LOC(66,1:3)=[372,200,0];
LOC(67,1:3)=[372,250,0];
LOC(68,1:3)=[372,300,0];
LOC(69,1:3)=[372,350,0];
%wall 3 points along midheight
LOC(70,1:3)=[500,175,0];
LOC(71,1:3)=[500,175,50];
LOC(72,1:3)=[500,175,100];
LOC(73,1:3)=[500,175,200];
LOC(74,1:3)=[500,175,300];
LOC(75,1:3)=[500,175,400];
LOC(76,1:3)=[500,175,500];
%wall 3 vertical profile at sensors
LOC(77,1:3)=[500,0,428];
LOC(78,1:3)=[500,50,428];
LOC(79,1:3)=[500,100,428];
LOC(80,1:3)=[500,150,428];
LOC(81,1:3)=[500,200,428];
LOC(82,1:3)=[500,250,428];
LOC(83,1:3)=[500,300,428];
LOC(84,1:3)=[500,350,428];
%wall 3 vertical profile at quarter point
LOC(85,1:3)=[500,0,214];
LOC(86,1:3)=[500,50,214];
LOC(87,1:3)=[500,100,214];
LOC(88,1:3)=[500,150,214];
LOC(89,1:3)=[500,200,214];
LOC(90,1:3)=[500,250,214];
LOC(91,1:3)=[500,300,214];
LOC(92,1:3)=[500,350,214];

%Create vectors listing which sensors is on which wall
W3=[1 2 7 8:42 70:92];
W1=[1 2 7 8:42 70:92];
W2=[6 43:69];

%Generate a matrix for each wall providing x, y, z, pressure, and impulse
%Wall 3
num=length(W3);
for k=1:1:num
   N=W3(k);
   Wall3(k,1:3)=LOC(N,1:3);
   Wall3(k,4)=max(P(:,N));
   Wall3(k,5)=max(imp(:,N));
end
%Wall 2
num=length(W2);
for k=1:1:num
   N=W2(k);
   Wall2(k,1:3)=LOC(N,1:3);
   Wall2(k,4)=max(P(:,N));
```

```
   Wall2(k,5)=max(imp(:,N));
end
%Replicate the wall 2 quarter point measurements which should be locations
%62-69
Wall2(29:36,1:5)=Wall2(21:28,1:5);
Wall2(29:36,1)=Wall2(29:36,1)-248;
%Wall 1
num=length(W1);
for k=1:1:num
   N=W1(k);
   Wall1(k,1:3)=LOC(N,1:3);
   Wall1(k,4)=max(P(:,N));
   Wall1(k,5)=max(imp(:,N));
end

%Create a grid and use the interpolation/extrapolation features to create
%contour plots of pressure and impulse across all 3 walls
%Wall 2
W2x=Wall2(:,1);
W2y=Wall2(:,2);
W2z(1:length(W2x))=[2];
W2p=Wall2(:,4);
W2i=Wall2(:,5);
x2=[0:4:500];
y2=[0:4:350];
[X2,Y2]=meshgrid(x2,y2);
P2=griddata(W2x,W2y,W2p,X2,Y2,'v4');
I2=griddata(W2x,W2y,W2i,X2,Y2,'v4');
LOC2=[W2x W2y];
clear W2p W2i x2 y2
%plot pressure
figure(1)
[C,h]=contour(X2,Y2,P2)
set(h,'ShowText','on','TextStep',get(h,'LevelStep')*1)
colormap('bone')
hold on
plot(LOC2(:,1),LOC2(:,2),'ko','MarkerSize',4);
xlabel('Distance From Wall #3 (cm)')
ylabel('Height Above Chamber Floor (cm)')
%plot impulse
figure(2)
[C,h]=contour(X2,Y2,I2)
set(h,'ShowText','on','TextStep',get(h,'LevelStep')*1)
colormap('bone')
hold on
plot(LOC2(:,1),LOC2(:,2),'ko','MarkerSize',4);
xlabel('Distance From Wall #3 (cm)')
ylabel('Height Above Chamber Floor (cm)')

%Wall 1
W3x=Wall3(:,3);
```

```
W3y=Wall3(:,2);
W3p=Wall3(:,4);
W3i=Wall3(:,5);
x3=[0:4:500];
y3=[0:4:350];
[X3,Y3]=meshgrid(x3,y3);
P3=griddata(W3x,W3y,W3p,X3,Y3,'v4');
I3=griddata(W3x,W3y,W3i,X3,Y3,'v4');
LOC3=[W3x W3y];
clear W3p W3i x3 y3
%plot pressure
figure(3)
[C,h]=contour(X3,Y3,P3)
set(h,'ShowText','on','TextStep',get(h,'LevelStep')*1)
colormap('bone')
hold on
plot(LOC3(:,1),LOC3(:,2),'ko','MarkerSize',4);
xlabel('Distance From Wall #2 (cm)')
ylabel('Height Above Chamber Floor (cm)')
xlim([0 472])
%plot impulse
figure(4)
[C,h]=contour(X3,Y3,I3)
set(h,'ShowText','on','TextStep',get(h,'LevelStep')*1)
colormap('bone')
hold on
plot(LOC3(:,1),LOC3(:,2),'ko','MarkerSize',4);
xlabel('Distance From Wall #2 (cm)')
ylabel('Height Above Chamber Floor (cm)')
xlim([0 472])

%Wall 3
W3x=Wall3(:,3);
W3y=Wall3(:,2);
W3p=Wall3(:,4);
W3i=Wall3(:,5);
x3=[0:4:500];
y3=[0:4:350];
[X3,Y3]=meshgrid(x3,y3);
P3=griddata(W3x,W3y,W3p,X3,Y3,'v4');
I3=griddata(W3x,W3y,W3i,X3,Y3,'v4');
LOC3=[W3x W3y];
clear W3p W3i x3 y3
%plot pressure
figure(5)
[C,h]=contour(X3,Y3,P3)
set(h,'ShowText','on','TextStep',get(h,'LevelStep')*1)
colormap('bone')
hold on
plot(LOC3(:,1),LOC3(:,2),'ko','MarkerSize',4);
xlabel('Distance From Wall #2 (cm)')
```

```
ylabel('Height Above Chamber Floor (cm)')
xlim([0 428])
%plot impulse
figure(6)
[C,h]=contour(X3,Y3,I3)
set(h,'ShowText','on','TextStep',get(h,'LevelStep')*1)
colormap('bone')
hold on
plot(LOC3(:,1),LOC3(:,2),'ko','MarkerSize',4);
xlabel('Distance From Wall #2 (cm)')
ylabel('Height Above Chamber Floor (cm)')
xlim([0 428])
```

D.7. Script for Wall #3

This script generates the K_{LM} factors for one way spanning members. It also computes elastic deflections, and resistance function values. The script as included here is specifically for Wall #3.

```
%%%%%%%%%%%BEGIN INPUTS%%%%%%%%%%%%%%%%%%%%%%%
%Process the blast load parameters.  This comes from a vector of data
%reduced from the 2D loading profiles shown in Section 5.7.
%Input a vector "y" which is the position from the top of the wall to the
%bottom.  Input a vector "z" which is the normalized impulse.

%Basic Structural Dimensions
L1=35.98;   %inches, height of bottom part of wall up to window bottom
L2=108.036;   %inches, total wall height minus L1
hw=84.02;   %inches, height of window opening
numit=2000;   %Number of segments into which to divide the wall
R=0.4822;    %Ratio of solid width to total width of wall section
E=614e3;   %psi, modulus of elasticity
I=144;    %in^4, wall moment of inertia per unit width, not including window openings
t=12;    %inches, thickness of wall
ft=250;     %psi, tensile strength of masonry normal to bed joints
P=0;    %lbs per unit width applied axial surcharge.  Positive = compression.
A=12;   %square inches of cross section per unit width
mass=(115+25)/144/32.2/12;   %aerial mass in inches per second squared
%%%%%%%%%%ND INPUTS%%%%%%%%%%%%%%%%%%%%%%%%%%%

%%%%%%%%%%%BEGIN COMPUTATIONS%%%%%%%%%%%%%%%%%%%%
%Divide the wall into even segments
dx=(L1+L2)/numit;
x(1)=0;
for j=2:1:numit
   x(j)=x(j-1)+dx;
end
```

```
%Create a vector providing the moment of inertia of the wall section at
%each location along x.  Allows inclusion of non-uniform stiffness.
MOMI(1)=I;
for j=2:1:numit
   if x(j)<=(L2-hw)
      MOMI(j)=I;
   end
   if x(j)<=L2
      if x(j)>(L2-hw)
         MOMI(j)=R*I;
      end
   end
   if x(j)>L2
      MOMI(j)=I;
   end
end

%Create a normalized moment of inertia vector which will serve to reduce
%the applied load in areas with window openings

preduce=MOMI/max(MOMI);

%Generate the loading vector by interpolating the supplied z vector
 for j=1:1:numit
    p(j)=interp1(y,z,x(j))*preduce(j);
 end

%Find the centroid of the shear curve and thus also compute the top and
%bottom wall reactions, which allow the corrected shear and moment curves
%to be generated.
 for j=1:1:numit
    V=cumtrapz(x,p);
    R1=V(j);
    V=V-R1;
    M=cumtrapz(x,V);
    if max(M)<=0
       cgv=x(j);  %this is the x location of the shear curve centroid
       Rbot=V(numit);
       Rtop=abs(V(1));
       V=V-Rtop;  %Created corrected shear curve
       break
    end
 end

  %Create the M/EI curve for subsequent integrations.
 for j=1:1:numit
    c(j)=M(j)/(E*MOMI(j));
 end

%Create the rotation curve
```

```
 rot=cumtrapz(x,c);
%The lefthand and righthand support rotations can be determined knowing that the
%deflection at x=L1+L2 must equal 0.
for j=1:1:numit
    rot=rot-rot(j);
    defl=cumtrapz(x,rot);
    if defl(numit)>=0
       break
    end
    xmax=x(j);
end

%find the maximum tensile stress and its location.
sratio(1)=[0];
for j=2:1:length(x)
   mcrack=M(j);
   stress(j)=abs(mcrack)*(t/2)/MOMI(j);
   sratio(j)=stress(j)/(ft+P/A);
end
%Take advantage of the fact that the structure is linear and all results
%can be scaled using the actual to cracking stress ratio
smax=max(stress);
SR=smax/(ft+P/A);
pcrack=p/SR;
stress=stress/SR;

%Scale up the deflected shape and moment using the stress ratio because the
%deformation should be linear with respect to loading
defl=defl/SR;
M=M/SR;

%compute deflection at assumed height of crack
deflcrack=defl(round(L2/dx));
deflmax=max(defl);
%compute moment at assumed crack height
mcrack=M(round(L2/dx));
%check stress at assumed crack height
fcrack=abs(mcrack)*t/2/(R*I);
R1=max(cumtrapz(x,pcrack));   %elastic resistance, total load on wall in lbs
X1=deflcrack;    %deflection at onset of tensile cracking, inches
K1=R1/X1;   %elastic stiffness at the cracking load as observed at the location of the crack, lb/in
%%%%%%%%%END CRACKING LOAD DEFL CALC%%%%%%%%%%%%

%%%%%%%%%%ELASTIC TRANSFORMATION FACTORS%%%%%%%%%%
%Given the complicated loading and deflected shape, use numerical
%integration to compute the elastic KL, KM, and KLM factors.

 %Create a mass vector
 MASS(1)=mass;
 for j=2:1:numit
    if x(j)<=(L2-hw)
```

```
        MASS(j)=mass;
    end
    if x(j)<=L2
        if x(j)>(L2-hw)
            MASS(j)=R*mass;
        end
    end
    if x(j)>L2
        MASS(j)=mass;
    end
end

%Total mass
masstot=max(cumtrapz(x,MASS)); %lbs/in

%Normalize the deflection function to the point being tracked
deflnorm=defl/X1;

%compute the KM function
for j=1:1:numit
    f1(j)=MASS(j)*(deflnorm(j))^2;
end
KMe=max(cumtrapz(x,f1))/masstot;

%compute the KL function
 for j=1:1:numit
    f1(j)=pcrack(j)*(deflnorm(j));
end
KLe=max(cumtrapz(x,f1))/R1;

KLMe=KMe/KLe;

%compute the KR function
 for j=1:1:numit
    f1(j)=1*(deflnorm(j));
end
KRe=max(cumtrapz(x,f1))/(L1+L2);

%%%%%END ELASTIC TRANSFORMATION FACTORS%%%%%%%%%%%

%%%%%POST ELASTIC TRANSFORMATION FACTORS%%%%%%%%%%%
% The wall's post elastic deflection has its maximum value at x=L2.

m1=1/L2;   %slope of the curve between x=0 and x=L2
m2=1/L1;   %slope of curve between x=L2 and x=L1+L2
for j=1:1:numit
    if x(j)<=L2
        crackdefl(j)=x(j)*m1;
    elseif x(j)>L2
        crackdefl(j)=crackdefl(j-1)-m2*dx;
    end
```

```
end

%compute the KM function
 for j=1:1:numit
    f1(j)=MASS(j)*(crackdefl(j))^2;
 end
 KMc=max(cumtrapz(x,f1))/masstot

 %compute the KL function
  for j=1:1:numit
    f1(j)=pcrack(j)*(crackdefl(j));
 end
KLc=max(cumtrapz(x,f1))/R1;

KLMc=KMc/KLc;

%compute the KR function
  for j=1:1:numit
    f1(j)=1*(crackdefl(j));
 end
KRc=max(cumtrapz(x,f1))/(L1+L2);

%%%%%END POST ELASTIC TRANSFORMATION FACTORS%%%%%%%%

%%%%%ARCHING RESISTANCE FUNCTION CALULATIONS%%%%%%%%
%If the load were uniform, it would be possible to develop a closed form
%solution for the arching resistance as is reported in Chapter 6.  Due to
%nonuniformity, use the equations of moment equilibrium about points of
%rocking to solve for the maximum total resultant the wall can withstand.
%Note that the equilibrium equations do not include wall self weight.

%create a normalized load vector
pnorm=p/max(p);
n=round(L2/dx);
%normalized total force for each component
ftop=max(cumtrapz(x(1:n),pnorm(1:n)));
fbot=max(cumtrapz(x(n:numit),pnorm(n:numit)));
%Find the top half centroid
for j=2:1:n
   if max(cumtrapz(x(1:j),pnorm(1:j)))>=ftop/2
      cgtop=x(j);
      break
   end
end
%Find the bottom half centroid
for j=n+1:1:numit
   if max(cumtrapz(x(n:j),pnorm(n:j)))>=fbot/2
      cgbot=x(j);
      break
   end
end
```

```
%Compute wall part weights
Mtop=max(cumtrapz(x(1:n),MASS(1:n)));
Mbot=masstot-Mtop;

Wtop=Mtop*32.2*12;
Wbot=Mbot*32.2*12;

%Top half equilibrium
Ftop=(Wtop+P)*(t-X1)/cgtop;
%factor up the normalized load according to this result
ratio=Ftop/ftop;
R2top=max(cumtrapz(x,ratio*pnorm));

%Bottom half equilibrium
Fbot=(Wbot+P)*(t-X1)/(L2+L1-cgbot);
%factor up the normalized load according to this result
ratio=Fbot/fbot;
R2bot=max(cumtrapz(x,ratio*pnorm));

%Determine maximum arching resistance
R2=min(R2top,R2bot);
%%%%%%%END ARCHING RESISTANCE FUNCTION CALCULATION%%%%%

Pmax=max(cumtrapz(x,p));

%%%%%%%CREATE ANALYSIS REPORT%%%%%%%%%%%%%%%%%%%%
R1
X1
KLMe
R2
KLMc
Pmax
%%%%%%%END REPORT%%%%%%%%%%%%%%%%%%%%%%%%%%%%%%
```

D.8. Script for Wall #1 ESDOF Factors

This script performs the numerical integration of deformed shapes to compute the elastic and post-elastic ESDOF factors for Wall #1. The program requires input files containing data from an ANSYS FEA model. This script generates the post-elastic deflected shape based on standard SBEDS assumptions.

```
%This program will compute the transformation factors for a two dimensional
%structure given inputs that define the loading and deflected shape.  The
%following computations assume a uniform distribution of mass and stiffness
%THIS PROGRAM IS SPECIFICALLY FOR WALL#1

%%%%%%%%BEGIN INPUTS%%%%%%%%%%%%%%%%%%
NODELOC=NODELOC*2.54;
DISPSHAPE=DISPSHAPE*2.54;
L=max(NODELOC(:,1));
H=max(NODELOC(:,2));
amass=46.115/(12*12*2.54*2.54);   %kg per square centimeter, aerial mass, any constant will
work...
totalmass=amass*L*H;
ymeet=min(104.8*2.54,H);   %distance from base where yield lines meet, this
%is derived from the SBEDS methodology manual, Table 4-4

%Grid the deflected shape from the FEA model node location matrix (NODELOC)
dx=NODELOC(5,1)-NODELOC(4,1);  %grid spacing in x direction for nodes
dy=NODELOC(57,2)-NODELOC(56,2);  %grid spacing in y direction for nodes
xvect=[0:dx:L];
yvect=[0:dy:H];
[X,Y]=meshgrid(xvect,yvect);
%Grid the FEA displaced shape vecotr (DISPSHAPE)
Z=griddata(NODELOC(:,1),NODELOC(:,2),DISPSHAPE,X,Y,'v4');
%convert the grid to metric for use with the applied loading

%scale the loading function slightly to encompass the deflected shape so
%that the interpolation algorithm will function
scalex=max(max(X))/max(max(X1))+0.001;
scaley=max(max(Y))/max(max(Y1))+0.001;
X1=X1*scalex;
Y1=Y1*scaley;

%normalize the deflected shape at the point where displacement is tracked
%in the SDOF model - i.e midspan in both directions for this case
dispcrack=interp2(X,Y,Z,L/2,H);
Z=Z/dispcrack;
%%%%%%%%%END INPUTS%%%%%%%%%%%%%%%%%%
```

```
%%%%%%ELASTIC TRANSFORMATION FACTORS%%%%%%%%%%%%%
%Given the complicated loading and deflected shape, use numerical
%integration to compute the elastic KL, KM, and KLM factors.
%assumes constant mass.

%compute the KM factor:
%square every entry in the deflected shape matrix to get the mass factor
rows=length(Z(:,1));
cols=length(Z(1,:));
for k=1:1:rows
   for j=1:1:cols
   if (j==1 || k==1 || j==cols || k==rows)
         Zsq(k,j)=Z(k,j)^2*amass*(dx*dy)/2;
      else
         Zsq(k,j)=Z(k,j)^2*amass*(dx*dy);
   end
   end
end

KMe=sum(sum(Zsq))/totalmass;

Lsum=0;
%compute the KL factor:
for k=1:1:rows
   for j=1:1:cols
   if (j==1 || k==1 || j==cols || k==rows)
         ZL(k,j)=Z(k,j)*interp2(X1,Y1,I1,X(k,j),Y(k,j))*(dx*dy)/2;
         Lsum=Lsum+interp2(X1,Y1,I1,X(k,j),Y(k,j))*(dx*dy)/2;
   else
         ZL(k,j)=Z(k,j)*interp2(X1,Y1,I1,X(k,j),Y(k,j))*(dx*dy);
         Lsum=Lsum+interp2(X1,Y1,I1,X(k,j),Y(k,j))*(dx*dy);
   end
   end
end
KLe=sum(sum(ZL))/Lsum;
KLMe=KMe/KLe

%compute the KR factor:
for k=1:1:rows
   for j=1:1:cols
   if (j==1 || k==1 || j==cols || k==rows)
         ZL(k,j)=Z(k,j)*1*(dx*dy)/2;
   else
         ZL(k,j)=Z(k,j)*1*(dx*dy);
   end
   end
end
rsum=L*H*1;
KRe=sum(sum(ZL))/rsum;
```

```
%%%%%%%%END  ELASTIC TRANSFORMATION FACTORS%%%%%%%%%%

%%%%%%%%POST ELASTIC TRANSFORMATION FACTORS%%%%%%%%%%
%Wall is assumed to crack along classic yield line pattern from SBEDS
%manual

%yield line slope:
m=ymeet/(L/2);

%Create the deflected shape:
rows=length(X(:,1));
cols=length(X(1,:));
for j=1:1:cols
   for k=1:1:rows
      if (Y(k,j)>=X(k,j)*m)&&(X(k,j)<=L/2)  %Upper Left
      Zcrack(k,j)=(X(k,j)/(L/2));
      end
      if (Y(k,j)>=ymeet-m*(X(k,j)-L/2))&&(X(k,j)>L/2);  %Upper Right
      Zcrack(k,j)=(1-(X(k,j)-L/2)/(L/2));
      end
      if (Y(k,j)<ymeet-m*(X(k,j)-L/2))&&(Y(k,j)<X(k,j)*m)  %Bottom Middle
      Zcrack(k,j)=Y(k,j)/(H-(H-ymeet));
      end
   end
end

%compute the Km factor:
%square every entry in the deflected shape matrix

for k=1:1:rows
   for j=1:1:cols
   if (j==1 || k==1 || j==cols || k==rows)
         Zsqc(k,j)=Zcrack(k,j)^2*amass*(dx*dy)/2;
      else
         Zsqc(k,j)=Zcrack(k,j)^2*amass*(dx*dy);
   end
   end
end
KMc=sum(sum(Zsqc))/totalmass;

Lsum=0;

%compute the load factor
for k=1:1:rows
   for j=1:1:cols
   if (j==1 || k==1 || j==cols || k==rows)
         ZLc(k,j)=Zcrack(k,j)*interp2(X1,Y1,I1,X(k,j),Y(k,j))*(dx*dy)/2;
         Lsum=Lsum+interp2(X1,Y1,I1,X(k,j),Y(k,j))*(dx*dy)/2;
   else
         ZLc(k,j)=Zcrack(k,j)*interp2(X1,Y1,I1,X(k,j),Y(k,j))*(dx*dy);
```

```
        Lsum=Lsum+interp2(X1,Y1,I1,X(k,j),Y(k,j))*(dx*dy);
   end
   end
end
KLc=sum(sum(ZLc))/Lsum;
KLMc=KMc/KLc

%compute the resistance factor
for k=1:1:rows
   for j=1:1:cols
   if (j==1 || k==1 || j==cols || k==rows)
        ZLc(k,j)=Zcrack(k,j)*1*(dx*dy)/2;
   else
        ZLc(k,j)=Zcrack(k,j)*1*(dx*dy);
   end
   end
end
rsum=H*L*1;
KRc=sum(sum(ZLc))/rsum;

%%%%%%%%END POST ELASTIC TRANSFORMATION FACTORS%%%%%%%%%%

%plot elastic deflected shape.
figure(1)
[C,h]=contour(X,Y,Z,[0.2 0.4 0.6 0.8 1])
clabel(C,h,'LabelSpacing',200)
colormap('bone')
hold on
%plot(LOC2(:,1),LOC2(:,2),'ko','MarkerSize',2);
xlabel('X (cm)')
ylabel('Y (cm)')
xlim([0 L])
ylim([0 H])

%plot plastic deflected shape.
figure(2)
[C,h]=contour(X,Y,Zcrack,[0.2 0.4 0.6 0.8 1])
clabel(C,h,'LabelSpacing',200)
colormap('bone')
hold on
%plot(LOC2(:,1),LOC2(:,2),'ko','MarkerSize',2);
xlabel('X (cm)')
ylabel('Y (cm)')
xlim([0 L])
ylim([0 H])
```

D.9. Script for Wall #2 ESDOF Factors

This script performs the numerical integration of deformed shapes to compute the elastic and post-elastic ESDOF factors for Wall #2. The program requires input files containing data from an ANSYS FEA model. This script generates the post-elastic deflected shape based on standard SBEDS assumptions.

```
%This program will compute the transformation factors for a two dimensional
%structure given inputs that define the loading and deflected shape.  The
%following computations assume a uniform distribution of mass and stiffness
%THIS PROGRAM IS SPECIFICALLY FOR WALL#2

%%%%%%%%%%%BEGIN INPUTS%%%%%%%%%%%%%%%%%%%
NODELOC=NODELOC*2.54;
DISPSHAPE=DISPSHAPE*2.54;
L=max(NODELOC(:,1));
H=max(NODELOC(:,2));
amass=63.5/(12*12*2.54*2.54);   %kg per square centimeter, aerial mass, any constant will
work...
totalmass=amass*L*H;
xmeet=min(83.52*2.54,L/2);   %distance from vertical edges where yield lines meet, this
%is derived from the SBEDS methodology manual, Table 4-4

%Grid the deflected shape from the FEA model node location matrix (NODELOC)
dx=NODELOC(5,1)-NODELOC(4,1);  %grid spacing in x direction for nodes
dy=NODELOC(57,2)-NODELOC(56,2);  %grid spacing in y direction for nodes
xvect=[0:dx:L];
yvect=[0:dy:H];
[X,Y]=meshgrid(xvect,yvect);
%Grid the FEA displaced shape vecotr (DISPSHAPE)
Z=griddata(NODELOC(:,1),NODELOC(:,2),DISPSHAPE,X,Y,'v4');
%convert the grid to metric for use with the applied loading

%scale the loading function slightly to encompass the deflected shape so
%that the interpolation algorithm will function
scalex=max(max(X))/max(max(X2))+0.001;
scaley=max(max(Y))/max(max(Y2))+0.001;
X2=X2*scalex;
Y2=Y2*scaley;

%normalize the deflected shape at the point where displacement is tracked
%in the SDOF model - i.e midspan in both directions for this case
dispcrack=interp2(X,Y,Z,L/2,H/2);
Z=Z/dispcrack;
%%%%%%%%%%%END INPUTS%%%%%%%%%%%%%%%%%%%%
```

```
%%%%%%%%ELASTIC TRANSFORMATION FACTORS%%%%%%%
%Given the complicated loading and deflected shape, use numerical
%integration to compute the elastic KL, KM, and KLM factors.
%assumes constant mass.

%compute the KM factor:
%square every entry in the deflected shape matrix to get the mass factor
rows=length(Z(:,1));
cols=length(Z(1,:));
for k=1:1:rows
   for j=1:1:cols
   if (j==1 || k==1 || j==cols || k==rows)
         Zsq(k,j)=Z(k,j)^2*amass*(dx*dy)/2;
      else
         Zsq(k,j)=Z(k,j)^2*amass*(dx*dy);
   end
   end
end

KMe=sum(sum(Zsq))/totalmass;

Lsum=0;
%compute the KL factor:
for k=1:1:rows
   for j=1:1:cols
   if (j==1 || k==1 || j==cols || k==rows)
         ZL(k,j)=Z(k,j)*interp2(X2,Y2,I2,X(k,j),Y(k,j))*(dx*dy)/2;
         Lsum=Lsum+interp2(X2,Y2,I2,X(k,j),Y(k,j))*(dx*dy)/2;
   else
         ZL(k,j)=Z(k,j)*interp2(X2,Y2,I2,X(k,j),Y(k,j))*(dx*dy);
         Lsum=Lsum+interp2(X2,Y2,I2,X(k,j),Y(k,j))*(dx*dy);
   end
   end
end
KLe=sum(sum(ZL))/Lsum;

KLMe=KMe/KLe

%compute the KRe factor:
for k=1:1:rows
   for j=1:1:cols
   if (j==1 || k==1 || j==cols || k==rows)
         ZL(k,j)=Z(k,j)*1*(dx*dy)/2;
   else
         ZL(k,j)=Z(k,j)*1*(dx*dy);
   end
   end
end
rsum=L*H*1;
KRe=sum(sum(ZL))/rsum;
```

```
%%%%%%%%%END ELASTIC TRANSFORMATION FACTORS%%%%%%%%%%%%

%%%%%%%%%POST ELASTIC TRANSFORMATION FACTORS%%%%%%%%%%%%
%Wall is assumed to crack along classic yield line pattern from SBEDS
%manual

%yield line slope:
m=H/2/xmeet;

%Create the deflected shape:
rows=length(X(:,1));
cols=length(X(1,:));
for j=1:1:cols
   for k=1:1:rows
      if (X(k,j)<=Y(k,j)/m)&&(Y(k,j)<=H/2)  %Lower left quadrant
      Zcrack(k,j)=(X(k,j)/xmeet);
      end
      if (X(k,j)<=(xmeet-(Y(k,j)-H/2)/m))&&(Y(k,j)>H/2)  %Upper left quadrant
      Zcrack(k,j)=(X(k,j)/xmeet);
      end
      if (X(k,j)>=(L-xmeet+(Y(k,j)-H/2)/m))&&(Y(k,j)>H/2);  %Right top
      Zcrack(k,j)=(1-(X(k,j)-(L-xmeet))/xmeet);
      end
      if (X(k,j)>=(L-Y(k,j)/m))&&(Y(k,j)<=H/2)      %Right bottom
      Zcrack(k,j)=(1-(X(k,j)-(L-xmeet))/xmeet);
      end
      if (X(k,j)>Y(k,j)/m)&&(X(k,j)<(L-Y(k,j)/m))&&(Y(k,j)<=H/2)  %Center bottom
      Zcrack(k,j)=(Y(k,j)/(H/2));
      end
      if (X(k,j)>(xmeet-(Y(k,j)-H/2)/m))&&(X(k,j)<(L-xmeet+(Y(k,j)-H/2)/m))&&(Y(k,j)>H/2)
      Zcrack(k,j)=(2-2*Y(k,j)/H);   %Center Top
      end
   end
end

%compute the Km factor:
%square every entry in the deflected shape matrix

for k=1:1:rows
   for j=1:1:cols
   if (j==1 || k==1 || j==cols || k==rows)
         Zsqc(k,j)=Zcrack(k,j)^2*amass*(dx*dy)/2;
      else
         Zsqc(k,j)=Zcrack(k,j)^2*amass*(dx*dy);
   end
   end
end
KMc=sum(sum(Zsqc))/totalmass;

Lsum=0;
```

```
%compute the load factor
for k=1:1:rows
   for j=1:1:cols
   if (j==1 || k==1 || j==cols || k==rows)
         ZLc(k,j)=Zcrack(k,j)*interp2(X2,Y2,I2,X(k,j),Y(k,j))*(dx*dy)/2;
         Lsum=Lsum+interp2(X2,Y2,I2,X(k,j),Y(k,j))*(dx*dy)/2;
   else
         ZLc(k,j)=Zcrack(k,j)*interp2(X2,Y2,I2,X(k,j),Y(k,j))*(dx*dy);
         Lsum=Lsum+interp2(X2,Y2,I2,X(k,j),Y(k,j))*(dx*dy);
   end
   end
end
KLc=sum(sum(ZLc))/Lsum;

KLMc=KMc/KLc

%compute the resistance factor
for k=1:1:rows
   for j=1:1:cols
   if (j==1 || k==1 || j==cols || k==rows)
         ZLc(k,j)=Zcrack(k,j)*1*(dx*dy)/2;
   else
         ZLc(k,j)=Zcrack(k,j)*1*(dx*dy);
   end
   end
end
rsum=L*H*1;
KRc=sum(sum(ZLc))/rsum;

%%%%%%%%%END POST ELASTIC TRANSFORMATION FACTORS%%%%%
%plot elastic deflected shape.
figure(1)
[C,h]=contour(X,Y,Z,[0.2 0.4 0.6 0.8 1.0000])
clabel(C,h,'LabelSpacing',200)
%set(h,'ShowText','on','TextStep',get(h,'LevelStep')*1)
colormap('bone')
hold on
%plot(LOC2(:,1),LOC2(:,2),'ko','MarkerSize',2);
xlabel('X (cm)')
ylabel('Y (cm)')
xlim([0 L])
ylim([0 H])

%plot plastic deflected shape.
figure(2)
[C,h]=contour(X,Y,Zcrack,[0.2 0.4 0.6 0.8 1.0])
clabel(C,h,'LabelSpacing',200)
%set(h,'ShowText','on','TextStep',get(h,'LevelStep')*2)
colormap('bone')
hold on
%plot(LOC2(:,1),LOC2(:,2),'ko','MarkerSize',2);
```

```
xlabel('X (cm)')
ylabel('Y (cm)')
xlim([0 L])
ylim([0 H])
```

D.10. Script for Locating Contacts in Cubic LSDYNA Meshes

This script will identify contacts and write the required input cards for an LSDYNA model; the domain must be meshed with cubic elements with their faces oriented on planes parallel to the global XYZ axes. Furthermore, the nodal XYZ coordinates must all be non-negative. The program will directly read the *NODE and *ELEMENT cards of an LSDYNA input file provided each input card is written in a separate text file with all non-numeric data removed.

```
%This code will search two files titled 'nodes.txt' and 'elements.txt'
%and will identify contacting surfaces.  The code will then write the
%required *set_segment and *contact cards

DX=4;       %Manually specify the cubic mesh size

%Read in the node numbers and locations, delete the last two columns which
%contain no data
%Format is |node number|x-coord|y-coord|z-coord|
node=dlmread('nodes.txt');
%node(:,6)=[];
%node(:,5)=[];

%Read in the element data
%Format is
%|elnumber|partnumber|node1|node2|node3|node4|node5|node6|node7|node8|
elems=dlmread('elements.txt');

%Now create a list of every element face in the entire model
%First determine the total number of faces
numels=length(elems(:,1));
numfaces=numels*6;

%Preallocate all vectors
faces(:,1)=(1:1:numfaces);
faces(:,2:6)=0;
xmin(1:numfaces)=0;
xmax(1:numfaces)=0;
ymin(1:numfaces)=0;
```

```
ymax(1:numfaces)=0;
zmin(1:numfaces)=0;
zmax(1:numfaces)=0;
A(1:numfaces,1:4)=0;
normal(1:numfaces,1:3)=0;
fcenter(1:numfaces,1:3)=0;
contact(1:numfaces,1:2)=0;
ecenter(1:numels,1:3)=0;

%Loop through one element at a time forming 4 node sets that comprise each
%of the six faces

for k=1:1:numels
   enum=k
   %Number the second column according to which element the face is associated
   faces(6*k-5:6*k,2)=enum;
   %Number the third through the sixth column with the nodes defining the
   %faces
   faces(6*k-5,3:6)=elems(enum,3:6);
   faces(6*k-4,3:6)=elems(enum,7:10);
   faces(6*k-3,3:6)=[elems(enum,3),elems(enum,4),elems(enum,7),elems(enum,8)];
   faces(6*k-2,3:6)=[elems(enum,5),elems(enum,6),elems(enum,9),elems(enum,10)];
   faces(6*k-1,3:6)=[elems(enum,4),elems(enum,5),elems(enum,8),elems(enum,9)];
   faces(6*k,3:6)=[elems(enum,3),elems(enum,6),elems(enum,7),elems(enum,10)];
end

%Create the symbolic vector for later calculations
syms x y z;
P=[x,y,z];

%Split up the nodes of each face into 4 seperate vectors for computation
node1(1:numfaces)=faces(1:numfaces,3);
node2(1:numfaces)=faces(1:numfaces,4);
node3(1:numfaces)=faces(1:numfaces,5);
node4(1:numfaces)=faces(1:numfaces,6);

%Obtain the xyz coordinates of every node of every face
%Preallocate the vectors to speed memory performance
vect1(1:numfaces,1:3)=[0];
vect2(1:numfaces,1:3)=[0];
vect3(1:numfaces,1:3)=[0];
vect4(1:numfaces,1:3)=[0];
for k=1:1:numfaces
   facevector=k
vect1(k,1:3)=node(node1(k),2:4);
vect2(k,1:3)=node(node2(k),2:4);
vect3(k,1:3)=node(node3(k),2:4);
vect4(k,1:3)=node(node4(k),2:4);
end

%Compute the properties of areas defining every face including the x,y,z
```

```
%center of each face
%preallocate the vectors to speed memory performance
xmax(1:numfaces)=[0];
ymax(1:numfaces)=[0];
zmax(1:numfaces)=[0];
xmin(1:numfaces)=[0];
ymin(1:numfaces)=[0];
zmin(1:numfaces)=[0];
facecenter(1:numfaces,1:3)=[0];
for k=1:1:numfaces
   currentface=k
   xmax(k)=max([vect1(k,1),vect2(k,1),vect3(k,1),vect4(k,1)]);
   ymax(k)=max([vect1(k,2),vect2(k,2),vect3(k,2),vect4(k,2)]);
   zmax(k)=max([vect1(k,3),vect2(k,3),vect3(k,3),vect4(k,3)]);
   xmin(k)=min([vect1(k,1),vect2(k,1),vect3(k,1),vect4(k,1)]);
   ymin(k)=min([vect1(k,2),vect2(k,2),vect3(k,2),vect4(k,2)]);
   zmin(k)=min([vect1(k,3),vect2(k,3),vect3(k,3),vect4(k,3)]);
   %compute the center of the face

facecenter(k,1:3)=[round((xmin(k)+xmax(k))/2),round((ymin(k)+ymax(k))/2),round((zmin(k)+z
max(k))/2)];
end

%construct a matrix which calculates the centroid of every element in the
%model.  This will be used to construct the 3D search matrix
%preallocate vectors for performance
ecenter(1:numels,1:3)=[0];
for j=1:1:numels
   xavg=sum(node(elems(j,3:10),2))/8;
   yavg=sum(node(elems(j,3:10),3))/8;
   zavg=sum(node(elems(j,3:10),4))/8;
   ecenter(j,1)=xavg;
   ecenter(j,2)=yavg;
   ecenter(j,3)=zavg;
end

%Now associate the center of every face with the element to which it is
%attached
%preallocate vectors for performance
fcenter(1:numels,1:3)=[0];
for j=1:1:numfaces
   fcenter(j,1:3)=ecenter(faces(j,2),1:3);
end

%Construct a matrix that represents the xyz location of every element for
%use as a screening tool to minimize nearest neighbor searches

%Determine the global minimum coordinates
gxmin=min(xmin);
gymin=min(ymin);
gzmin=min(zmin);
```

```
%Convert the element centers into index coordinates for a three dimensional
%matrix
eloc(1:numels,1)=(ecenter(1:numels,1)-DX/2)+1;
eloc(1:numels,2)=(ecenter(1:numels,2)-DX/2)+1;
eloc(1:numels,3)=(ecenter(1:numels,3)-DX/2)+1;

%Do a little memory clean up
clear vect1 vect2 vect3 vect4

%Now write the element number into the spatially correct position inside a
%3D matrix that will aid the nearest neighbor search
%preallocate vectors
for j=1:1:numels
   xpos=round(eloc(j,1));
   ypos=round(eloc(j,2));
   zpos=round(eloc(j,3));
   LOC(xpos,ypos,zpos)=j;
end

%Increment through each element of this matrix.  At each position, look in
%all six directions and take note of the elements surround each other
%element
LOCsize=size(LOC)
LOCx=LOCsize(1);
LOCy=LOCsize(2);
LOCz=LOCsize(3);

%Step through the location matrix LOC one entry at a time through each
%slice.  Compare each element to the ones near it and create a list called
%bucket that will detail what other elements each element could have a
%contact with.
%Initialize the matrix to correct size.
bucket(1,1:6)=[0];

for j=1:1:LOCx
   for k=1:1:LOCy
      for l=1:1:LOCz
         if (LOC(j,k,l)==0)
            continue
         end
         %Look in+/- x direction
         if (j>=1) && (j<LOCx)
            masterel=LOC(j,k,l);
            bucket(masterel,1)=LOC(j+DX,k,l);
            if j>1
            bucket(masterel,2)=LOC(j-DX,k,l);
            end
         end
         %Look in the +/- y direction
         if (k>=1) && (k<LOCy)
```

```
            masterel=LOC(j,k,l);
            bucket(masterel,3)=LOC(j,k+DX,l);
            if k>1
            bucket(masterel,4)=LOC(j,k-DX,l);
            end
         end
         %Look in the +/- z direction
         if (l>=1) && (l<LOCz)
            masterel=LOC(j,k,l);
            bucket(masterel,5)=LOC(j,k,l+DX);
            if l>1
            bucket(masterel,6)=LOC(j,k,l-DX);
            end
         end
      end
   end
end

%Now translate these lists of nearest neighbor elements into a list
%of faces that are near each other.  Translate the bucket matrix into a
%matrix that contains face numbers, rather than element numbers.

for k=1:1:length(bucket(:,1))
   CurrentElement=k
   masterfaces=[6*k 6*k-1 6*k-2 6*k-3 6*k-4 6*k-5];
   SL1=bucket(k,1);
   SL2=bucket(k,2);
   SL3=bucket(k,3);
   SL4=bucket(k,4);
   SL5=bucket(k,5);
   SL6=bucket(k,6);
   %Create vector lists of the possible slave face matches
   slave(1,1:6)=[SL1*6 SL1*6-1 SL1*6-2 SL1*6-3 SL1*6-4 SL1*6-5];
   slave(2,1:6)=[SL2*6 SL2*6-1 SL2*6-2 SL2*6-3 SL2*6-4 SL2*6-5];
   slave(3,1:6)=[SL3*6 SL3*6-1 SL3*6-2 SL3*6-3 SL3*6-4 SL3*6-5];
   slave(4,1:6)=[SL4*6 SL4*6-1 SL4*6-2 SL4*6-3 SL4*6-4 SL4*6-5];
   slave(5,1:6)=[SL5*6 SL5*6-1 SL5*6-2 SL5*6-3 SL5*6-4 SL5*6-5];
   slave(6,1:6)=[SL6*6 SL6*6-1 SL6*6-2 SL6*6-3 SL6*6-4 SL6*6-5];
   %Now loop through each of the master/slave sets and identify contacting
   %faces
   for l=1:1:6
      for m=1:1:6
         for n=1:1:6
            r=masterfaces(l);
            t=slave(m,n);
            if (r<=0) || (t<=0)
               continue
            end
            %If any of the nodes are shared then there is no contact
            if (node1(r)==node1(t)) || (node1(r)==node2(t))  || (node1(r)==node3(t))  ||
(node1(r)==node4(t))
```

```
            continue
         end
         if (facecenter(r,1:3)~=facecenter(t,1:3))
            continue
         end
         if (facecenter(r,1:3)==facecenter(t,1:3))
            if (contact(t,2)~=r)  %this makes sure it hasn't been written elsewhere
               contact(r,1)=r;
               contact(r,2)=t;
            end
         end
      end
   end
end

%this code will write the resulting contact pairs to a text file in the
%appropriate format for *set_segment and *contact cards

%Now loop through all faces having a contact and create node sets that
%correspond to segments with normals pointing at each other
nset(1:length(faces),1:4)=0;
for j=1:1:length(contact)
   currentcontact=j
   if (contact(j,1)>0)
      %Get the numbers of the faces involved in the contact
      face1=contact(j,1);
      face2=contact(j,2);
      %get the locations of the associated elements
      f1x=fcenter(face1,1);
      f1y=fcenter(face1,2);
      f1z=fcenter(face1,3);
      f2x=fcenter(face2,1);
      f2y=fcenter(face2,2);
      f2z=fcenter(face2,3);
      if (f1x>f2x) || (f1y>f2y) || (f1z>f2z)
         %renumber faces if we had them backwards, always want face 1 to
         %be closer to the origin so segments are facing +x, +y or +z
         face1=contact(j,2);
         face2=contact(j,1);
         f1x=fcenter(face1,1);
         f1y=fcenter(face1,2);
         f1z=fcenter(face1,3);
         f2x=fcenter(face2,1);
         f2y=fcenter(face2,2);
         f2z=fcenter(face2,3);
      end
      %Handle an X facing contact.  We want face 1 to have a +x facing
      %normal and face 2 to have a -x facing normal.
      if (f1z==f2z) && (f1y==f2y)
         contact(j,3)=[1];
```

```
        xnorm=[1 0 0];
          %FIRST DO THE POSITIVE FACING FACE
          %arbitrarily choose the first node as being fixed, then fill in
          %the remaining three
          %get location vectors of nodes
          n(1,1:3)=node(faces(face1,3),2:4);
          n(2,1:3)=node(faces(face1,4),2:4);
          n(3,1:3)=node(faces(face1,5),2:4);
          n(4,1:3)=node(faces(face1,6),2:4);
          %write node numbers as last column
          n(1,4)=faces(face1,3);
          n(2,4)=faces(face1,4);
          n(3,4)=faces(face1,5);
          n(4,4)=faces(face1,6);
          %create a permutation matrix
          nlist=[2 3 4];
          indx=perms(nlist);
          %Now test each possible combination using dot and cross product
          for q=1:1:length(indx)
             edge1=n(indx(q,1),1:3)-n(1,1:3);
             edge2=n(indx(q,2),1:3)-n(indx(q,1),1:3);
             edge3=n(indx(q,3),1:3)-n(indx(q,2),1:3);
             edge4=n(1,1:3)-n(indx(q,3),1:3);
             if (dot(cross(edge2,edge1),xnorm)>0) && (dot(cross(edge3,edge2),xnorm)>0) &&
(dot(cross(edge4,edge3),xnorm)>0) && (dot(cross(edge1,edge4),xnorm)>0)
                nset(face1,1)=face1;
                nset(face1,2:6)=[n(1,4),n(indx(q,1),4),n(indx(q,2),4),n(indx(q,3),4),1];  %Last 1
indicates z-facing contact
             end
          end
          %NOW DO THE NEGATIVE FACING FACE
          %arbitrarily choose the first node as being fixed, then fill in
          %the remaining three
          %get location vectors of nodes
          n(1,1:3)=node(faces(face2,3),2:4);
          n(2,1:3)=node(faces(face2,4),2:4);
          n(3,1:3)=node(faces(face2,5),2:4);
          n(4,1:3)=node(faces(face2,6),2:4);
          %write node numbers as last column
          n(1,4)=faces(face2,3);
          n(2,4)=faces(face2,4);
          n(3,4)=faces(face2,5);
          n(4,4)=faces(face2,6);
          %create a permutation matrix
          nlist=[2 3 4];
          indx=perms(nlist);
          %Now test each possible combination using dot and cross product
          for q=1:1:length(indx)
             edge1=n(indx(q,1),1:3)-n(1,1:3);
             edge2=n(indx(q,2),1:3)-n(indx(q,1),1:3);
             edge3=n(indx(q,3),1:3)-n(indx(q,2),1:3);
```

```
            edge4=n(1,1:3)-n(indx(q,3),1:3);
            if (dot(cross(edge2,edge1),xnorm)<0) && (dot(cross(edge3,edge2),xnorm)<0) &&
(dot(cross(edge4,edge3),xnorm)<0) && (dot(cross(edge1,edge4),xnorm)<0)
               nset(face2,1)=face2;
               nset(face2,2:6)=[n(1,4),n(indx(q,1),4),n(indx(q,2),4),n(indx(q,3),4),1];  %Last 1
indicates z-facing contact
            end
         end
      end
      %Handle a Y facing contact.  We want face 1 to have a +Y facing
      %normal and face 2 to have a -Y facing normal.
      if (f1x==f2x) && (f1z==f2z)
         contact(j,3)=[2];
        ynorm=[0 1 0];
         %FIRST DO THE POSITIVE FACING FACE
         %arbitrarily choose the first node as being fixed, then fill in
         %the remaining three
         %get location vectors of nodes
         n(1,1:3)=node(faces(face1,3),2:4);
         n(2,1:3)=node(faces(face1,4),2:4);
         n(3,1:3)=node(faces(face1,5),2:4);
         n(4,1:3)=node(faces(face1,6),2:4);
         %write node numbers as last column
         n(1,4)=faces(face1,3);
         n(2,4)=faces(face1,4);
         n(3,4)=faces(face1,5);
         n(4,4)=faces(face1,6);
         %create a permutation matrix
         nlist=[2 3 4];
         indx=perms(nlist);
         %Now test each possible combination using dot and cross product
         for q=1:1:length(indx)
            edge1=n(indx(q,1),1:3)-n(1,1:3);
            edge2=n(indx(q,2),1:3)-n(indx(q,1),1:3);
            edge3=n(indx(q,3),1:3)-n(indx(q,2),1:3);
            edge4=n(1,1:3)-n(indx(q,3),1:3);
            if (dot(cross(edge2,edge1),ynorm)>0) && (dot(cross(edge3,edge2),ynorm)>0) &&
(dot(cross(edge4,edge3),ynorm)>0) && (dot(cross(edge1,edge4),ynorm)>0)
               nset(face1,1)=face1;
               nset(face1,2:6)=[n(1,4),n(indx(q,1),4),n(indx(q,2),4),n(indx(q,3),4),2];  %Last 2
indicates z-facing contact
            end
         end
         %NOW DO THE NEGATIVE FACING FACE
         %arbitrarily choose the first node as being fixed, then fill in
         %the remaining three
         %get location vectors of nodes
         n(1,1:3)=node(faces(face2,3),2:4);
         n(2,1:3)=node(faces(face2,4),2:4);
         n(3,1:3)=node(faces(face2,5),2:4);
         n(4,1:3)=node(faces(face2,6),2:4);
```

```
        %write node numbers as last column
        n(1,4)=faces(face2,3);
        n(2,4)=faces(face2,4);
        n(3,4)=faces(face2,5);
        n(4,4)=faces(face2,6);
        %create a permutation matrix
        nlist=[2 3 4];
        indx=perms(nlist);
        %Now test each possible combination using dot and cross product
        for q=1:1:length(indx)
           edge1=n(indx(q,1),1:3)-n(1,1:3);
           edge2=n(indx(q,2),1:3)-n(indx(q,1),1:3);
           edge3=n(indx(q,3),1:3)-n(indx(q,2),1:3);
           edge4=n(1,1:3)-n(indx(q,3),1:3);
           if (dot(cross(edge2,edge1),ynorm)<0) && (dot(cross(edge3,edge2),ynorm)<0) &&
(dot(cross(edge4,edge3),ynorm)<0) && (dot(cross(edge1,edge4),ynorm)<0)
              nset(face2,1)=face2;
              nset(face2,2:6)=[n(1,4),n(indx(q,1),4),n(indx(q,2),4),n(indx(q,3),4),2];  %Last 2
indicates z-facing contact
           end
        end
     end
     %Handle a Z facing contact.  We want face 1 to have a +Z facing
     %normal and face 2 to have a -Z facing normal.
     if (f1x==f2x) && (f1y==f2y)
        contact(j,3)=[3];
        znorm=[0 0 1];
        %FIRST DO THE POSITIVE FACING FACE
        %arbitrarily choose the first node as being fixed, then fill in
        %the remaining three
        %get location vectors of nodes
        n(1,1:3)=node(faces(face1,3),2:4);
        n(2,1:3)=node(faces(face1,4),2:4);
        n(3,1:3)=node(faces(face1,5),2:4);
        n(4,1:3)=node(faces(face1,6),2:4);
        %write node numbers as last column
        n(1,4)=faces(face1,3);
        n(2,4)=faces(face1,4);
        n(3,4)=faces(face1,5);
        n(4,4)=faces(face1,6);
        %create a permutation matrix
        nlist=[2 3 4];
        indx=perms(nlist);
        %Now test each possible combination using dot and cross product
        for q=1:1:length(indx)
           edge1=n(indx(q,1),1:3)-n(1,1:3);
           edge2=n(indx(q,2),1:3)-n(indx(q,1),1:3);
           edge3=n(indx(q,3),1:3)-n(indx(q,2),1:3);
           edge4=n(1,1:3)-n(indx(q,3),1:3);
           if (dot(cross(edge2,edge1),znorm)>0) && (dot(cross(edge3,edge2),znorm)>0) &&
(dot(cross(edge4,edge3),znorm)>0) && (dot(cross(edge1,edge4),znorm)>0)
```

```
                nset(face1,1)=face1;
                nset(face1,2:6)=[n(1,4),n(indx(q,1),4),n(indx(q,2),4),n(indx(q,3),4),3];  %Last 3
indicates z-facing contact
             end
          end
          %NOW DO THE NEGATIVE FACING FACE
          %arbitrarily choose the first node as being fixed, then fill in
          %the remaining three
          %get location vectors of nodes
          n(1,1:3)=node(faces(face2,3),2:4);
          n(2,1:3)=node(faces(face2,4),2:4);
          n(3,1:3)=node(faces(face2,5),2:4);
          n(4,1:3)=node(faces(face2,6),2:4);
          %write node numbers as last column
          n(1,4)=faces(face2,3);
          n(2,4)=faces(face2,4);
          n(3,4)=faces(face2,5);
          n(4,4)=faces(face2,6);
          %create a permutation matrix
          nlist=[2 3 4];
          indx=perms(nlist);
          %Now test each possible combination using dot and cross product
          for q=1:1:length(indx)
             edge1=n(indx(q,1),1:3)-n(1,1:3);
             edge2=n(indx(q,2),1:3)-n(indx(q,1),1:3);
             edge3=n(indx(q,3),1:3)-n(indx(q,2),1:3);
             edge4=n(1,1:3)-n(indx(q,3),1:3);
             if (dot(cross(edge2,edge1),znorm)<0) && (dot(cross(edge3,edge2),znorm)<0) &&
(dot(cross(edge4,edge3),znorm)<0) && (dot(cross(edge1,edge4),znorm)<0)
                nset(face2,1)=face2;
                nset(face2,2:6)=[n(1,4),n(indx(q,1),4),n(indx(q,2),4),n(indx(q,3),4),3];  %Last 3
indicates z-facing contact
             end
          end
       end
    end
end

%Now open the output file for writing and begin writing cards
fid=fopen('contacts.k','a+');

%Write the *set_segment cards
a='*SET_SEGMENT';
b='$#     sid       da1       da2       da3       da4';
c='$#      n1        n2        n3        n4        a1        a2        a3        a4';
indx=0;
for j=1:1:length(contact)
   if (contact(j,1)>0)
      %write *set_segment
      fprintf(fid,'%s\n',a);
      %write the header for the SID line
```

```
        %fprintf(fid,'%s\n',b);
        %write the SID as the current face number
        fprintf(fid,'%10.0f\n',contact(j,1));
        %write the next header line
        %fprintf(fid,'%s\n',c);
        %now write the nodes that comprise this set
        node1=nset(contact(j,1),2);
        node2=nset(contact(j,1),3);
        node3=nset(contact(j,1),4);
        node4=nset(contact(j,1),5);
        fprintf(fid,'%10.0f%10.0f%10.0f%10.0f\n',[node1 node2 node3 node4]);
        %write the second face's card
        fprintf(fid,'%s\n',a);
        %write the header for the SID line
        %fprintf(fid,'%s\n',b);
        %write the SID as the current face number
        fprintf(fid,'%10.0f\n',contact(j,2));
        %write the next header line
        %fprintf(fid,'%s\n',c);
        %now write the nodes that comprise this set
        node1=nset(contact(j,2),2);
        node2=nset(contact(j,2),3);
        node3=nset(contact(j,2),4);
        node4=nset(contact(j,2),5);
        fprintf(fid,'%10.0f%10.0f%10.0f%10.0f\n',[node1 node2 node3 node4]);
    end
end

%Now write the contact cards to file using the set segment numbers in each
%pair
a='*CONTACT_AUTOMATIC_SURFACE_TO_SURFACE_TIEBREAK_ID';
b='$#     cid';
c='$#    ssid      msid     sstyp     mstyp    sboxid    mboxid       spr       mpr';
d='$#      fs        fd        dc        vc       vdc    penchk        bt        dt';
e='  0.750000  0.500000     0.000     0.000      2.00         0     0.0001.0000E+20';
f='$#     sfs       sfm       sst       mst      sfst      sfmt       fsf       vsf';
g='  1.000000  1.000000     0.000     0.000  1.000000  1.000000  1.000000  1.000000';
h='$#    nfls      sfls    tblcid';
%hh='         2  93.24000  100.0000';
%hhh='         2  200.0000  100.0000';
hh='         7   85.8000    75.000       7.2    0.0571     0.337';
hhh='         7   150.000    75.000       7.2    0.0571     0.337';

clear face;
for j=1:1:length(contact)
    if (contact(j,1)>0)
        face=contact(j,1);
        %write the headers before the set ID's
        fprintf(fid,'%s\n',a);
        %fprintf(fid,'%s\n',b);
        fprintf(fid,'%10.0f\n',j);  %this is the contact ID number
```

```
      %now write the contact slave and master id's
      %fprintf(fid,'%s\n',c);
      fprintf(fid,'%10.0f%10.0f%10.0f%10.0f\n',[contact(j,1),contact(j,2)],0,0);
      %now write the rest of the lines
      %fprintf(fid,'%s\n',d);
      fprintf(fid,'%s\n',e);
      %fprintf(fid,'%s\n',f);
      fprintf(fid,'%s\n',g);
      %fprintf(fid,'%s\n',h);
      if (fcenter(face,1)<300)&&(contact(j,3)==2)
         fprintf(fid,'%s\n',hhh);
      elseif (fcenter(face,1)>300)&&(contact(j,3)==1)
         fprintf(fid,'%s\n',hhh);
      else
         fprintf(fid,'%s\n',hh);
      end
      %fprintf(fid,'%s\n',hhh);
      %fprintf(fid,'%s\n',hhhh);
   end
end

fclose(fid);

%This will write the *PART cards

fid=fopen('parts.k','a+');

%Write the *set_segment cards
a='*PART';
b='Part Definitions';
c='$PID     SECID    MID      EOSID    HGID';
%d='*DAMPING_PART_STIFFNESS'
%dd='$#     pid      coef'
numparts=5748;

for j=1:1:numparts
   fprintf(fid,'%s\n',a);
   fprintf(fid,'%s\n',b);
   fprintf(fid,'%s\n',c);
   fprintf(fid,'%10.0f%10.0f%10.0f%10.0f%10.0f\n',[j,1,1,0,0]);
  %fprintf(fid,'%s\n',d);
  %fprintf(fid,'%s\n',dd);
  %fprintf(fid,'%10.0f%10.4f\n',[j,0.100]);
end

fclose(fid);
```

APPENDIX E: INPUT FILES FOR CTH SIMULATIONS

This appendix contains the CTH input files used during this investigation. At the beginning of each input file is a brief description of the simulation's purpose.

E.1. INPUT #1

This input file simulates the BPS-10 and BPG-14 blast events documented in Chapter 3 and again in Chapter 5.

```
************************************************************************
*eor* cthin
************************************************************************
2D Test of Eo=5kJ/cc – BPS-10 and BPG-14 - Free Air
*
control
  mmp
  tstop = 6e-3
endc

spy

 PlotTime(0.0, 5e-4);

 SaveTime(0.0, 5e-4);
 Save("M,VOLM,VX,VY,P");

 ImageFormat(800,600);

 define main()
 {
   pprintf(" PLOT: Cycle=%d, Time=%e\n",CYCLE,TIME);
   XLimits(0,400);
   YLimits(0,80);

   Image("Mats");
    Window(0,0,0.75,1);
    MatColors(PERU,LIGHT_BLUE);
    Label(sprintf("Materials at %0.2e s.",TIME));
    Plot2DMats;
    Draw2DBlockEdges;
    MatNames("TNT","Air");
    DrawMatLegend("",0.75,0.2,0.99,0.9);
   EndImage;
```

```
  Image("Pressure");
   Window(0,0,0.75,1);
   ColorMapRange(1e6,7e7,LOG_MAP);
   Label(sprintf("Pressure at %0.2e s.",TIME));
   Plot2D("P");
   Draw2DMatContour;
   Draw2DTracers(3);
   DrawColorMap("(dyn/cm^2^)",0.75,0.4,0.9,0.9);
  EndImage;
  Image("Vmag");
   Window(0,0,0.75,1);
   ColorMapRange(1e2,1e6,LOG_MAP);
   Label(sprintf("Velocity Magnitude at %0.2e s.",TIME));
   Plot2D("VMAG");
   Draw2DMatContour;
   Draw2DTracers(3);
   DrawColorMap("(cm/s)",0.75,0.4,0.9,0.9);
  EndImage;
 }

 HisTime(0,1e-6);
 SaveTracer(ALL);
 SaveHis("GLOBAL,POSITION,P");

 define spyhis_main()
 {
  HisLoad(1,"hscth");
  Label("Pressure at Tracer 1");
  TPlot("P.1",1,AUTOSCALE);
 }
endspy

* AMR calculation
amr
 2dc
 debug
 nx=10
 ny=10
 bx=10
 by=4
 gmin = 0,   0
 gmax = 400, 160
 maxl = 4
 maxb = 5000

 * unrefine everywhere refinement not indicated
```

```
 indicator
  val void
  unrabove -1
 endi

 * refine explosive until burn complete
 indicator
  mat 1
  val dens
  refabove 1
  maxl=4
 endi

 * refine moving air shock
 indicator
  ton=1e-6
  maxl=4
  val P
  linhistogram
  vmin 1.2e6
  refabove 0.15
  unrbelow 0.15
 endi

enda

convct
   interface = smyra
endc

*  equation of state inputs
eos
   *dynamite
   mat1  jwl tnt
   R0=1.5 AG=2.3435e12 BG=9.5127e10
   DCJ=5.856e5 PCJ=1.46502e11 R1=4.35916869 R2=1.39146798
   WG=0.249751967 TCJ=0.35 E0=0 CV=0 BRN=1
   *air at gastonia range conditions
   mat2  ses  air T0=0.0255239 R0=1.197e-3
endeos

tracer
 add 293.4,50.8 fixed=xy
 add 297.5,50.8 fixed=xy
endtracer
heburn
```

```
  mat 1  d 5.856e5
  dp 0,40
  r 45
  time 0.0
endh

* material insertion inputs
diatom
    package 'explosive'
     mat 1
     insert box
       p1=0,40.65
       p2=4.46837,60.95
     endinsert
    endpackage
    package 'air'
     mat 2
     insert box
      p1 0,   0
      p2 2000, 2000
     endi
    endp
enddiatom

edit
  shortt
    tim = 0.,  dt = 1e-3
  ends
  longt
    tim = 0.,  dt = 1.0
  endl
  restt
    tim = 0.
    dtf = 3e-3
  endr
ende

*  spall parameters
 fracts
   pfrac1  -1.0e12
   pfrac2  -1.0e12
 endf
*
boundary
   bhy
      bxb = 0 , bxt = 1
```

```
      byb = 0 , byt = 1
   endh
endb
mindt
   time = 0.  dt = 1.e-12
endn
```

E.2. INPUT #2

This input file simulates the A1 blast event using two-dimensional cylindrical symmetry.

```
*************************************************************************
*eor* cthin
*************************************************************************
Shot A1 with unimax Eo of 5 kJ/cc
*
control
  mmp
  tstop = 9e-3
endc

spy
 PlotTime(0.0, 5e-4);
 SaveTime(0.0, 5e-4);
 Save("M,VOLM,VX,VY,P");
 ImageFormat(800,600);

 define main()
 {
   pprintf(" PLOT: Cycle=%d, Time=%e\n",CYCLE,TIME);
   XLimits(0,251.5);
   YLimits(0,503);

   Image("Mats");
    Window(0,0,0.75,1);
    MatColors(PERU,SNOW);
    Label(sprintf("Materials at %0.2e s.",TIME));
    Plot2DMats;
    Draw2DBlockEdges;
    MatNames("TNT","Air");
    DrawMatLegend("",0.75,0.2,0.99,0.9);
   EndImage;
   Image("Pressure");
    Window(0,0,0.75,1);
```

```
   ColorMapRange(1e6,7e7,LOG_MAP);
   Label(sprintf("Pressure at %0.2e s.",TIME));
   Plot2D("P");
   Draw2DMatContour;
   ReverseGrayMap;
   Draw2DTracers(3);
   DrawColorMap("(dyn/cm^2^)",0.75,0.4,0.9,0.9);
  EndImage;
  Image("Vmag");
   Window(0,0,0.75,1);
   ColorMapRange(1e2,1e6,LOG_MAP);
   Label(sprintf("Velocity Magnitude at %0.2e s.",TIME));
   Plot2D("VMAG");
   Draw2DMatContour;
   Draw2DTracers(3);
   ReverseGrayMap;
   DrawColorMap("(cm/s)",0.75,0.4,0.9,0.9);
  EndImage;

 }

 HisTime(0,1e-6);
 SaveTracer(ALL);
 SaveHis("GLOBAL,POSITION,P");

 define spyhis_main()
 {
  HisLoad(1,"hscth");
  Label("Pressure at Tracer 1");
  TPlot("P.1",1,AUTOSCALE);
 }
endspy

* AMR calculation
amr
 2dc
  debug

 nx=10
 ny=10
 bx=4
 by=8
 gmin = 0,0
 gmax = 251.5,503
 maxl = 7
 maxb = 5000
```

```
* unrefine everywhere refinement not indicated
indicator
 val void
 unrabove -1
endi

* refine explosive until burn complete
indicator
 mat 1
 toff=1e-3
 val dens
 refabove 1
 maxl=7
endi

* refine moving air shock
indicator
 ton=1e-5
 maxl=6
 value P
 linhistogram
 vmin 1.1e6
 refabove 0.15
 unrbelow 0.15
endi

*refine reflection zone
indicator
mat 2
maxl=7
val vmag
refabove 1000
unrbelow 900
p1=240,0
p2=251.5,503
endi

enda

convct
  interface = smyra
endc

*  equation of state inputs
eos
```

```
   *dynamite
   mat1  jwl tnt
   R0=1.5 AG=2.3435e12 BG=9.5127e10
   DCJ=5.856e5 PCJ=1.46502e11 R1=4.35916869 R2=1.39146798
   WG=0.249751967 TCJ=0.35 E0=0 CV=0 BRN=1

   *Mid day macon GA air
   mat2  ses  air T0=0.02642 R0=1.172e-3
endeos

tracer
 add 251.5,42 fixed=xy
 add 251.5,136 fixed=xy
 add 251.5,203 fixed=xy
 add 5,503 fixed=xy
 add 251.5,138 fixed=xy
 add 251.5,0 fixed=xy
 add 251.5,50 fixed=xy
 add 251.5,100 fixed=xy
 add 251.5,150 fixed=xy
 add 251.5,200 fixed=xy
 add 251.5,250 fixed=xy
 add 251.5,300 fixed=xy
 add 251.5,350 fixed=xy
 add 251.5,400 fixed=xy
 add 251.5,450 fixed=xy
 add 251.5,503 fixed=xy
endtracer

heburn
  mat 1  d 5.856e5
  dp 0,70
  r 45
  time 0.0
endh

* material insertion inputs
diatom
    package 'explosive'
     mat 1
     insert box
       p1=0,30.48
       p2=5.8136,71.48
     endinsert
    endpackage
    package 'air'
```

```
     mat 2
     insert box
      p1 0,   0
      p2 2000, 2000
     endi
    endp
enddiatom

edit
  shortt
    tim = 0.,  dt = 1e-3
  ends
  longt
    tim = 0.,  dt = 1.0
  endl
  restt
    tim = 0.
    dtf = 6e-3
  endr
ende

*  spall parameters
 fracts
   pfrac1  -1.0e12
   pfrac2  -1.0e12
 endf
*
boundary
   bhy
      bxb = 0 , bxt = 0
      byb = 0 , byt = 0
   endh
endb
mindt
   time = 0.  dt = 1.e-12
endn
```

E.3. INPUT #3

This input file simulates the B blast event using two-dimensional cylindrical symmetry. Input file for Wall #2 (ref Chapter 2 for wall designations).

```
**********************************************************************
*eor* cthin
```

```
**************************************************************************
Shot B wall 2 with Eo of 5 kJ
*
control
  mmp
  tstop = 13e-3
endc

spy
 PlotTime(0.0, 5e-4);
 SaveTime(0.0, 5e-4);
 Save("M,VOLM,VX,VY,P");
 ImageFormat(800,600);

 define main()
 {
   pprintf(" PLOT: Cycle=%d, Time=%e\n",CYCLE,TIME);
   XLimits(0,428);
   YLimits(0,321);

   Image("Mats");
    Window(0,0,0.75,1);
    MatColors(PERU,SNOW);
    Label(sprintf("Materials at %0.2e s.",TIME));
    Plot2DMats;
    Draw2DBlockEdges;
    MatNames("TNT","Air");
    DrawMatLegend("",0.75,0.2,0.99,0.9);
   EndImage;
   Image("Pressure");
    Window(0,0,0.75,1);
    ColorMapRange(1e6,7e7,LOG_MAP);
    Label(sprintf("Pressure at %0.2e s.",TIME));
    Plot2D("P");
    Draw2DMatContour;
    ReverseGrayMap;
    Draw2DTracers(3);
    DrawColorMap("(dyn/cm^2^)",0.75,0.4,0.9,0.9);
   EndImage;
   Image("Vmag");
    Window(0,0,0.75,1);
    ColorMapRange(1e2,1e6,LOG_MAP);
    Label(sprintf("Velocity Magnitude at %0.2e s.",TIME));
    Plot2D("VMAG");
    Draw2DMatContour;
    Draw2DTracers(3);
```

```
   ReverseGrayMap;
   DrawColorMap("(cm/s)",0.75,0.4,0.9,0.9);
  EndImage;
 }

HisTime(0,1e-6);
 SaveTracer(ALL);
 SaveHis("GLOBAL,POSITION,P");
 define spyhis_main()
 {
  HisLoad(1,"hscth");
  Label("Pressure at Tracer 1");
  TPlot("P.1",1,AUTOSCALE);
 }
endspy

* AMR calculation
amr
 2dc
  debug
 nx=10
 ny=10
 bx=8
 by=6
 gmin = 0,0
 gmax = 428,321
 maxl = 7
 maxb = 5000

 * unrefine everywhere refinement not indicated
 indicator
  val void
  unrabove -1
 endi

 * refine explosive until burn complete
 indicator
  mat 1
  toff=1e-3
  val dens
  refabove 1
  maxl=7
 endi

 * refine moving air shock
 indicator
```

```
 ton=1e-5
 maxl=6
 value P
 linhistogram
 vmin 1.1e6
 refabove 0.15
 unrbelow 0.15
endi

*refine reflection zone
indicator
mat 2
maxl=7
val vmag
refabove 1000
unrbelow 900
p1=418,0
p2=428,321
endi

enda

convct
  interface = smyra
endc

*  equation of state inputs
eos
  *dynamite
  mat1  jwl tnt
  R0=1.5 AG=2.3435e12 BG=9.5127e10
  DCJ=5.856e5 PCJ=1.46502e11 R1=4.35916869 R2=1.39146798
  WG=0.249751967 TCJ=0.35 E0=0 CV=0 BRN=1

  *Macon GA air at mid day
  mat2  ses  air T0=0.02642 R0=1.172e-3
endeos

tracer
add 428,160 fixed=xy
add 428,0 fixed=xy
add 428,50 fixed=xy
add 428,100 fixed=xy
add 428,150 fixed=xy
add 428,200 fixed=xy
add 428,250 fixed=xy
```

```
 add 428,300 fixed=xy
 add 428,321 fixed=xy
endtracer

heburn
  mat 1  d 5.856e5
  dp 0,70
  r 45
  time 0.0
endh

* material insertion inputs
diatom
    package 'explosive'
     mat 1
     insert box
       p1=0,30.48
       p2=6.714235,71.48
     endinsert
    endpackage
    package 'air'
     mat 2
     insert box
      p1 0,   0
      p2 2000, 2000
     endi
    endp
enddiatom

discard
mat=-1
dens=1000
denl=3
ton=5e-4
toff=20e-3
dti=5e-5
endd

edit
  shortt
    tim = 0.,  dt = 1e-3
  ends
  longt
    tim = 0.,  dt = 1.0
  endl
```

```
  restt
    tim = 0.
    dtf = 9e-3
  endr
ende

*  spall parameters
 fracts
   pfrac1  -1.0e12
   pfrac2  -1.0e12
 endf

boundary
   bhy
      bxb = 0 , bxt = 0
      byb = 0 , byt = 0
   endh
endb
mindt
   time = 0.  dt = 1.e-12
endn
```

E.4. INPUT #4

This input file simulates the B blast event using two-dimensional cylindrical symmetry. Input file for Wall #3 (ref Chapter 2 for wall designations).

```
**********************************************************************
*eor* cthin
**********************************************************************
Shot B wall 3 with Eo of 5 kJ
*
control
  mmp
  tstop = 9e-3
  tbad=500000000
endc

spy
 PlotTime(0.0, 5e-4);
 SaveTime(0.0, 5e-4);
 Save("M,VOLM,VX,VY,P");
 ImageFormat(800,600);

 define main()
```

```
{
 pprintf(" PLOT: Cycle=%d, Time=%e\n",CYCLE,TIME);
 XLimits(0,248);
 YLimits(0,372);

 Image("Mats");
  Window(0,0,0.75,1);
  MatColors(PERU,SNOW);
  Label(sprintf("Materials at %0.2e s.",TIME));
  Plot2DMats;
  Draw2DBlockEdges;
  MatNames("TNT","Air");
  DrawMatLegend("",0.75,0.2,0.99,0.9);
 EndImage;
 Image("Pressure");
  Window(0,0,0.75,1);
  ColorMapRange(1e6,7e7,LOG_MAP);
  Label(sprintf("Pressure at %0.2e s.",TIME));
  Plot2D("P");
  Draw2DMatContour;
  ReverseGrayMap;
  Draw2DTracers(3);
  DrawColorMap("(dyn/cm^2^)",0.75,0.4,0.9,0.9);
 EndImage;
 Image("Vmag");
  Window(0,0,0.75,1);
  ColorMapRange(1e2,1e6,LOG_MAP);
  Label(sprintf("Velocity Magnitude at %0.2e s.",TIME));
  Plot2D("VMAG");
  Draw2DMatContour;
  Draw2DTracers(3);
  ReverseGrayMap;
  DrawColorMap("(cm/s)",0.75,0.4,0.9,0.9);
 EndImage;
}

HisTime(0,1e-6);
SaveTracer(ALL);
SaveHis("GLOBAL,POSITION,P");

define spyhis_main()
{
 HisLoad(1,"hscth");
 Label("Pressure at Tracer 1");
 TPlot("P.1",1,AUTOSCALE);
}
```

```
endspy

* AMR calculation
amr
 2dc
  debug
 nx=10
 ny=10
 bx=4
 by=6
 gmin = 0,0
 gmax = 248,372
 maxl = 7
 maxb = 5000

 * unrefine everywhere refinement not indicated
 indicator
  val void
  unrabove -1
 endi

 * refine explosive until burn complete
 indicator
  mat 1
  toff=1e-3
  val dens
  refabove 1
  maxl=7
 endi

 * refine moving air shock
 indicator
  ton=1e-5
  maxl=6
  value P
  linhistogram
  vmin 1.1e6
  refabove 0.15
  unrbelow 0.15
 endi

 *refine reflection zone
 indicator
 mat 2
```

```
 maxl=7
 val vmag
 refabove 1000
 unrbelow 900
 p1=238,0
 p2=248,372
 endi
enda

convct
  interface = smyra
endc

*  equation of state inputs
eos
  *dynamite
  mat1  jwl tnt
  R0=1.5 AG=2.3435e12 BG=9.5127e10
  DCJ=5.856e5 PCJ=1.46502e11 R1=4.35916869 R2=1.39146798
  WG=0.249751967 TCJ=0.35 E0=0 CV=0 BRN=1

  *Macon GA air at mid day
  mat2  ses  air T0=0.02642 R0=1.172e-3
endeos

tracer
 add 248,45 fixed=xy
 add 248,159 fixed=xy
 add 248,0 fixed=xy
 add 248,50 fixed=xy
 add 248,100 fixed=xy
 add 248,150 fixed=xy
 add 248,200 fixed=xy
 add 248,250 fixed=xy
 add 248,300 fixed=xy
 add 248,350 fixed=xy
 add 248,372 fixed=xy
endtracer

heburn
  mat 1  d 5.856e5
  dp 0,70
  r 45
  time 0.0
endh
```

```
* material insertion inputs
diatom
    package 'explosive'
     mat 1
     insert box
       p1=0,30.48
       p2=6.714235,71.48
     endinsert
    endpackage
    package 'air'
     mat 2
     insert box
      p1 0,   0
      p2 2000, 2000
     endi
    endp
enddiatom

discard
mat=-1
dens=100
denl=3
ton=5e-4
toff=9e-3
dti=1e-4
endd

edit
  shortt
    tim = 0.,  dt = 1e-3
  ends
  longt
    tim = 0.,  dt = 1.0
  endl
  restt
    tim = 0.
    dtf = 6e-3
  endr
ende

*  spall parameters
 fracts
   pfrac1  -1.0e12
   pfrac2  -1.0e12
 endf
*
```

```
boundary
  bhy
     bxb = 0 , bxt = 0
     byb = 0 , byt = 0
  endh
endb
mindt
  time = 0.  dt = 1.e-12
endn
```

E.5. INPUT #5

This input file simulates shot B in three dimensions.

```
*************************************************************************
*eor* cthin
*************************************************************************
Shot B in 3D with unimax Eo of 5 kJ/cc
*
control
 mmp0
 tstop = 25e-3
 tbad=5000000000
 pvo=10
 rdu=14.4e3
endc

spy
 PlotTime(0.0, 5e-4);
 SaveTime(0.0, 5e-4);
 Save("M,VOLM,VX,VY,P");
 ImageFormat(800,600);
 define main()
 {
  pprintf(" PLOT: Cycle=%d, Time=%e\n",CYCLE,TIME);
  XLimits(0,500);
  YLimits(0,350);
  ZLimits(0,500);

  Image("Mats");
   Window(0,0,0.75,1);
   MatColors(PERU,NO_COLOR);
   RotateAbout(250,150,250);
   RotateY(45);
   RotateZ(10);
   RotateX(10);
```

```
  Label(sprintf("Materials at %0.2e s.",TIME));
  Plot3DMats;
  Draw3DBlockEdges;
  MatNames("TNT","Air");
  DrawMatLegend("",0.75,0.2,0.99,0.9);
 EndImage;
 Image("Pressure");
  Window(0,0,0.75,1);
  RotateAbout(250,150,250);
  RotateY(45);
  RotateZ(10);
  RotateX(10);
  MatColors(NO_COLOR,NO_COLOR);
  Plot3DMats;
  ColorMapRange(1.1e6,2e8,LIN_MAP);
  ColorMapClipping(ON,OFF);
  ReverseGrayMap;
  Label(sprintf("Pressure at %0.2e s.",TIME));
  Paint3DMat(1,"P");
  Paint3DMat(2,"P");
  DrawColorMap("(dyn/cm^2^)",0.75,0.4,0.9,0.9);
 EndImage;
 Image("Pressure2");
  Window(0,0,0.75,1);
  RotateAbout(250,150,250);
  RotateY(15);
  RotateZ(5);
  RotateX(10);
  MatColors(NO_COLOR,NO_COLOR);
  Plot3DMats;
  ColorMapRange(1.1e6,2e8,LIN_MAP);
  ColorMapClipping(ON,OFF);
  ReverseGrayMap;
  Label(sprintf("Pressure at %0.2e s.",TIME));
  Paint3DMat(1,"P");
  Paint3DMat(2,"P");
  DrawColorMap("(dyn/cm^2^)",0.75,0.4,0.9,0.9);
 EndImage;
}

HisTime(0,1e-6);
SaveTracer(ALL);
SaveHis("GLOBAL,POSITION,P");

define spyhis_main()
{
```

```
 HisLoad(1,"hscth");
 Label("Pressure at Tracer 1");
 TPlot("P.1",1,AUTOSCALE);
}
endspy

* AMR calculation
amr
 3dr
 debug
 nx=8
 ny=8
 nz=8
 bx=10
 by=7
 bz=12
 gmin = 0,0,0
 gmax = 500,350,600
 maxl = 6
 maxb = 1600

 * unrefine everywhere refinement not indicated
 indicator
  val void
  unrabove -1
 endi

 * refine explosive until burn complete
 indicator
  mat 1
  toff=5e-5
  val dens
  refabove 0.25
  maxl=6
 endi

 * refine moving air shock
 indicator
  maxl=6
  value P
  linhistogram
  vmin 1.3e6
  refabove 0.05
  unrbelow 0.04
 endi
```

```
enda

convct
  interface = smyra
  convct=0
endc

*  equation of state inputs
eos
  *dynamite
  mat1  jwl tnt
  R0=1.5 AG=2.3435e12 BG=9.5127e10
  DCJ=5.856e5 PCJ=1.46502e11 R1=4.35916869 R2=1.39146798
  WG=0.249751967 TCJ=0.35 E0=0 CV=0 BRN=1

  *Mid day macon GA air
  mat2  ses  air T0=0.02642 R0=1.172e-3
endeos

tracer
 *instruments
 add 500,45,428 fixed=xyz   *P1
 add 500,159,428 fixed=xyz  *P2
 add 500,350,428 fixed=xyz  *P3
 add 500,159,428 fixed=xyz  *P4
 add 500,45,428 fixed=xyz   *P5
 add 248,160,0 fixed=xyz  *P6
 add 500,160,212 fixed=xyz  *P7
 *Wall 1 horizontal profile
 add 500,175,0 fixed=xyz
 add 500,175,50 fixed=xyz
 add 500,175,100 fixed=xyz
 add 500,175,150 fixed=xyz
 add 500,175,200 fixed=xyz
 add 500,175,250 fixed=xyz
 add 500,175,300 fixed=xyz
 add 500,175,350 fixed=xyz
 add 500,175,400 fixed=xyz
 add 500,175,450 fixed=xyz
 add 500,175,500 fixed=xyz
 *Wall 1 central vertical profile
 add 500,0,236 fixed=xyz
 add 500,50,236 fixed=xyz
 add 500,100,236 fixed=xyz
 add 500,150,236 fixed=xyz
 add 500,200,236 fixed=xyz
```

add 500,250,236 fixed=xyz
add 500,300,236 fixed=xyz
add 500,350,236 fixed=xyz
*Wall 1 quarter point vertical profile
add 500,0,118 fixed=xyz
add 500,50,118 fixed=xyz
add 500,100,118 fixed=xyz
add 500,150,118 fixed=xyz
add 500,200,118 fixed=xyz
add 500,250,118 fixed=xyz
add 500,300,118 fixed=xyz
add 500,350,118 fixed=xyz
*Wall 1 quarter point vetical profile
add 500,0,354 fixed=xyz
add 500,50,354 fixed=xyz
add 500,100,354 fixed=xyz
add 500,150,354 fixed=xyz
add 500,200,354 fixed=xyz
add 500,250,354 fixed=xyz
add 500,300,354 fixed=xyz
add 500,350,354 fixed=xyz
*Wall 2 horizontal profile
add 0,175,0 fixed=xyz
add 50,175,0 fixed=xyz
add 100,175,0 fixed=xyz
add 150,175,0 fixed=xyz
add 200,175,0 fixed=xyz
add 250,175,0 fixed=xyz
add 300,175,0 fixed=xyz
add 350,175,0 fixed=xyz
add 400,175,0 fixed=xyz
add 450,175,0 fixed=xyz
add 500,175,0 fixed=xyz
*Wall 2 vertical profile
add 248,0,0 fixed=xyz
add 248,50,0 fixed=xyz
add 248,100,0 fixed=xyz
add 248,150,0 fixed=xyz
add 248,200,0 fixed=xyz
add 248,250,0 fixed=xyz
add 248,300,0 fixed=xyz
add 248,350,0 fixed=xyz
*Wall 2 vertical quarter point profile
add 372,0,0 fixed=xyz
add 372,50,0 fixed=xyz
add 372,100,0 fixed=xyz

```
 add 372,150,0 fixed=xyz
 add 372,200,0 fixed=xyz
 add 372,250,0 fixed=xyz
 add 372,300,0 fixed=xyz
 add 372,350,0 fixed=xyz
 *wall 3 points along midheight
 add 500,175,0 fixed=xyz
 add 500,175,50 fixed=xyz
 add 500,175,100 fixed=xyz
 add 500,175,200 fixed=xyz
 add 500,175,300 fixed=xyz
 add 500,175,400 fixed=xyz
 add 500,175,500 fixed=xyz
 *wall 3 vertical profile at sensors
 add 500,0,428 fixed=xyz
 add 500,50,428 fixed=xyz
 add 500,100,428 fixed=xyz
 add 500,150,428 fixed=xyz
 add 500,200,428 fixed=xyz
 add 500,250,428 fixed=xyz
 add 500,300,428 fixed=xyz
 add 500,350,428 fixed=xyz
 *wall 3 vertical profile at quarter point
 add 500,0,214 fixed=xyz
 add 500,50,214 fixed=xyz
 add 500,100,214 fixed=xyz
 add 500,150,214 fixed=xyz
 add 500,200,214 fixed=xyz
 add 500,250,214 fixed=xyz
 add 500,300,214 fixed=xyz
 add 500,350,214 fixed=xyz
endtracer

heburn
  mat 1  d 5.856e5
  dp 250,70,428
  r 50  time 0.0
endh

* material insertion inputs
diatom
    package 'explosive'
     mat 1
     numsub=12
     iteration=4
     insert cylinder
```

```
      ce1=250,30.48,428
      ce2=250,71.48,428
      r=6.714235
    endinsert
   endpackage
   package 'air'
    mat 2
    insert box
     p1 0,0,0
     p2 2000,2000,2000
    endi
   endp
enddiatom

discard
*mat=1 ton=1e-7 toff=25e-3 dti=1e-7 dens=100 denl=0 pres=1e2
mat=1 ton=5e-3 toff=25e-3 dti=1e-5 dens=100 enrg=1
*mat=1 ton=1.01e-5 toff=25e-3 dti=1e-6 dens=100 enrg=1
endd

edit
 shortt
   tim = 0.,  dt = 5e-3
 ends
 longt
   tim = 0.,  dt = 1.0
 endl
 restt
   tim = 0.
   dtf = 30e-3
 endr
ende

*  spall parameters
 fracts
  pfrac1  -1.0e12
  pfrac2  -1.0e12
 endf
*
boundary
  bhy
     bxb = 0 , bxt = 0
     byb = 0 , byt = 0
     bzb = 0 , bzt = 2.1
  endh
endb
```

```
mindt
  time = 0.  dt = 1.e-12
endn
```

APPENDIX F: TIME HISTORY PLOTS OF PRESSURES FROM CTH SIMULATIONS AND EXPERIMENTS

This appendix contains plots overlaying the CTH predicted blast pressure time histories from two-dimensional simulations with those measured during Shots A1 and B.

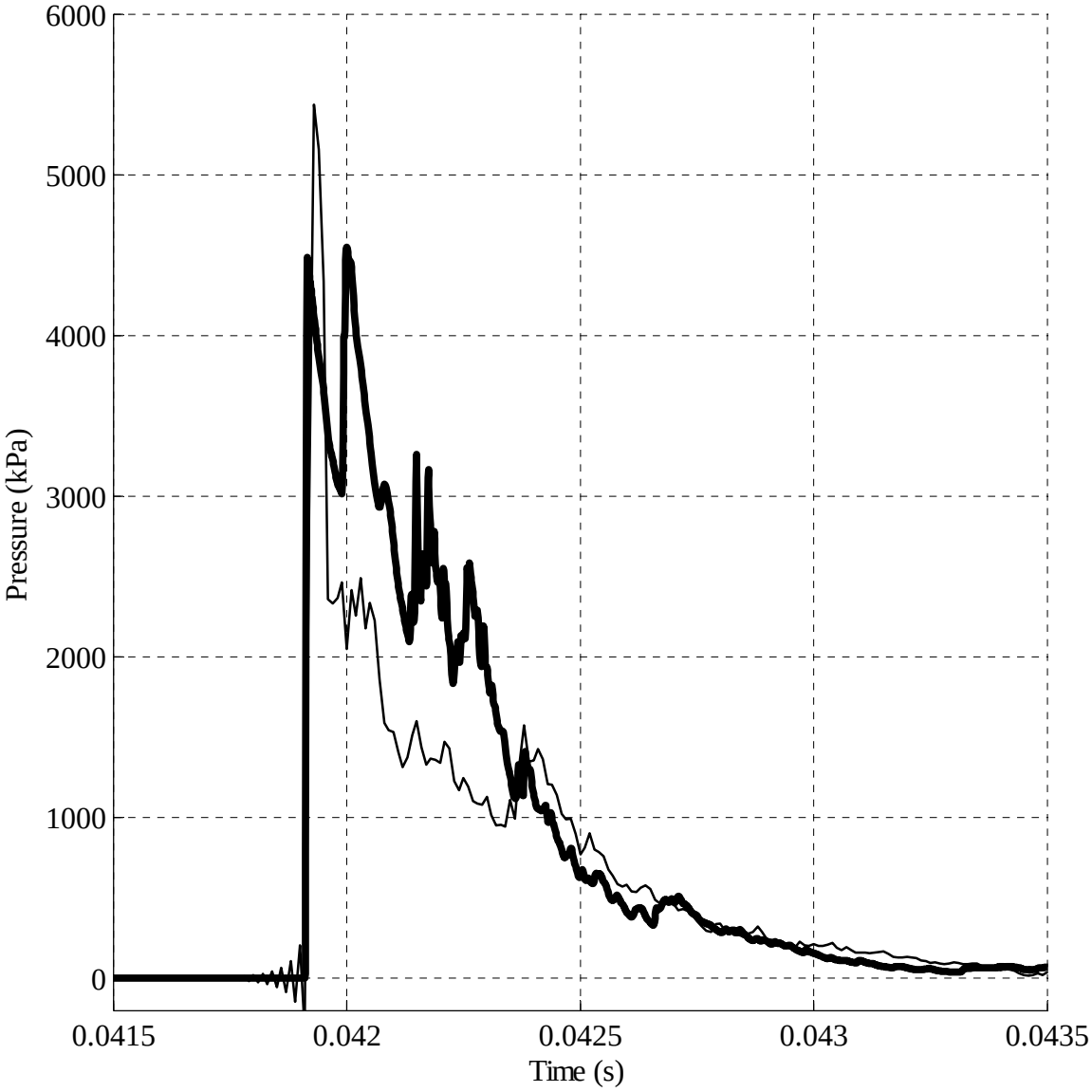

FIGURE F.1: Shot A1, Sensor P1 – Comparison of CTH pressure pulse to that measured at Sensor P1. CTH prediction is the thicker line. P1 time of arrival manually synchronized. All other arrival times are similarly shifted relative to P1.

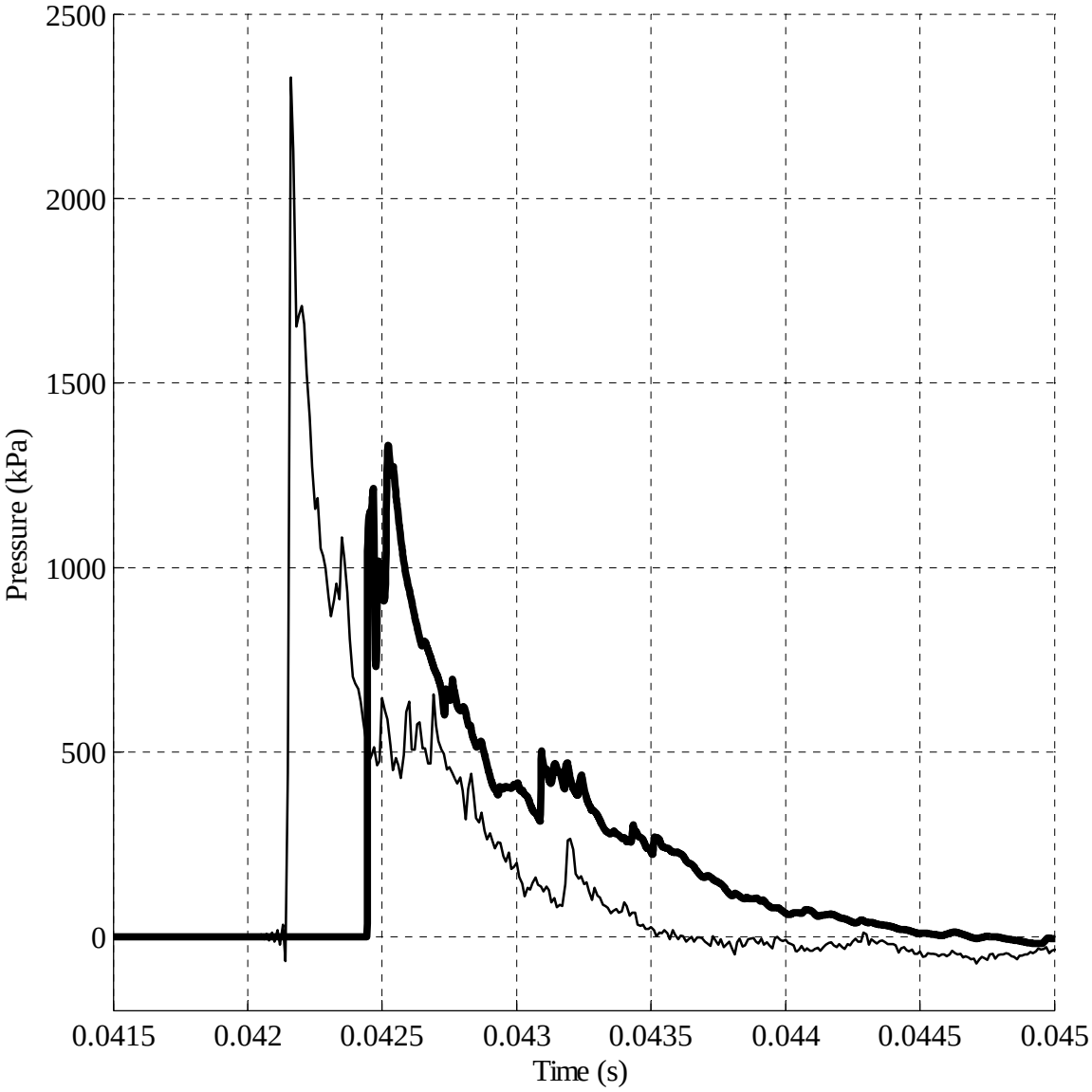

FIGURE F.2: Shot A1, Sensor P2 – Comparison of CTH pressure pulse to that measured at Sensor P2. CTH prediction is the thicker line. P1 time of arrival manually synchronized. All other arrival times are similarly shifted relative to P1.

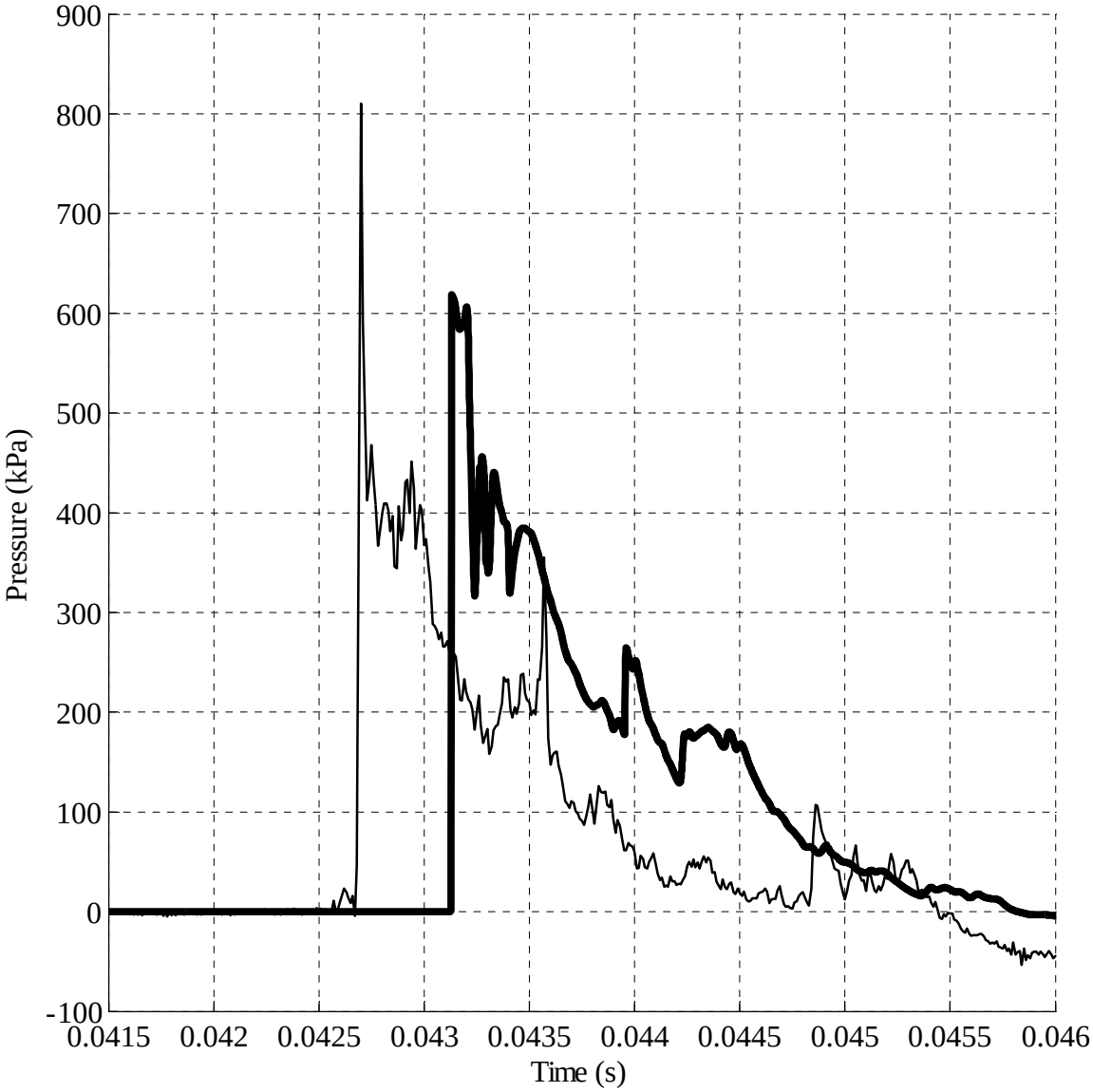

FIGURE F.3: Shot A1, Sensor P3 – Comparison of CTH pressure pulse to that measured at Sensor P3. CTH prediction is the thicker line. P1 time of arrival manually synchronized. All other arrival times are identically shifted relative to P1.

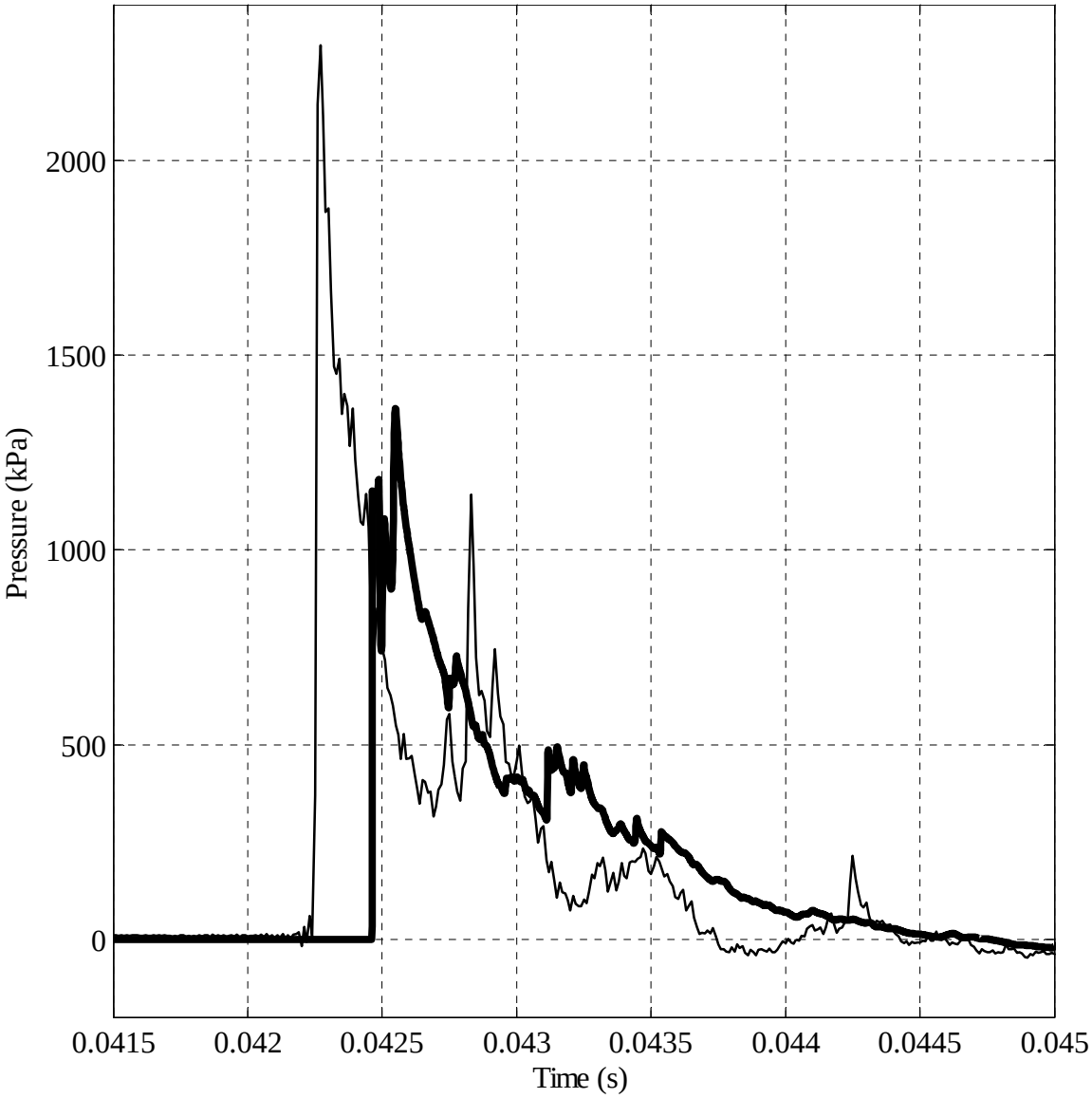

FIGURE F.4: Shot A1, Sensor P5 – Comparison of CTH pressure pulse to that measured at Sensor P5. CTH prediction is the thicker line. P1 time of arrival manually synchronized. All other arrival times are identically shifted relative to P1.

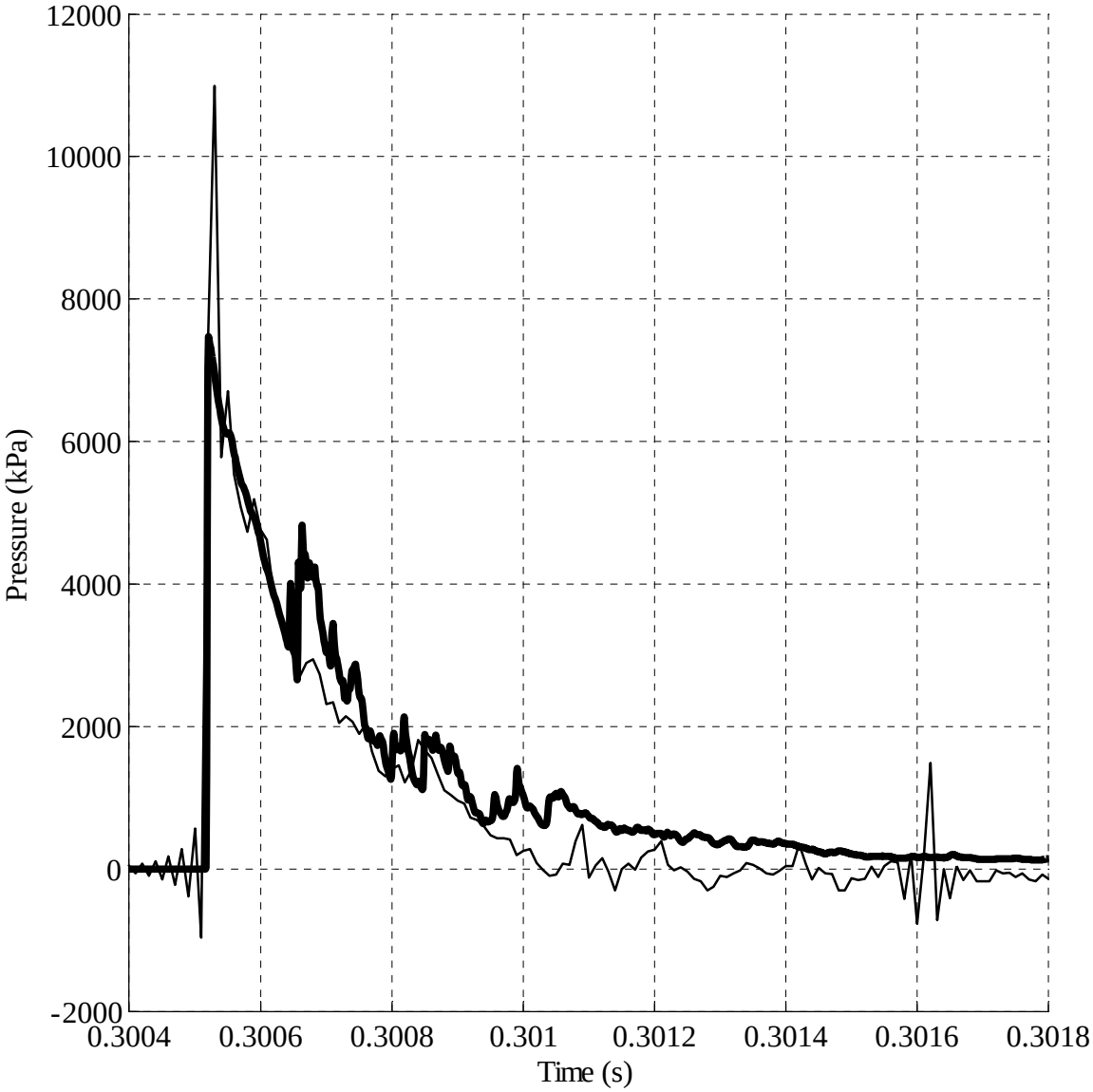

FIGURE F.5: Shot B, Sensor P1 – Comparison of CTH pressure pulse to that measured at Sensor P1. CTH prediction is the thicker line. P1 time of arrival manually synchronized. All other arrival times are identically shifted relative to P1.

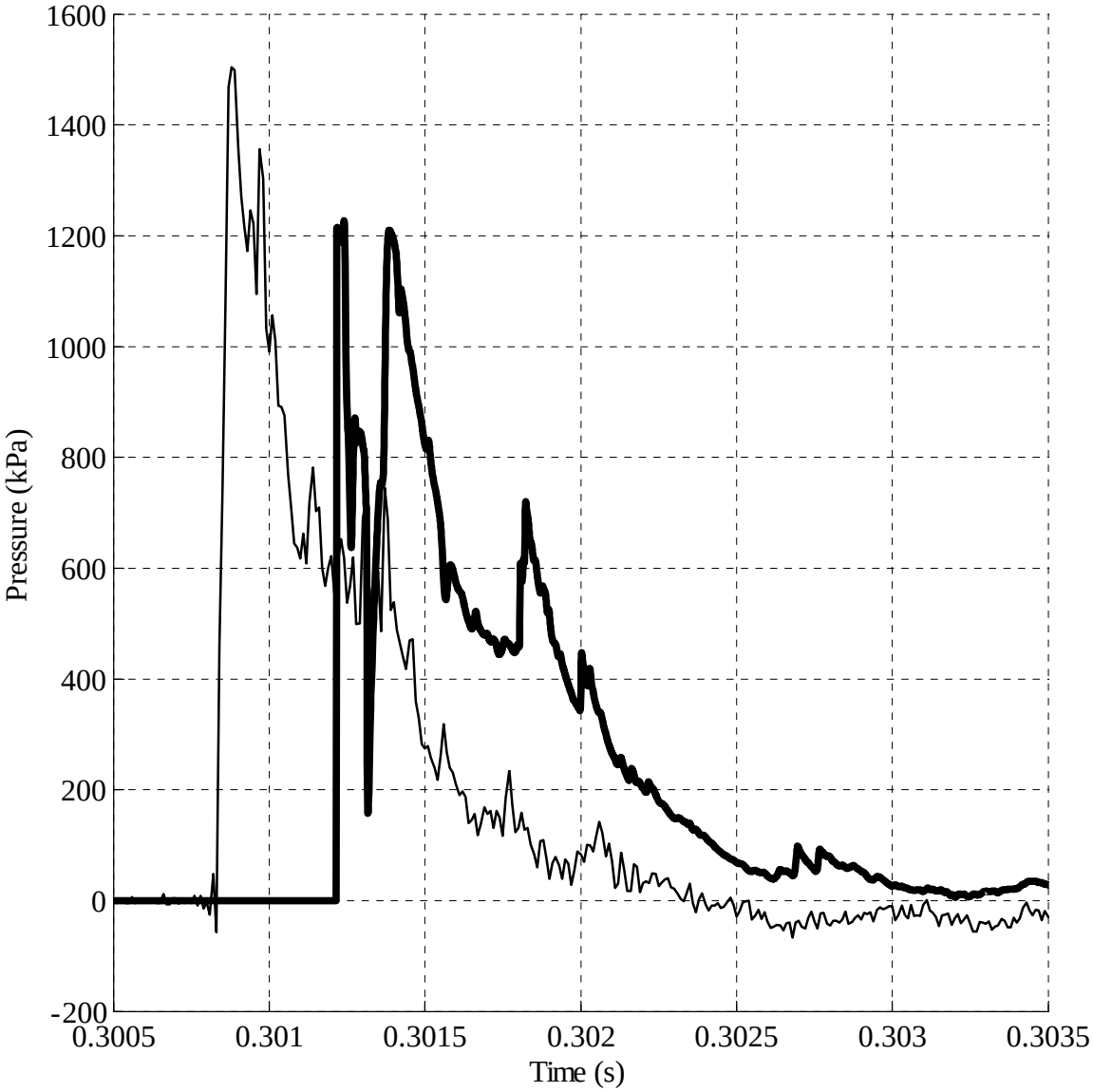

FIGURE F.6: Shot B, Sensor P2 – Comparison of CTH pressure pulse to that measured at Sensor P2. CTH prediction is the thicker line. P1 time of arrival manually synchronized. All other arrival times are identically shifted relative to P1.

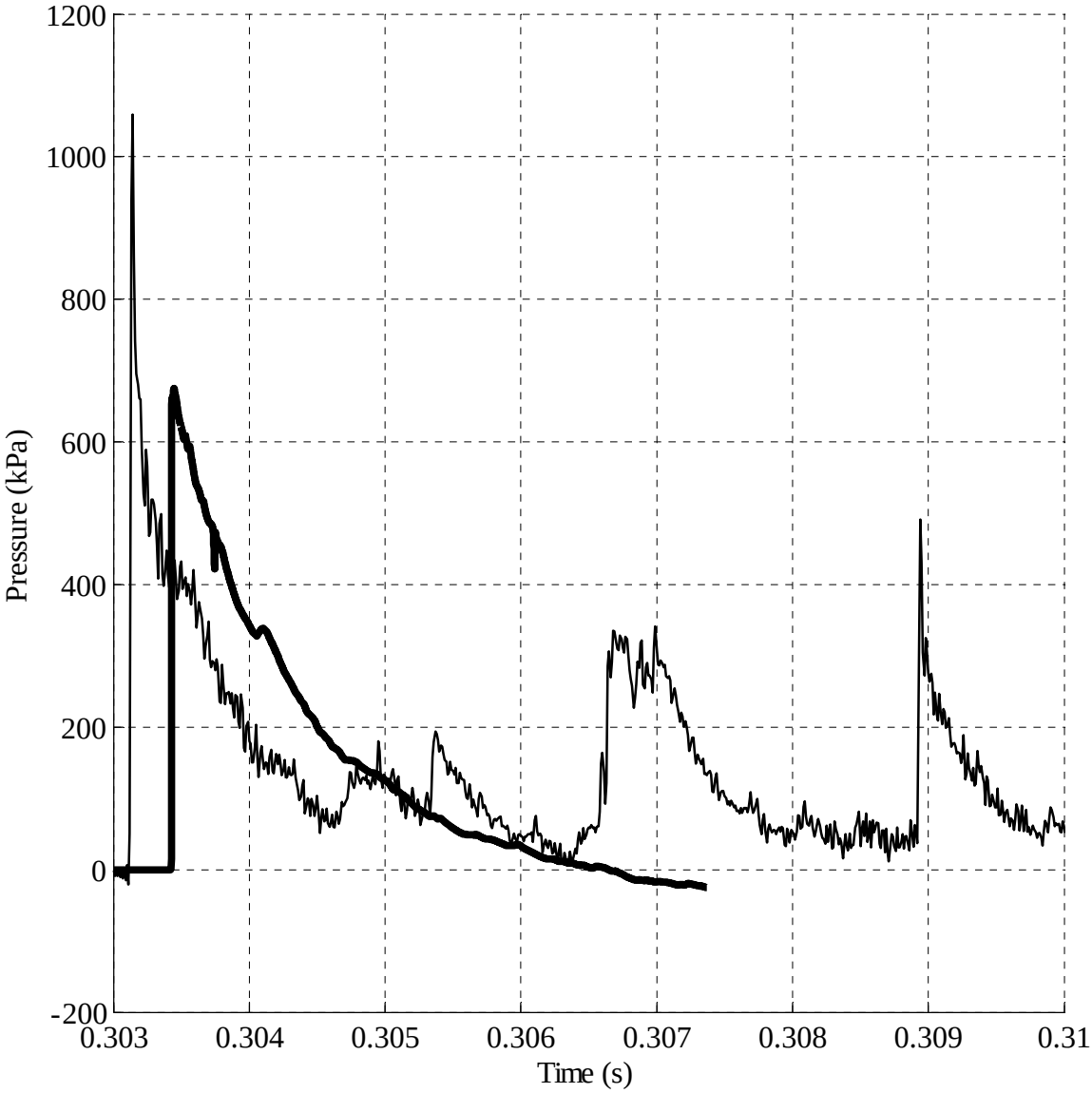

FIGURE F.7: Shot B, Sensor P6 – Comparison of CTH pressure pulse to that measured at Sensor P6. CTH prediction is the thicker line. P1 time of arrival manually synchronized. All other arrival times are identically shifted relative to P1.